

# Multiaxial and variable amplitude fatigue in steel bridges

THÈSE N° 7044 (2016)

PRÉSENTÉE LE 21 OCTOBRE 2016

À L'ÉCOLE POLYTECHNIQUE FÉDÉRALE DE LAUSANNE  
À LA FACULTÉ DE L'ENVIRONNEMENT NATUREL, ARCHITECTURAL ET CONSTRUIT  
LABORATOIRE DES STRUCTURES MÉTALLIQUES RÉSILIENTES

ET

À L'INSTITUTO SUPERIOR TÉCNICO (IST) DA UNIVERSIDADE DE LISBOA

PROGRAMME DOCTORAL EN GÉNIE CIVIL ET ENVIRONNEMENT  
DOUTORAMENTO EM ENGENHARIA CIVIL

POUR L'OBTENTION DU GRADE DE DOCTEUR ÈS SCIENCES (PhD)

PAR

**Cláudio Alexandre PEREIRA BAPTISTA**

acceptée sur proposition du jury:

Prof. A. Schleiss, président du jury  
Prof. A. Nussbaumer, Prof. A. J. Reis, directeurs de thèse  
Prof. M. Al-Emrani, rapporteur  
Prof. V. de Ville de Goyet, rapporteur  
Prof. F. Virtuoso, rapporteur



Suisse  
2016





# Acknowledgements

The work presented in this thesis was carried out at the Steel Structures Laboratory (ICOM) of the Swiss Federal Institute of Technology in Lausanne (EPFL), and at Instituto Técnico de Lisboa (IST) from the University of Lisbon. All the experimental work was carried out at EPFL with the financial support of the Steel Structures Laboratory (ICOM), and the author was financial supported by the Portuguese Ministry of Science with a grant from the National Foundation for Science and Technology (FCT).

The research was carried out under the supervision of Prof. António Reis (IST) and Prof. Alain Nussbaumer (EPFL) to whom I would like to express my gratitude for their patient guidance and support.

I am also very grateful to the members of my jury, Prof. F. Virtuoso, Prof. M. Al-Emrani, Prof. V. de Ville de Goyet and Prof. A. Schleiss (chairman) for their valuable comments and advices.

The laboratory work would not have been possible without the assistance of the incredible and high quality team of technicians at the ICOM/IIC laboratories. I am especially grateful to Gérald Rouge, Sylvain Demierre, Frédérique Dubugnon, Gilles Guignet and Armin Krkic with whom I had the pleasure to work. I am also greatfull to Prof. Nitschke-Pagel to have performed the residual stress measurements at IFS Braunschweig University in Germany.

Over the course of the thesis, I had the pleasure to meet other ICOM researchers to whom I would like to thank for interesting discussions, their friendship and support, especially Albano de Castro e Sousa, Jagoda Cupac, Raphael Thiebaud, Farshid Zamiri and Yadav Santosh.

*Lausanne, 29 May 2016*

Claudio Baptista



# Abstract

Modern bridge construction all over Europe in the last decades, has highlighted the importance of steel solutions for the design of bridges. Steel bridges have become slender and lighter with the generalisation of welded connections. These features increased the relevance of fatigue phenomena, and as a result, fatigue design has become a leading ultimate limit state verification. This research is focused on the fatigue behavior of welded joints in two domains: variable amplitude under bridge loadings and multiaxial interaction between normal and shear stress.

For the assessment of weld details under variable amplitude loads, fatigue tests have been conducted under constant and variable amplitude in a typical bridge detail. Experimental crack growth curves were obtained using the Alternative Current Potential Drop method (ACPD) which showed the detrimental effect of stress ranges below the conventional Constant Amplitude Fatigue Limit (CAFL). A two-step model with initiation and propagation was used to estimate the experimental fatigue lives, using a local strain approach for the initiation life and fracture mechanics for long crack propagation. The model was then used in a probabilistic Monte Carlo framework to include variability on the main parameters and establish S-N curves for Constant and Variable amplitude fatigue. The results allowed to correlate the load spectra sequence with the shape of the S-N curves, namely the 2<sup>nd</sup> slope value below the Constant Amplitude Fatigue Limit.

For the multiaxial interaction under shear and normal stress, a large scale setup was built that allowed tests on transversal attachments to be performed under proportional and non-proportional loads. Significant fatigue life reduction was observed under proportional multiaxial loads. The multiaxial experimental results were successfully described by a local notch approach with principal stress.

A probabilistic traffic generation model was finally established for typical highway traffic loads from bridges in Europe. The model allowed to characterise the stress spectra shapes that influence the 2<sup>nd</sup> slope value of the variable amplitude S-N curves. The results of the traffic generation model were used to calibrate partial safety factors for the design code format safety checks, both for uniaxial and multiaxial fatigue.

Key words:

Multiaxial fatigue tests, Variable amplitude tests, Multiaxial criteria, Alternative Current Potential Drop method (ACPD), S-N curves, Lateral attachments, Transversal attachments, Highway bridges, Fatigue traffic model



# Résumé

La construction de ponts en Europe au cours de la dernière décennie a mis en évidence l'importance de solutions en acier pour la conception des ponts. Les ponts en acier sont devenus plus minces et légers avec la généralisation d'assemblages soudés. Ces tendances ont accentué l'importance des phénomènes de fatigue, et par conséquent, les vérifications à l'état limite ultime fatigue sont ainsi devenues déterminantes. Cette recherche se concentre sur le comportement à la fatigue des joints soudés dans deux domaines: les chargements d'amplitude variable et l'interaction entre contraintes normale et de cisaillement. Pour l'évaluation à la fatigue sous chargement d'amplitude variable, des essais ont été menés sur un détail typique de pont. Les courbes de propagation des fissures ont été obtenues expérimentalement en utilisant une méthode de chute de potentiel à courant alternatif (ACPD), qui a montré l'effet endommageant des variations de contrainte en-deçà de la limite convenue de fatigue à amplitude constante. Un modèle combinant amorçage et propagation a été utilisé afin d'estimer les durées de vie, ceci grâce à une approche locale pour la vie en amorçage et en utilisant la mécanique de la rupture pour la propagation des fissures. Le modèle a ensuite été utilisé dans un cadre probabiliste pour inclure la variabilité des principaux paramètres et établir les courbes S-N sous amplitude constante et variable. Les résultats ont permis de corréliser la forme des spectres de chargement avec la forme des courbes S-N, soit la valeur de la 2<sup>ème</sup> pente sous la limite de fatigue à amplitude constante. Un bâti a été développé pour étudier l'interaction multiaxiale entre contraintes normale et de cisaillement. Il a permis de tester des joints soudés à attaches transversales sous chargement multiaxial proportionnel et non-proportionnel. Une réduction significative de la durée de vie a été observée sous chargement proportionnel. Une approche en contrainte locale effective a permis de décrire les résultats expérimentaux avec succès. Par ailleurs, le développement d'un modèle probabiliste de génération de trafic routier a permis de caractériser la forme des spectres de contrainte qui influence la valeur de la 2<sup>ème</sup> pente des courbes S-N. Les résultats du modèle de génération de trafic ont été utilisés afin d'étalonner les facteurs partiels pour les vérifications de la sécurité à la fatigue uniaxiale et multiaxiale.

Mots clés:

Essais multiaxiaux en fatigue, Essais d'amplitude variable, critères de fatigue multiaxiale, Méthode de chute de potentiel à courant alternatif (ACPD), Courbes S-N, Attaches latérales, Attaches transversales, Ponts routiers, Modèle de charge de fatigue



# Resumo

A construção de Pontes nas últimas décadas tem mostrado a importância de soluções metálicas para o projeto de Pontes. Com a generalização das ligações soldadas, aumentou a importância dos fenômenos de fadiga, e conseqüentemente, a verificação ao Estado Limite Último de Fadiga tornou-se condicionante. Esta investigação focou-se no comportamento à fadiga de ligações soldadas em dois domínios: fadiga sob amplitude variável e interação multiaxial entre tensões normais e de corte. Para avaliar o comportamento à fadiga sob tensões de amplitude variável, realizaram-se ensaios num detalhe soldado, sob cargas de amplitude constante e variável. Obtiveram-se curvas experimentais de propagação de fissura, utilizando um método de queda de potencial sob corrente alternada (ACPD), que mostrou o efeito prejudicial dos ciclos de tensão abaixo do limite de fadiga a amplitude constante. Desenvolveu-se um modelo incluindo a iniciação e propagação de fissuras, que foi utilizado para estimar a vida em fadiga obtida experimentalmente. Para a iniciação utilizou-se uma abordagem em tensões locais no entalhe, tendo a propagação de fissuras sido modelada com recurso à Mecânica da Fractura. Utilizando uma abordagem probabilística de forma a incluir a variabilidade dos principais parâmetros do modelo, estabeleceram-se as curvas S-N sob amplitude constante e variável. Os resultados permitiram correlacionar a forma dos espectros de carga com o valor do declive das curvas S-N abaixo do limite de fadiga a amplitude constante. Para a interação multiaxial sob tensões normais e de corte, realizaram-se ensaios num detalhe soldado com reforços transversais, sob cargas proporcionais e não-proporcionais. Uma redução significativa da vida em fadiga foi observada sob cargas multiaxiais a actuar proporcionalmente. A influência da não-proporcionalidade de cargas foi pequena. Os resultados foram descritos com sucesso utilizando uma análise de elementos finitos com tensões principais locais no entalhe. Por fim, desenvolveu-se um modelo de geração de tráfego probabilístico para cargas rodoviárias. O modelo permitiu caracterizar a forma dos espectros de carga que influenciam o valor do declive das curvas S-N a amplitude variável. Os resultados do modelo de geração de tráfego foram usados para calibrar factores parciais de segurança para a verificação da segurança à fadiga sob tensões uniaxiais e multiaxiais.

Palavras chave:

Testes de fadiga multiaxiais, Testes de fadiga a amplitude variável, Critérios de fadiga multiaxial, Método de queda de potencial sob corrente alternada (ACPD), Curvas S-N, Reforços laterais e transversais, Pontes rodoviárias, Modelo de tráfego de fadiga





# Contents

<b>List of figures</b>	<b>xiii</b>
<b>List of tables</b>	<b>xxi</b>
<b>List of symbols</b>	<b>xxiii</b>
<b>Introduction</b>	<b>1</b>
Motivation and Background . . . . .	2
Objectives . . . . .	6
Structure of the thesis and Methodology . . . . .	7
<b>I FATIGUE RESISTANCE</b>	<b>9</b>
<b>1 Literature Review</b>	<b>11</b>
1.1 Constant amplitude fatigue . . . . .	11
1.2 Variable amplitude fatigue . . . . .	19
1.3 Multiaxial fatigue . . . . .	27
<b>2 In-plane interaction - Flange crossings</b>	<b>31</b>
2.1 Flange tip attachments . . . . .	34
2.1.1 Rectangular flange tip attachments . . . . .	35
2.1.2 Flange tip attachments with transition radius . . . . .	37
2.1.3 Summary of conclusions . . . . .	39
2.2 Experimental setup . . . . .	40
2.2.1 The matrix of experiments . . . . .	40
2.2.2 Specimens . . . . .	42
2.2.3 The Alternating Current Potential Drop (ACPD) . . . . .	45
2.3 Exploratory tests under multiaxial load . . . . .	51
2.3.1 Test setup . . . . .	52
2.3.2 Analysis of results with local stress approaches . . . . .	53
2.3.3 Hot spot method . . . . .	54
2.3.4 Effective notch stress method . . . . .	57
2.3.5 Summary of conclusions . . . . .	59

## Contents

---

2.4	Experiments under constant amplitude . . . . .	60
2.4.1	Initiation model . . . . .	67
2.4.2	Propagation model . . . . .	71
2.4.3	Summary of conclusions . . . . .	75
2.5	Experiments under variable amplitude . . . . .	76
2.5.1	Analysis of results in nominal stress . . . . .	77
2.5.2	Analysis of ACPD curves . . . . .	80
2.5.3	Initiation-Propagation model . . . . .	80
2.5.4	Summary of conclusions . . . . .	89
2.6	Probabilistic fatigue model . . . . .	90
2.6.1	Stage I - Initiation . . . . .	91
2.6.2	Stage II - Propagation . . . . .	93
2.6.3	Constant amplitude simulations . . . . .	95
2.6.4	Variable amplitude simulations . . . . .	102
2.6.5	The threshold drop . . . . .	110
2.6.6	Summary of conclusions . . . . .	112
<b>3</b>	<b>Out-of-plane interaction - Web crossings</b>	<b>113</b>
3.1	The experimental setup . . . . .	114
3.2	Experiments under uniaxial stress . . . . .	117
3.3	Experiments under multiaxial stress . . . . .	121
3.4	Fatigue life estimation . . . . .	125
3.5	Summary of conclusions . . . . .	129
<b>II</b>	<b>FATIGUE LOADS</b>	<b>131</b>
<b>4</b>	<b>Highway traffic</b>	<b>133</b>
4.1	Highway traffic generation model . . . . .	134
4.1.1	Vehicle weight . . . . .	135
4.1.2	Traffic density . . . . .	138
4.1.3	Traffic composition . . . . .	139
4.1.4	Traffic flow . . . . .	141
4.1.5	Traffic jam influence . . . . .	144
4.2	Comparison between FLM3, FLM4 and FLMG . . . . .	145
4.3	Results from traffic simulations . . . . .	148
4.3.1	Load-effects spectra shape . . . . .	149
4.3.2	Equivalent stress range for fatigue reliability . . . . .	155
4.4	Summary of conclusions . . . . .	158

<b>III</b>	<b>FATIGUE RELIABILITY</b>	<b>159</b>
<b>5</b>	<b>Uniaxial fatigue reliability</b>	<b>161</b>
5.1	The reliability model . . . . .	162
5.2	Partial safety factors for fatigue design . . . . .	164
5.3	Summary of conclusions . . . . .	171
<b>6</b>	<b>Multiaxial fatigue reliability</b>	<b>173</b>
6.1	Fatigue tests collected from literature . . . . .	173
6.2	Stress based multiaxial interaction criteria . . . . .	175
6.3	Fatigue life estimation . . . . .	178
6.4	Calibration of partial safety factors . . . . .	182
6.5	Summary of conclusions . . . . .	185
<b>IV</b>	<b>CONCLUSIONS</b>	<b>187</b>
<b>V</b>	<b>APPENDIX</b>	<b>195</b>
<b>A</b>	<b>Uniaxial fatigue database</b>	<b>197</b>
A.1	Statistical evaluation of fatigue results . . . . .	197
A.2	Flange tip attachments . . . . .	201
A.3	Flange tip attachments with transition radius . . . . .	207
A.4	Transversal attachments . . . . .	211
A.5	Longitudinal attachments . . . . .	218
A.6	Shear . . . . .	223
A.7	Plates with holes . . . . .	225
A.8	Tubular connections . . . . .	230
A.9	Cope holes . . . . .	236
<b>B</b>	<b>Multiaxial fatigue database</b>	<b>239</b>
B.1	Plate specimens . . . . .	239
B.1.1	Longitudinal attachments . . . . .	239
B.1.2	Welded box beams . . . . .	240
B.1.3	Transversal attachments . . . . .	242
B.2	Tubular Specimens . . . . .	243
B.2.1	Circular tubes with flanges . . . . .	243
B.2.2	Circular tubes with end plate . . . . .	245
B.2.3	Square tubes with end plate . . . . .	247
B.3	Stud connectors . . . . .	247
B.3.1	Normal stress on base plate . . . . .	248
B.3.2	Shear stress on stud . . . . .	249
B.3.3	Shear-normal stress interaction . . . . .	252

**Contents**

---

**C Experimental results** **253**

    C.1 Experiments under constant amplitude . . . . . 254

    C.2 Experiments under variable amplitude . . . . . 266

    C.3 Experiments under non-proportional load . . . . . 278

**Bibliography** **301**

**Curriculum Vitae** **303**

# List of Figures

1	Layout of the Third Tagus River crossing in Lisbon (© GRID 2011) . . .	2
2	Cross section of the Third Tagus River crossing in Lisbon (© GRID 2011)	2
3	Viaduc de la Deule (Bouley, 1993), Viaduc de Donzère (© GREISH 1999)	3
4	Approach viaduct to the suspension bridge over Tagus River in Lisbon . .	3
5	Twin girder and Box girder bridges (© GRID 2008) . . . . .	3
6	Typical bridge deck grillage connection . . . . .	4
7	Simplified details investigated in this thesis . . . . .	5
1.1	Schematic double S–N curve for Very High Cycle Fatigue regime . . . . .	12
1.2	Schematic double slope S–N curve for Very High Cycle Fatigue regime . .	12
1.3	Welded steel details in Very High Cycle Fatigue regime . . . . .	13
1.4	Beams with cover-plates in Very High Cycle Fatigue regime . . . . .	14
1.5	Butt welds tested in the Very High Cycle Fatigue regime . . . . .	14
1.6	Relation between propagation law and the S–N curve . . . . .	15
1.7	Fatigue tests in notched specimens, quenched tempered steel . . . . .	16
1.8	Residual stress relaxation under variable amplitude fatigue . . . . .	18
1.9	Load spectra and CAFL after Keating and Fisher (1989) . . . . .	19
1.10	Effect of over-strains in constant amplitude fatigue . . . . .	19
1.11	Variable amplitude tests with Rayleigh spectra by Tilly and Nunn (1980)	20
1.12	Variable amplitude tests by Dahle (1994) . . . . .	21
1.13	Variable amplitude tests by Marquis (1995) . . . . .	22
1.14	Block loading tests on wing plates . . . . .	22
1.15	Simplified variable amplitude curves for AASHTO . . . . .	22
1.16	Normalised stress range exceedance distribution . . . . .	23
1.17	Material plastic sequence effects . . . . .	25
1.18	Gassner curves for variable amplitude fatigue . . . . .	25
1.19	Unified scatter band for welded steel details . . . . .	26
1.20	Multiaxial equivalent stress for plate and tubular specimens . . . . .	28
1.21	Multiaxial experimental results according to the Hot Spot method . . . .	29
2.1	Bridge grillage detail and specimen configuration . . . . .	31
2.2	Fatigue improvement by stress concentration reduction . . . . .	31
2.3	Fatigue improvement with transition plates . . . . .	32
2.4	Fatigue tests on welded beams . . . . .	32

## List of Figures

---

2.5	Details for connections between main and cross girders . . . . .	33
2.6	Definition of flange details . . . . .	33
2.7	FAT classification for rectangular flange tip attachments . . . . .	36
2.8	FAT category for flange tip attachments with transition radius . . . . .	38
2.9	Detail for flange tip attachments with transition radius . . . . .	39
2.10	Geometry of specimens in Test Setup 1 . . . . .	40
2.11	Geometry of specimens in Test Setup 2 . . . . .	42
2.12	Rigidifying beam welded over the butt-welded plates . . . . .	43
2.13	Root and 2 <sup>nd</sup> pass before grinding . . . . .	44
2.14	View of the root pass after turning the specimen . . . . .	44
2.15	Welds flush ground and sealing fillet welds done with auxiliary plates . . . . .	44
2.16	Test machine “Schenck” 100 ton used for the fatigue tests . . . . .	45
2.17	ACPD schematic representation . . . . .	46
2.18	Calibration test: Definition of block loading . . . . .	48
2.19	Calibration test: ACPD probes and beach-marks on crack surfaces . . . . .	49
2.20	Calibration test: ACPD measured potential values and filtered data . . . . .	49
2.21	Calibration test: Estimated crack depths with different flow equations . . . . .	50
2.22	Calibration test: Estimated crack depths (log-log scale) . . . . .	50
2.23	Schematics of the biaxial loads . . . . .	51
2.24	Test kinematic for Test Setup 2 . . . . .	52
2.25	ACPD potential for specimen 5 and crack depth estimate for ACPD1 . . . . .	53
2.26	Load cases for the local analysis . . . . .	54
2.27	Structural Hot Spot type a) and b) . . . . .	55
2.28	Detail of the finite element mesh for hot spot evaluation . . . . .	55
2.29	Experimental hot-spot measurements . . . . .	56
2.30	Fine mesh extrapolation for Hot Spot type b) . . . . .	57
2.31	Fictitious 1mm notch radius . . . . .	58
2.32	Master curve for the notch stress method . . . . .	58
2.33	Maximum crack size for brittle and plastic failure . . . . .	61
2.34	Constant amplitude tests for Intersected Flanges and Lateral Attachments . . . . .	61
2.35	Lateral attachments and Intersected flanges tested by Haibach (1979) . . . . .	62
2.36	Literature results for flange tip attachments and intersected flanges . . . . .	62
2.37	Residual stress measurements from literature . . . . .	63
2.38	Residual stress profile measured by X-Ray diffraction . . . . .	64
2.39	Crack paths for Flange tip lateral attachments and Intersected flanges . . . . .	65
2.40	Micro-structure of parent material, HAZ and weld metal . . . . .	66
2.41	Crack propagation curves measured for tests in both configurations . . . . .	67
2.42	Similitude concept for the local notch strain approach . . . . .	68
2.43	Schematic representation of the 1 <sup>st</sup> and 2 <sup>nd</sup> load reversal . . . . .	69
2.44	Initiation life for Lateral attachments and Intersected flanges . . . . .	70
2.45	Observed crack types and SIF correction factors $Y_i$ and $M_k$ . . . . .	72
2.46	LA-CA-1: ACPD potential, crack depths and growth rates . . . . .	74

2.47	Block loading definition used for the variable amplitude tests . . . . .	76
2.48	Variable amplitude tests plotted according to equivalent stress . . . . .	77
2.49	Multilinear regression coefficients for Miner sum on single slope curve . . . . .	78
2.50	Damage and estimated lives for 3 different S-N curves ( $\Delta\sigma_{m,2.10^6} = 60$ ) . . . . .	79
2.51	Total fatigue life divided into measured initiation and propagation lives . . . . .	80
2.52	LA-VA-20: Electric potential measurements and crack depth . . . . .	81
2.53	LA-VA-20: Schematic representation of the cyclic load reversal . . . . .	82
2.54	Damage sum for initiation life . . . . .	83
2.55	LA-VA-20: Measured and estimated initiation life . . . . .	83
2.56	LA-VA-20: Crack surface and fracture mechanics life estimation . . . . .	84
2.57	LA-VA-20: Progressive crack propagation threshold measurements . . . . .	85
2.58	LA-VA-21: Progressive crack threshold drop test . . . . .	86
2.59	Equivalent stress plot with effective life . . . . .	88
2.60	Fatigue life estimations with effective life and Haibach's model . . . . .	88
2.61	Schematic crack stages for the I-P model . . . . .	91
2.62	Ramber-Osgood curves for structural steels defined in EN10025 . . . . .	92
2.63	Initial imperfections: cold-laps and undercuts . . . . .	94
2.64	Monte Carlo model for constant amplitude . . . . .	96
2.65	Statistical analysis for the flange tip attachments "sample" . . . . .	97
2.66	Constant amplitude S-N curve (Flange tip attachments "sample") . . . . .	98
2.67	Constant amplitude simulations (Flange tip attachments "population") . . . . .	98
2.68	Statistical analysis of constant amplitude simulations: ( $N_i$ ) + ( $N_p$ ) . . . . .	99
2.69	Statistical analysis of constant amplitude simulations: ( $N_p$ ) . . . . .	100
2.70	Constant amplitude S-N curve (Flange tip attachments "population") . . . . .	101
2.71	Constant amplitude S-N curve for W and L up to 500mm . . . . .	101
2.72	Load spectra influence on fatigue life . . . . .	102
2.73	Spectrum Shape Factor (SSF) after Heuler and Klatschke (2005) . . . . .	103
2.74	Schematic relation between a concave and convex spectra and the CAFL . . . . .	103
2.75	Monte Carlo model for variable amplitude . . . . .	104
2.76	Probability density and exceedance for the load spectra cases . . . . .	105
2.77	Effective and nominal stress for $2^{nd}$ slope calculation . . . . .	107
2.78	$2^{nd}$ slope simulations for concave spectra . . . . .	107
2.79	$2^{nd}$ slope simulations for linear and convex spectra . . . . .	108
2.80	S-N curve for concave spectra with simulations and experiments ("sample") . . . . .	109
2.81	CAFL threshold drop definition after Haibach (1970) . . . . .	110
2.82	Threshold drop curves by spectra type for an edge crack on a plate . . . . .	111
2.83	Threshold drop curves by spectra type for flange tip attachments . . . . .	112
3.1	Multiaxial normal-shear stress interaction: basic cases of fillet welds . . . . .	113
3.2	Specimen geometry for multiaxial tests . . . . .	114
3.3	Experimental setup for multiaxial tests . . . . .	116
3.4	Uniaxial setup for tests under normal stress . . . . .	117

## List of Figures

---

3.5	Detail of weld toe end on plate edge . . . . .	118
3.6	Typical crack pattern for tests under uniaxial normal stress . . . . .	118
3.7	Tests under uniaxial normal stress . . . . .	119
3.8	“Proof of concept” shear test on slotted hole plate . . . . .	119
3.9	Typical crack pattern for tests under uniaxial shear stress . . . . .	120
3.10	Tests under uniaxial shear stress . . . . .	121
3.11	Overall view of a failed specimen under proportional load . . . . .	121
3.12	Typical crack pattern for tests under multiaxial stress . . . . .	122
3.13	Test results under multiaxial stress and comparison . . . . .	123
3.14	Shear friction mechanism . . . . .	124
3.15	Estimation of initiation life for Fe360 and $\sigma_{res} = 0$ . . . . .	124
3.16	Global and sub-model for the multiaxial specimens . . . . .	125
3.17	Notch stress output from the FEM sub-model . . . . .	126
3.18	Notch stress S-N curve . . . . .	127
3.19	Fatigue life estimation with the local notch stress . . . . .	127
3.20	Life estimations for proportional tests using the damage sum criteria . . . . .	128
4.1	Schematics of the traffic generation model . . . . .	134
4.2	Lorry types and weight distribution (JRC, 2008) . . . . .	135
4.3	Recent traffic surveys (Mladen et al., 2010) . . . . .	138
4.4	Histogram of the different generated lorry types (FLM4 and FLMG) . . . . .	140
4.5	Typical “Stop and Go Waves” . . . . .	142
4.6	Inter-vehicle distances in 24 hour with 2 periods of congested traffic . . . . .	142
4.7	Model for traffic flow with jams . . . . .	142
4.8	Distances between lorries on a 24 hour traffic generation . . . . .	143
4.9	Typical inter-vehicle histogram obtained for a single slow lane simulation . . . . .	143
4.10	Damage for different traffic flow scenarios . . . . .	144
4.11	$\lambda_{max}$ and $\lambda_{tot}$ for the entire span range . . . . .	147
4.12	Typical output of the traffic generation model for 24hours . . . . .	148
4.13	Transversal traffic arrangement and longitudinal structural systems . . . . .	149
4.14	Rainflow for load-effects: 1-year traffic simulations . . . . .	150
4.15	Exceedance plots for highway traffic simulations . . . . .	151
4.16	Exceedance plot for FLM axle loads . . . . .	152
4.17	Exceedance plot for Eurocode railway mix axle loads . . . . .	153
4.18	Cross section of the 3 <sup>rd</sup> Bosphoro bridge . . . . .	153
4.19	Exceedance plot for highway/railway mix on hanger12 . . . . .	154
4.20	Characteristic load-effect on rainflow histogram . . . . .	155
4.21	Calibration of the 0,95 load fractile with the 0.05 resistance fractile . . . . .	156
4.22	Example of convergence of both $\mu_{\Delta\sigma_{eq}}$ and $\sigma_{\Delta\sigma_{eq}}$ for 250 days of traffic . . . . .	156
4.23	Log <sub>10</sub> -normal distribution for 2 design cases . . . . .	157
5.1	Reliability problem with 2 variables, adapted from (Melchers, 1999) . . . . .	162
5.2	Limit state function in the basic variables and normalised space . . . . .	163



5.3	Partial safety factors $\gamma_S$ and $\gamma_R$ against the $\nu_L$ . . . . .	167
5.4	Partial safety factor $\gamma_S \cdot \gamma_R$ against the $\nu_L$ . . . . .	167
5.5	Unified S-N curve for the database uniaxial FAT details . . . . .	169
5.6	Partial safety factors $\gamma_S$ and $\gamma_R$ against the $\nu_L$ (re-calibration) . . . . .	170
5.7	Partial safety factor $\gamma_S \cdot \gamma_R$ against the $\nu_L$ (re-calibration) . . . . .	171
6.1	Experimental results and interaction formulas in normalised stress $d_\sigma, d_\tau$ . . . . .	176
6.2	Multiaxial experimental results by $\rho = \frac{\Delta\tau}{\Delta\sigma}$ . . . . .	177
6.3	Multiaxial experimental results by stress proportionality . . . . .	177
6.4	Life estimations for the multiaxial database with mean strength values . . . . .	178
6.5	Life estimations for the multiaxial database with FAT values . . . . .	179
6.6	Life estimations with the log-fitted criteria (mean strength values) . . . . .	180
6.7	Life estimations with the log-fitted criteria (FAT values) . . . . .	181
6.8	Experimental results and log-fitted criteria in normalised stress $d_\sigma, d_\tau$ . . . . .	182
6.9	Experimental results and log-fitted criteria . . . . .	182
6.10	Generalised Extreme Value distribution fit to the limit state function $g(z_i)$ . . . . .	183
6.11	Log-normal fit to the IIW criteria results on the multiaxial database . . . . .	184
6.12	$\beta$ computations for the IIW multiaxial interaction formula . . . . .	185
A.1	S-N curve for “wing plates” . . . . .	203
A.2	S-N curve for flange tip attachments according to IIW . . . . .	205
A.3	Statistical analysis of rectangular flange tip attachments . . . . .	206
A.4	FAT classification for rectangular flange tip attachments . . . . .	207
A.5	S-N curve for flange tip attachments with transition radius . . . . .	209
A.6	Tests with grounded 15mm transition radius (Gurney, 1993) . . . . .	210
A.7	FAT category, influence of geometry on SCF and comparison with tests . . . . .	211
A.8	Typical details with transversal attachments (EN 1993 1-9, 2005) . . . . .	211
A.9	Thickness effect on offshore design after Gordon et al. (1997) . . . . .	213
A.10	Datasets with results at the five different stress range level . . . . .	213
A.11	Normality of fatigue tests on transversal attachments . . . . .	214
A.12	Experimental results for transversal attachments by $R_\sigma$ ratio . . . . .	215
A.13	FAT classification for transversal attachments . . . . .	215
A.14	Statistical analysis of transversal attachments ( $l \leq 80$ ) . . . . .	216
A.15	Statistical analysis of transversal attachments ( $l > 80$ ) . . . . .	217
A.16	General plot for the database of longitudinal attachments . . . . .	218
A.17	Longitudinal attachments distinguished by R ratio . . . . .	219
A.18	Longitudinal attachments with tapered transition . . . . .	219
A.19	Longitudinal attachments with rounded transition . . . . .	220
A.20	Longitudinal attachments distinguished by attachment length . . . . .	220
A.21	Statistical analysis of longitudinal attachments ( $L_{attach} \leq 100$ ) . . . . .	221
A.22	Statistical analysis of longitudinal attachments ( $L_{attach} > 100$ ) . . . . .	222
A.23	Experimental setup for tubes under pure shear . . . . .	223
A.24	Statistical analysis of shear in tubes . . . . .	224

## List of Figures

---

A.25	Characteristic fatigue curves obtained with fracture mechanics . . . . .	227
A.26	Data pooling check for plates with holes (Quality Group 1 and 2) . . . . .	227
A.27	Statistical analysis of plates with holes (Quality group 1) . . . . .	228
A.28	Statistical analysis of plates with holes (Quality group 2) . . . . .	229
A.29	Nominal net-stress FAT classification for plates with holes . . . . .	230
A.30	FAT classification for tube to plate connections . . . . .	231
A.31	Specimen configuration for tubular experiments . . . . .	231
A.32	Re-analysis of tests reported by Zirn (1975) . . . . .	232
A.33	Fatigue tests in tubular connections . . . . .	232
A.34	Statistical analysis of tubular connections . . . . .	233
A.35	Statistical analysis of tubular connections (fillet welds) . . . . .	234
A.36	Recommended connections for different exposed environments . . . . .	235
A.37	FAT classification for tubular connections . . . . .	235
A.38	Cope hole classification in ENV 1993 (Sedlacek et al., 2000) . . . . .	236
A.39	Cope holes cracks . . . . .	236
A.40	Statistical analysis of cope holes . . . . .	237
B.1	Box beam with longitudinal attachments tested by Archer (1987) . . . . .	239
B.2	S-N curves for tests by Archer (1987) . . . . .	240
B.3	Welded box beams tested by Dahle et al. (1997) . . . . .	240
B.4	Results for longitudinal shear cracks on fillet welds (L) . . . . .	241
B.5	Results for transversal cracks (T) and (TW) . . . . .	242
B.6	Transversal attachments tested by Kim and Yamada (2005) . . . . .	242
B.7	Results for longitudinal (L) and transversal (T) attachments . . . . .	243
B.8	Tubes with welded flanges Yung and Lawrence (1986) . . . . .	244
B.9	Tube-to-flange data (Yung and Lawrence, 1986), (Siljander et al., 1992) . . . . .	244
B.10	Results for tube to end-plate Razmjoo (1996) . . . . .	245
B.11	Results for tube to end-plate Sonsino et al. (1999) . . . . .	245
B.12	Tubes to end-plate by Amstutz et al. (2001) and Yousefi et al. (2001) . . . . .	246
B.13	S-N curve for tubes to end-plate . . . . .	246
B.14	Square tubes to end-plate Bäckström (2003) . . . . .	247
B.15	Failure modes for shear studs . . . . .	247
B.16	Influence of stress ratio $R_\sigma$ on plates with studs . . . . .	249
B.17	Statistical analysis of plates with studs . . . . .	250
B.18	Statistical analysis of studs in shear . . . . .	251
B.19	Multiaxial fatigue interaction for shear studs . . . . .	252
C.1	LA-CA-1: ACPD potential, estimated and measured crack depths . . . . .	254
C.2	LA-CA-1: Crack growth rate . . . . .	255
C.3	LA-CA-3: ACPD probes and measured potential values . . . . .	256
C.4	LA-CA-3: ACPD potential, estimated and measured crack depths . . . . .	256
C.5	LA-CA-4: Estimated and measured crack depths . . . . .	258
C.6	IF-1, IF-3 and IF-5: Crack measurements and fracture mechanics . . . . .	259

C.7 IF-6: ACPD potential, estimated and measured crack depths . . . . . 260  
C.8 IF-6: Crack growth rate . . . . . 261  
C.9 IF7: ACPD probes and measured potential values . . . . . 262  
C.10 IF-7: ACPD potential, estimated and measured crack depths . . . . . 262  
C.11 IF-7: Crack growth rate . . . . . 263  
C.12 IF-8: ACPD potential, estimated and measured crack depths . . . . . 264  
C.13 IF-8: Crack growth rate . . . . . 265



# List of Tables

2.1	FAT for “Rectangular Flange Tip Attachments” and “Intersected Flanges”	35
2.2	FAT classification for “Flange Tip Attachments with Transition Radius”	38
2.3	Matrix of experiments for constant amplitude tests	41
2.4	Matrix of experiments for variable amplitude tests	41
2.5	Welding procedure for Flange Tip Attachments and Intersected Flanges	43
2.6	Experimental results under non-proportional load	52
2.7	Results of the hot spot analysis under uniaxial tension (T)	56
2.8	Hot spot for the different load cases (linear quadrilateral shell element S4R)	56
2.9	Notch stress for the different load cases	59
2.10	Experimental results for constant amplitude tests	60
2.11	Cyclic material parameters, (Radaj et al., 2006), (Haibach, 2006)	70
2.12	Variable amplitude test results for lateral attachments	76
2.13	LA-VA-20: Schematic representation of the 1 <sup>st</sup> load reversal	81
2.14	LA-VA-22: Variable amplitude test with load spectra below CAFL	87
2.15	Minimum reference detectable crack values with NDT	94
2.16	Recommended FAT for “Flange Tip Attachments” and “Intersected Flanges”	102
2.17	2 <sup>nd</sup> slope values for Flange tip attachments	109
3.1	Matrix of experiments for multiaxial tests	114
3.2	Welding procedure for Transversal attachments	115
3.3	Experimental results under uniaxial normal stress	117
3.4	Experimental results under multiaxial stress	122
3.5	Notch stress values for the multiaxial specimens	125
4.1	Traffic parameters adopted in the model	135
4.2	Fatigue Load model 4 (FLM4) (EN 1991-2, 2003)	136
4.3	Vehicle weights registered at Auxerre compared with FLM4	136
4.4	Comparison between traffic data from Brohtal 2004 and Auxerre 1986	137
4.5	GVW registers in European traffic background	137
4.6	Heavy vehicles ( $N_{obs}$ ) and ADTT for European motorways	139
4.7	Traffic composition for the Auxerre traffic data (JRC, 2008)	140
4.8	Distributions for inter-vehicle distances	141
4.9	Equivalent damage factors, $\lambda_i$ for mid-span moment	145

## List of Tables

---

4.10	Equivalent stress at $2.10^6$ cycles [N/mm <sup>2</sup> ] . . . . .	146
4.11	Equivalent damage factors, $\lambda_{v,i}$ for shear connectors . . . . .	147
4.12	Equivalent stress for FAT90 in shear connectors . . . . .	147
4.13	Weibull shape parameter for simulations on 36 design cases . . . . .	152
4.14	Train types and traffic mixes for railway traffic . . . . .	154
4.15	Log <sub>10</sub> -normal distribution parameters for $\Delta\sigma_{eq,2}$ on the 36 design cases . .	157
5.1	Partial safety factor $\gamma_R$ (EN 1993 1-9, 2005) . . . . .	165
5.2	$\beta$ index and safety factor $\gamma_R$ in Eurocode background . . . . .	166
5.3	$\beta_{target}$ values adapted from Eurocode 0 . . . . .	168
5.4	Summary of uniaxial FAT details . . . . .	169
6.1	Summary of mean and characteristic values for literature multiaxial tests	174
A.1	Comparison of $k_p$ (coverage method) with $t_p$ (prediction method) . . . . .	201
A.2	FAT categories for rectangular flange tip attachments . . . . .	201
A.3	Database of experimental results for flange tip lateral attachments . . . . .	202
A.4	Experimental setups with symmetrical and non-symmetrical specimens . .	203
A.5	FAT classification for “Flange Tip Attachments with Transition Radius” .	208
A.6	Database of literature tests on transversal attachments . . . . .	212
A.7	Database for fatigue experiments in longitudinal attachments . . . . .	218
A.8	Database for fatigue experiments in plates with holes . . . . .	225
B.1	Database for fatigue experiments in plates with studs . . . . .	248
B.2	Database for fatigue experiments in plates with studs . . . . .	249
C.1	Crack surfaces - 1 . . . . .	275
C.2	Crack surfaces - 2 . . . . .	276
C.3	Crack surfaces - 3 . . . . .	277

# List of symbols

## Abbreviations:

ULCF	Ultra Low Cycle Fatigue $N < 100$	
LCF	Low Cycle (oligocyclic) Fatigue $N < 100.000$	
HCF	High Cycle Fatigue $N < 10.000.000$	
VHCF	Very High Cycle Fatigue $N > 10.000.000$	
FAT	Detail category, resistance at $2 \cdot 10^6$ cycles	[MPa]
CAFL	Constant amplitude fatigue limit	[MPa]
VAFL	Variable amplitude fatigue limit	[MPa]
SCF	Stress concentration factor	
SIF	Stress intensity factor	[Nmm <sup>-3/2</sup> ]
I-P model	Initiation-Propagation model	
NDT	Non-destructive tests	

## Stress, Loads

$\Delta\sigma$	normal stress range	[MPa]
$\Delta\tau$	shear stress range	[MPa]
$\rho$	shear to normal stress ratio $\frac{\Delta\tau}{\Delta\sigma}$	
N	Number of cycles	
$N_C$	$2 \cdot 10^6$ cycles, per definition	
$\Delta\sigma_C$	stress range at $N_C$	[MPa]
$\Delta\sigma_{R,2}$	mean fatigue strength at $2 \cdot 10^6$ cycles	[MPa]
$\Delta\tau_{R,2}$	mean fatigue strength at $2 \cdot 10^6$ cycles	[MPa]
$N_D$	$5 \cdot 10^6$ cycles, per definition	
$\Delta\sigma_D$	CAFL, stress range at $N_D$ (Dauerfestigkeit)	[MPa]
$\Delta\sigma_{th,i}$	instantaneous threshold stress range at $N_{th,i}$ (Schadenfestigkeit)	[MPa]
$\Delta\sigma_{Q,fat}$	stress range due to the passage of a single design truck	[MPa]
$R_\sigma$	stress ratio $R_\sigma = \frac{\Delta\sigma_{min}}{\Delta\sigma_{max}}$	
$K_t$	stress concentration factor (SCF)	
$E_s$	modulus of elasticity of steel	[GPa]
$f_y$	yield stress	[MPa]
$\lambda$	damage equivalence factor	

**Alternative Current Potential Drop ACPD:**

$\delta$	skin depth	[mm]
$\mu_r$	relative magnetic permeability	
$\mu_0$	magnetic permeability of the free space	[H/m]
$\sigma_e$	electric conductivity of the material	[S/m]
f	current frequency	[Hz]

**Geometrical parameters:**

W	Width	[mm]
L	Length	[mm]
t	thickness	[mm]
$\rho$	notch radius	[mm]

**Probability and statistics:**

$m_x$	mean value for a sample of the random variable (x)
$\mu_x$	population mean
$s_x$	standard deviation for a sample of the random variable (x)
$\sigma_x$	standard deviation of the population
$\nu$	coefficient of variation COV
$p_f$	probability of failure
p	probability of an event
$x_p$	fractile $p$ or 100. $p$ % percentile ( $P(X \leq x_p) = F(x_p) = p$ )
F()	cumulative density function CDF
$F^{-1}()$	inverse of the cumulative density function
$F_E()$	complementary cumulative density function CCDF: Exceedance
f()	probability density function PDF
$\Phi()$	density function for the standard normal distribution
$\Phi^{-1}()$	inverse density function for the standard normal distribution
$\phi()$	cumulative density function for the standard normal distribution
$\phi^{-1}()$	inverse cumulative density function for the standard normal
log	Logarithm base 10
ln	Natural Logarithm base $e$

**Reliability:**

R	statistical variable for resistance
S	statistical variable for solicitations (loads or effects)
G()	limit state function
$\beta$	reliability index
$\beta_{target}$	target reliability index
$\gamma_{F,f}$	Partial safety factor for fatigue design loads
$\gamma_{M,f}$	Partial safety factor for fatigue design resistance
$\gamma_S$	Partial safety factor for design loads
$\gamma_R$	Partial safety factor for design resistance



**Crack propagation:**

C	Paris law coefficient	
m, m <sub>1</sub>	Paris law exponent and SN curve first slope	
m <sub>2</sub>	SN curve 2 <sup>nd</sup> slope for constant amplitude	
k	SN curve 2 <sup>nd</sup> slope for variable amplitude	
$\nu$	Spectra Weibull shape parameter	
a	crack depth	[mm]
a <sub>0</sub>	crack depth in the as-welded state	[mm]
a <sub>i</sub>	crack depth in the as-welded state	[mm]
a <sub>c</sub>	critical crack depth - failure	[mm]
a/c	crack aspect ratio	
(a/c) <sub>0</sub>	initial crack aspect ratio	
c	half surface length of semi-elliptical and corner cracks	[mm]
K	stress intensity factor (K <sub>I</sub> opening mode)	[Nmm <sup>-3/2</sup> ]
Y(a)	global correction factor	
Y <sub>b</sub>	correction factor for the bending stress case	
Y <sub>e</sub>	shape correction factor (for an elliptical crack)	
Y <sub>g</sub>	non-uniform stress distribution along the crack path	
Y <sub>s</sub>	free surface correction factor	
Y <sub>w</sub>	correction factor to account for the finite thickness of the plate	
$\Delta K$	stress intensity factor range	[Nmm <sup>-3/2</sup> ]
$\Delta K_{th}$	threshold stress intensity factor range	[Nmm <sup>-3/2</sup> ]



# Introduction

The construction of high speed railway lines all over Europe in the last 20 years has highlighted the importance of steel solutions for the design of long span bridges. The demand of aesthetic and efficient bridges prompted steel structures to become slender and lighter, outcome achieved through the development of normalized and thermomechanical steels with improved toughness and the increase of the plate thickness at acceptable carbon content. This enabled the reduction of the total number of structural connections as well as the generalisation of welded connections. The use of high strength steels up to S460 or S690 is however very limited by the fact that fatigue life of welded details is essentially independent from steel strength. Fatigue details as low as FAT40 for lateral attachments, FAT56 for cover-plates or FAT71 for cope holes are very limitative in exploring the high strength steel capacities because their allowable stress under fatigue remains roughly 10% of the yield stress.

These features increased the importance of fatigue phenomena and dynamic behavior of the steel superstructure whereas fatigue design is generally the leading ultimate limit state verification. Stress amplitudes due to trains are high and dynamic effects of high speed trains may further amplify the fatigue effects, also controlling deformation, track stability and passenger comfort design under service. Fatigue and dynamic behavior have become intrinsic to the process of concept design since both phenomena are highly dependent on the choice of structural solutions.

Some specific issues remain however an open subject, particularly the multiaxial fatigue behaviour of welded joints and the treatment of very large number of cycles at low stress amplitudes, specially when lower than the Constant Amplitude Fatigue Limit (CAFL). Safety against fatigue in bridge design is typically assessed by uniaxial procedures, but welded connections are often subjected to multiaxial stress/strains due to both local constraints and external loading. Recent investigations have shown the detrimental effect of multiaxial stress states and inconsistency in design codes to accurately correlate test results. Under variable amplitude load spectra, both highway and railway bridges are subjected to occasional overloads and stress peaks, followed by millions of cycles at low amplitudes. The damage process due to stress ranges below the CAFL, depends on the load spectra, and design provisions have shown to be unsafe under some conditions.

## Motivation and Background

Warren truss solutions are one of the most current typologies for the superstructure of steel and composite bridges, figure 1 and 2. They are efficient and aesthetically attractive design solutions in bridge engineering and have been adopted in several bridges of the European high speed railway network (Reis, 2001, 2008; Reis and Oliveira Pedro, 2011). They are also economically interesting since man work costs are optimised by the reduction of structural connections between steel elements (Nussbaumer and Schumacher, 2002). This, on the other hand, leads to large scale connection details, for which fatigue assessment procedures and multiaxial behaviour are not yet well established. Truss nodes between diagonals, chords and crossbeams or deck grillage connections with welded crossbeams and stringers are typical examples of these large scale details.



Figure 1 – Layout of the Third Tagus River crossing in Lisbon (© GRID 2011)

Typical deck grillage systems for Warren truss or Bow-string bridges are usually made of I girders welded orthogonally, as exemplified in figure 2 and 3.



Figure 2 – Cross section of the Third Tagus River crossing in Lisbon (© GRID 2011)



Figure 3 – Viaduc de la Deule (Bouley, 1993) and Viaduc de Donzère (© GREISH 1999)

This type of welded connection is also frequent for twin-girder bridges, connecting cross beams to the main girders or stringers to cross beams and its use is wide spread both in railway, figure 4, and highway bridges, figure 5.



Figure 4 – Approach viaduct to the suspension bridge over Tagus River in Lisbon (© GRID 1998)

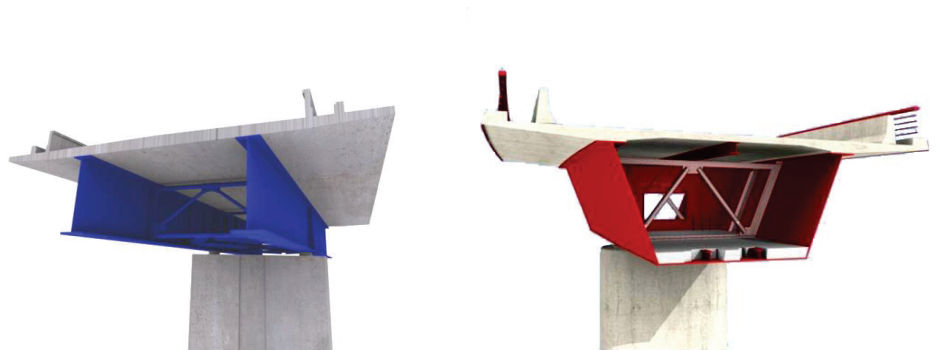


Figure 5 – Twin girder and Box girder bridges (© GRID 2008)

The cross-girder connection between two orthogonal beams with flanges welded at  $90^\circ$  is a typical example of a bridge deck grillage solution. The detail as shown in figure 6 is the starting point for the work presented in this thesis.

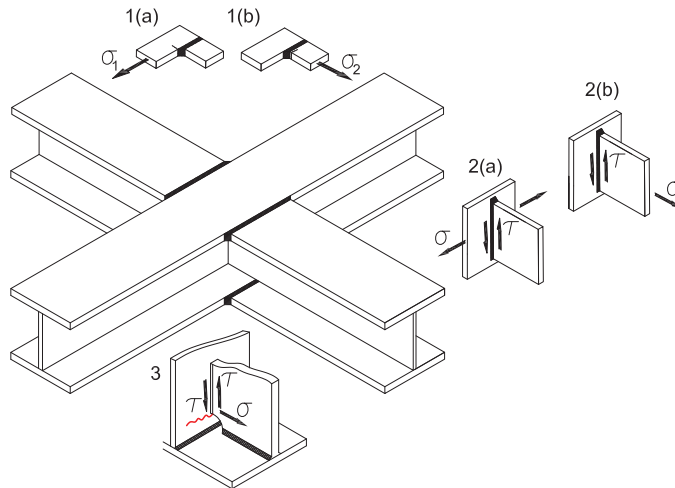


Figure 6 – Typical bridge deck grillage connection with the different details composing it

For the fatigue assessment of these type of connections, a technique proposed by Gurney (1979) is to decompose it in its basic FAT details. This is still the general procedure in bridge design. However, under variable traffic load conditions, the details are subjected to multiaxial stresses so that even in this “simple” connection, three basic multiaxial cases may be identified:

1. Beam flanges under biaxial loading ( $\sigma_1, \sigma_2$ )
  - (a) Flange tip attachment
  - (b) Intersected flange
2. Web under biaxial stress ( $\sigma, \tau$ )
  - (a) Non-load-carrying fillet weld (transversal attachment)
  - (b) Load-carrying fillet weld
3. Cope hole under a multiaxial stress state ( $\sigma, \tau$ )

The intersection between the beam flanges under biaxial loading (detail 1a and 1b) is characterised by one of the lowest fatigue categories, FAT40 in Eurocode 3 (EN 1993 1-9, 2005), if no transition radius is adopted on the welded flanges. Under traffic loads, the connection is under biaxial bending combined with normal stress, so that the multiaxial stress state at the weld toe may have to be considered.

The web connection (detail 2a and 2b) is under shear stress and normal stress interaction, due to bending of the elements or membrane behavior of the stringers. The multiaxial



interaction may in this case also influence the fatigue resistance of the connection.

The approach followed in this thesis to investigate the behaviour of the cross-girder connection is to simulate their behaviour through simplified details as shown in figure 7.

In-plane intersections of the flanges (detail 1(a) and 1(b)) are investigated through experimental tests on plate elements under in-plane uniaxial loadings. The multiaxial influence of loads acting in two perpendicular directions ( $\sigma_1$  and  $\sigma_2$ ) is investigated and the detail is used for tests under variable amplitude focusing the influence of stress ranges below the CAFL and the effect of the load spectra on the 2<sup>nd</sup> slope value of the S-N curve.

Out-of-plane intersections (detail 2(a)), are investigated with a simplified structural component, using orthogonal plates under multiaxial loads. A special large scale experimental setup was built to test this detail under multiaxial stress  $\Delta\sigma / \Delta\tau$  interaction.

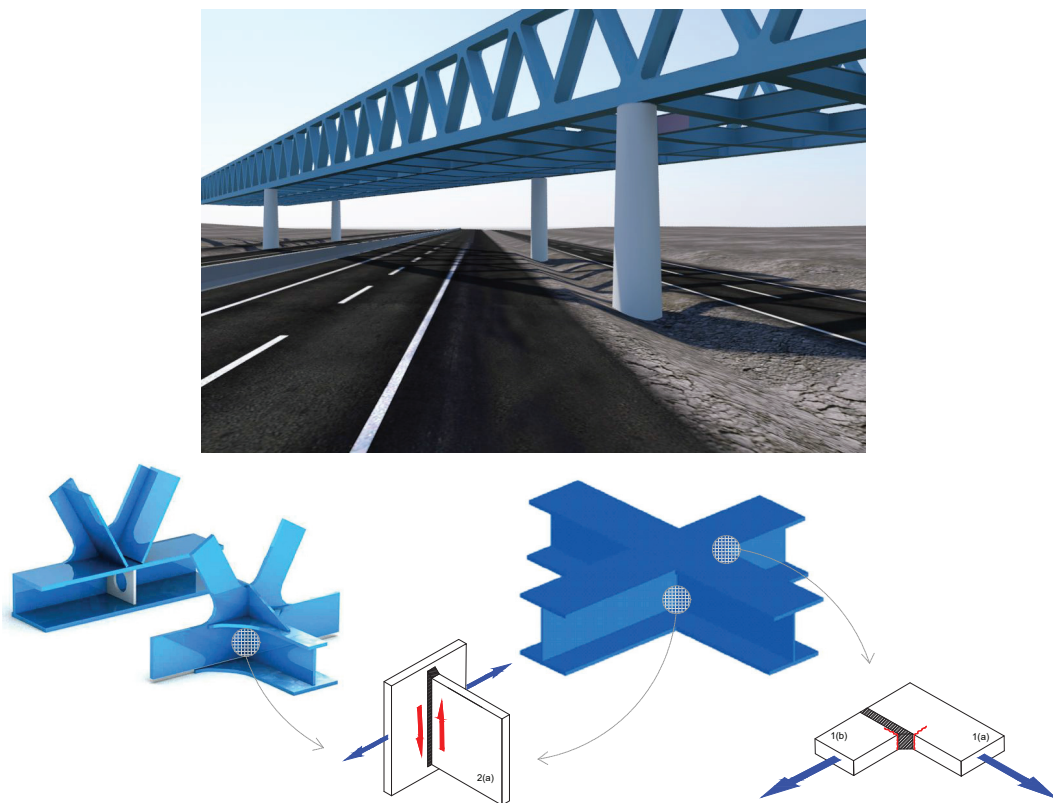


Figure 7 – Simplified details investigated in this thesis

## Objectives and Scope

Bridge elements under traffic loads are subjected to fatigue lives up to  $200 \cdot 10^6$  cycles or more. While the majority of these stress ranges are below the Constant Amplitude Fatigue Limit (CAFL), some few high stress cycles, can trigger the start of fatigue damage and lead stress ranges below CAFL to become propagating. For that reason, variable amplitude fatigue tests in very high cycle regime ( $N > 10 \cdot 10^6$  cycles) are fundamental to predict fatigue life under service loads. Experimental data to justify the  $2^{nd}$  slope value on a double slope S-N curve is very limited, because they are expensive and time consuming. Very few results have been obtained in relevant bridge details under constant amplitude after  $5 \cdot 10^6$  cycles and even less, can be found under variable amplitude for lives above 5 to  $10 \cdot 10^6$  cycles. In this thesis, results up to  $70 \cdot 10^6$  are presented, both under constant and variable amplitude, allowing a better insight on the damaging character of stress cycles with amplitudes below the CAFL. Crack propagation measurements were used to calibrate a fracture mechanics model using a Monte Carlo procedure to incorporate the random nature of the main parameters on simulations and characterise the shape of the S-N curve for variable amplitude loads. Multiaxial fatigue for welded details in the high-cycle regime was investigated with a specific experimental setup, devised to allow tests under shear-normal stress ( $\sigma, \tau$ ) interaction, both with proportional and non-proportional load application. New experimental results were obtained in the High-Cycle Regime under multiaxial interaction. Traffic generation models for typical steel bridges were developed to characterise load spectra and allow the reliability calibration of the fatigue models proposed in this thesis.

The objectives accomplished with this thesis can be summarised as:

- Devise a fatigue model for variable amplitude loads, that incorporates load spectra shape effects in a double slope S-N curve.
- Investigate interaction formulas for multiaxial stress using typified uniaxial FAT details for welded plates
- Calibration of partial safety factors for uniaxial and multiaxial safety checks based on a random traffic generation model.

The conclusions are limited to:

- The fatigue model for variable amplitude loads with the load spectra shape effects in the double slope S-N curve is limited to flange tip lateral attachments
- Multiaxial stress stress interaction based on principal stress is limited to the specific case of transversal attachments with full penetration fillet welds.
- The reliability computations and partial safety factors for uniaxial and multiaxial safety checks are based only on highway traffic for influence lines  $L \geq 20\text{m}$ .



## Structure and Methodology

The thesis is structured in three different parts: Resistance, Loads and Reliability.

### Part I - Resistance

Chapter 1 presents the state of art of the fatigue theory used in this thesis. Chapter 2 analyses the fatigue resistance of lateral flange tip attachments. Classification according to several Standards is analysed and compared with results collected from literature. The detail is characterised for the most important parameters. Experiments carried out under uniaxial load with constant and variable amplitude are presented. The experimental crack growth curves obtained from these tests are presented in Appendix. The results are analysed with an initiation+propagation model using fracture mechanics. The behaviour of lateral attachments is then fully characterised through a probabilistic fracture mechanics approach using a Monte Carlo technique, first to establish the CAFL position, and then to investigate the S-N curve shape below the CAFL.

Chapter 3 presents the results for multiaxial tests performed on out of plane normal-shear stress interactions. The large scale setup is presented along with the interpretation of the experimental results using the 1mm effective notch stress approach in principal stress. Life estimations based on nominal stress criteria is presented.

### Part II - Loads

Chapter 4 characterises fatigue traffic loads for highway bridges. Traffic parameters and their variability are identified from literature and a traffic generation model is developed using a Monte Carlo simulation procedure.

### Part III - Reliability

The fatigue safety assessment is done on a reliability basis on the third part of the thesis. Partial safety factors are calibrated for uniaxial safety checks based on a semi-probabilistic method on Chapter 5. Chapter 6 presents a probabilistic model used for the reliability of multiaxial verification based on nominal uniaxial details. In both cases, a database of uniaxial and multiaxial fatigue details, with experimental results collected from literature, had to be established. The re-analysis of these details was also necessary as a base for interaction of multiaxial experimental results, both the ones obtained under this investigation and the ones collected from literature. This database and the re-analysis is presented in Appendix along with the statistical approach used throughout the thesis.



# FATIGUE RESISTANCE **Part I**



# 1 Literature Review

## 1.1 Constant amplitude fatigue

The SN curves for constant amplitude generally specify a Constant Amplitude Fatigue Limit (CAFL), a so called “endurance limit” under constant amplitude cyclic loadings that defines a “knee-point” in the S-N curve, see figure 1.6. The CAFL concept was originally established by Woehler at  $2 \cdot 10^6$  cycles as the “safe working stress” under which no fatigue failure would occur (Socie and Marquis, 2000). Experiments in the 60’s and 70’s, showed that fatigue failures under constant amplitude loads could still occur after  $2 \cdot 10^6$  cycles (Haibach, 1971), so by the time the first IIW Recommendations were implemented in 1975, the CAFL was set, by inspection, at  $5 \cdot 10^6$  cycles (Hobbacher, 2010). Recent experimental investigations indicate that the knee point should be more conservatively defined at  $10 \cdot 10^6$  cycles as included nowadays in some fatigue standards.

Regardless of the specific endurance at which the CAFL is defined, all European standards place the knee-point at a given endurance level, independent of the notch category, which is advantageous for example in devising equivalent load models based on real traffic. The American and Japanese approach on the other hand, is to move the “knee-point” towards higher endurance as the notch effect increases (AASHTO, 2002), (JSSC, 1995). This seems to be more realistic when comparing to experimental results. The lower the FAT category, the more the knee point shifts towards higher number of cycles, approaching  $10 \cdot 10^6$  cycles for the lowest notch categories (Schönborn and Nitschke-Pagel, 2015).

Experiments in the giga-cycle regime up to  $1 \cdot 10^{11}$  cycles, have highlighted the fact that fatigue crack initiation under constant amplitude loads still occurs beyond  $10 \cdot 10^6$  cycles and the non-existence of a fatigue limit for some steels (Bathias and Paris, 2005), (Bathias, 2010). Tests in plain material from a large number of alloys have shown that for face-centered cubic lattice metals like austenitic steels, aluminium alloys or copper, a double slope S–N curve could be defined, with knee point around  $10 \cdot 10^6$  cycles, after which a  $2^{nd}$  S-N curve for internal crack initiation appears (Pyttel et al., 2011), figure 1.1.

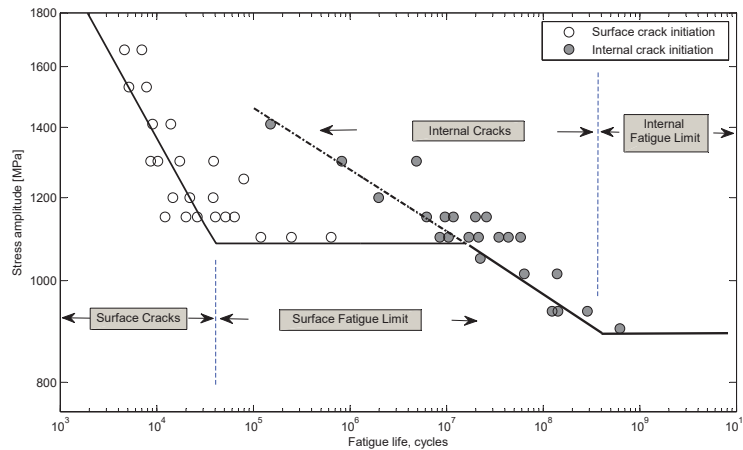


Figure 1.1 – Schematic double S–N curve for VHCF with results on bearing steel,  $f_u = 2320$  MPa and 1% carbon, data from (Dowling, 1993)

For body-centered cubic lattice metals like ferritic low or high-strength steels and quenched or tempered steels, a less pronounced trend and a possible asymptotic line at very low stress amplitudes is found. However the conventional fatigue limit is very difficult to justify as fatigue strength decreases with increasing number of cycles (Pyttel et al., 2011). Sonsino (2007a) proposed 2<sup>nd</sup> slope values dependant on the material microstructure,  $m_2=45$  for steels, cast irons and magnesium alloys and  $m_2=22$  for aluminium alloys, welded magnesium alloys and welded steels. Figure 1.2 shows the schematic single S–N curve with 2 slopes, for body-centered cubic metals with constant amplitude tests reported by Mayer (2007), for a low-strength steel under tension-compression.

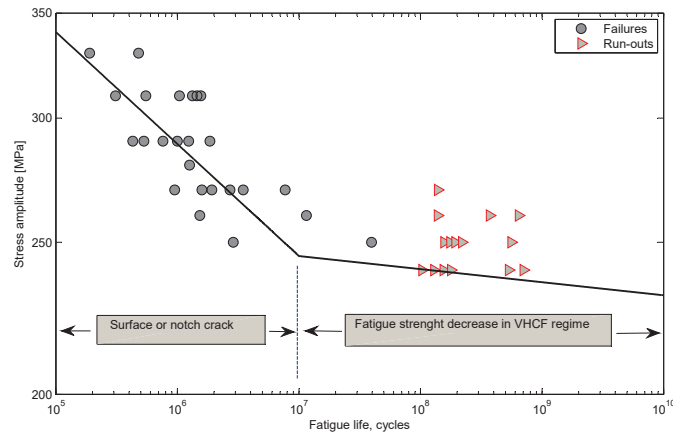


Figure 1.2 – Schematic double slope S–N curve for VHCF, results on low-strength steel with 0.15% carbon, data from (Mayer, 2007)

These trends on the constant amplitude S–N curves after the knee-point, are material features, mostly dependent on the material micro-structure. They are based on tests with smooth cylindrical specimens ( $\phi=6$  to 8mm) where approximately 90% of the experimental fatigue life corresponds to the initiation of a crack up to  $\approx 1$ mm.

In welded details, initial crack-like imperfections up to 0,5mm are common in weld toes, so the entire fatigue life corresponds to propagation of those initial cracks. The conventional fatigue limit is in this case dependent on the propagation threshold, and thus, less influenced by the material microstructure than the initiation life. Consequently, the conclusions about the fatigue limit on base material, cannot be directly extrapolated to the analysis of welded details, because initiation and propagation, correspond to different mechanisms ( see also figure 2.61).

The existing experimental results for welded steel details, have been re-analysed by Sonsino et al. (2005) (Sonsino, 2007a). Figure 1.3 shows the “normalized Wohler-curve”, a concept from Haibach (2006), for results in longitudinal stiffeners, butt-welds and girth welded tubes. A slope  $m_2=22$  is recommended after the knee point at  $10 \cdot 10^6$  cycles, to account for the decline in fatigue resistance in the very high cycle regime.

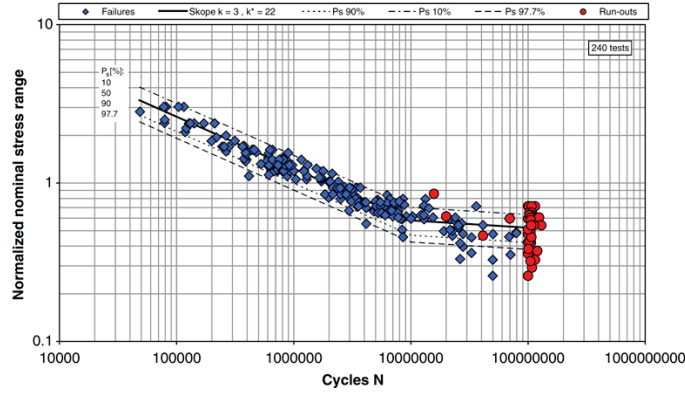


Figure 1.3 – Welded steel details in very-high cycle regime (Sonsino et al., 2005)

Although the experimental data on figure 1.3 could also justify a single slope  $m=3$  curve and a CAFL at  $50 \cdot 10^6$  cycles, the aim of specifying a  $2^{nd}$  slope, is to avoid designs based on a fatigue limit, by considering a 10% loss in stress per decade:

$$(\Delta\sigma)^{m_2} \cdot 10^n = ((1 - 0,1)\Delta\sigma)^{m_2} \cdot 10^{n+1} \rightarrow m_2 = \frac{-1}{\log 0,9} \approx 22$$

A probabilistic approach for estimation of the constant amplitude S-N curve slope was recently presented by D Angelo (2015). The method combines a Maximum Likelihood method with Monte Carlo simulations to fit a random CAFL non-linear model to experimental data points. The method allows the  $2^{nd}$  slope value  $m_2$  to be defined by considering both failures and run-outs.

The allowable stress ranges for welded details in the high-cycle regime up to  $10 \cdot 10^6$  cycles are generally so low, that a smooth, almost asymptotic curve in the very-high cycle regime appears, considered in general as the CAFL. A look at other databases support this dispute. Among these, an extensive and interesting database of fatigue tests in beams with cover-plates, developed in Lehigh University along the years. Several test

## Chapter 1. Literature Review

programs produced results under low stress amplitude in the very high cycle regime, including tests under constant and variable amplitude (Fisher et al., 1970), (Slockblower and Fisher, 1978), (Schilling and Klippstein, 1978), (Fisher, 1979), (Fisher et al., 1983). Figure 1.4 shows the results for beams with coverplates narrower than the flange width and beam flange thickness less than 20 mm. Coverplates with or without transversal end welds are included because this end weld was seen to have little influence on the fatigue strength. A distinctive CAFL can be seen for constant amplitude and a lower Variable Amplitude Fatigue Limit (VAFL). As a result, the American Standard for bridge design, (AASHTO, 2002), defines a single slope constant amplitude curve, without knee-point, extrapolated below the CAFL until the variable amplitude fatigue limit, defined at  $VAFL \approx 0,5 CAFL$ , which, in turn, can be used for infinite life check if the maximum traffic stress range is below VAFL.

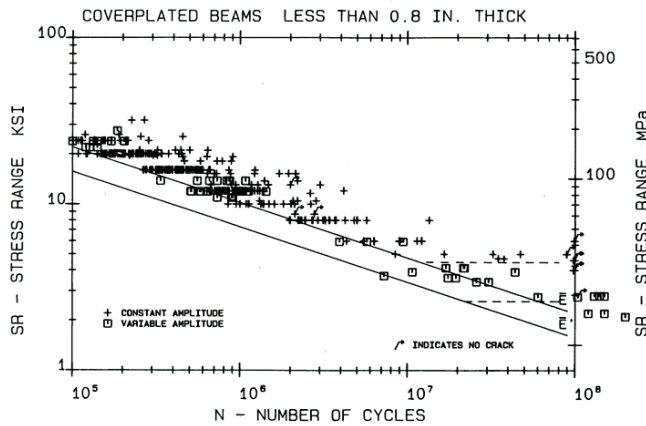


Figure 1.4 – Beams with cover-plates in VHCF regime (Keating and Fisher, 1986)

More recent tests up to  $1.10^9$  cycles in butt-welds on 4mm thick plates made of S355J2+N, have shown again that many run-outs are obtained (Schaumann and Steppeler, 2013). The data shows a distinct fatigue limit under constant amplitude, in this case below  $5.10^6$  cycles, consistent with the relatively low notch value of butt-welds, figure 1.5.

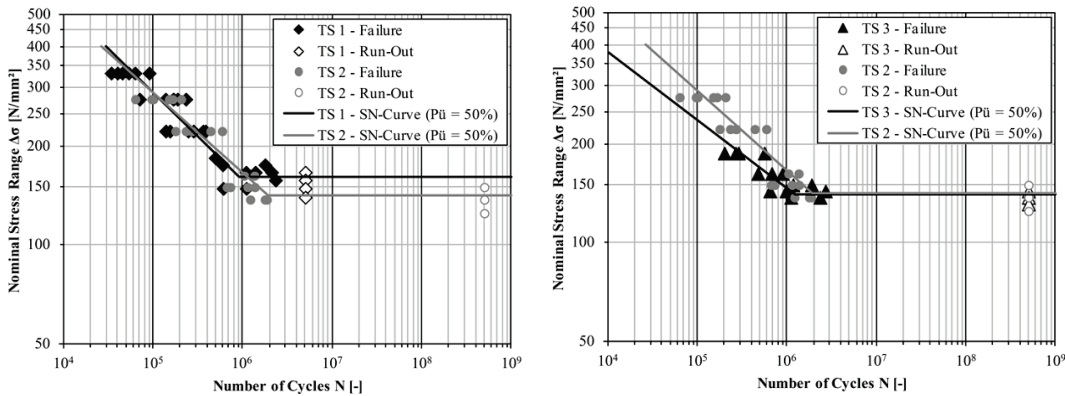


Figure 1.5 – Butt welds tested in the giga-cycle regime (Schaumann and Steppeler, 2013)



## 1.1. Constant amplitude fatigue

Under the assumption that the propagation phase accounts for the majority of the fatigue life of welded details (Maddox, 1974), the fatigue life of welded joints may be described by fracture mechanics (Hobbacher, 1992). Thus, ignoring crack initiation and short crack behaviour, S-N curves can be derived based on Paris law (Paris and Erdogan, 1963):

$$\frac{da}{dN} = C \cdot \Delta K_I^m \quad \text{and} \quad \Delta K_I = K_{max} - K_{min} \quad (1.1)$$

$C$  and  $m$  are constants that depend mainly on the material properties and loading conditions, measured with specific crack propagation tests (Maddox, 1973).

Rewriting Paris law with the Stress Intensity Factor range ( $\Delta K_I$ ):

$$\frac{da}{dN} = C \cdot \Delta K_I^m = C(Y(a)\Delta\sigma\sqrt{\pi a})^m \Rightarrow dN = \frac{1}{C(Y(a)\Delta\sigma\sqrt{\pi a})^m} da \quad (1.2)$$

For constant amplitude and stable crack growth (Stage II in figure 1.6), equation 1.2 may be integrated to estimate the number of cycles to propagate an initial crack  $a_i$ , real or postulated crack like imperfection or inclusion, to a given final crack size  $a_f$ :

$$\int_0^N dN = \int_{a_i}^{a_f} \frac{1}{C(Y(a)\Delta\sigma\sqrt{\pi a})^m} da \Rightarrow N = \frac{1}{C\Delta\sigma^m} \int_{a_i}^{a_f} \frac{1}{(Y(a)\sqrt{\pi a})^m} da \quad (1.3)$$

Considering  $Y(a)$  constant during propagation from  $a_i$  to  $a_f$  leads to ( $\int x^n = \frac{1}{n+1}x^{n+1}$ ):

$$N = \frac{1}{C(Y\Delta\sigma\sqrt{\pi})^m} \int \frac{1}{\sqrt{a}^m} da = \frac{a_f^{1-\frac{m}{2}} - a_i^{1-\frac{m}{2}}}{(1-\frac{m}{2})C(Y\Delta\sigma\sqrt{\pi})^m}, \quad m \neq 2 \quad (1.4)$$

Under constant amplitude fatigue, and for a given pair of values  $a_i$ ,  $a_f$  if  $C$ ,  $m$  and  $Y$  are known, the expression of a single slope S-N curve is obtained:

$$N\Delta\sigma^m = \frac{a_f^{1-\frac{m}{2}} - a_i^{1-\frac{m}{2}}}{(1-\frac{m}{2})C(Y\sqrt{\pi})^m}, \quad m \neq 2 \Rightarrow N\Delta\sigma^m = \text{Const} \quad (1.5)$$

$$\Rightarrow \log N + m \log \Delta\sigma = \log \text{Const}$$

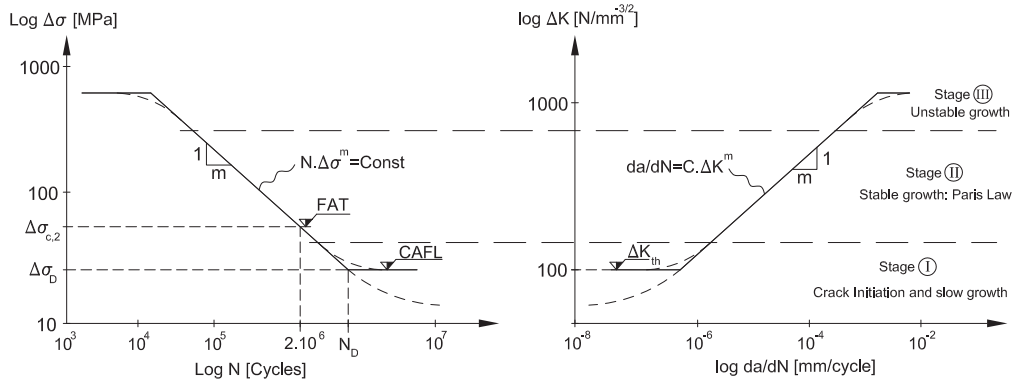


Figure 1.6 – Relation between propagation law and the S-N curve

## Chapter 1. Literature Review

The validity of equation 1.5 has been confirmed by many experimental programs on welded details with lives dominated by crack growth, (Fisher et al., 1970), (Fisher et al., 1974), (Bremen, 1989). The existence of weld imperfections prior to any fatigue loading, “eliminates” the initiation phase (Smith and Smith, 1982), (Husset, Lieurade, Maltrud, 1985). Experimental results show that the S-N slope for most of the welded details is generally close to the Paris law exponent for C-Mn steels, i.e.  $m=3$ . S-N curves for welded details are “propagation” curves, the slope corresponding to Paris Law, expressing the same crack propagation mechanism.

Apart from the natural scatter on the Paris law exponent, shallower S-N curves with higher slope values are obtained for non-welded component details where crack initiation represents an important part of total life, particularly  $m \approx 5$  for tests on non-welded details such as rolled beams or plates with holes, figure 1.7. Shallower S-N curves have also been obtained for tubular joints of small dimensions (Mang et al., 1987). Secondary bending stresses (non-linear with load level) and initiation are believed to explain these slopes values close to 5. Thick tubular welded joints tend to follow the  $m=3$  slope.

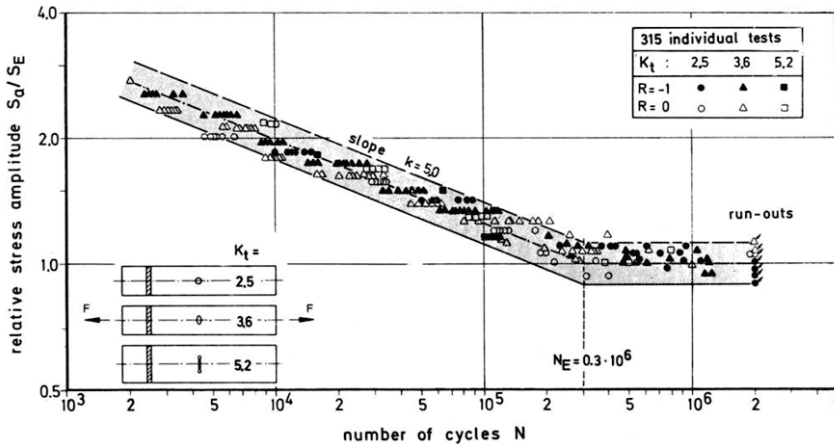


Figure 1.7 – Fatigue tests in notched specimens, quenched and tempered steel 42CrMo4 (Spindel and Haibach, 1981)

The constant amplitude fatigue limit  $\Delta\sigma_D$  is thus directly related to the fatigue crack growth threshold  $\Delta K_{th}$ , (Topper and Haddad, 1981) and can be justified based on Fracture Mechanics (Gurney, 2006). Although a matter of disagreement (Sonsino, 2007a), the threshold stress intensity,  $\Delta K_{th}$ , defines the limit below which no propagation exists:

$$\frac{da}{dN} = 0 \quad \text{if} \quad \Delta K_I < \Delta K_{th} \quad (1.6)$$

Assuming a fixed  $\Delta K_{th}$  value for steel, the maximum allowable initial size for non-propagating cracks on a given geometry may be defined. Alternatively, the maximum allowable stress range  $\Delta\sigma_D$  for a given crack size  $a_i$  may be estimated, defining the level below which, run-outs are due to non propagating cracks. Introducing the threshold

stress intensity factor range in equation 1.1 leads to:

$$\frac{da}{dN} = C(\Delta K_I^m - \Delta K_{th}^m) \quad (1.7)$$

and introducing the effective stress intensity factor concept (Bremen, 1989):

$$\frac{da}{dN} = C(\Delta K_{eff}^m - \Delta K_{th}^m) \quad (1.8)$$

The threshold stress intensity factor,  $\Delta K_{th}$ , depends on the material characteristics and load conditions, mainly stress ratio and mean load, highly dependent on residual stresses. The residual stress field in the crack region modifies the mean stress and the applied stress cycle at which the crack opens (Krebs and Kassner, 2007). The effective opening stress is consequently dependent on the residual stresses with an important influence on the onset of propagation. With compressive residual stress, the effective range may be below the threshold. On the opposite, tensile residual stresses may cause the effective stress to be above the threshold, even if the applied stress range is in compression. Crack closure effects may be taken into account by Elber's model, under constant amplitude Elber (1971) or spectrum loading (Elber, 1976). Although originally observed in aluminum, the plastic induced crack closure (which add to the effect of residual stress) was generalised for steels by Schijve (1988). A crack can remain closed at the tip during part of the tensile stress cycle due to previous yielding and residual extension, thus only part of the stress range is effective. The opening stress above which the stress range is effective is given by:

$$\Delta\sigma_{eff} = \sigma_{max} - \sigma_{op} \quad \text{if} \quad \sigma_{min} < \sigma_{op} \quad (1.9)$$

Open cracks do not propagate until the effective stress intensity factor is below the threshold  $\Delta K_{eff} > \Delta K_{th}$ . The tensile residual stresses may however suppress crack closure so that:

$$\sigma_{op} = -(\sigma_{res} + \sigma_{pl}) \quad \text{and} \quad \Delta\sigma_{eff} = \sigma_{max} + (\sigma_{res} + \sigma_{pl}) \quad (1.10)$$

with  $\sigma_{res}$  and  $\sigma_{pl}$  negative if creating closure i.e. compressive  $\sigma_{res}$ .

Fracture mechanics models to take crack closure effects into account may be found in (Vasudevan et al., 2016). A simplified form of Elber model due to Bremen (1989) is to ignore the plastic closure effect and define the opening stress as the residual stress if in compression:

$$\sigma_{op} = \sigma_{res} \quad \text{and} \quad \sigma_{res} < 0 \quad (1.11)$$

For the practical design of as-welded details directly with S-N curves, it is generally assumed that high residual tensile stress up to yield strength magnitude are present.

These residual stresses overcome the opening stress and as a result the fatigue crack is held open through the entire load cycle and the applied stress range is fully effective, cycling from yield stress down (Gurney, 1979), (Maddox, 1991). Fatigue life is thus dependent only on the applied stress range even if compressive. The assumption that life is independent from applied mean stress is conservative, by ignoring compressive residual stresses that are present in some welded details, however, there is also evidence of stress relaxation and re-distribution of compressive residual stresses during fatigue loads (Maddox, 2003), a major drawback for most of the improvement methods that rely on these compressive residual stresses. On the other hand, there is also evidence of residual stress relaxation for tensile stress, as reported by Blom (1995) on fatigue tests obtained under variable amplitude loads, with linear and concave spectra, figure 1.8. Initial as-welded residual stress were found in the range of the base material yield stress and residual stress relaxation was monitored using an X-ray diffraction technique, repeatedly during the fatigue tests. Around 50% of the tensile residual stress is relaxed within 10% of total fatigue life, with loads in the VHCF regime with lives up to  $10 \cdot 10^6$ . Similar conclusions were found by Zhang and Maddox (2009) and (Mikkola et al., 2015).

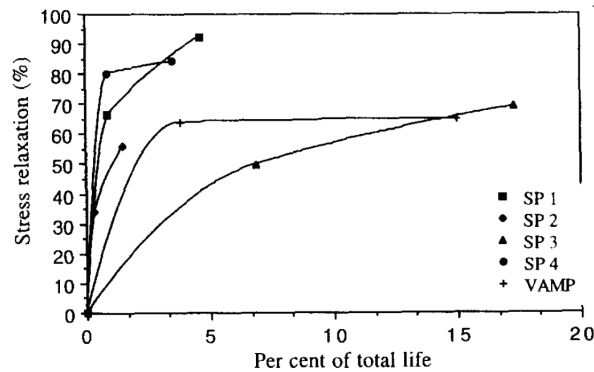


Figure 1.8 – Residual stress relaxation under variable amplitude fatigue after Blom (1995)

For details in as-welded conditions, the existence of the CAFL is arguable but the discussion about the shape of the S-N curve beyond the knee point under constant amplitude is of little importance for steel bridges. Real loadings are variable, and stress peaks or maximum loads are not easily predictable in highway or even railway bridges. For that reason, load models defined in EN 1991-2 (2003) to verify “infinite life”, are based on “frequent loads”, which correspond to the vehicle weights producing less than 1% of the total damage. These frequent loads for infinite life check have a mean return period of one week (JRC, 2008). If none of the design stress ranges reaches the CAFL, the life of the detail is considered infinite (ECCS, 2000), see figure 1.9 (Case 3). The “infinite life” check is made against a characteristic fatigue limit, but the definition of a characteristic CAFL level based on fatigue tests is also very difficult due to high variability on initial cracks size, stress concentration, stress intensity factors, residual stress and other factors, which require a considerable number of tests. Finally, fatigue experiments in the VHCF regime have shown the fatigue limit to be dependent on the

presence of micro-structural inhomogeneities and corrosion, both unavoidable in practice.

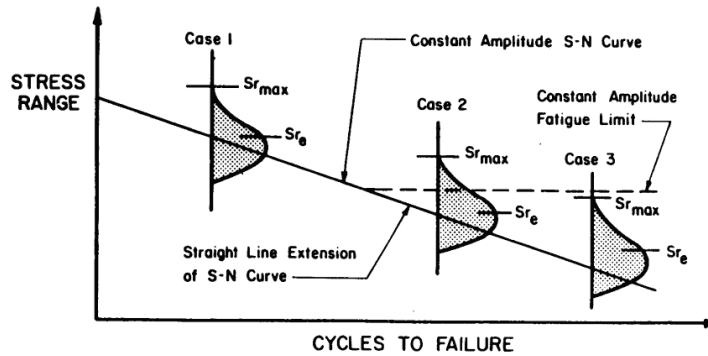


Figure 1.9 – Load spectra and CAFL after Keating and Fisher (1989)

The conclusion is that designs based on “infinite life” concepts should be avoided because the difference between finite and infinite life is too sensitive to the CAFL definition and to the maximum peak stress range.

## 1.2 Variable amplitude fatigue

Experiments on large beams reported by Fisher et al. (1993) have shown that exceeding the characteristic CAFL only once in 10.000 cycles, 0,01% of the total number of cycles, was enough to trigger crack propagation, while these overloads produced less than 1% of the total damage.

The same effect had already be highlighted by Brose et al. (1974), with constant amplitude tests on low strength steel. Periodic overstrains applied every 100.000 cycles corresponding only to a few percents of the total damage, made cycles below the CAFL to become damaging, figure 1.10.

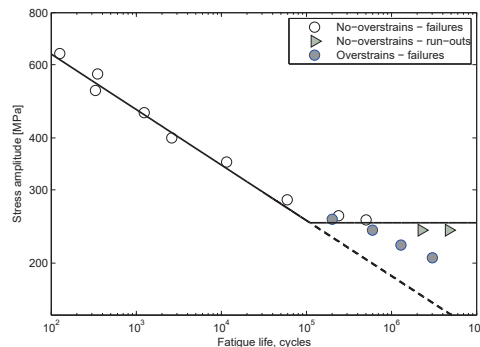


Figure 1.10 – Effect of over-strains

Experiments in fillet welded joints presented by Miki et al. (1989), both under constant and variable amplitude stress, with generated highway and railway loads, showed failures even with the equivalent stress range ( $S_{req}$ ) lower than the CAFL. Same conclusions were found in (Miki et al., 1990) using large scale beams with lateral flange tip attachments tested under random highway loads.

It is clear that for bridges, with load spectra composed by large number of cycles at stress below CAFL with some occasional overloads, the damage due to overloads may be

small, but life for stress ranges below the CAFL cannot be considered “infinite”.

Infinite life designs are based on the concept that crack-like imperfections do not propagate below a certain level  $\Delta\sigma_D$ , assuming the Stress Intensity Factor  $\Delta K$  is lower than the propagation threshold  $\Delta K_{th}$ , either because cracks are too small or because stress range is too low. Under variable amplitude loading, occasional overloads higher than  $\Delta\sigma_D$  will however cause some damage and, although negligible, it produces a small crack size increase. The Stress Intensity Factor  $\Delta K$  will increase, eventually getting higher than the threshold  $\Delta K_{th}$  at some point. As a consequence, some load cycles that were below the original CAFL level become damaging, and the propagation level continues to drop. This behaviour was first recognised by Haibach (1970), who proposed a model for welded steels, based on a decreasing threshold level,  $\Delta\sigma_{th,i}$  dependent on accumulated damage  $D$ , equation 1.12, leading to the definition of a  $2^{nd}$  slope,  $k=2m-1$ , below the CAFL  $\Delta\sigma_D$ .

$$\frac{\Delta\sigma_{th,i}}{\Delta\sigma_D} = (1 - D)^{1/(m-1)} \quad \text{where } D = \sum \frac{n_{E,i}}{N_{R,i}} \quad (1.12)$$

One comprehensive experimental work including both constant amplitude tests to define the CAFL and variable amplitude tests in plates with longitudinal attachments, was presented by Tilly and Nunn (1980) using a Rayleigh narrow band convex spectrum, figure 1.11. The results clearly showed that stress ranges below the CAFL were damaging and that Haibach’s model with a  $2^{nd}$  slope  $k=5$  gave the best estimation, while the model with a single slope  $k=m=3$  was found over-conservative. For the highest experimental lives achieved, up to 400 million cycles, the stress history was composed by only 25 % of stress cycles above the CAFL, which were responsible for only 9% of the total damage.

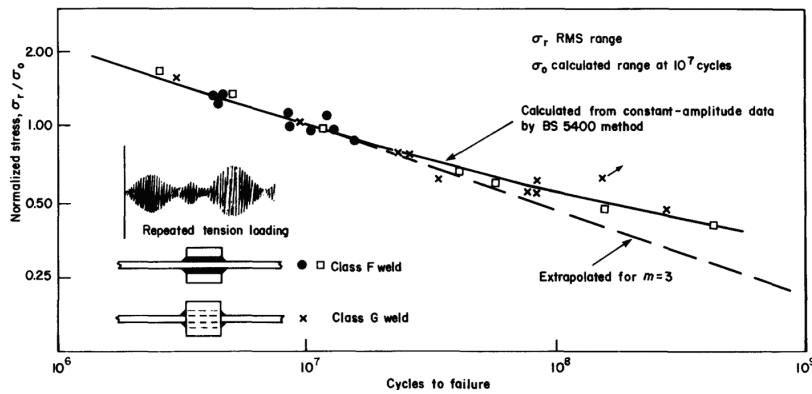


Figure 1.11 – Variable amplitude tests with Rayleigh spectra by Tilly and Nunn (1980)

Several experimental works, followed the tests reported by Tilly and Nunn (1980) and argued Haibach’s model to be too conservative, giving overall preference to damage accumulation on a straight S-N curve (i.e. extrapolated beyond the CAFL without changing slope). Failures were in general plotted using the equivalent root mean cube or the root mean stress. Fatigue tests in beams with cover plates and longitudinal

attachments on the web reported by Fisher et al. (1983), figure 1.4, were performed under a Rayleigh spectrum (block size  $\approx 1000$  cycles) and showed Haibach's model to be unsafe. Better estimation of fatigue lives was found with single slope  $k=m=3$ . The exceedance of characteristic CAFL was between 0.1% and 12%. Experiments reported later by Fisher et al. (1993) on large beams have led to the same conclusion with CAFL exceedance of only 0,01% of the total number of cycles in some cases.

Dahle and Larsson (1992) also confirmed Haibach's model to be unsafe with a concave spectrum on tests performed with longitudinally welded box beams and longitudinal non-load-carrying fillet welds. Later, under two different types of load spectra, Dahle (1993) and Dahle (1994) suggested that the slope of the S-N curve below the "knee-point" could be related to the load spectra shape, figure 1.12.

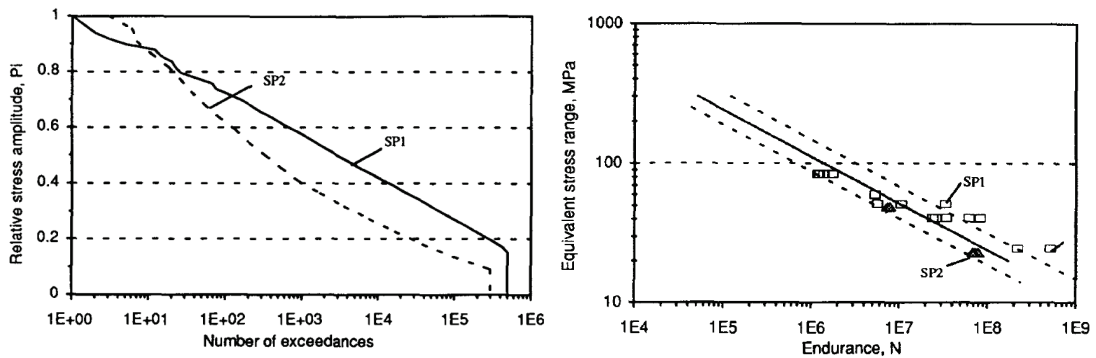


Figure 1.12 – Variable amplitude tests by Dahle (1994)

A concave load spectrum with  $R_\sigma = -1$  was used by Marquis (1995) for tests on box beams and longitudinal attachments. The spectrum had large peak stress ranges truncated at 33%, 50% and 100% of the mean CAFL found in constant amplitude tests, equivalent to approximately 10%, 16% and 31% of the peak stress. Haibach's model showed to be unsafe and the single slope S-N curve a conservative estimation of fatigue lives. In this case a 2<sup>nd</sup> slope between 3 and 5 would have lead to more accurate life estimations. These results show the importance of a truthful definition of the CAFL "knee-point" in order to establish the 2<sup>nd</sup> slope of the S-N curve. In these tests, the CAFL was identified experimentally as  $\Delta\sigma_D=110\text{MPa}$  at  $1.10^6$  cycles but this is a rather high value for the constant amplitude limit if we compare with the experimental database of longitudinal attachments on figure A.22. Truncation at 33% CAFL means that the minimum applied stress range was  $\Delta\sigma_{min}=37\text{MPa}$ , which indicates that the spectra stress ranges were mainly above a more conservative CAFL value, and thus, plot mainly on a slope  $m=3$  S-N curves, figure 1.13.

Variable amplitude tests under block loading presented by Gurney (2001) on wing plates, suggested that stress ranges below the CAFL were equally damaging as those above, leading to use a single slope S-N curve. Stress ranges as low as  $\Delta\sigma = 10 \text{ N/mm}^2$  were found damaging, figure 1.14. The same conclusions were later drawn by Zhang and



Maddox (2009) with tests under a concave spectra.

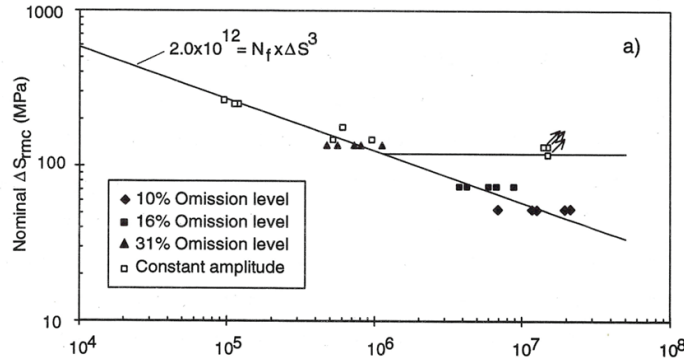


Figure 1.13 – Variable amplitude tests by Marquis (1995)

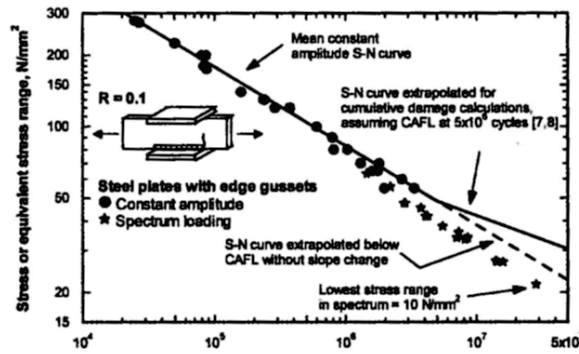


Figure 1.14 – Block loading tests on wing plates (Gurney, 2001)

To resume, several experimental works have shown the accuracy of Haibach’s model while other’s have claimed it to be non-conservative. A state-of-art presented by Albrecht and Lenwari (2009) revised several variable amplitude datasets, and proposed a simplified model with smooth transition between the single slope S-N curve and the VAFL, figure 1.15. The smooth transition between the CAFL and the VAFL is in agreement with the European concept of changing slope below the CAFL up to a cut-off at the VAFL.

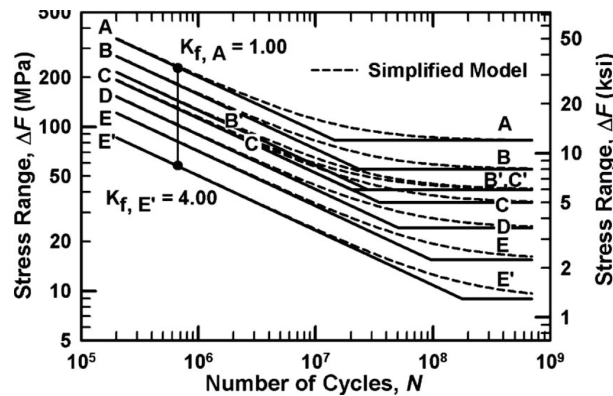


Figure 1.15 – Variable amplitude curves for AASHTO after Albrecht and Lenwari (2009)



The accuracy of the 2<sup>nd</sup> slope model as proposed by Haibach (1970) depends on the load spectra shape and the relation of the spectra with the CAFL. It will be shown in Chapter 2, that a 2<sup>nd</sup> slope dependent on the spectrum shape parameter, relative to the original CAFL, is able to predict fatigue life under several variable load conditions.

Variable amplitude load-sequences may be described by standardised load spectra for many practical applications (Berger et al., 2002), (Sonsino, 2007b). One typical way of representing stress spectra is by the cumulative frequency of occurrence of stress ranges at different levels. These diagrams are usually normalised to the maximum load of the spectra and expressed per million cycles, see figure 1.16 (Heuler and Klatschke, 2005). The exceedance diagram may conveniently be defined with a Weibull distribution, differentiating between spectra types with shape parameter,  $\nu$ . The probability density function  $f(x)_{PDF}$  is fitted to the histogram of stress ranges obtained by rainflow counting. The histogram may be obtained from actual bridge measurements or by simulated traffic as in Chapter 4. The spectra types are characterised by their shape (concave, linear or convex), a characteristic seen on their semi-log plots, figure 1.16. While the ordinates denote the stress ratio normalised to the maximum spectra stress, the abscissa in log scale is the Cumulative Exceedance number of cycles. For that reason it is convenient to express the exceedance function also on a logarithmic base:

$$\ln(N_{E,i}) = \left[ 1 - \left( \frac{\Delta S_i}{\Delta S_{max}} \right)^\nu \right] \cdot \ln(N_{tot}) \quad (1.13)$$

where:

- $N_{E,i}$  is the n<sup>o</sup> of cycles exceeding  $\frac{\Delta S_i}{\Delta S_{max}}$
- $\Delta S_{max}$  the maximum stress range
- $N_{tot}$  is the total number of cycles
- $\nu$  is the shape parameter

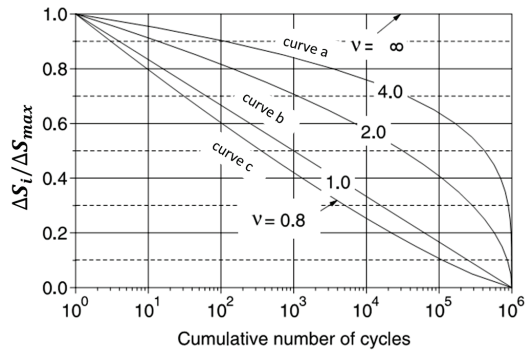


Figure 1.16 – Normalised stress range exceedance distribution

**Curve a** with shape parameter  $\nu > 1$ , defines a convex spectra. With shape parameter  $\nu = 2$  the curve corresponds to a stationary narrow band Gaussian process, typical of elastic structures, produced for example by road roughness, gusts or waves (Haibach, 1976). The exceedance in this case, is the skewed Rayleigh distribution, typically used for bridges, representing loads with a minimum value but without a maximum limit. It has been used for variable amplitude tests under traffic loads on bridges by several authors (Schilling and Klippstein, 1978), (Tilly and Nunn, 1980), (Gurney, 2001). With shape parameter  $\nu \approx 3,44$  it is equivalent to a normal distribution.

Shape parameter values  $\nu < 2$  represent load sequences not necessarily stationary. **Curve b** with  $\nu = 1$  corresponds to a linear exceedance diagram, equivalent to an Exponential distribution of loads. **Curve c** with shape parameter  $\nu < 1$ , defines a concave spectra.

The suitability of the 2<sup>nd</sup> slope model also depends on the damage accumulation method and the cut-off limit for the lowest stress ranges. A common practice is to extend the 2<sup>nd</sup> slope up to  $100.10^6$  cycles defining a cut-off level, i.e a VAFL, that eliminates the small cycles, from vibrations or resonance. Small cycles in a stress spectrum should not contribute significantly to the damage because the crack lengths required to have these stress ranges above the propagation threshold are in general close to the failure of the detail. It was shown by Fisher et al. (1993) and Tilly and Nunn (1980) that stress ranges below  $\approx 0,25$  CAFL  $\approx 0,18$  FAT could be ignored in the fatigue damage computation. This was also confirmed with our tests, see Section 2.5.

For damage computations, Miner's linear rule is the most widespread method (Miner, 1945) because of its simplicity (also referred to as Palmgren-Miner rule). It may be derived by fracture mechanics, based on the assumption that fatigue life is entirely in propagation (Maddox, 1975), (Schjive, 2003).

$$\frac{n}{N} = \frac{\int_{a_i}^a \frac{1}{(Y(a)\sqrt{\pi a})^m} da}{\int_{a_i}^{a_f} \frac{1}{(Y(a)\sqrt{\pi a})^m} da}$$

Miner's rule assumes a linear damage accumulation, independent from the real load sequence, which is often held as a major drawback to Miner's rule, because the sequence of each individual load occurrence, indeed plays an important effect on the damage sum.

Sequence effects have been classified by Vormwald (2015) in two categories: material and geometric effects. Material sequence effects are due to plastic deformation, inducing crack retardation/acceleration due to overloads, figure 1.17. Geometric sequence effects are due to crack growth, causing a progressive drop on the crack propagation threshold  $\Delta K_{th}$  as crack length increases, i.e. as damage accumulates.

Two different approaches are found in literature to take sequence effects into account. One approach has been to define non-linear damage accumulation models, mainly to account for material crack retardation/acceleration effects. Another, followed in this thesis, is to consider the sequence effects in the fatigue life models, using linear damage sum with Miner's rule.

For welded steel details, with high residual stresses, this 2<sup>nd</sup> approach is made easier under high cycle fatigue, because material sequence effects have a very small influence due to restricted plasticity (Kulak and Smith, 1993), (Bannantine, 1990). According to Dowling (1993), for two subsequent loads, if one is considered as  $\Delta\sigma_{peak}$  and the other  $\Delta\sigma_{regular}$ , load sequence effects should be considered important only for  $\frac{\Delta\sigma_{peak}}{\Delta\sigma_{regular}} > 2$ .

## 1.2. Variable amplitude fatigue

One overload over 10.000 cycles is usually referred to be the optimum rate to develop important retardation effects (Tilly and Nunn, 1980), but for variable amplitude load histories typical from bridges, peaks occur much more often, so their damaging effect is more important than retardation (Niemi, 1997).

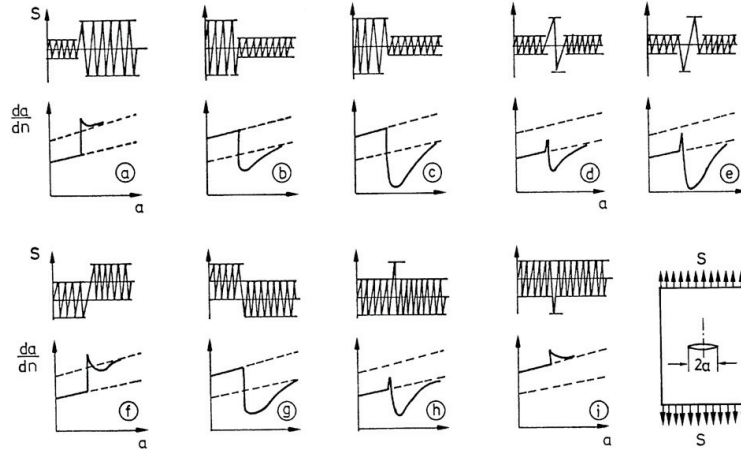


Figure 1.17 – Material plastic sequence effects (Haibach, 2006)

Geometric sequence effects are considered by appropriate variable amplitude S-N curves. One approach extensively developed in Germany (Berger et al., 2002), is the use of “Gassner” curves, figure 1.18.

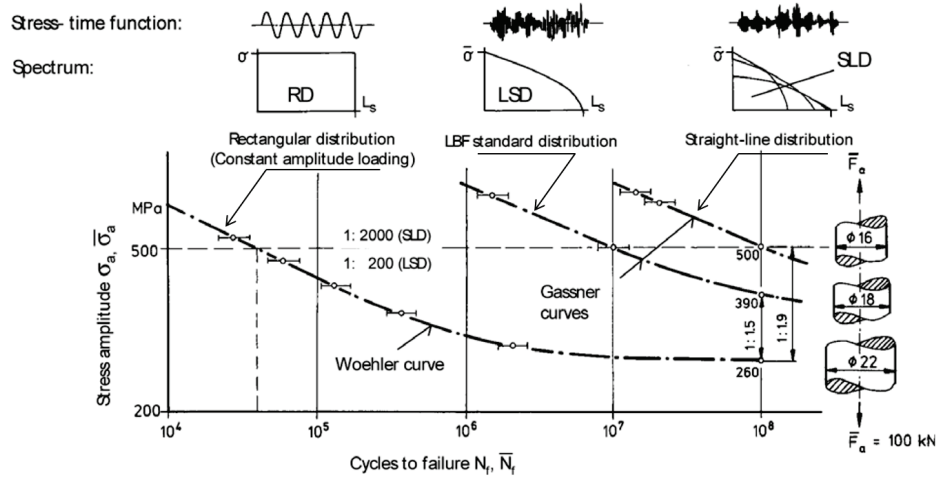


Figure 1.18 – Gassner curves for variable amplitude fatigue (Sonsino, 2007b)

Gassner curves are defined for specific load spectra shapes, giving a direct relation between the maximum stress amplitude,  $\bar{\sigma}_a$  and fatigue life,  $N$ . The advantage of this design procedure, mostly developed for mechanical component design, is that maximum stress amplitude  $\bar{\sigma}_a$  may be directly compared to tensile ( $f_y$ ) or ultimate ( $f_u$ ) steel strength and also with the CAFL from the Woehler curve. On the other hand, each component needs to be tested under several load spectra.

## Chapter 1. Literature Review

The strategy to account for the geometric sequence effects using Miner's linear damage sum, is to define suitable variable amplitude S-N curves, namely, the  $2^{nd}$  slope model by Haibach (1970), that introduces the progressive drop of the crack propagation threshold  $\Delta K_{th}$  in the constant amplitude S-N curves. This approach is followed in this thesis, because of its practical character, by using the existing database of constant amplitude tests for typical bridge details.

Miner's rule was originally proposed as  $D = \sum \frac{n_{E,i}}{N_{R,i}} = D_{max}$  with  $D_{max}$  set by definition at 1 for failure. However, many experimental programs have shown damage sum values different than unity, with values ranging from 0,1 to 9 found in re-analysing existing databases (Gurney and Maddox, 1982), (Berger et al., 2002) (Zhang and Maddox, 2009). In consequence, sequence effects and fatigue scatter are considered by using characteristic values for Constant amplitudes curves and by reducing the maximum damage sum  $D_{max}$ , requiring a variety of "semi-empirical" rules to define the damage sum values. IIW (2008) Recommendations for example, define  $D_{max} = 0,5$  in general and  $D_{max} = 0,2$  for cases under variable amplitude with varying mean stress.

When accounting for variability in the damage sum  $D_{max}$ , even with sequence effects considered in the fatigue resistance models, it is reasonable to assume that scatter under variable amplitude is similar than obtained under constant amplitude (Gurney and Maddox, 1982). Considering the unified scatter band for fatigue life as proposed by Haibach (1968), represented by probability of survival of 10% and 90% by  $\frac{1}{T_N} = \frac{N_{10\%}}{N_{90\%}}$ , figure 1.19, a scatter band for the expected damage sum  $D_{max}$  may be derived. For log  $N$  normally distributed,  $P_{10\%}$  and  $P_{90\%}$  correspond to  $\mu_x \pm 1,25\sigma_x$  and

$$\sigma_x = \frac{1}{2,54} \log \frac{1}{T_N}. \text{ If } D_{max} = 1 \text{ for } N_{P_f} = 50\%, \text{ then } D_{max,10\%,90\%} = 10^{\pm \log \left( \frac{1}{T_N} \right) / 2}$$

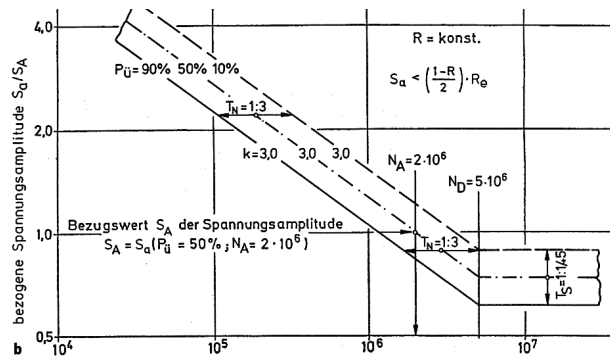


Figure 1.19 – Unified scatter band for welded steel details (Haibach, 2006)

A value of  $\frac{1}{T_N} = \frac{1}{3}$  is commonly accepted for constant amplitude experimental lives. In this case, the corresponding damage sum lies between 0,6 and 1,75 and for  $\frac{1}{T_N} = \frac{1}{4}$ , between 0,5 and 2. As a random variable, the maximum value of the damage sum,  $D_{max}$ , is often used in literature, as a Gaussian variable, centered at mean=1 and stdv=0,3 (Wirsching, 1984).

### 1.3 Multiaxial fatigue

Besides the variable character of traffic loads, they may also induce multiaxial stress states. Several experimental works have shown the assessment under multiaxial fatigue to be potentially more damaging than the uniaxial case (Socie and Marquis, 2000), (Sonsino, 2009). Design codes such as BS (BS 5400: Part 10 1980), IIW Recommendations (IIW 2008) or Eurocode (EN 1993 1-9 2005), have adopted a wide range of multiaxial fatigue criteria but the accuracy of those is limited.

The re-analysis of existing fatigue test results, specially weld toe failures, has shown that design code interaction formulas do not accurately reproduce the test results (Bäckström and Marquis, 2001), (Backstrom and Marquis, 2004). On the other hand, Lotsberg (2009) and Bokesjö et al. (2012) have shown good agreement between those code interaction formulas and fatigue tests both in plates and tubular specimens, involving weld root failure. Among those criteria, equations based on the interaction of each independent uniaxial stress component are the most interesting in bridge design practice. The reason is that the general procedure in bridge design is to compute stress components independently based on classical beam theory (ex. shear and normal stress) but most importantly, the resistance is related to the extensive database of uniaxial FAT details defined in Design Standards.

The majority of multiaxial criteria in literature, were developed to explain the behaviour of the base material (Socie and Marquis, 2000), (Sonsino, 2009) and (Mladen et al., 2010). It is a general convention to divide multiaxial criteria in three groups:

- stress-based criteria,
- strain-based criteria
- energy-based criteria.

For the specific problem of multiaxial fatigue in welded details, interaction formulas may be divided in nominal and equivalent stress criteria. Interaction equations based on nominal shear and normal stress are very useful from a design point of view, since resistance is related to the uniaxial FAT detail database.

The formula presented in EN 1993 1-9 (2005) is based on a linear damage accumulation according to Miner's rule (Sedlacek et al., 2000):

$$D_{\sigma} + D_{\tau} \leq 1 \Leftrightarrow \left( \frac{\Delta\sigma_{Ed,2}}{FAT_{\sigma}} \right)^3 + \left( \frac{\Delta\tau_{Ed,2}}{FAT_{\tau}} \right)^5 \leq 1 \quad (1.14)$$

Although not specifically defined in the current version of EN 1993 1-9 (2005), the damage sum equation 1.14 was originally adopted for non-simultaneous loads (ECCS, 1985). Due to the lack of clear guidance for assessment under principal stress, the interaction

formula 1.14 is often adopted for both proportional and non-proportional cases.

Under proportional loads, the maximum principal stress due to fatigue loading would be used, however no specific resistance curve was indeed defined. It is assumed that the FAT category applicable for normal stress  $\Delta\sigma$  may also be used for the verifications using the principal stress. For evaluating the fatigue resistance of cope holes in stringers of orthotropic decks, the principal stress range is still required, limiting it to FAT 56.

IIW Recommendations (IIW, 2008) have instead adopted a formula based on Gough-Pollard interaction (Gough and Pollard, 1935), with different comparison values, CV, for proportional loads and non-proportional loads:

$$\left(\frac{\Delta\sigma_{Ed,2}}{FAT_\sigma}\right)^2 + \left(\frac{\Delta\tau_{Ed,2}}{FAT_\tau}\right)^2 \leq CV \quad \begin{cases} CV = 1 \text{ proportional stress} \\ CV = 0.5 \text{ non-proportional} \end{cases} \quad (1.15)$$

The IIW Recommendations also specify a principal stress criteria to be used for constant amplitude proportional loads, as long as the principal stress direction is within  $\pm 60^\circ$  of the normal to the weld toe.

Interaction equations based on equivalent stress require the definition of an equivalent resistance (Maddox and Razmjoo, 2001), which is done on a case by case basis and is generally not defined in design standards. An important observation regarding the interaction between shear and normal stress in equivalent stress, is the significant difference between direct shear in welded plate details and torsion shear in shafts or tubes. The interaction behaviour of welded plate details, where usually shear levels are not too high, is controlled by propagation under normal stress with cracks in Mode I (Maddox and Razmjoo, 2001). In other words, when plate results are represented in an S-N curve, a slope  $m=3$  is observed, figure 1.20 (left side). For tubular specimens or shafts, shear cracks in Mode II and III dominate, and the results under interaction correspond to a slope  $m=5$ , figure 1.20 (right side).

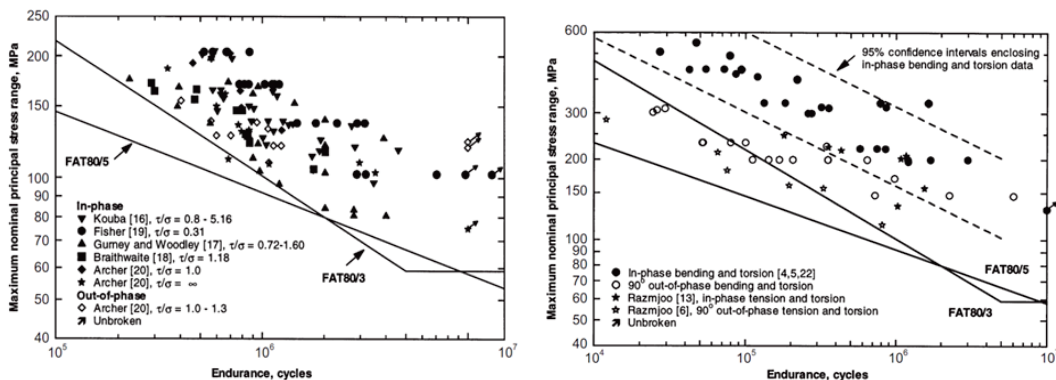


Figure 1.20 – Multiaxial equivalent stress for plate and tubular specimens (Maddox and Razmjoo, 2001)

### 1.3. Multiaxial fatigue

Equivalent stress procedures are useful in evaluating non-welded base metal or in case where complex loadings may not be decomposed. In the case of welded plates, the equivalent stress approach is also interesting for the verification in terms of notch stress approach (Susmel et al., 2011). In terms of the Hot-Spot method, the multiaxial normal-shear stress interaction has been investigated by (Bäckström, 2003). Based on results for fillet weld toe failures a FAT 84 (m=3) classification was proposed for the maximum principal stress range, figure 1.21.

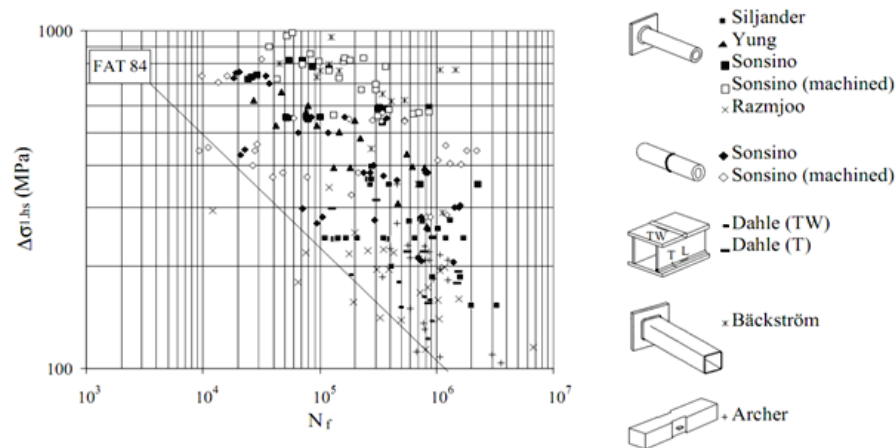


Figure 1.21 – Multiaxial experimental results according to the Hot Spot method (Bäckström, 2003)





## 2 In-plane interaction - Flange crossings

The intersection between beam flanges under uniaxial or biaxial loading is characterised by one of the lowest fatigue categories, FAT40, if no transition radius is adopted, detail 1(a) and 1(b), figure 2.1.

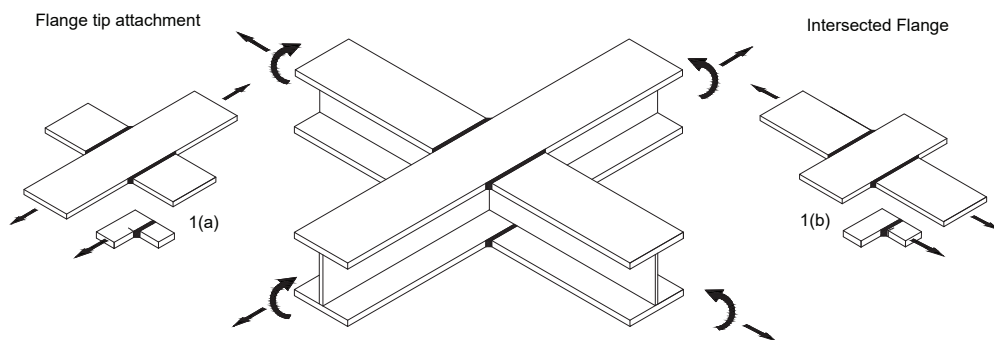


Figure 2.1 – Bridge grillage detail and specimen configuration

It has early been recognised that the fatigue behaviour of the weld between co-planar flanges could be improved by reducing the stress concentration from the sealing weld toe, by tapering or rounding the attachment and further machining the weld, figure 2.2.

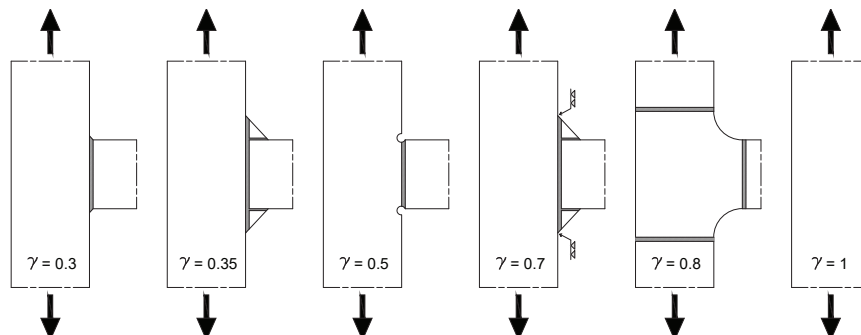


Figure 2.2 – Fatigue improvement by stress concentration reduction (Radaj, 1990)  
( $\gamma$  is a reduction factor for the FAT compared with the reference FAT for flat bars)

## Chapter 2. In-plane interaction - Flange crossings

If the sealing weld profile is rounded by grinding, some improvement of the fatigue resistance is achieved (Gurney, 1979), the same being true for attachments with a drilled hole at each end (Lesniak, 1960), (Miki, 2010). Similar effects have been obtained by spot heating, as experiments in the 50's and 60's showed that this method could introduce local compressive residual stresses at the weld tip, and increase the fatigue strength by 150% (Puchner, 1959), (Gurney and Trepka, 1959), or slightly around 100% at  $2.10^6$  cycles (Gurney, 1962). However, tests were conducted at low stress ratios  $R_\sigma = 0$  and 0.1 and the heating process showed difficult to control, without means of trustfully estimating the residual stress induced.

Research on real scale beams showed that further improvement could be achieved by assembling the flanges with a suitable shaped plate, butt-welded, far away from the stress concentration zone. The lateral sealing fillet weld is eliminated and replaced by a butt-weld, away from the stress concentration zone, with ground edges. Another solution is to add triangular plates before the crossing, this way the stress in the flange is reduced by the tapered plates and edge fillets carefully grounded. These details are recommended by the IIW (2008), figure 2.3.

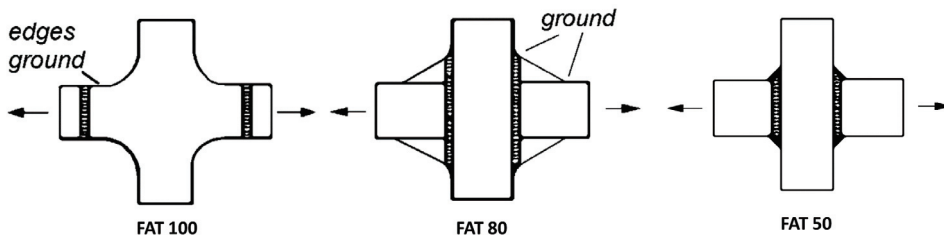


Figure 2.3 – Fatigue improvement with transition plates (IIW, 2008)

Tests performed on beams have shown  $\Delta\sigma_{mean,2.10^6} \approx 60N/mm^2$  in the connection with flanges welded at  $90^\circ$  while for beams with tapered transition plates this value increased to  $\Delta\sigma_{mean,2.10^6} \approx 92N/mm^2$  (Gurney, 1979) (Braithwaite and Gurney, 1967), figure 2.4.

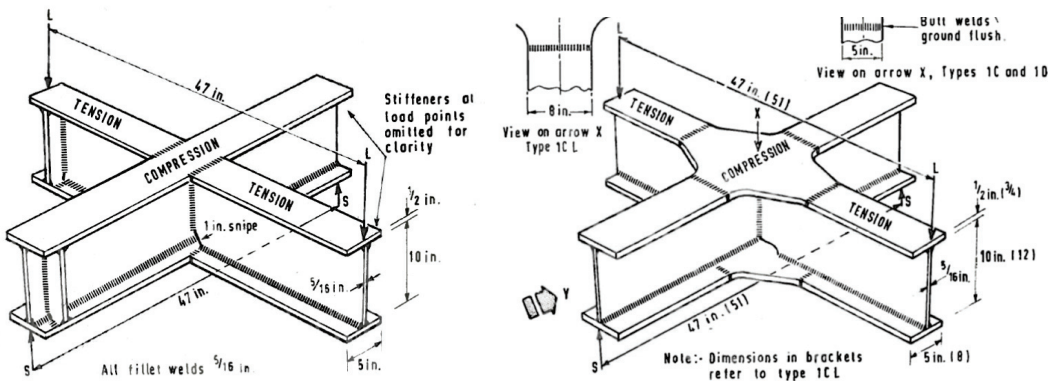


Figure 2.4 – Fatigue tests on welded beams (Braithwaite and Gurney, 1967)

Further tests performed by (UIC/ORE, 1971) compared orthogonal beams with sharp corners and beams using thicker plates with rounded corners to do the intersection. An increase in fatigue strength of about 30% was reported and the detail is recommended in UIC 775 R (1984), figure 2.5.

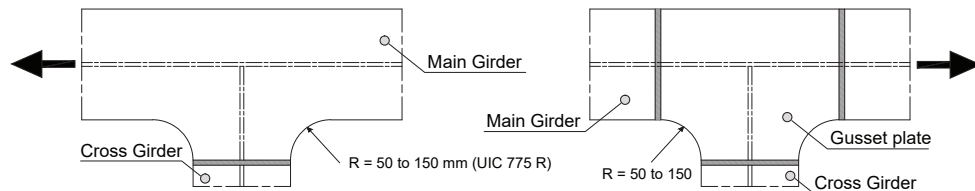


Figure 2.5 – Details for connections between main and cross girders (UIC 775 R, 1984)

The connection between beam flanges is thus usually specified with a transition radius but this solution has a significant economical impact increasing weld length, requiring complex plate geometry and extra grinding work, see figure 2.9. It may be argued that the increase in fabrication costs is compensated by savings in material weight as the allowable fatigue stresses are higher and thinner plates may be used. However, this is only the case if fatigue limit state controls the element design, but the design of modern bridge decks is often driven by deflection and vibration control, defining the deck elements by inertia requirements and not by fatigue. Due to fabrication complexity of the rounded flange transition, the general trend is to adopt flanges welded at  $90^\circ$  whenever possible. They are simple and allow for significant savings on steel fabrication costs. This justifies the attention put on this detail in this thesis.

The detail designation used in this thesis is adopted from (Keating and Fisher, 1986) as “**flange tip attachment**”. Other authors use “in-plane gusset” (Xiao and Yamada, 2004) or “edge gusset” (Niemi, 2000), (Radaj, 1990). Further distinction is made between load and non-carrying load butt welds. The detail with load carrying butt-welds is designated as an “**intersected flange**”.

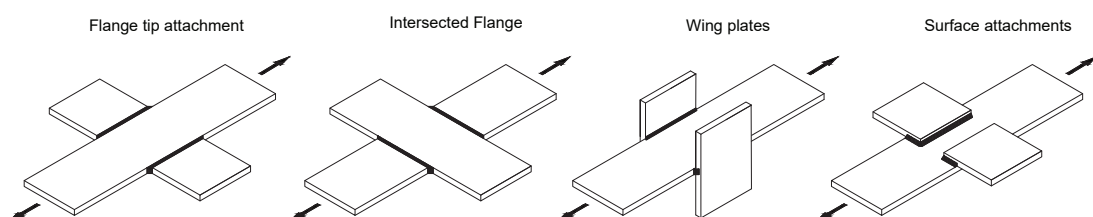


Figure 2.6 – Definition of flange details

### 2.1 Flange tip attachments

The establishment of a relevant fatigue database was the necessary 1<sup>st</sup> step to enable the fatigue classification of flange tip attachments and analysis of the most important parameters. Fatigue tests were collected from several sources and a reasonable amount of tests performed under different test conditions could be found. Some restrictions were however necessary for the pooling of datasets. Only datasets where the original report or article was available were considered and furthermore, only representative steel grades and specimen sizes were kept. It is a common practice to include variable amplitude tests in the form of an equivalent stress range. These are excluded from our database because the aim is to define a constant amplitude reference value in order to discuss variable amplitude results. A detailed description of the datasets collected from literature is presented in Appendix A.2.

A consistent analysis was made in 1973 with the existing results at that time in the British database (Gurney and Maddox, 1973) and an extensive database has also been developed and published in Germany at the “Fraunhofer Institut für Betriebsfestigkeit” at Darmstadt (Olivier and Ritter, 1982). A re-analysis and a database of the existing data was later done at Lehigh University by (Keating and Fisher, 1986). The results included in our database were cross-checked with the German and American databases for the experimental works performed before 1982 and 1986 respectively. Cross check was also made whenever possible with several of the Eurocode Background Documents (Sedlacek et al., 2003), (Stötzel et al., 2007), but these were found not completely coherent.

Several individual datasets confirmed that fatigue life can be considered independent from steel grade. No significant difference between steel grades was found by Haibach (1979) comparing Fe E355 and Fe E460 steels or in (Bae, 2004) where high-strength steels were compared to mild steels. In this later case, authors reported higher crack propagation rates in high-strength steel, concluding that fatigue decreases with higher steel grades, but this remains to be proven.

Flange surface attachments were seen to give very low fatigue lives in general (Hirt, M. A., Crisinel, 1975), (Fisher et al., 1980). These findings were the base for the prohibition of this detail in the AASHTO (2002) Specifications. The behavior of attachments welded on the flange surface is different from the ones welded to the plate edge (Maddox, 2003) and they are thus excluded from our re-analysis.

“Wing plates” were also excluded. Although usually included in the rectangular flange tip attachment category by other authors (Gurney and Maddox, 1973), (Olivier and Ritter, 1982), wing plates give higher propagation rates because while cracks propagate in the main plate the fillet weld in the interior part of the attachment increases the stress intensity factor. More important, is that specimens are often fabricated without the return fillet weld on the main plate thickness, as reported in (Zhang and Maddox, 2009).

2.1.1 Rectangular flange tip attachments

Rectangular flange tip attachments are classified with different FAT categories, according to different Fatigue Standards. The same holds true for Intersected Flanges. The FAT categories are summarised in table 2.1, where differences in FAT up to 25% (in allowable characteristic stress range at  $2.10^6$  cycles) may be found, which means roughly a factor of 3 in life for the high-cycle regime. For details with such a widespread use in bridges, the economical impact of this discrepancies is important.

Standart	FAT	Geometrical conditions	Detail
Eurocode 3 (2005)	40		
IIW (2013) (*)	50	$L_{attach} < 150 \text{ mm}$	
	45	$150 \text{ mm} \leq L_{attach} < 300 \text{ mm}$	
	40	$L_{attach} \geq 300 \text{ mm}$	
AASHTO (2002)	55	$t \leq 25 \text{ mm}$	
	40	$t \geq 25 \text{ mm}$	
DNV (2010)	50	$L_{attach} < 150 \text{ mm}$	
	45	$150 \text{ mm} \leq L_{attach} < 300 \text{ mm}$	
	40	$L_{attach} \geq 300 \text{ mm}$	
UIC 778-1 (1984)	80	$L_{attach} < 100 \text{ mm}$	
	50	$L_{attach} \geq 100 \text{ mm}$	
JSSC (1995)	50	finished weld toe	
	40	as-welded	
SETRA (1996)	56	$R/W \leq 1/6$	
<hr/>			
Eurocode 3 (2005)	40		
IIW (2013)	50		
DNV (2010)	50	$L < 150 \text{ mm}$	
	45	$150 \text{ mm} \leq L < 300 \text{ mm}$	
	40	$L \geq 300 \text{ mm}$	
SETRA (1996)	71	NDT full penetration weld	
	56	full penetration weld	
	36 (**)	partial penetration or fillet welds	

(\*) 1,12 FAT if  $t_{attach} \leq 0,7t$ , (\*\*) Stress on the weld throat

Table 2.1 – FAT for “Rectangular Flange Tip Attachments” and “Intersected Flanges”

Size Effect

The attachment length is the main geometric factor influencing the fatigue resistance of the detail. Longer attachments allow higher load transfers to the attachment, increasing the stress concentration at the weld toe. Fatigue strength is essentially independent from the main plate width and thickness. The thickness of the attachment has however

## Chapter 2. In-plane interaction - Flange crossings

an influence in fatigue life. If the attachment thickness ( $t_2$ ) is smaller than the main plate ( $t_1$ ), the increase in FAT category is estimated in 12%, for any attachment length if  $t_2 < 0.7t_1$ , IIW (2008).

For the classification in nominal stress, the size effect may be accounted for by classifying the fatigue resistance based on the attachment length. Results in database were organised according to the attachment length ( $L_{attachment}$ ), with the FAT categories defined by IIW (2008) in good agreement, see Appendix A.2. For details in bridge design, attachment lengths below 150mm are of little practical importance, so that a simplified FAT category may be defined.

The statistical analysis for the flange tip attachments allows to define them as FAT50, see figure 2.7 and figure A.3. Eurocode 3 classification FAT40 is not justified by tests and was probably set by using  $k_p = 2$  standard deviations while our database with a sample size  $n = 721$  allows for  $k_p = 1.685$ . Note that in this case the CAFL is defined at  $10 \cdot 10^6$  cycles. 21 run-outs ( $N_{run-out} > 10 \cdot 10^6$  cycles) are shown in the plot.

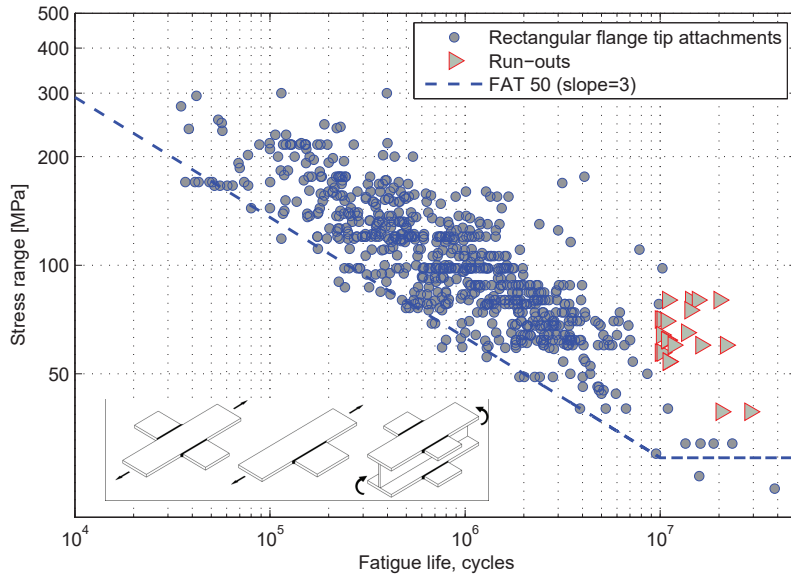


Figure 2.7 – FAT classification for rectangular flange tip attachments

The unified scatter band for fatigue life, represented by a probability of survival  $P_{10\%}$  and  $P_{90\%}$  with  $\mu_x = \pm 1,25\sigma_x$ , is given by  $\frac{1}{T_N} = \frac{N_{10\%}}{N_{90\%}}$  and may be expressed as:

$$\sigma_x = \frac{1}{2,54} \log \frac{1}{T_N} \rightarrow \frac{1}{T_N} = 10^{2,54\sigma_x}$$

The standard deviation  $\sigma_x = 0,3$  obtained by the statistical analysis for a fixed slope  $m = 3$ , figure A.3 leads to  $T_N \approx 5$ . Compared to  $T_N = 4$  as proposed by Haibach

(1968) for the representative scatter at  $2.10^6$ , although higher, is still a reasonable scatter band, considering these pooling conditions. The re-analysis includes tests performed in **9** countries, more than **15** different steel grades and more than **20** different manufacturers with tests performed in the last **50** years. Main plate thickness ranging from 10 to 100 mm and tests performed in beams or flat plates with symmetrical and non-symmetrical attachments, attachments with transition radius  $R < 50$  mm and details in as-welded and slightly quenched states.

An important conclusion from the analysis of the database is the presence of failures under the characteristic CAFL value, and at more than  $5.10^6$  cycles. Failures up to  $6,8.10^6$  cycles were obtained by Yamada and Hirt (1982) in beams with rectangular attachments. Flat plates with lateral attachments were tested in (Kondo and Yamada, 2002) and one failure at very low constant amplitude,  $\Delta\sigma = 24$  MPa was obtained at more than 38 million cycles, clearly the lowest CAFL limit of all database. On the other hand interesting run-outs with  $\Delta\sigma = 23$  MPa and up to 220 million cycles were reported. Yamada and Shigetomi (1989) tested the detail under constant amplitude in the long life regime to define the CAFL and obtained run-outs for tests in beams at  $\Delta\sigma = 39,2$  MPa with no crack initiation observed after more than  $20.10^6$  cycles.

### 2.1.2 Flange tip attachments with transition radius

The severe notch case that characterises the rectangular flange tip attachments can be eliminated by adopting a transition radius between plates. The beneficial effect of a smooth transition radius between the lateral attachment and the tip of the main plate is recognized in the fatigue classification of the Fatigue Design Codes, table 2.2. Eurocode 3 and IIW Recommendations allow an increase to FAT90 with the classification being dependent on the ratio between the transition radius (R) and the main plate width (W). In Eurocode 3, since the “zero” radius classifies as FAT40, a minimum 50mm radius should be required for the FAT50 category, and not only a R/W minimum value, since a simple weld toe grinding has not been shown to increase the detail from FAT40 to 50. This is done in AASHTO (2002) where the detail classifies as a FAT40 if  $R < 50$ mm, which is the reference for rectangular flange tip attachments without any transition radius.

The analysis of the database shows that no real improvement can be achieved by minor re-shaping of the attachment or by grinding the sealing fillet weld of a rectangular attachment. The minimum radius to allow an increase on the FAT category should be fixed at 50 mm. The effect of shaping the attachment weld toe is very small unless the weld toe is also completely ground removing the weld toe concentration and most importantly, its imperfections. The effects of grinding can even be unfavorable, as reported in cases where sub-surface defects appear on the surface after grinding (Miki, 2010), (Keating and Fisher, 1986).

## Chapter 2. In-plane interaction - Flange crossings

The lack of good shape and removal of weld toe imperfections is also the main reason why no improvement can be achieved with tapered attachments because the weld toe and its imperfections are not eliminated. Several experimental programs showed that no significant difference was achieved when comparing tests on rectangular and tapered attachments (Puchner, 1959), (Haibach, 1979), (Comeau and Kulak, 1979).

Standard	FAT	Geometrical conditions	Detail
<b>Eurocode 3 (2005)</b>	90	$R/W \geq 1/3$ or $R \geq 150\text{mm}$	
	71	$1/6 \leq R/W < 1/3$	
	50	$R/W < 1/6$ (*)	
<b>IIW (2013)</b>	90	$R/W \geq 1/3$	
	71	$1/6 \leq R/W < 1/3$	
	50	$R/W < 1/6$	
<b>AASHTO (2002)</b>	110	$R \geq 600$ mm	
	71	$150 \text{ mm} \leq R < 600$ mm	
	56	$50 \text{ mm} \leq R < 150$ mm	
	40	$0 \text{ mm} < R < 50$ mm	
<b>DNV (2010)</b>	80	$R/W \geq 1/3$ or $R \geq 150\text{mm}$	
	71	$1/6 \leq R/W < 1/3$	
	63	$1/10 \leq R/W < 1/6$	
	56	$1/16 \leq R/W < 1/10$	
	50	$1/25 \leq R/W < 1/16$	

(\*)  $R \geq 50$  mm should be specified

Table 2.2 – FAT classification for “Flange Tip Attachments with Transition Radius”

Within this work, new fracture mechanics calculations are carried out and a simplified FAT category is defined, by fitting the characteristic value of each test batch performed at a defined  $R/W$  ratio. Our re-analysis of rectangular attachments proposed a FAT50, and consequently a unified classification may in this case be defined as  $FAT=50(1 + R/W)$  valid for both types of attachments, figure 2.8.

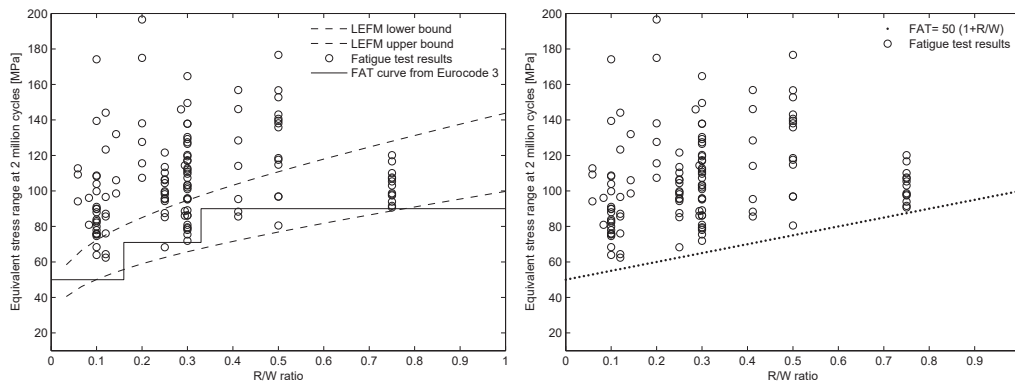


Figure 2.8 – FAT category for flange tip attachments with transition radius



## 2.1. Flange tip attachments

The transition radius should ideally have  $1/3$  of the plate width (ECCS, 2000) or a minimum of 150mm, and in any case higher than 50 mm as recommended by (UIC 775 R, 1984). The transition should be shaped on the attachment plate by machining or flame cut, prior to welding, leaving a strip on the edge with a minimum height of 50mm to be welded on the main plate. The final shape is achieved by grinding after weld, to completely remove the weld toe flaws and imperfections (SETRA, 1996), figure 2.9.

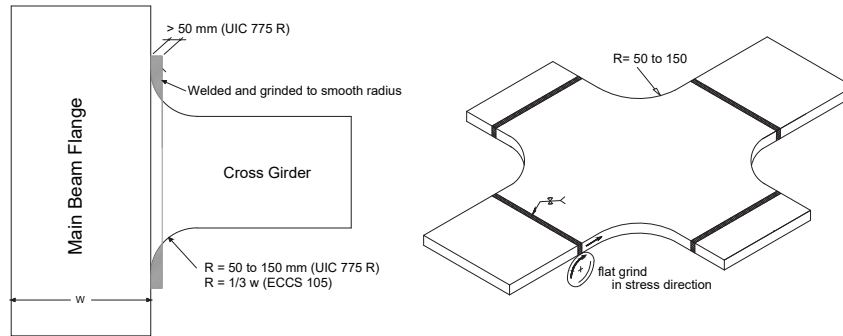


Figure 2.9 – Detail for flange tip attachments with transition radius

### 2.1.3 Summary of conclusions

- Fatigue life of flange tip lateral attachments can be considered independent from steel grade.
- Fatigue classification in nominal stress can take into account the effect of the flange tip attachment length. IIW's classification is in good agreement with the fatigue database.
- The influence of attachment thickness ( $t_2$ ) being smaller than the main plate ( $t_1$ ), may be accounted by increasing 12% the FAT category, if  $t_2 < 0,7t_1$ , for any attachment length.
- The classification of rectangular flange tip attachments can be updated to FAT50 independently from the attachment length. For attachments with transition radius, a simplified FAT relationship may be defined as  $FAT=50(1 + R/W)$  with  $R \geq 50$ mm. These conclusions are based on the re-analysis of the experimental database. It will be seen in Section 2.6 that a probabilistic approach shows that these values are too high.
- The characteristic CAFL value is below the conventional endurance limit at  $N_D=5.10^6$  cycles. It should be defined at  $10.10^6$  cycles with  $\Delta\sigma_D = 29,2$  in a FAT50 S-N curve with slope  $m=3$ .

## 2.2 Experimental setup

Flange Tip Lateral Attachments and Intersected Flanges were tested with different load conditions, on flat specimens under pure tensile loads, simulating beam flanges, as previous tests showed to be a reasonable assumption (Gurney, 1979), (Yamada and Sakai, 1986). “Test Setup 1” involved a total of **40** tests, covering the uniaxial behaviour, both under constant and variable amplitude, at very high number of cycles and relatively low stress ranges, in a regime dominated by threshold behavior and initiation (Smith and Smith, 1983), see also Section 2.6. “Test Setup 2” involved **5** multiaxial tests, under non-proportional constant amplitude loading on flange crossings, at a relatively high stress range in order to have notch stresses higher than the threshold and clearly in the propagation domain.

### 2.2.1 The matrix of experiments

“Flange Tip Lateral Attachments” were first tested under constant amplitude loads, table 2.3, with the aim of extending the existing database over the range from 2 to  $10 \cdot 10^6$  cycles, considering that the fatigue curve was well established with the existing database of fatigue results in the range below  $2 \cdot 10^6$  cycles. These tests enabled the definition of the propagation threshold for constant amplitude, the CAFL, important to understand the variable amplitude tests that followed. **6** tests were performed on the geometry shown in figure 2.10. The constant amplitude experimental matrix was complemented with **10** tests on “Intersected Flanges”, table 2.3, with the geometry shown in figure 2.10.

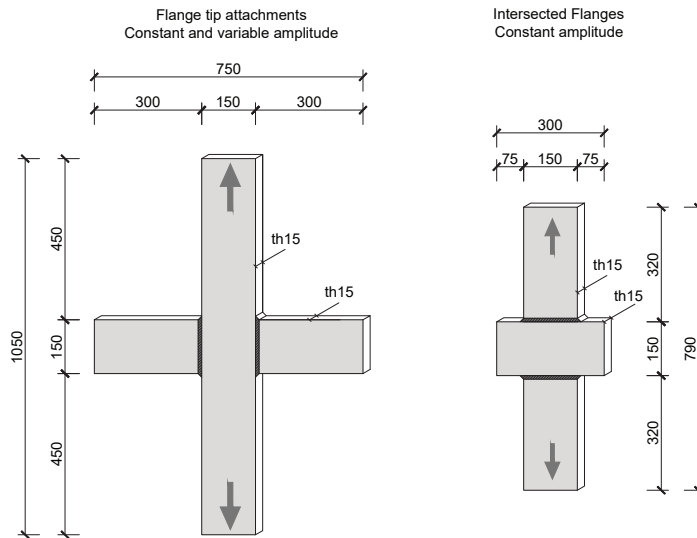
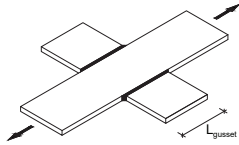


Figure 2.10 – Geometry of specimens in Test Setup 1

These tests aimed to investigate the difference in fatigue behavior between “Flange Tip Lateral Attachments” and “Intersected Flanges”, previously revealed by the analysis of

## 2.2. Experimental setup

the database with the existing fatigue tests from literature. All tests were conducted at high stress ratios  $R_\sigma \geq 0,5$  to get consistent results, eliminating the residual stress as a parameter, and possible crack closure effects or effective stress range variations.

$\Delta\sigma$ [MPa]	$R_\sigma$	frequency [Hz]	N° of tests	Lateral Attachment
100	0,5	5	2	
50	0,5	15	3	
25	0,5	15	1	

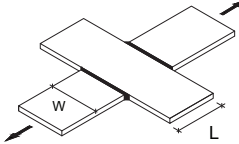
$\Delta\sigma$ [MPa]	$R_\sigma$	frequency [Hz]	N° of tests	Intersected Flange
100	0,5	5	2	
50	0,5	15	3	
45	0,72	15	3	
40	0,75	15	2	

Table 2.3 – Matrix of experiments for constant amplitude tests

The same geometry was used for **23** tests under variable amplitude block loading, with the number of cycles ranging from 10 to 70 million cycles, with the following objectives:

- Investigate the fatigue damage contribution of cycles below the Constant Amplitude Fatigue Limit in spectrum loading
- Measure initiation life under variable load histories and crack propagation rates at several stress levels below the CAFL using ACPD crack propagation measurements

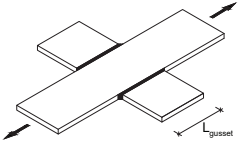
N° of tests	Stress Amplitude $\Delta\sigma$ [MPa]										Lateral Attachment
	100	80	60	50	40	30	20	15	10		
2	x				x	x					
2	x	x	x								
3		x			x	x					
3		x		x	x						
2		x	x	x							
4			x		x	x					
2			x	x	x						
3				x	x	x					
1					x	x	x				
1	x	x	x	x	x	x	x	x	x	x	

Table 2.4 – Matrix of experiments for variable amplitude tests

## Chapter 2. In-plane interaction - Flange crossings

A “stalactite” load sequence was adopted for the variable amplitude load history, by cycling all stress ranges down from a constant maximum tensile stress. This eliminates mean stress effects from the results, and is coherent with the constant amplitude tests at  $R_\sigma \geq 0,5$  (Tilly and Nunn, 1980) (Ohta et al., 1994).

“Test Setup 2” included 5 exploratory tests under non-proportional multiaxial loading to simulate flange crossings with the geometry shown in figure 2.11. These tests were carried out at relatively high stress ranges  $\Delta\sigma=100\text{MPa}$  and  $R_\sigma=0,5$  with notch stresses higher than the threshold and clearly in the propagation domain (Smith and Smith, 1983).

The objective of these non-proportional multiaxial tests was to investigate the notch stress, perpendicular to the load direction to characterise the multiaxial effect.

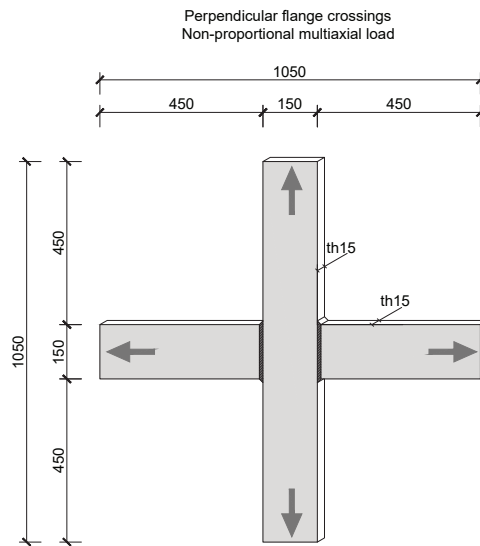


Figure 2.11 – Geometry of specimens in Test Setup 2

### 2.2.2 Specimens

All specimens were fabricated at ICOM laboratory by the author, with commercial flat bars  $150 \times 15 \text{ mm}^2$  in steel grade S235JR.

The welding procedure adopted is summarised in table 2.5. Each pass is made in 2 steps, from the edges to the middle of the plate. The central part of the butt weld is the last to cool down so that compressive residual stresses may be expected on the edges. This procedure with the start/stop position in the center of the plate also avoids end craters at the critical plate edge. The full weld is composed by eight passes, made alternately on each side to minimise distortion. MAG process was used because it is of widespread use in bridge construction. The welding is considered representative of typical bridge

## 2.2. Experimental setup

details because fatigue life of welded specimens is relatively independent from the welding process, provided the execution quality is the same.

MAG 136 - Welding procedure for butt welds		
Steel grade	S235 JR	thickness 15mm
Filler material	OK autorod 12.51	thickness 1mm
<div style="display: flex; justify-content: space-around; align-items: flex-start;"> <div style="text-align: center;"> <p>K-joint chamfer</p> </div> <div style="text-align: center;"> <p>Welding pass</p> </div> <div style="text-align: center;"> <p>Weld sequence</p> </div> </div>		
Type of gaz	82%Argon/18%CO2 (M21) Arcal 5	
Debit	15 liters/minute	
Position	Horizontal	
Polarity	DC+	
	Root pass	2 <sup>nd</sup> , 3 <sup>rd</sup> , 4 <sup>th</sup>
Voltage [V]	23	24
Wire speed [m/min]	5	8.8
Current [A]	140	200
Welding speed [cm/min]	17	20
Pre heating [deg]	No	No
Inter-pass temperature [deg]	<250	<250

Table 2.5 – Welding procedure for Flange Tip Attachments and Intersected Flanges

All plates were cut and chamfered in a water cooled continuous saw machine. For the assembly and welding, plates were aligned, joined with small tack weld points, and a “rigidifying beam” is welded over the plates on **Side B** in order to do the first two weld passes on **Side A**, figure 2.12. The root and 2<sup>nd</sup> filling pass are done (out of the total of 4) on side **Side A**, opposite to the rigidifying beam, figure 2.13. All passes are ground, cleaned, and inspected visually and with dye penetrant, before the next one is done.

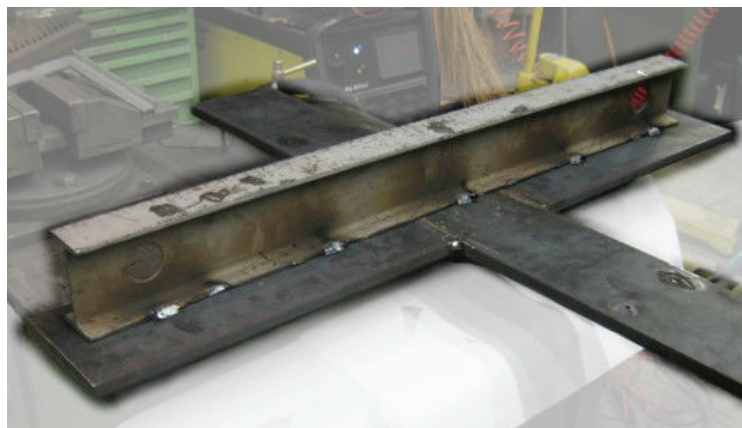


Figure 2.12 – Rigidifying beam welded over the butt-welded plates **Side B**

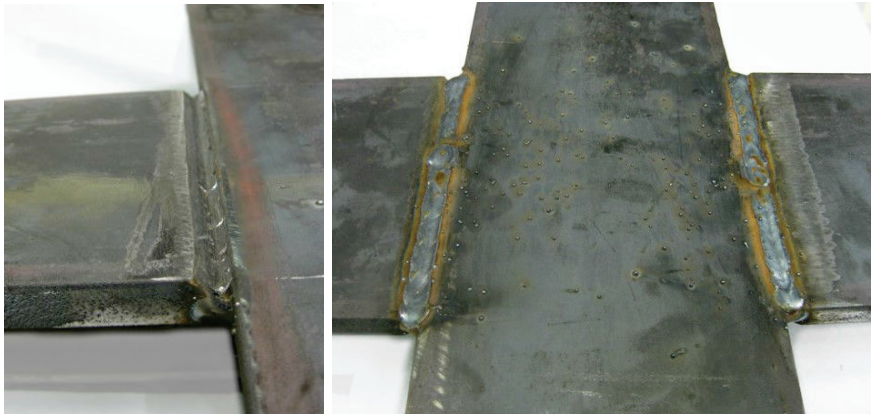


Figure 2.13 – Root and 2<sup>nd</sup> pass before grinding (Side A)

After the 2<sup>nd</sup> pass is finished, a new “rigidifying beam” is welded on **Side A**, the specimen is turned, and the total 4 passes on **Side B** are done. This procedure avoids angular distortions due to the weld shrinkage. After turning and taking the 1<sup>st</sup> rigidifying beam out on **Side B** one can see the root pass done from **Side A**, figure 2.14.

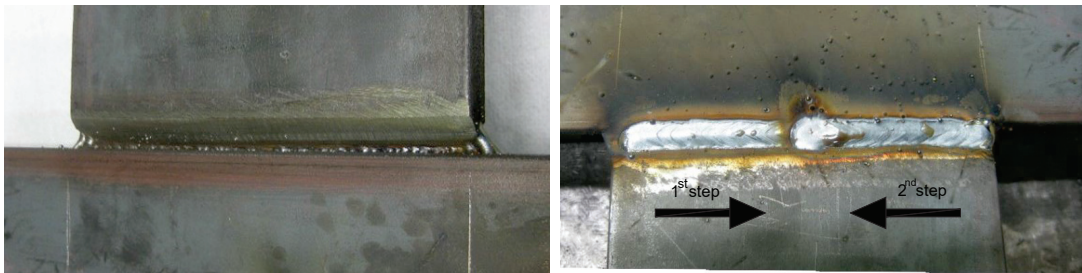


Figure 2.14 – Root pass from **Side A** and 2<sup>nd</sup> pass on **Side B**

After the four weld passes are completed on **Side B**, the rigidifying beam is welded again, allowing the last two last passes from **Side A** to be finished. This procedure assures that the plates remain in-plane, reducing the misalignments. After completion and cooling, the welds are ground flush.



Figure 2.15 – Welds flush ground and sealing fillet welds done with auxiliary plates



## 2.2. Experimental setup

The finishing sealing fillet welds along the thickness of the plate, are done with the aid of auxiliary “run-on run-off” plates, allowing the weld pass to start and stop on these plates, figure 2.15. This leaves a clean fillet on the specimen thickness and avoids magnetic edge effects. The auxiliary plates are removed after completion of the fillet welds, plates are ground flush and the specimen is left in the as-welded condition.

All specimens from “Test Setup 1” and “Test Setup 2” were produced in the same way and tested on a servo-hydraulic machine “Schenck” 100 ton, 50 ton in dynamic regime, figure 2.16. Applied loads were measured from the load cell on the machine base and controlled with measurements from strain gauges, placed on undisturbed areas of the specimen, away from the weld toe. All specimens were equipped with an electrical potential drop technique in order to get initiation and propagation curves.

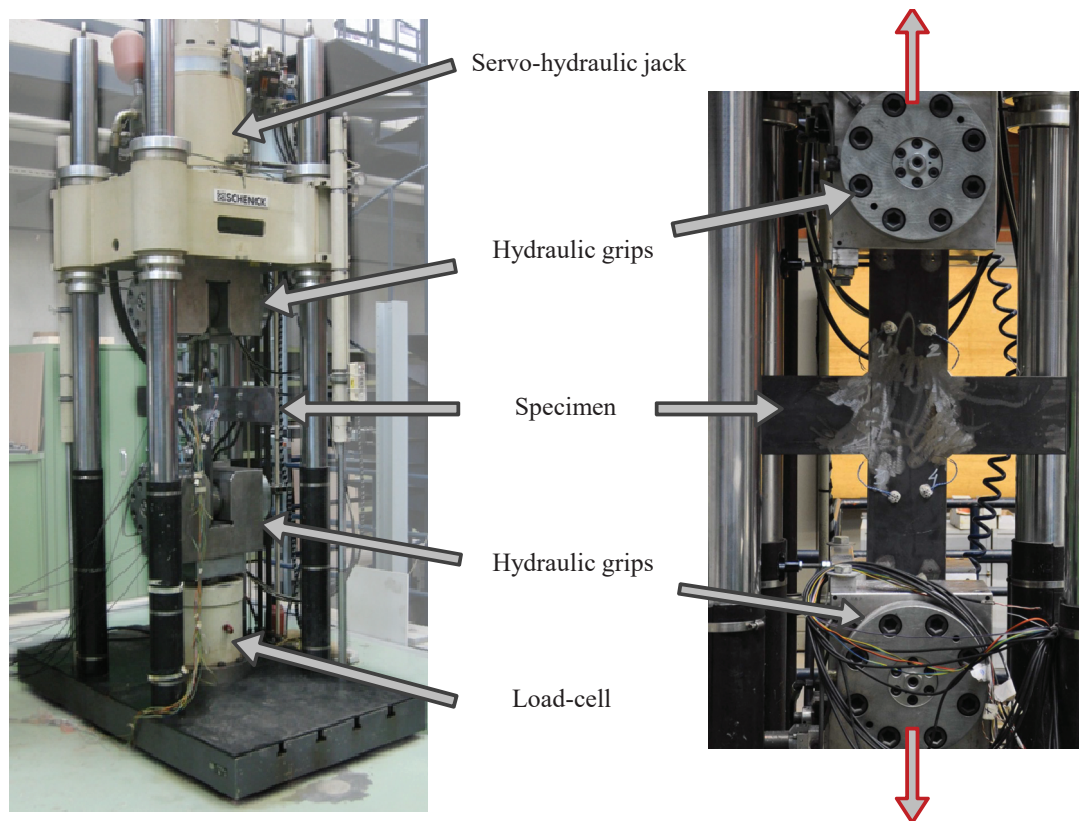


Figure 2.16 – Test machine “Schenck” 100 ton used for the fatigue tests

### 2.2.3 The Alternating Current Potential Drop (ACPD)

The potential drop technique is based on the principle that a conductive specimen exhibits a voltage drop if its resistance is changed by the presence of a surface crack or defect. Specially for cracks propagating under cyclic loads, if a constant electric current is kept, the measurement of the electrical potential drop due to the change in resistance of the

## Chapter 2. In-plane interaction - Flange crossings

specimen, allows the detection of the initiation and monitoring of the crack propagation. The method is non-destructive with two variants, depending on the type of current, either direct or alternating.

The Alternating Current Potential Drop (ACPD) technique was used to measure the change in electric potential during the fatigue tests performed on “test setup 1” and “test setup 2”. A constant alternating current is established between the two extremities of the specimen,  $I_{input}$  and  $I_{output}$ , as schematically shown in figure 2.17.

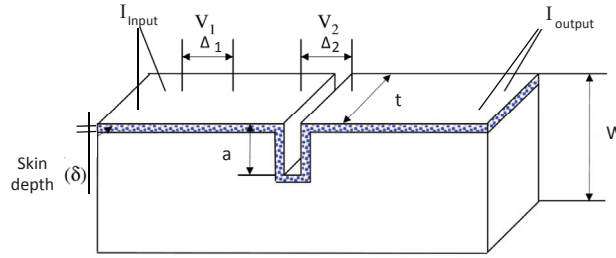


Figure 2.17 – ACPD schematic representation

The alternating current flows through the metallic specimen on a peripheral superficial layer, a phenomena called ‘skin effect’ (Saguy and Rittel, 2007). The skin depth ( $\delta$ ) depends on the conductor’s properties and the frequency of the alternating current, and may be approximated by equation 2.1:

$$\delta = \frac{1}{\sqrt{\pi \mu_r \mu_0 \sigma_e f}} \quad (2.1)$$

where:

$\delta$  is the skin depth [mm]

$\mu_r$  is the relative magnetic permeability

$\mu_0$  is the magnetic permeability of the free space [H/m]

$\sigma_e$  is the electric conductivity of the material [S/m]

$f$  is the current frequency [Hz]

If the conductor has a surface crack with depth ( $a$ ), the current has to flow around the crack, and the voltage ( $V_2$ ) can be measured by a fixed probe with distance  $\Delta_2$  between the electrodes. If a reference probe is welded in an undisturbed area of the conductor, a reference voltage ( $V_1$ ) is measured and the potential drop due to the presence of the crack ( $V_2/V_1$ ) is translated into crack depth ( $a$ ) by a theoretical transfert function or by calibration. The method relies on the relative potential change so that the absolute value of the material resistance or voltage is not required.

The equivalence between potential drop and crack depth depends on the flow conditions, especially on the current frequency and on the relation between “skin depth” ( $\delta$ ) and the crack depth ( $a$ ) defining two theoretical flow models, “thin” and “thick” skin conditions.



“Thin skin” conditions are generally obtained at high frequency of current, when the current flows in a very thin superficial layer. This condition is schematically represented in figure 2.17 in which case the crack depth ( $a$ ) may be obtained by the proportionality expressed in equation 2.2:

$$\frac{V_1}{\Delta_1} \propto \frac{V_2}{(\Delta_2 + 2a)} \quad (2.2)$$

If the distance between electrodes of each probe is the same ( $\Delta$ ) or if the potential readings ( $V_1$  and  $V_2$ ) are done in the same probe with electrodes around the crack, the indices 1 and 2 refer to two different time steps in this case, the crack depth for “thin skin” conditions is estimated by equation 2.3:

$$V_1 \Delta_1 \propto V_2 (\Delta_2 + 2a) \Rightarrow a = \frac{\Delta}{2} \left( \frac{V_2}{V_1} - 1 \right) \quad (2.3)$$

Under “thick skin” conditions, an expression for the crack depth ( $d$ ) was defined by (Michael and Collins, 1982), equation 2.4. According to (Saguy and Rittel, 2007) the following expression gives a lower bound for the crack depth:

$$a = \frac{\Delta}{2} \left( \frac{V_1}{V_2} \right)^{1/2} \left( \frac{V_2}{V_1} - 1 \right) \quad (2.4)$$

An expression accounting for the transition regime between “thin” and “thick” skin was proposed by (Saguy and Rittel, 2005):

$$\frac{V_2}{V_1} = \frac{\Delta + 2a - f_1(\Delta, \delta) - f_2(a, \delta)}{\Delta} \quad (2.5)$$

$$f_1(\Delta, \delta) = \Delta \cdot e^{-\frac{(\Delta/2)+\delta}{\delta}} \quad f_2(d, \delta) = 2a \cdot e^{-\frac{a+\delta}{\delta}} \quad (2.6)$$

Functions  $f_1$  and  $f_2$  represent the “corner effect” for the flow around the crack:  $f_1$  compensates the decrease of voltage on the surface;  $f_2$  compensates the decrease of voltage on the crack plane. Equation 2.5 gives non-zero values for ( $V_1 = V_2$ ) because  $f_1(\Delta, \delta)$  is constant for each specimen (slight variations for  $\Delta$  exist from specimen to specimen, otherwise  $f_1(\Delta, \delta)$  would be a constant for all specimens).

According to (Saguy and Rittel, 2005) “thin skin” flow may be considered if the following conditions are met:

$$\frac{w}{\delta} > 10, \quad \frac{a}{\delta} > 10, \quad \frac{t}{a} > 10 \quad (2.7)$$

The ACPD equipment available at the ICOM/IIC laboratories allows to record up to 8

## Chapter 2. In-plane interaction - Flange crossings

channels with current intensity of 50, 150 or 300 A (150 Amperes were used) at a frequency of 5 Hz. Using equation 2.1, the skin depth for a 5Hz alternating current is  $\delta = 4,18$  mm using the electrical properties taken from (Blitz, 1997):  $\mu_r=500$ ,  $\mu_0 = 4\pi \cdot 10^{-7} [\frac{H}{m}]$ ,  $\sigma = 5,8 \cdot 10^6 [S/m]$ . Conditions of equation 2.7 are not met for 5Hz current and cracks ranging from 0,1mm to 50mm. Mixed flow conditions between “thin” and “thick” skin have to be considered.

$$\frac{w}{\delta} = \frac{150}{4,18} = 35,88 > 10, \frac{a}{\delta} = \frac{a}{4,18} > 10 \Rightarrow a > 42mm, \frac{t}{a} = \frac{15}{a} > 10 \Rightarrow a < 1,5mm$$

The geometric and electrical flow conditions not being purely “thin skin”, required a calibration test to fit the crack depth estimation theories to the real current flow conditions achieved in our setup . The test was performed on a “Flange Tip Lateral Attachments” configuration, figure 2.10.

Taking advantage of the fact that a modification of the load amplitude, or frequency, produces a “beach-mark” on the crack surface, by producing several “beach-marks” at regular intervals, it becomes possible to trace back the crack front by analyzing the crack surface after failure. A block loading with 2 steps of 50.000 cycles each, was applied with stress range  $\Delta\sigma_1 = 100$  MPa and  $\Delta\sigma_2 = 50$  MPa keeping the test frequency constant at 5Hz, figure 2.18. To avoid stress relaxation or overloading retardation phenomena, the maximum stress was kept constant at  $\sigma_{max} = 200$  MPa with the stress ratio  $R_{\sigma_1} = 0,5$ .

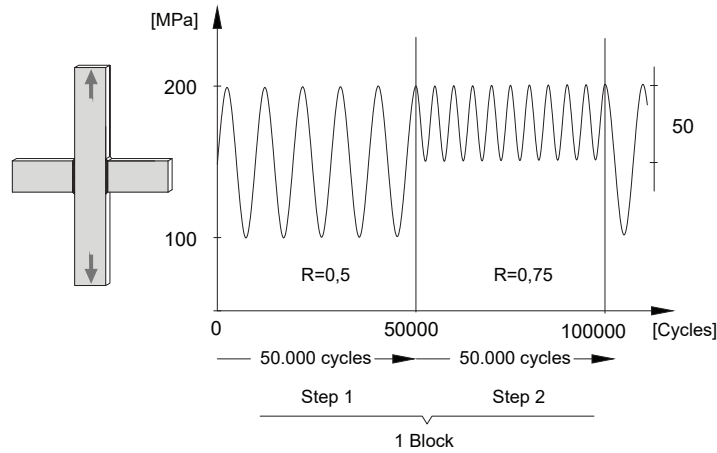


Figure 2.18 – Calibration test: Definition of block loading

Figure 2.19 shows the ACPD location and the fracture surfaces obtained, with the corresponding beach-marks identified after failure.

The measured potential values are shown in figure 2.20 where it can be seen that weld toes 1, 3 and 4 had cracks. The “raw” potential values as measured have some noise due to the difference between the acquisition and the sinusoidal load frequency. A moving

## 2.2. Experimental setup

average filter is applied to the measured potential values with a sample of 51 points corresponding to a lapse of approximately 7650 cycles. A potential (V) versus time is obtained. A close snapshot of the filtered data versus “raw” data is shown in figure 2.20.

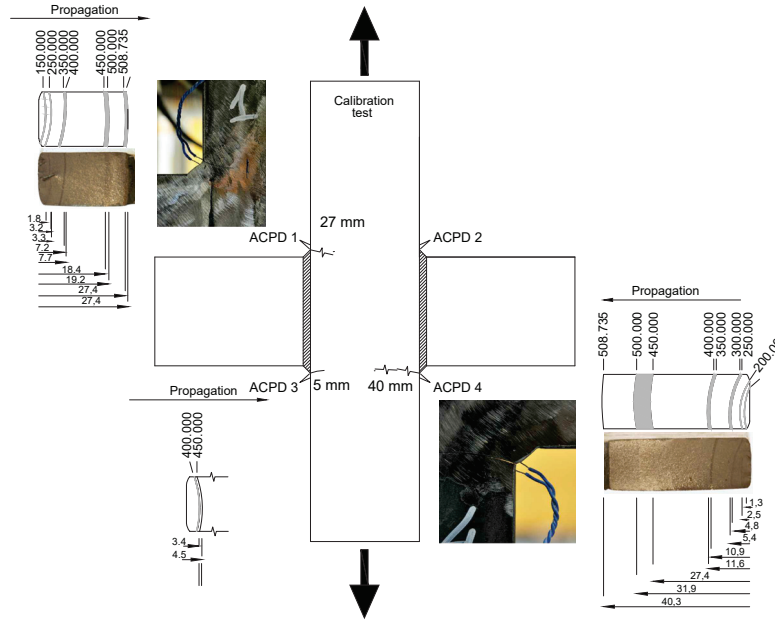


Figure 2.19 – Calibration test: ACPD probes and beach-marks on crack surfaces

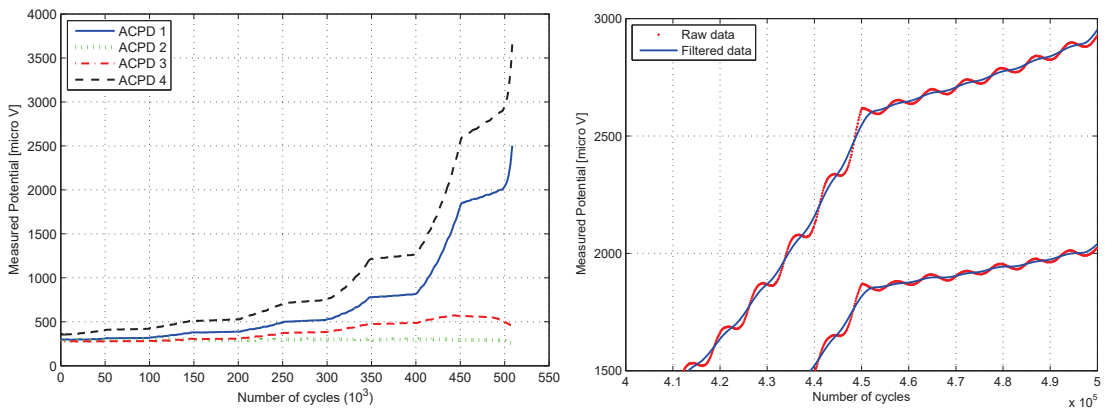


Figure 2.20 – Calibration test: ACPD measured potential values and filtered data

The estimated crack depth ( $a$ ) versus number of cycles ( $N$ ) according to the different flow theories are shown in figure 2.21. The crack depth ( $a$ ) is estimated with the “thin skin” theory, equation 2.3, the “thick skin” theory, equation 2.4 and the equation 2.5 for the transition regime. The best fit with the measured crack depths is obtained by the “thin skin” theory with a correction factor of 2,2 shown in figure 2.22.

$$a = \alpha \frac{\Delta}{2} \left( \frac{V_2}{V_1} - 1 \right) \text{ with } \alpha = 2,2 \quad (2.8)$$

## Chapter 2. In-plane interaction - Flange crossings

An iterative formula for the step by step calculation of the crack depth is given by:

$$a_{i+1} = \alpha \left( \frac{\Delta}{2} \left( \frac{V_{i+1}}{V_i} - 1 \right) + \frac{V_{i+1}}{V_i} a_i \right) \quad (2.9)$$

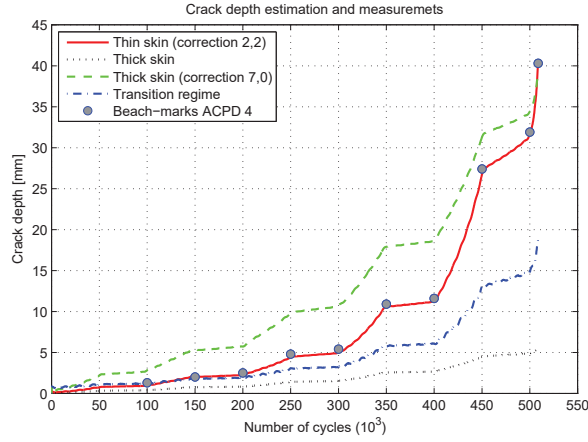


Figure 2.21 – Calibration test: Estimated crack depths with different flow equations

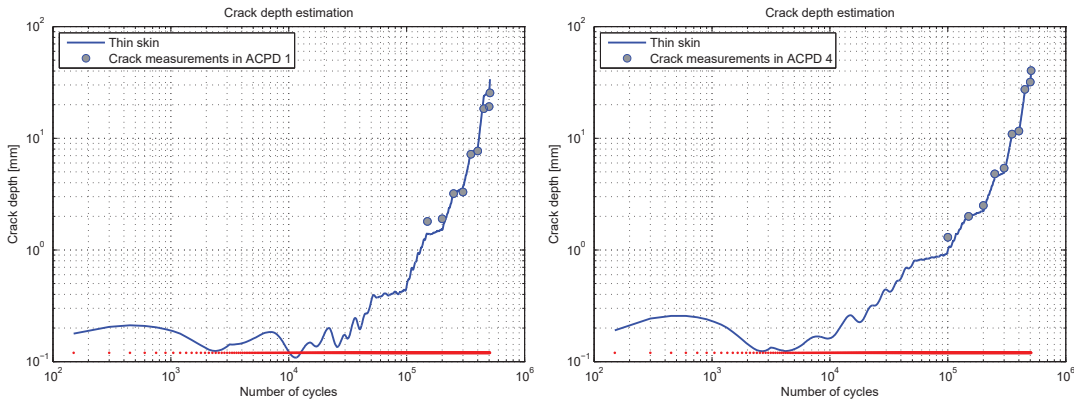


Figure 2.22 – Calibration test: Estimated crack depths (log-log scale)

The treatment of the measured potentials for the fatigue tests presented in the following sections follows a 3 step procedure:

- 1** - Measured potential values are filtered with a “moving average algorithm” (sample points depending on each test). The potential ( $V$ ) versus number of cycles ( $N$ ) is obtained.
- 2** - Crack depth ( $a$ ) is estimated with the calibrated equation 2.8. The crack depth ( $a$ ) relation versus number of cycles ( $N$ ) is obtained.
- 3** - Crack growth rate is obtained by derivation of the crack depth ( $a$ ) curve. Crack growth rate ( $da/dN$ ) versus number of cycles ( $N$ ) can be plotted.

## 2.3 Exploratory tests under multiaxial load

The bridge deck grillage detail as shown in figure 2.1, may be subjected to biaxial loadings, with each beam flange under proportional or non-proportional cyclic or static loads. At the intersection between beam flanges, the sealing weld toe is under a co-planar biaxial stress state  $(\sigma_1, \sigma_2)$  which may reduce the fatigue strength of the uniaxial detail, figure 2.23. No specific provisions exist for the fatigue assessment of the detail under these conditions, so the fatigue behavior is verified for the nominal uniaxial stress on each flange independently, without accounting for the local bi-axial stress state.

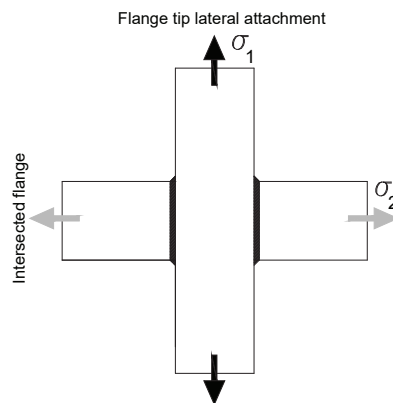


Figure 2.23 – Schematics of the biaxial loads

Literature results on orthogonal beams under biaxial loads are scarce, but they generally showed that the fatigue strength under proportional biaxial loading was not lower than under uniaxial loads (Braithwaite and Gurney, 1967) (UIC/ORE, 1971).

A numerical analysis with a notch approach, shows that the local stress at the weld toe, has indeed some influence of the multiaxial load condition. In view of these results, five exploratory tests were made under non-proportional loads where the beam crossing detail was simulated by a simple flange intersection specimen as figure 2.23 ( $\sigma_1$  refers to lateral attachments and  $\sigma_2$  to intersected flanges). The objective of the tests was to separately measure the influence of each stress component ( $\sigma_1, \sigma_2$ ) on crack growth, calibrate the ACPD measurement procedure and the test procedure in general, for the subsequent constant and variable amplitude tests on this detail.

Similar specimens were tested by Yamada et al. (1998b). Lateral attachments were loaded with cyclic constant amplitude  $\Delta\sigma_1$  and constant static stress  $\sigma_2 \approx \pm 100\text{MPa}$ , both tensile or compressive. Tests were also performed on Intersected flanges (Yamada et al., 1998a) with cyclic  $\Delta\sigma_2$  and constant  $\sigma_1 \approx \pm 100\text{MPa}$ , again tensile or compressive. Results showed the biaxial static forces have little effect on the fatigue strength in the as-welded conditions. For stress-relieved welds, transversal compressive static forces increased fatigue life while tensile static forces had little influence.

2.3.1 Test setup

The experiments under non-proportional multiaxial loading were conducted using the geometry shown in figure 2.11. All 5 tests were carried out with the same load conditions:

- Max load .....450 kN ( $\sigma = 200$  MPa)
- Min load .....225 kN ( $\sigma = 100$  MPa)
- Load range .....225kN ( $\Delta\sigma=100$  MPa)
- $R_\sigma$  .....0,5
- frequency ..... 5Hz (sinusoidal shape signal)

The multiaxial load is applied by blocks of 50.000 cycles, in two stages as shown in figure 2.24. During the 1<sup>st</sup> stage, cracks propagate from the weld toe through the plate width, perpendicular to the principal stress. During the 2<sup>nd</sup> stage, with the specimen rotated at 90°, these cracks are approximately parallel to the stress field.

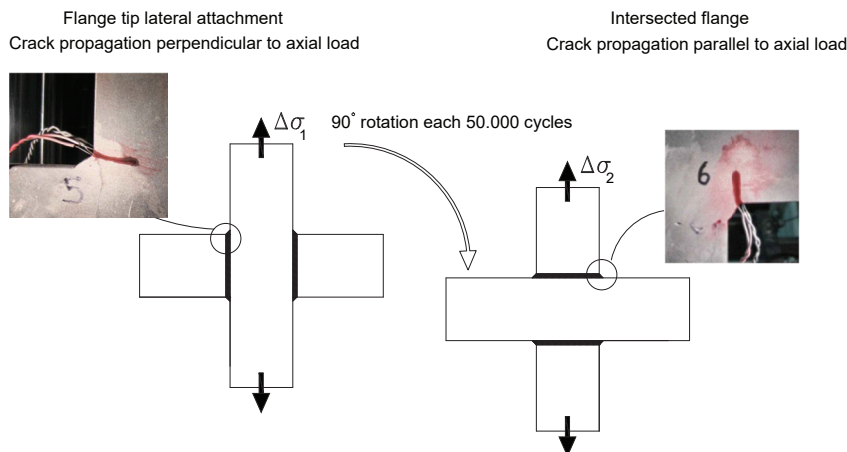


Figure 2.24 – Test kinematic for Test Setup 2

Each test started as Lateral attachment configuration and after several rotations, it achieved failure. The number of cycles to failure consist on blocks of 50.000 cycles. Under the Intersected flange configuration, after the last rotation, it was decided to leave the specimens in the same orientation up to failure, table 2.6.

Specimen	Stress Amplitude $\Delta\sigma$ [MPa]		crack size [mm]		Blocks to failure
	$\Delta\sigma_1=100$	$\Delta\sigma_2=100$	$a_{failure}$		
	Stage LA	Stage IF	Stage LA	Stage IF	
ts2-sp1	300.000	250.000	45 (ACPD4)	45 (ACPD6)	6
ts2-sp2	350.000	600.000	42 (ACPD3)	31 (ACPD5)	7
ts2-sp3	350.000	400.000	27 (ACPD1)	28 (ACPD5)	7
ts2-sp4	300.000	481.000	26 (ACPD3)	37 (ACPD7)	6
ts2-sp5	400.000	648.000	25 (ACPD1)	24 (ACPD8)	8

Table 2.6 – Experimental results under non-proportional load

### 2.3. Exploratory tests under multiaxial load

Each of the eight weld toes was monitored with ACPD probes and crack growth readings performed in continuous up to failure. Crack growth curves obtained in this way show the clear demarcation between each non-proportional stage. Figure 2.25 shows the example for the critical crack under flange tip attachment configuration (i.e.  $\Delta\sigma_1$  cyclic). The ACPD curves for the other specimens are presented in Appendix C.3.

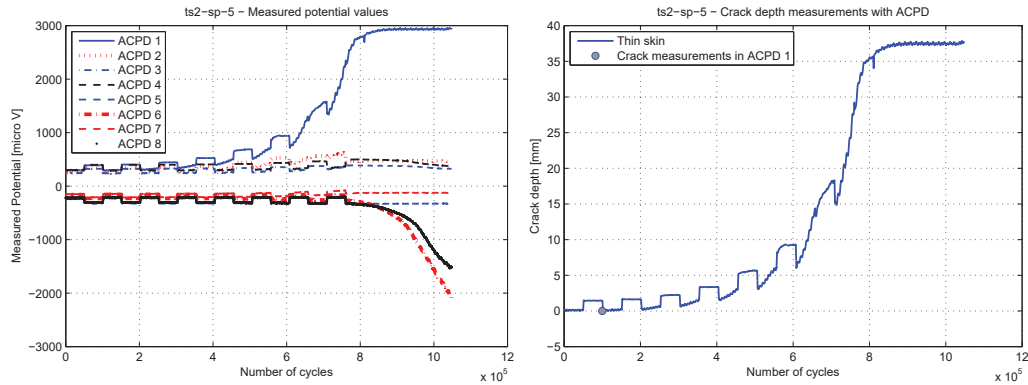


Figure 2.25 – ACPD potential for specimen 5 and crack depth estimate for ACPD1

Some influence under Mode II was observed for very long cracks ( $a > 25$  to 30mm) by optical microscope monitoring during tests. The Mode II activity is also visible on ACPD measurements, but the crack depth is over-estimated by this method. Mode II cracks induce crack front friction which influences the current flow, and some of the crack driving force is also lost in this process. It is concluded that the biaxial load is not expected to have any measurable influence on the crack propagation mechanism, although locally on the notch, the perpendicular stress may decrease initiation life. This is further investigated with a local finite element method analysis.

#### 2.3.2 Analysis of results with local stress approaches

The nominal stress approach based on FAT details is the most practical and widespread design procedure for the fatigue assessment of bridge details. It is limited however to classified details, relatively simple joints and uniaxial load cases. Non classified details, complex connections or multiaxial stress states may alternatively be assessed by finite element methods with local approaches such as the Hot-Spot or the Effective Notch Stress Method. By modeling the local geometry of the detail, global and local stress concentrations are taken into account. These methods rely on fewer generic fatigue resistance curves, which in the case of the Hot Spot Method differentiate only between the weld type (Niemi et al., 2006), while the Effective Notch Stress Method uses a single S-N master-curve (Radaj et al., 2006). Both methods are well established for the analysis of typical bridge details such as flange tip lateral attachments or transversal attachments.

Both the Hot-Spot and the local effective notch method are used in this work. The analysis is done with the same geometry as the tested specimens with the three following load cases:

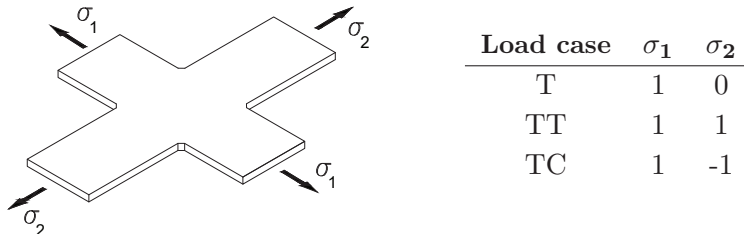


Figure 2.26 – Load cases for the local analysis

### 2.3.3 Hot spot method

The Hot Spot method was originally developed for off-shore tubular structures and later extended to welded plate details (Niemi, 2002). The method and its application may be handled according IIW (2008) or (Niemi et al., 2006). It is based on the structural stress at the potential weld toe crack location, known as the hot-spot. One limitation of the method is the root crack assessment, partly restricted to definite cases of application. In the case of weld root cracks, simple stress extrapolation is not suitable. Alternative approaches use local nominal stress obtained from internal forces or from stress distribution in the weld itself (Fricke, 2013).

The structural stress accounts for the macroscopic stress concentration due to the weld geometry but excludes the local stress peak due to the weld toe notch, that is included in the resistance curve. The hot-spot stress is obtained by extrapolating computed or measured stresses, from two or three points near the weld toe. Two types of hot spots, a) and b) are defined, see figure 2.27.

If the weld toe is placed along the plate width, the non-linear stress concentration due to the weld toe notch, is distributed along the plate thickness. This is Hot Spot Type a) with the interpolation of the structural stress done along the plate surface approaching the weld toe notch, see figure 2.27. If the relevant weld toe is on the plate edge, the non-linear stress concentration is seen along the plate width. This is Hot Spot Type b) and the extrapolation is done along the plate edge. Hot Spot type b) cracks, initiate at the edge of the member and propagate as through-thickness cracks (Maddox, 2001b). Flange tip attachments are clearly of the type b).

Several authors have made the re-analysis of existing fatigue results in nominal stress into the Hot Spot domain (Maddox, 2001a), (Aygül et al., 2013). Hot Spot Stress extrapolation for lateral attachments was extensively discussed in (Niemi, 2000; Niemi et al., 2006) were several quadratic extrapolation functions were analysed. The interpolation formula with three fixed extrapolation points at 4, 8 and 12 mm from the weld toe, Hot Spot type b),



### 2.3. Exploratory tests under multiaxial load

proved to be the best fit to the fatigue test results (Wagner, 1998), (Kim and Kang, 2008). This is the formula adopted in the IIW Recommendations (IIW, 2008). According to (Xiao and Yamada, 2004) HSS extrapolation techniques where the extrapolation points are thickness dependent are not suitable, because the stress distribution near the weld toe does not depend on the plate thickness.

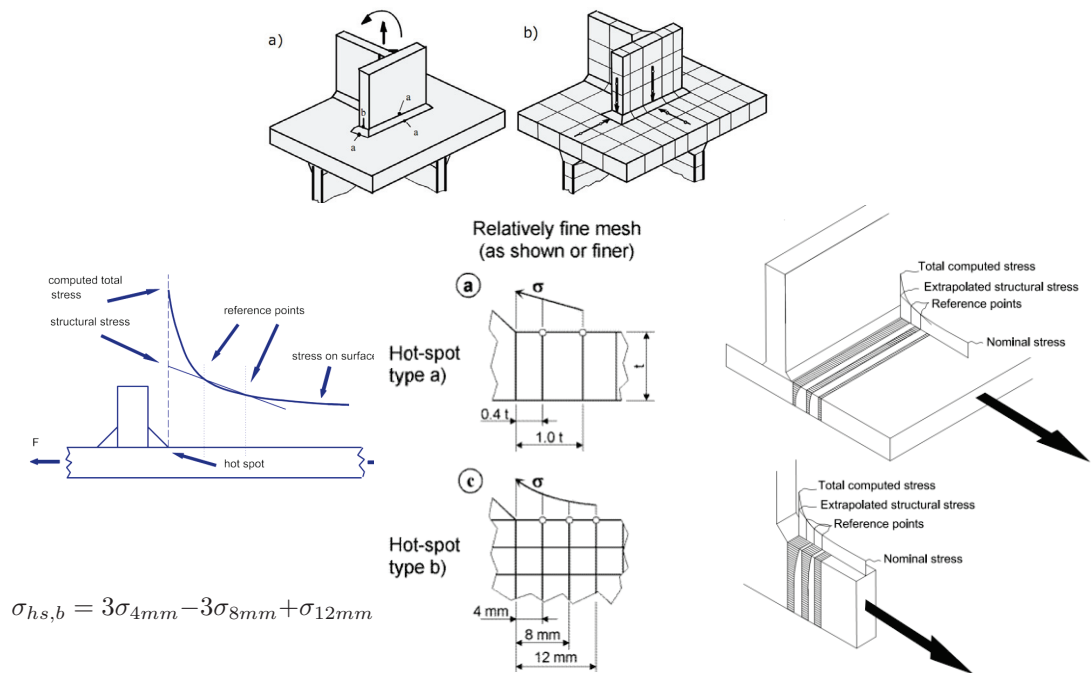


Figure 2.27 – Structural Hot Spot type a) and b) (IIW, 2008), (Niemi, 2002)

The quadratic extrapolation function with fixed extrapolation points at 4, 8 and 12 mm is thus adopted for the hot-spot geometric stress:  $\sigma_{hot-spot} = 3(\sigma_{4mm} - \sigma_{8mm}) + \sigma_{12mm}$ . Finite element models with both shell and solid elements were developed in ABAQUS, with a 4mm mesh size in both cases. For the solid models, two extrapolation paths were investigated: 1) surface path and 2) mid-thickness path.

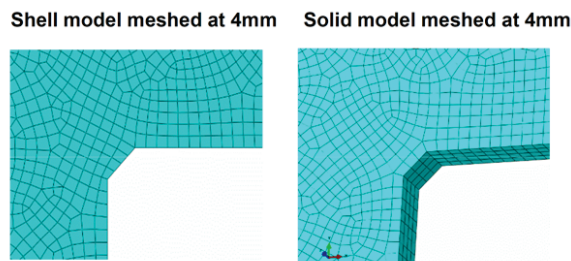


Figure 2.28 – Detail of the finite element mesh for hot spot evaluation

The finite element results are shown in table 2.7. The hot spot value is strongly dependent on the element type and integration order as other studies in literature had already

## Chapter 2. In-plane interaction - Flange crossings

shown (Rother and Rudolph, 2011). The resistance curves for Hot Spot type b are FAT 90 or FAT 100 depending on the attachments length. In this case we use FAT 100 for  $L_{attach}=150\text{mm}$ . The mean hot spot SCF for all models is  $SCF_{hot-spot}=2,3$  which corresponds to a nominal FAT43,5.

Element type	Path	4mm	8mm	12mm	Hot Spot SCF	FAT <sub>nominal</sub> 40 / FAT <sub>HS</sub> 100 $\sigma_{HS}$	Life ( $10^6$ )	Life factor
<b>S4R</b>	mid-thick	1,73	1,42	1,30	2,23	89,20	2,82	1,41
<b>S8R</b>	mid-thick	1,64	1,40	1,29	2,01	80,40	3,85	1,92
<b>S4</b>	mid-thick	1,85	1,40	1,30	2,65	106,00	1,68	0,84
<b>C3D8R</b>	surface	1,62	1,40	1,30	1,96	78,40	4,15	2,08
	mid-thick	1,67	1,40	1,28	2,09	83,60	3,42	1,71
<b>C3D8</b>	surface	1,83	1,44	1,32	2,49	99,60	2,02	1,01
	mid-thick	1,90	1,46	1,31	2,63	105,20	1,72	0,86

Table 2.7 – Results of the hot spot analysis under uniaxial tension (T)

Adopting the general linear quadrilateral shell element with reduced-integration (S4R) leads to  $SCF_{hot-spot}=2,23$  for the uniaxial tension load case T, the other load cases TT and TC are estimated in table 2.8.

Hot spot SCF			
Load case	T	TT	TC
	2,23	2,58	1,81

Table 2.8 – Hot spot for the different load cases (linear quadrilateral shell element S4R)

The values obtained for the uniaxial T case with quadratic extrapolation of stress measured at 4, 8 and 12mm, were confirmed experimentally. One tested specimen was instrumented with chain strain gages with 5 gages (4mm spacing) at each weld toe. Two weld toes on the flange tip lateral attachment configuration were measured, figure 2.29.

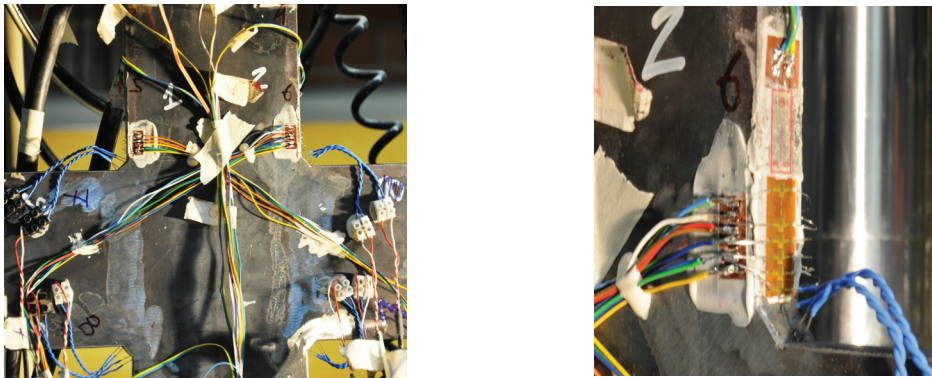


Figure 2.29 – Experimental hot-spot measurements

The measurements and extrapolation results are shown in figure 2.30. The initial measurements on an uncracked specimen were made after a few load cycles to obtain

### 2.3. Exploratory tests under multiaxial load

stable values. Two different values are obtained:  $SCF_{hot-spot}=2,63$  (strain gauge 1) and  $SCF_{hot-spot}=2,18$  (strain gauge 2). The measurements were repeated after a crack  $a \approx 4\text{mm}$  was created at the weld toe 1, represented on the right side of figure 2.30. The stress at this weld toe drops drastically.

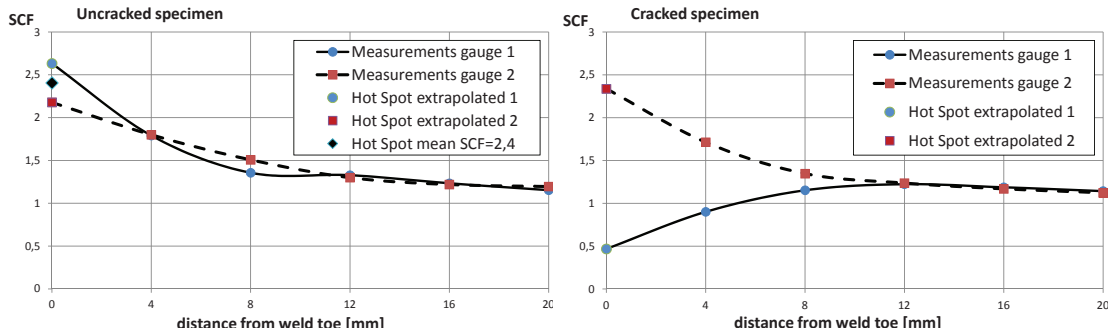


Figure 2.30 – Fine mesh extrapolation for Hot Spot type b)

The hot-spot method is able to estimate the SCF for the flange tip attachments. However, the sensitivity of the estimation to the finite element model is high, which justifies the approach of the effective notch stress approach as presented next.

#### 2.3.4 Effective notch stress method

The *effective notch stress method* is a local notch stress approach based on Neuber's notch concept (Neuber (1961), (Neuber, 1968), and extended by Radaj (1990), (Radaj et al., 2006)). The *effective notch stress method* is based on a local stress averaging approach achieved by a fictitious notch rounding, accounting for the microstructural support effect of the material and the effect of inhomogeneous material structure under a stress gradient (Amstutz and Olivier, 2011). This fictitious notch radius has to be added to the actual notch radius, which is usually assumed to be zero in a conservative way. Therefore it is recommended to assume  $r_{ref}=1\text{mm}$  for design purposes. The result is an effective notch stress that accounts for the variability in the weld shape or, if related to the nominal stress, a fatigue notch factor  $K_f$ . Any notch at the expected crack location, weld toe or root, is modeled by the fictitious radius of 1mm, eliminating the discontinuity and allowing a linear-elastic finite stress to be obtained, figure 2.31. A minimum of 4 quadratic elements in the radius is advised (Wagner, 1998). This gives the local stress including both the macroscopic stress concentration due to the weld shape and the local one from the weld toe or root. Extensive experimental research to validate the 1mm notch stress approach was carried out by Olivier et al. (1989) and (Olivier et al., 1994), for several weld configurations, including the scatter due to different notch values and the effect of stress ratio. The application to welded plate details has been investigated, in particular for the ship industry (Fricke and Paetzoldt, 1995), (Fricke et al., 2002) including the assessment of fillet weld root cracking (Fricke, 2013).

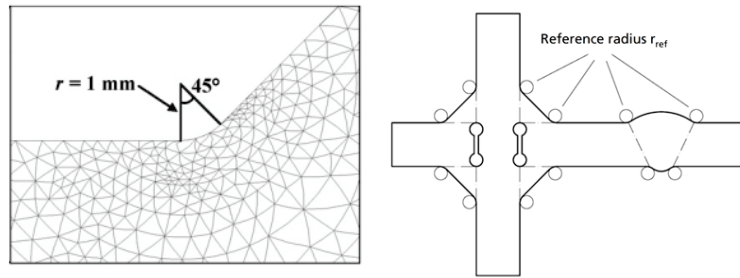


Figure 2.31 – Fictitious 1mm notch radius (IIW, 2008)

Several typical bridge details were re-analysed by Pedersen et al. (2010) and Aygül et al. (2013). An interesting conclusion was that scatter of the test results, re-plotted in effective notch stress, remains basically the same than for nominal stress range. Still, this method is more powerful since it includes all geometries. Cruciform non-load carrying fillet welds, for example, have been tested by Barsoum and Jonsson (2008). These are transversal attachments and all specimens cracked at weld toe. Results were found to be widely scattered and the characteristic notch fatigue strength was found to be FAT194 instead of FAT225.

For structural steels used in bridge and ship welded construction, fatigue assessment resumes to comparing the notch stress with a resistance master curve of FAT 225 (225 MPa at 2 million cycles and  $m = 3$ ), figure 2.32. The S-N curve provides then the intrinsic fatigue resistance of a weld toe or root with its micro-structural imperfections. Radaj (1990) proposed a design fatigue strength of 240 MPa for 95% survival probability that was later downgraded to a FAT 225 with 97,7% survival probability in (IIW, 2008), to account for the residual stress effects and stress ratio as high as  $R = 0,5$ .  $K_w$  is the ratio between the 1mm notch stress and the structural stress at 2mm from the weld.  $K_w = 1,6$  allows the assessment of mild notches at welds with large toe radius. An effective notch fatigue class of FAT 200 should be used in this case as found in (Fricke and Kahl, 2007). The author believes that details with lower values of  $K_w$  cannot be assessed with this method, as the imperfection influence becomes predominant to express fatigue strength.

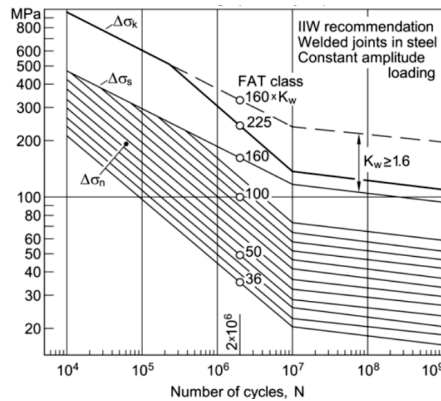


Figure 2.32 – Master curve for the notch stress method (IIW, 2008)

### 2.3. Exploratory tests under multiaxial load

The flange tip attachment was analysed with the notch stress approach, with a numerical model developed in ABAQUS. The mesh adopted for modelling the weld toe with a 1mm transition radius is shown in table 2.9 along with the results. Quadratic 20-node elements with full integration are used in a linear elastic analysis. According to (Fricke, 2008), the principal notch stress should be used for the multiaxial case. A stress concentration of 5,5 is obtained under uniaxial tension (Case T). Using the 225 MPa master curve for the notch stress, the equivalent nominal strength is FAT 41, coherent with the Hot-Spot analysis, which gave FAT43,5, also in terms of influence of the TT and TC load cases. The results for the multiaxial case in tension (TT) show an increase of 28% on the interaction SCF compared to the uniaxial one. For the tension-compression case (TC) there is a reduction of the same level.

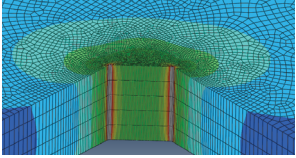
Load case	$K_{notch}$	FAT <sub>nominal</sub> [MPa]	
T	5,5	41	
TT	7,1	32	
TC	3,9	57	

Table 2.9 – Notch stress for the different load cases

#### 2.3.5 Summary of conclusions

- Five exploratory tests under non-proportional loads allowed crack measurements under the influence of each stress component ( $\sigma_1, \sigma_2$ ). Mixed mode Mode I + Mode II was observed under non-proportional loads, but only for very long cracks, with crack depths close to failure. No major influence is thus expected as Mode I prevails over Mode II propagation. This should be confirmed with tests under proportional loads.
- Local notch stress analysis shows that the local stress at the weld toe may influence the initiation life. However, for as-welded conditions, the residual stress effects and inherent scatter, will probably eliminate this influence and under non-proportional loads, the notch stress perpendicular to the load direction is well below the threshold. Under proportional loads, some influence on the notch is expected, which may reduce the initiation life.
- Literature results with cyclic loads in one direction and constant static loads on the perpendicular direction, showed that the biaxial static forces have little influence on the fatigue strength in as-welded conditions. These findings are important because many biaxial loadings in steel bridges may be treated as mean static stress, which is the case for example of a crossing between a stringer and a cross-beam, where cross beams have many cycles due to axle loads while the stringer may be loaded by a single cycle due to the presence of a vehicle or train in the bridge.
- No specific provisions are anticipated for the fatigue assessment of the detail under bi-axial stress state conditions.

## 2.4 Experiments under constant amplitude

The results of the constant amplitude tests carried out on both Flange tip attachments and Intersected flanges are summarised in table 2.10. These tests provided valuable information for the calibration of a fracture mechanics model, identifying typical crack shapes, propagation rates and threshold value, as well as the mean S-N curve. This information is important for the interpretation of variable amplitude tests and for the development of the probabilistic fracture mechanics model.

Specimen	$\Delta\sigma$ [MPa]	$R_\sigma$	f [Hz]	$N_{\text{failure}}$	crack size [mm]	Figure
LA-CA-1	50	0,5	15	3.801.150	54	C.2
LA-CA-2	25	0,5	15	32.200.000 <sup>+</sup>	-	-
LA-CA-3	50	0,5	15	7.961.384	70	C.4
LA-CA-4	50	0,5	15	3.322.000*	50	C.5
LA-CA-5	100	0,5	5	358.000	23	-
LA-CA-6	100	0,5	5	340.000	27	-
IF-1	50	0,5	15	5.000.000	48	C.6
IF-2	40	0,5	15	22.000.000 <sup>+</sup>	-	-
IF-3	45	0,72	15	5.651.618	40	C.6
IF-4	40	0,75	15	34.000.000 <sup>+</sup>	-	-
IF-5	45	0,72	15	11.657.405	48	C.6
IF-6	50	0,5	15	4.543.545	31	C.7
IF-7	50	0,5	15	2.636.500*	50	C.10
IF-8	45	0,72	15	5.921.400*	50	C.12
IF-9	100	0,5	5	710.000	27	-
IF-10	100	0,5	5	581.065	32	-

\* extrapolated  
+ run-outs

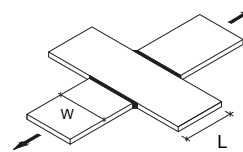
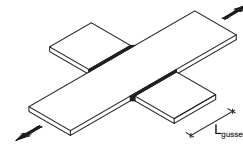


Table 2.10 – Experimental results for constant amplitude tests

Tests showed the remaining number of cycles to be negligible after a long crack was achieved  $a \approx \frac{W}{3} = 50\text{mm}$ . The critical crack depth  $a_{cr}$  for brittle failure or the maximum crack size  $a_{pl}$  for plastic collapse are both higher than 50mm for the range of maximum



## 2.4. Experiments under constant amplitude

stress used in the tests. Maximum stress range was  $\Delta\sigma = 100$  with  $R_\sigma = 0,5$  leading a maximum stress  $\sigma = 200$  MPa. Figure 2.33 shows  $a_{cr}$  and  $a_{pl}$  assuming  $K_{Ic} = 3000 \text{ Nmm}^{-3/2}$ , an edge crack with  $Y = 1,1$  and  $f_u = 360$  MPa (Sedlacek et al., 2008). For the sake of coherence on the treatment of experimental results in nominal stress and by the fracture mechanics model, the number of cycles is reported in general to a crack depth of  $a_f = 50 \text{ mm}$  (see table 2.10), considered as failure for the specimens used on the experiments.

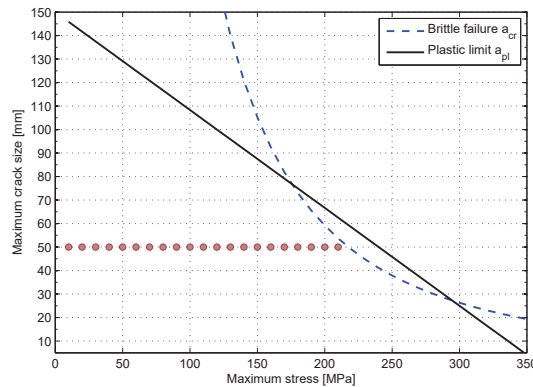


Figure 2.33 – Maximum crack size for brittle and plastic failure

The results of the constant amplitude tests are shown in figure 2.34 including the five tests at  $\Delta\sigma = 100$  MPa presented in Section 2.3. The detail is characterised by  $\Delta\sigma_{m,2.10^6} = 60$  MPa and CAFL at  $5 \cdot 10^6$  equal to  $\Delta\sigma_{m,D} = 44$  MPa. Also shown are the results along with the tests from the uniaxial database. The new tests obtained are below the mean value obtained for the database, FAT75 with  $m = 3$ , see figure A.3. This may be explained by the high stress ratio that was adopted in our tests,  $R_\sigma \geq 0,5$  which practically eliminates all beneficial residual stresses and crack closure effects. The run-outs obtained under our experimental program are in the range where failures were observed by other authors but the threshold value is considered valid for the remaining batch of specimens tested under variable amplitude.

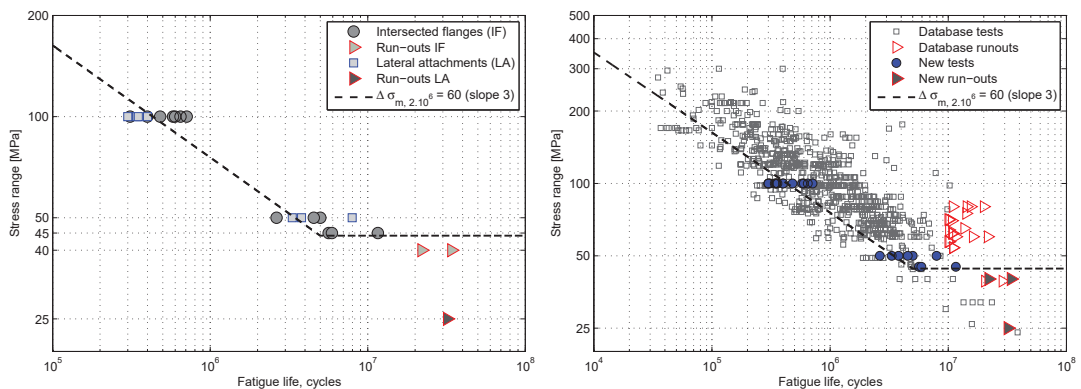


Figure 2.34 – Constant amplitude tests for Intersected Flanges and Lateral Attachments

“Flange tip attachments” versus “intersected flanges”

It was seen in table 2.1 that Flange tip attachments and Intersected flanges may have different FAT classifications. IIW (2008) Recommendations assign FAT50 to Intersected flanges without dependence on the attachment length, while the Lateral flange tip attachment may be as low as FAT40. It was not possible to find the experimental results justifying this difference, but according to the editor, Prof A. Hobacher, the FAT50 value resulted from discussions with the British Welding Institute, which classified the detail on the G-curve (BS 5400: Part 10, 1980), that is about FAT50.

Tests carried out at  $\Delta\sigma = 100\text{MPa}$  showed indeed some difference between the flange tip attachments and intersected flanges. The difference vanishes however for tests at lower stress ranges,  $\Delta\sigma = 50\text{MPa}$ , figure 2.34.

Looking at experimental results from the uniaxial database, only two setups, where both configurations were tested and compared, could be found. They are presented in Appendix A but it is of special interest to recall them here to settle the case. Haibach (1979) presented tests on both lateral attachments (Type II and III) and intersected flanges (Type IV and V) in  $200 \times 20 \text{ mm}^2$  plates, at stress ratio  $R_\sigma=0,15$ , figure 2.35. Fatigue strength of intersected flanges was found to be 15% higher than lateral attachments, figure 2.36.

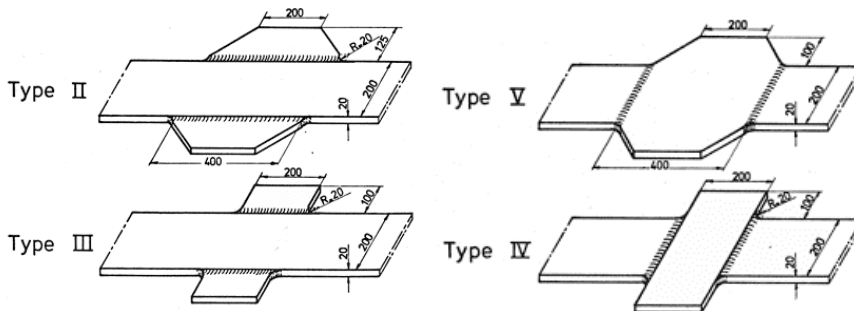


Figure 2.35 – Lateral attachments and Intersected flanges tested by Haibach (1979)

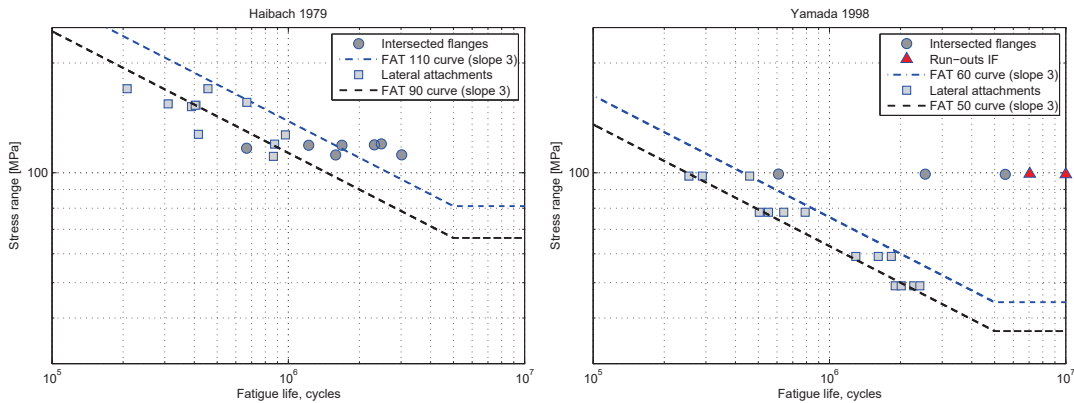


Figure 2.36 – Literature results for flange tip attachments and intersected flanges



## 2.4. Experiments under constant amplitude

Yamada et al. (1998b) presented an experimental program with 35 fatigue tests 200mm wide plates with lateral attachments 200mm long. The same type of specimens was then tested in the intersected flange configuration in (Yamada et al., 1998a). Stress ratio  $R_\sigma = 0,1$  was used for both configurations and conclusion was that Intersected flanges had better fatigue behaviour, figure 2.36.

It may thus be argued that the difference in fatigue behaviour is supported by tests. Several factors were considered to explain this difference, but most of the parameters considered were discarded. The Stress Concentration Factor at the weld toe in our specimens, is the same for both configurations as they were made in a systematic and symmetric way, all welded the same way by the author. The same holds true for the weld imperfections at the weld toe, that should be expected to be similar given that the same welding process is adopted and the sealing weld toe is symmetrical.

The difference in fatigue life may possibly be attributed to the residual stress field effect at the crack tip. Residual stress for both configurations were measured by Yamada et al. (1998b) using the sectioning method with strain gauges. They showed a clear difference between both configurations, with tensile residual stresses at the weld toe of lateral attachments and compression at the intersected flange weld toe, figure 2.37.

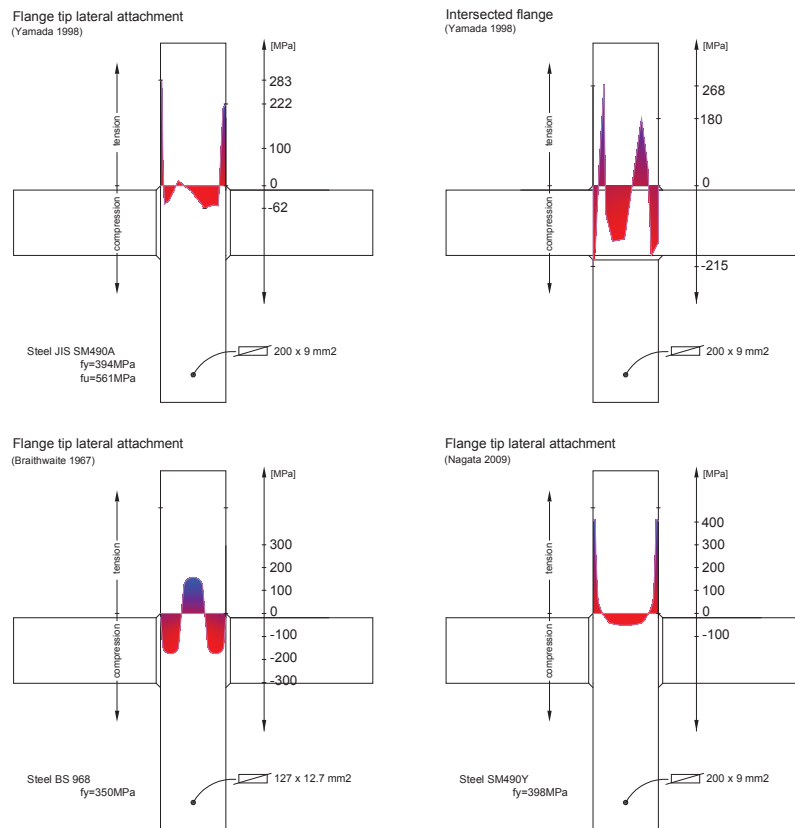


Figure 2.37 – Residual stress measurements from literature

## Chapter 2. In-plane interaction - Flange crossings

Tensile residual stresses for the flange tip configuration were confirmed by measurements presented by Nagata et al. (2009) but, measurements on the outmost fiber of cross girders welded beams published by Dawes (1965) and Braithwaite and Gurney (1967) showed compression in the region of the weld toe.

To compare with this values, one of our specimens was produced for residual stress measurements. Four intersected flange weld toes and four lateral attachment weld toes were measured at IFS (Braunschweig University, Germany) by X-Ray diffraction. X-ray method is based on the estimation of the lattice spacing to calculate the residual strains. These are surface residual strains on the weld toe region as X-ray only penetrates up to 0,025 mm deep. The results show that lateral attachment weld toes were found mainly in compression while intersected flanges could be both in tension or compression, figure 2.38.

The residual stress measurements indicate that it seems reasonable to expect some degree of tensile residual stress at the weld toe of lateral attachments, and on the other hand, compression may be present at the intersected flange weld toe. Our tests however, were performed at  $R_\sigma=0,5$  so that the beneficial compressive residual stresses would have been relieved. Indeed, an analysis in effective stress would allow an opening stress to be defined, accounting for a non-effective part of the stress cycle for the intersected flanges. The difference does however disappear in the long life regime so that this model loses its logic.

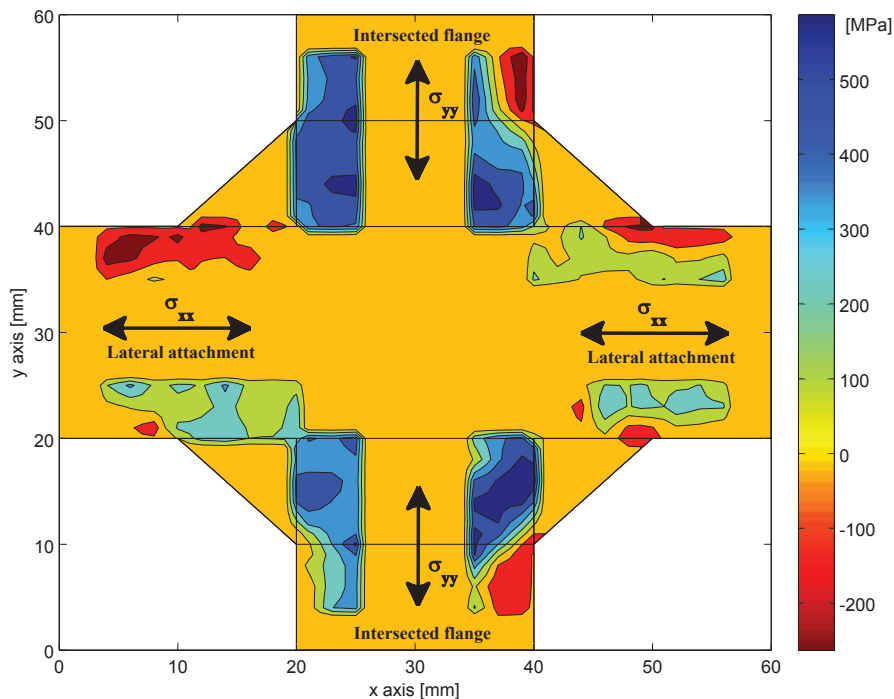


Figure 2.38 – Residual stress profile measured by X-Ray diffraction

Another possible parameter is the crack propagation rate. Although both cracks start

## 2.4. Experiments under constant amplitude

at the sealing weld toe, a fundamental difference between the crack paths on both configurations exists. For the lateral attachment configuration, cracks initiate from the weld toe and propagate through a first strip of Heat Affected Zone (HAZ) about 2mm deep. The remaining of the crack path is entirely in base material. Cracks under the Intersected flange on the other hand, after getting out the HAZ from the weld toe, propagate through a mix of micro-structures. Close to surface they propagate through the weld metal, while at mid-thickness the path is in the parent metal due to the chamfer of the plate, figure 2.39. Transition micro-structures are found in between. The micro-structures found at the weld toe region and along the crack paths corresponding to the plate surface and also the mid-thickness plane are shown in figure 2.40.

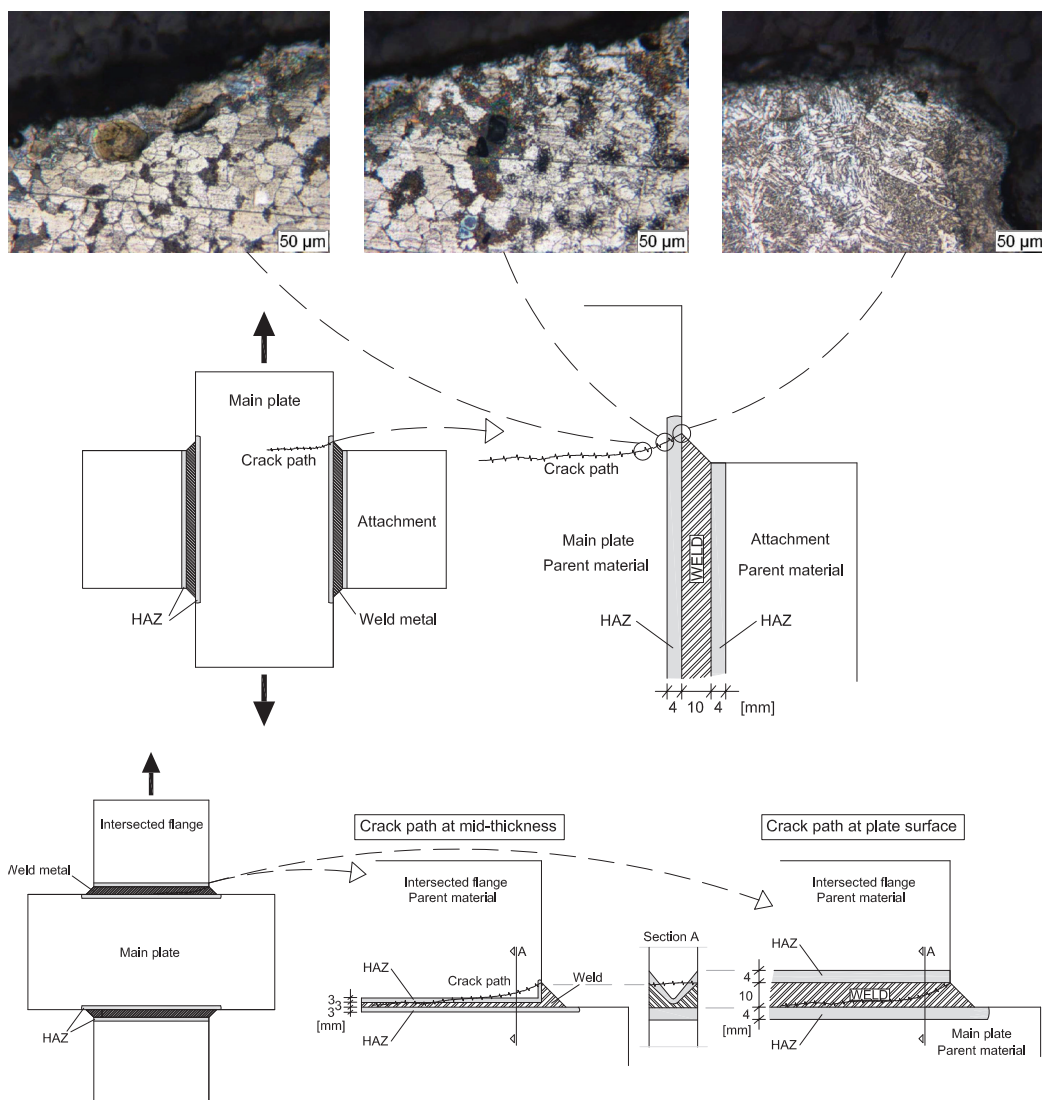


Figure 2.39 – Crack paths for Flange tip lateral attachments and Intersected flanges



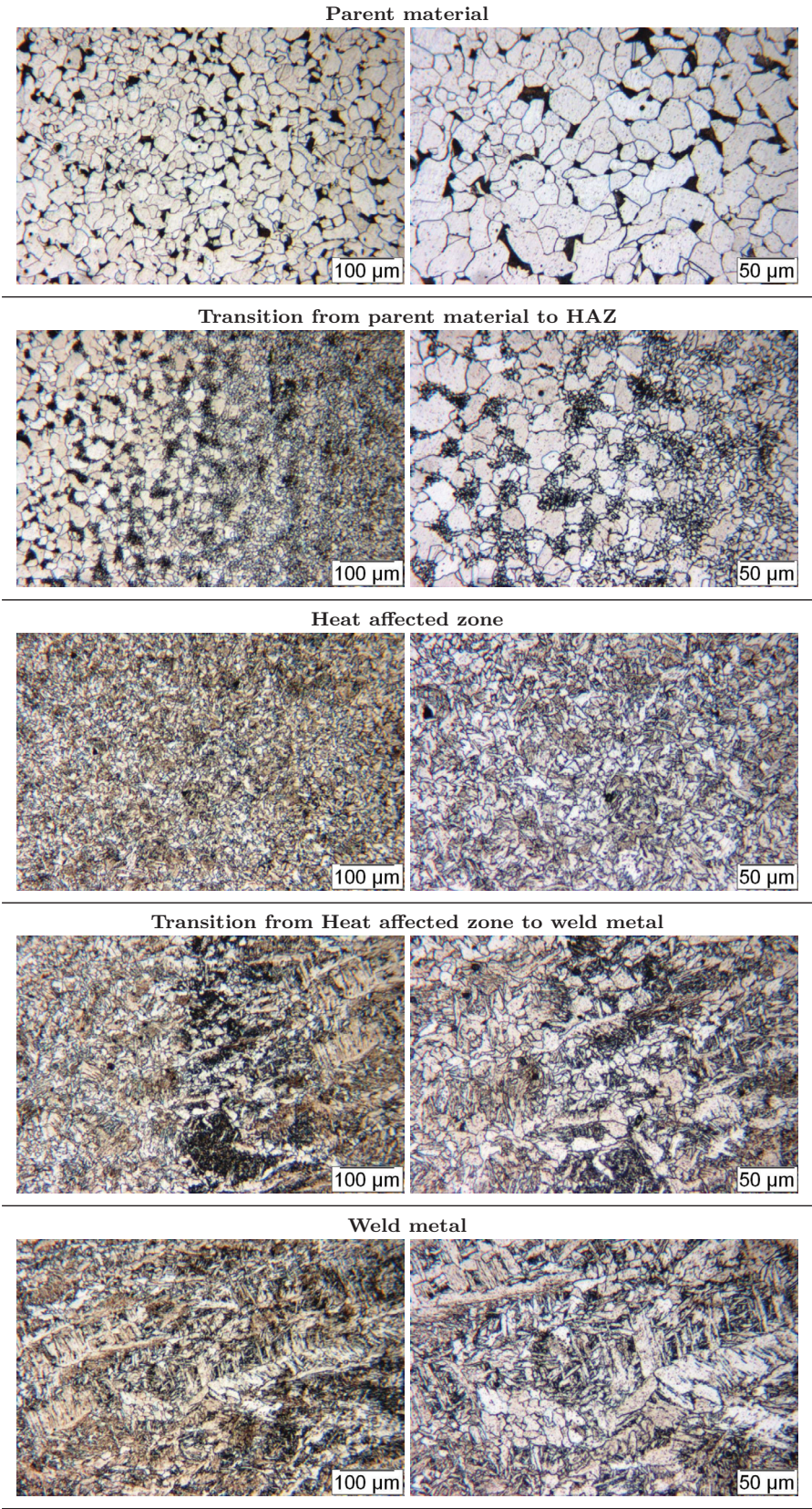


Figure 2.40 – Micro-structure of parent material, HAZ and weld metal

## 2.4. Experiments under constant amplitude

Although cracks propagate through different micro-structures, the hypothesis that crack propagation rates justify the difference in life observed for both configurations is not supported by tests. ACPD measurements show that no difference in propagation rates is observed, as indeed, the propagation life for both configurations can be modeled by fracture mechanics using the same Paris Law constants, see Appendix C.1. This is in line with current assumptions that the same propagation rates are observed for base material, HAZ or weld metal (Maddox, 1970), (Virkler et al., 1979) and (Maddox, 1992).

Some ACPD crack growth curves under constant amplitude are shown in figure 2.41 and their initiation life in figure 2.44. For tests performed at  $\Delta\sigma=100\text{MPa}$  (left side), the crack growth curves for Intersected flanges, are shifted towards higher number of cycles, indicating higher initiation life. For tests performed at  $\Delta\sigma=50\text{MPa}$  (right side), with total lives above  $2.10^6$  cycles, the percentage of initiation life becomes less important, exception made for the lateral attachment (LA-CA-3) with 50% of life in initiation.

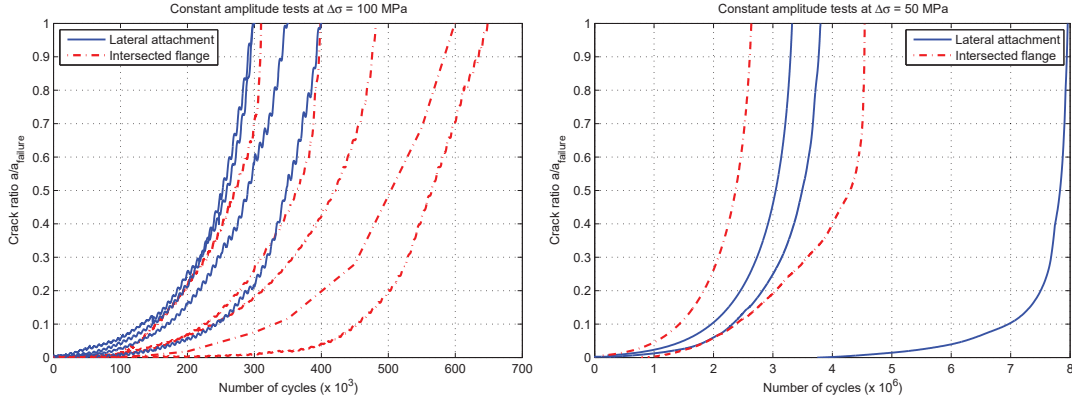


Figure 2.41 – Crack propagation curves measured for tests in both configurations

### 2.4.1 Initiation model

The difference in initiation thus explains some higher lives observed for Intersected flanges. To model initiation life, a local notch strain approach is adopted to account for local repeated yielding (Radaj, 1996), (Glinka and Chattopadhyay, 2009). Local elasto-plastic strains are considered by Neuber's notch rule and material cyclic strain-stress curve is modeled according to Ramberg-Osgood relation. Solving both equations it is possible to calculate the local elasto-plastic maximum, mean stress and stress range. These quantities are then used to estimate fatigue life using Coffin-Manson equation with Morrow's mean stress correction (Dowling, 1993).

The basic assumption of the analytical local notch strain approach is that fatigue life to crack initiation at a weld toe notch, is similar to the life of a smooth material specimen ( $\phi=6$  to  $8\text{mm}$ ) if the stress-strain state in the weld toe is the same as in the smooth material specimen (similitude concept), figure 2.42.

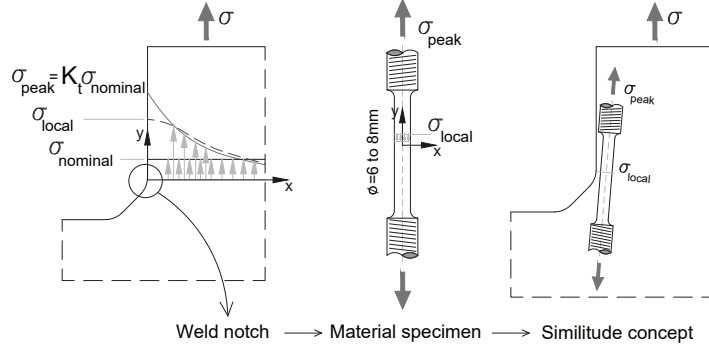


Figure 2.42 – Similitude concept for the local notch strain approach

Neuber’s rule gives an energy balance between the fictitious linear elastic stress-strain state at the notch (herein called pseudo-elastic) and the local notch elasto-plastic stress and strain (herein called local) (Neuber, 1961), (Neuber, 1968), (Topper et al., 1967). With the pseudo-elastic stress defined elastically by  $K_t\sigma$ , and considering the locally measured residual stress, Neuber’s rule can be written as:

$$(\sigma.\varepsilon)_{pseudo-elastic} = (\sigma.\varepsilon)_{elasto-plastic} \Rightarrow \frac{(K_t.\sigma_{max} + \sigma_{residual})^2}{E} = (\sigma.\varepsilon)_{local} \quad (2.10)$$

A 2<sup>nd</sup> equation relating  $\sigma_{local}$  and  $\varepsilon_{local}$  becomes available by considering a material cyclic stress-strain curve. The Ramberg-Osgood relation is considered assuming the cyclic strength coefficient  $K'$  and the cyclic strain hardening exponent  $n'$  to be stable, (Ramberg and Osgood, 1943):

$$\varepsilon_{local} = \frac{\sigma_{local}}{E} + \left(\frac{\sigma_{local}}{K'}\right)^{\frac{1}{n'}} \quad (2.11)$$

By replacing equation 2.11 in 2.10, the maximum local stress  $\sigma_{max,local}$  corresponding to the 1<sup>st</sup> load reversal, is obtained by solving:

$$\frac{(K_t.\sigma_{max,nominal} + \sigma_{residual})^2}{E} = \sigma_{max,local} \left( \frac{\sigma_{max,local}}{E} + \left(\frac{\sigma_{max,local}}{K'}\right)^{\frac{1}{n'}} \right) \quad (2.12)$$

Once the maximum elasto-plastic stress  $\sigma_{max,local}$  is defined for the 1<sup>st</sup> load reversal using equation 2.12, the same procedure is applied to calculate the effective local stress range and local mean stress. The pseudo-elastic stress range is  $K_t\Delta\sigma$  and Neuber’s rule is used in this case to calculate the stress-strain point at the 2<sup>nd</sup> load reversal:

$$\frac{(K_t.\Delta\sigma_{nominal})^2}{E} = (\Delta\sigma.\Delta\varepsilon)_{local} \quad (2.13)$$

The material cyclic stress-strain curve provides the 2<sup>nd</sup> equation between  $\Delta\sigma_{local}$  and  $\Delta\varepsilon_{local}$ , with the stabilised hysteresis loop obtained by doubling the basic Ramberg-Osgood



## 2.4. Experiments under constant amplitude

material stress-strain curve (Massing's hypothesis) (Glinka and Chattopadhyay, 2009):

$$\Delta\varepsilon_{local} = \frac{\Delta\sigma_{local}}{E} + 2 \cdot \left( \frac{\sigma_{local}}{2K'} \right)^{\frac{1}{n'}} \quad (2.14)$$

The local stress range  $\Delta\sigma_{local}$  is obtained by replacing equation 2.14 in equation 2.13:

$$\frac{(K_t \Delta\sigma_{nominal})^2}{E} = \Delta\sigma_{local} \left( \frac{\Delta\sigma_{local}}{E} + 2 \left( \frac{\Delta\sigma_{local}}{2K'} \right)^{\frac{1}{n'}} \right) \quad (2.15)$$

and the local mean stress by:  $\sigma_{mean,local} = \sigma_{max,local} - \frac{\Delta\sigma_{local}}{2}$ , see figure 2.43

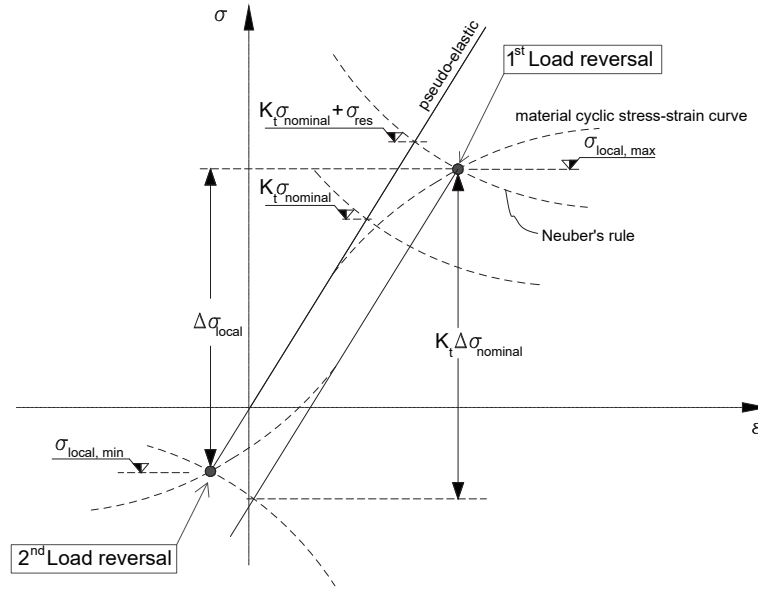


Figure 2.43 – Schematic representation of the 1<sup>st</sup> and 2<sup>nd</sup> load reversal

Finally, using Coffin-Manson equation with Morrow's mean stress correction, fatigue life to crack initiation at the weld toe notch tip is estimated by:

$$\frac{\Delta\varepsilon_{local}}{2} = \left( \frac{\sigma_f' - \sigma_{m,local}}{E} \right) (2N_r)^b + \varepsilon_f' (2N_r)^c \quad (2.16)$$

where  $\Delta\varepsilon_{local}$  is the fully reversible local strain range  $\frac{\Delta\sigma_{local}}{E}$ ,  $N_r$  the number of reversals to failure (1 rev = 1/2 cycle,  $N=2N_r$ ),  $\sigma_{m,local}$  the local notch mean stress,  $b$  the fatigue strength exponent (Basquin's exponent) and  $\sigma_f'$  is the fatigue strength coefficient, approximately equal to the true fracture strength. For the plastic strain,  $c$  is the fatigue ductility exponent and  $\varepsilon_f'$  is the fatigue ductility coefficient, approximately equal to the true strain at fracture.

Cyclic material parameters for the Coffin-Manson curve and Ramber-Osgood law are taken according to the Uniform Material Law, after Baumel and Seeger (1990), (Boller

## Chapter 2. In-plane interaction - Flange crossings

and Seeger, 1987).

$\sigma_f' = 1,5f_u$	fatigue strength coefficient	[MPa]
$b=-0,087$	fatigue strength exponent	
$\varepsilon_f' = 0,59$	fatigue ductility coefficient	
$c=-0,58$	fatigue ductility exponent	
$K'=1,65f_u$	cyclic strength coefficient	[MPa]
$n'=0,12$	cyclic strain hardening exponent	
$E=210.10^3$	modulus of elasticity	[MPa]

Table 2.11 – Cyclic material parameters, (Radaj et al., 2006), (Haibach, 2006)

By considering initiation for the Lateral attachments given in the base plate material (S235JR  $\Rightarrow$  Fe 360:  $f_u=360$ MPa) and for Intersected flanges on the weld material (“OK autorod 12.51”, see table 2.5,  $f_u=560$ MPa, equivalent to an S355  $\Rightarrow$  Fe 510), the initiation life for both configurations can be estimated as shown in figure 2.44.

Initiation curves for both materials are shown on the left, for the fatigue tests at  $\Delta\sigma=100$ MPa,  $\sigma_m=150$ MPa. Residual stresses up to yield stress  $f_y$  are considered,  $\sigma_{res}=235$ MPa for Lateral attachments and  $\sigma_{res}=355$ MPa for Intersected flanges. Estimated initiation life ranges from 400.000 cycles for Lateral attachments to 500.000 for Intersected flanges. Initiation curves for the tests at  $\Delta\sigma=50$ MPa,  $\sigma_m=75$ MPa are shown on the right side, with initiation life ranging from 2.300.000 cycles for Lateral attachments to 14.000.000 for Intersected flanges. Both estimations are coherent with experimental initiation life re-plotted from figure 2.41.

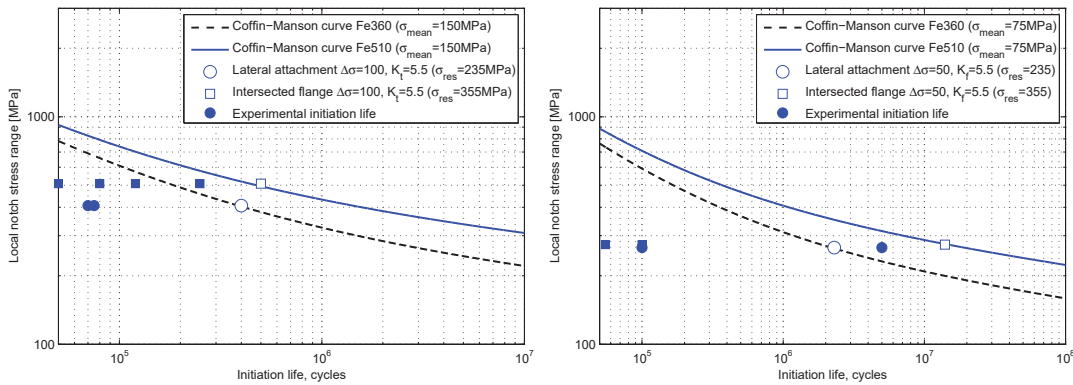


Figure 2.44 – Initiation life for Lateral attachments and Intersected flanges

To conclude, higher initiation lives are expected for the Intersected flange configuration mainly due to a difference in the weld toe micro-structure. It must be noted however that although welds are generally produced with overmatching material, different FAT categories are not justified because specimens with significant initiation can only define



## 2.4. Experiments under constant amplitude

---

the upper bound of the S-N curve, while the lower bound values are given by purely propagation curves. Furthermore, crack initiation at weld toes is most likely to occur from the Heat Affected Zone and although Weld Metal and Heat Affected Zone have higher mean fatigue strength properties, they also have wider scatter. The assessment of welded joints should thus be based exclusively on the cyclic stress strain properties of Base Metal. The same applies for the propagation parameters.

### 2.4.2 Propagation model

Although some initiation was observed, the most important part of fatigue life was seen to be in propagation. Three crack types were identified from crack surface analysis carried out after testing, figure 2.45: **edge**, **semi-elliptical** and **corner crack**. These cracks initiated at one or more weld toes (out of four) but only the one leading to failure is considered for analysis. Macroscopically the crack path was found to be predominantly perpendicular to the principal stress field as represented in figure 2.39. No important short crack effects were detected and the crack propagation life could be estimated by a Linear Elastic Fracture Mechanics model. The crack propagation model is based on the integral of Paris Law equation, to calculate the number of cycles in propagation from an initial crack  $a_i$  to a final crack size  $a_f$ :

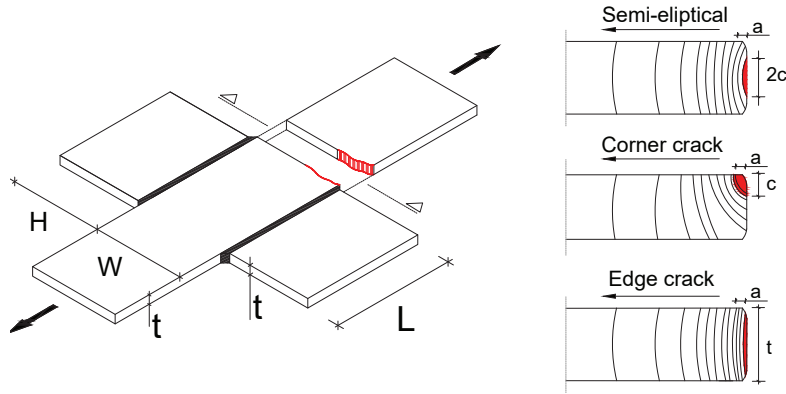
$$\frac{da}{dN} = C \Delta K_I^m = C (Y M_k \Delta \sigma \sqrt{\pi a})^m \quad \text{if} \quad \Delta K_I > \Delta K_{th} \quad (1.1 \text{ rep})$$

$$\frac{da}{dN} = 0 \quad \text{if} \quad \Delta K_I < \Delta K_{th}$$

$$\int_0^N dN = \int_{a_i}^{a_f} \frac{1}{C (Y M_k \Delta \sigma \sqrt{\pi a})^m} da = \frac{1}{C (\Delta \sigma \sqrt{\pi})^m} \int_{a_i}^{a_f} \frac{1}{(Y M_k \sqrt{a})^m} da \quad (2.17)$$

where  $C=1,5 \cdot 10^{-13}$ ,  $m=3$ ,  $\Delta K_{th}=100 \text{ Nmm}^{-3/2}$ ,  $Y$  and  $M_k$  are defined in figure 2.45.

In presence of tensile residual stresses close to the yield limit at the crack location, the crack propagation is independent from mean stress, and the stress intensity factor depends only on the stress range:  $\Delta K_I = \Delta K_{ap} = K_{ap,max} - K_{ap,min}$ . Under these conditions, the values of  $C$  and  $\Delta K_{th}$  are considered independent from the loading conditions. The stress intensity factor is given in the form  $\Delta K_I = Y M_k \Delta \sigma \sqrt{\pi a}$  where  $Y$  is a geometric function for the crack shape and  $M_k$  accounts for the non-uniform stress distribution along the crack path due to the weld toe concentration. The geometric correction factor  $Y$  is calculated according to the decomposition procedure described in (Albrecht and Yamada, 1977). The method consists in defining partial  $Y_i$  factors that apply a correction to the fundamental Stress Intensity Factor for a through-thickness elliptical crack (length  $2a$ ), in a infinite plate under tensile stress, for which  $Y_{ref} = 1$  and  $\Delta K_I = \Delta \sigma \sqrt{\pi a}$ .



**Semi-elliptical crack:**

$$Y_S^{3D} = 1 + 0,12 \left(1 - 0,75 \frac{a}{c}\right)$$

$$Y_W^{3D} = \sqrt{\frac{2W}{\pi a} \tan \frac{\pi a}{2W}}$$

$$Y_E^{3D} = \frac{1}{\sqrt{1 + 1,464 \left(\frac{a}{c}\right)^{1,65}}}$$

**Edge crack:**

$$Y_S = \frac{0,752 + 2,02 \frac{a}{W} + 0,37 \left(1 - \sin \frac{\pi a}{2W}\right)^3}{\cos \frac{\pi a}{2W}}$$

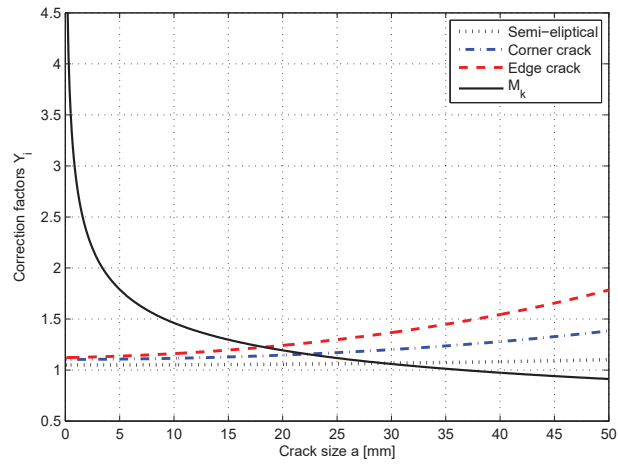
$$Y_W = \sqrt{\frac{2W}{\pi a} \tan \frac{\pi a}{2W}}$$

**Corner crack:**

$$Y_S^{3D} = \left(M_1 + M_2 \left(\frac{a}{W}\right)^2 + M_3 \left(\frac{a}{W}\right)^4\right) g_\phi$$

$$Y_W^{3D} = \sqrt{\frac{2W}{\pi a} \tan \frac{\pi a}{2W}}$$

$$Y_E^{3D} = \frac{1}{\sqrt{1 + 1,464 \left(\frac{a}{c}\right)^{1,65}}}$$



$$M_1 = 1,08 - 0,03 \frac{a}{c}$$

$$M_2 = -0,44 + \frac{1,06}{0,3 + \frac{a}{c}}$$

$$M_3 = -0,5 + 0,25 \frac{a}{c} + 14,8 \left(1 - \frac{a}{c}\right)^{15}$$

$$g_\phi = 1 + \left(0,08 + 0,15 \left(\frac{a}{W}\right)^2\right)$$

**$M_k$  - local non-uniform stress distribution**

$$M_k = C \cdot \left(\frac{a}{W}\right)^b$$

$$\log 10C = -0,2979 + 0,04406 \frac{L}{W} - 0,005056 \left(\frac{L}{W}\right)^2 + 0,2084 \frac{H}{W} - 0,1291 \left(\frac{H}{W}\right)^2$$

$$b = 0,2643 + 0,02848 * (H/W)$$

Figure 2.45 – Observed crack types and SIF correction factors  $Y_i$  and  $M_k$

## 2.4. Experiments under constant amplitude

---

Four partial  $Y_i$  factors were originally defined in (Albrecht and Yamada, 1977) as:

$$Y = Y_E \cdot Y_S \cdot Y_W \cdot Y_G \quad \text{where } Y_G \text{ is defined here as } M_k \quad (2.18)$$

- $Y_{E(elliptical)}$  is a correction for the elliptical crack front dependent on the  $a/c$  ratio and valid only for the tri-dimensional crack propagation case.
- $Y_{S(surface)}$  is the surface correction for cracks on a free surface.
- $Y_{W(width)}$  is a correction for finite width plates.
- $M_k$  function corrects the Stress Intensity Factor for the local non-uniform stress distribution due to the weld geometry. A specific function was defined by Hobbacher (1992) for flange tip attachments and is considered here.

Both the initiation and propagation model for the fatigue life estimates were validated against experimental crack growth curves. Figure 2.46 shows the example for the specimen LA-CA-1 while all others are presented in Appendix C.1. The correlation of the electric potential measurements is done with both the crack surface analysis after failure and crack measurements during tests. The estimated crack depth (a) versus number of cycles (N) is checked against the measured crack depths during fatigue tests.

Given that no “beach-marks” are produced under constant amplitude load, tracing back the crack front, is not possible just by observation of the crack surface after failure. Crack measurements with non-destructive dye penetrant method were done with a red dye penetrant applied near the sealing weld toe. The seeped dye was drawn up to surface with a white developer allowing the crack depth to be measured and creating a sort of “colored beach-mark” at the crack surface, which could be correlated with the measurements after failure and opening of cracks, figure 2.46. The process is done on both surfaces allowing corner cracks to be identified. Measurements on both surfaces are shown in the graphs.

Figure 2.46 shows a schematic layout of the specimen to allow ACPD location and fracture surfaces to be identified. The filtered potential values are shown for the four monitored weld toes. Crack depth estimation using the calibrated thin-skin theory based on the measured potentials, equation 2.9, are shown along with the crack measurements during tests and the fracture mechanics computations. Initiation life, when relevant, is accounted and initial crack size and shape (semi-elliptical, edge or corner) as identified by the ACPD record is considered to start with the fracture mechanics computations, as shown in the log-scale plot with crack depth (a) versus number of cycles (N).

For all tests, accurate propagation life estimations were obtained, also in agreement with crack growth curves, see Appendix C.1.

## Chapter 2. In-plane interaction - Flange crossings

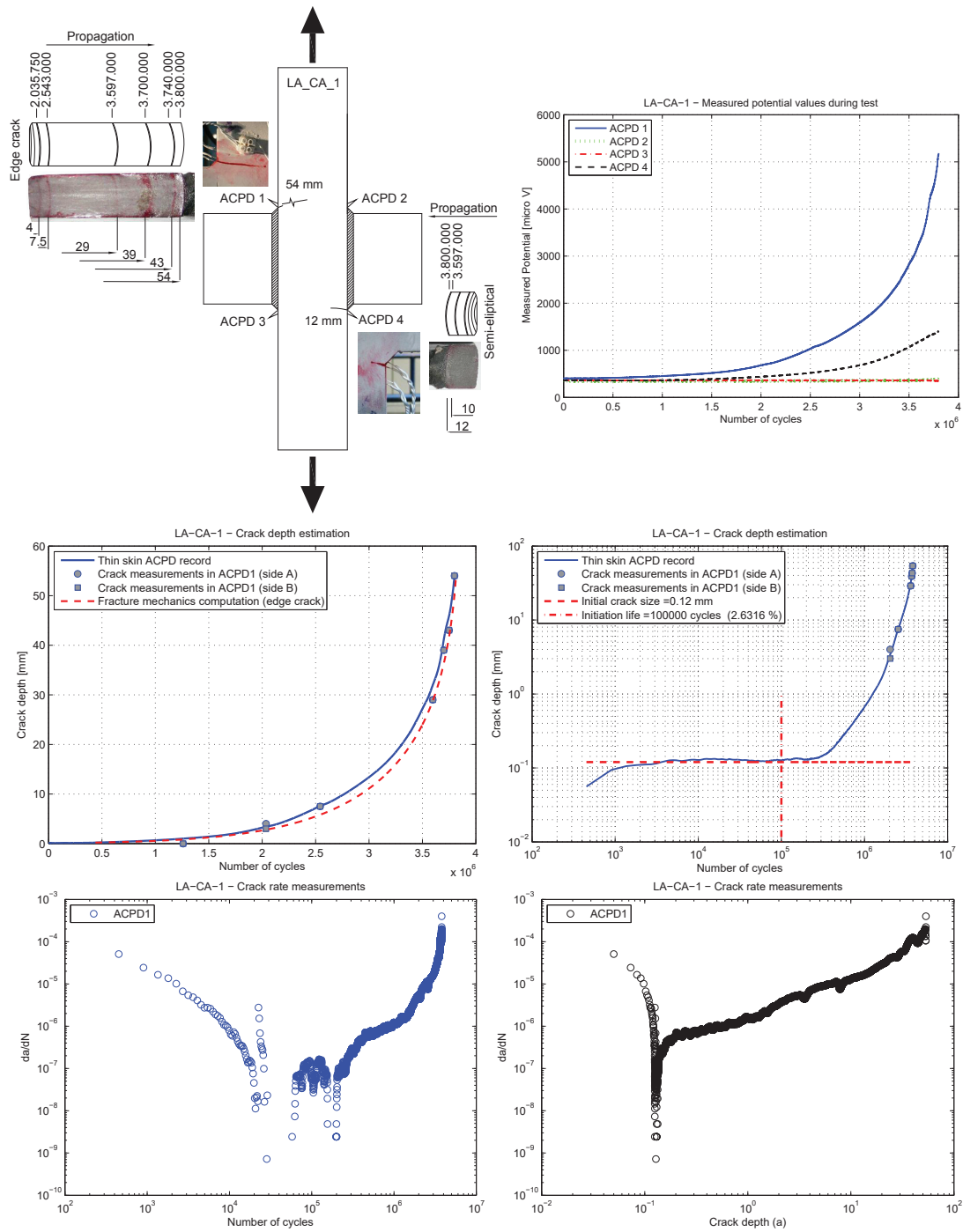


Figure 2.46 – LA-CA-1: ACPD potential, crack depths and growth rates

### 2.4.3 Summary of conclusions

- Constant amplitude tests carried out in Flange tip attachments and Intersected flanges were presented. A single detail with  $\Delta\sigma_{mean,2.10^6} = 60\text{MPa}$  was identified. Several run-outs obtained under the experimental program allow the definition of a mean experimental CAFL at  $5.10^6$  equal to  $\Delta\sigma_{mean,D} = 44\text{MPa}$ .
- The new experimental results are below the mean value obtained from the database of existing results in literature,  $\Delta\sigma_{mean,2.10^6} = 75\text{MPa}$ . The difference is attributed to the high stress ratio that was adopted in our tests,  $R_\sigma \geq 0,5$  eliminating mean stress effects.
- Residual stress measurements showed that tensile residual stress may be expected at the weld toe of lateral attachments, while compression may be present at the intersected flange weld toe.
- Micro-structures along various crack paths were analysed. Some difference was found between Flange tip and Intersected flange configuration. The different micro-structure at the Intersected flanges weld toe was identified as the cause for higher initiation lives of this configuration compared to flange tip attachments.
- Initiation lives ranging from 1 to 50% of total fatigue life were observed. A local stress approach using Coffin-Manson equation with Morrow's mean stress correction successfully estimates fatigue life to crack initiation.
- Propagation live was computed with a Linear elastic fracture mechanics model using three different crack types and their sizes identified from tests. Accurate propagation life estimations were obtained with the fracture mechanics model in good agreement with experimental crack growth curves.

## 2.5 Experiments under variable amplitude

The experimental program with variable amplitude in the high cycle regime, included a total of 23 tests on flange tip attachments. A concave shape spectra was used to increase the influence of small stress range cycles in the results. The n<sup>o</sup> of cycles for each block was chosen to produce equal damage according to a single slope S-N curve with m=3, similar as adopted by Gurney (2006). These were reproduced by block loading, figure 2.47, with maximum stress  $\sigma_{max}$  defined by  $R_{\sigma,1}=0,1$  for the 1<sup>st</sup> block, and kept constant for all stress cycles. Experimental results are summarised in table 2.12.

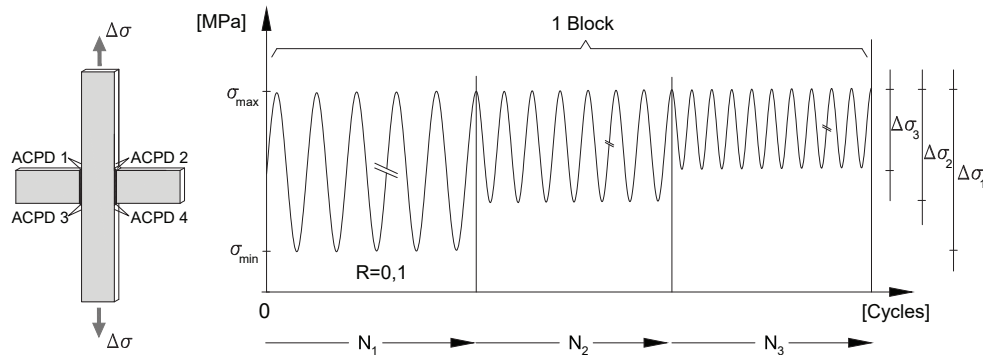


Figure 2.47 – Block loading definition used for the variable amplitude tests

Specimen	Stress range $\Delta\sigma_1$ [MPa]						Blocks to failure	$N_{failure}$ run-outs +
	100	80	60	50	40	30		
LA-VA-0	800	1562	3701				182	1.103.466
LA-VA-5	800	1562	3701				194	1.176.222
LA-VA-8	800				12500	29600	158	6.778.200
LA-VA-11	800				12500	29600	225	9.652.500
LA-VA-1		800	1896	3278			269	1.607.006
LA-VA-6		800	1896	3278			407	2.431.418
LA-VA-9		800			6400	15200	589	13.193.600
LA-VA-12		800			6400	15200	408	9.139.200
LA-VA-17		8000		33000	64000		30	3.150.000
LA-VA-18		8000		33000	64000		34	3.570.000
LA-VA-19		8000		33000	64000		35	3.675.000
LA-VA-20		8000			64000	152000	68	15.232.000
LA-VA-2			800	1383	2700		944	4.609.552
LA-VA-3			800	1383	2700		968	4.726.744
LA-VA-10			800		2700	6400	961	9.513.900
LA-VA-13			800		2700	6400	2236	22.136.400+
LA-VA-14			800		2700	6400	1515	14.998.500
LA-VA-16			800		2700	6400	2000	19.800.000+
LA-VA-4				800	1560	3700	6601	40.002.060+
LA-VA-7				800	1560	3700	1709	10.356.540
LA-VA-15				800	1560	3700	2318	14.047.080

Table 2.12 – Variable amplitude test results for lateral attachments

## 2.5.1 Analysis of results in nominal stress

For the analysis of variable amplitude tests, it is common to use the “equivalent stress range” concept, a fictitious constant amplitude stress range, that produces the same damage as the variable stress spectra. The equivalent stress is derived based on Miner’s rule,  $D = \sum \frac{n_{E,i}}{N_{R,i}} = D_{max}$  with  $D_{max} = 1$  at failure. In the simplest case, using a single slope S-N curve, the equivalent stress range is a weighted average:

$$\Delta\sigma_{eq,n_i} = \left( \frac{\sum \Delta\sigma_i^m n_i}{\sum n_i} \right)^{\frac{1}{m}} \quad \text{or} \quad \Delta\sigma_{eq,2} = \left( \frac{\sum \Delta\sigma_i^m n_i}{2 \cdot 10^6} \right)^{\frac{1}{m}} \quad (2.19)$$

For the typical welded details under normal stress,  $m=3$ , and the equivalent stress range expressed by equation 2.19 is the root mean cube (r.m.c). Figure 2.48 shows the equivalent stress range plotted against the experimental lives. The points are inside the constant amplitude scatter band, but it is evident that there is a non-explained effect on the scatter of the lowest stress range tests.

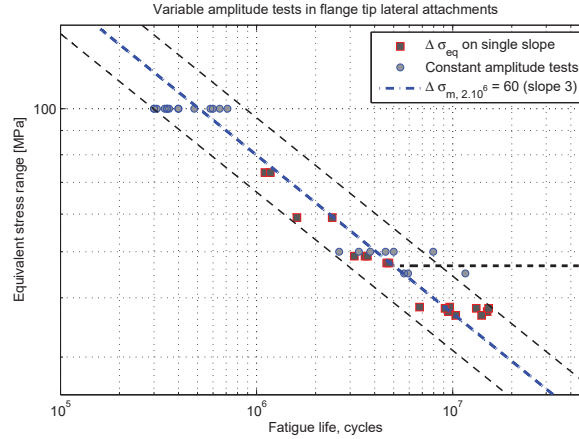


Figure 2.48 – Variable amplitude tests plotted according to equivalent stress

The variable amplitude block loading, a concave shape spectra, was designed to have a relatively large number of stress ranges below the CAFL, and equal damage produced by each stress range level, in a single slope S-N curve without “knee-point” and  $m=3$ :

$$\Delta\sigma_i^3 \cdot N_i = \Delta\sigma_j^3 \cdot N_j \Rightarrow D = \sum \frac{n_i}{N_i} = 1$$

With this definition of load spectra, all partials in the Miner’s sum would have the same weight ( $\alpha_i$ ), if all were equally damaging. A multilinear regression on the  $\alpha$  coefficients allows them to be calculated as:

$$D = \sum \frac{\Delta\sigma_1^3 \cdot N_1}{C} + \sum \frac{\Delta\sigma_2^3 \cdot N_2}{C} + \sum \frac{\Delta\sigma_3^3 \cdot N_3}{C} + \sum \frac{\Delta\sigma_i^3 \cdot N_i}{C} = 1$$

where  $C$  is the S-N curve intercept  $C = \Delta\sigma_{2,mean}^3 \cdot N_{ref}$ .

## Chapter 2. In-plane interaction - Flange crossings

Taking  $\Delta\sigma_{2,mean} = 60$  MPa as defined in Section 2.4 based on constant amplitude tests, we can write:

$$\alpha_1\Delta\sigma_1^m \cdot N_1 + \alpha_2\Delta\sigma_2^m \cdot N_2 + \alpha_3\Delta\sigma_3^m \cdot N_3 + \alpha_i\Delta\sigma_i^m \cdot N_i = 4,32 \times 10^{11} \quad (2.20)$$

Figure 2.49 shows the damage sum coefficients ( $\alpha_i$ ), where the small contribution of stress ranges  $\Delta\sigma = 30$ MPa is evident.

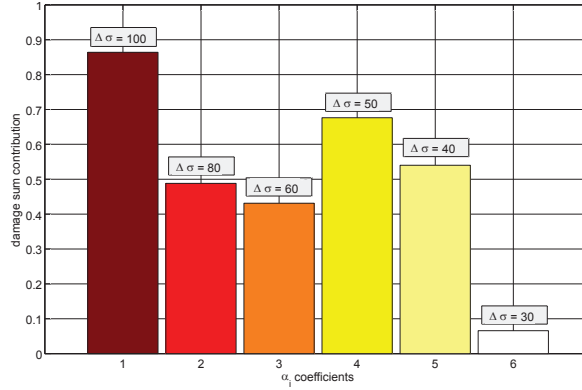


Figure 2.49 – Multilinear regression coefficients for Miner sum on single slope curve

To represent variable amplitude tests on a S-N plot, the equivalent stress range converts the entire variable load history into a single dot data. However, this representation is not the most convenient to investigate the influence of the different S-N curve shapes on the damage computation.

The influence of three different S-N curve shapes on the damage computation is shown in figure 2.50. The computations are based on the mean  $\Delta\sigma_{m,2.10^6} = 60$ MPa with knee-point at  $N_D = 5.10^6$  cycles, as defined with constant amplitude tests, figure 2.34.

Life estimations based on single slope S-N curve with CAFL at  $\Delta\sigma_{m,D} = 44$ MPa are non-conservative. Estimated lives are higher than experimental ones because computed damage is less than unity,  $D_{mean} = 0,65$ . This indicates the damaging character of stress ranges below the CAFL, as shown in figure 2.49 for  $\Delta\sigma = 40$ MPa.

By computing damage on a single slope curve  $m=3$  without “knee-point”, all stress ranges are supposed equally damaging, but estimated lives are lower than experimental ones. Damage is higher than one,  $D_{mean} = 1,21$ , meaning that stress ranges below the CAFL,  $\Delta\sigma = 40$  and  $\Delta\sigma = 30$ , contribute to damage, but not as predicted by the extension of the S-N curve below the “knee-point” with  $m=3$ .

Haibach’s model is able to translate this effect, with a 2<sup>nd</sup> slope  $k=5$  after the knee-point. Stress ranges below the CAFL are not ignored but their damaging effect increases as the CAFL progressively decreases with damage accumulation. Life estimations based on the double slope model, agree with experimental lives and damage is  $D_{mean} = 1,02$ .



## 2.5. Experiments under variable amplitude

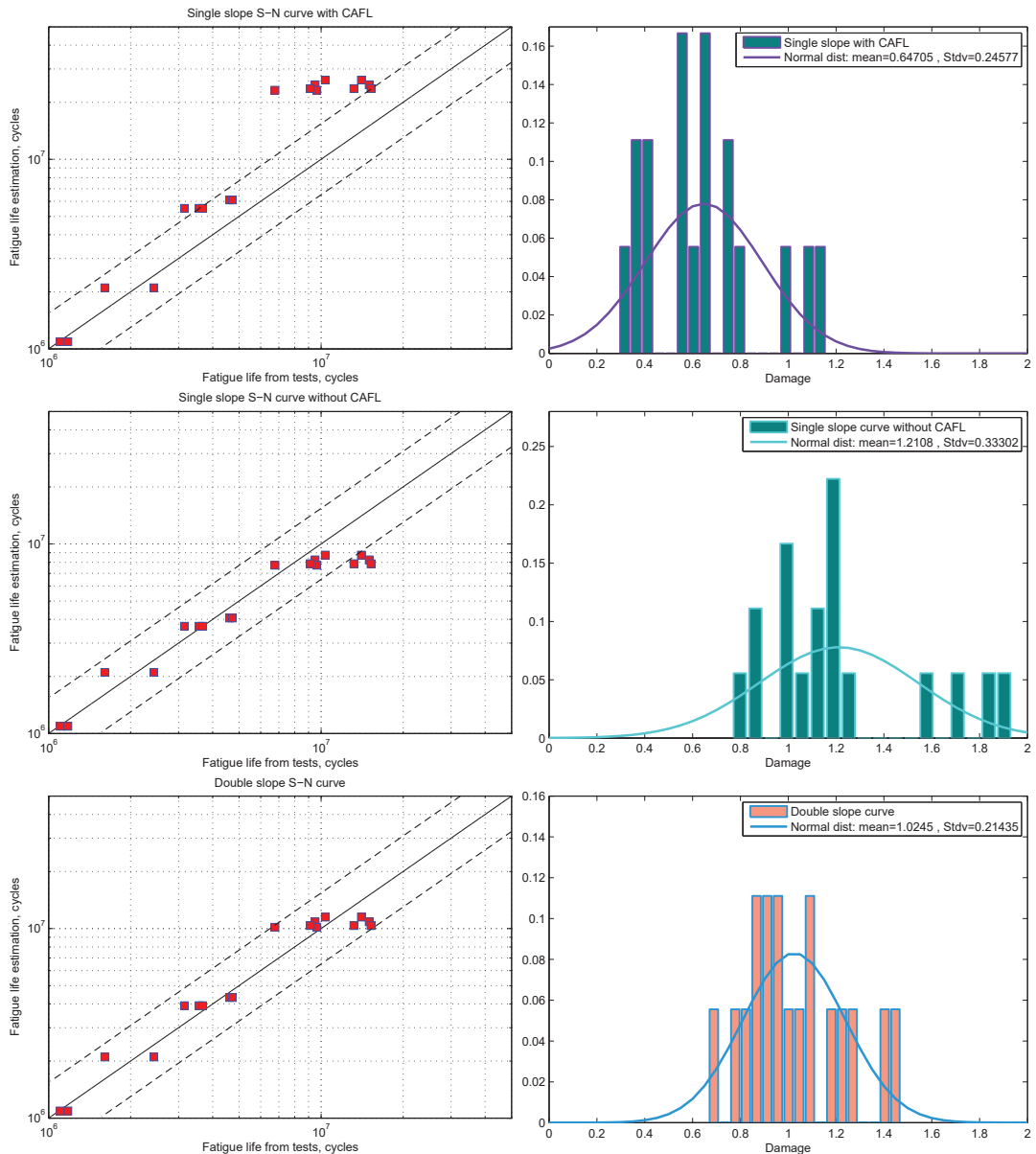


Figure 2.50 – Damage and estimated lives for 3 different S-N curves ( $\Delta\sigma_{m,2.10^6} = 60$ )

The analysis of experimental results under variable amplitude using an equivalent stress approach or by comparison of damage values for different S-N curves is limited by the fact that further information is required to characterise the non-linear effects influencing the damage sum. It is often the case in literature, that differences between the experimental results and life estimation based on equivalent stress and single slope S-N curves, are attributed to different types of sequence effects, but without experimental observation of those effects, because only the experimental life is generally measured. This has resulted in a variety of damage sum rules being proposed, or in different proposals of  $D_{max} \neq 1$  for Miner's linear damage sum rule. Herein, ACPD measurements are used to better quantify these effects for our block loading sequence.

### 2.5.2 Analysis of ACPD curves

Further analysis of the variable amplitude effects is done with the information from ACPD measurements, for which all specimens were monitored with probes. The analysis of the crack growth curves (a-N) and the damage contribution of stress ranges below the CAFL, indicate that there are sequence effects. As discussed in Chapter 1, two main effects are known to influence variable amplitude results, namely, crack retardation/acceleration due to overloads and the progressive drop of the crack propagation threshold.

While the absence of crack retardation/acceleration is confirmed by the ACPD readings, a third important effect was identified: the initiation life. The wide scatter obtained for the tests with significant parts of the spectra below the CAFL, is mainly attributed to the life required to initiate cracks, with registered initiation lives up to 45% of total fatigue life, see Appendix C.2. Figure 2.51 shows the total fatigue life divided by the measurements of initiation and propagation life.

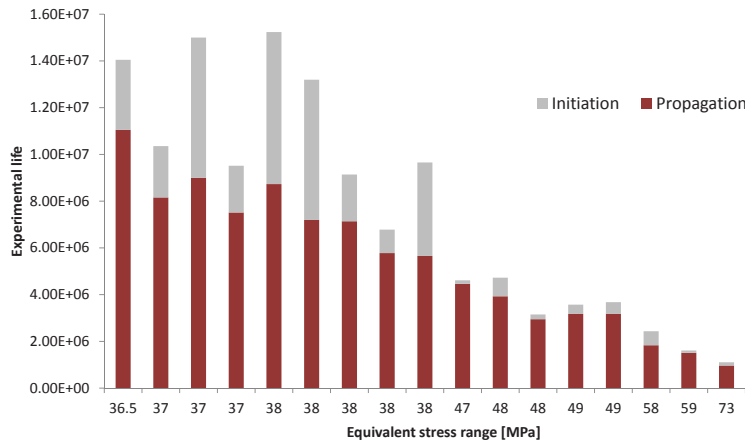


Figure 2.51 – Total fatigue life divided into measured initiation and propagation lives

### 2.5.3 Initiation-Propagation model

The initiation and propagation models that were used to estimate fatigue life under constant amplitude loads in Section 2.4 are extended here to the case of variable amplitude loads. By using the measured initiation and propagation lives and the crack shapes observed after analysis of the crack surface propagation, fatigue life is estimated for each specimen and calibrated to the experimental crack growth curve, by adopting different crack shapes, initial crack sizes and a/c ratios. These calculations are presented in Appendix C.2 for all tests from table 2.12, along with their ACPD curves and crack shapes. The example of LA-VA-20 is presented here to explain the model and to highlight the conclusions drawn from the experiments. Figure 2.52 shows the ACPD record and the crack depth for the critical crack (ACPD 2) of specimen LA-VA-20.

## 2.5. Experiments under variable amplitude

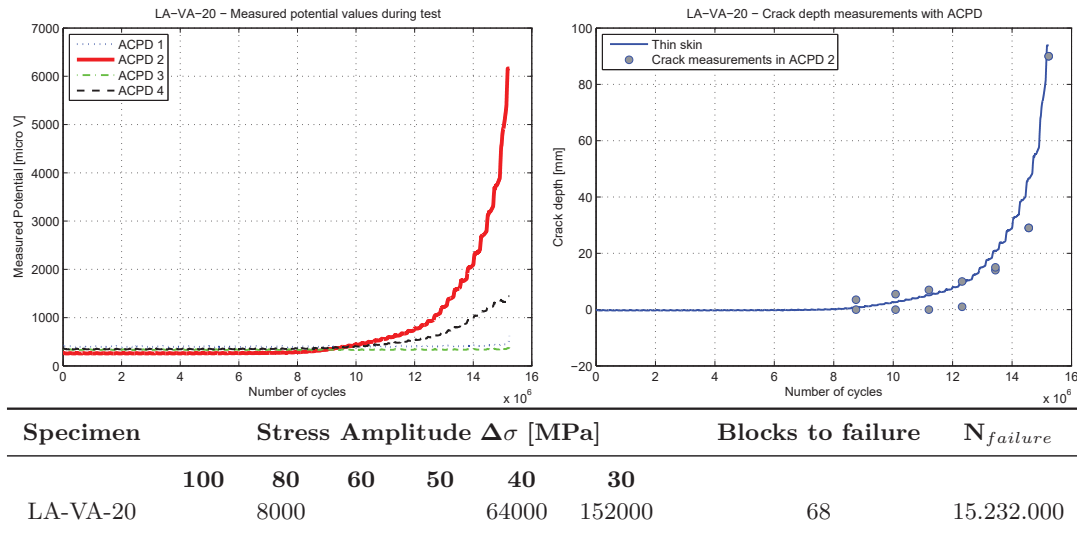


Figure 2.52 – LA-VA-20: Electric potential measurements and crack depth

### Initiation model

The local notch strain approach presented in Section 2.4 to estimate initiation life under constant amplitude, is applied here to variable amplitude. The stalactitical nature of the load spectra used for the experimental tests, figure 2.47 is characterised by having a constant maximum load. The corresponding maximum local stress  $\sigma_{max,local}$ , for the 1<sup>st</sup> load reversal, is obtained by solving equation 2.12.

$$\frac{(K_t \sigma_{max,nominal} + \sigma_{residual})^2}{E} = \sigma_{max,local} \left( \frac{\sigma_{max,local}}{E} + \left( \frac{\sigma_{max,local}}{K'} \right)^{\frac{1}{n'}} \right) \quad (2.12 \text{ rep})$$

#### 1<sup>st</sup> load reversal

$\sigma_{max, nominal}$	88,9
$\sigma_{max, notch, pseudo-elastic}$	515,6
$\sigma_{notch, residual}$	0
$\sigma_{max, notch, elasto-plastic}$	256,6
$\sigma_{notch, residual}$	235
$\sigma_{max, notch, elasto-plastic}$	287,7 [MPa]

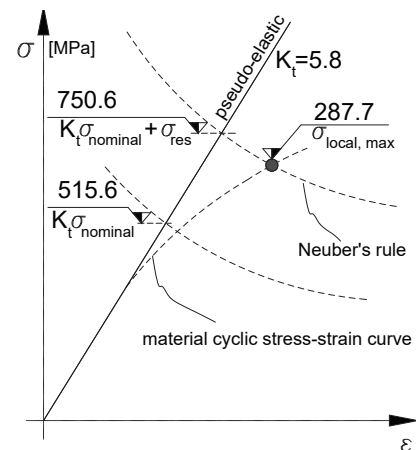


Table 2.13 – LA-VA-20: Schematic representation of the 1<sup>st</sup> load reversal

## Chapter 2. In-plane interaction - Flange crossings

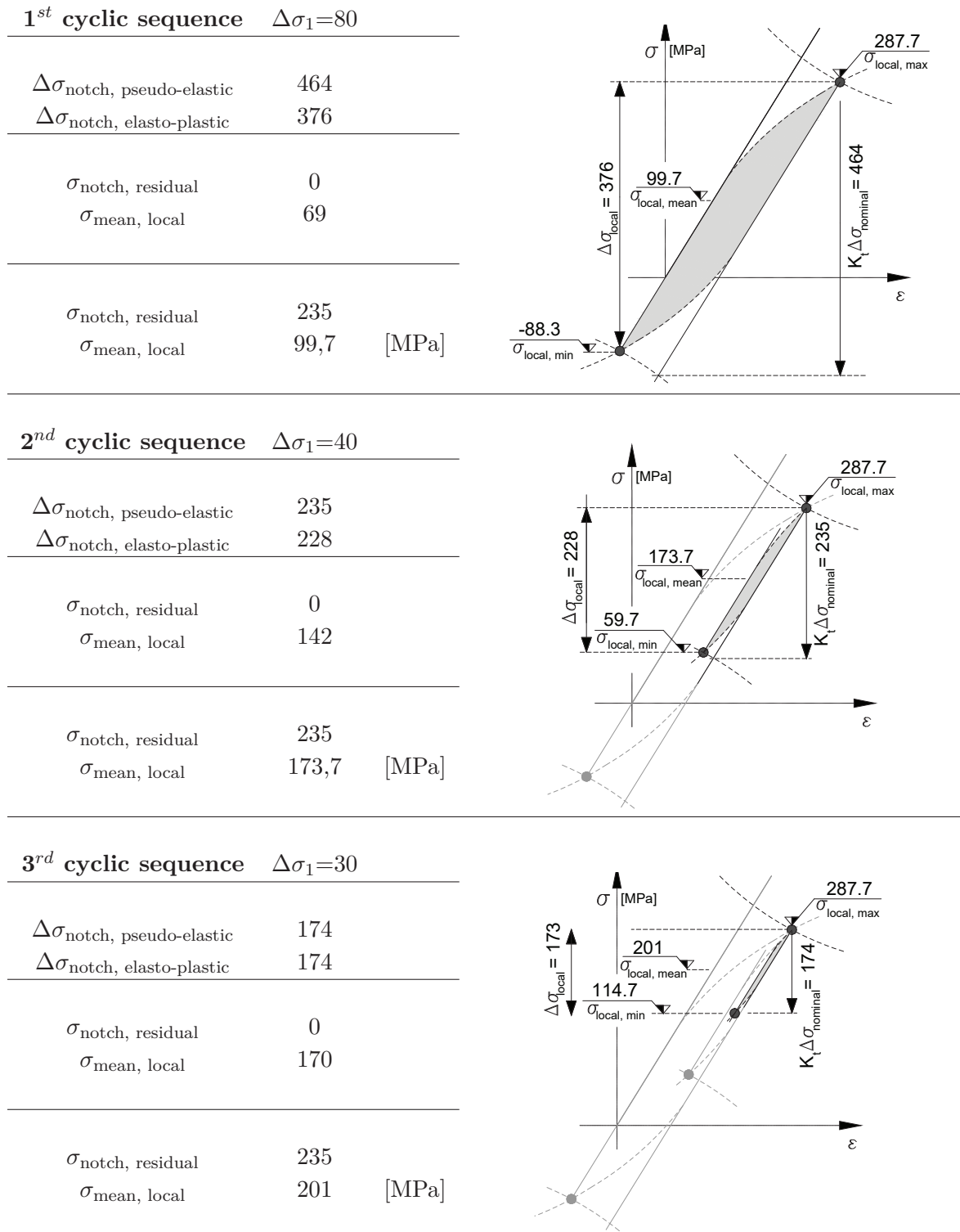


Figure 2.53 – LA-VA-20: Schematic representation of the cyclic load reversal

## 2.5. Experiments under variable amplitude

The maximum local stress  $\sigma_{max,local}$  is kept constant for the entire test and for each load sequence, the local stress range  $\Delta\sigma_{local}$  corresponding to  $\Delta\sigma_1$ ,  $\Delta\sigma_2$  and  $\Delta\sigma_3$  is obtained by equation 2.15 and the local mean stress, for each stress range level by:  $\sigma_{mean,local} = \sigma_{max,local} - \frac{\Delta\sigma_{local}}{2}$ , see figure 2.53.

Fatigue life to crack initiation is estimated with Miner's rule for each load sequence  $\Delta\sigma_1$ ,  $\Delta\sigma_2$  and  $\Delta\sigma_3$ , using Coffin-Manson equation 2.16 for total life for each stress range:

$$D = \frac{n_1}{N_1} + \frac{n_2}{N_2} + \frac{n_3}{N_3} \quad (2.21)$$

$$= \frac{8.000}{681.508} + \frac{64.000}{4.485.123} + \frac{152.000}{18.686.329} = 0,0117 + 0,0143 + 0,0081 = 0,0341$$

$$N_{initiation} = \frac{1}{D} = 6.560.800 \text{ cycles} \quad \text{with} \quad \sigma_{residual} = 235 \text{ [MPa]}$$

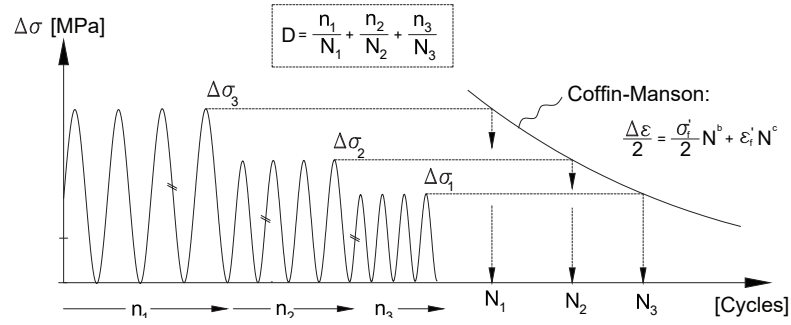


Figure 2.54 – Damage sum for initiation life

Estimated and measured initiation life is shown in figure 2.55. A range for the estimated life is given by the bounds  $\sigma_{residual} = [0; f_y]$ . The estimated initiation life  $N_{initiation} = 6.560.800$  cycles obtained for the case of  $\sigma_{residual} = f_y$  is in good agreement with the ACPD measurements  $N_{initiation,exp} \approx 6.500.000$

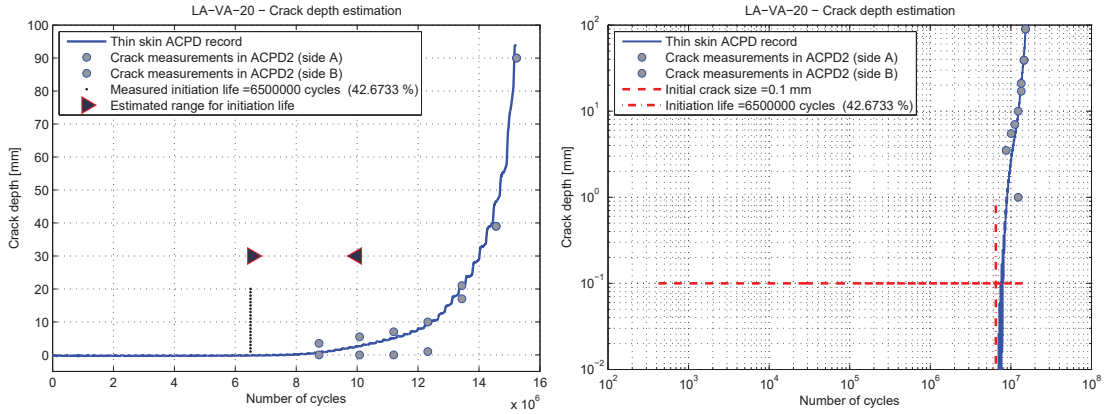


Figure 2.55 – LA-VA-20: Measured and estimated initiation life

Fracture mechanics model

To evaluate fatigue life under long crack propagation, the fracture mechanics model that was calibrated to constant amplitude experiments in Section 2.4 is applied here to variable amplitude load cycles.

Because the damage parameter  $D$  is not a measurable quantity, the crack depth is taken as a physical measure of fatigue damage. The theoretical damage evolution up to failure is thus given by the measurements of crack growth by considering the equivalence:  $D = 0 \xrightarrow{t_0} 1 \Rightarrow a = a_i \xrightarrow{t_0} a_f$

Since the load spectra is defined by specific sequences  $(n_1, n_2, n_3)$ , integration of Paris Law, equation 1.1, is done numerically, cycle by cycle. For each load cycle, the crack increment  $da$  is calculated for  $n_i = 1$ . The calculation process starts with an initial crack  $a_i$ , and goes numerically from  $N = 0 \xrightarrow{t_0} n_1$  using the corresponding stress range  $\Delta\sigma_1$ , then from  $N = n_1 \xrightarrow{t_0} (n_1 + n_2)$  using  $\Delta\sigma_2$  and from  $N = (n_1 + n_2) \xrightarrow{t_0} (n_1 + n_2 + n_3)$  with  $\Delta\sigma_3$ . The calculation stops when  $a = a_f$  returning the life estimate for the propagation from  $a = a_i \xrightarrow{t_0} a_f$ .

The fracture mechanics estimations are then checked visually by plotting them against the experimental crack growth curve. Figure 2.56 shows the crack growth curve up to failure, along with the corresponding crack surface. The crack propagation curve is obtained by considering a corner crack up to  $a/c=0,6$  ( $a \approx 9mm$ ) and an edge crack up to failure with  $C=1,5 \cdot 10^{-13}$  and  $m=3$  in Paris Law. Non-propagating cycles are defined with a crack growth threshold  $\Delta K_{th} = 100$  [Nmm<sup>-3/2</sup>] and a Stress Intensity Factor for corner cracks.

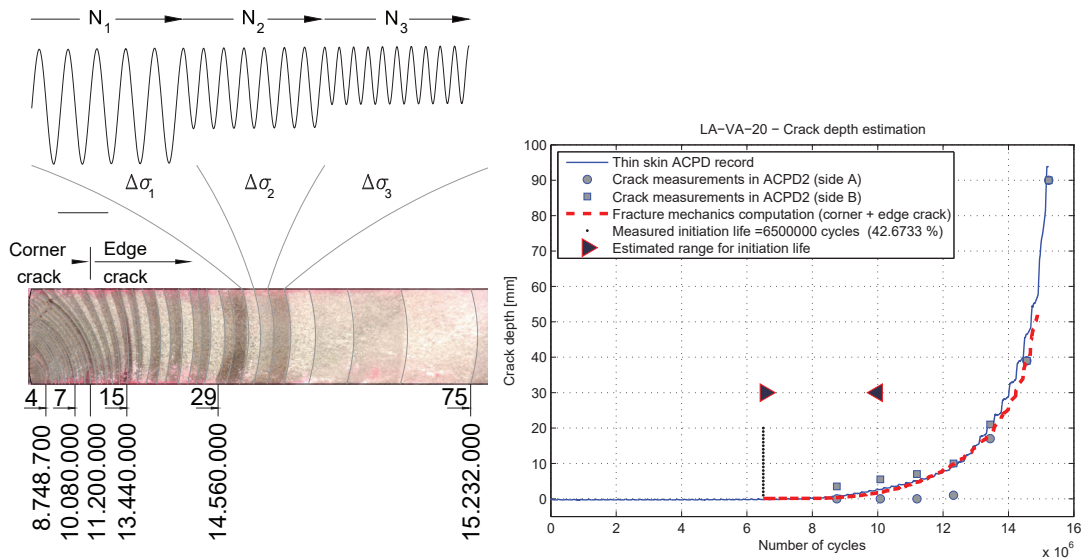


Figure 2.56 – LA-VA-20: Crack surface and fracture mechanics life estimation

## 2.5. Experiments under variable amplitude

The fracture mechanics computations are in good agreement with the experimental life, see all other computations in Appendix C.2. The variable amplitude model accounts for the crack propagation threshold effects which are the basis of S-N curves with a  $2^{nd}$  slope model. It is important to emphasise that the  $2^{nd}$  slope  $k$ , as proposed by Haibach, is an engineering model, and the slope value  $k$ , has no physical meaning. Consequently, it cannot be measured. However, the model seeks to account for the progressive drop on the crack propagation threshold, which is a physically measurable effect that can be observed experimentally as shown next.

For the variable amplitude tests, many of the load blocks were defined to have one or more stress levels below the mean CAFL, which was identified as  $\Delta\sigma_{m,D} = 44$  MPa, corresponding to  $\Delta\sigma_{m,2.10^6} = 60$  MPa . This is also the case for LA-VA-20 which had two stress levels below the CAFL, namely  $\Delta\sigma_1 = 40$  and  $\Delta\sigma_2 = 30$ . However, the identification of non-propagating stress levels, after the crack has start to grow, is not straightforward, specially because long cyclic periods are required to have stable ACPD results. For that reason, the block length for LA-VA-20 was increased to  $N_1 = 8000$  cycles, and ACPD records were made at 0,1 seconds intervals. The ACPD curves show that the stress range  $\Delta\sigma_3 = 30$  is not immediately effective, and that the initial crack growth in this case is given by propagation under  $\Delta\sigma_1$  and  $\Delta\sigma_2$ , figure 2.57.

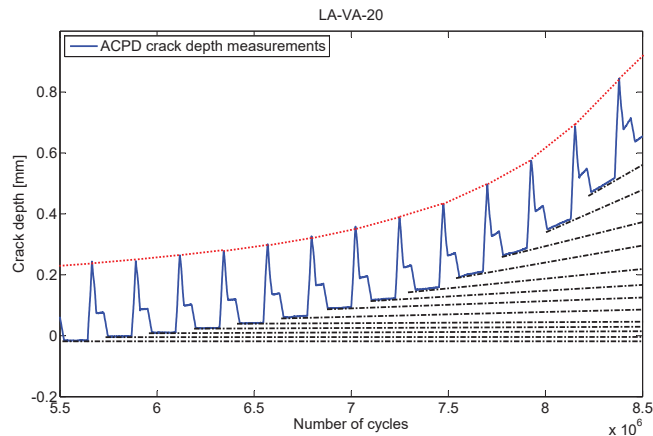


Figure 2.57 – LA-VA-20: Progressive crack propagation threshold measurements

An easier way to confirm the progressive crack threshold drop was achieved by an exemplary test. LA-VA-21 was conducted following a decreasing stress spectrum, carefully driven by “in loco” monitoring of the crack propagation measurements with ACPD. The test started with  $\Delta\sigma_1=100$  MPa, and after 50.000 cycles, a crack was already propagating, see figure 2.58. The stress range was then lowered to  $\Delta\sigma_2=80$  MPa and again after 50.000 cycles the crack was clearly propagating. The stress ranges were then continuously decreased following the same principle, down to  $\Delta\sigma_9=10$  MPa which was the highest non-propagating stress range. The test achieved 56.850.000 cycles, practically with all the cycles effective. This particularly test shows the accuracy and physical meaning of the progressive threshold drop model.

## Chapter 2. In-plane interaction - Flange crossings

Specimen LA-VA-21									$N_{Blocks}$
Stress Amplitude $\Delta\sigma$ [MPa]									
100	80	60	50	40	30	20	15	10	
50.000	50.000	50.000	100.000	100.000	500.000	4.000.000			1
						2.000.000	2.000.000		6
							2.000.000	2.000.000	7
$N_{failure} = 56.850.000$									

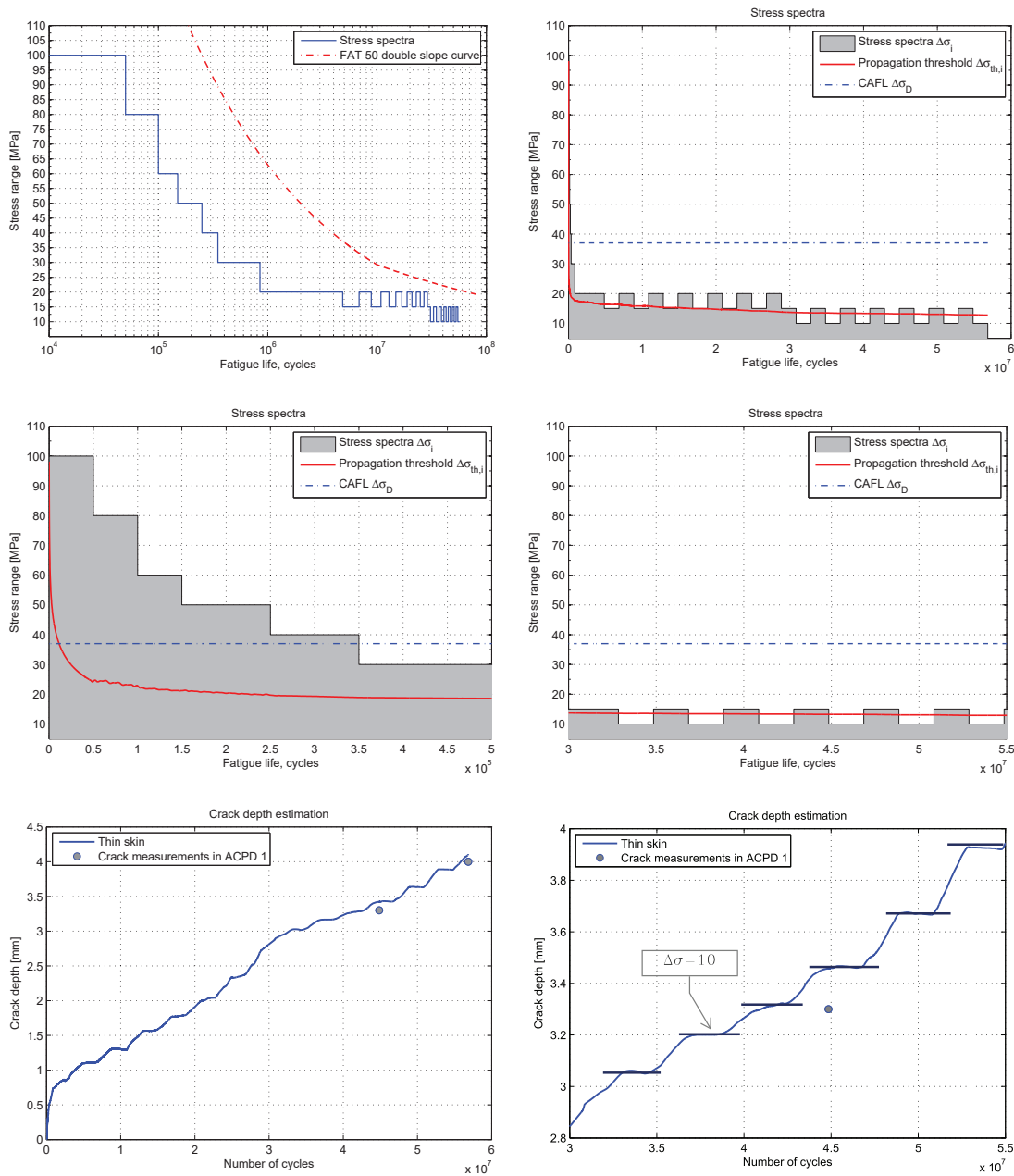


Figure 2.58 – LA-VA-21: Progressive crack threshold drop test



## 2.5. Experiments under variable amplitude

---

This test confirmed the cut-off level  $\Delta\sigma_L$ , with stress ranges below  $\Delta\sigma=15\text{MPa}$  being non-propagating, or by extrapolation, that the crack length required to have a propagation threshold drop to such low values, is very close to the failure crack. The “cut-off” limit for small stress ranges, i.e. the VAF<sub>L</sub>, is thus correctly defined at  $\approx 0,25$  FAT.

The LA-VA-21 test showed that it is possible to arrange the stress history in such a way, as to obtain a permanent crack propagation, i.e, a permanent drop of the propagation threshold. This is an extreme case of load spectra shape. In reality, the variable load spectra in bridges, contain many small stress range cycles that will load the crack tip with stress intensity factors below the propagation threshold. As a consequence, they do not contribute to the damage, and if all stress cycles from the load history are below this threshold, a technical endurance appears, and fatigue life is “infinite”. This is another extreme case, where independently from the load spectra shape, all stress ranges are below a technical endurance limit.

This lower extreme case was shown by some relevant run-outs obtained during this experimental program, specially with LA-VA-22, see table 2.14, which was extended up to  $70.10^6$  cycles without any measurable sign of crack propagation with ACPD or NDT. The maximum stress range for that particular test was fixed above the characteristic CAF<sub>L</sub>, corresponding to FAT50, i.e  $\Delta\sigma_{max} = (2/5)^{(1/3)}\text{FAT}50=37\text{MPa}$ . This endurance limit may be defined statistically as will be seen later, see figure 2.65 and 2.67. However, as discussed earlier, variable amplitude design, can hardly be based on this endurance limit. The LA-VA-22 test is thus considered as another important validation of the physical relevance of the propagation threshold drop model.

Specimen	Stress Amplitude $\Delta\sigma$ [MPa]			Blocks to failure	$N_{failure}$
	37	28	23		
LA-VA-22	1000	4000	11000	4375	70.000.000 <sup>+</sup> run-out <sup>+</sup>

Table 2.14 – LA-VA-22: Variable amplitude test with load spectra below CAF<sub>L</sub>

The previous conclusions, allow for the re-plotting of the variable amplitude results with the equivalent stress concept. Eliminating the scatter from initiation life, the equivalent stress concept may be applied using only the experimental propagation life, considered as effective. In this case, the experimental points align on a S-N single slope propagation curve with  $m=3$ , which corresponds to fully effective propagation, figure 2.59.

The concept of effective propagation life, gives the last proof of accuracy to the 2<sup>nd</sup> slope model. Fatigue lives estimated with fracture mechanics computations, that were demonstrated to be in good agreement with the experimental crack growth curves, are used as effective propagation life estimations. In that case, fatigue life estimation is performed on a single slope S-N curve with  $m=3$ , representing the fully effective propagating cycles.

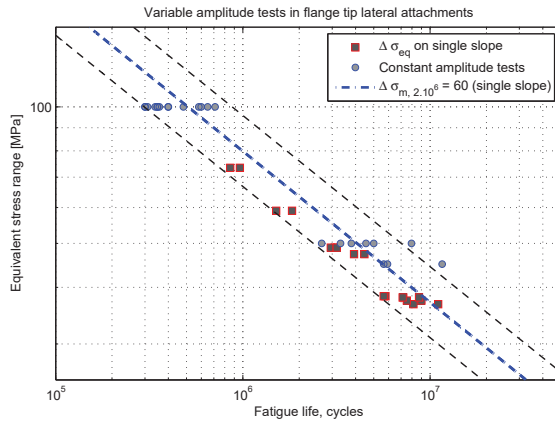


Figure 2.59 – Equivalent stress plot with effective life

The effective propagating life estimation is shown in figure 2.60, left side. On the other hand, the 2<sup>nd</sup> slope model, takes the non-effective stress ranges into account, by an artificial increase of fatigue life for points below the original threshold. This is shown on the right side of figure 2.60, where the total experimental lives are used. The equivalence of both life plots in figure 2.60, shows that the 2<sup>nd</sup> slope model is able to take the main sequence effect into account.

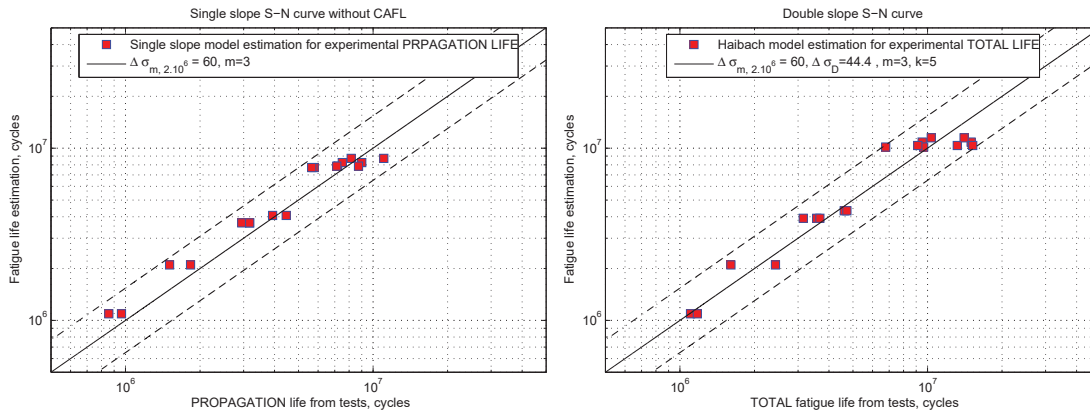


Figure 2.60 – Fatigue life estimations with effective life and Haibach's model

### 2.5.4 Summary of conclusions

- The experimental variable amplitude block loading was defined to have each stress range with similar damage on a single slope S-N curve without “knee-point”. A multilinear regression on the partials of Miner’s sum, showed smaller damage contribution for stress ranges below CAFL.
- Life estimations based on single slope S-N curve with CAFL were non-conservative with computed damage  $D_{mean} = 0,65$ . On the other hand, damage computation on a single slope curve without “knee-point”, was over-conservative with  $D_{mean} = 1,21$ . The best life estimations were achieved with a 2<sup>nd</sup> slope  $k=5$ , after the knee-point, with  $D_{mean} = 1,02$ .
- The experimental crack growth curves (a-N) allowed sequence effects to be identified. The progressive drop of the crack propagation threshold was experimentally recreated and measured. The wide scatter obtained for the tests with significant parts of the spectra below the CAFL, was mainly attributed to initiation life, with registered initiation up to 45% of total fatigue life.
- Both the local strain approach for initiation and the fracture mechanics model for propagation, were applied under variable amplitude loads. Very good agreement of the computed life estimates was achieved.
- Some important run-outs with lives ranging from 20 to  $70 \cdot 10^6$  cycles were obtained and showed no propagation for stress spectra with all stress ranges below a technical endurance limit.
- The cut-off level  $\Delta\sigma_L$  for small negligible stress ranges was experimentally measured. The VAFL, is suitable defined at  $\approx 0,25$  FAT lower than  $\Delta\sigma_L = 0,4$  FAT defined in Eurocode 3.
- The concept of effective propagation life was introduced. It proved that all propagating ranges do agree with an effective single slope propagation curve. The 2<sup>nd</sup> slope model proved accurate in taking the non-effective stress ranges into account, by an artificial increase of fatigue life for points below the original threshold. The 2<sup>nd</sup> slope model is thus able to include the main sequence effects.

### 2.6 Probabilistic fatigue model

The success of any experimental campaign with variable amplitude tests to explain the 2<sup>nd</sup> slope model, depends on the previous identification of the CAFL level. Constant amplitude tests performed to define the CAFL level are time consuming by nature, because trustful “run-outs” need to be obtained. Variable amplitude tests under various conditions of load spectra shapes and relative position to CAFL, are even more time demanding and expensive, because long initiation periods slow the crack propagation process. As an example, for the longest test presented on this thesis,  $70.10^6$  cycles were achieved. At 15Hz, the test takes 54 days with the test machine working 24h/day without any interruption.

The limitations on obtaining a reasonable number of experimental points justify a simulation model, where “virtual tests” are generated, based on the fatigue models previously calibrated on “real tests”. A probabilistic Monte Carlo simulation framework is used here, developing generalised constant and variable amplitude S-N curves for the flange tip attachments. The simulations include uncertainties such as crack shape, initial depth, crack growth parameters, geometry and material strength.

Several probabilistic models based on Linear Elastic Fracture Mechanics for constant amplitude fatigue can be found in literature, (Walbridge, 2005), (Leander et al., 2013), including approaches using a Monte Carlo technique to estimate the CAFL, extrapolating the fatigue results at constant amplitude in the long life regime (Yamada et al., 1989a) (Yamada and Shigetomi, 1989). An early probabilistic model considering both fatigue and brittle fracture limit states was developed by Banz and Nussbaumer (2001).

One general trend common to all these works is the lack of a crack initiation stage which is generally assumed to be zero. This is a conservative approach suited to define characteristic constant amplitude S-N curves, defined only by propagation, but the assumption of negligible initiation life does not hold under variable amplitude fatigue with high number of cycles below the CAFL, as was clearly shown with the experiments presented in Section 2.5. Moreover, variable amplitude probabilistic models have relied on equivalent stress range approaches, (Miki et al., 1989), (Zhao et al., 1994) for example, which cannot account for the sequential threshold drop effects, as the fracture mechanics model proposed here. The model presented in this section, extends the previous procedures to variable amplitude fatigue, by extrapolating the variable amplitude fracture mechanics model to different load spectra shapes, with due account for variability in the main parameters: propagation threshold and initiation life. Two different simulation frameworks are developed for the definition of general S-N curves:

**1 - Constant amplitude S-N curve** (*definition of scatter bands and CAFL*)

**2 - Variable amplitude S-N curve** (*second slope estimation for specific load spectra*)

The division of total fatigue life in technical crack initiation and propagation has been suggested by Lawrence et al. (1978) for welded structures. A review of similar models is presented in (Radaj et al., 2006) and has been previously adopted by the author, for plates with holes (Baptista and Nussbaumer, 2014). Total fatigue life ( $N_{total}$ ) is given by crack initiation ( $N_i$ ) and propagation ( $N_p$ ). Short crack behaviour is not explicitly considered and is inherently included in the initiation model. The explicit modeling of short crack behaviour requires calibration over measurements with capacity to register propagation below  $100\mu\text{m}$ . The two stage Initiation-Propagation model (I-P model) is summarised in figure 2.61 with the technical crack initiation **Stage I**, and long crack propagation **Stage II** represented in figure 1.6.

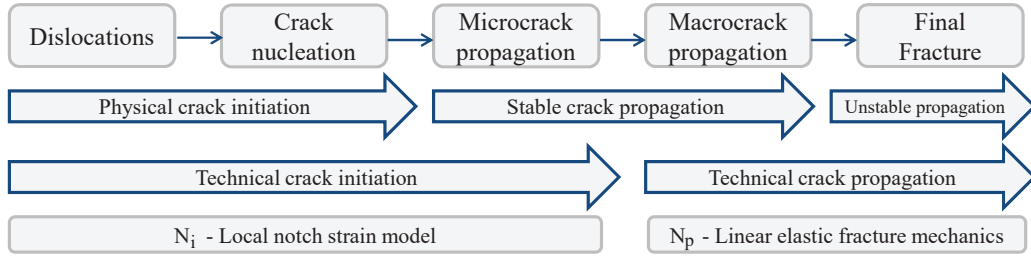


Figure 2.61 – Schematic crack stages for the I-P model

### 2.6.1 Stage I - Initiation

Initiation life is estimated with the local elasto-plastic strain approach presented in Section 2.4. Local mean stress and material micro-structure were identified as important factors influencing crack initiation. Variability on the local mean stress  $\sigma_{m,local}$  is considered by estimating the local mean strain, with due account for the local plastic effects. For a given random set of nominal stress range  $\Delta\sigma$ , stress concentration  $K_f$  and  $R_\sigma$ , Neuber's notch rule is numerically solved with the Ramberg-Osgood curve to estimate the local maximum  $\sigma_{max,local}$ , using a random pair of pseudo-values ( $K_t\Delta\sigma$ ;  $\sigma_{residual,local}$ ). Under constant amplitude, a positive stress ratio is considered according to a uniform distribution defining the maximum nominal stress  $\sigma_{max} = \frac{\Delta\sigma}{1-R_\sigma}$ :

$$R_\sigma \rightarrow \text{uniform}(\min = 0, 1; \max = 0, 75)$$

For variable amplitude spectra, the maximum stress is given by a random value of  $R_\sigma$  for the highest stress range in the spectra. This maximum stress is kept constant for all other smaller stress ranges following a stalactite spectra shape. Both compressive and tensile residual stress at the notch are considered by random values according to a uniform distribution:

$$\sigma_{residual,local} \rightarrow \text{uniform}(-f_y; +f_y) \text{ [MPa]}$$

## Chapter 2. In-plane interaction - Flange crossings

The local strain range  $\Delta\sigma_{local}$ , is evaluated by the same numerical procedure with equation 2.15 and local mean stress obtained by  $\sigma_{m,local} = \sigma_{max,local} - \frac{\Delta\sigma_{local}}{2}$ .

Both the Coffin-Manson relation, equation 2.16, and the Ramber-Osgood cyclic material curves, equation 2.11, are influenced by the tensile stress  $f_u$ . Variability is introduced in the fatigue strength coefficient  $\sigma'_f = 1,5f_u$  and in the cyclic strength coefficient  $K'=1,65f_u$ , by randomly defining the material tensile stress  $f_u$ , with an uniform distribution corresponding to steel grades S235 to S460:

$$f_u \rightarrow \text{uniform}(\min = 360; \max = 720) \text{ [MPa]}$$

All other parameters are kept constant as defined in table 2.11. Figure 2.62 shows the material curves for the relevant steel grades considered in the simulation.

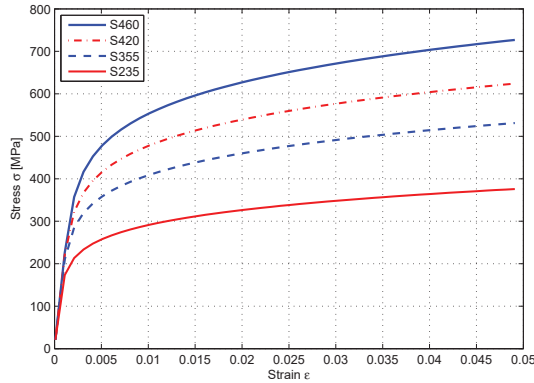


Figure 2.62 – Ramber-Osgood curves for structural steels defined in EN10025

The theoretical Stress Concentration Factor for the flange tip attachments with weld flank angle of  $45^\circ$  and toe radius of 1mm was calculated based on a finite element analysis using the effective 1mm notch method,  $K_t = 5,5$  but variability on the weld toe geometrical parameters is expected to influence  $K_t$ . Several authors have defined statistical distributions for the weld flank angle at the toe radius and confirmed the statistical independence of both parameters, (Yakubovski and Valteris, 1989), (Barsoum and Jonsson, 2008). Based on literature measurements, both variables were seen to follow a normal distribution with a COV=0.1. The  $K_t$  values were confirmed by finite element analysis for some discrete relevant values of weld flank angle. The stress concentration factor is thus considered as a gaussian variable:

$$K_t \rightarrow \text{normal}(\mu = 5,5; \text{stdv} = 0,55)$$

The initiation period finishes when the microcrack growth is no longer dependant on the microstructure or surface conditions, and thus, the crack growth resistance of the material starts to control the crack growth. The size of the microcrack at the transition stage is thus material dependant and the initiation stage is assumed to include crack

nucleation and micro-crack growth. The transition from short to long crack regime is assumed at roughly 5 grains, i.e.  $100\mu\text{m}$  considering  $20\mu\text{m}$  grain size. This showed to be the minimum value measurable with our ACPD equipment, see Appendix C. The initiation model thus estimates fatigue life to initiate a crack of  $0,1\text{mm}$ .

### 2.6.2 Stage II - Propagation

Propagation life is estimated with fracture mechanics, taking crack depth as a damage parameter. For constant amplitude, Paris law is integrated from an initial crack  $a_i$  to a final crack size  $a_f$ , while under variable spectra load, the integration is done for the  $N_i$  cycles of the spectra blocks, under the condition of being above the the propagation threshold  $\Delta K_{th}$ :

$$\int_0^N dN = \int_{a_i}^{a_f} \frac{1}{C(YM_k\Delta\sigma\sqrt{\pi a})^m} da = \frac{1}{C(\Delta\sigma\sqrt{\pi})^m} \int_{a_i}^{a_f} \frac{1}{(YM_k\sqrt{a})^m} da \quad (2.22)$$

Scatter sources depend on the initial crack size and crack growth parameters, considering all three types of cracks presented in figure 2.45 and their combinations.

Cracks start to grow as one of the three configurations: **edge**, **semi-elliptical** or **corner crack**. The model choses randomly between each type. Once the propagation life is initiated with either a semi-elliptical or corner crack, a criteria based on the  $a/c$  ratio defines the transition for edge crack propagation. A lognormal distribution was adopted for the  $a/c$  ratio as proposed by Yamada et al. (1989b), with mean and standard deviation based on the observed crack types from our tests:

$$a/2c \rightarrow \text{lognormal} (\mu = 0,2; \sigma = 0,05) , \text{ semi-elliptical crack}$$

$$a/c \rightarrow \text{lognormal} (\mu = 0,5; \sigma = 0,05) , \text{ corner crack}$$

The crack depth,  $a_i$ , defining the transition to an edge crack during the integration of equation 2.22, is defined at  $2c=t$  (for the semi-elliptical crack) and  $c=t$  (for the corner crack), see figure 2.45 for definitions. Limit state function for crack failure as an edge crack is assumed as  $a_{final} = \frac{W}{3}$ .

#### Initial imperfections in welds

The initial crack-like imperfections have an important influence on the estimated propagation life using fracture mechanics computation. The initial crack size should ideally be taken as the crack detected by weld inspection, but the acceptable crack size is often too high, and the minimum detectable crack size for the NDT technique too small, table 2.15. The initial crack size is then usually taken as  $a_{initial} = 0,1\text{mm}$  which is considered the theoretical minimum value that assures Linear Fracture Mechanics validity (Broek,



## Chapter 2. In-plane interaction - Flange crossings

1986). The Stress Intensity Factor concept to describe the stress field at the crack tip, is based on linear and isotropic elastic theory. The equations that describe the stress field at the crack tip are an approximation of that field with dimensions around  $a/10$ . If the region  $a/10$  is considered to be at least equivalent to a grain, a minimum grain size of  $10\mu\text{m}$  allows for  $a_{min} = 100\mu\text{m}$ . The initial crack  $a_{initial} = 0,1\text{mm}$ , may also be obtained by back calculation, “fitted”, to allow life estimation by Linear Elastic Fracture Mechanics, ignoring initiation and micro-crack growth. In a more conservative approach,  $a_{initial} = 0,15\text{mm}$  is recommended in (IIW, 2008) and alternatively a value of  $a_{initial} = 0,75\%t$  ( $t$  - plate thickness) is proposed in (Hobbacher, 2010). For a worst case scenario  $a_{initial} = 0,5\text{mm}$  is sometimes assumed (Guerrera, 1982) which was the maximum value reported by Signes et al. (1967).

	Visual	DP	MP	EC	PD	US	Rx	[mm]
Crack depth (a)	-	0,5	0,1	0,1	0,1	1	0,02 t	
Crack width (b)	0,1	0,01	0,001	0,01	0,01	0,001	0,1	
Crack length (c)	2	1	1	1	2	1	1	

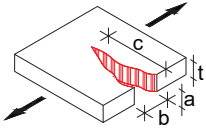


Table 2.15 – Minimum reference detectable crack values with NDT

Welding imperfections in the vicinity of the weld toe have been measured by several authors (Maddox, 1974), (Yang and Manning, 1980), (Martinez and Korsgren, 1993). Sharp small cracks, or microcracks, typically 0,1 to 0,4 mm deep are generally present in weld toes, (Husset, Lieurade, Maltrud, 1985). Signes et al. (1967) reported an average depth of 0,15mm and a maximum of 0,5mm. A maximum of 0,4mm was reported by Watkinson et al. (1971). Average depths of  $45\mu\text{m}$  and some of the imperfections with a depth above  $100\mu\text{m}$  were reported by Smith and Smith (1982) in non-load carrying fillet welds made with manual metal arc. Barsoum and Samuelsson (2006) found imperfections of 0,1 to 0,2 mm deep in transversal non-load carrying MAG welds, figure 2.63.

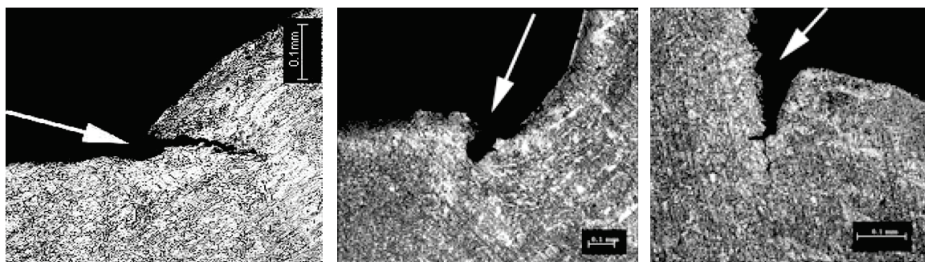


Figure 2.63 – Initial imperfections: cold-laps and undercuts (Samuelsson et al., 2008)

The variability of the initial crack depth is assumed in our model to follow a lognormal distribution as proposed by Engesvik and Moan (1983). This distribution was previously adopted in other studies (Banz and Nussbaumer, 2001), and is in generally agreement with measurements reported in literature:

$$a_i \rightarrow \text{lognormal} (\mu = 0,125; \sigma = 0,045) [\text{mm}]$$



### Fatigue crack threshold Stress Intensity Factor

$\Delta K_{th}$  has a strong dependency on stress ratio  $R_\sigma$  and relations between  $\Delta K_{th}$  and  $R_\sigma$  are defined in (BS 7910, 2005) for example. These are mainly applicable for non-welded or stress-relieved components, while in welded structures, tests to define  $\Delta K_{th}$  are carried out at high stress ratios, accounting for high welding residual stresses. The usual approach is thus to define  $\Delta K_{th}$  independent from stress ratio, based on measurements at high  $R_\sigma$ . Values between  $70 < \Delta K_{th} < 130$  have been adopted in other studies (Bremen, 1989) and a characteristic value  $\Delta K_{th} = 63 \text{Nmm}^{-3/2}$  is recommended in (IIW, 2008) or (BS 7910, 2005) for  $R_\sigma=0,5$ . The threshold stress intensity factor  $\Delta K_{th}$  is defined in our model as a lognormal variable after Walbridge (2005):

$$\Delta K_{th} \rightarrow \text{lognormal} (\mu = 100; \sigma = 15) [\text{Nmm}^{-3/2}]$$

### Paris law parameters

Maddox (1973) has experimentally obtained crack propagation rates for base metal, Heat Affected Zone (HAZ) and filler metal. He found the Paris law parameters to be independent for a given steel type, without remarkable difference between the HAZ, plain material or weld metal. This means that a Paris law with one pair of material parameters,  $C$  and  $m$ , is applicable for the crack propagation along any of those three different micro-structures. For low-alloy carbon steels in general, he proposed  $m=3$  and  $C_{min} = 0,9 \cdot 10^{-13}$ ,  $C_{max} = 3 \cdot 10^{-13}$ .

Uncertainty in the crack propagation rate is considered by assuming  $\text{Log}(C)$  normally distributed with  $C_{mean} = 1,1 \cdot 10^{-13}$  as proposed by Banz and Nussbaumer (2001) and defined in (DNV, 2014). The exponent  $m$  is given by  $C = (1,315 \cdot 10^{-4}) / (895,4^m)$  after Gurney (1978), (Gurney, 1979):

$$C \rightarrow \text{lognormal} (\mu = -29,84; \sigma = 0,55)$$

### 2.6.3 Constant amplitude simulations

The Monte Carlo framework for the simulation of S-N curves under constant amplitude is schematically shown in figure 2.64.

The first step for each simulation, is to generate a random pair or nominal stress range,  $\Delta\sigma$ , and stress concentration  $K_f$ . Stress range is generated with an uniform distribution:

$$\Delta\sigma \rightarrow \text{uniform}(min = 10; max = 0,5f_y) [\text{MPa}]$$

with  $f_y$  obtained by solving  $f_u = f_y(1 - 0,72 \cdot e^{-0,0027f_y})^{-1}$  (Raoul and Günther, 2005)

## Chapter 2. In-plane interaction - Flange crossings

Maximum stress range is limited to  $\Delta\sigma_{max} = 1,5f_y$  according to EN 1993 1-9 (2005) but values of this magnitude are in Low Cycle Fatigue regime, with number of cycles ranging from 762 (S460) to 5700 (S235) considering a FAT50. This range is of little importance for steel bridges so the maximum stress range is limited to  $\Delta\sigma_{max} = 0,5f_y$ , considering that the ratio between traffic loads and permanent loads is often close to unit.

After all random variables for loads, geometry and material are defined, the initial crack size is evaluated. If  $a_i > 0,1\text{mm}$ , one of the three possible crack shapes is chosen randomly and the Stress Intensity factor,  $\Delta K$  is compared to the threshold  $\Delta K_{th}$ . If  $\Delta K > \Delta K_{th}$ , the fracture mechanics model estimates propagation life up to failure. In case  $\Delta K < \Delta K_{th}$ , a new crack is allowed to initiate, the calculations run the same way as for the case where the initial random crack was  $a_i < 0,1\text{mm}$ . Initiation life is estimated and  $a_i = 0,1\text{mm}$  is assumed. A random crack shape is attributed to this new crack, and the Stress Intensity Factor is again evaluated. If  $\Delta K < \Delta K_{th}$ , the point is a run-out, with life given only by initiation (final non-propagating crack  $a_i = 0,1\text{mm}$ ). If  $\Delta K > \Delta K_{th}$ , the fracture mechanics model estimates propagation life up to failure and  $N_{total} = N_i + N_p$ .

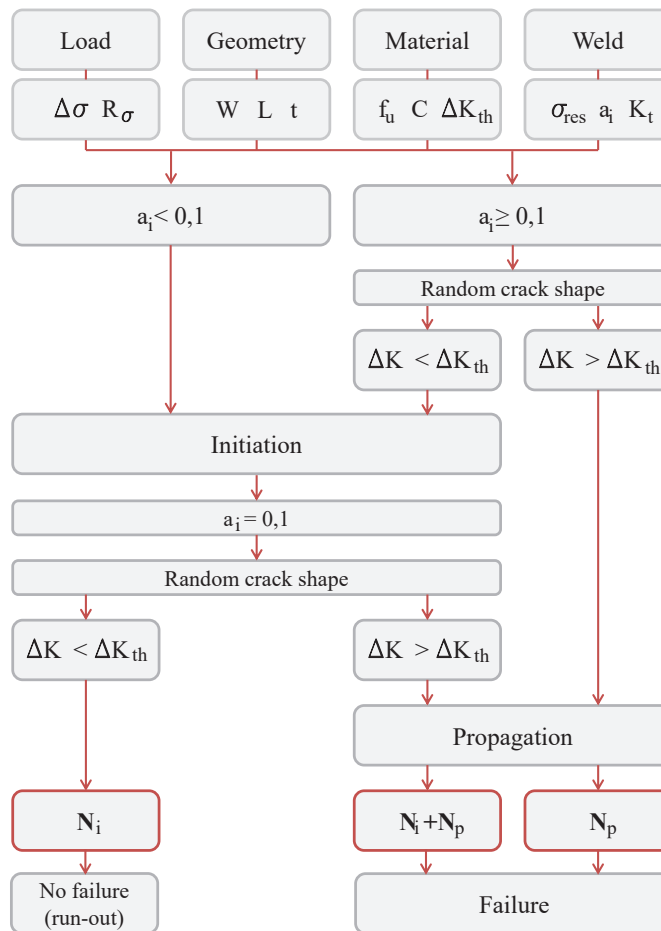


Figure 2.64 – Monte Carlo model for constant amplitude

Two different cases are investigated with results generally based on 100.000 simulations:

- **Flange tip lateral attachments “test sample”**

The random variables of the model, are restricted to the case of Lateral attachments and Intersected flanges tested in this thesis. This means restricting geometric parameters to  $W=L=150\text{mm}$  and  $t=15\text{mm}$ , and  $f_u$  between 360 and 510MPa.

- **Flange tip lateral attachments “population”**

The random variables apply to a wider range of geometric configurations with parameters given by a range of values representative for steel bridges:

- $W \rightarrow$  uniform ( $min = 100; max = 1000$ ) [mm]
- $L \rightarrow$  uniform ( $min = 100; max = 500$ ) [mm]
- $t \rightarrow$  uniform ( $min = 10; max = 100$ ) [mm]

Figure 2.65 shows the results for the simulations on the “sample” group of lateral attachments. A Type II Generalized Extreme Value (GEV) is used to fit the histogram of CAFL estimation. Characteristic 5% percentile (95% survival probability) is  $\Delta\sigma_D = 33$  MPa, and the 50% percentile is  $\Delta\sigma_{D,50\%} = 46$  MPa which is in very good agreement with the experimental values  $\Delta\sigma_{D,50\%} = 44$  MPa obtained experimentally, see Section 2.4.

The statistical analysis for the characteristic FAT value based on propagation life, right side on figure 2.65 gives a slope  $m=3,09$ . Fixing the slope to  $m=3$ , the mean value for the S-N curve is  $\Delta\sigma_{mean,2.10^6} = 60\text{MPa}$  and characteristic value for 95% survival probability is FAT50. These values confirm both the experimental results obtained under constant amplitude and the re-analysis of the database of literature results. Combining the characteristic 5% percentile values of CAFL and FAT, the knee-point is given at:

$$N_D 33^3 = 2.10^6 50^3 \rightarrow N_D = 7.10^6 \text{cycles}$$

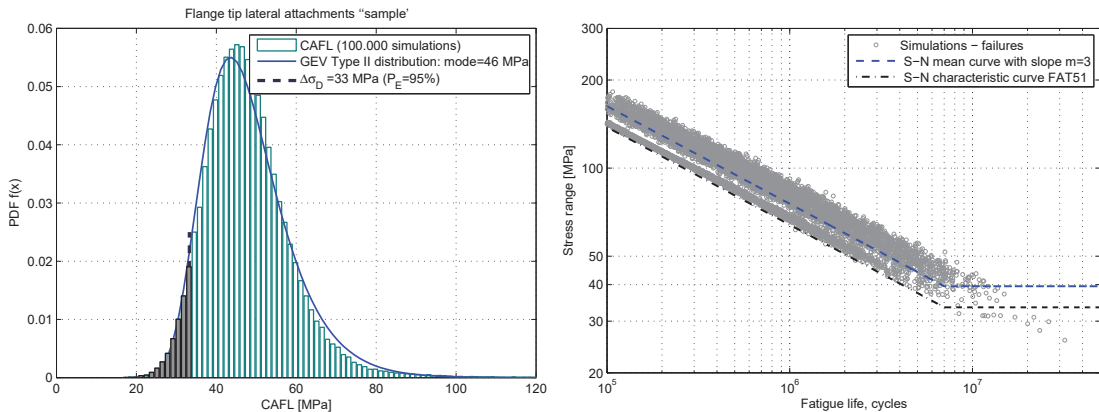


Figure 2.65 – Statistical analysis for the flange tip attachments “sample”

Figure 2.66 shows the set of simulations along with our experimental results and the S-N curve. Run-outs are represented by life to initiate a crack  $a_i = 0, 1$  whose Stress Intensity Factor was below the threshold,  $\Delta K < \Delta K_{th}$  without subsequent propagation.

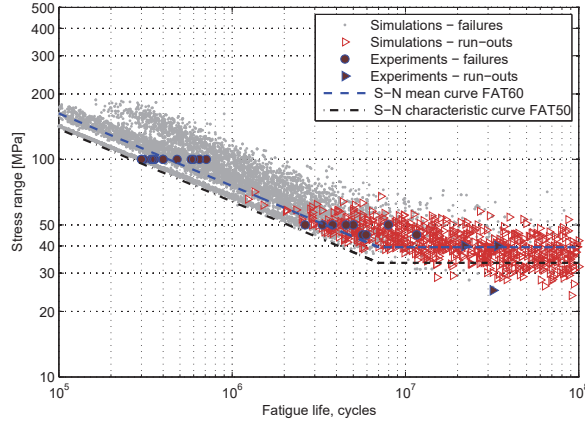


Figure 2.66 – Constant amplitude S-N curve (Flange tip attachments “sample”)

The Initiation-Propagation simulations for the “population” of flange tip lateral attachments, require variation in the most important geometric parameters. Size effects identified in Section 2.1 and Appendix A.2, are the attachment length and the plate width with less influence. Both influence  $YM_k$ . Plate width  $W$  is extended to 1000mm, attachment length  $L$  to 500mm and thickness to 100mm. Figure 2.67 shows the simulations obtained under these conditions. Again a Type II GEV distribution is used to fit the CAFL simulations and lower values of characteristic 5% percentile (95% survival probability)  $\Delta\sigma_D = 25$  MPa, and 50% percentile  $\Delta\sigma_{D,50\%} = 37$  MPa are obtained. A characteristic FAT45 S-N curve is obtained, that combined with the 5% percentile CAFL value, defines the knee-point at:

$$N_D 25^3 = 2.10^6 45^3 \rightarrow N_D = 11,6.10^6 \text{ cycles}$$

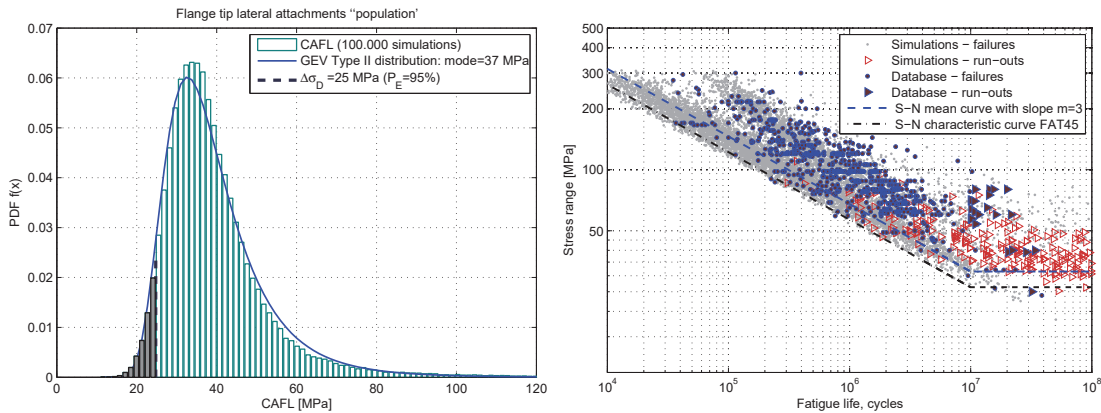


Figure 2.67 – Constant amplitude simulations (Flange tip attachments “population”)

## 2.6. Probabilistic fatigue model

Figure 2.67 shows the FAT45 S-N curve with knee-point adjusted to  $10 \cdot 10^6$  cycles. The results from the literature database and from our experiments are shown with 100.000 “virtual tests”. The run-outs from simulations again correspond to the initiation life of non-propagating cracks.

The statistical analysis for the set of simulations on the “population” is shown in figure 2.68. Two different cases are shown to justify the statistical analysis and linear regression based only on the simulated failures without initiation life. For the definition of the mean S-N curve by linear regression, normality, independence and homoscedasticity is assumed for the residuals. These assumptions are checked by a quantile plot of the residuals against the independent variable of the regression  $\log \Delta\sigma$ . For the linear regression on failure points including initiation, the variance increases with  $\log \Delta\sigma$ . The assumption about the normality of experimental lives ( $\log C$ ) is checked on a probability plot for the linearity of the cumulative frequency distribution of  $\log C$ . Also in this case, normality of fatigue lives is not assured, mainly because initiation introduce scatter on the upper bound.

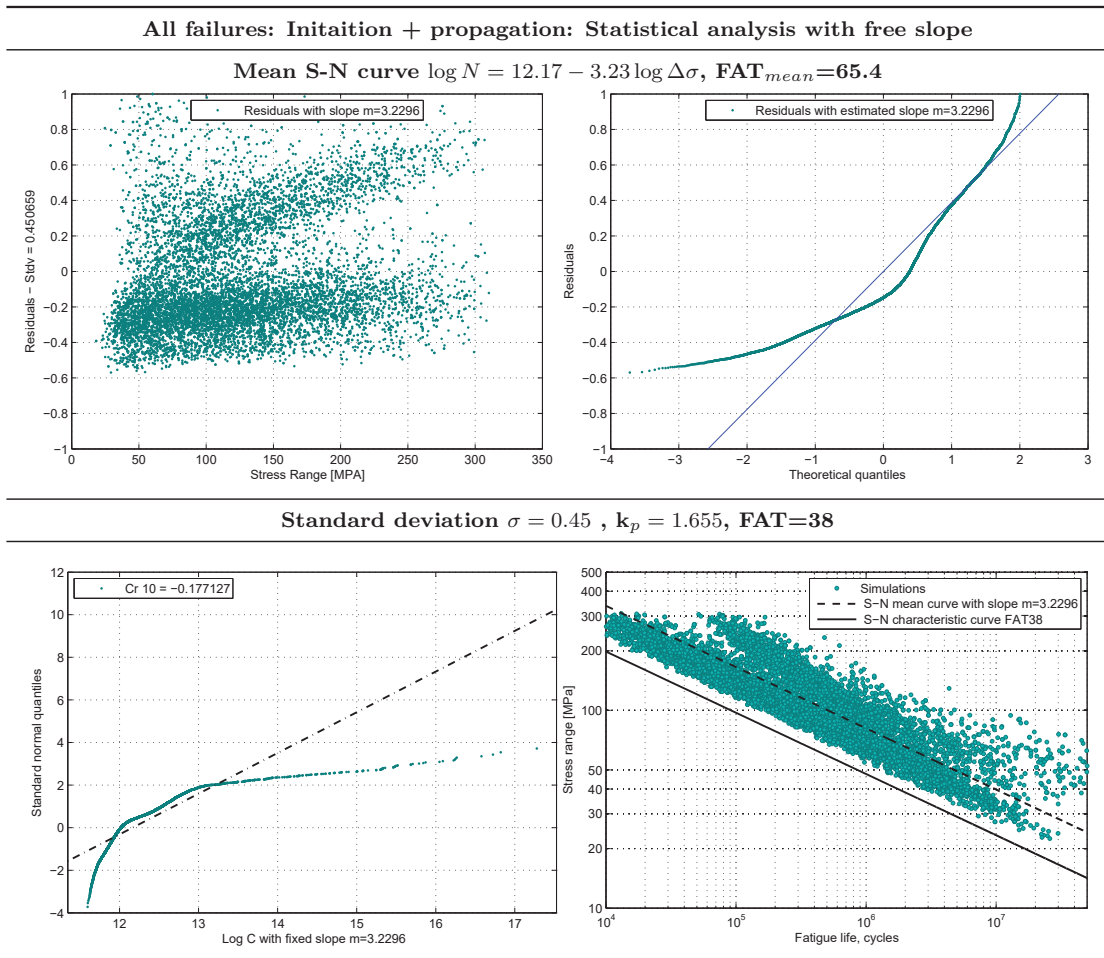


Figure 2.68 – Statistical analysis of constant amplitude simulations:  $(N_i) + (N_p)$

## Chapter 2. In-plane interaction - Flange crossings

The definition of FAT values based on our probabilistic model, is thus based only on failures under propagation. Figure 2.69 shows the statistical analysis for slope  $m=3$ .

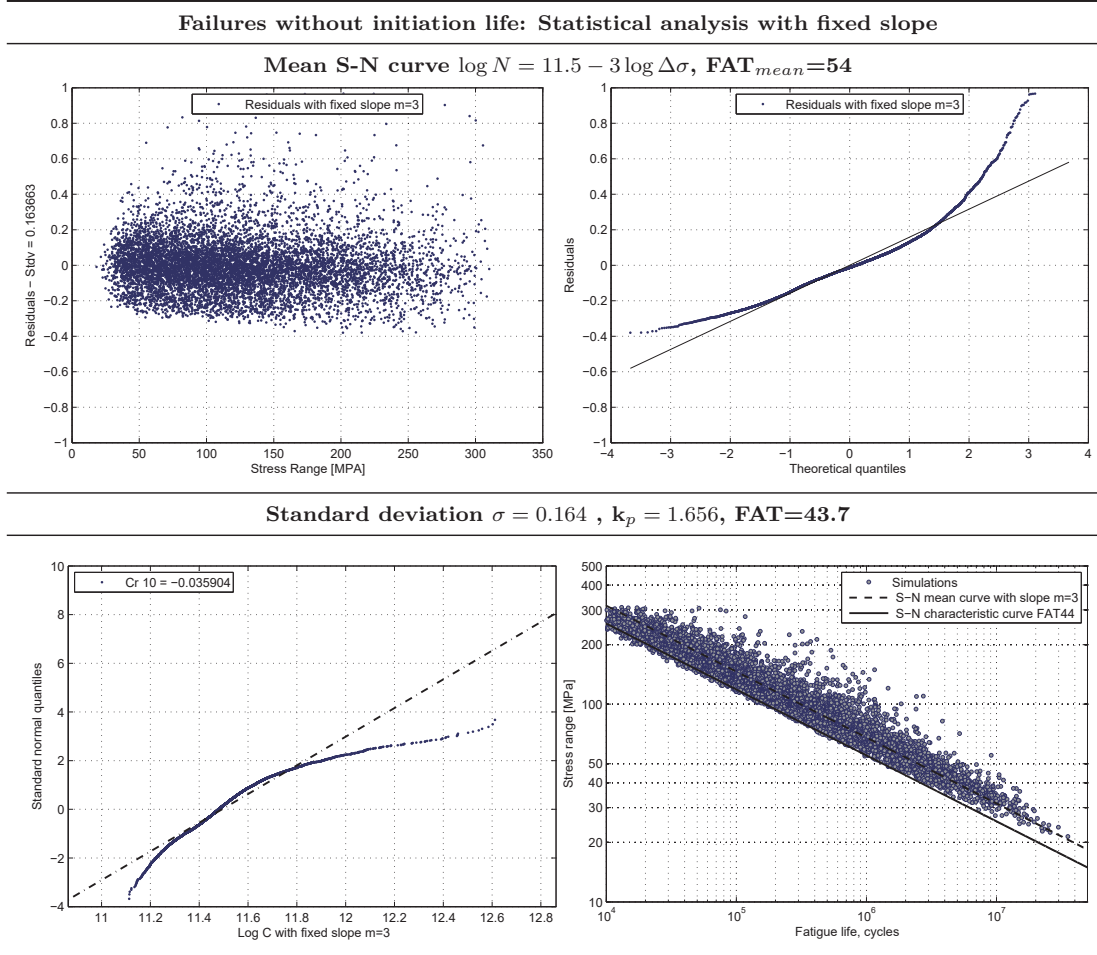


Figure 2.69 – Statistical analysis of constant amplitude simulations: ( $N_p$ )

The complete set of simulations is shown in figure 2.70, along with the recommended S-N curve. Run-outs corresponding to non-propagating cracks,  $a_i = 0, 1$  and  $\Delta K < \Delta K_{th}$  are represented by their initiation life. They define a 2<sup>nd</sup> slope after the threshold knee-point at  $N_D = 10 \cdot 10^6$  cycles.

While the 1<sup>st</sup> slope  $m_1=3$  corresponds to the Paris Law exponent, the 2<sup>nd</sup> slope  $m_2=12$  is given by the exponent  $(1/b)$  of the elastic part from the Coffin-Manson equation 2.16:  $\frac{\Delta \epsilon}{2} = \frac{\sigma_f}{E} (2N_r)^b$ . The simulations were based on Uniform Material Law, after Baumel and Seeger (1990), to estimate cyclic material parameters for the Coffin-Manson curve, see table 2.11. The Uniform Material Law is widely accepted for the high-cycle with good life estimations, with constant values averaged values for the parameters. Our model assumes variability on the fatigue strength coefficient with constant  $b=-0,087$  ( $m_2=1/0,087 \approx 12$ ), but other values could be assumed for the exponent. An extensive

statistical evaluation for the Coffin–Manson parameters presented by Meggiolaro (2004), defines the fatigue strength exponent for steels as  $b_{median} = -0,09$  with  $COV=40\%$ . Any value up to  $m_2 \approx 45$  as proposed by Sonsino (2007a) may be obtained. The definition of a probabilistic  $2^{nd}$  slope for constant amplitude curves is out of the scope of this thesis, mainly due to the variable character of bridge loads.

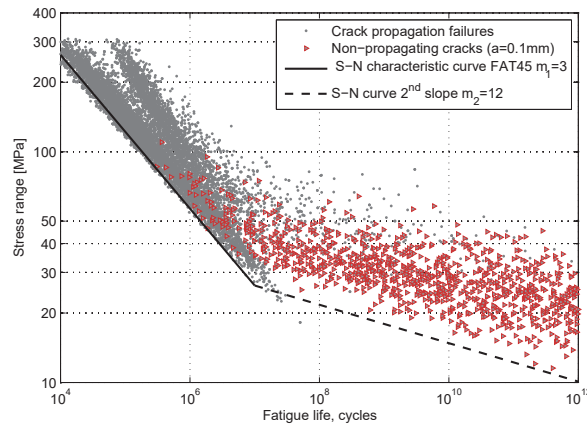


Figure 2.70 – Constant amplitude S-N curve (Flange tip attachments “population”)

The detail with geometric properties extended to the “population” of Lateral attachments and Intersected Flanges, has a characteristic FAT value of 44MPa. It seems that the FAT40 category should be recommended. However, classifying all the geometric configurations in this category would be unduly conservative. A look to the database of literature results supports this statement. Experimental results are available for maximum width up to 380mm (Shimokawa et al., 1985) and maximum attachment length of 440mm, with tapered attachments, (Puchner, 1959) which were seen in agreement with a FAT50.

In view of a rational classification, a limit of W and L up to 500mm is set by inspection, representing the vast majority of practical application of this detail in steel bridges.

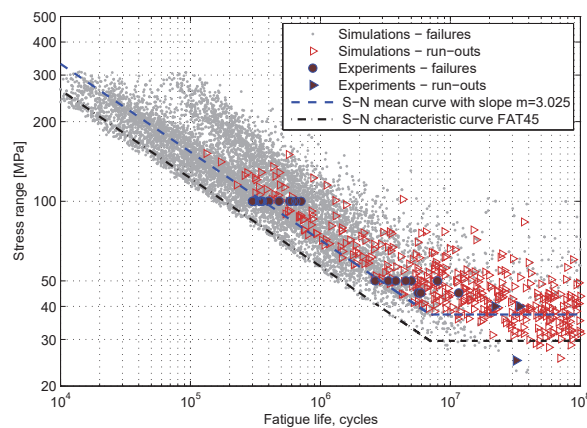


Figure 2.71 – Constant amplitude S-N curve for W and L up to 500mm



## Chapter 2. In-plane interaction - Flange crossings

The simulations for this scenario are shown in figure 2.71 and justify the definition of two different categories: FAT 45 for  $W$  and  $L$  up to 500mm, and FAT 40 above those geometries, mainly due to lack of experimental background, table 2.16.

FAT	Geometry	Detail
45(1+1,25R/W)	$L_{attach} \leq 500$ mm $W \leq 500$ mm $t \leq 100$ mm $R \geq 50$ mm	
40(1+1,6 R/W)	$L_{attach} > 500$ mm $W \leq 1000$ mm $t \leq 100$ mm $R \geq 50$ mm	

Table 2.16 – Recommended FAT for “Flange Tip Attachments” and “Intersected Flanges”

### 2.6.4 Variable amplitude simulations

The Monte Carlo framework with the I-P model as developed for constant amplitude loads, is now applied under variable amplitude loading. By this, the random character of the variables is included in both the initiation and propagation models, that were calibrated in Section 2.5. To account for the influence of the load spectra effects on the 2<sup>nd</sup> slope  $k$  value, different load sequences are considered. The load spectra shape is known to have a strong influence on fatigue life (Fisher et al., 1993) (Dahle, 1994) (Gurney, 2006), which can be seen directly on the “Gassner curves”, where the load spectra shape define different design curves for variable amplitude, figure 2.72.

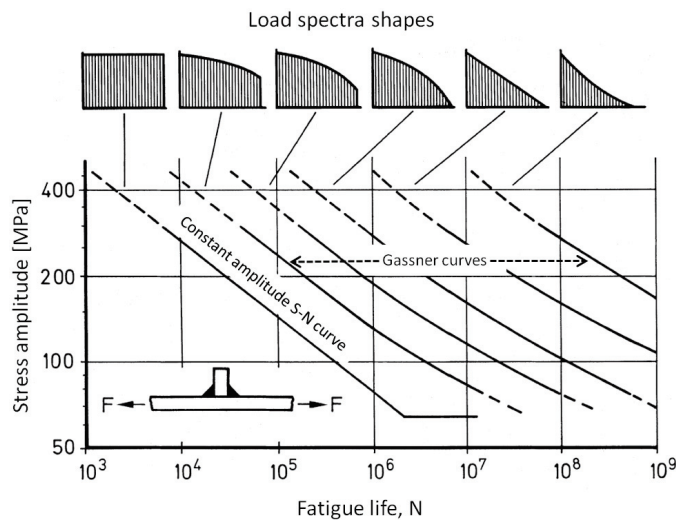


Figure 2.72 – Load spectra influence on fatigue life (Haibach, 2006)



The difference between “Gassner curves” is quantified according to Heuler and Klatschke (2005) by a “spectrum shape factor” (SSF), which defines the distance between Constant amplitude S-N curve and each “Gassner” variable amplitude curve, corresponding to different stress spectra shapes, figure 2.73.

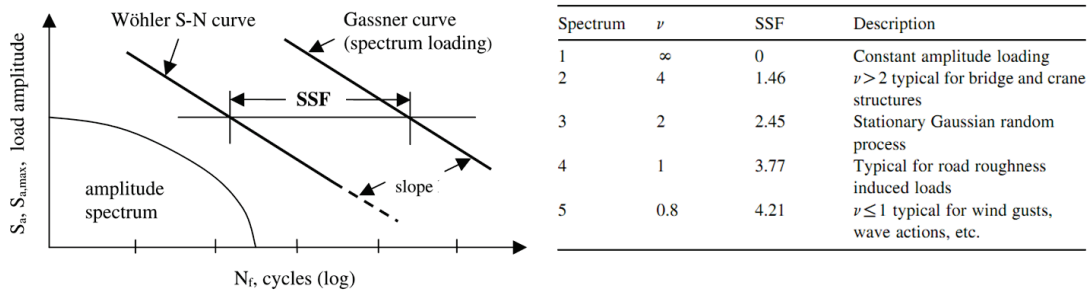


Figure 2.73 – Spectrum Shape Factor (SSF) after Heuler and Klatschke (2005)

Although the effect of the spectra type is clearly defined for designs based on “Gassner curves”, the same is not true for designs based on double slope S-N curves, which is the case for steel bridges, where a single double slope S-N curve is used, regardless of the spectra shape. An attempt to include the spectra shape on the 2<sup>nd</sup> slope is made here. We anticipate that, to be fully equivalent to the range of “Gassner curves” as shown in figure 2.72, different spectra shapes, will define different 2<sup>nd</sup> slope values.

Our experimental results in Section 2.5 showed that stress ranges below the CAFL could have different damage contributions, depending on the particular load sequence. The experiments were obtained with concave spectra, shape parameter  $\nu < 1$ , and a double slope S-N curve with  $m=3$  and  $k=5$  was seen to give a good estimation of fatigue life. Figure 2.74 shows schematically the potential damage contribution of stress ranges below CAFL, for 2 different load spectra shapes. The number of stress cycles below the CAFL is very large for the concave spectra ( $\nu < 1$ ), while for a convex spectra ( $\nu \geq 2$ ), there are relatively few of those below the CAFL. In this last case the drop of the threshold is expected to be faster, and the 2<sup>nd</sup> slope closer to  $m$ .

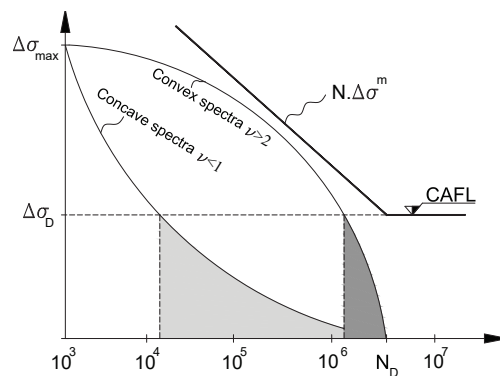


Figure 2.74 – Schematic relation between a concave and convex spectra and the CAFL

## Chapter 2. In-plane interaction - Flange crossings

By applying the I-P model to different spectra, the threshold drop effect is naturally accounted for. The model is solved numerically, considering the random character of the variables, and estimates life to failure for each spectra. The 2<sup>nd</sup> slope is evaluated with the *effective stress cycle* concept, as this method showed accurate in estimating experimental lives under variable amplitude loads, Section 2.5. The framework for the simulations is schematically shown in figure 2.75.

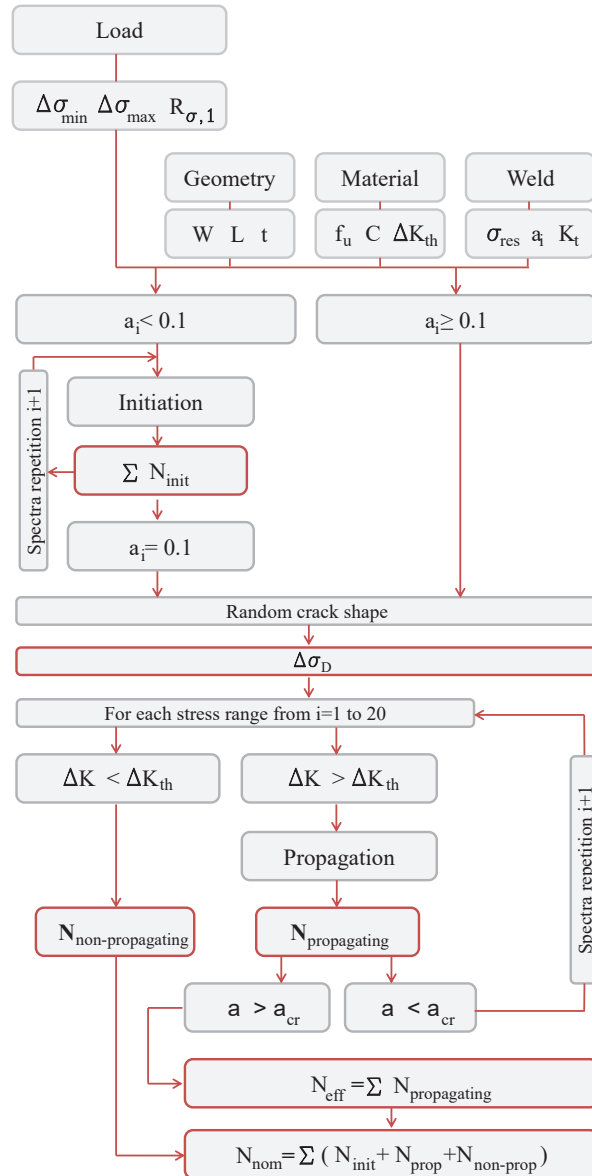


Figure 2.75 – Monte Carlo model for variable amplitude

The simulations are carried out with four different spectra: concave, linear (Exponential), convex (Rayleigh) and convex (Gauss), with each standard spectra discretized in 20 load levels, considering 20 steps sufficient to describe a stress range histogram, figure 2.76.

## 2.6. Probabilistic fatigue model

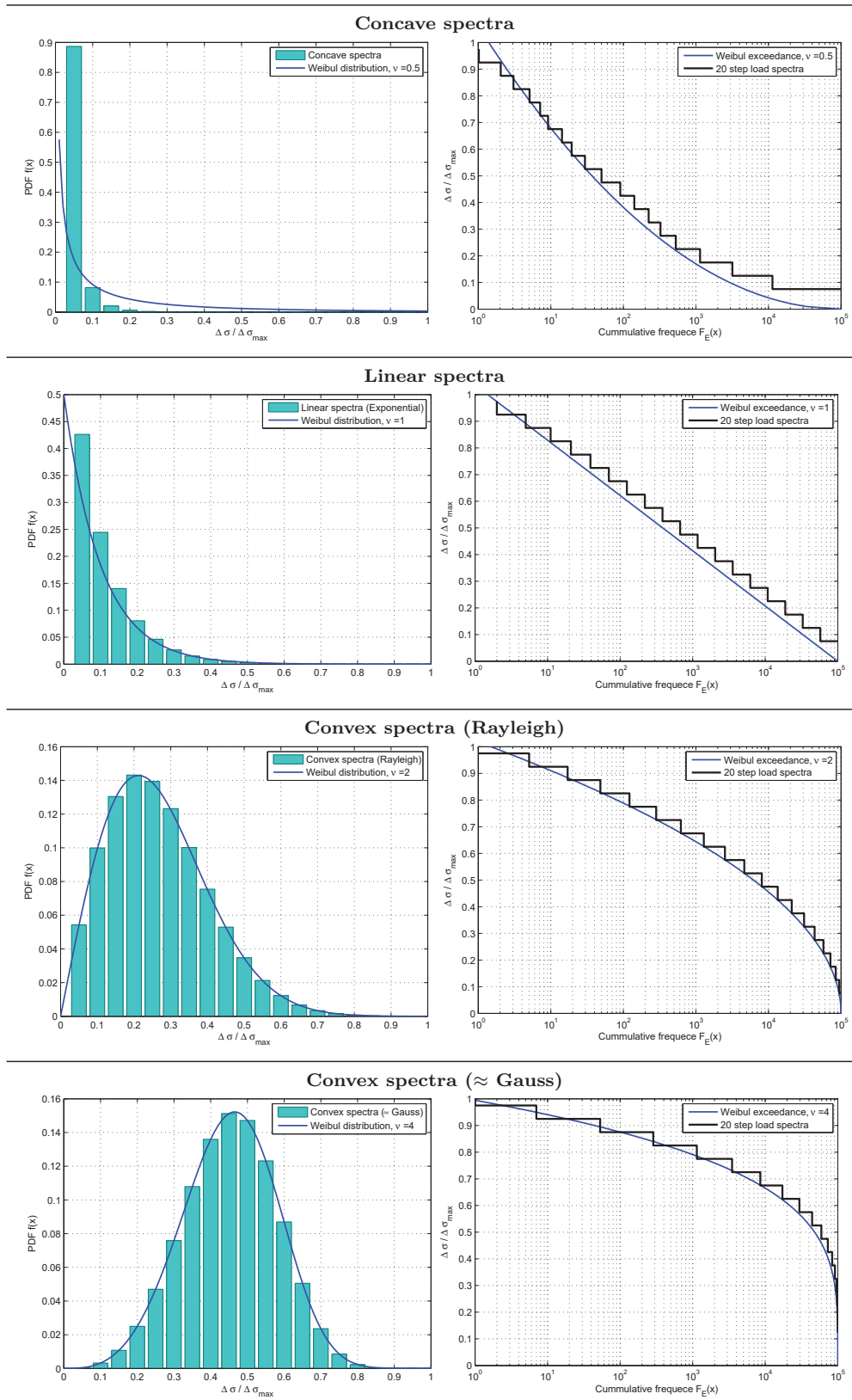


Figure 2.76 – Probability density and exceedance for the load spectra cases

## Chapter 2. In-plane interaction - Flange crossings

---

Preliminary simulations with block lengths from  $10 \cdot 10^3$  to  $1 \cdot 10^6$  showed that the block size influence is small, which agrees with conclusions from Gurney (2006). For the simulations shown here, we use a standard spectra with block size of 100.000 cycles. All four spectra are fully described with a Weibull distribution with shape parameter  $\nu$ , and cumulative exceedance function:

$$P_i \left( \frac{\Delta\sigma}{\Delta\sigma_{max}} \geq \frac{\Delta\sigma_i}{\Delta\sigma_{max}} \right) = \exp \left[ - \left( \frac{\Delta\sigma_i}{\Delta\sigma_{max}} \right)^\nu \ln(100.000) \right] \quad (2.23)$$

The first necessary step for each simulation, is to generate a random set of material and weld parameters, using the geometry of the “test sample”, i.e.  $W=L=150\text{mm}$  and  $t=15\text{mm}$ . With a given random pair of initial weld toe imperfection, crack shape and crack propagation threshold  $\Delta K_{th}$ , the *original* CAFL ( $\Delta\sigma_D$ ) is established, i.e. the CAFL that corresponds to a Constant amplitude curve, with the same material and geometric parameters.

The stress range for each spectra shape is generated with an uniform distribution:

$$\Delta\sigma_{max} \rightarrow \text{uniform}(min = 30; max = 0,5f_y) \text{ [MPa]}$$

$$\Delta\sigma_{min} \rightarrow \text{uniform}(min = 0,3\Delta\sigma_{max}; 0,5\Delta\sigma_{max}) \text{ [MPa]}$$

The initial imperfection  $a_i < 0,1\text{mm}$  leads to an initiation life, estimated by the local strain approach using Miner’s rule, equation 2.21. The load spectra is iteratively applied up to an estimated life corresponding to Coffin-Manson equation 2.16, see figure 2.54. At the end,  $a_i = 0,1\text{mm}$  is assumed.

Then with  $a_i \geq 0,1\text{mm}$ , for each stress range on the spectra, the Stress Intensity factor  $\Delta K_i$ , is evaluated against the threshold  $\Delta K_{th,i}$ . Crack propagation occurs for stress ranges above the threshold  $\Delta K_i > \Delta K_{th,i}$ , and only those are considered effective, while regardless of their damaging character, the nominal life includes all cycles on the spectra. This process is repeated cycle by cycle up to failure while  $a_i \leq a_{cr}$ .

Each simulated “virtual” failure, is ultimately defined by a single value of *original* CAFL,  $\Delta\sigma_D$ , an effective equivalent stress range ( $\Delta\sigma_{eq,eff}$ ) defined with the effective propagating life ( $N_{eff} = \sum n_{eff}$ ), and nominal life ( $N_{nom}$ ), i.e. the total number of cycles of the spectra up to failure. With those quantities, the effective ratio  $\frac{N_{nom}}{N_{eff}} \geq 1$  enables the calculation of the 2<sup>nd</sup> slope with equation 2.24, see figure 2.77:

$$\Delta\sigma_{eq,eff} = \left( \frac{\sum \Delta\sigma_{propagating}^m n_{eff}}{\sum n_{eff}} \right)^{\frac{1}{m}}$$

$$\left\{ \begin{array}{l} \Delta\sigma_{eq,eff}^m \cdot N_{eff} = \Delta\sigma_D^m \cdot N_D \\ \Delta\sigma_{eq,eff}^k \cdot N_{nom} = \Delta\sigma_D^k \cdot N_D \end{array} \right\} \Rightarrow \frac{N_{eff}}{N_{nom}} = \left( \frac{\Delta\sigma_{eq,eff}}{\Delta\sigma_D} \right)^{k-m} \quad (2.24)$$

The concept of effective and nominal life is schematically shown in figure 2.77 with the I-P model simulations for the concave spectra, considering both the Initiation and Propagation on the effective and nominal stress. Although initiation plays an important role, it is not suited for the definition of a **characteristic** 2<sup>nd</sup> slope value, because it spreads the result scatter and increases the nominal life. The 2<sup>nd</sup> slope value are thus derived here, based on simulations considering only propagation life, in line to what was assumed to define characteristic S-N curves for constant amplitude.

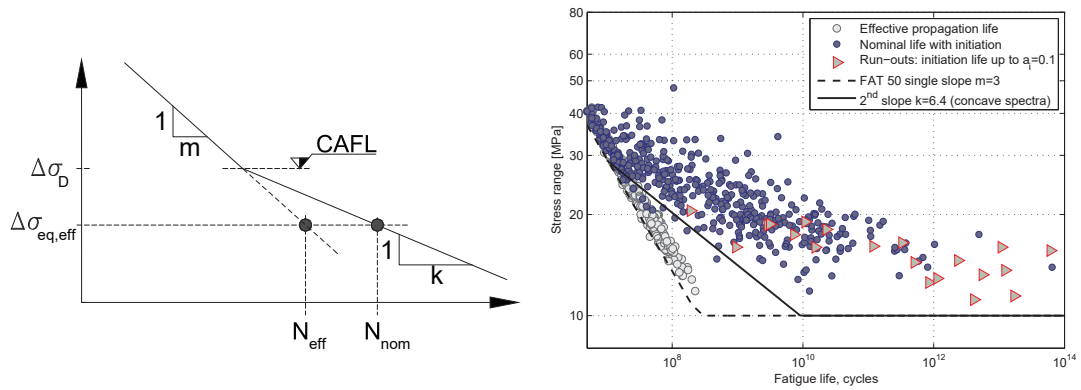


Figure 2.77 – Effective and nominal stress for 2<sup>nd</sup> slope calculation

For each simulated failure where  $(\Delta\sigma_{eq,eff}) < \Delta\sigma_D$ , the 2<sup>nd</sup> slope is solved with equation 2.24 and a Type II Generalised Extreme Value distribution is fitted to the histogram of all simulated k values. Figures 2.78 and 2.79 show the variable amplitude S-N curves for the “test sample” group, based on 15.000 simulations for each spectra. The “knee-point” is placed at  $7 \cdot 10^6$  cycles which is the characteristic CAFL previously derived with constant amplitude simulations.

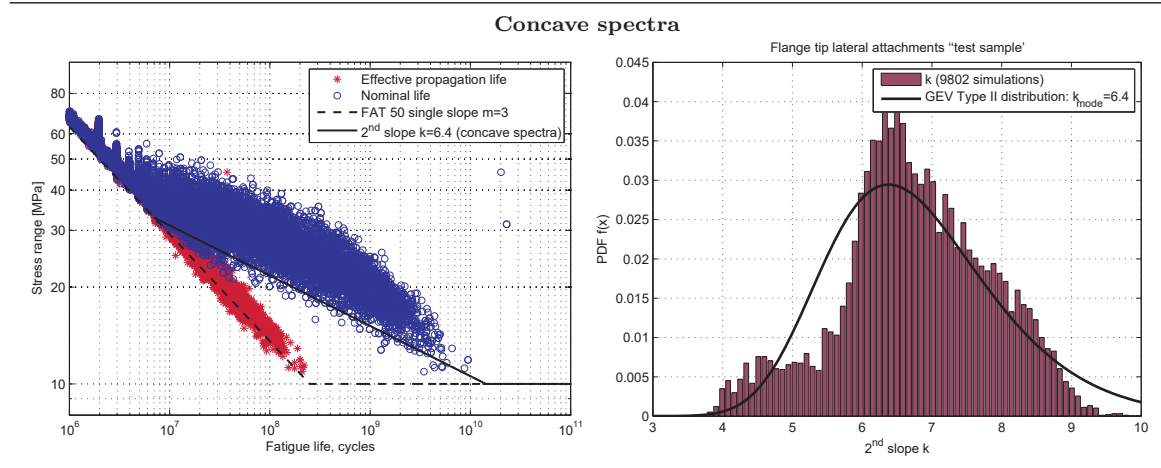


Figure 2.78 – 2<sup>nd</sup> slope simulations for concave spectra

## Chapter 2. In-plane interaction - Flange crossings

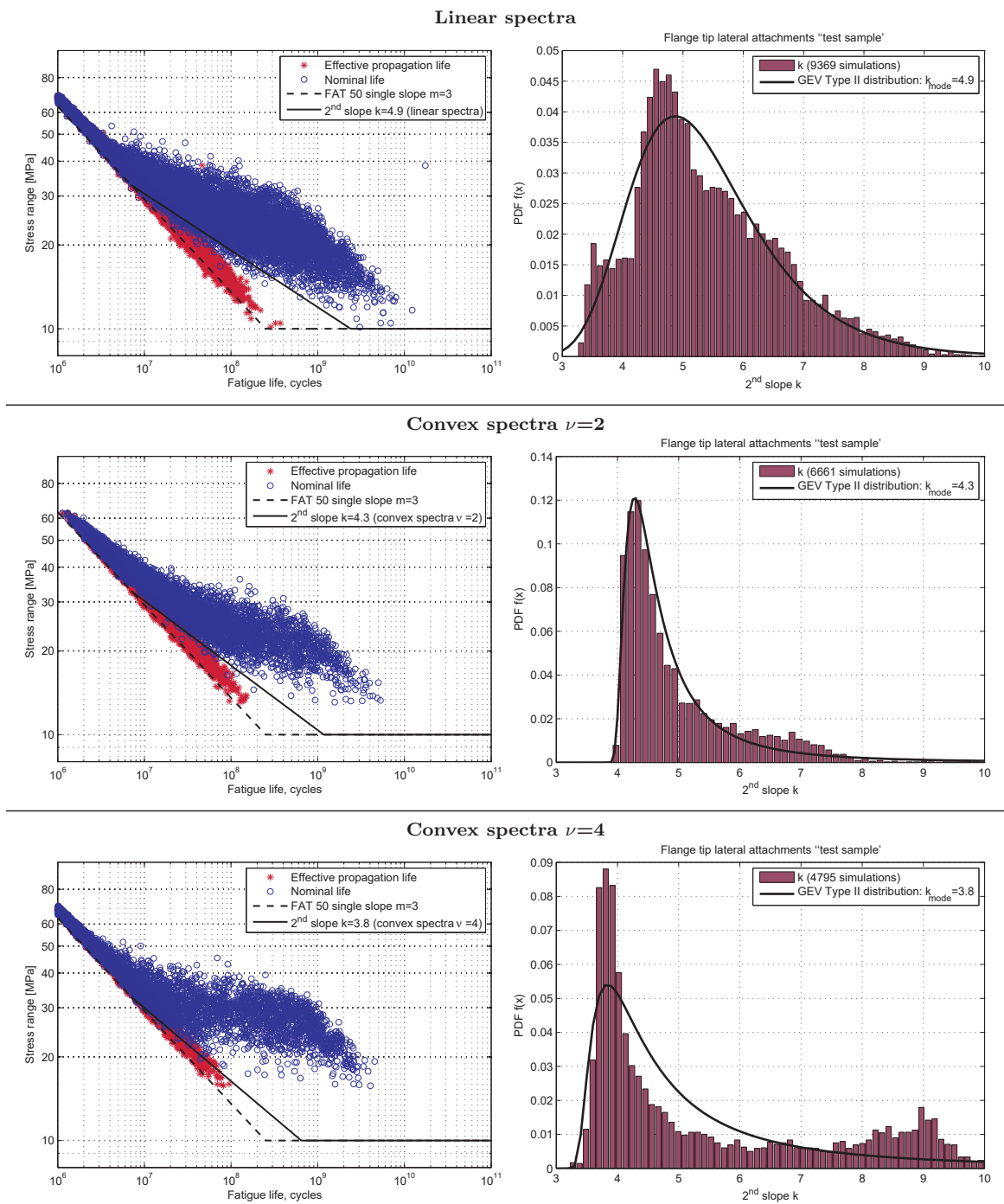


Figure 2.79 –  $2^{nd}$  slope simulations for linear and convex spectra

The  $2^{nd}$  slope values as obtained for the “test sample” are summarised in table 2.17.

The final characteristic S-N curve for concave spectra with the experimental results from Section 2.5 and 2.4 is shown in figure 2.80. The “virtual tests” in this plot include the simulations under both constant and variable amplitude for the “test sample” geometry.

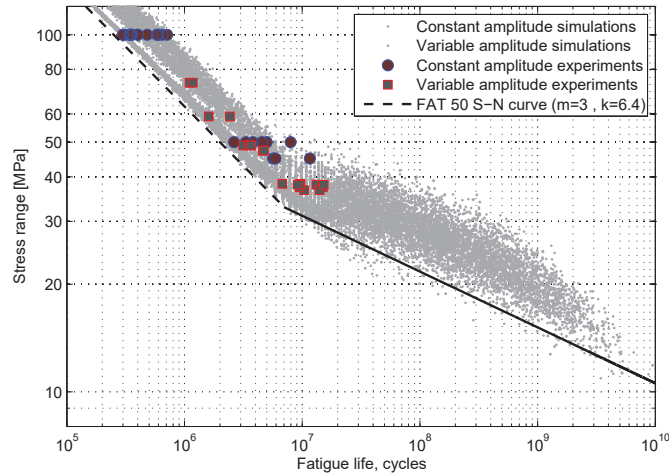


Figure 2.80 – S-N curve for concave spectra with simulations and experiments (“sample”)

The simulations with variable amplitude spectra show that some correlation between the spectra shape factor  $\nu$  and the  $2^{nd}$  slope can indeed be identified as indicated by the “Gassner” curves, figure 2.72 and figure 2.73. The  $2^{nd}$  slope values are summarised in table 2.17. They range 3,8 to 6,4 and although these may seem a small difference in the slope, if one takes a stress range of half the CAFL, fatigue life will depend linearly on a factor of  $2^k$  which means that increasing one unit in the slope  $k$ , will double the fatigue life.

	Spectra shape factor			
	Concave $\nu = 0,5$	Linear $\nu = 1$	Convex $\nu = 2$	Convex $\nu = 4$
<b><math>2^{nd}</math> slope <math>k</math> (simulations)</b>	6,4	4,9	4,3	3,8
<b><math>k=m+2/\nu</math> (formula)</b>	7,0	5,0	4,0	3,5

Table 2.17 –  $2^{nd}$  slope values for Flange tip attachments

It is seen that the  $2^{nd}$  slope increases the number of repetitions of stress range below the CAFL. The damage sum on a double S-N curve gives good estimations for spectra with a large number of low stress ranges, because the damage caused by these low stress ranges, depends on the exceedance of the CAFL level.

On the other hand, it was seen in Chapter 1, that existing experimental results reported in literature, are not unanimous in the correlation between the spectra shape effects and the  $2^{nd}$  slope  $k$ . This is attributed to the lack of sufficient tests under different spectra. Our simulations including initiation and propagation at long lives, figure 2.77, show that to correctly characterise scatter in the “knee-point” region and beyond, a considerable amount of tests is required. Due to time and economic constraints, each experimental setup reported in literature, has a limited quantity of results, as is also the case for the experiments presented in this thesis. The result is that regardless of the spectra type, experimental results point out slopes between 3 and 5.

A second drawback from the lack of experimental results, is the CAFL definition based on few experimental points. This usually leads to a rather non-conservative “knee-point” definition that is too high, coincident with the experimental CAFL, while a probabilistic assessment shows that the “knee-point” should be placed at minimum at  $10.10^6$  cycles. This is in agreement with several authors that proposed a 2<sup>nd</sup> slope model with the “knee-point” lower than the CAFL, figure 1.11 (Tilly and Nunn, 1980), figure 1.12 (Dahle, 1994), and figure 1.15 (Albrecht and Lenwari, 2009).

### 2.6.5 The threshold drop

The effect of the threshold drop on a 2<sup>nd</sup> slope model was introduced by Haibach (1970), considering that the ratio between the instantaneous threshold limit  $\Delta\sigma_{th,i}$ , and the CAFL  $\Delta\sigma_D$ , could be related as a function of the accumulated damage D, figure 2.81:

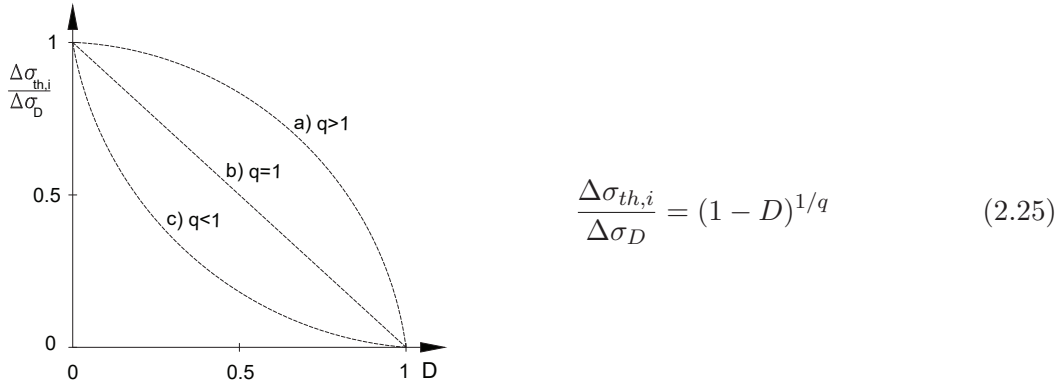


Figure 2.81 – CAFL threshold drop definition after Haibach (1970)

The damage sum with Miner’s rule is  $D_{(\Delta\sigma_i > \Delta\sigma_D)} = \frac{n_i}{N_{R,0}}$  for stress ranges above the CAFL. As damage accumulates, the fraction of stress ranges below the threshold decreases with (1-D). The damage considering both stress ranges above and below the CAFL is:

$$D = \sum_{\Delta\sigma_i > \Delta\sigma_D} \frac{n_i}{N_{R,i}} + \sum_{\Delta\sigma_i < \Delta\sigma_D} \frac{n_j(1 - D)}{N_{R,i}} \quad (2.26)$$

Replacing the constant amplitude S-N curve expression, where  $D=0$ ,  $N_{R,i} = N_D \frac{\Delta\sigma_i}{\Delta\sigma_D}^{-m}$  and considering the decrease (1-D) on the number of cycles below the CAFL, as a fictitious increase in fatigue life on  $N_{R,i}$ , the damage sum writes:

$$D = \sum_{\Delta\sigma_i > \Delta\sigma_D} \frac{n_i}{N_D \frac{\Delta\sigma_i}{\Delta\sigma_D}^{-m}} + \sum_{\Delta\sigma_i < \Delta\sigma_D} \frac{n_j}{(1 - D)^{-1} \cdot N_D \frac{\Delta\sigma_i}{\Delta\sigma_D}^{-m}} \quad (2.27)$$

Using the threshold drop definition given in 2.25 to replace (1-D), the expression for the



double slope S-N curve becomes:

$$D = \sum_{\Delta\sigma_i > \Delta\sigma_D} \frac{n_i}{N_D} \frac{\Delta\sigma_i^{-m}}{\Delta\sigma_D^{-m}} + \sum_{\Delta\sigma_i < \Delta\sigma_D} \frac{n_j}{N_D} \frac{\Delta\sigma_i^{-k}}{\Delta\sigma_D^{-k}} \quad (2.28)$$

where  $k=m+q$  is the fictive  $2^{nd}$  slope below the CAFL. Haibach defined  $q=m-1$  for a narrow band gaussian load spectra, where the stress ranges follow a Rayleigh distribution. For welded steel with  $m=3$ ,  $q=2$  in expression 2.25, which corresponds to a smooth drop on the instantaneous threshold  $\Delta\sigma_{th,i}$ .

Kunz (1992) defined expression 2.25 by  $\frac{\Delta\sigma_{th,i}}{\Delta\sigma_D} = (1 - D)^\xi$  and derived the  $\xi$  exponent by fracture mechanics. For the integration of Paris Law, see equation 2.29, he assumed  $Y(a)$  constant resulting in  $\xi = 1/(m - 2)$ . By assuming  $Y(a)$  variable but both  $dY(a)/da$  and  $\Delta\sigma$  constant, he derived  $\xi = 1/(m - 1)$ , similar to Haibach's assumption. These bounds for the exponent of expression 2.25, represent threshold drop curves between the smooth curve **a** ( $\xi = 1/(m - 1)$ ) and the more aggressive **b** ( $\xi = 1/(m - 2)$ ). Figure 2.82 shows simulations on an edge crack in a plate, considering ( $M_k Y(a) = 1$ ), in agreement with ( $\xi$ ) exponents as derived by Kunz (1992).

For the lateral attachments as presented in the previous section, or any weld notch in general, the integral of Paris Law, also includes the  $M_k$  correction for the local non-uniform stress distribution. This is a highly non-linear factor, see figure 2.45, and the previous assumptions for the integration of Paris law are no longer valid, so the integral has to be solved numerically, as the I-P model considers.

$$\int_0^N dN = \int_{a_1}^{a_2} \frac{1}{C(Y(a)M_k\Delta\sigma\sqrt{\pi a})^m} da \Rightarrow N = \frac{1}{C\Delta\sigma^m} \int_{a_1}^{a_2} \frac{1}{(M_k Y(a)\sqrt{\pi a})^m} da \quad (2.29)$$

Under these circumstances, the exponent  $\xi$  is higher than 1, defining concave threshold drop curves as curve **c** in figure 2.81. This is shown in figure 2.83 for an edge crack on the weld toe with  $M_k Y(a) > 1$ .

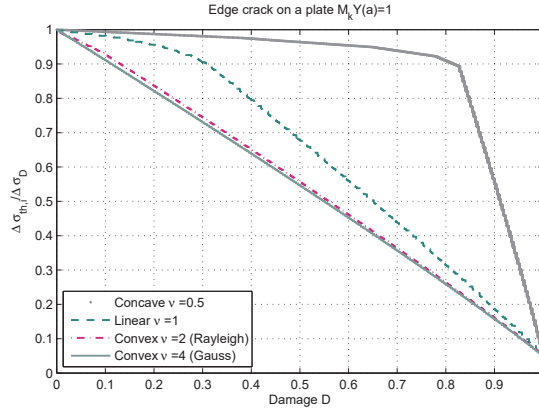


Figure 2.82 – Threshold drop curves by spectra type for an edge crack on a plate

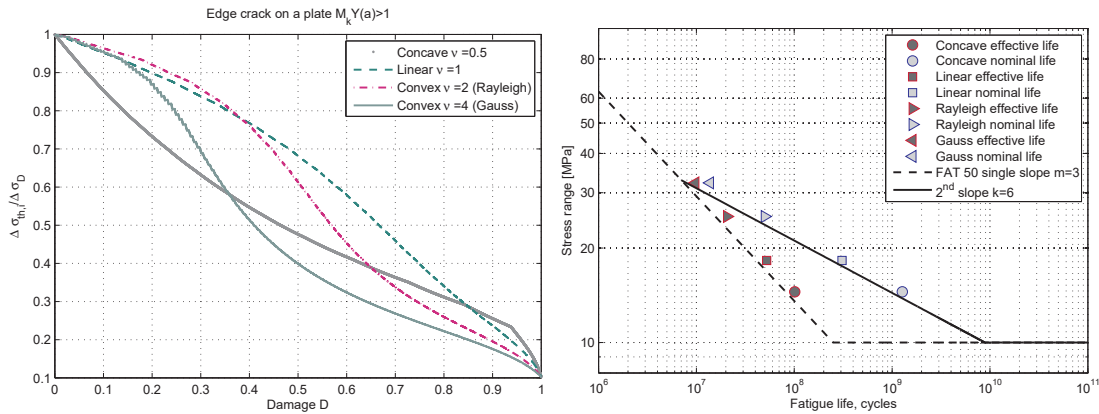


Figure 2.83 – Threshold drop curves by spectra type for flange tip attachments

The  $2^{nd}$  slope value is both dependent on the load spectra and the notch case. For flange tip lateral attachments, the slope  $k$  values obtained by numeric integration of Paris law, table 2.17 allow for defining equation 2.25 as  $\frac{\Delta\sigma_{th,i}}{\Delta\sigma_D} = (1 - D)^{\nu/2}$  with the  $2^{nd}$  slope defined as  $k=m+2/\nu$ , where  $\nu$  is the Weibull shape parameter.

### 2.6.6 Summary of conclusions

- This Section applied an Initiation-Propagation model under a Monte Carlo probabilistic framework, suitable to devise characteristic S-N curves under both constant and variable amplitude. This procedure was applied to flange tip attachments but may be used to define the S-N curves for any other detail.
- Constant amplitude simulations showed that the CAFL for lateral attachments is placed around  $10.10^6$  cycles, much lower than Eurocode 3 definition at  $5.10^6$ , and in line with the American bridge standard procedure (AASHTO, 2002) where endurance at fatigue limit depend on the notch category.
- For long lifes under variable amplitude, the  $2^{nd}$  slope model is justified. The model requires an accurate estimation of the ‘knee-point’ and may include the spectra shape for the definition of the  $2^{nd}$  slope  $k$ . The  $2^{nd}$  slope value depends both on the notch case and the load spectra and could be defined by simulations. For load spectra characterised by a Weibull frequency distribution, the  $2^{nd}$  slope is reasonably estimated by  $k=m+2/\nu$ , where  $\nu$  is the Weibull shape parameter.

### 3 Out-of-plane interaction - Web crossings

The majority of welded connections under multiaxial shear-normal stress interaction in bridges are fillet weld details. They can be typified by two fundamental cases: load carrying and non-load carrying fillet welds, figure 3.1.

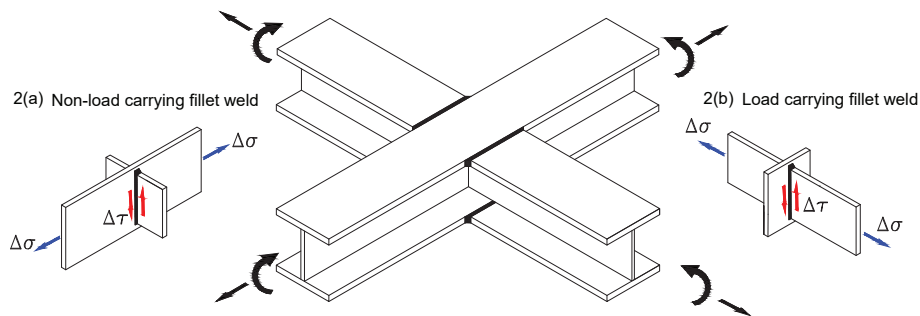


Figure 3.1 – Multi-axial normal-shear stress interaction: basic cases of fillet welds

Detail 2(a) represents a continuous plate under tensile stress, with transversal non-load carrying fillet welds on its surface. This is the widespread “transversal attachment” detail. If the transversal attachment is loaded in shear, the weld toe on the main plate will have an additional shear stress interacting with the main normal stress. The weld toe on the main plate becomes the relevant critical damage location under multiaxial stress state, where both normal and shear stress quantities, act on a continuous strip of plate, rather than on the weld. In detail 2(b) on the contrary, the main tensile stress is carried by the weld, so the critical location under multiaxial stress state is the weld throat (or toe) under both shear and normal stress. Detail 2(b) is relatively well reported in literature. It is characterised by root failure with cracks developing into the weld throat section (Lotsberg, 2009), (Bokesjö et al., 2012). Detail 2(a) was chosen for our experimental investigation, due to its widespread use in bridge design, and because no fatigue tests under multiaxial non-proportional loads were found in literature. This means that the focus is put on multiaxial failures at the weld toe, with the relevant stress quantities in the main element under tension.

### 3.1 The experimental setup

An experimental program with 20 fatigue tests under uniaxial and multiaxial stress was carried out on plates with transversal attachments (detail 2a), according to the matrix of experiments shown in table 3.1. The experimental campaign under combined normal-shear stress, included 6 tests with proportionality between stress ranges and 6 tests with shear and normal stress acting non-proportionally, with a  $90^\circ$  out-of-phase angle. All tests were done at stress ratio  $R_{\sigma,\tau} = 0,1$  and test frequency of 3Hz.

$\Delta F_{hor}$ [kN]	$\Delta F_{vert}$ [kN]	Phase $^\circ$	N $^\circ$ of tests	Detail
100	100	0	6	
100	100	90	6	
-	100	-	1	
180	-	-	1	
150	-	-	3	
120	-	-	1	
100	-	-	1	

Table 3.1 – Matrix of experiments for multiaxial tests

The specimens were produced by the author at the ICOM laboratory with commercial flat bars, steel grade S235JR. Bars with  $100 \times 12 \text{ mm}^2$  cross section were used for the longitudinal main plate (plate 1) and  $160 \times 20 \text{ mm}^2$  for the attachment plate (plate 2), see figure 3.2. The longitudinal plate under normal stress had a “control section” on the weld toe region with thickness reduced to 10mm, machined out of the 12mm plate, along 200mm . All plates were cut in a water cooled continuous saw machine and the chamfer and cope hole on the transversal attachment were made in a water jet cutting machine.

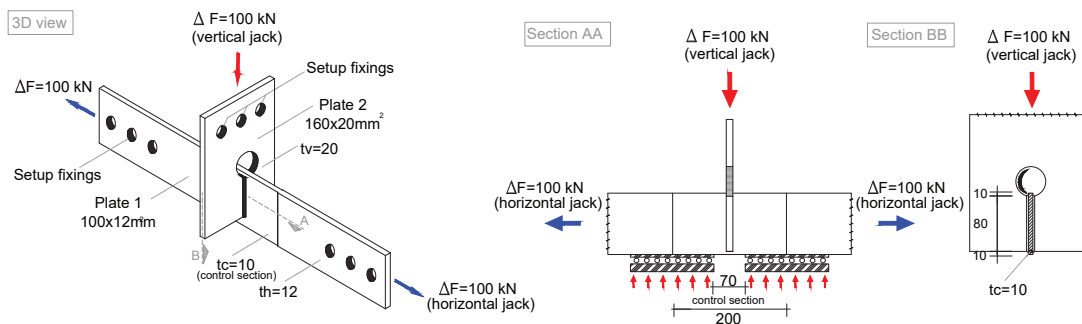


Figure 3.2 – Specimen geometry for multiaxial tests

### 3.1. The experimental setup

To avoid weld defects at the main plate edge, the full-penetration welds were only 80mm long, leaving 10mm on each side of the fillet. The welding procedure is summarised in table 3.2 with each weld composed by four passes, made alternately to minimise distortion of the main plate.

MAG 136 - Welding procedure for full penetration fillet welds		
Steel grade	S235 JR	thickness 15 / 20 mm
Filler material	OK autorod 12.51	thickness 1mm
Type of gas	82%Argon/18%CO2 (M21) Arcal 5	
Debit	15 liters/minute	
Position	Horizontal	
Polarity	DC+	
	Root pass	2 <sup>nd</sup> , 3 <sup>rd</sup> , 4 <sup>th</sup>
Voltage [V]	23,5	23
Wire speed [m/min]	5	8.8
Current [A]	170	140
Welding speed [cm/min]	18	17
Pre heating [deg]	No	No
Inter-pass temperature [deg]	<250	<250

Table 3.2 – Welding procedure for Transversal attachments

#### The setup

An original large scale test setup was developed for the multiaxial tests on plate specimens, figure 3.3. Two servo-hydraulic actuators with 300 kN capacity in dynamic regime were used in perpendicular directions, one horizontal and other vertical. The horizontal actuator works in tension, applying tensile normal stress on the main plate, while the vertical actuator works in compression. The vertical compression force applied to the attachment, deviates at the cope hole, and is transferred in shear through the weld. The weld toe in the main plate is also under shear, and these forces transfer to linear sliding bearings, supporting the main plate under tension. This ensures the transmission of vertical forces through the sliding bearings, eliminating friction effects for the horizontal tension load. The specimen is attached by pre-stressed friction connections to a clamping system connecting with the jacks. A frequency of 3Hz could be achieved, limiting the global vibration of the setup and possibility of fatigue cracks in the test setup components, specially on the welds of the clamping system.

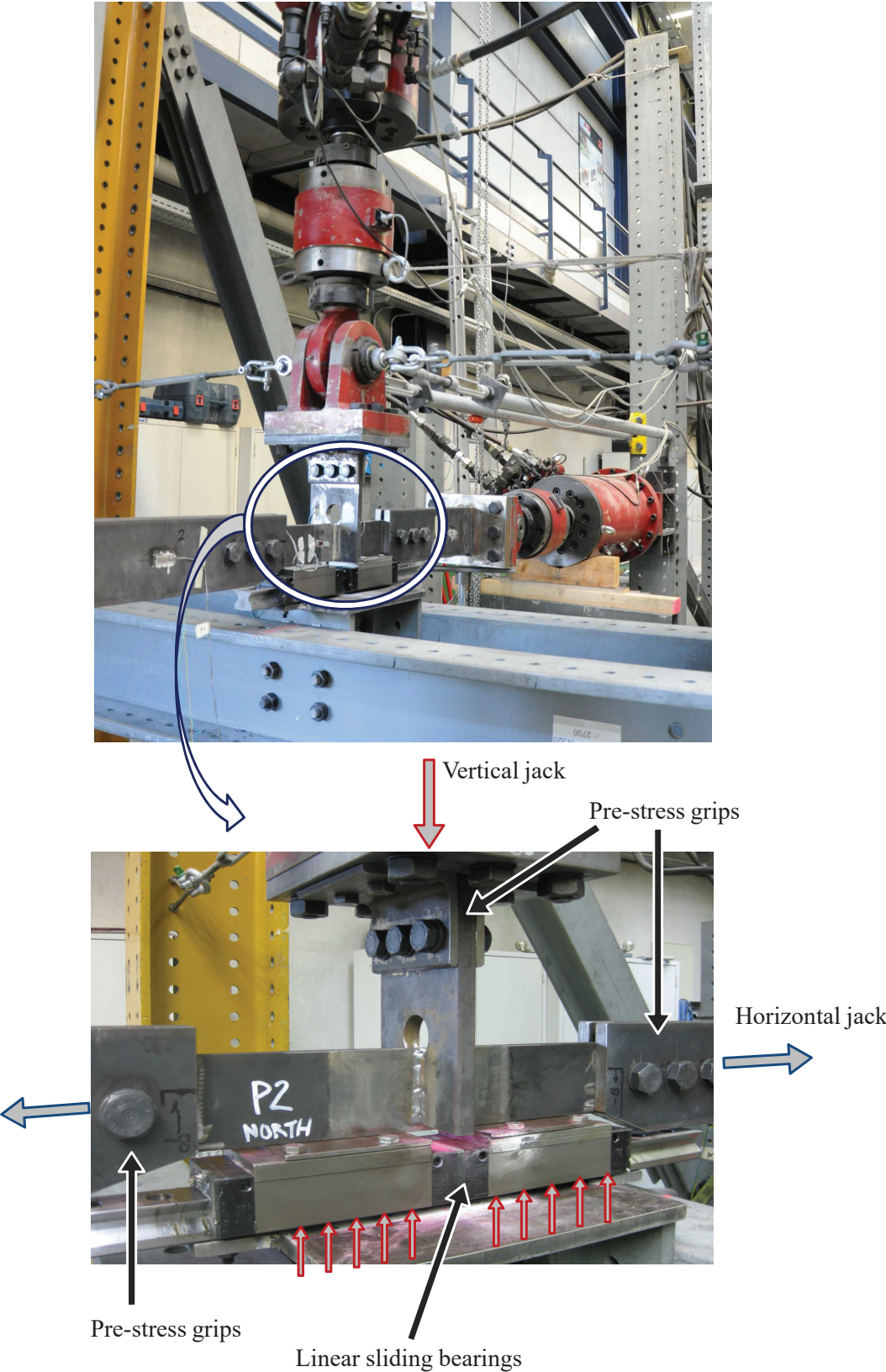


Figure 3.3 – Experimental setup for multiaxial tests



### 3.2 Experiments under uniaxial stress

Six specimens were tested under uniaxial normal stress to allow for the FAT classification of the detail as designed and fabricated. The detail actually represents a typical case of non-load carrying transversal attachments. The results are summarised in table 3.3. The tests were conducted at different stress levels to enable the S-N slope estimate. As much of the available time was spent on building and tuning the multiaxial setup, uniaxial tests under normal stress range had to be done in another setup, namely the servo-hydraulic “Schenck” 100 ton showed in figure 2.16. Applied loads measured with the machine’s load cell were controlled with strain gauges far from the weld toes and the specimens were equipped with ACPD probes, figure 3.4. The ACPD measurements on these specimens revealed to be difficult to use, mainly because only 4 probes could be used along each weld toe (100mm long) and propagation is remarkably 2-dimensional.

Specimen	$\Delta F_{\text{horiz.}}$ [kN]	$\Delta \sigma$ [N/mm <sup>2</sup> ]	$R_{\sigma}$	$N_{\text{fail}}$
N1	180	180	0,1	261.740
N2	150	150	0,1	657.361
N3	120	120	0,1	2.721.534
N4	150	150	0,1	1.390.893
N5	150	150	0,1	626.458
N6	100	100	0,1	9.000.000*

(\*) run-out

Table 3.3 – Experimental results under uniaxial normal stress

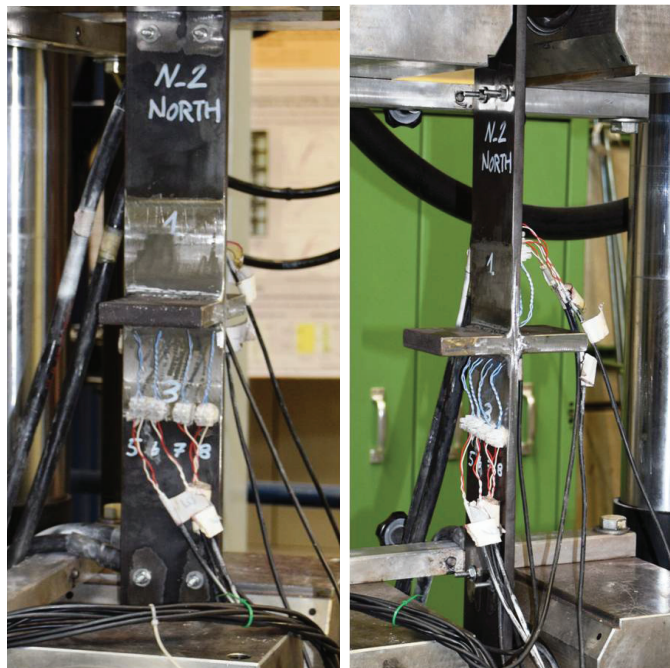


Figure 3.4 – Uniaxial setup for tests under normal stress

### Chapter 3. Out-of-plane interaction - Web crossings

All specimens presented the same crack pattern, with typical multiple semi-elliptical cracks initiated at the weld toe. Multiple initiation points were observed, originating coalescence from single small semi-elliptical cracks to larger cracks (at different depths) to finally a large crack with  $a/c \approx 0,25$ . The end of the weld toes at the edge of the main stressed plate were carefully machined to eliminate any notch or indentation, figure 3.5. Consequently, no preferential crack initiation point was observed, and the cracks did not propagate from the edges, rather initiated at the weld toe on the main plate and propagated essentially perpendicular into the main plate.

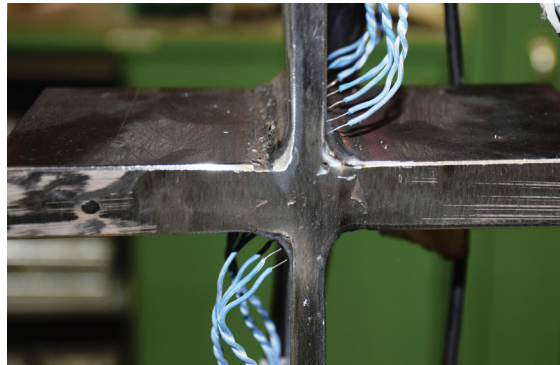


Figure 3.5 – Detail of weld toe end on plate edge

Some examples of the crack patterns obtained under uniaxial normal stress are shown in figure 3.6. The crack surfaces are smooth, a typical feature for Mode I cracks.

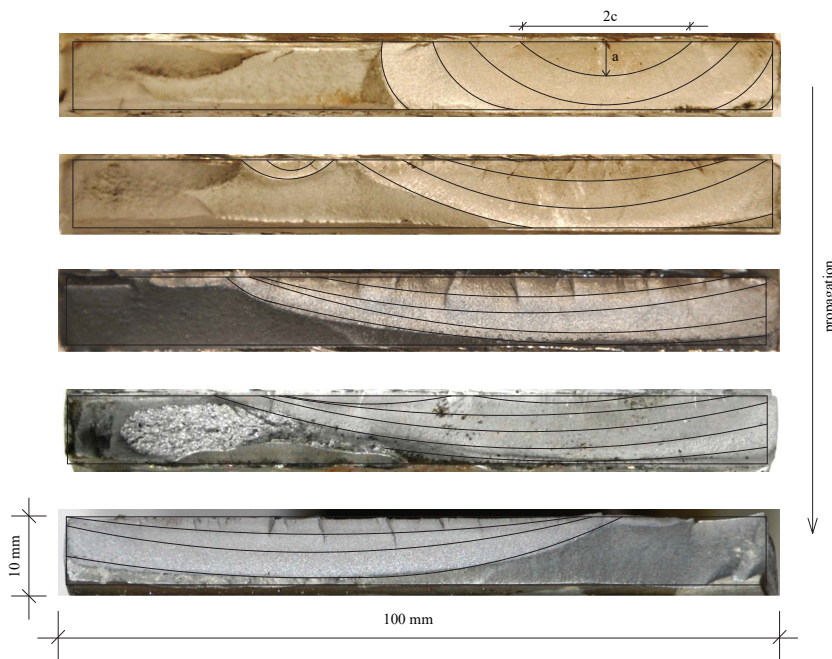


Figure 3.6 – Typical crack pattern for tests under uniaxial normal stress



### 3.2. Experiments under uniaxial stress

The results for the tests under uniaxial normal stress are shown in figure 3.7 along with their mean S-N curve. The slope obtained by linear regression is high,  $m=5,75$ , but the  $n^{\circ}$  of tests is limited. Considering a fixed slope  $m=3$ , the detail can be classified as  $\Delta\sigma_{2.10^6, mean} = 110\text{MPa}$ . For the sake of comparison, a database of uniaxial experiments collected from literature was established. Details of the database and re-analysis of experimental results are shown in Appendix A.4. The detail could be classified as FAT80, for toe-to-toe length up to  $l=80\text{mm}$ , see figure A.8. Our experimental results are plotted along with the database in figure 3.7, showing overall good agreement with the database results.

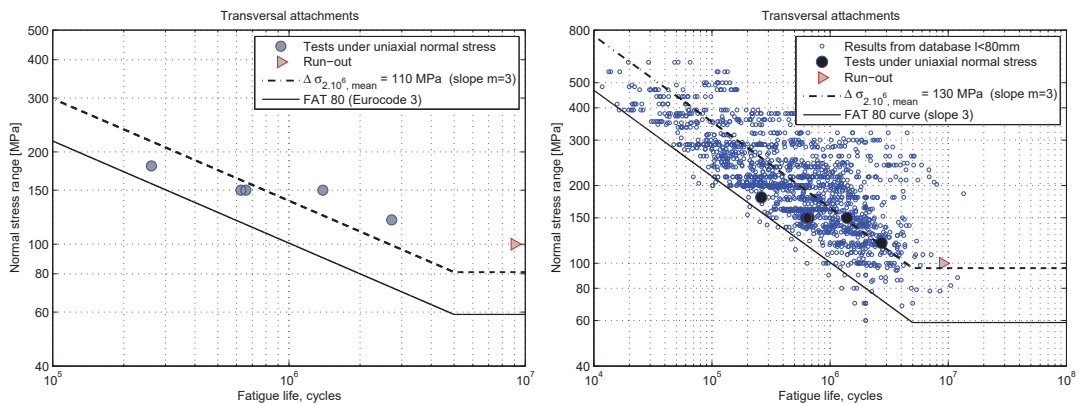


Figure 3.7 – Tests under uniaxial normal stress

Two tests were carried under pure shear. One of them, was a “proof of concept” specimen, tested in shear on a  $180 \times 8\text{mm}^2$  steel plate (S355) with a 50mm slot hole done by water jet on each side of the fillet weld, figure 3.8. The specimen was loaded to a nominal gross section stress of 150MPa, i.e. a nominal shear stress on each weld throat ( $100 \times 4\text{mm}^2$ ) of 135MPa, achieving failure at 416.319 cycles, which corresponds to a mean FAT of  $135 \sqrt[5]{\frac{416.319}{2.000.000}} = \text{FAT}98$ , shown in figure 3.10. The fillet welds for this preliminary test were partial penetration and consequently, fatigue crack started at the root and the crack was “perfectly” aligned with the throat section, i.e.  $\approx 45^{\circ}$ .



Figure 3.8 – “Proof of concept” shear test on slotted hole plate

### Chapter 3. Out-of-plane interaction - Web crossings

---

A second test was done using one of the multiaxial specimens with full penetration fillet welds. The test was performed on the multiaxial setup under the same conditions as the proportional and non-proportional tests. The specimen failed at 3.780.000 cycles. The crack is located in the weld toe section of the main plate, i.e. the same section and crack plane as under uniaxial normal stress, although it is globally rugged and presented small branches along the slag lines of the fillet weld, figure 3.9. These are typical Mode II/III cracks, similar as reported in literature for other shear cracks on tubes in Appendix B.



Figure 3.9 – Typical crack pattern for tests under uniaxial shear stress

Both Mode II and III are known to be difficult to obtain in plate details and it is usually assumed that these failure modes are not important for plate structures, where tangential stress is not obtained by torsion but mainly by shear forces. In this aspect the original design of the multiaxial setup proved successful. The cracks obtained under pure shear are in Mode II/III as shown in figure 3.9 and this is also the case for the cracks obtained under interaction as shown in figure 3.12.

One disadvantage of the multiaxial setup that could not be avoided is that it does not allow a clear definition of the nominal shear stress. While under longitudinal normal stress, the horizontal jack at  $\Delta F=100$  kN ( $A=100 \times 10$  mm<sup>2</sup>) clearly defines  $\Delta \sigma_{nominal}=100$  MPa, nominal shear stress under vertical jack load of  $\Delta F=100$  kN ( $A=100 \times 10$  mm<sup>2</sup>) is not realistic due to proximity of the rolling bearing supports, see figure 3.2 and 3.3. The bearings had to be placed as close as possible from the center axle of the vertical jack to avoid major bending effects, but on the other hand not too close, to avoid direct load transfer from the vertical plate without inducing a shear stress state at the weld toe. A compromise position was adopted but the results are still influenced by some degree of bending due to the vertical jack, especially under proportional loads. An equivalent nominal shear stress was derived from a local notch stress analysis (the 1mm notch approach), using a three-dimensional finite element model in ABAQUS, with 3-D 20-node quadratic solid elements (C3D20). The model showed that the assumption about nominal

### 3.3. Experiments under multiaxial stress

shear stress using the full cross section of the longitudinal plate (100x10mm<sup>2</sup>) is not reasonable due to the particular transfer of the vertical load to the linear roller bearings. A nominal shear stress was thus defined by assuming equivalence between the nominal stress system and the notch stress. This equivalence has been established by Amstutz and Olivier (2011) by re-analysing experimental results on the local 1mm system. The majority of the experimental results considered in the re-analysis by Amstutz and Olivier (2011) is included in Appendix A.6. By considering  $\frac{\Delta\tau_{notch,ref}}{\Delta\tau_{nominal,ref}} = \frac{225}{80} = \frac{\Delta\tau_{local}}{\Delta\tau_{nominal}}$  where  $\Delta\tau_{local}=280$  was derived with the finite element model, figure 3.17, a nominal equivalent shear range of  $\Delta\tau_{nominal}=99,6$  MPa is defined.

Both shear tests are shown in figure 3.10. By assuming a fixed slope  $m=5$ , the mean strength at  $2.10^6$  results  $\Delta\tau_{2.10^6,mean} = 106$ MPa. Once again a relevant database of existing fatigue results was collected from literature. The re-analysis presented in Appendix A.6, showed that the mean strength at  $2.10^6$  is  $\Delta\tau_{2.10^6,mean} = 128$ MPa. Our experimental results are in line with the database as shown in figure 3.10, although lower, a common trend for welded plate details.

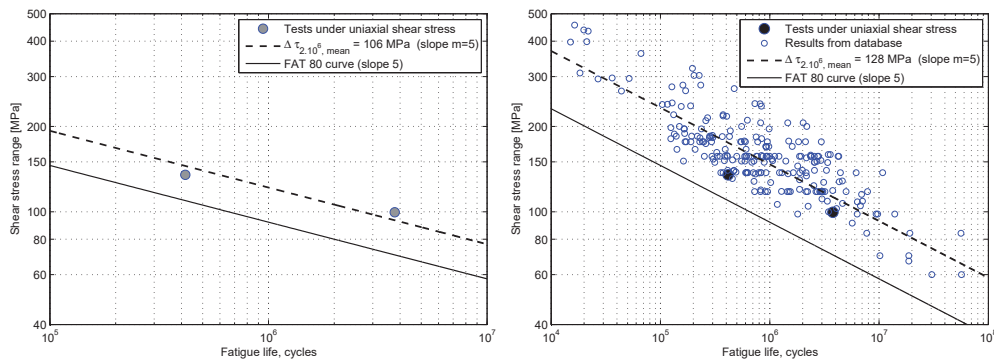


Figure 3.10 – Tests under uniaxial shear stress

### 3.3 Experiments under multiaxial stress

A total of twelve tests were done under multiaxial shear-normal stress, six under proportional loads and other six under non-proportional, table 3.4.



Figure 3.11 – Overall view of a failed specimen under proportional load

### Chapter 3. Out-of-plane interaction - Web crossings

Specimen	$\Delta F_{\text{horiz.}}$ [kN]	$\Delta \sigma$ [N/mm <sup>2</sup> ]	$\Delta F_{\text{vert.}}$ [kN]	$\Delta \tau$ [N/mm <sup>2</sup> ]	Phase shift (°)	$N_{\text{fail}}$
NP-0	100	100	100	99,6	90°	1.550.000
NP-1	100	100	100	99,6	90°	4.052.629
NP-2	100	100	100	99,6	90°	3.200.000
NP-3	100	100	100	99,6	90°	2.000.000
NP-4	100	100	100	99,6	90°	5.000.000
NP-5	100	100	100	99,6	90°	5.500.000
P-0	100	100	100	99,6	0°	173.840
P-1	100	100	100	99,6	0°	240.500
P-2	100	100	100	99,6	0°	192.560
P-3	100	100	100	99,6	0°	306.120
P-4	100	100	100	99,6	0°	330.000
P-5	100	100	100	99,6	0°	253.000

Table 3.4 – Experimental results under multiaxial stress

The specimens failed at the weld toe, both under proportional and non-proportional loads, in a similar way as the uniaxial tests, figure 3.11. It was seen that due to the static behaviour of the experimental setup, cracks were initiated mainly on the lower half of the 80mm fillet weld, both due to the concentration of shear stress and secondary bending effects. Some examples of the observed crack patterns are shown in figure 3.12.

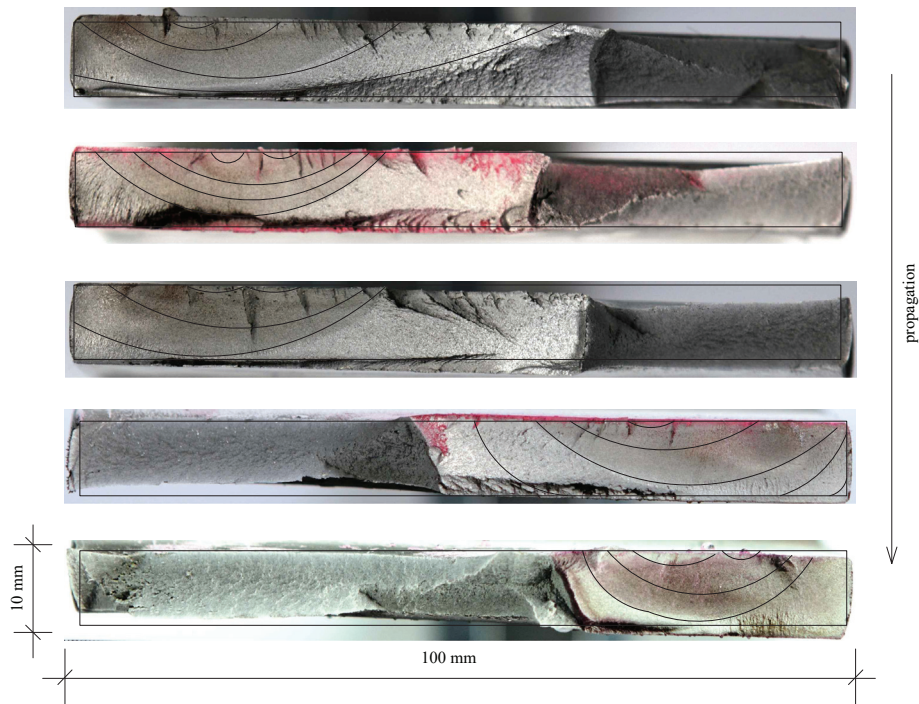


Figure 3.12 – Typical crack pattern for tests under multiaxial stress

Crack coalescence was observed, with small semi-elliptical cracks initiating from different spots at the weld toe. After parallel growth and coalescence, these cracks turned into

### 3.3. Experiments under multiaxial stress

a single crack, semi-elliptical but with high  $a/c$  ratios, closer to semi-circular than the crack patterns observed under uniaxial normal stress. This is attributed to the influence of the shear load. No clear distinction was seen between cracks due to proportional or non-proportional load case.

Three basic variables characterise the multiaxial tests:  $\Delta\sigma$ ,  $\Delta\tau$  and  $N$ . By defining the shear to normal stress ratio as  $\rho = \frac{\Delta\tau}{\Delta\sigma} \approx 1$ , we may plot the multiaxial results, based on the normal stress range. This is shown in figure 3.13 where the vertical axis defines  $\Delta\sigma$ . A linear regression on the non-proportional results with fixed slope  $m=3$  gives  $\Delta\sigma_{2,10^6,mean} = 117\text{MPa}$ . Comparing with the results obtained under uniaxial normal stress, see figure 3.13, and corresponding  $\Delta\sigma_{2,10^6,mean} = 110\text{MPa}$ , one concludes that the interaction effect under the non-proportional case is low. On the contrary, the proportional load case, significantly reduces fatigue life. If correlated based on the normal stress range, a mean S-N curve  $\Delta\sigma_{2,10^6,mean} = 50\text{MPa}$  is obtained by linear regression with fixed slope  $m=3$ .

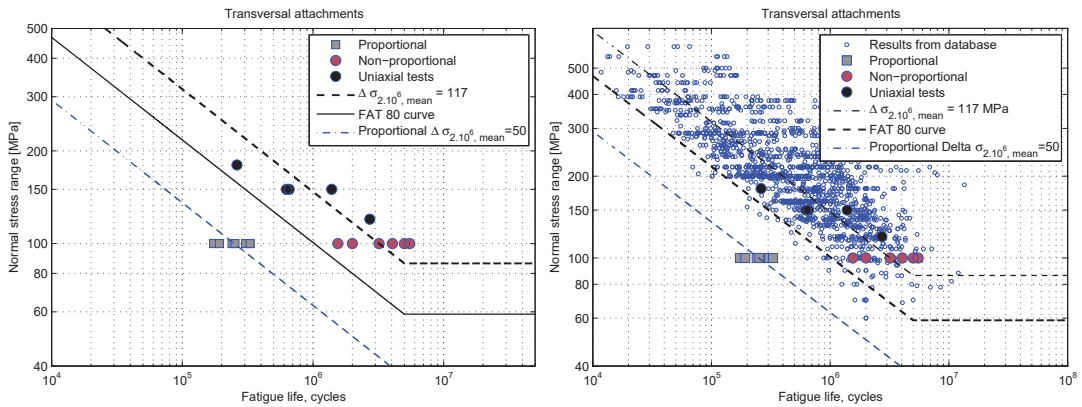


Figure 3.13 – Test results under multiaxial stress and comparison

The proportional load case proves to significantly reduce uniaxial fatigue life due to the interaction of shear and normal stress. In fact, it was seen that the non-proportional case did not significantly influence fatigue life under normal stress. This conclusion, is somehow contrary to what has been observed in multiaxial tests on tubular specimens where the non-proportional load case has been reported as more damaging, see Appendix B. These tests also show the anisotropic nature of the multiaxial fatigue phenomena in welded plate details. The failure modes are expected mainly under Mode I due to the unavoidable weld toe imperfections. Mode II/III cracks were obtained with pure shear tests. Most of the crack driving force is lost in friction so these modes have higher lives than their corresponding Mode I cracks. The shear friction may however be severely reduced under the presence of a normal stress. This is illustrated in figure 3.14. The idea of factorising the shear damage for the normal stress influence can be found in most of the important strain based criteria: Brown-Miller, Fatemi-Socie or Findley. This is believed here to be the main reason for the proportional load case to give the lowest fatigue lives. The



### Chapter 3. Out-of-plane interaction - Web crossings

normal stress influence, acting in phase with the shear, greatly reduces friction between the crack surfaces, increasing the damaging character of the shear forces.

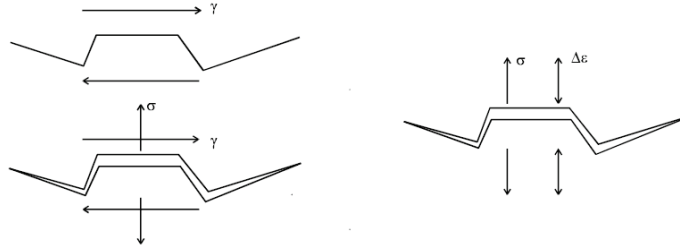


Figure 3.14 – Shear friction mechanism

The transverse longitudinal residual stresses at the weld toe of transversal attachments (non-load cruciform fillet welds) are usually compressive, as shown for example with residual stress measurements presented by (Barsoum and Samuelsson, 2006) or (Barsoum and Jonsson, 2008). The proportional load cases greatly reduces these favorable compressive stresses, although some relaxation is expected also for the non-proportional load case, at a smaller rate though. The lack of detailed measurements greatly reduces the scope of possible posterior analysis. This is the case for instance for the lack of information about initiation life. An estimation based on the Coffin Manson relation using Neuber's notch rule is presented in figure 3.15. Using the notch values from the local 1mm finite element analysis, the estimated initiation lives are, between the proportional and non-proportional load cases, significantly different, by a factor of  $\approx 10$ . It must be stressed out that in presence of compressive residual stresses due to the welding, initiation life will increase, but on the other hand, relaxation under proportional loads is expected to be faster than for the non-proportional case. Another great limitation is the lack of crack propagation measurements that would allow calibration of a fracture mechanics model, most importantly for the shear propagation under mixed Mode II and III. This is believed to be part of necessary future works as Mode II/III stress intensity factors are calibrated case by case after experiments as shown for example by Amstutz et al. (2001).

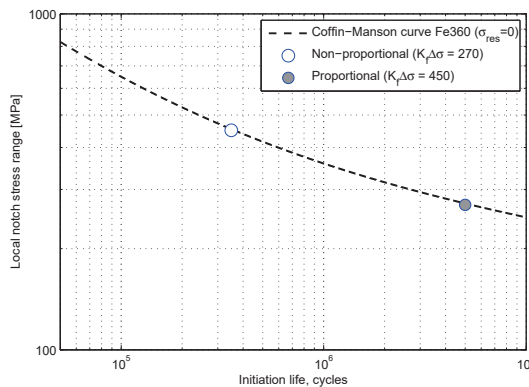


Figure 3.15 – Estimation of initiation life for Fe360 and  $\sigma_{res} = 0$

### 3.4 Fatigue life estimation

A suitable method to estimate fatigue life for the tests is the local 1mm notch stress approach. The principal maximum stress under each load condition is calculated at the weld toe, whose notch is rounded to 1mm. Each load case is solved by the global 3-D model taking into account the boundary conditions from the setup, with a relatively coarse mesh. The linear bearings were modeled with 2 rows of spring elements supporting the edge of the main horizontal plate, which were calibrated based on the registered displacement from the specimen under vertical loads,  $\delta_{vert} \approx 0,4mm$  on the vertical jack axis, between bearing supports. The local maximum principal stress were computed using a sub-model technique, with the weld region isolated from the global model, allowing for the local notch rounding and refined mesh. The same 20-node quadratic solid elements are used on both the main model and the sub-model, the sub-model being meshed to 0,25mm at the weld toe rounded to 1mm (minimum 4 elements per radius), figure 3.16, following the guideline presented by Fricke (2008).

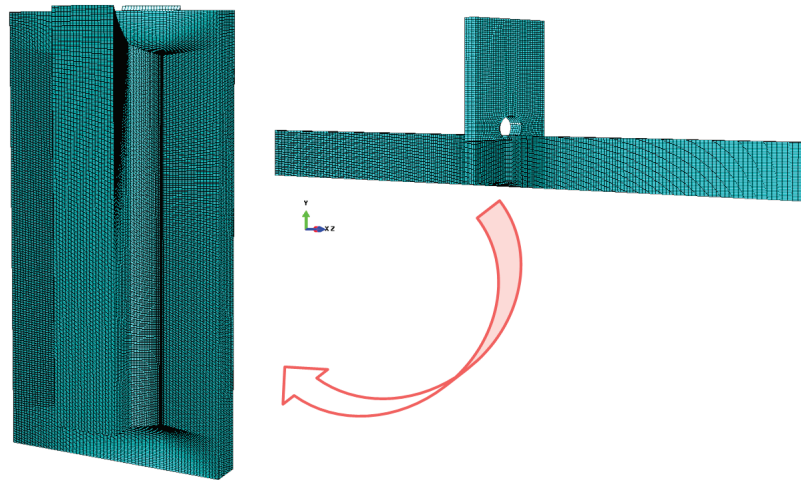


Figure 3.16 – Global and sub-model for the multiaxial specimens

The notch stress results are summarised in table 3.5 and shown in table 3.17.

Load case	$\Delta F_{horiz.}$ [kN]	$\Delta F_{vert.}$ [kN]	$\Delta \sigma_{max,local}$
Uniaxial N	180	-	486
Uniaxial N	150	-	405
Uniaxial N	120	-	324
Uniaxial N	100	-	270
Non-proportional	100	-	270
Proportional	100	100	580
Uniaxial S	-	100	280

Table 3.5 – Notch stress values for the multiaxial specimens

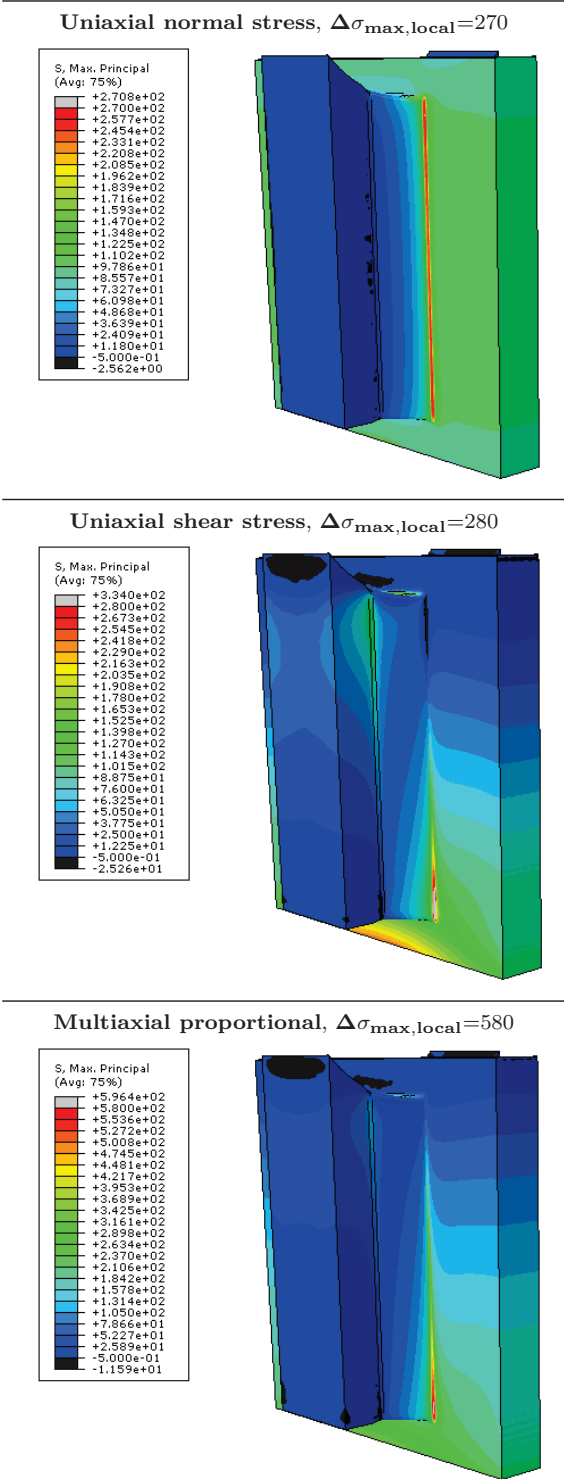


Figure 3.17 – Notch stress output from the FEM sub-model



### 3.4. Fatigue life estimation

The representation of the results in a notch S-N diagram is shown in figure 3.18 along with the master curve FAT225.

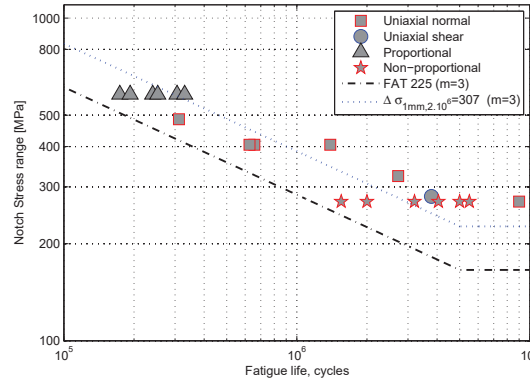


Figure 3.18 – Notch stress S-N curve

A linear regression with all results pooled gives in a S-N slope  $m=3,7$ . Assuming a fixed slope  $m=3$  one obtains a mean notch FAT value  $\Delta\sigma_{1mm,2.10^6}=307$  MPa and FAT220 with  $k=1,94$  accounting for the sample size.

The notch stress has the ability to regroup the different load cases in a single scatter band, supported by the standard deviation of  $\sigma=0,22$  similar to what is obtained for several uniaxial datasets, see Appendix A. Fatigue life estimation using the notch stress results is shown in figure 3.19. The scatter bands obtained with standard deviation  $\sigma=0,22$  and  $k=1,94$  are shown for both cases of characteristic FAT225 and mean strength at  $2.10^6$   $\Delta\sigma_{mean,2.10^6}=307$  MPa. The design FAT225 is seen to give safe estimates for the fatigue life.

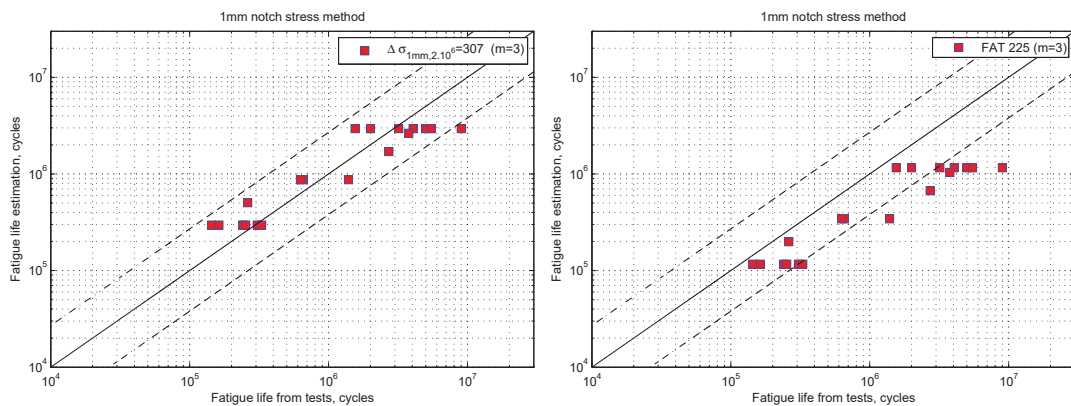


Figure 3.19 – Fatigue life estimation with the local notch stress

A simplified estimation of fatigue life may also be attempted using the nominal stress quantities  $\Delta\sigma$  and  $\Delta\tau$ , using the interaction equations presented in Section 1.3. The damage accumulation rule from Eurocode 3 adds the fatigue damage computed under

### Chapter 3. Out-of-plane interaction - Web crossings

normal stress ranges with damage due to shear stress ranges:

$$D_\sigma + D_\tau \leq CV \Leftrightarrow \frac{n_{test}}{N_{R,\sigma}} + \frac{n_{test}}{N_{R,\tau}} \leq CV \Leftrightarrow \frac{1}{N_{R,\sigma}} + \frac{1}{N_{R,\tau}} \leq \frac{CV}{n_{test}} \quad (3.1)$$

$$\text{where: } N_{R,\sigma} = \frac{2.10^6 \Delta\sigma_{R,2}^3}{\Delta\sigma_{test}^3} \quad ; \quad N_{R,\tau} = \frac{2.10^6 \Delta\tau_{R,2}^5}{\Delta\tau_{test}^5}$$

The criteria defined by IIW Recommendations is a quadratic equation for the equivalent stress ranges at  $2.10^6$  cycles. It writes:

$$\left( \frac{\Delta\sigma_{Ed,2}}{\Delta\sigma_{R,2}} \right)^2 + \left( \frac{\Delta\tau_{Ed,2}}{\Delta\tau_{R,2}} \right)^2 \leq CV \quad (3.2)$$

$$\text{where: } \Delta\sigma_{Ed,2} = \sqrt[3]{\frac{n_{test} \cdot \Delta\sigma_{test}^3}{2.10^6}} \quad ; \quad \Delta\tau_{Ed,2} = \sqrt[5]{\frac{n_{test} \cdot \Delta\tau_{test}^5}{2.10^6}}$$

Life estimations for the proportional tests are obtained by solving both equations 3.1 and 3.2. The results are shown in figure 3.20. Both equations are solved for the characteristic FAT values  $FAT_\sigma=80$  and  $FAT_\tau=80$  and the mean resistance values at  $2.10^6$  which were shown earlier,  $\Delta\sigma_{R,2}=110$  and  $\Delta\tau_{R,2}=106$ . Life scatter bands for  $\sigma=0,27$  according to figure 5.5 and  $k=1,64$  are included. The damage accumulation formula from Eurocode 3, equation 3.1 has to be solved with the damage comparison value  $CV=0,2$ , to give mean life estimation coherent with the experimental results and characteristic values for  $FAT_\sigma$  and  $FAT_\tau$  coincident with the uniaxial scatter band for the 95% percentile. On the other hand, IIW elliptical interaction gives good results by solving equation 3.2 with  $CV=0.6$ , the mean estimation matching the experimental results, and the characteristic values yielding conservative estimations. This is in agreement with findings by Backstrom and Marquis (2004) and Sonsino (2009) who have proposed  $CV=0,5$  as defined now in (IIW, 2008). The discussion about these interaction formulas will be held in chapter 6, but it is seen that the conclusion about non-proportional stress states in tubular specimens are equivalent to proportional states as presented in this Chapter.

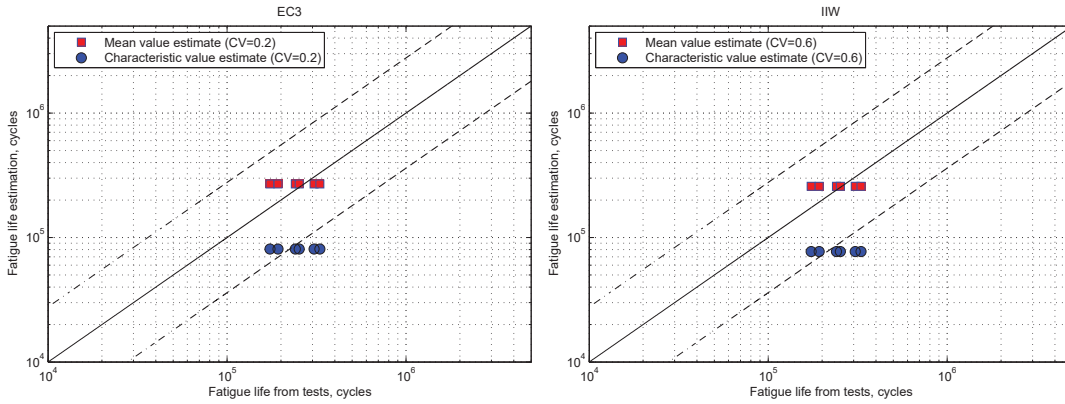


Figure 3.20 – Life estimations for proportional tests using the damage sum criteria

## 3.5 Summary of conclusions

- A new multiaxial setup was presented in this section that allowed proportional and non-proportional multiaxial tests in a typical welded plate detail. Under pure shear, Mode II/III cracks were obtained. The results on a transversal attachments loaded both in normal stress  $\Delta\sigma$  and shear stress  $\Delta\tau$  clearly showed the detrimental effect of the proportional load case. Under non-proportional stresses, fatigue life was dominated by Mode I behaviour under normal stress, and fatigue life was little affected by the presence of shear loads.
- The local 1mm notch approach was shown suited to the analysis under multiaxial stress states. Maximum principal stresses at the rounded notch allowed all load cases to be defined in the same notch category. The FAT225 master curve gives safe life estimations.
- The experimental results were analysed with Interaction formulas based on uniaxial nominal stress components. The Gough-Pollard elliptical interaction equation with  $CV=0,5$  as defined in IIW Recommendations for non-proportional stress states, was seen to be in good agreement with the experimental results obtained under proportional conditions.



# FATIGUE LOADS **Part II**



## 4 Highway traffic

A probabilistic highway traffic model is developed in this chapter for the traffic spectra characterisation and reliability simulations. The model allows the interaction between vehicles in multiple lanes, multiple presence of lorries in the same lane over the bridge length and interaction with railway traffic.

Current European procedure for fatigue verification of highway bridges is based on five different fatigue load models (EN 1991-2, 2003), (Nussbaumer, A; Borges, L; Davaine, 2011). FLM1 and FLM2 for short influence lines, are used for infinite life checks on S-N curves with a CAFL fatigue limit. They are defined as “frequent loads” to cover 99% of the damage due to free-flowing traffic (Calgaro et al., 2010). These models were calibrated with S-N curves with CAFL at  $5 \cdot 10^6$  cycles, so that they may be unsafe for the lowest FAT categories. Load models based on a fatigue limit design are not considered here due to considerable lack of accurate knowledge on maximum loads for bridges. FLM3 is a simplified “damage equivalent load model” limited to critical span lengths of 80m. It is the most important and widespread load model for highway bridges and is considered here to investigate some of the difficulties faced with the use of equivalent damage factors. FLM4 is important because it allows a damage accumulation procedure that is helpful for cases where damage equivalent factors are not valid or if interaction between highway and railway loads is required. Although originally developed for local effects on slow lane traffic (influence lines  $L < 10\text{m}$ ) (Bruls, 1996), it is often used for other cases where vehicle interaction can be neglected. The FLM5 is finally a load model based on traffic measurements that allows specific bridges to be designed for particular load cases. It is limited by the fact that real traffic data is seldom available at design stage of a new bridge. The traffic model developed in this chapter is intended to be a generalised FLM5, representative of European traffic, allowing fatigue design of bridges in a general way. The model was already used in the fatigue design of the 3<sup>rd</sup> Bosphoro bridge, where interaction of 8 highway lanes with 2 railway tracks was investigated with influence lines up to 400m (Baptista and Nussbaumer, 2015).

## 4.1 Highway traffic generation model

The traffic generation model is based on a Monte Carlo simulation of highway loads using statistical data of traffic parameters. A daily traffic spectrum is generated as output. The model generates vehicles, within given traffic densities and composition, accounting for variability in lorry weights with random distances ( $d_i$ ) between vehicles. The traffic generation is schematically shown in figure 4.1.

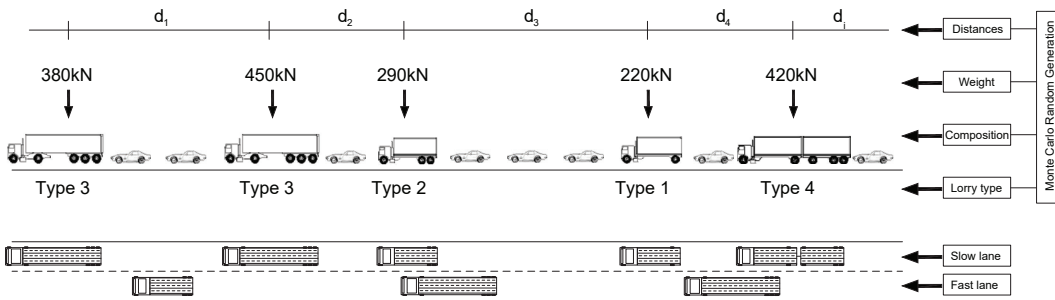


Figure 4.1 – Schematics of the traffic generation model

The model is based on traffic survey data from Eurocode Background (JRC, 2008), (SETRA, 1996) and (Sanpaolesi and Croce, 2005). This ensures consistency between the generated traffic and Eurocode Fatigue Load Models, namely FLM3 and FLM4. More specifically, the traffic measured on the French A6 Paris-Lyon motorway at Auxerre (4-lane motorway - 2 on each direction) during 1986 is considered because it was taken as the “European long distance traffic” and as the basis of the European Load Models. The choice of Auxerre data as representative of European motorway traffic was justified by the following reasons (JRC, 2008) :

- The traffic composition corresponded to estimated future trends, namely the high percentage of type 3 vehicles, figure 4.1
- Very high percentages of lorries in traffic composition, 33% in the slow Lane
- Loaded lorries corresponded to about 66% of total lorry number, what was considered to mirror future efficient logistic systems
- Traffic data was fully documented for a long period on both slow and fast lane
- Auxerre had the highest frequency of large axle loads

During the development of the European fatigue load models, it was considered that future traffic growth trend was implicitly taken into account by adopting Auxerre traffic data (JRC, 2008). Traffic growth trends mainly affect the vehicle weight ( $G$ ) and density ( $N_{obs}$ ). Growth tendencies for Swiss traffic, for example, measured between 2003 and 2009 were characterised in (Maddah et al., 2012) defining annual development index of 0,078% and 0,027% for the Average Gross Weight of Trucks (AGWT) and Average Gross Weight



## 4.1. Highway traffic generation model

of Heavy Vehicles (AGWHV) respectively. For the Average Daily Truck Traffic (ADTT) and the Average Daily Heavy Vehicle Traffic (ADHVT) annual development index of 0,35% and 0,40% were defined. Similar trends were reported in (Boer, 2010). On the other hand, motorway capacities defined by TRB (2000) vary between 2250 vehicles/lane/hour (at 90km/h) and 2400 vehicles/lane/hour (at 120km/h). Considering 90km/h as the reference value for lorries, and further considering that traffic background data already considers 1800vehicles/lane/hour, one may have a maximum annual development index of 0,22% during the 100 year design life. This means that the traffic density considered to develop the Eurocode fatigue load models is high, close the maximum motorway capacity, which is why no traffic growth tendency is included in our model.

The main parameters of the traffic generation model are summarised in table 4.1.

Traffic	Parameter	Variable	Model
Weight	Lorry weight	G	Normal distribution
Density	N° vehicles/year	$N_{obs}$	Constant
Composition	N° lorries N° total vehicles	%	Deterministic
Flow	Distance between vehicles	Free flow Congested	Gamma distribution Beta distribution
	Vehicle speed	v	Discrete variation

Table 4.1 – Traffic parameters adopted in the model

### 4.1.1 Vehicle weight

Lorry types and mean vehicle weight for the traffic generation model, are taken from the traffic at Auxerre (JRC, 2008), figure 4.2. After statistical data treatment, four types of vehicles were categorised and bi-modal normal distributions attributed to each type, both for loaded and unloaded lorries.

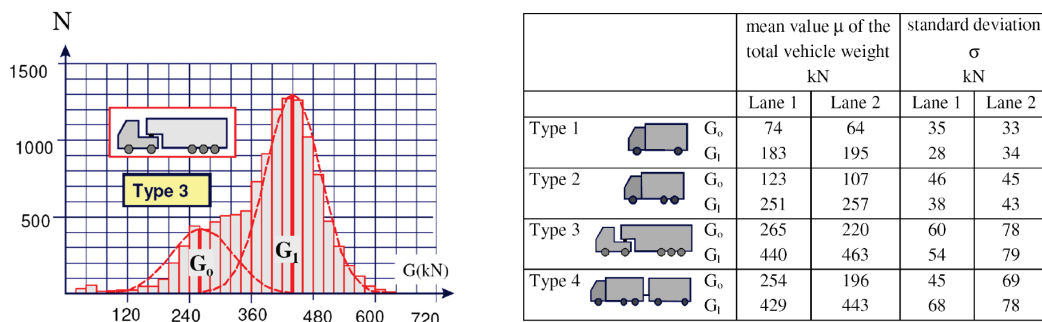


Figure 4.2 – Lorry types and weight distribution (JRC, 2008)

## Chapter 4. Highway traffic

The lorry categories and weight distributions as shown in figure 4.2 were used in the European background to calibrate fatigue safety coefficients based on defined reliability indexes and characteristic S-N curves (Merzenich and Sedlacek, 1995), (Sedlacek and Jaquemoud, 1984), (Bruls, 1996). A similar model is defined by the FLM4 with representative values for highway traffic, table 4.2. Although developed for influence lines smaller than 10m, the Fatigue Load Model 4 is well suited to generate characteristic fatigue loads, as long as for longer spans the vehicle interactions are taken into account, both for single and multiple lanes. For short influence lines, traffic generation based on FLM4 needs to account for the specific axle load probabilistic distribution using axle loads normally distributed with mean values given by FLM4 and standard deviation defined for example in (Mensingher, 2000).

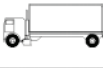




VEHICLE TYPE			TRAFFIC TYPE			
1	2	3	4	5	6	7
			Long distance	Medium distance	Local traffic	
LORRY	Axle spacing (m)	Equivalent axle loads (kN)	Lorry percentage	Lorry percentage	Lorry percentage	Wheel type
	4,5	70 130	20,0	40,0	80,0	A B
	4,20 1,30	70 120 120	5,0	10,0	5,0	A B B
	3,20 5,20 1,30 1,30	70 150 90 90	50,0	30,0	5,0	A B C C C
	3,40 6,00 1,80	70 140 90 90	15,0	15,0	5,0	A B B B
	4,80 3,60 4,40 1,30	70 130 90 80 80	10,0	5,0	5,0	A B C C C

Table 4.2 – Fatigue Load model 4 (FLM4) (EN 1991-2, 2003)

A comparison between the mean values of Auxerre traffic (figure 4.2) and the FLM4 (table 4.2) shows that they are very similar, table 4.3. Type 3 from Auxerre traffic corresponds to articulated lorries which was subdivided in Type 3 and 4 from FLM4 to distinguish between 2 and 3 axles trailers, important for short influence lines. Type 4 from Auxerre corresponds to Type 5 from FLM4.

Auxerre	Lane 1	Lane 2	Mean	FLM4	FLM4/Mean %
Type 1	183	195	189	200	5,8%
Type 2	251	257	254	310	22%
Type 3	440	463	452	467*	3,3%
Type 4	429	443	436	450	3,2%

(\*mean of FLM4 Type 3 and 4 for long distance)

Table 4.3 – Vehicle weights registered at Auxerre compared with FLM4

## 4.1. Highway traffic generation model

As an example, recent measurements from 2004 in Germany (Brohtal) showed that the data from Auxerre was still representative of lorry weights and distribution, table 4.4.







Recorded data at Brohtal (2004) and comparison with data from Auxerre				
type of vehicle		mean value $\mu$ of the total vehicle weight kN	standard deviation $\sigma$ kN	relative frequency %
Type 1 	$G_o$	59,6	14,6	5
	$G_l$	91,7	44,0	6
Type 2 	$G_o$	190,3	23,2	1
	$G_l$	208,4	73,9	4
Type 3 	$G_o$	276,8	59,5	12
	$G_l$	414,5	32,5	5
Type 4 	$G_o$	156,7	18,8	3
	$G_l$	211,4	52,8	5
Type 5 	$G_o$	259,6	92	37
	$G_l$	405,3	24,8	22
Statistical parameters of the traffic records of Auxerre (1986)				
Type 5 	$G_o$	265	60	28,0
	$G_l$	440	54	30,4

Table 4.4 – Comparison between traffic data from Brohtal (2004) and Auxerre (1986) (Sedlacek, 2010)

Overloaded trucks are not considered in our traffic generation model. Although their relative importance in the fatigue damage should be low, because of their usually low number of occurrences, they are extremely important for designs based on fatigue limit. Our models do not assume the existence of a fatigue limit, rather assuming all traffic loads to be damaging, accounting for the propagation threshold with a double slope S-N curve according to Haibach's model. Unfortunately, design assumptions on the fatigue limit are too sensitive to the overload characterisation and multi-lane behaviour, and may lead to unconservative designs in the current code verification format.

The real scenario with the growing tendency of overloads seems however to be important. The data for the European background had shown already some relevance of the Maximum Gross Vehicle Weight (GVW) with values generally around 60 ton, table 4.5.

Measured site	ADTT/slow lane	GVW <sub>mean</sub> [kN]	Stdv <sub>GVW</sub> [kN]	GVW <sub>max</sub> [kN]
Brohtal (D) 1984	4793	245,8	127,3	650,0
Garonor (F) 1984	3686	186,5	118,0	560,0
Auxerre (F) 1986	2630	326,7	144,9	630,0
Fiano R. (I) 1987	4000	204,5	130,3	590,0
Piacenza (I) 1987	5000	235,2	140,0	630,0
Sasso M. (I) 1987	3500	224,9	149,0	620,0

Table 4.5 – GVW registers in European traffic background

Measurements reported for European Weight-in-motion (WIM) data collected between 2005 and 2008 show that Maximum Gross Vehicle Weight (GVW) may largely exceed 100ton, with records of 165ton in Netherlands (Enright and O'Brien, 2011). Some detailed data for a specific Dutch case is presented in (Boer, 2010) with measurements at the

Moerdijk Bridge on the A16 motorway, showing some important presence of vehicles above 100ton. This data was analysed and compared with the specific Auxerre traffic (Caramelli and Croce, 2010) concluding that Auxerre traffic, still covers fatigue effects induced by heavier traffic similar to Moerdijk measurements, excluding overload and exceptional vehicles, which cannot be treated statistically. Similar conclusions were reported by (Mladen et al., 2010) based on weigh-in-motion data for vehicle and axle loads, collected during 1 year in an access highway to Rotterdam in the Netherlands, figure 4.3.

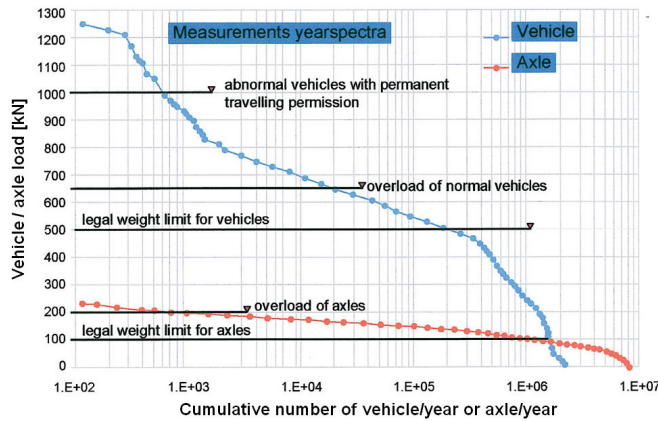


Figure 4.3 – Recent traffic surveys (Mladen et al., 2010)

#### 4.1.2 Traffic density

Traffic density is defined by the number of heavy vehicles per year. Heavy vehicles (lorries) are defined as having a minimum Gross Vehicle Weight of 100kN. Four different traffic categories were defined with the yearly number of observed (or estimated) heavy vehicles ( $N_{obs}$ ) given for the slow lane (or lanes dedicated to heavy traffic). The traffic generation model considers traffic category 1, with  $N_{obs} = 2.10^6$  as defined for the European fatigue checks.

Traffic density of  $2.10^6$  lorries/year (8000 lorries/day) represents a rather high volume of traffic and was not observed in Auxerre, it was registered on Paris Peripherique (SETRA, 1996). For lorry traffic, the maximum was registered at Limburger Bahn (D) with 8600 lorries/day/slow-lane, but measurements were not considered reliable. This ensures that Eurocode traffic model is conservative as it combines two separate maximums, assuming also traffic growth trends are included by this way. Table 4.6, shows ADTT data collected from three different sources, data from (JRC, 2008) with the measurements done between 1978 and 1988 for the European traffic models background, Swiss data from 2005 (Maddah et al., 2012) and recent Weigh-in-motion (WIM) data collected in Europe between 2005 and 2008 (Enright and O'Brien, 2011). The variability on the Average Daily Truck Traffic (ADTT) may be accounted statistically with a  $\beta$  distribution (parameters  $a=1.53$ ,  $b=$

## 4.1. Highway traffic generation model

2.85 and  $\min=2000$  and  $\max=10000$  lorries/day). However, traffic density is considered in our model as a predefined service level, specific of each bridge location, and in this case,  $ADTT=8000$ , corresponding to Eurocode traffic category 1, with  $N_{obs}=2.10^6$  heavy vehicles/year/slow lane.

Measured site	Country	Year	ADTT/slow lane	$N_{obs}/year$ ( $\times 10^3$ )
A6 - Auxerre	(FR)	1986	2630	986
Péripherique - Paris	(FR)	1983	<b>8076</b>	<b>1866</b>
A1 - Garanor	(FR)	1982	2570	1060
A1 - Garanor	(FR)	1984	3686	1060
Limburger Bahn	(D)	1978	8600*	2150*
Brothtal	(D)	1984	4793	1198
Haseltal	(D)	1986	5010	1253
Haseltal	(D)	1988	5620	1405
Rheden	(NL)	1978	3240	810
Leidersdorp	(NL)	1980	6823	1706
Fiano R.	(I)	1987	4000	1000
Piacenza	(I)	1987	5000	1250
Sasso M.	(I)	1987	3500	875
A1 Mattstetten	(CH)	2005	3540	885
A12 - Woerden	(NL)	2005	6545	1636
D1 - Sedlice	(CZ)	2008	4490	1123
A1 - Vransko	(SL)	2006	3158	790
A4 - Wroclaw	(PL)	2008	3708	927
(*) unreliable data				
<b>Traffic Category (Eurocode)</b>				
1 - Motorways with 2 or more lanes per direction with high flow rates				<b>2000</b>
Haagse Schouw	(NL)	1978	1352	338
Forth	(GB)	1978	1250	313
A2 Götthard	(CH)	2005	1472	368
A13 Plazzas	(CH)	2005	533	133
A1 Denges	(CH)	2005	1606	402
A13 Trübbach	(CH)	2005	1048	262
A2 Ceneri	(CH)	2005	1836	459
A1 Oberbüren	(CH)	2005	1752	438
D1 - Branisko	(SK)	2006	1031	258
<b>Traffic Categories (Eurocode)</b>				
2 - Motorways with medium flow rates				500
3 - Main roads with low flow rates of lorries				125
4 - Local roads with low flow rates of lorries				50

Table 4.6 – Heavy vehicles ( $N_{obs}$ ) and ADTT for European motorways (slow lanes)

### 4.1.3 Traffic composition

Traffic composition is defined by the type of lorries and their percentage in the traffic. European background data shows that the percentage of heavy vehicles in traffic varies between 9% and 59%, with a mean around 33%. The reference value was taken from Auxerre, where 33% was registered from which 66% were loaded. This leads to 25% of loaded lorries on slow lanes. On fast lanes, the proportion of lorries in traffic is 10% and one considers, conservatively that they are all loaded (JRC, 2008). The traffic composition

## Chapter 4. Highway traffic

registered at Auxerre is shown in table 4.7. It can be seen that the composition of the FLM4 for long distance traffic is the same, table 4.2.





	mean value $\mu$ of the total vehicle weight kN		standard deviation $\sigma$ kN		relative frequency %		
	Lane 1	Lane 2	Lane 1	Lane 2	Lane 1	Lane 2	
Type 1 	$G_o$	74	64	35	33	13,3	17,2
	$G_i$	183	195	28	34	9,4	10,4
Type 2 	$G_o$	123	107	46	45	0,3	1,3
	$G_i$	251	257	38	43	1,0	2,2
Type 3 	$G_o$	265	220	60	78	17,1	28,0
	$G_i$	440	463	54	79	48,1	30,4
Type 4 	$G_o$	254	196	45	69	3,6	4,1
	$G_i$	429	443	68	78	7,2	6,4

Table 4.7 – Traffic composition for the Auxerre traffic data (JRC, 2008)

Considering  $N_{obs} = 2.10^6$  lorries per year and 50 weeks of 5 days, i.e. 250 days per year, the traffic model generates ADTT=8000 lorries/day for the slow lanes and 3200 lorries/day for the fast lanes. A traffic density of 8000 heavy vehicles generated per day, corresponding to 25% of the total daily traffic on the slow lane, leads to a total of 32000 generated vehicles per day, where 24000 are light vehicles (cars). For the fast lanes, 32000 vehicles in total per day are generated, where only 10% correspond to heavy vehicles. Figure 4.4 shows the distribution of the different lorry type generated by the model. The histogram corresponding to FLM4 has lorry type 1 to 5 and type 6 represents light vehicles (left side of each histogram). For the histogram corresponding to FLMG (right side), type 1 to 8 are the 4 types of lorries separated by loaded (Lorries 1, 3, 5, 7) and unloaded (Lorries 2, 4, 6, 8), while in this case type 9 represents the light vehicles. Light vehicles are considered in the model because they influence the inter-lorry distance. Their weight is however not considered, introducing in this way a natural cut-off for low amplitude stress ranges.

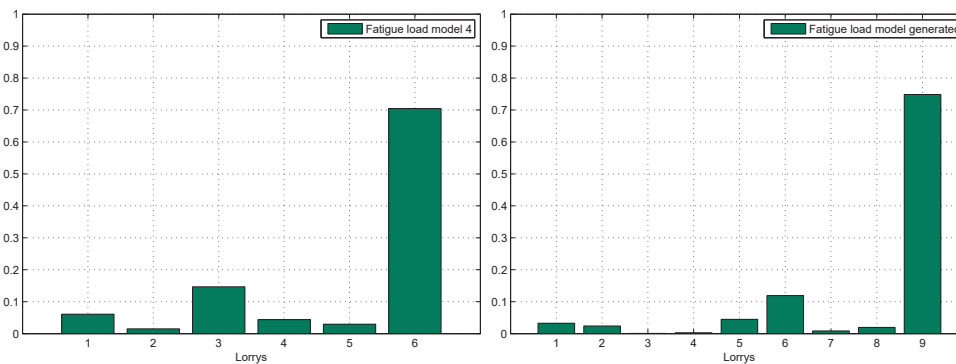


Figure 4.4 – Histogram of the different generated lorry types (FLM4 and FLMG)

4.1.4 Traffic flow

Traffic flow is characterised by the distance between vehicles, which in turn depends on traffic conditions. In other words, traffic flow depends on vehicle speed and traffic jam frequencies. The traffic flow parameters considered in the model are thus: Inter-vehicle distances and Flow conditions. For bridges with span lengths larger than the vehicle length ( $\approx 20m$ ), a mix between free-flow and congested traffic has to be considered in order to maximise fatigue damage in a realistic way. The inter-vehicle distances are generated in the model with continuous distributions of distances between vehicles, considering discrete variations of vehicle speed. The inter-vehicle distance is randomly sampled in a *Gamma distribution* for free-flow conditions (JRC, 2008), and in a *Beta distribution* for congested flow conditions (Bailey and Bez, 1999).

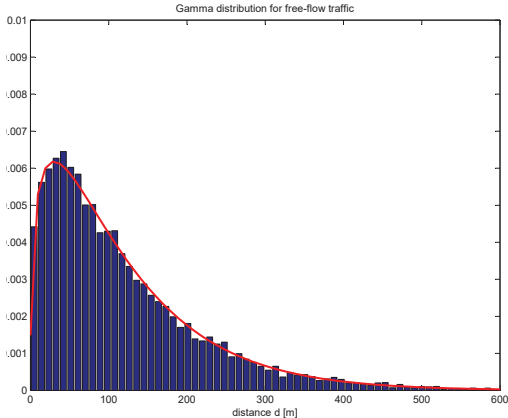
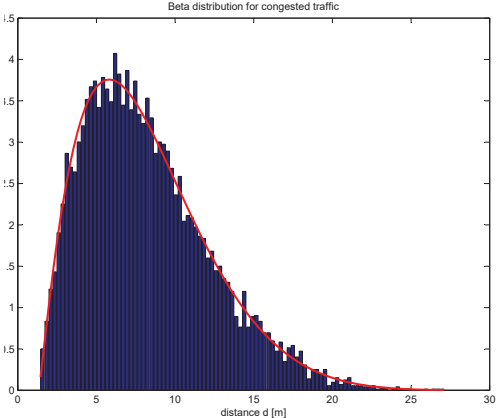
Free flowing traffic	Congested traffic
$f(d) = \text{gammaPDF}(d, \alpha, \beta)$ $\alpha = \frac{d_0}{d_0 - d_m} = \frac{4}{3} ; \beta = \frac{1}{d_0 - d_m} = \frac{1}{90}$ $d_0 = 120m \rightarrow \text{mean value}$ $d_m = 30m \rightarrow \text{modal value}$	$f(d) = \text{betaPDF}(d, \alpha, \beta)$ $\alpha = 2, 15 ; \beta = 9, 0$ $v = 20 \text{ km/h}$ $d_{min} = \frac{v}{15} = 1,33m$ $d_{max} = 15 + 1,1v = 37m$
 <p>Gamma distribution for free-flow traffic</p>	 <p>Beta distribution for congested traffic</p>

Table 4.8 – Distributions for inter-vehicle distances

The conditions for traffic jam generation are based on self induced traffic jams, namely “Stop and Go Waves” (SGW) with two main characteristics (Schönhof and Helbing, 2007):

- Perturbations triggered only for certain traffic volumes (rush hours, holidays)
- Perturbations characterised by a sequence of moving jams between free-flow traffic with an upstream wave propagation at constant speed ( $\approx 16km/h$ )

Traffic measurements on German A5 motorway (Frankfurt – Bad Homburg) have shown the frequency of these SGW to be approximately 4 waves/hour with duration of  $\approx 5$  minutes per perturbation during 4 hours, figure 4.5 (Schönhof and Helbing, 2007) .

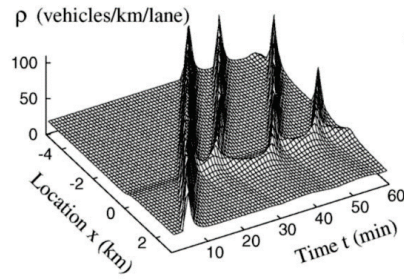


Figure 4.5 – Typical “Stop and Go Waves” (Schönhof and Helbing, 2007)

Rush hours on the French A6 Paris-Lyon motorway are characterised by a morning period from 6 to 10 am and afternoon from 16 to 20 pm (information gathered on the official A6 motorway website). If the traffic is considered congested during each of these 4 rush hours, a daily spectrum of inter-vehicle distances displays like figure 4.6.

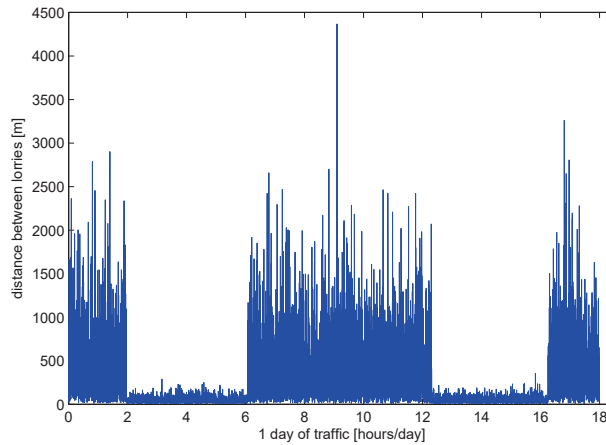


Figure 4.6 – Inter-vehicle distances in 24 hour with 2 periods of congested traffic

In order to have a realistic generation of inter-vehicle distances during the rush hours, we assume four hours of SGW on the morning rush period and four hours of SGW on the afternoon rush period.

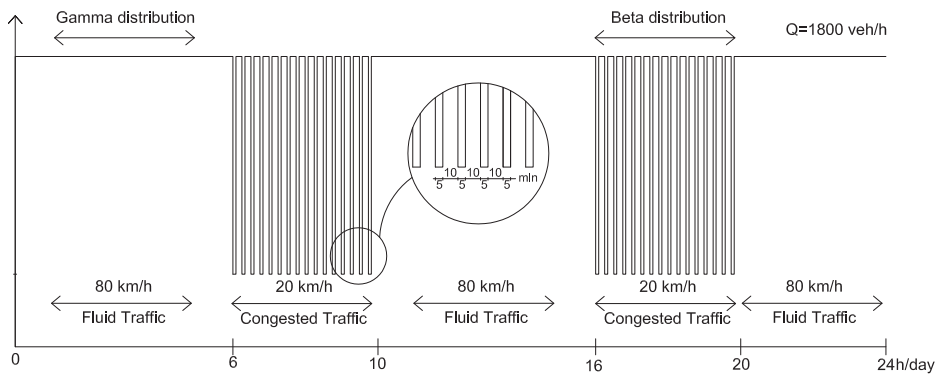


Figure 4.7 – Model for traffic flow with jams



## 4.1. Highway traffic generation model

During each four hour period of congested traffic, we assume four waves/hour with durations of 5 minutes. We further assume all lanes to be congested at the same time. The flow is thus composed by mixed traffic, congested and free, during these 2 periods of rush hours, see figure 4.7. Traffic is generated through a decrease in velocity from 80km/h to 20km/h, keeping flow constant at 1800 veh/lane/hour (Treiber et al., 2000), (Schönhof and Helbing, 2007).

The assumptions for mixed flow conditions, being based on real traffic measurements, allow to maximise the damage compared to free flow conditions, keeping a realistic scenario of two rush periods per day. The inter-lorry distance generated with this scenario on 24hours is shown in figure 4.8, corresponding to 8000 heavy vehicles.

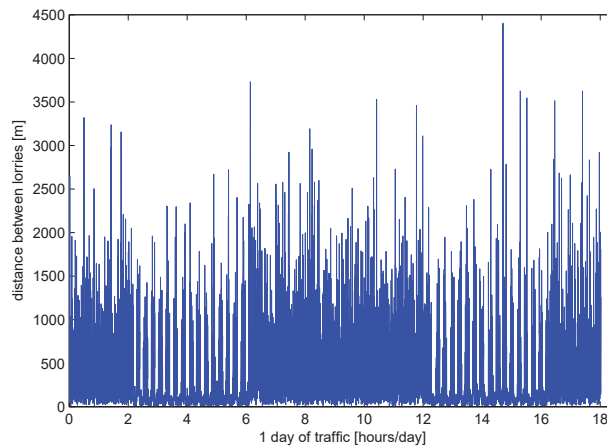


Figure 4.8 – Distances between lorries on a 24 hour traffic generation

A typical inter-vehicle histogram obtained for a single slow lane traffic generation gives a modal inter-lorry distance of  $\approx 25\text{m}$ , a value lower than the 30m mode value for the free-flowing *Gamma* distribution, due to the period of congested traffic, figure 4.9. This value may be used as rule of thumb when applying the FLM4 for influences lines higher than the lorry length.

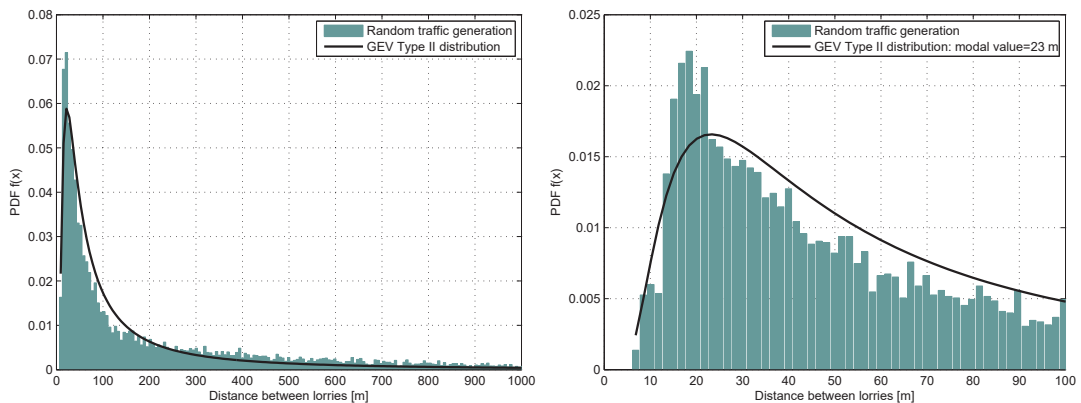


Figure 4.9 – Typical inter-vehicle histogram obtained for a single slow lane simulation

### 4.1.5 Traffic jam influence

From a point of view of maximising fatigue damage, the flow conditions to be adopted depend on the length of the influence line. Figure 4.10 shows an example of the relative damage index obtained with simulations on a simply supported beam with one lane of heavy traffic. Traffic was generated assuming  $N_{obs} = 2.10^6$  heavy vehicles/year corresponding to 25% of total generated traffic with three types of flow scenarios: congested traffic during all day, free-flowing traffic and mixed as adopted in our model. The model for mixed flow conditions with a scenario of two rush periods per day, was adopted to maximise damage in a realistic way. It can be seen in figure 4.10, that for influence lines shorter than 40m, the effect of the flow conditions is not important, because the influence line is in the range of the vehicle length (plus a minimum distance between lorries) so that each vehicle produces one load cycle on the bridge, regardless of the flow conditions. For longer influence lines, the congested traffic distance distribution maximises damage, since it is able to place several lorries on the bridge and still allowing the traffic to unload the bridge, keeping a good ratio between load and cycles. However, for very long influence lines, it is a mix traffic flow scenario that actually maximises fatigue damage. The congested scenario is able to maximise the load on the bridge but drastically reduces the total number of cycles, because the influence line is permanently loaded, and the rainflow counting cycles, drastically decrease.

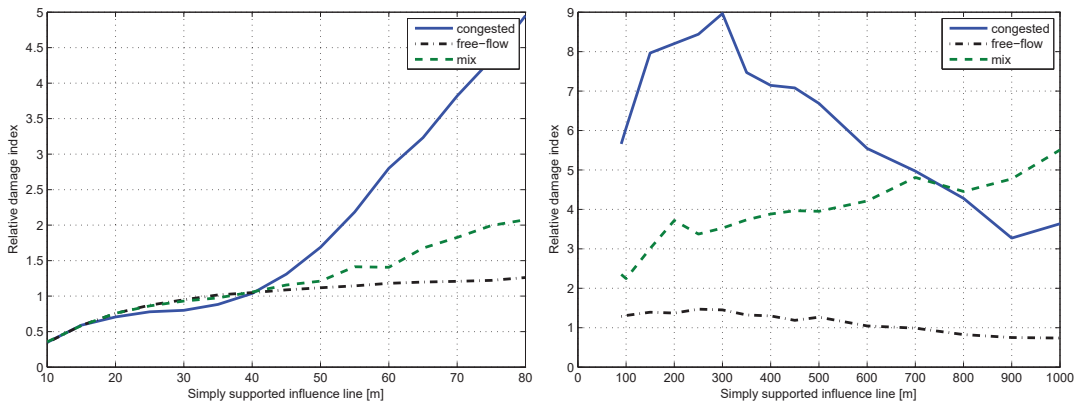


Figure 4.10 – Damage for different traffic flow scenarios

The relative damage index curves in Figure 4.10 were obtained by calibrating a relation between load and stress, so that the damage computed for free-flow traffic was approximately  $D=1$ , and using the same load/stress relation for the other flow conditions. An S-N curve (FAT100) with  $m = 3, k = 5$ , CAFL at  $5.10^6$  without cut-off was considered. The load/stress relation  $f(L)$  was first calibrated for span lengths between 10 and 80m, by assuming damage due to FLM3 as  $D=1$ . The damage equivalent load for FLM3 is given by  $Q_{FLM3} \cdot \lambda_1 \cdot \lambda_2 \cdot \lambda_3 \cdot \lambda_4 \leq Q_{FLM3} \cdot \lambda_{max}$ :

$$\frac{M_{\lambda_i} Q_{FLM3} [\text{kN}]}{f(L)} = 100 [\text{MPa}] \text{ where } f(L) = 0,003L^2 + 2,0583L + 8,9209$$

## 4.2 Comparison between FLM3, FLM4 and FLMG

In order to compare the results from the traffic generation model to the design loads FLM3 and FLM4, a simple design cases is analysed. The traffic generated with the four types of lorries characterising traffic from Auxerre, figure 4.2, is referred as “Fatigue Load Model Generated”, (FLMG), where the weight of each lorry is described by a bi-modal normal distribution for loaded and un-loaded lorries. On the other hand, for the sake of comparison, the random traffic model is also used to generate traffic using the five types of lorries from FLM4 with their representative weight, table 4.2, this being referred as “Fatigue Load Model 4 Generated”, (FLM4). For the structural systems, a simple supported beam with 1 Lane of traffic is used, see figure 4.13.

To translate the internal load effects obtained from the simulation model, in stress ranges, a transfer function  $\alpha$  defining a linear relation between internal load effects and stress is used. The  $\alpha$  transfer function is obtained by assuming that fatigue is the leading limit state of the design, and the design was done using the reference fatigue load model from Eurocode - FLM3. Assuming fatigue damage  $D_{FLM3} = 1$ , for a given FAT detail, the  $\alpha$  transfer function can be obtained by the fatigue safety equation:  $S_{\lambda Q_{FLM3}} \alpha = FAT$ . Exemplifying with a simply supported beam, for a detail under the influence line of bending moment, stress range is given by the maximum bending moment at mid-span:

$$M_{\lambda Q_{FLM3}} \alpha = FAT \rightarrow \lambda Q_{FLM3} \frac{L}{4} \alpha = FAT \rightarrow \alpha = \frac{4FAT}{\lambda Q_{FLM3} L}$$

The equivalent damage load effect for FLM3 is given by:

$$\lambda_1 \cdot \lambda_2 \cdot \lambda_3 \cdot \lambda_4 Q_{FLM3} \leq \lambda_{max} Q_{FLM3}$$

where both  $\lambda_1$  and  $\lambda_{max}$  are span length dependent, table 4.9.

$\lambda_i$	Parameter	Expression	Observations
$\lambda_1$	Parameter for influence line	$\lambda_1 = 2,55 - 0,7 \cdot (L - 10) / 70$	
$\lambda_2$	Traffic volume parameter	$\lambda_2 = 1,224$	$N_{obs} = 2 \cdot 10^6, Q_{m1} = 445$ (FLM4)
$\lambda_3$	Design life of 100years	$\lambda_3 = 1$	
$\lambda_4$	1 Lane traffic	$\lambda_4 = 1$	
$\lambda_{max}$	Maximum $\lambda$ factor	$\lambda_{max} = 2,5 - 0,5 \cdot (L - 10) / 15 \geq 2$	

**Eurocode Traffic Category 1 - Motorways with 2 or more lanes per direction with high flow rates**

Table 4.9 – Equivalent damage factors,  $\lambda_i$  for mid-span moment

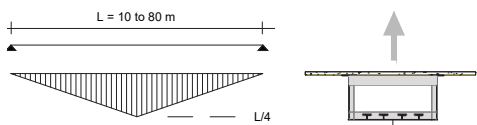
Each FAT is defined in a double slope S-N curve with  $m = 3$  and  $k = 5$  with the “knee-point” defined for  $\Delta\sigma_D$  at  $5 \cdot 10^6$  without cut-off. The equivalent stress range for the traffic generation model is calculated by simulations of daily sum of the power-stress-cycle product as:

$$\sum \Delta\sigma^m N = \sum n_k \Delta\sigma_k^{m_k} = \sum n_i \Delta\sigma_i^{m_1} + \Delta\sigma_D^{m_1-m_2} \sum n_j \Delta\sigma_j^{m_2}$$

The daily sum of the power-stress-cycle product is sampled out of the Monte Carlo model, with 250 samples, which corresponds to 1 year of traffic simulation. The output of the 250 simulations is approximated with a normal distribution and extrapolated to 100 years. The equivalent stress range at  $2.10^6$  cycles is then computed by assuming the “knee-point” defined for  $\Delta\sigma_D$  at  $5.10^6$  in the original FAT:

$$\Delta\sigma_{eq,2} = \left( \frac{(\sum n_i \Delta\sigma_i^{m_1} + \Delta\sigma_D^{m_1-m_2} \sum n_j \Delta\sigma_j^{m_2}) 25000}{2000000} \right)^{\frac{1}{m_1}}$$

The simulation results are summarised in table 4.10. It is seen that using FLM4 gives higher equivalent stress than our model. This is expected because no randomness is applied on the FLM4 weight. These conclusions are however restricted to this example. Comparison between FLM3 and FLM4 given here, cannot be extrapolated for other influence lines of Traffic Categories.



L	FLM3	FLM4	FLMG	FLMG/FLM3	FLMG/FLM4
10	40	65,8	53,9	1,35	0,82
10	71	116,9	95,7	1,35	0,82
10	100	164,6	134,9	1,35	0,82
10	160	263,4	215,8	1,35	0,82
50	40	63,7	51,2	1,28	0,80
50	71	113,1	90,9	1,28	0,80
50	100	159,2	127,9	1,28	0,80
50	160	254,8	204,7	1,28	0,80
80	40	70	55,7	1,39	0,80
80	71	124,3	98,9	1,39	0,80
80	100	175	139,3	1,39	0,80
80	160	280,1	222,8	1,39	0,80

Table 4.10 – Equivalent stress at  $2.10^6$  cycles [N/mm<sup>2</sup>]

The results from our simulation model (FLMG) are also higher than the FLM3 based design. This is attributed in this case to the fact that  $\lambda_{max}$  controls the design. In fact, a bridge subjected to the representative Traffic Category 1 is defined by  $N_{obs} = 2.10^6$  and  $Q_{m1} = 445kN$  so that  $\lambda_2 = 1,224$ . If the design life is fixed to 100 years,  $\lambda_3 = 1$  and considering a single lane, the product  $\lambda_1 \lambda_2 \lambda_3 = 1,224$ . That means that further considering the influence line parameter  $\lambda_1$ , leads total  $\lambda$  factor above  $\lambda_{max}$  for the entire range of span length, figure 4.11, Further influence of multi-lane behaviour on  $\lambda_4$  will also not have any effect on the design because  $\lambda_{max}$  is governing.

## 4.2. Comparison between FLM3, FLM4 and FLMG

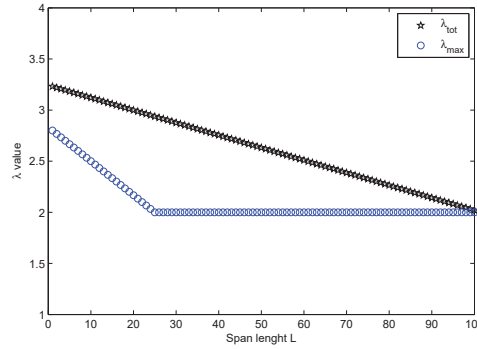


Figure 4.11 –  $\lambda_{max}$  and  $\lambda_{tot}$  for the entire span range

It is further noted that  $\lambda_{max}$  was defined based on simulations with the CAFL at  $5 \cdot 10^6$  (Sedlacek et al., 2000). A rough estimate is  $\lambda_{max} = \sqrt[3]{\frac{\Delta\sigma_c}{\Delta\sigma_D}} = \sqrt[3]{\frac{5}{2}} \approx 1,4$  and the sensitivity to the CAFL shifts from 5 to  $10 \cdot 10^6$  cycles,  $\lambda_{max} = \sqrt[3]{\frac{10}{2}} \approx 1,7$  i.e. 20%.

Similar simulations, without limiting the equivalent damage factor to  $\lambda_{max}$ , i.e. using the line  $\lambda_{tot}$  from figure 4.11 showed that the decrease of  $\lambda_1$  with the span length is not consistent. The same conclusion was drawn by (Maddah, 2013) that obtained  $\lambda$  factors practically constant for critical length up to 100m. Further comparison or calibration of  $\lambda_i$  factors is out of the scope of this thesis, but a final example for the case of stud connectors under shear on a simply supported influence line shows that using constant  $\lambda_1$ , as defined for shear studs, see table 4.11, leads to equivalent stress that are constant with the influence line length, which shows good agreement with the simulation results, table 4.12.

$\lambda_i$	Parameter	Expression	Observations
$\lambda_{v,1}$	Parameter for influence line	$\lambda_{v,1} = 1,55$	
$\lambda_{v,2}$	Traffic volume parameter	$\lambda_{v,2} = 1,224$	$N_{obs} = 2 \cdot 10^6, Q_{m1} = 445kN$ (FLM4)
$\lambda_{v,3}$	Design life of 100years	$\lambda_{v,3} = 1$	
$\lambda_{v,4}$	1 Lane traffic	$\lambda_{v,4} = 1$	

Table 4.11 – Equivalent damage factors,  $\lambda_{v,i}$  for shear connectors

L	FLM3	FLMG	FLMG/FLM3
10	90	75,6	0,84
50	90	75,9	0,84
80	90	87,9	0,98

Table 4.12 – Equivalent stress for FAT90 in shear connectors

### 4.3 Results from traffic simulations

The reliability of the fatigue limit state under the condition  $\Delta\sigma_{S,k,eq}\gamma_S = \frac{\Delta\sigma_{R,k}}{\gamma_R}$ , treats the load effects as an equivalent damage stress range at  $N_{eq} = 2 \cdot 10^6$ . The partial safety factors  $\gamma_S$  and  $\gamma_R$  are defined in Section 5 based on a First Order Reliability Method (FORM), where the statistical distribution of  $\Delta\sigma_{S,k,eq}$  is required to define the tail behaviour above the characteristic value. The probabilistic traffic generation model is used here to characterise the statistics of the equivalent damage stress range  $\Delta\sigma_{S,k,eq,2 \cdot 10^6}$ . On the other hand it was seen in Section 2.6 that the 2<sup>nd</sup> slope of the S-N curves was dependent on the aggressiveness of the loads, characterised by the load spectra shape. It is thus of special interest to identify the type of spectra shape that may be expected in typical cases of highway bridges. The traffic simulations are used here for that purpose, characterising the load spectra by the Weibull shape parameter  $\nu$ .

The traffic model parameters presented in the previous section were defined on a daily basis, so it is logical to define the traffic model variability also on that base. A typical daily output of the traffic generation model is shown in figure 4.12. The model produces an array with the lorry weight (in ordinates) and the accumulated inter-lorry distance (abscissa) for 24hours of traffic random generation. Small zooms on the free-flowing and congested periods are also shown where the difference in inter-lorry distance is clear.

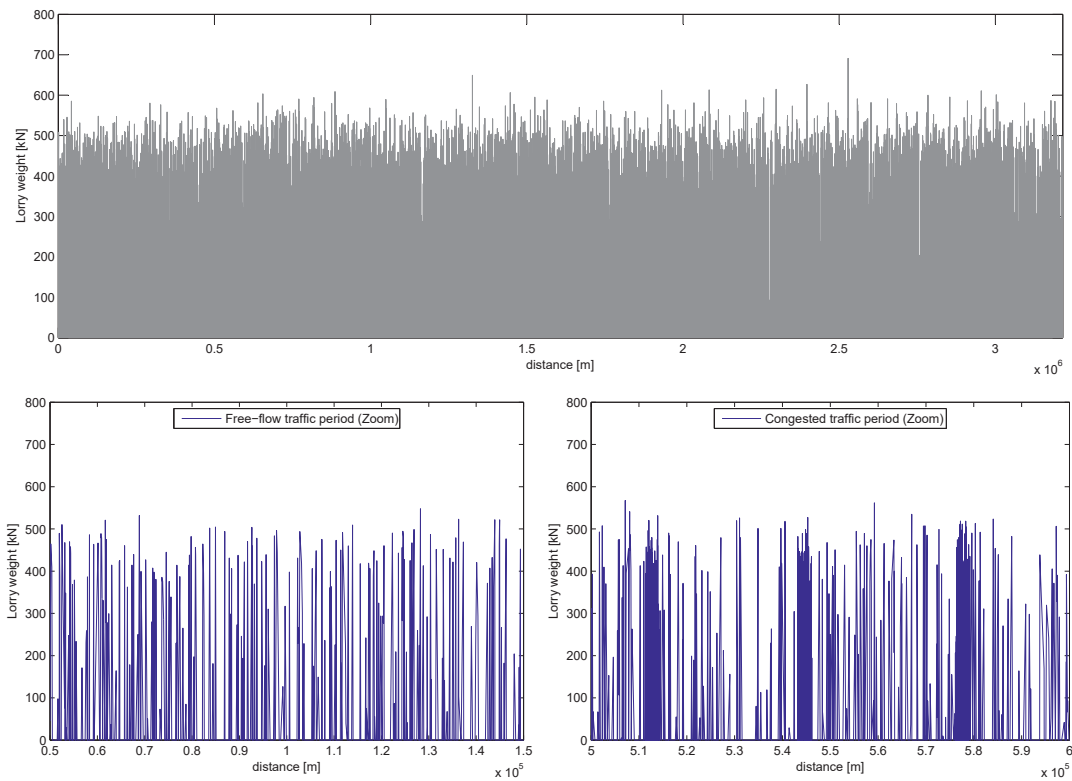


Figure 4.12 – Typical output of the traffic generation model for 24hours

A total of 36 design cases are investigated with the combination of 3 longitudinal influence lines, 3 transversal lane arrangements and 4 discrete cases of span length. For transversal load distributions, a box-girder with 3 possible traffic lane arrangements is used in simulations, figure 4.13, this cross section being chosen because multilane influence is higher with torsional stiffer cross sections. The longitudinal influence lines are considered representative of the vast majority of practical problems.

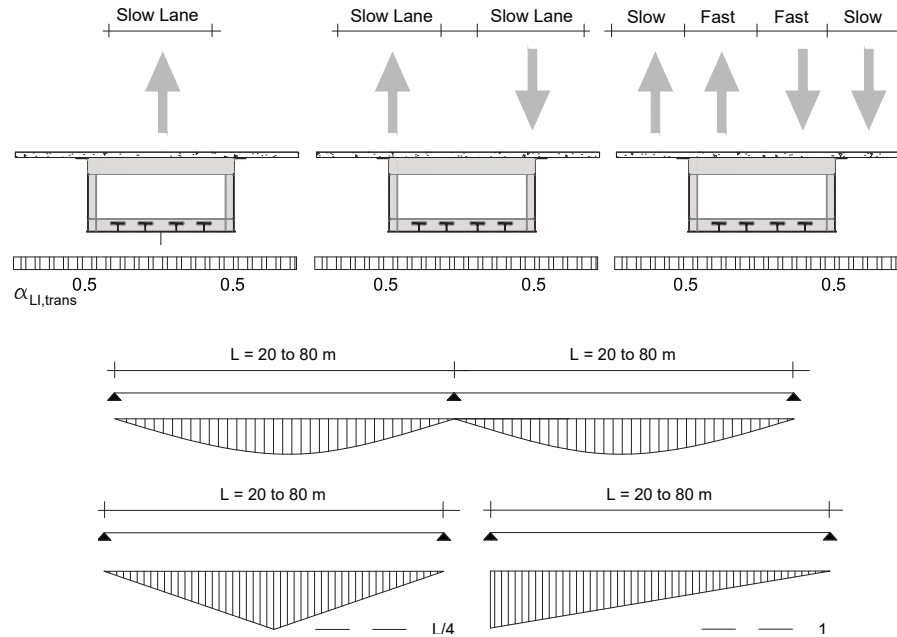


Figure 4.13 – Transversal traffic arrangement and longitudinal structural systems

These structural systems with due account for the transversal load distributions and longitudinal influence lines are implemented in the probabilistic traffic generation model, with the resulting internal load effects being obtained. The artificial traffic arrays generated for each case of transversal lane distribution, are computed over each longitudinal influence line, on a step by step procedure.

### 4.3.1 Load-effects spectra shape

The output of the traffic simulations on the structural systems from figure 4.13, is the resulting internal load effects during 1 day of traffic. A rainflow counting procedure is implemented in the model giving an histogram of load-effects and corresponding number of cycles (Brozzetti and Chabrolin, 1986). A typical rainflow histogram is shown in figure 4.14 for the 20 meter simply supported beam under bending. As vehicle weights were characterised by gaussian distributions, the weighted sum of the vehicle weight mean is  $\mu_G = \sum_1^8 r_i \cdot \mu_{G,i}$  where  $r_i$  is the relative frequency of each of the 8 weight distributions with mean  $\mu_{G,i}$ . Taking these values from table 4.7 for Lane 1 one gets  $\mu_{average} = 327$ . For these values, the load effect M is  $M_{\mu_G} = \alpha_{LI,trans} \frac{L \cdot \mu_G}{4} = 818$  and the

most likely value  $M_{type3,G_1} = \alpha_{LI,trans} \frac{L \cdot \mu_{G_{type3,1}}}{4} = 1100$  given by the loaded lorry type 3 with  $r_{type3,G_1} = 48,1\%$ . Both these rough estimates agree well with the simulations output in figure 4.14.

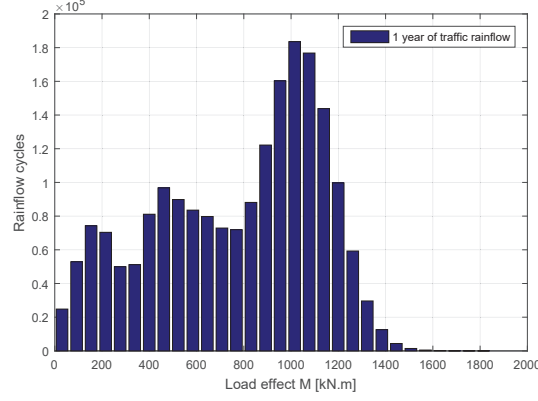


Figure 4.14 – Rainflow for load-effects: 1-year traffic simulations

The histograms of 1 year of load-effects as figure 4.14, are fitted with a Weibull probability distribution function. The cumulative  $P(X \leq x)$  is defined by:

$$F(x)_{cdf} = 1 - e^{-\left(\frac{x}{\lambda}\right)^\nu} \quad \text{where } \lambda > 0 \text{ is the scale parameter} \quad (4.1)$$

Defining  $\lambda = \frac{\Delta\sigma_{max}}{\nu \sqrt{Ln(N_{tot})}}$ , the cumulative function  $F(x)$  re-writes:

$$F_{cdf}\left(\frac{\Delta\sigma_i}{\Delta\sigma_{max}}\right) = 1 - e\left[-\left(\frac{\Delta\sigma_i}{\Delta\sigma_{max}}\right)^\nu Ln(N_{tot})\right] \quad (4.2)$$

The Exceedance function given by the complementary cumulative,  $F(x)_E = 1 - F(x)_{cdf}$ :

$$F_E\left(\frac{\Delta\sigma}{\Delta\sigma_{max}} \geq \frac{\Delta\sigma_i}{\Delta\sigma_{max}}\right) = e\left[-\left(\frac{\Delta\sigma_i}{\Delta\sigma_{max}}\right)^\nu Ln(N_{tot})\right] \quad (4.3)$$

The exceedance cycles at each level are  $N_{tot} \cdot F\left(\frac{\Delta\sigma_i}{\Delta\sigma_{max}}\right)_E$  and the exceedance function in cycles is:

$$N_i = Ln(N_{tot}) \cdot e\left[-\left(\frac{\Delta\sigma_i}{\Delta\sigma_{max}}\right)^\nu Ln(N_{tot})\right] \Rightarrow Ln(N_i) = Ln(N_{tot}) \cdot \left[1 - \left(\frac{\Delta\sigma_i}{\Delta\sigma_{max}}\right)^\nu\right] \quad (4.4)$$

The output in terms of spectra shape parameter for 250 days of traffic simulations for each of the 36 design cases are summarised in table 4.13. All the load histogram were fitted by a Weibull exceedance function with shape parameter between  $1 \leq \nu \leq 4$ . In general either Rayleigh or Gauss distributions may be used to characterise highway traffic, that is found mainly as convex type spectra. The results were grouped according to  $\nu$  and it is seen that the load spectra shape depends on the global structural system,



### 4.3. Results from traffic simulations

namely span length and traffic lane arrangement. For influence lines in the range of the vehicle length with single lane cross sections, spectra shape are remarkably convex, typically gaussian ( $\nu \approx 4$ ). They tend to smoothen with the span length and multiple lane arrangements, generally being of a Rayleigh convex type, with Weibull shape  $\nu \approx 2$ . Longer span lengths and the presence of multiple lane tends to give linear shape spectra with Weibull shape  $\nu \approx 1$ . The resulting exceedance plots are shown in figure 4.15 grouped as indicated in table 4.13 and normalised to  $N_{tot} = 1.10^6$ .

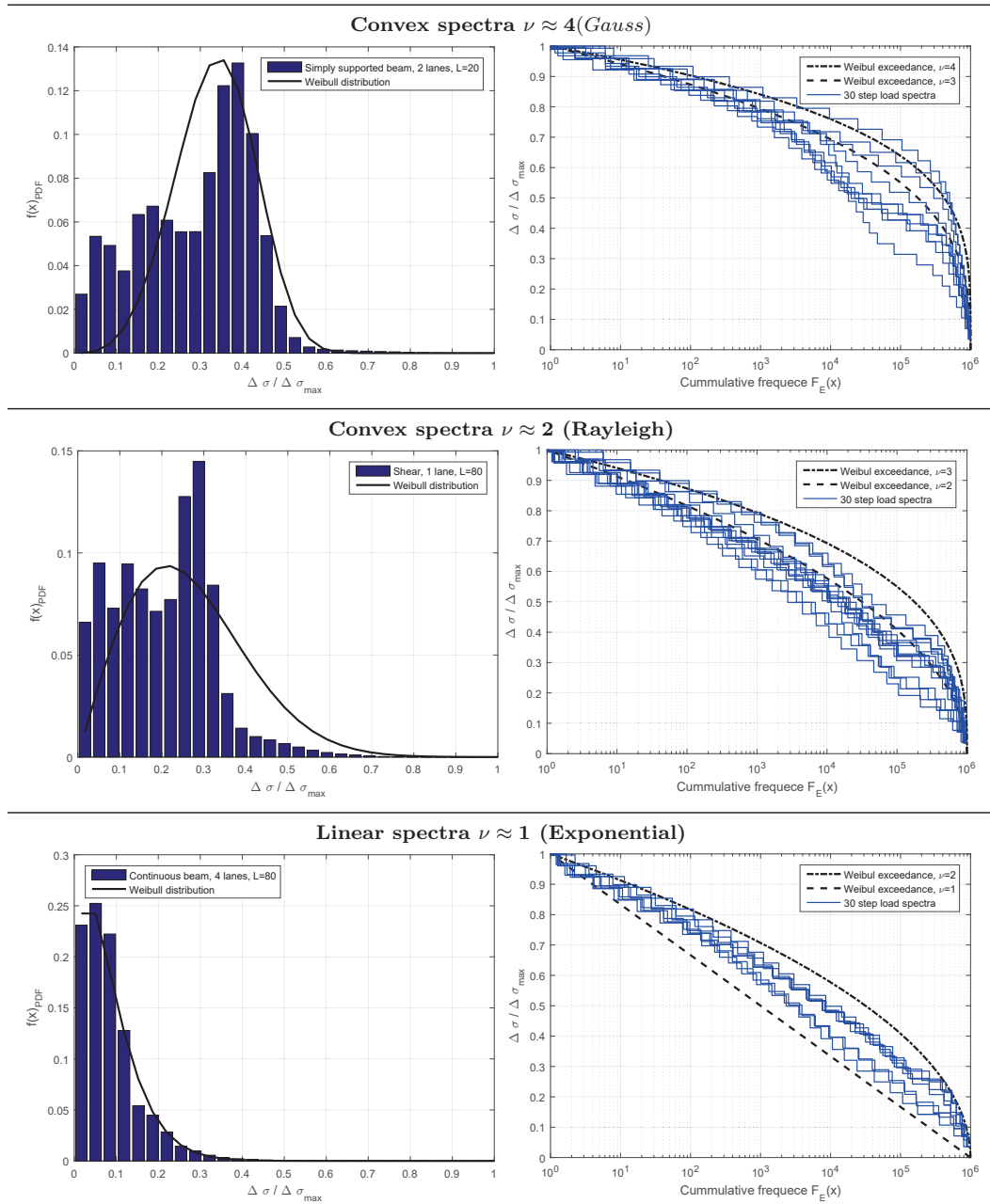
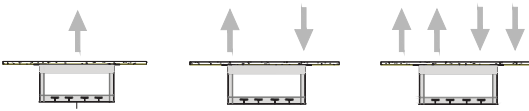


Figure 4.15 – Exceedance plots for highway traffic simulations



L=20	simple beam continuous beam shear	$4 \geq \nu \geq 3$	
L=40	simple beam continuous beam shear		
L=60	simple beam continuous beam shear	$3 \geq \nu \geq 2$	
L=80	simple beam continuous beam shear		
			$2 \geq \nu \geq 1$

Table 4.13 – Weibull shape parameter for simulations on 36 design cases

The typified load spectra types for highway bridges spectra found with our simulation model agree with others in literature. It is a common assumption to use the Rayleigh distribution for the stress effects from highway traffic (Tilly and Nunn, 1980), essentially due to the work reported by Schilling and Klippstein (1978) who characterised different Rayleigh distribution types based on extensive field data in the USA. Also for European traffic, measurements have been seen to follow Rayleigh type distributions (Vrouwenvelder and Waarts, 1993). On the other hand, Gurney (2006) reported data from measurements in U.K and Holland, finding concave and linear spectra, or slightly convex. More recently, Maljaars and Steenbergen (2012) reported 3-week measurements on a stay-cable highway bridge with 6 traffic lanes 320m long. The relevant influence lines had approximately 150 meters with influence of 4 lanes, and both measured and simulated spectra where linear.

Exceptions are probably to be expected for short influence lines (5 to 10m) on orthotropic decks, per example, where the allowable axle load frequency is more important than the global vehicle weight. As an example, the exceedance frequency for the FLM4 axle loads is shown in figure 4.16 and the same holds for railway axle loads.

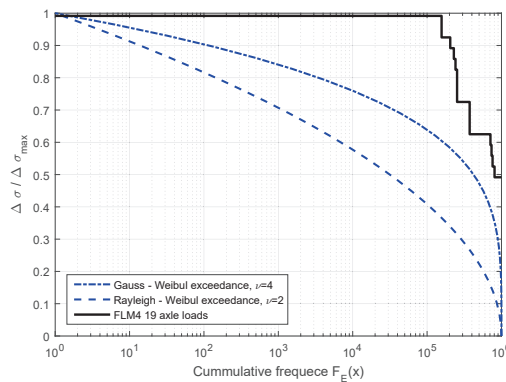


Figure 4.16 – Exceedance plot for FLM axle loads

### 4.3. Results from traffic simulations

Also for railway loads, as the influence line length increases, spectra become more smooth, as reported for example (UIC, 1979) or (Kuehn and Lukić, 2008), where these have been characterised mainly concave or linear. Figure 4.17 shows the exceedance plot for both European traffic mix 1 and 2 (EN 1991-2, 2003).

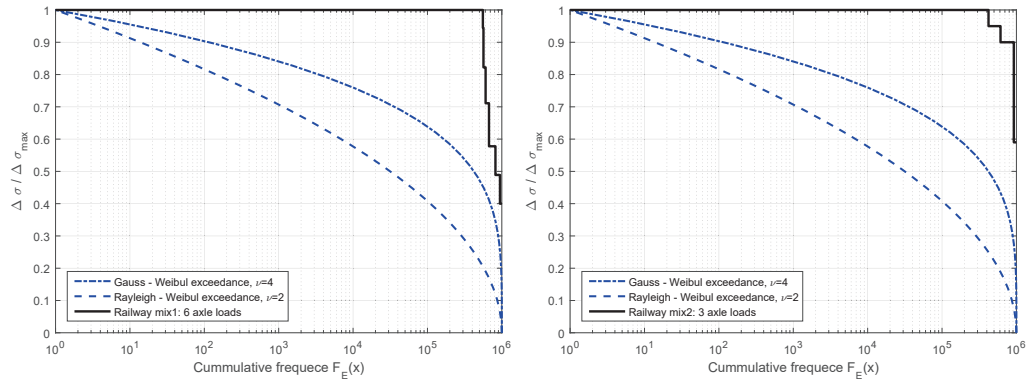


Figure 4.17 – Exceedance plot for Eurocode railway mix axle loads

An interesting example is the case of an interaction between 8 highway lanes and 2 railway tracks on the same bridge, figure 4.18. The bridge is 2164m long, hybrid suspended/stay-cable bridge, with a main span of 1408m.

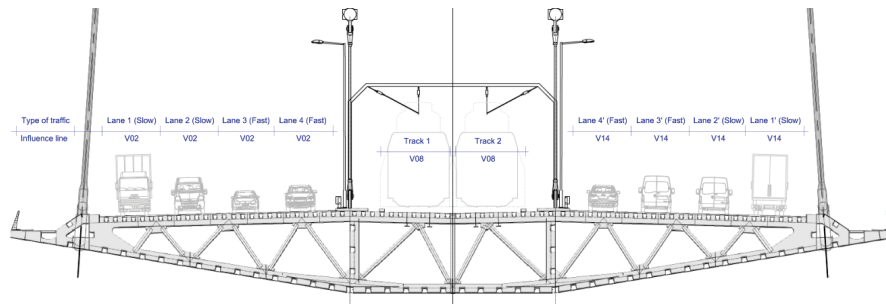


Figure 4.18 – Cross section of the 3<sup>rd</sup> Bosphoro bridge (Baptista and Nussbaumer, 2015)

The railway traffic generation model was based on the European traffic mixes: Traffic mix 1 for standard traffic mix with maximum axle loads of 22,5 tons and Traffic mix 2 for Heavy traffic mix with maximum axle loads of 25 tons. Both traffic mixes correspond to a traffic volume of  $\approx 25 \cdot 10^6$  tons/year since railway damage has been shown to be controllable by the traffic volume (Nussbaumer, A; Borges, L; Davaine, 2011), (Fryba, 1996). The total weight of each train type  $Q$  [kN] and the linear weight  $q$  [kN/m] are given in table 4.14.

To combine the railway traffic in our highway generation model, the number of trains per year for each rail mix reported to 365 days per year, was converted to 250 days per year, keeping the traffic volume constant. Traffic densities for both mixes and scenarios are defined in table 4.14. This assures that railway and highway traffic are modeled each

## Chapter 4. Highway traffic

day simultaneously, i.e. all weekend traffic is reported to daily work days. The railway traffic was distributed uniformly along the daily highway traffic generation. The highway traffic is generated at a constant flow of 1800 vehicles/hour, so the generation of 32000 vehicles takes around 18 hours per day. The length of the generated traffic depends on the random inter-lorry distance, and corresponds to about 3200 km of generated traffic per day. For each highway simulation, the length of the total generated highway traffic is taken, and the railway traffic is uniformly distributed along this length, defining the distance between trains. This ensures that for each track, there is only 1 train at the time in the track

Train type definition and characteristics					Traffic mix definitions [Trains/day]			
Train type	Q [kN]	v [km/h]	L [m]	q [kN/m]	Mix 1		Mix 2	
					365 days/year	250 days/year	365 days/year	250 days/year
1	6630	200	262,1	25,3	12	17		
2	5300	160	281,1	18,9	12	17		
3	9400	250	385,52	24,4	5	7		
4	5100	250	237,6	21,5	5	7		
5	21600	80	270,3	80	7	11	6	9
6	14310	100	333,1	43	12	17	13	19
7	10350	120	196,5	52,7	8	12		
8	10350	100	212,5	48,7	6	9		
9	2960	120	134,8	22				
10	3600	120	129,6	27,8				
11	11350	120	198,5	57,2			16	24
12	11350	100	212,5	53,4			16	23
<b>Total</b>					<b>67</b>	<b>97</b>	<b>51</b>	<b>75</b>

Table 4.14 – Train types and traffic mixes for railway traffic

For the simultaneity of railway traffic in both tracks, a percentage of 12% for crossings is considered. The train types are generated so that in 12% of the train crossings in track 1, there is a train in track 2, but the train types generated are completely random. The percentage of each train type in the traffic composition depends on the traffic mix and is shown in table 4.14. The distribution of the train type along the daily generated traffic is random. Several long influence lines were tested. Figure 4.19 shows an example of an hanger, with an influence line roughly 1200m long. The spectra obtained were all either of a concave or linear type. An example for the rail mix 2 is shown in figure 4.19.

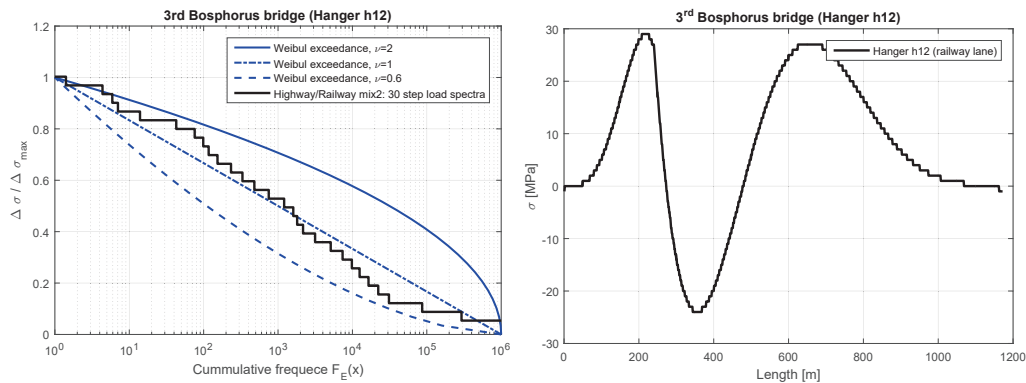


Figure 4.19 – Exceedance plot for highway/railway mix on hanger12

### 4.3.2 Equivalent stress range for fatigue reliability

To transform the highway rainflow histograms of load effects into an equivalent stress range, a damage sum hypothesis is required. The histograms as shown in figure 4.14 represent internal load effects, bending moments  $M$  and shear  $V$ . To obtain stress ranges, specific information such as section modulus and cross section areas would be required. To solve this matter around, and for the specific aim of characterising equivalent stress range variability, load effects are transformed in stress ranges by assuming that the 95% load-effect percentile from the spectra, is equivalent to a stress range at  $2.10^6$  cycles (which is the resistance 5% percentile), i.e.  $\alpha.M_{95\%} = \Delta\sigma_{M_{95\%}} = FAT$  where  $\alpha$  may be seen as a simple linear coefficient between load and stress, an equivalent section modulus or cross section area. To estimate the upper 0,95 load fractile, an Extreme value distribution is fitted to the rainflow histogram so that  $M_{95\%} = F_{cdf}^{-1}(0, 95)$ . An example is shown on figure 4.20 with the histogram of the simply supported (20m, 1Lane) and the continuous beam under bending (80m, 4Lanes).

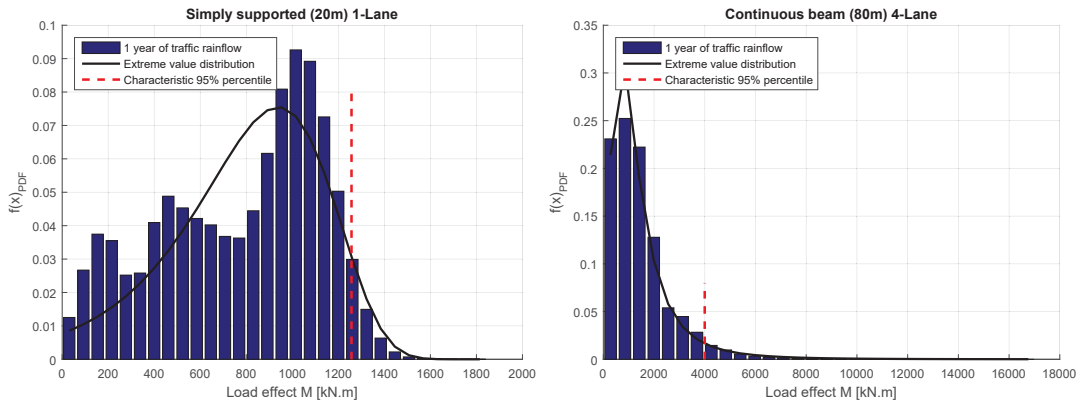


Figure 4.20 – Characteristic load-effect on rainflow histogram

By further scaling the S-N curve to a standardised S-N curve where  $FAT=1$ , the damage sum procedure gets greatly simplified by the use of a single S-N curve, see figure 4.21. By fixing the 95% load effect at  $FAT$ , the load spectra is “forced” on both S-N curve branches. This ensures that the effect of the damage accumulation on a double slope curve, is included in the variability of  $\Delta\sigma_{eq}$ . It should be noted however that traffic spectra with these amount of cycles, roughly  $200 \cdot 10^6$ , are necessarily placed entirely on the  $2^{nd}$  slope branch of the S-N curve, which is confirmed here by obtaining  $\Delta\sigma_{eq} \leq \sqrt[3]{\frac{2}{5}} = 0,74$ . Using this procedure, the load histogram on figure 4.14 is transformed into a normalised stress-cycle histogram, figure 4.21.

The equivalent stress range is computed using Miner’s rule  $D = \sum \frac{n_{S,i}}{N_{R,i}} = D_{max}$  with  $D_{max}$  set to 1. For normal stress ranges the standardised  $FAT$  is defined in a double slope S-N curve with  $m = 3$  and  $k = 5$  with the “knee-point” for  $\Delta\sigma_D$  at  $N_D = 5 \cdot 10^6$ , without cut-off. For shear stress a single slope  $m=5$  curve is used.

The equivalent stress range at  $2.10^6$  cycles is then computed by:

$$\Delta\sigma_{eq} = \sqrt[m]{\frac{\Delta\sigma_D^{m-k} \sum_0^{\Delta\sigma_D} n_j \Delta\sigma_j^k + \sum_{\Delta\sigma_D}^{\Delta\sigma_{max}} n_i \Delta\sigma_i^m}{N_{eq}}}; \quad \Delta\sigma_2 = \sqrt[m]{\frac{N_{eq}}{2.10^6}} \Delta\sigma_{eq} \geq \Delta\sigma_D$$

$$\Delta\sigma_{eq} = \sqrt[k]{\frac{\sum_0^{\Delta\sigma_D} n_j \Delta\sigma_j^k + \Delta\sigma_D^{k-m} \sum_{\Delta\sigma_D}^{\Delta\sigma_{max}} n_i \Delta\sigma_i^m}{N_{eq}}}; \quad \Delta\sigma_2 = \sqrt[m]{\frac{N_D}{2.10^6}} \sqrt[k]{\frac{N_{eq}}{N_D}} \Delta\sigma_{eq} < \Delta\sigma_D$$

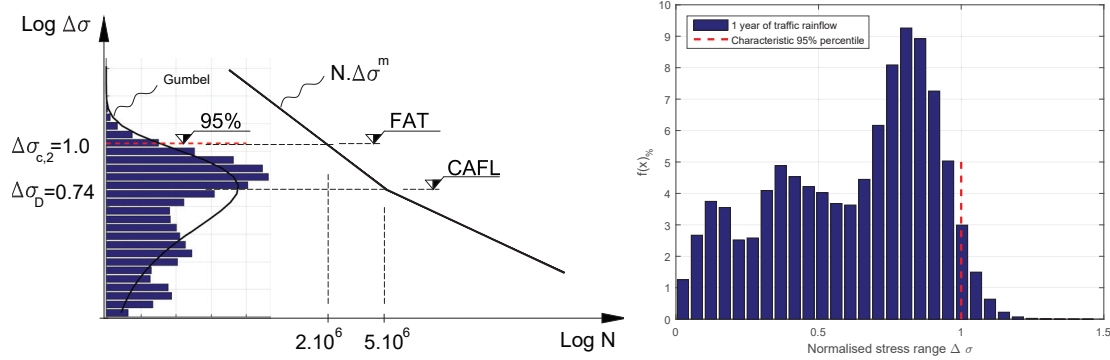


Figure 4.21 – Calibration of the 0,95 load fractile with the 0.05 resistance fractile

The equivalent stress  $\Delta\sigma_{eq}$  is sampled out of the Monte Carlo model, with the number of samples sufficient to give a difference of less than 10% between the estimated parameter and the 95%  $(1-\alpha)$  confidence bounds of each parameter. The confidence interval for the mean is given by a t-student  $\mu \pm t_{\alpha/2} \frac{\sigma}{\sqrt{n}}$  and by a  $\chi^2$  for the standard deviation  $\sqrt{\frac{n-1}{\chi_{n-1}^2(\alpha/2)}} \cdot \sigma$ ;  $\sqrt{\frac{n-1}{\chi_{n-1}^2(1-\alpha/2)}} \cdot \sigma$  where n is the number of days traffic simulation. This is achieved with 250 samples, which corresponds to 1 year of traffic simulation, figure 4.22.

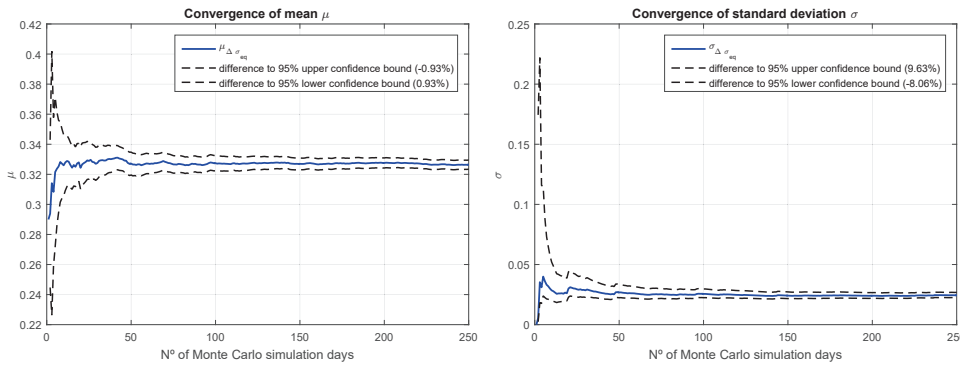


Figure 4.22 – Example of convergence of both  $\mu_{\Delta\sigma_{eq}}$  and  $\sigma_{\Delta\sigma_{eq}}$  for 250 days of traffic

Based on conclusions from Section 2.6, the  $2^{nd}$  slope k value for the S-N curve could be related to the spectra Weibull shape parameter  $\nu$  by  $k=m+2/\nu$  meaning that resistance model, ultimately depends on the main structural system. In view of these findings,

### 4.3. Results from traffic simulations

different slope values could be adopted based on the load spectra shape. Considering different  $2^{nd}$  slope values has little impact on the variability on the load side  $\Delta\sigma_{eq,2}$ , rather changing the design point  $S_k = R_k$ . The statistical characteristics are thus derived assuming  $k=5$  (i.e  $\nu \approx 1$ ) without loss of representativeness for the reliability computation.

Two examples of the final distribution of equivalent stress range at  $2 \cdot 10^6$  cycles  $\Delta\sigma_{eq,2}$  are shown in figure 4.23 for the simply supported (20m, 1Lane) and the continuous beam under bending (80m, 4Lanes). The histograms are skewed and the log-normal distribution (log base 10) are used to fit the histograms of 250  $\Delta\sigma_{eq,2}$  simulations. The numerical values for the  $\text{Log}_{10}$  normal distributions are summarised in table 4.15, and are used in Section 5 to compute the partial safety factors.

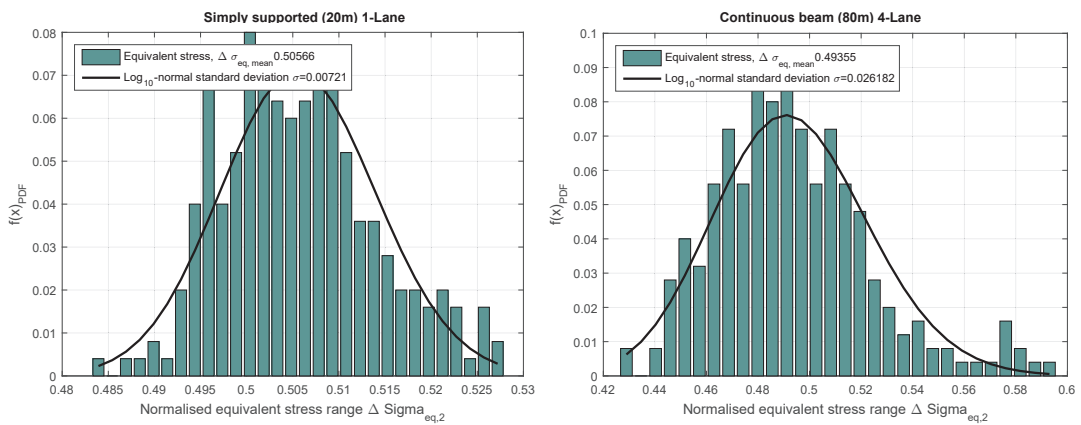


Figure 4.23 –  $\text{Log}_{10}$ -normal distribution for 2 design cases

		$\mu$	$\sigma$	$\mu$	$\sigma$	$\mu$	$\sigma$
<b>L=20</b>	simple beam	-0,2962	0,0072	-0,2518	0,0159	-0,2181	0,015
	continuous beam	-0,2943	0,0184	-0,2231	0,0183	-0,1977	0,0194
	shear	-0,2141	0,006	-0,1856	0,0135	-0,1704	0,0158
<b>L=40</b>	simple beam	-0,315	0,0079	-0,2803	0,0146	-0,2501	0,0162
	continuous beam	-0,338	0,0208	-0,2718	0,0238	-0,2393	0,0215
	shear	-0,2426	0,0111	-0,1919	0,0128	-0,1727	0,0144
<b>L=60</b>	simple beam	-0,359	0,0137	-0,3016	0,0168	-0,2866	0,0185
	continuous beam	-0,383	0,0232	-0,3266	0,0256	-0,2836	0,0276
	shear	-0,2551	0,0158	-0,2025	0,0159	-0,181	0,0199
<b>L=80</b>	simple beam	-0,3949	0,0149	-0,3299	0,0178	-0,3098	0,0204
	continuous beam	-0,4298	0,0291	-0,3663	0,031	-0,3075	0,0262
	shear	-0,269	0,0157	-0,2061	0,0169	-0,1915	0,0196

Table 4.15 –  $\text{Log}_{10}$ -normal distribution parameters for  $\Delta\sigma_{eq,2}$  on the 36 design cases

For the reliability analysis, the combination of all design cases, is considered as a population of possible outcomes of the limit state function. That means combining the statistics of each individual outcome, to define the entire design points population.



Combining the standard deviation  $\sigma_{\Delta\sigma_{eq,2}}$  for the population of (d) design cases is a typical problem of Analysis of Variance. The common standard deviation for the entire set of design points is a mean square estimation, which is the variance of a set of random observation from the same population. Knowing the variance  $V_i = \sigma_i^2$  of each design case, where  $\sigma_i$  values are summarised in table 4.15, the error sum of squares is given by  $SSE = \sum_1^d V_i \cdot (n_i - 1)$  where  $n_i$  is the size of each design cases sample,  $n=250$  for our annual traffic simulations, and  $d=36$  the total number of design cases. To correct for the deviations between the individual mean  $\mu_{\Delta\sigma_{eq,i}}$  and the total mean  $\Delta\sigma_{eq} = \frac{\sum_1^d \mu_i}{d}$  we use the sum of squares of the differences from the mean:

$$SSM = \sum_1^d [(\mu_{\Delta\sigma_{eq,i}} - \mu_{\Delta\sigma_{eq}})^2 \cdot n_i]$$

The total sum of squares (mean and error) is  $SS = SSE + SSM$  and the variance is given by  $V = \frac{SS}{N-1}$ , where  $N$  is the total number of simulation,  $N = n \cdot d$ . The standard deviation for the entire set of design cases is  $\sigma_{\Delta\sigma_{eq}} = \sqrt{V}$ . For the 36 design cases analysed with the traffic simulation model, the computation with the values from table 4.15 results in  $\sigma_{\Delta\sigma_{eq,2}} = 0,0695 \approx 0,07$ . This corresponds to a Coefficient of Variation of 16%. It is however arguable to correct for the individual mean deviations between from the overall mean, because each simulated structure corresponds to a design point for reliability. Thus the standard deviation may be estimated simply by the sum of squares of the error SSE and thus  $V = \frac{SS}{N-1}$  and  $\sigma_{\Delta\sigma_{eq,2}} = 0,0187$ . For reliability computation we will consider the maximum standard deviation from the simulations  $\sigma_{\Delta\sigma_{eq,2}} = 0,031$  (continuous beam) which in this case corresponds to a Coefficient of Variation of 7,15%.

## 4.4 Summary of conclusions

- The load effects near the fatigue limit are traduced in damage, given by the sum of a large number of cycles of several individual stress ranges. None of these stress ranges has a dominant trend above all others, and as a result, the variability of the total load effect expressed by  $\Delta\sigma_{eq}$  is greatly reduced, because this value represents a weighted average. This is not the case if traffic growth scenarios are adopted. However, many unknown parameters, influence the possible future trends of traffic. It is expected that the impact of future traffic weight growth is considerable for designs based on the CAFL, while it should impact, to a lesser extend, the current procedure with damage sum.
- The results of the traffic simulations allowed to characterise the expected stress range spectra for fatigue analysis. The spectra shapes varied from remarkably convex for small influence lines and single lane traffic, to almost linear under multilane traffic and long influence lines. This indicates that for short influence lines, where axle loads are important, an S-N curve with  $2^{nd}$  slope  $k=5$  would be unsafe and on the contrary, the increase of span length to a range where global vehicle weight and multilane effects prevail, tend to produce smoother spectra profile, where  $k=5$  was shown to be suitable.



# FATIGUE RELIABILITY **Part III**



## 5 Uniaxial fatigue reliability

The input parameters of the limit state function for fatigue design are characterised by both variability and uncertainty. This chapter re-analyses the fatigue limit state partial safety factors  $\gamma_R$  and  $\gamma_S$  for the reliability levels defined in Eurocode 0, based on a statistical treatment of load (S) and resistance (R). The analysis is done for the nominal stress approach based on a representative group of FAT details, whose results, presented in this thesis or taken from literature, were statistically re-analysed to define characteristic strength. Fatigue strength based on characteristic 5% percentile values includes the effect of misalignments, welding residual stresses, mean stress, weld geometry, weld process and imperfections, metallurgical defects, crack shapes and others. Although the influence of some of these parameters is important, their implicit inclusion on resistance scatter greatly simplifies fatigue safety check.

On the load side, the main sources of uncertainty are the traffic loads and flow conditions, while the number of cycles is set to a representative (characteristic) value defining a service level. For the fatigue limit state of welded connections, the traffic loads on the structure are translated to stress ranges with a cycle counting technique and damage accumulation on a pre-defined S-N curve shape. Hence, the partial safety factor on the load side includes traffic variability but also, inherent model uncertainties due to conversion from load to stress, stress-cycle counting and damage summation. Stress calculation finite element models may have considerable differences to measured values as seen in Section 2.3, where still a 7% difference was achieved with the best calibration for the measured and calculated hot-spot stress. Many authors have reported on the other hand, measured stress lower than predicted by the model. This is usually attributed to the participation of other structural elements such as bracings, cross girders, ballast or rails.

### 5.1 The reliability model

The basic reliability problem involving two statistical variables, resistance R and S, is generically described by a limit state function  $G(z_i)$ , where  $z_i$  are the relevant variables (Melchers, 1999). Considering the structural safety condition  $S \leq R$ , the probability of failure is  $P_f = P(R - S < 0)$ . Defining the variable  $Z=R-S$ , the limit state function represents failure for  $G(Z(R, S)) < 0$  and the probability of failure  $p_f = P(G(z_i) < 0) = P(R - S < 0)$  the area under the PDF of  $G(z_i)$ , for which  $G(z_i) < 0$ , figure 5.1. If both R and S are independent and defined by probability density functions  $f_R$  and  $f_S$ , the probability of failure  $p_f$  is expressed as:

$$p_f = P(R - S \leq 0) = \int_{-\text{inf}}^{\text{inf}} \int_{-\text{inf}}^{s \geq r} f_R(r) \cdot f_S(s) dr ds \tag{5.1}$$

Using the cumulative distribution of R,  $F_R(r) = \int_{-\text{inf}}^r f_R(x) dx$  the probability of failure may be given by a single integral:

$$p_f = P(R - S < 0) = \int_{-\text{inf}}^{\text{inf}} F_R(x) \cdot f_S(x) dx = P(G(z_i)) < 0 = \int_{G(z_i) < 0} f(z_i) dz \tag{5.2}$$

The integral in equation 5.2 is designated as the convolution integral and its direct integration is of limited scope while most usually it is solved numerically with Monte Carlo methods (MC) or analytical methods such as the first order second moment method (FOSM) using only the first two moment  $\mu$  and  $\sigma^2$  from the probability distributions.

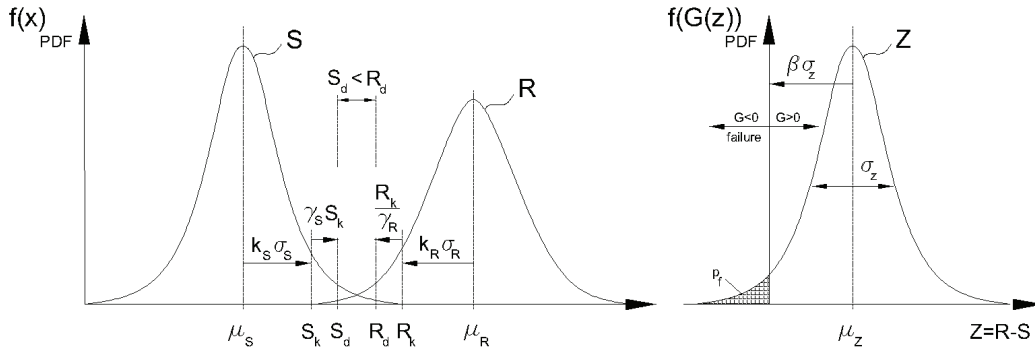


Figure 5.1 – Reliability problem with 2 variables, adapted from (Melchers, 1999)

If both S and R are represented by normal Gaussian distributions as shown in figure 5.1, the convolution integral 5.2 may be solved directly and the probability of failure,  $p_f$ , expressed analytically:

$$p_f = \Phi \left( \frac{-(\mu_R - \mu_S)}{\sqrt{\sigma_R^2 + \sigma_S^2}} \right) = \Phi(-\beta) = 1 - \Phi(\beta) \tag{5.3}$$

where  $\mu$  is the mean,  $\sigma$  the standard deviation and  $\Phi$  the standard normal distribution

CDF. The reliability index is expressed by  $\beta = -\Phi^{-1}(p_f)$  which can be interpreted as the distance between the mean of  $G(Z)$  distribution and the origin, in standard deviation units. The random normal variable  $Z$  is shown in figure 5.1 where the failure region corresponds to  $Z \leq 0$ :

$$\beta = \frac{\mu_G}{\sigma_G} = \frac{\mu_R - \mu_S}{\sqrt{\sigma_R^2 + \sigma_S^2}} \quad (5.4)$$

Figure 5.2 represents the linear limit state function in the space of the basic variables  $S$  and  $R$  defined by their moments  $\mu$  and  $\sigma$ .

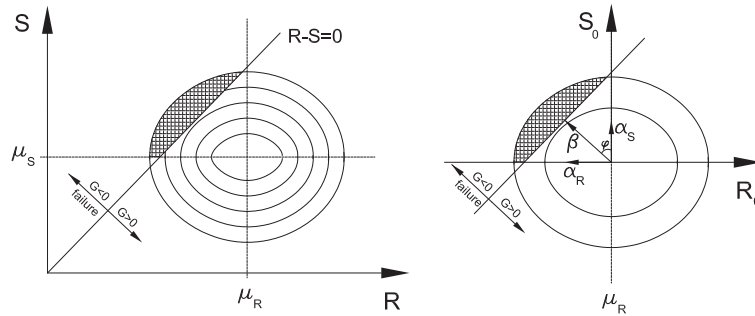


Figure 5.2 – Limit state function in the basic variables and normalised space, adapted from (Melchers, 1999)

By transforming the normal variables  $S$  and  $R$  to a standard normal form by  $S_0 = \frac{S - \mu_S}{\sigma_S}$  and  $R_0 = \frac{R - \mu_R}{\sigma_R}$  where  $S_0; R_0 \rightarrow Normal(\mu = 0; \sigma = 1)$ , their distance to the limit state function in the normalised space  $S_0; R_0$ , becomes measured in units of  $\sigma_{S_0} = \sigma_{R_0} = 1$ , figure 5.2. The joint probability function  $f_{G_z}$  becomes the bivariate normal distribution  $\Phi_2(Y)$  which is symmetrical about the origin in the  $S_0; R_0$  space. The initial limit state function is also transformed to the normalised space:

$$g(S_0, R_0) = \mu_R - \mu_S + R_0\sigma_R - S_0\sigma_S \quad (5.5)$$

The limit state function  $g(S_0, R_0) = 0$  defines a failure line given by  $S_0 = \frac{\sigma_R}{\sigma_S} R_0 + \frac{\mu_R - \mu_S}{\sigma_S}$  and the shortest distance between the limit state function and the origin defines the reliability index  $\beta$ . The design point is defined with coordinates:

$$S_0^* = \frac{\mu_R - \mu_S}{\sigma_R^2 + \sigma_S^2} \sigma_S \quad ; \quad R_0^* = -\frac{\mu_R - \mu_S}{\sigma_R^2 + \sigma_S^2} \sigma_R \quad (5.6)$$

The coordinates of the design point may be re-written using trigonometric relations, see figure 5.2 leading to the direction cosines (sensitivity factors), defined as:

$$\alpha_S = \frac{-\sigma_S}{\sqrt{\sigma_R^2 + \sigma_S^2}} \quad ; \quad \alpha_R = \frac{\sigma_R}{\sqrt{\sigma_R^2 + \sigma_S^2}} \quad (5.7)$$

## Chapter 5. Uniaxial fatigue reliability

---

The coordinates of the design point may be defined by replacing  $\beta$  in equation 5.6 and using the sensitivity factors to get  $S_0^* = \alpha_S \beta$  and  $R_0^* = \alpha_R \beta$ . Re-writing the design coordinates in the original space of the variables S and R one gets:

$$S^* = \mu_S - \alpha_S \beta \sigma_S \quad ; \quad R^* = \mu_R - \alpha_R \beta \sigma_R \quad (5.8)$$

The characteristic values for S and R, figure 5.1, are defined as:

$$S_k = \mu_S + k_S \sigma_S = \mu_S(1 + k_S \nu_S) \quad ; \quad R_k = \mu_R - k_R \sigma_R = \mu_R(1 - k_R \nu_R) \quad (5.9)$$

where  $\nu$  is the coefficient of variation (COV)  $\nu = \sigma/\mu$ . The design point may be expressed in terms of these characteristic values by replacing equation 5.9 in equation 5.8:

$$\begin{aligned} S_d = S^* &= \mu_S(1 - \alpha_S \beta \nu_S) = \frac{1 - \alpha_S \beta \nu_S}{1 + k_S \nu_S} S_k \\ R_d = R^* &= \mu_R(1 - \alpha_R \beta \nu_R) = \frac{1 - \alpha_R \beta \nu_R}{1 - k_R \nu_R} R_k \end{aligned} \quad (5.10)$$

To obtain the partial safety factors one replaces  $S_d = \gamma_S \cdot S_k$  and  $R_d = \frac{R_k}{\gamma_R}$  in equation 5.10:

$$\gamma_S = \frac{1 - \alpha_S \beta \nu_S}{1 + k_S \nu_S} \quad ; \quad \gamma_R = \frac{1 - k_R \nu_R}{1 - \alpha_R \beta \nu_R} \quad (5.11)$$

For linear limit state functions, the sensitivity factors may be defined as  $\alpha = 0,75 \pm 0,06$  given that  $\frac{1}{3} \leq \frac{\sigma_S}{\sigma_R} \leq 3$  and  $\alpha_R = -\alpha_S$  (Melchers, 1999). Eurocode has adopted  $\alpha_R = 0,8$  and  $\alpha_S = -0,7$  for  $0,16 \leq \frac{\sigma_S}{\sigma_R} \leq 7,6$ .

## 5.2 Partial safety factors for fatigue design

The FOSM method presented in the previous Section, may be applied to a fatigue limit state, considering that both S and R follow a log-normal distribution and using  $\log(S)$  and  $\log(R)$ , both normally distributed. The limit state function for the fatigue check is  $Z = \log(\Delta\sigma_R) - \log(\Delta\sigma_S)$  where  $m \log(\Delta\sigma_R) + \log(N) = C$  is the expression for the S-N curve and  $\Delta\sigma_S$  the equivalent stress range at  $N_{ref}$ . The reliability index is expressed by:

$$\beta = \frac{\mu_{\log(\Delta\sigma_R)} - \mu_{\log(\Delta\sigma_S)}}{\sqrt{\sigma_{\log(\Delta\sigma_R)}^2 + \sigma_{\log(\Delta\sigma_S)}^2}} \quad (5.12)$$

The standard normal form of  $\log(\Delta\sigma_R)$  and  $\log(\Delta\sigma_S)$  is:

$$S_0 = \frac{\log(\Delta\sigma_S) - \mu_{\log(\Delta\sigma_S)}}{\sigma_{\log(\Delta\sigma_S)}} \quad ; \quad R_0 = \frac{\log(\Delta\sigma_R) - \mu_{\log(\Delta\sigma_R)}}{\sigma_{\log(\Delta\sigma_R)}} \quad (5.13)$$

## 5.2. Partial safety factors for fatigue design

---

and the transformed limit state function:

$$g(S_0, R_0) = \mu_{\log(\Delta\sigma_R)} - \mu_{\log(\Delta\sigma_S)} + R_0\sigma_{\log(\Delta\sigma_R)} - S_0\sigma_{\log(\Delta\sigma_S)} \quad (5.14)$$

The coordinates of the design point at the original space of  $\log(S)$  and  $\log(R)$  are:

$$\begin{aligned} \log(\Delta\sigma_S)_d &= \mu_{\log(\Delta\sigma_S)} - \alpha_S\beta\sigma_{\log(\Delta\sigma_S)} \\ \log(\Delta\sigma_R)_d &= \mu_{\log(\Delta\sigma_R)} - \alpha_R\beta\sigma_{\log(\Delta\sigma_R)} \end{aligned} \quad (5.15)$$

The characteristic values for  $\log(S)$  and  $\log(R)$  are defined as:

$$\begin{aligned} \log(\Delta\sigma_S)_k &= \mu_{\log(\Delta\sigma_S)} + k_S\sigma_{\log(\Delta\sigma_S)} = \mu_{\log(\Delta\sigma_S)}(1 + k_S\nu_{\log(\Delta\sigma_S)}) \\ \log(\Delta\sigma_R)_k &= \mu_{\log(\Delta\sigma_R)} + k_R\sigma_{\log(\Delta\sigma_R)} = \mu_{\log(\Delta\sigma_R)}(1 + k_R\nu_{\log(\Delta\sigma_R)}) \end{aligned} \quad (5.16)$$

Expressing the design point in terms of characteristic values by replacing 5.16 in 5.15:

$$\begin{aligned} \log(\Delta\sigma_S)_d &= \mu_{\log(\Delta\sigma_S)}(1 - \alpha_S\beta\nu_{\log(\Delta\sigma_S)}) = \frac{1 - \alpha_S\beta\nu_{\log(\Delta\sigma_S)}}{1 + k_S\nu_{\log(\Delta\sigma_S)}} \log(\Delta\sigma_S)_k \\ \log(\Delta\sigma_R)_d &= \mu_{\log(\Delta\sigma_R)}(1 - \alpha_R\beta\nu_{\log(\Delta\sigma_R)}) = \frac{1 - \alpha_R\beta\nu_{\log(\Delta\sigma_R)}}{1 - k_R\nu_{\log(\Delta\sigma_R)}} \log(\Delta\sigma_R)_k \end{aligned} \quad (5.17)$$

and the partial safety factors are obtained by:

$$\begin{aligned} \log(\gamma_S) &= -\alpha_S\beta\sigma_{\log(\Delta\sigma_S)} - k_S\sigma_{\log(\Delta\sigma_S)} \\ \log(\gamma_R) &= \alpha_R\beta\sigma_{\log(\Delta\sigma_R)} - k_R\sigma_{\log(\Delta\sigma_R)} \end{aligned} \quad (5.18)$$

The partial safety factors defined in EN 1993 1-9 (2005), summarised in table 5.1, were obtained with equation 5.18 (Chabrolin, 1988) and defined for the fatigue limit state function at  $N_{eq} = 2.10^6$  as:

$$\Delta\sigma_{S,k}\gamma_S = \frac{\Delta\sigma_{R,k}}{\gamma_R} \quad (5.19)$$

Only  $\gamma_R$  is shown in table 5.1 because  $\gamma_S$  was set to 1,0 by definition. They depend on both the failure consequence and safety concept adopted for fatigue design: damage tolerant and safe life. The damage tolerant concept, avoids fatigue failure by regular inspections in service. Partial safety factors are lower based on the service life defined between each inspection. Safe-life concept assumes no inspection and must allow for the full development of crack growth until failure.

Assessment concept	Consequence of failure	
	Low consequence	High consequence
Damage tolerant	1,0	1,15
Safe life	1,15	1,35

Table 5.1 – Partial safety factor  $\gamma_R$  (EN 1993 1-9, 2005)

## Chapter 5. Uniaxial fatigue reliability

The values from table 5.1, were based on the Eurocode background (Brozzetti et al., 1989). The original values are recalled in table 5.2, with the corresponding  $\beta$  given as a range, inside which the safety factors were chosen.

Assessment concept	Consequence of failure			
	Low consequence		High consequence	
	$\beta$	$\gamma_R$	$\beta$	$\gamma_R$
<b>Damage tolerant</b>	<b>2.0</b> → 2,5	1,0	<b>3.0</b> → 3,5	1,25
<b>Safe life</b>	<b>2.5</b> → 3,0	1,15	<b>3.5</b> → 4	1,35

Table 5.2 –  $\beta$  index and safety factor  $\gamma_R$  in Eurocode background (Brozzetti et al., 1989)

The statistical parameters used in equation 5.18 to define the values in table 5.2, are discussed below. These values are often questioned so it is justified to re-analyse them here. Note that the partial safety factors shown in table 5.1 and 5.2, do in fact represent the product  $\gamma_S \cdot \gamma_R$ , i.e. variability on the loading side was not explicitly considered.

### Reliability index $\beta$ :

The background values were defined for the range of reliability index  $\beta$  indicated in table 5.2, with the bold values defined as minimum values for each case of assessment concept and failure consequence. It is unclear for which service life these bold  $\beta$  values correspond but the range of  $\beta$  values defined in table 5.2 may be assumed valid for a design life of 100 years.

### Standard deviation $\sigma_{\log(\Delta\sigma_R)}$ and fractile deviate $k_R$ :

Fatigue strength standard deviation  $\sigma_{\log(\Delta\sigma_R)}$  is defined by the standard deviation in life  $\sigma_N$  (units of log, base 10), obtained from the statistical analysis of fatigue tests. Given that the S-N curve is linear in log-log coordinates,  $\sigma_{\log(\Delta\sigma_R)} = \frac{\sigma_N}{m}$ , where  $m$  is the S-N curve slope and  $\sigma_N$  the variability in life that is measurable with fatigue tests at a pre-defined  $\Delta\sigma$  level. The values in table 5.2 were obtained with  $m=3$  and  $\sigma_N=0,21$ , which results in  $\sigma_{\log(\Delta\sigma_R)} = 0,07$ . The standard deviation  $\sigma_N=0,21$ , was chosen as representative on a typical range from 0,1 to 0,25, after extensive statistical analysis of fatigue tests under uniaxial loads, see for example (BS7608, 2014), (ECCS, 1985), (Brozzetti et al., 1989), (Sedlacek et al., 2003), (Stötzel et al., 2007), (Olivier and Ritter, 1980) or (Olivier and Ritter, 1982). For the definition of characteristic values,  $k_R = 2$  was assumed, corresponding to a 97.7% percentile rather than the usual 95% percentile.

### Standard deviation $\sigma_{\log(\Delta\sigma_S)}$ and fractile deviate $k_S$ :

The characteristic value  $\log(\Delta\sigma_k)$  in the limit state function corresponds to an equivalent stress  $\Delta\sigma_{eq}$  defined at  $N_{ref} = 2.10^6$  cycles. It accounts for the variability on vehicle loads and traffic conditions as defined in Section 4 but it further includes a cycle-stress range procedure (the rainflow counting) and the damage sum by Miner's rule on a specific S-N



## 5.2. Partial safety factors for fatigue design

curve. This process averages the stress ranges so that  $\sigma_{\Delta\sigma_{eq}}$  may be smaller than the standard deviation of the vehicle loads. No detailed information about the variability in  $\Delta\sigma_{eq}$  was used in Eurocode background (Brozzetti et al., 1989), so the standard deviation for the equivalent stress was approximated by the load coefficient of variation  $\nu_L$ . The loading COV is a non log variable so the relation to a log standard deviation is defined as:  $\sigma_{\log(\Delta\sigma_S)} = \log(e)\sqrt{Ln(1 + \nu_L^2)}$  (Chabrolin, 1988). The value adopted was  $\nu_L = 0,15$  ( $\sigma_{\log(\Delta\sigma_S)} = 0,065$ ) and further rounded to  $\sigma_{\log(\Delta\sigma_S)} = 0,07$  ( $\nu_L \approx 0,162$ ). For these values,  $\alpha_R = 0,7$  and  $\alpha_S = -0,7$  for  $\frac{\sigma_{\log(\Delta\sigma_S)}}{\sigma_{\log(\Delta\sigma_R)}} = 1$ . For the definition of the characteristic value,  $k_S = 1,645$  was used to comply with a 95% percentile. The influence of the load COV  $\nu_L$  on the partial safety factors  $\gamma_S$  and  $\gamma_R$  was computed and may be seen in figure 5.3.

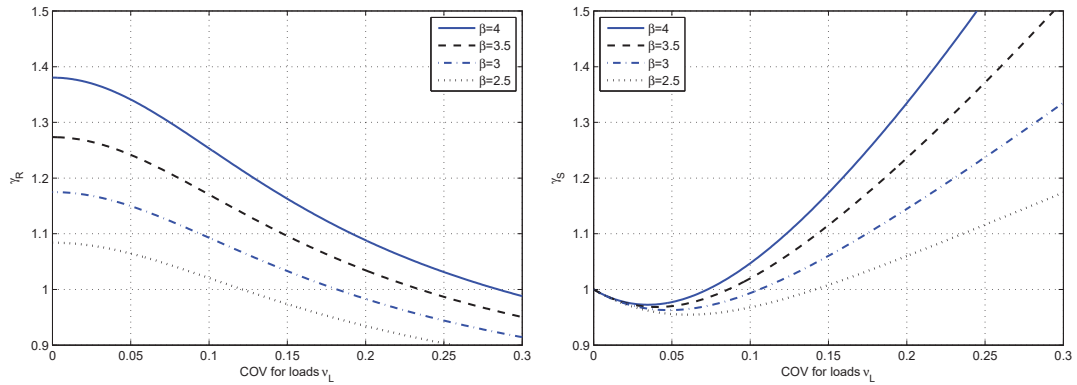


Figure 5.3 – Partial safety factors  $\gamma_S$  and  $\gamma_R$  against the  $\nu_L$

Figure 5.4 shows the product  $\gamma_S \cdot \gamma_R$  and the influence of  $\nu_L$ . The partial safety factor values from EN 1993 1-9 (2005) in table 5.2, can be read at  $\nu_L \approx 0,16$ . The sensitivity to the pre-defined value of  $\nu_L$  is important, and justifies the simulation carried out on Section 4 to better define  $\sigma_S$ .

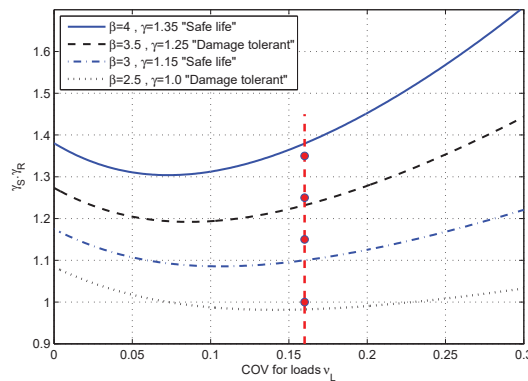


Figure 5.4 – Partial safety factor  $\gamma_S \cdot \gamma_R$  against the  $\nu_L$

Re-calibration of the partial safety factors

Reliability index  $\beta$ :

The necessary first step to calibrate partial safety factors is to set an acceptable probability of failure, or an equivalent  $\beta_{target}$ . These are defined in Eurocode 0 as a  $\beta_{50year}=1,5$  to 3,8 corresponding to  $\beta_{1year}=3,0$  to 4,7. However, the  $\beta_{target}$  values are not linked to the safety assessment method and consequence class as given in table 5.2. Following a similar procedure as recommended in (Nussbaumer, A; Borges, L; Davaine, 2011), we adopt the code max  $\beta_{100}= 3,65$  for high consequence and the code min  $\beta_{100}=1,15$  for low consequence, table 5.3.  $\beta$  target values of 3,6 for 100 years of service life have also been used by other authors (Vrouwenvelder and Waarts, 1993).

In case of damage tolerant design, a minimum number of intermediate inspections  $n_{insp.} \geq 3$  is assumed for a design life of 100 years, with a maximum time between inspections of  $t_{insp.} = 25$ years. That means that at each inspection, there is an upgrade of the reliability index. So one may assume that the target reliability of  $\beta_{target} = 3.65$  required for 100 years, has to be met between each inspection, i.e.  $\beta_{25years} = 3.65$  which leads to an equivalent target  $\beta=3.25$  at 100 years. It is noted that this is a simplified assumption by considering the Probability of detection (POD) as 100%.

The reliability index for n years is given by  $\Phi\beta_n = (\Phi\beta_1)^n$ , or in terms of probability of failure  $p_{f,n} = 1 - (1 - p_{f,1})^n$ , assuming that the variability on the loads is time invariant. This ergodicity implies that load variability is not time correlated which may only be assumed without traffic growth scenarios.

Assessment concept	Service life	Consequence of failure			
		Low consequence		High consequence	
		$\beta$	$p_f$	$\beta$	$p_f$
	1 year	3,0	$1,3^{-3}$	4,7	$1,3^{-6}$
	50 years	1,5*	$6,68^{-2}$	3,8*	$7,23^{-5}$
<b>Damage tolerant</b>	100 years	1,0**	$1,58^{-1}$	3,25	$5,77^{-4}$
<b>Safe life</b>	100 years	1,15	$1,2^{-1}$	3,65	$1,3^{-4}$

(\*) values recommended in Eurocode 0

(\*\*) set as minimum

Table 5.3 –  $\beta_{target}$  values adapted from Eurocode 0

Standard deviation  $\sigma_{\log(\Delta\sigma_R)}$  and fractile deviate  $k_R$ :

Standard deviation  $\sigma_N$  for individual experimental setups may range from 0,1 to 0,25 depending on the detail and notch intensity. However, when several datasets are merged, higher variability is obtained, which naturally accounts for different sources of variability such as welding procedures, steel types, fabrication quality and measurement errors. This is intended to be accounted by the partial safety approach, so that the fatigue strength

## 5.2. Partial safety factors for fatigue design

standard deviation  $\sigma_{\log(\Delta\sigma_R)}$ , is defined based on a probabilistic re-analysis of several datasets. The data-pooling of individual experimental setups for several different details is presented in Appendix A, where  $\sigma_N$  is denoted by  $\sigma$ . Table 5.4 summarises the main results considered in the re-analysis of each individual detail.

Detail	$\Delta\sigma_{\text{mean},2}$	$\sigma_N$	FAT (EC3)	FAT	remarks	$N^\circ$ tests
Lateral attachments	75.3	0.2967	40	50	Lattach<500mm	721
Long. attachments	99.3	0.14	63	80	Lattach<100mm	74
Long. attachments	94	0.2	56	71	Lattach>100mm	551
Plates with holes	144.2	0.31	90	90	Quality group 1	202
Plates with holes	99	0.28	90	71	Quality group 2	169
Tubular connections	78.6	0.3	71	56	Tubes with holes	161
Tubular connections	57	0.32	71	45	Tubes with fillet welds	40
Cope holes	105	0.267	71	71	$\frac{\Delta\tau}{\Delta\sigma} \approx 0$	59
Plates with studs	117.6	0.267	80	80	$\Delta\sigma$ on plate	279

Table 5.4 – Summary of uniaxial FAT details

Merging these datasets through an unified FAT curve, where each individual detail is normalised to the FAT category given by the statistical re-analysis, allows to define a common variability for the reliability index computation. This common S-N curve is shown in figure 5.5 with the database points summarised in table 5.4. A standard deviation  $\sigma_N=0,27$  (units of log, base 10) is obtained from the statistical analysis of these tests, and  $\sigma_{\log(\Delta\sigma_R)} = \frac{\sigma_N}{m} = 0,0933$ , where  $m=3$  is the S-N curve slope (free slope regression  $m=2,66$ ) and  $k_R = 1,645$ .

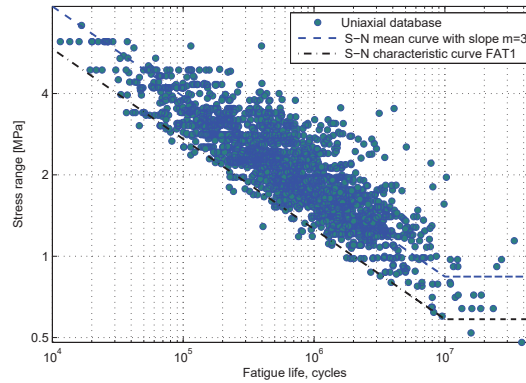


Figure 5.5 – Unified S-N curve for the database uniaxial FAT details

Some details were seen to be inconsistently classified in Eurocode. The partial safety factors do not cover mis-interpretations of the FAT category, so that these details were re-classified and these new FAT category was used for computation of  $\sigma_N$ . Re-classified details include lateral attachments, plates with holes or tubular connections, see Appendix A for more details.

**Standard deviation  $\sigma_{\log(\Delta\sigma_S)}$  and fractile deviate  $k_S$ :**

To cover the lack of background for the variability of the equivalent stress  $\Delta\sigma_{eq,2.10^6}$ , simulations were carried out with the probabilistic traffic model in Section 4. Thirty six design cases were simulated, and the equivalent stress  $\Delta\sigma_{eq,2.10^6}$  was seen to follow a log-normal distribution. Table 4.15 summarises the individual values from simulations in Section 4. The standard deviation of the log-normal distribution for the full set of simulated design cases can be taken as the maximum obtained with simulations:  $\sigma_{\log_{10}(\Delta\sigma_{eq})} = 0,031$  with the deviate  $k_S = 1,645$ . Compared to  $\sigma_{\log_{10}(\Delta\sigma_{eq})} = 0,07$  from Eurocode background (Brozzetti et al., 1989), one can only conclude that the estimate based on the load COV  $\nu = 0,16$  is rather pessimistic, mainly because one of the load variables, the number of cycles, is fixed to a conservative upper bound value, and on the other, the lorry weight, is averaged by the damage sum procedure. Unduly conservative design may be avoided by re-defining traffic categories, allowing for intermediate values of  $N_{obs}$  between  $5.10^5$  and  $2.10^6$  heavy vehicles/year.

The partial  $\gamma$  safety factors derived for the equivalent damage stress range are equally valid for damage accumulation procedures, because the calibration already involved the rainflow counting technique, the linear Miner's damage sum and a double slope S-N curve. They are shown in figures 5.6 and 5.7.

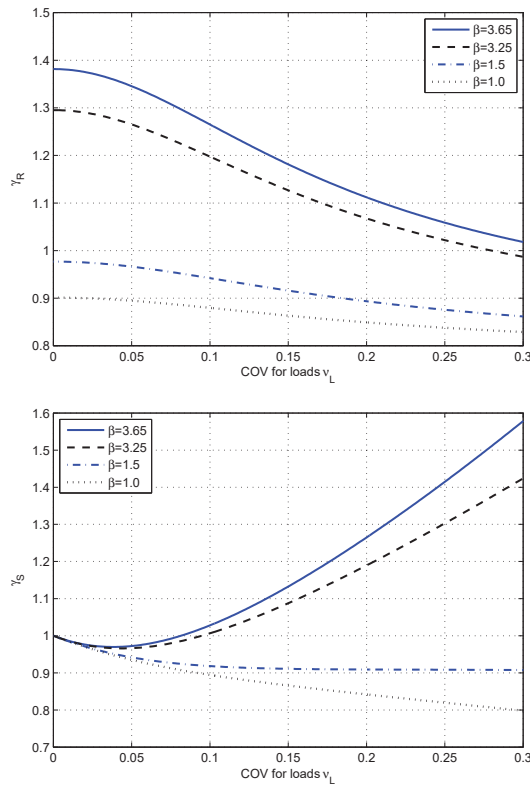


Figure 5.6 – Partial safety factors  $\gamma_S$  and  $\gamma_R$  against the  $\nu_L$  (re-calibration)

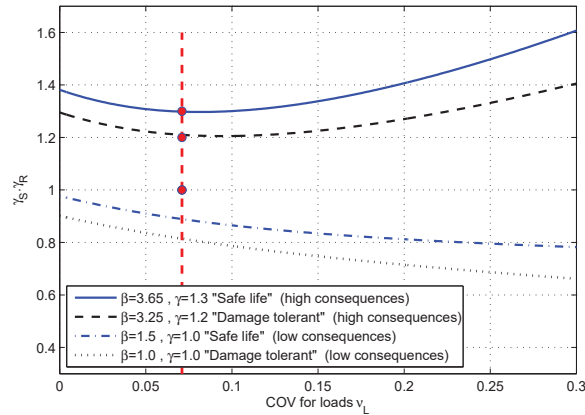


Figure 5.7 – Partial safety factor  $\gamma_S \cdot \gamma_R$  against the  $\nu_L$  (re-calibration)

### 5.3 Summary of conclusions

- This chapter revised the First Order Reliability approach used to define the partial safety factors for fatigue checks in Eurocode 3. Based on the same approach, the partial safety factors were re-calculated with revised  $\beta_{target}$  values and statistical definitions for both loads and resistance.
- The results of the traffic generation model were used to characterise the variability on the load side  $\Delta\sigma_{eq}$ . The results showed that a conservative approach had been previously adopted in the Eurocode 3 background.
- Statistical analysis of a variety on uniaxial detail, allowed for a re-definition of the resistance curve with higher standard deviation as originally considered. The re-calibrated partial safety factors are similar to Eurocode 3 background.
- The establishment of a database of several fatigue details allowed the re-classification of some FAT details. This was the case of plates with holes that were re-classified based on the fabrication quality of the hole edges and also tubular connections which were classified based on the weld type and chamfer detailing. Both showed the actual Eurocode FAT categories to be unsafe.



# 6 Multiaxial fatigue reliability

This chapter is focused on the multiaxial fatigue assessment with criteria based on uniaxial FAT details. In detail, the damage sum rule as proposed by Eurocode 3 and the elliptical interaction formula as defined in IIW Recommendations are analysed. The IIW criteria is calibrated for the target reliability index.

## 6.1 Fatigue tests collected from literature

A database of multiaxial experiments was established based on results collected from different literature sources. Their re-analysis is presented in Appendix B. The database is restricted to comparable experiments that resulted in weld toe failure. These are both welded plate details and tubular specimens with fillet welded attachments or flanges. All tests presented in Appendix B and considered here for interaction analysis, presented some degree of interaction under combined loads. However, it is indeed not possible to generalise and classify the effect of proportional and non-proportional loads, so they are pooled in our analysis. Following the classification proposed by Maddox and Razmjoo (2001), figure 1.20, welded plate details or tubular specimens could be dealt with separately. For the experiments on welded plates described in Appendix B, it is clear that the proportional case with  $\Delta\sigma$  and  $\Delta\tau$  produces a reduction on the number of cycles to failure, when compared to the reference uniaxial case of any of those stress quantities. Similar conclusions were reported by (Lotsberg, 2009) and (Bokesjö et al., 2012) for plate details where failure was due to root crack on the weld throat section. However, exception made for the beams tested by Archer (1987), which have a very small weld toe under shear, none of the other experimental setups with plates, produced non-proportional stress states. This justifies the relevance of the multiaxial tests presented in Chapter 3, where indeed, proportional interactions greatly reduced fatigue life, while the non-proportional case was found to have no relevant interaction effects, with failures at the weld toe. These conclusions however, contradict the observations reported by several authors on tubular specimens, where the non-proportional case has

## Chapter 6. Multiaxial fatigue reliability

repeatedly been reported as more damaging than the proportional one. The data for circular tubular specimens summarised in Appendix B, shows that the proportional case is worst than the uniaxial one, but the non-proportional may give even lower fatigue lives. Exception is the data in square tubes where the degree of interaction was low.

For circular tubes welded on end plates or flanges, a plausible reason to justify that non-proportional stress states represent the worst case scenario, was not found. In pure material tests, the rotation of the principal stress direction allows for crack initiation in several planes, but for the welded tubular specimens, cracks develop on the weld toe for any case of combined loads. A closer look to the experimental results, shows that the weld toe is generally under transverse residual compressive stresses (Siljander et al., 1992), which in part justifies that experimental fatigue life is lower for stress relieved specimens (Yung and Lawrence, 1986). Transverse residual stresses are perpendicular to the weld toe. Any applied compression is also expected to reduce the shear effects. Furthermore, the fact is that under proportional torsion/bending, a significant part of the section is compressed due to direct bending stresses, which may also have a beneficial effect on reducing shear damage.

It seems thus that different design criteria should be put forward for tubes and plates, or in other words, for normal stress  $\Delta\sigma$  interactions with shear stress  $\Delta\tau$  due to torsion or from direct forces, respectively. The approach followed here, is to pool both tubular and plate specimens together, and analyse the entire set of multiaxial results to find a single interaction criteria. Data is analysed using their mean uniaxial fatigue life as devised for each experimental setup in Appendix B. The relevant parameters needed for the interaction analysis are summarised in table 6.1. In all cases the S-N constant amplitude slopes are considered  $m_\sigma=3$  and  $m_\tau=5$  and for stress relieved specimens under  $R_\sigma$ , only 60% of the compressive amplitude was considered for the stress range computation.

Detail	$\Delta\sigma_{\text{mean},2}$	FAT $_\sigma$	$\Delta\tau_{\text{mean},2}$	FAT $_\tau$	Reference
Longitudinal attachment	115	80	112	80	(Archer, 1987)
Continuous fillet welds	177	100	97	80	(Dahle et al., 1997)
Transverse butt-welds	102	90	97	80	(Dahle et al., 1997)
Transversal attachment	102	80	128	80	(Kim and Yamada, 2005)
Tube-to-flange	163	80	148	80	(Siljander et al., 1992)
Tube-to-flange	100	80	102	80	(Yung and Lawrence, 1986)
Tube-to-end plate	81	80	120	80	(Razmjoo, 1996)
Tube-to-end plate	140	80	178	80	(Sonsino et al., 1999)
Tube-to-end plate	124	80	131	80	(Amstutz et al., 2001)
Tube-to-end plate	144	80	184	80	(Yousefi et al., 2001)
Tube-to-end plate	87	80	159	80	(Bäckström, 2003)
Transversal attachment	110	80	106	80	Chapter 3

Table 6.1 – Summary of mean and characteristic values for literature multiaxial tests



Measurements of residual stresses in both transversal attachments (Barsoum, 2008), (Barsoum and Jonsson, 2008) or tubes with flanges (Yung and Lawrence, 1986), (Siljander et al., 1992), have shown the weld toe to be generally under transverse compression stresses. This justifies mixing as-welded and stress-relieved results.

## 6.2 Stress based multiaxial interaction criteria

For the comparison of the multiaxial interaction formulas, the concept of normalised stress components is useful, by defining the quantities  $d_\sigma$  and  $d_\tau$  as the ratio between each independent stress range component and fatigue uniaxial resistance:

$$d_\sigma = \frac{\Delta\sigma_E}{\Delta\sigma_R} \quad ; \quad d_\tau = \frac{\Delta\tau_E}{\Delta\tau_R} \quad (6.1)$$

For equation 1.14 presented in Eurocode 3, the fatigue damage computed under normal stress ranges,  $\Delta\sigma$ , is added to the damage due to shear stress ranges  $\Delta\tau$ . It means that the interaction is computed through the formula:

$$D_\sigma + D_\tau \leq 1 \Leftrightarrow \frac{n_i}{N_{R,\sigma}} + \frac{n_i}{N_{R,\tau}} \leq 1 \Leftrightarrow \frac{1}{N_{R,\sigma}} + \frac{1}{N_{R,\tau}} \leq \frac{1}{n_i} \quad (6.2)$$

$$\text{where } N_{R,\sigma} = \frac{2.10^6 FAT_\sigma^3}{\Delta\sigma_i^3} \text{ and } N_{R,\tau} = \frac{2.10^6 FAT_\tau^5}{\Delta\tau_i^5} \text{ so that:}$$

$$\left( \frac{\Delta\sigma_i}{FAT_\sigma} \right)^3 + \left( \frac{\Delta\tau_i}{FAT_\tau} \right)^5 \leq \frac{2.10^6}{n_i} \quad (6.3)$$

If the stress ranges are reported to an equivalent value at  $N=2.10^6$  by:

$$\Delta\sigma_{eq,2} = \sqrt[3]{\frac{n_i}{2.10^6}} \cdot \Delta\sigma_i \text{ and } \Delta\tau_{eq,2} = \sqrt[5]{\frac{n_i}{2.10^6}} \cdot \Delta\tau_i \text{ one gets:}$$

$$D_\sigma + D_\tau \leq 1 \Leftrightarrow \left( \frac{\Delta\sigma_{Ed,2}}{FAT_\sigma} \right)^3 + \left( \frac{\Delta\tau_{Ed,2}}{FAT_\tau} \right)^5 \leq 1 \quad (6.4)$$

which may be re-written in terms of normalised stress components as:

$$D_\sigma + D_\tau \leq 1 \Leftrightarrow d_\sigma^3 + d_\tau^5 \leq 1 \quad (6.5)$$

The International Institute of welding (IIW, 2008) presents an interaction formula that assumes a quadratic relation between normalised stress components:

$$\left( \frac{\Delta\sigma_{Ed,2}}{FAT_\sigma} \right)^2 + \left( \frac{\Delta\tau_{Ed,2}}{FAT_\tau} \right)^2 \leq CV \Leftrightarrow d_\sigma^2 + d_\tau^2 \leq CV \quad (6.6)$$

$$\text{where: } \Delta\sigma_{Ed,2} = \sqrt[3]{\frac{n_i \cdot \Delta\sigma_i^3}{2 \cdot 10^6}} \quad ; \quad \Delta\tau_{Ed,2} = \sqrt[5]{\frac{n_i \cdot \Delta\tau_i^5}{2 \cdot 10^6}}$$

with CV being the critical comparison value less or equal to 1,0.

Several variations of both IIW and Eurocode formulas have been proposed in literature based on the normalised stress concept. For the combined shear and torsion tests, Archer (1987) proposed a modified version of the damage sum formula with  $m_\tau=3$  and a modified version of the IIW equation:

$$d_\sigma + d_\tau^2 \leq 1 \Leftrightarrow \frac{\Delta\sigma_E}{\Delta\sigma_R} + \left(\frac{\Delta\tau_E}{\Delta\tau_R}\right)^2 \leq 1 \quad (6.7)$$

A new interaction formula was proposed by Baptista and de Castro e Sousa (2013) based on multi-linear regression analysis of the normalised stress components imposing  $CV=1$ :

$$1,1d_\sigma + 1,15d_\tau - 1,25d_\sigma d_\tau \leq 1 \quad (6.8)$$

The normalised stress space  $d_\sigma$  and  $d_\tau$  is shown in figure 6.1 with the experimental results, using the mean resistance values as summarised in table 6.1. The interaction equations discussed above are also shown: equation 6.4 (EC3), equation 6.6 (IIW), equation 6.8 (BCS), equation 6.7 (Archer) and equation B.1 (Linear) with  $CV=1,0$ .

Considerable scatter is seen in figure 6.1 and none of the interaction formulas seems to be suited. The linear interaction equations is a lower bound for the data, but it must be noted that the experimental data is plotted with their mean values of uniaxial fatigue strength.

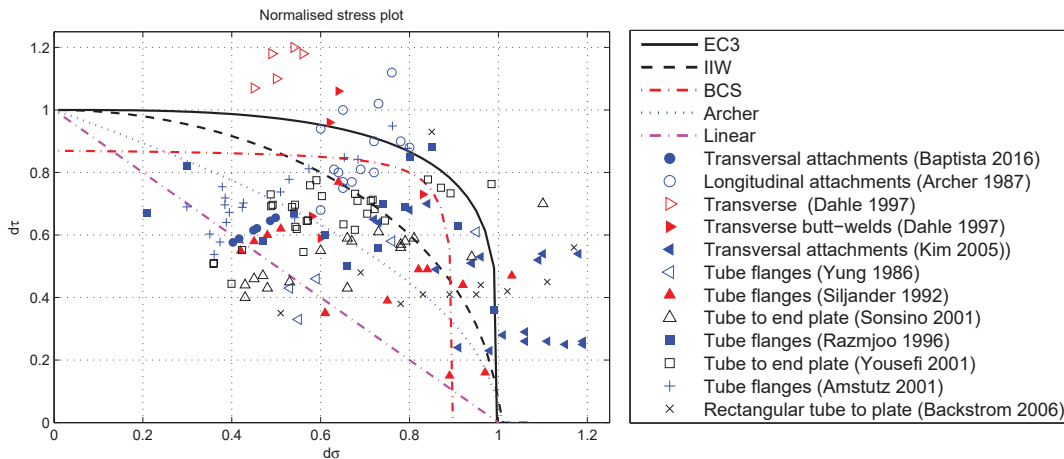


Figure 6.1 – Experimental results and interaction formulas in normalised stress  $d_\sigma$ ,  $d_\tau$

Design code models based on nominal stress ranges seem to have a very low correlation with the experimental results, and the experimental data is seen to be very scattered. This may suggest that the approach in nominal stress might be over simplified, and that

## 6.2. Stress based multiaxial interaction criteria

the problem of multiaxial fatigue interaction may not be treated with the few variables considered. The experimental data in figure 6.1 in terms of normalised stress  $d_\sigma$ ,  $d_\tau$ , includes both the load influence by  $\Delta\sigma$  and  $\Delta\tau$ , the number of cycles from tests and the uniaxial resistances,  $FAT_\sigma$  and  $FAT_\tau$ . One of the parameters often considered is the ratio between  $\rho = \frac{\Delta\tau}{\Delta\sigma}$  but this is seen in figure 6.2 to merely divide the normalised stress  $d_\sigma$ ,  $d_\tau$  in “slices”, and no clear trend is shown by this parameter.

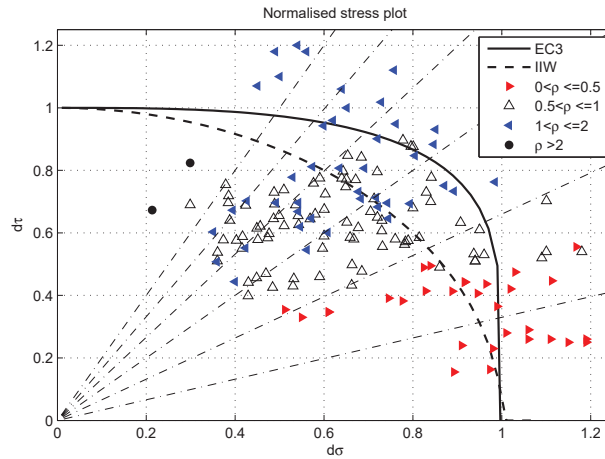


Figure 6.2 – Multi-axial experimental results by  $\rho = \frac{\Delta\tau}{\Delta\sigma}$

Many tentative models and parameters were tested based upon the normalised stress quantities  $d_\sigma$ ,  $d_\tau$  and only the example of equation 6.8 was presented here. The multi-axial interaction problem, even in its simplest form, has five basic variables,  $\Delta\sigma$ ,  $\Delta\tau$ ,  $\Delta\sigma_{R,2}$ ,  $\Delta\tau_{R,2}$  and  $N$ , and none of them can be treated directly within the interaction plot as figure 6.1 because the normalised stress quantities are not unique. Finally, figure 6.3 shows that the distinction between the proportional and non-proportional experiments is also not a factor that indicates any trend on the normalised stress  $d_\sigma$ ,  $d_\tau$ .

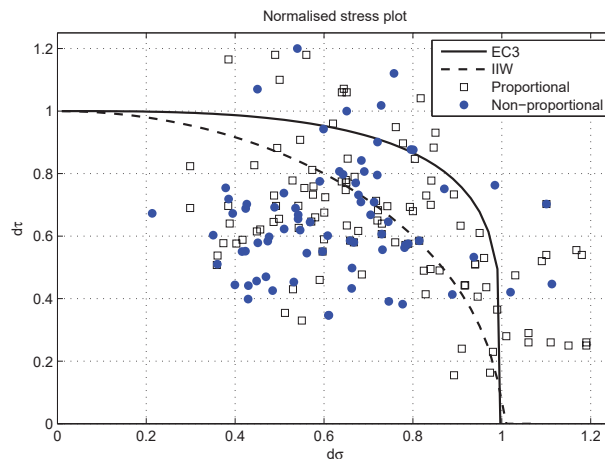


Figure 6.3 – Multi-axial experimental results by stress proportionality

The criteria are thus investigated via their ability to estimate directly the number of cycles under multiaxial stress states, and it may be anticipated that from the five equations plotted in figure 6.1, IIW quadratic interaction is the one giving the best results.

### 6.3 Fatigue life estimation

Life estimations for the database of multiaxial experiments are obtained for the damage sum equation (EC3) by solving equation 6.2 and for the quadratic Gough-Polard formula (IIW) by solving equation 6.6 with CV=1. The results for the mean resistance values at  $2 \cdot 10^6$  from table 6.1 are shown in figure 6.4.

The scatter bands shown in figure 6.4 are based on the 5 and 95% percentiles considering  $\text{Log}(N)$  normally distributed ( $k=1,64$ ) and centered with the mean line. Consequently, standard deviations ( $\sigma$ ) for  $\text{Log}(N)$  are shown. The uniaxial scatter band is based on the analysis done in the previous chapter, see figure 5.5 with  $\sigma=0,27$ , and the standard deviation for the multiaxial life estimations of each criteria, used as a comparison parameter, is computed by:

$$\sigma = \sqrt{\frac{\sum_1^n (\text{Log}(N_i)_{eq} - \text{Log}(N_i)_{test})^2}{n - 1}} \quad (6.9)$$

where  $\text{Log}(N_i)_{eq}$  is computed by the interaction criteria under analysis,  $\text{Log}(N_i)_{test}$  is the experimental life and  $n=165$  the number of multiaxial datapoints considered in the database. It is seen in figure 6.4, that the IIW criteria gives better life estimations with  $\sigma = 0,39$  than the damage accumulation from EC3 that has  $\sigma = 0,51$ .

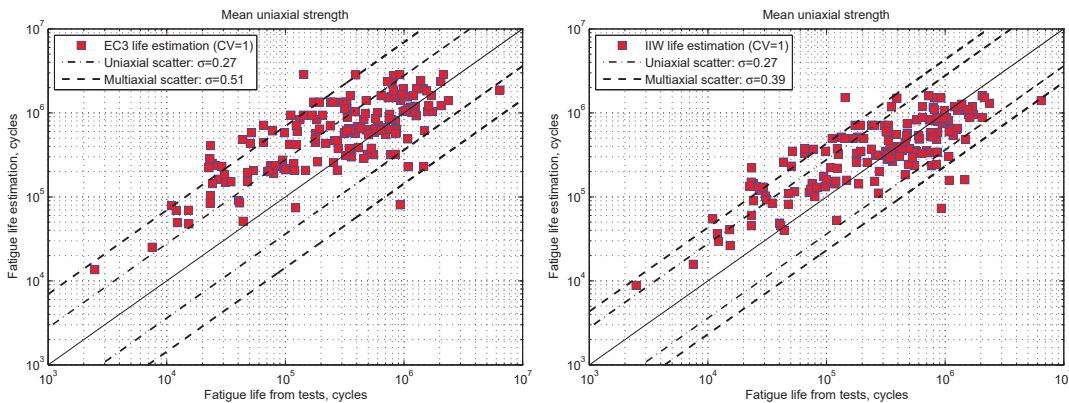


Figure 6.4 – Life estimations for the multiaxial database with mean strength values

Figure 6.5 shows the life estimates using the design code FAT values as summarised in table 6.1. A intermediate step would be to consider characteristic values based on the statistical analysis of each uniaxial case, but the accuracy of this estimate based on the few experimental results under each uniaxial case is low. The IIW criteria still has a

### 6.3. Fatigue life estimation

lower standard deviation on the life estimate, but the difference to the EC3 criteria is now lower. A linear regression on the life estimate is shown in figure 6.5. The scatter bands are centered on this mean line of the life estimations, and it is seen that for the IIW criteria, the 95% estimation scatter line, is practically coincident with the diagonal where estimated and experimental lives are the same. This means that 95% of the IIW life estimations are on the safe side. The EC3 formula, on the contrary, has the upper bound above the median diagonal line. From both analysis shown in figure 6.4 and 6.5, it is clear that the quadratic interaction formula from IIW handles better results as the Eurocode damage sum criteria.

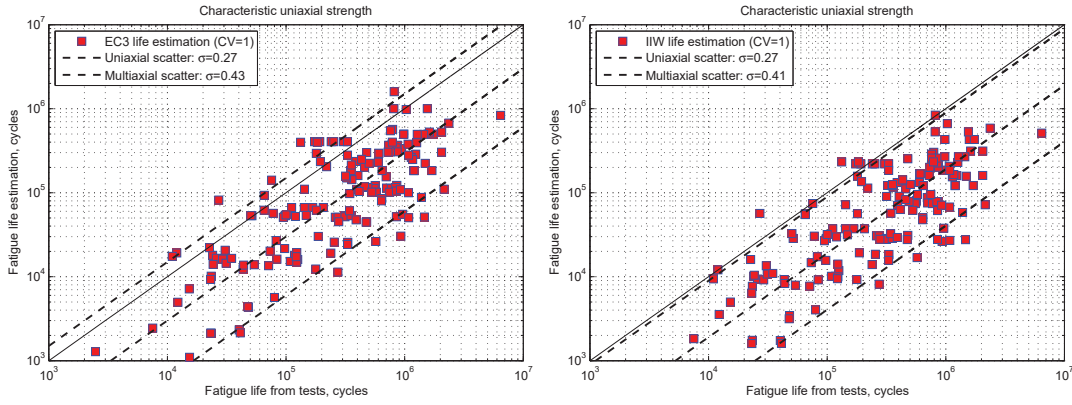


Figure 6.5 – Life estimations for the multiaxial database with FAT values

In an attempt to devise a criteria whose life estimation scatter is close to the one observed for uniaxial fatigue tests, ideally  $\sigma = 0,27$ , the most successful formula was achieved by developing the damage formula given in equation 6.2 using logarithmic components for each life quantities. This equation gives a direct relation between the quantities that indeed are measured from experiments and that characterise fatigue scatter, i.e. both uniaxial lives  $N_{R,\sigma}$ ,  $N_{R,\tau}$  and the multiaxial fatigue life  $n_i$ :

$$\text{Log}(n_i) = \text{Log}(N_{R,\sigma}) + \text{Log}(N_{R,\tau}) \quad (6.10)$$

By replacing  $N_{R,\sigma} = 2.10^6 \left( \frac{\Delta\sigma_{R,2}}{\Delta\sigma_i} \right)^{m_\sigma}$  and  $N_{R,\tau} = 2.10^6 \left( \frac{\Delta\tau_{R,2}}{\Delta\tau_i} \right)^{m_\tau}$  in equation 6.10:

$$\text{Log}(n_i) = \text{Log} \left( 2.10^6 \left( \frac{\Delta\sigma_{R,2}}{\Delta\sigma_i} \right)^{m_\sigma} \right) + \text{Log} \left( 2.10^6 \left( \frac{\Delta\tau_{R,2}}{\Delta\tau_i} \right)^{m_\tau} \right) \Rightarrow \quad (6.11)$$

$$\Rightarrow \text{Log}(n_i) = 2. \text{Log} \left( 2.10^6 \right) + m_\sigma. \text{Log} \left( \frac{\Delta\sigma_{R,2}}{\Delta\sigma_i} \right) + m_\tau. \text{Log} \left( \frac{\Delta\tau_{R,2}}{\Delta\tau_i} \right) \quad (6.12)$$

which is in the form  $y = \alpha_0. \text{const} + \alpha_1. x_1 + \alpha_2. x_2$  and may be solved through a multilinear regression to estimate the  $\alpha_j$  coefficients that better fit equation 6.13 to the experimental

database:

$$\text{Log}(n_i) = \alpha_0 \left( 2\text{Log}(2.10^6) \right) + \alpha_1 \left( m_\sigma \text{Log} \left( \frac{\Delta\sigma_{R,2}}{\Delta\sigma_i} \right) \right) + \alpha_2 \left( m_\tau \text{Log} \left( \frac{\Delta\tau_{R,2}}{\Delta\tau_i} \right) \right) \quad (6.13)$$

By using a matrix formulation to express equation 6.13, one has  $[Y] = [X] \cdot [\alpha]$  where  $[Y]$  ( $i \times 1$ ) is a column matrix with the  $i$  experimental results,  $[X]$  ( $i \times j$ ) is the model matrix with the  $j+1$  variables  $x_j$ , and  $[\alpha]$  ( $j \times 1$ ) is a vector with the  $\alpha_j$  model coefficients:

$$\begin{bmatrix} \text{Log}(n_1) \\ \text{Log}(n_2) \\ \vdots \\ \text{Log}(n_i) \end{bmatrix} = \begin{bmatrix} 2 \cdot \text{Log}(2.10^6) & m_\sigma \cdot \text{Log} \left( \frac{\Delta\sigma_{R,2}}{\Delta\sigma_1} \right) & m_\tau \cdot \text{Log} \left( \frac{\Delta\tau_{R,2}}{\Delta\tau_1} \right) \\ 2 \cdot \text{Log}(2.10^6) & m_\sigma \cdot \text{Log} \left( \frac{\Delta\sigma_{R,2}}{\Delta\sigma_2} \right) & m_\tau \cdot \text{Log} \left( \frac{\Delta\tau_{R,2}}{\Delta\tau_2} \right) \\ \vdots & \vdots & \vdots \\ 2 \cdot \text{Log}(2.10^6) & m_\sigma \cdot \text{Log} \left( \frac{\Delta\sigma_{R,2}}{\Delta\sigma_i} \right) & m_\tau \cdot \text{Log} \left( \frac{\Delta\tau_{R,2}}{\Delta\tau_i} \right) \end{bmatrix} \times \begin{bmatrix} \alpha_0 \\ \alpha_1 \\ \alpha_2 \end{bmatrix} \quad (6.14)$$

The coefficients in system 6.14 are obtained by solving  $[\alpha] = [X^T X]^{-1} [X^T Y]$  and one obtains  $\alpha_0=0,4423$  ;  $\alpha_1=0,7912$  and  $\alpha_2=0,3301$ . The coefficients  $\alpha_1$  and  $\alpha_2$  in equation 6.13 correct the S-N slopes  $m_\sigma = 3$  and  $m_\tau = 5$ . If one accepts these corrections and allows the slopes to be fitted, equation 6.13 may be redefined with  $\alpha_0=0,4423$  ;  $\alpha_{1'} = \alpha_1 m_\sigma = 2,37$  and  $\alpha_{2'} = \alpha_2 m_\tau = 1,65$  and written as:

$$\text{Log}(n_i) = \alpha_0 \left( 2\text{Log}(2.10^6) \right) + \alpha_{1'} \left( \text{Log} \left( \frac{\Delta\sigma_{R,2}}{\Delta\sigma_i} \right) \right) + \alpha_{2'} \left( \text{Log} \left( \frac{\Delta\tau_{R,2}}{\Delta\tau_i} \right) \right) \quad (6.15)$$

The fatigue life estimations for the log-fitted criteria, equation 6.15, are shown in figure 6.6. The standard deviation on the life estimates is  $\sigma = 0,35$  which is significantly lower than the damage accumulation equation from EC3,  $\sigma = 0,51$  and also lower than the quadratic IIW equation,  $\sigma = 0,39$ , compare to figure 6.4.

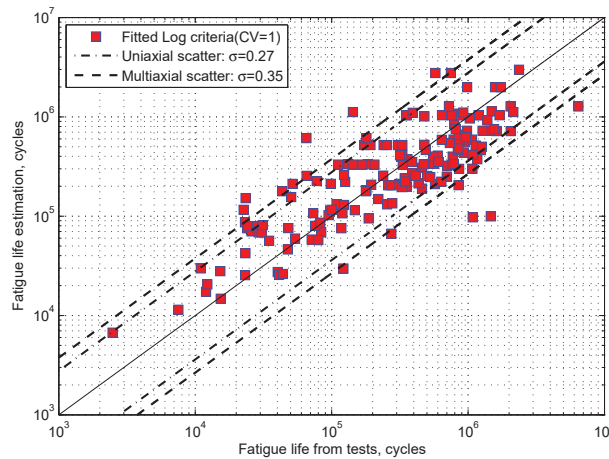


Figure 6.6 – Life estimations with the log-fitted criteria (mean strength values)

When used with the FAT values defined for each test setup based on design standard values, table 6.1, the log-fitted criteria 6.15 gives  $\sigma = 0,43$ , comparable to both Eurocode 3 and IIW formulations, figure 6.7. Of course the fitting of equation 6.15 could be done with  $\Delta\sigma_{R,2} = FAT_\sigma$  and  $\Delta\tau_{R,2} = FAT_\tau$ , leading to  $\alpha_0=0,4853$  ;  $\alpha_{1'} = 1,5486$  and  $\alpha_{2'} = 1,3724$ , but this biases the model because the FAT values do not necessarily correspond to the characteristic values of each dataset.

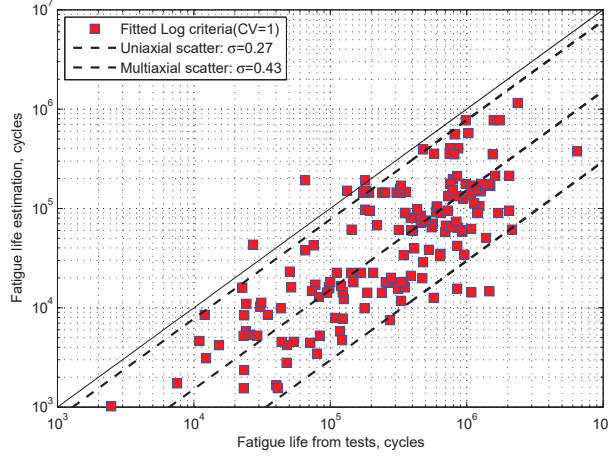


Figure 6.7 – Life estimations with the log-fitted criteria (FAT values)

By eliminating the logarithms in equation 6.15, we may write:

$$\text{Log} \left( \frac{n_i}{(2.10^6)^{2\alpha_0}} \right) = \text{Log} \left[ \left( \frac{\Delta\sigma_{R,2}}{\Delta\sigma_i} \right)^{\alpha_{1'}} \left( \frac{\Delta\tau_{R,2}}{\Delta\tau_i} \right)^{\alpha_{2'}} \right] \Rightarrow \quad (6.16)$$

$$\Rightarrow \frac{(2.10^6)^{2\alpha_0}}{n_i} = \left( \frac{\Delta\sigma_i}{\Delta\sigma_{R,2}} \right)^{\alpha_{1'}} \left( \frac{\Delta\tau_i}{\Delta\tau_{R,2}} \right)^{\alpha_{2'}} \quad (6.17)$$

which for the equivalent stress range at  $2.10^6$  is:

$$\Rightarrow (2.10^6)^{2\alpha_0-1} = \left( \frac{\Delta\sigma_{E,2}}{\Delta\sigma_{R,2}} \right)^{\alpha_{1'}} \left( \frac{\Delta\tau_{E,2}}{\Delta\tau_{R,2}} \right)^{\alpha_{2'}} \quad (6.18)$$

By replacing the coefficients  $\alpha_0=0,4853$ ;  $\alpha_{1'} = 1,5486$  and  $\alpha_{2'} = 1,3724$  and rounding:

$$\left( \frac{\Delta\sigma_{E,2}}{\Delta\sigma_{R,2}} \right)^{2,4} \left( \frac{\Delta\tau_{E,2}}{\Delta\tau_{R,2}} \right)^{1,6} \leq 0,2 \quad (6.19)$$

Equation 6.19 is re-plotted along with the experimental results from the multiaxial database in figure 6.8.

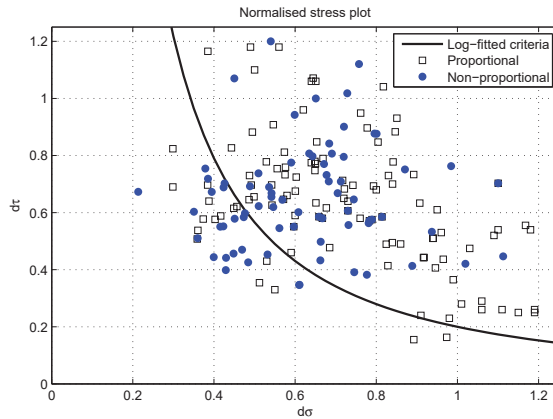


Figure 6.8 – Experimental results and log-fitted criteria in normalised stress  $d_\sigma, d_\tau$

The difference with the quadratic interaction or the damage sum, is that the best fit to the experimental data was achieved by inverting the equation curvature. By further limiting each individual damage check to  $\frac{\Delta\sigma_{E,2}}{\Delta\sigma_{R,2}} \leq 1$  and  $\frac{\Delta\tau_{E,2}}{\Delta\tau_{R,2}} \leq 1$  the interaction equation is shown in figure 6.9 along with the Eurocode and IIW criteria.

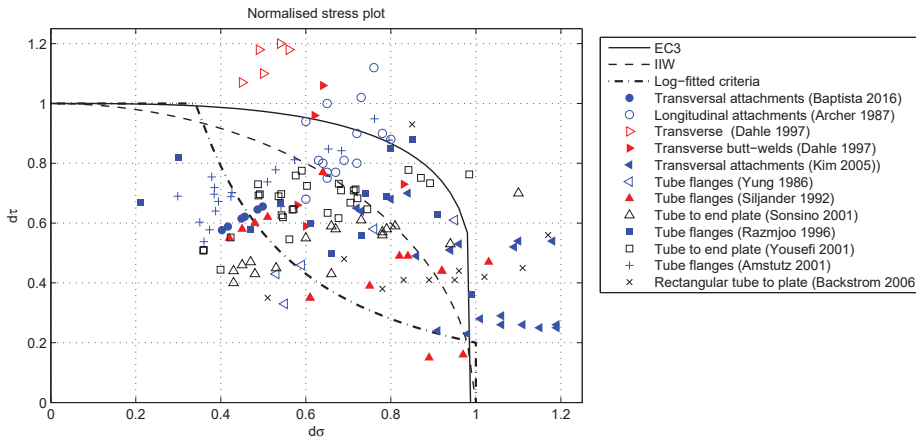


Figure 6.9 – Experimental results and log-fitted criteria

### 6.4 Calibration of partial safety factors

The analysis of Design Code interaction formulas shows that the quadratic IIW equation 6.6 is more accurate on multiaxial life estimations than the damage accumulation formula prescribed by Eurocode 3. A new criteria was presented whose accuracy is similar to the IIW formula. In view of the widespread use and acceptance of the IIW formula, we further calibrate the partial safety factors in order to recommend this criteria as an interim solution for the multiaxial interaction based on uniaxial FAT details. A code-calibration procedure as defined in (Faber and Sorensen, 2002) is used for the calibration of partial safety factors.



#### 6.4. Calibration of partial safety factors

The structural code design equation for multiaxial interaction is given by:

$$G(z_i) = \left( z_i \frac{\Delta\sigma_d}{FAT_{\sigma,d}} \right)^{\alpha_\sigma} + \left( z_i \rho \frac{\Delta\tau_d}{FAT_{\tau,d}} \right)^{\alpha_\tau} \leq CV \quad (6.20)$$

where the index  $d$  denotes design values given by the partial safety factors applied to characteristic  $k$  values, to ensure a minimum reliability level.

$$G(z_i) = \left( z_i \frac{\gamma_S \Delta\sigma_k}{FAT_\sigma / \gamma_R} \right)^{\alpha_\sigma} + \left( z_i \rho \frac{\gamma_S \Delta\tau_k}{FAT_\tau / \gamma_R} \right)^{\alpha_\tau} \leq CV \quad (6.21)$$

where  $z_i$  is a design variable;  $\alpha_\sigma = \alpha_\tau = 2$ ;  $\gamma_S = 1.0$ ;  $\Delta\sigma_k$  and  $\Delta\tau_k$  are the characteristic load effects;  $CV$  is the comparison value.

The solution of the design equation 6.21 for a given set of  $\gamma_R$ , load cases  $\Delta\sigma_{k,i}$  and  $\Delta\tau_{k,i}$  and FAT, yields the design variable  $z_i$  that ensures a given value of  $CV$ .

For each design variable  $z_i$ , the reliability index  $\beta$  is computed by solving the limit state function  $g(z_i)$ , which is of the same form as the design equation  $G(z_i)$ , but where the basic variables are random:

$$g(z_i) = CV - \left( \left( z_i \frac{\Delta\sigma_S}{\Delta\sigma_R} \right)^{\alpha_\sigma} + \left( z_i \rho \frac{\Delta\tau_S}{\Delta\tau_R} \right)^{\alpha_\tau} \right) = 0 \quad (6.22)$$

Since this interaction limit state functions is non-linear, a Monte Carlo procedure is implemented to solve for the probability of failure. To attain a  $\beta_{target} = 3,65$  the corresponding  $p_f = 1,3 \cdot 10^{-4}$  and a minimum n° of Monte Carlo trial given by  $n_{trial} = 1/p_f \approx 10.000$ . One hundred thousand trials are performed for any  $\beta$  computation corresponding to each design case  $z_i$ . The result of equation 6.22 is fitted to a Generalised Extreme Value distribution, figure 6.10 and the probability of  $g(z_i) \leq 0$  is computed on the fitted distribution.

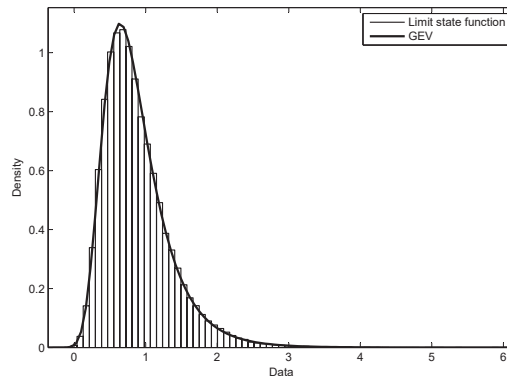


Figure 6.10 – Generalised Extreme Value distribution fit to the limit state function  $g(z_i)$

## Chapter 6. Multiaxial fatigue reliability

The 36 design cases issued from the probabilistic traffic model in Chapter 4 are used. All 24 normal stress cases and 12 shear stress cases as presented in table 4.15 are simulated as a design point  $z_i$ . This yields 288 computations of failure probability and corresponding  $\beta$ . The partial safety factor and the comparison value CV are calibrated to assure the required  $\beta_{target} = 3,65$ . The calibration is made for 4 different ratios  $\rho = \frac{\Delta\tau_{k,i}}{\Delta\sigma_{k,i}}$  set to  $\rho = 0,5$ ,  $\rho = 1$ ,  $\rho = 1,5$  and  $\rho = 2$  by inspection of figure 6.2.

The characteristic values of  $\Delta\sigma_{k,i}$  and  $\Delta\tau_{k,i}$  are calculated using the log-normal parameters from table 4.15. The FAT values are computed with standard deviation  $\sigma = 0,27$  for normal stress range according to figure 5.5 and  $\sigma = 0,36$  for the shear stress ranges according to figure A.24.

The random value CV in the limit state function 6.22 is defined by a log-normal distribution, fitted to the 165 experimental results on the multiaxial database from Appendix B. The distribution fitting is shown in figure 6.12.

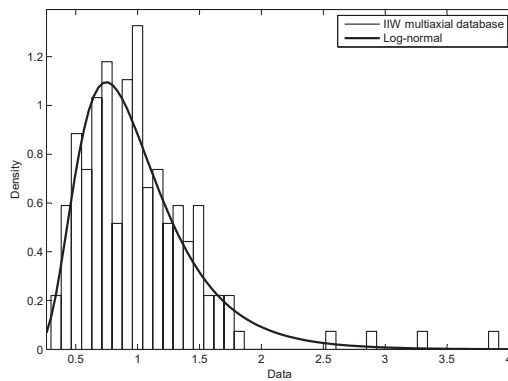


Figure 6.11 – Log-normal fit to the IIW criteria results on the multiaxial database

The  $\beta$  values computed for the four cases of  $\rho$  and for each design case ( $i=288$ ) are shown in figure 6.12. The calibration with  $CV=0,5$  allows the use of the uniaxial partial safety factor  $\gamma_R=1,45$ . For each  $\rho$  value, the mean  $\beta$  over the design cases is shown in the plot, comparable to the  $\beta_{target}$  value.

The overall mean is  $\beta=3,65$ . It is seen that higher  $\rho$  values give the lower  $\beta$  values, which is due to the higher standard deviation considered for shear loads. The influence of load correlation was also simulated with little influence on the  $\beta$  values. One can also see a tendency for the  $\beta$  values to increase with the design case number (the abscissa). This is the order of the load case combinations from table 4.15. In fact, the increase of design case index, corresponds to load cases with longer influence lines and multilane behaviour, in other words, to a decrease of the Weibull shape parameter as characterised in table 4.13.

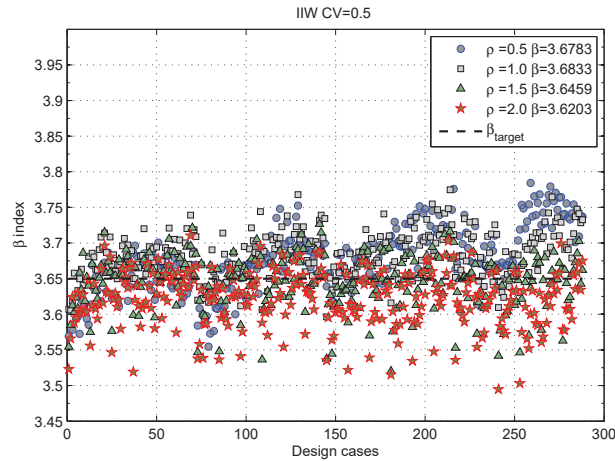


Figure 6.12 –  $\beta$  computations for the IIW multiaxial interaction formula

## 6.5 Summary of conclusions

- Multiaxial fatigue criteria based on the interaction of nominal uniaxial FAT details was investigated in this chapter, based on the experimental results obtained in this thesis and a relevant database from results collected from different literature sources.
- The elliptical Gough-Pollard formula as defined in IIW Recommendations proved to be better than the damage sum rule as proposed by Eurocode 3.
- A new criteria was presented but the overall results in terms of fatigue life estimation was found similar to the elliptical Gough-Pollard formula.
- An interim solution with the Gough-Pollard formula using a critical comparison value  $CV=0,5$  was defined with partial safety factor  $\gamma_R=1,45$  and target reliability index  $\beta=3,65$ .



# CONCLUSIONS **Part IV**



# Conclusions

One of the main goals of this thesis, based on the objective of investigating both the effects of variable amplitude and multiaxial loads on fatigue behaviour of common steel bridge details, was to produce relevant experimental results in the high-cycle regime under both of those load conditions. Under variable amplitude loads, fatigue tests up to 70 million cycles were conducted, and valuable results were obtained in the range above 5 million cycles, including constant amplitude tests to establish the Constant Amplitude Fatigue Limit. The experimental campaign on lateral flange tip attachments resulted in a total of 45 experimental results, giving an insight on different trends of the fatigue behaviour under variable amplitude. The second experimental campaign had the objective of producing multiaxial fatigue results on typical bridge plate details, with emphasis on the comparison between proportional and non-proportional loads. An original large scale setup was designed and built and a total of 20 experimental results were presented, under uniaxial shear, uniaxial normal stress and both proportional and non-proportional loads. Both experimental campaigns produced valuable fatigue tests that are believed to be a contribution to the database of existing fatigue results in two special domains and specific load conditions, where there was a clear lack of experimental data.

## Lateral Flange tip attachments

The behaviour of flange tip attachments was extensively investigated. This is an important detail in bridge construction practice, with one of the lowest FAT categories, and an important economical impact on steel bridge construction. An extensive database of experimental results was established based on tests reported in literature and our own experimental campaign. The detail could be re-classified from FAT40 to FAT50 based on the database with 721 experimental points. Further analysis with a probabilistic fracture mechanics approach showed that FAT45 would be recommended, for attachment length and main plate width up to 500mm, and FAT40 for higher values, although no experimental data is available to background this later classification. Experimental results for flange tip attachments with transition radius were re-analysed and their detail category was re-defined as  $FAT=45(1 + 1,25R/W)$  and  $FAT=40(1 + 1,6R/W)$  with  $R \geq 50\text{mm}$ , consistent with the rectangular attachments recommendation.

---

## Constant amplitude experiments

Constant amplitude experiments monitored with an Alternative Current Potential Drop (ACPD) technique allowed crack initiation lives and propagation curves to be obtained. These were used to calibrate both initiation and fracture mechanics models. Initiation lives up to 50% of total life to failure were measured. Successful crack initiation life estimates were obtained with a local notch strain approach, accounting for local repeated yielding by Neuber's notch rule and Ramberg-Osgood cyclic strain-stress curves. Local elasto-plastic stress ranges were used to estimate initiation life using Coffin-Manson equation with Morrow's mean stress correction. Experimental crack propagation curves were successfully modeled with a fracture mechanics model, with due account for the various crack shapes observed from tests.

Different fatigue lives were observed for Intersected flanges and Lateral attachments. The microstructures at the crack initiation spots and along the crack path were characterised. The difference was attributed to higher initiation lives for Intersected flanges due to a combination of compressive residual stresses and smaller microstructural grain size. Residual stresses measurements on both configurations showed that lateral attachment weld toes are mainly in compression while intersected flanges could be both in tension or compression. It is recommended that no FAT distinction should be made between both configurations because their propagation lives is similar and the beneficial effect of initiation is not guaranteed.

## Probabilistic fracture mechanics approach for the CAFL definition

The experimental results obtained under constant amplitude revealed the existence of an endurance level below which several run-outs were obtained. A probabilistic fracture mechanics model was established including variability in the main parameters to further investigate the position of the constant amplitude fatigue limit by numerical means. The results showed that the CAFL should be placed at  $10 \cdot 10^6$  cycles, much higher than the  $5 \cdot 10^6$  recommended for European bridge practice. The numerical results were confirmed with experimental data from literature. Furthermore, a re-analysis of other fatigue details revealed that longitudinal attachments should also be specified with a CAFL at  $10 \cdot 10^6$  cycles, indicating that the CAFL position may depend on the detail category, i.e. lower FAT categories correspond to higher number cycles.

## Variable amplitude experiments

Experiments under variable amplitude were performed with a concave spectra, having a considerable large number of cycles below the CAFL. This allowed the influence of small stress ranges cycles to be analysed. A double slope S-N curve with a 2<sup>nd</sup> slope value  $k=5$  below the CAFL gave the best estimates for the experimental lives. This was attributed to the CAFL threshold drop with damage accumulation. The concept of effective propagation life was used to show that by considering only the propagating ranges,



---

identified by ACPD measurements, good agreement with a single slope propagation curve was achieved. On the other hand, by considering also the non-effective stress ranges, the 2<sup>nd</sup> slope model proved accurate, by an artificial increase of fatigue life for points below the original CAFL threshold.

The experimental initiation-propagation curves were adequately described by applying the local notch strain approach with Coffin-Manson equation to estimate initiation life and the fracture mechanics model under variable amplitude, as previously calibrated with constant amplitude tests.

Experimental crack growth curves (a-N) allowed sequence effects to be identified, namely the progressive drop of the crack propagation threshold. Initiation lives up to 45% of total lives were measured. The crack threshold drop was experimentally confirmed using a progressively decreasing stress spectrum, carefully driven so that a continuous crack propagation was achieved. This showed the dependency between the crack threshold drop and the accumulated damage. Stress ranges as low  $\Delta\sigma=15$  MPa were propagating. The “cut-off” limit for small stress ranges was tentatively established at  $\approx 0,25$  FAT, considerably lower than  $\Delta\sigma_L = 0,4$  FAT defined in Eurocode 3, though the establishment of the “cut-off” levels needs further confirmation. On the other hand, under variable amplitude tests with the maximum stress range at the CAFL, several run-outs were obtained. The set of experiments conducted under variable amplitude, clearly validated the physical relevance of the crack threshold drop model and the use of an S-N double slope curve.

### **Probabilistic fracture mechanics approach for variable amplitude loads**

The probabilistic Initiation-Propagation model as established and calibrated for constant amplitude loads, was extended and used under variable amplitude. The model showed to be suitable to devise characteristic S-N curves under both constant and variable amplitude. The model was used to correlate the load spectra shape with the crack threshold drop model. The 2<sup>nd</sup> slope value for the variable amplitude S-N curves were shown to depend on both the notch case and the load spectra shape. By applying different load types characterised by a Weibull frequency distribution with shape parameter  $\nu$ , the 2<sup>nd</sup> slope value was seen dependent on the aggressiveness of the load spectrum, represented by  $k=m+2/\nu$ .

### **Experiments under multiaxial stress**

Fatigue experiments under multiaxial stress were conducted to investigate the influence of proportional and non-proportional loads in a typical welded plate detail. Mode II/III cracks were obtained under pure shear, Mode I under uniaxial normal stress and under both proportional and non-proportional loads. The results on a transversal attachment detail clearly showed the detrimental effect of the proportional load case. Under non-proportional loads, fully out-of-phase, fatigue life was dominated by Mode I

---

behaviour under normal stress, and no major influence from shear stress was observed. Fatigue life under non-proportional loads were similar to the uniaxial normal stress case, without measurable influence from shear. The local 1mm notch approach was used for the analysis of the experimental results and showed capable of estimating experimental lives using the maximum principal stress at the rounded notch and the FAT225 master curve. Using nominal stress quantities to estimate experimental fatigue lives, the best result was achieved with the elliptical Gough-Pollard equation as defined in the IIW Recommendations, using  $CV=0,5$  as the critical comparison value.

### **Highway traffic generation model**

The influence of the load spectra shape on the  $2^{nd}$  slope value of the resistance curve, that was established with the probabilistic fracture mechanics model, justified further investigation on the type of load spectra to expect on bridges. For that, a traffic generation model was established based on a probabilistic definition of the main traffic parameters, in link to the background data of European fatigue load models for the sake of compatibility. The simulations on different influence lines for bending moments and shear, and several cases of multilane behaviour, allowed to characterise the expected stress range spectra for fatigue analysis. The spectra shapes varied from remarkably convex for small influence lines and single lane traffic, to almost linear under multilane traffic and long influence lines. In view of the results obtained by the fracture mechanics model, this indicates that for short influence lines, where axle loads are important, an S-N curve with  $2^{nd}$  slope  $k=5$  would be unsafe and on the contrary, the increase of span length to a range where global vehicle weight and multilane effects prevail, tend to produce smoother spectra profile, where  $k=5$  was shown to be suitable.

### **Fatigue reliability**

The traffic simulations on several design cases allowed to characterise the variability on the load side  $\Delta\sigma_{eq}$ . The results were used to calibrate the partial safety factors for fatigue checks with the design code format. The First Order Reliability approach was used with revised  $\beta_{target}$  values, and a statistical analysis of a variety of uniaxial detail. The re-calibrated partial safety factors are similar to the ones specified in Eurocode 3.

The establishment of a database of relevant fatigue details, lead to the re-classification of some FAT details. This was the case of plates with holes that were re-classified based on the fabrication quality of the hole edges FAT90 (Drilled and Reamed holes), FAT71 (Punched, Flame and Plasma cut holes). Also tubular connections with gusset extremity plates welded on a slit, were classified based on the weld type and chamfer detailing, FAT56 (full-penetration welds, single slit with a hole and double slit with fillet welds) and FAT45 (single slit with fillet welds).

For the multiaxial interaction with criteria based on the nominal uniaxial FAT details, the re-analysis with experimental results collected from literature, showed the elliptical

---

Gough-Pollard formula more accurate than the damage sum rule as proposed by Eurocode 3. An interim solution with the Gough-Pollard formula using a critical comparison value  $CV=0,5$  was defined for a target reliability index  $\beta=3,65$  and safety factor  $\gamma_R = 1,45$ , pooling both proportional and non-proportional results, from plate and tubular specimens.

### **Future works**

In view of the results obtained in this thesis, it is believed that further research on the following topics are of interest:

- The probabilistic initiation-propagation model as presented in this thesis for the lateral flange tip attachments, is extensible to other typical fatigue details. This analysis would allow to settle the CAFL position and a comprehensive definition of the design code S-N curves for each detail class.
- An improvement on the highway traffic generation model as presented in this thesis would include variability on the number of heavy vehicles. This is achievable by further dividing the traffic categories from Eurocode 1 in smaller ranges. The definition of 2 million heavy vehicles per year seems to be extremely conservative in view of the measurements that were analysed.
- The typified load spectra based on different Weibull shape parameters could be further investigated. A comprehensive characterisation of highway traffic loads in this way, has the potential of allowing generic spectra shapes to be used in design, eliminating the limitations of the current procedure based on equivalent damage factors ( $\lambda$  factors), and incorporating different  $2^{nd}$  slope values on the damage computations.
- For the behaviour of plate details under multiaxial stress interaction, the influence of the normal stress components on the shear damage process, would allow a better insight to the interaction phenomena, specially for details characterised by failures at the weld toe. The treatment of the multiaxial interaction by fracture mechanics is still an open subject.
- A comprehensive fatigue reliability analysis for steel bridges would allow to establish the sensitivity of the partial safety factors to the main parameters of the load and resistance models.



# APPENDIX **Part V**



# A Uniaxial fatigue database

Several uniaxial fatigue details are used in this thesis. This Appendix presents the database of experimental results collected from literature, along with the re-analysis of their FAT categories.

## A.1 Statistical evaluation of fatigue results

The statistical procedure for the treatment of experimental results is presented. This procedure was adopted both for the interpretation of the experimental results obtained under this thesis, as well as the re-analysis of the fatigue database from literature.

### Data-pooling of experimental results

“Data pooling” of existing fatigue tests is a common practice in classifying fatigue details (Schneider and Maddox, 2003). This is of course not the most advisable technique in terms of the Design of Experiments, but the cost and the time involved in testing specimens that are representative of real bridge details and loads is considerable. “Data pooling” has however its advantages in the sense that data representative of several countries, steels and manufacturers may be pooled so that the natural scatter faced in bridge constructions and required in the Eurocode approach is somehow included.

Statistical tests for verifying the quality of the data being merged are applied to check if each sample set can be regarded as part of the same population. Checking that data sets belong to the same statistical population is also applied to identify parameters that lead to a differentiation in fatigue category, such as size effects or execution quality. No specific method for the pooling analysis is defined in (EN 1993 1-9, 2005), so the procedures recommended in IIW Recommendations (IIW, 2008) and (Huther et al., 2011) are adopted.

The collection of data sets from literature is of course analysed and a first engineering

## Appendix A. Uniaxial fatigue database

---

judgment allows for the data to be interpreted. After this analysis, and in order to determine the FAT category of a specific constructional detail,  $n$  datasets are pooled as they are believed to belong to the same detail, and statistical check performed as follows:

1. For each sample dataset  $1 \rightarrow n$ , a linear regression estimates the mean S-N curve by fitting the experimental results with a least-square fit. Stress range ( $\log \Delta\sigma$ ) is taken as independent variable and number of cycles ( $\log N$ ) as dependent. Due to limited sample size that generally characterizes each individual experimental set, the slope  $m$  is fixed using previous knowledge so that only the intercept  $\log C$  is estimated by regression

$$C = \Delta\sigma^m N \rightarrow \log N = \log C - m \log \Delta\sigma$$

2. The intercept  $\log C$  for each test of each independent  $n$  samples is pooled and compared in a Normal probability plot with  $\log C$  in abscissa plotted against the estimated cumulative distribution function in ordinate. This allows an assessment of the goodness-of-fit from the fatigue data to the normal distribution
3. If the data is reasonably linear in the normal probability plot, then one compares sets 2 by 2, assuming that the two sets of test results follow the same S-N curve, a two-tailed t-student test for unpaired samples is done with a 5% probability to reject the hypothesis of equivalence:

- Estimated variance for each sample  $v_i = \frac{\sum (X_i - X_m)^2}{n_i - 1}$

- Estimated common variance  $v = \frac{(n_1 - 1)v_1 + (n_2 - 1)v_2}{n_1 + n_2 - 2}$

- Estimated difference variance  $v_d = v \left( \frac{1}{n_1} + \frac{1}{n_2} \right)$

- Critical value for two-sided t-student  $t(p = 0.95; f = (n_1 + n_2) - 2)$

4. The criteria is  $Cr = |m_1 - m_2| - t(p, f)\sqrt{v_d}$  where  $t$  is the critical value for two-sided t-student at  $p$  significance,  $f = (n_1 + n_2) - 2$  degrees of freedom and  $m_1, m_2$  the mean for each dataset. The hypothesis of equivalence is rejected if  $Cr > 0$ .

### Linear model for the S-N curve

The model for the S-N curve is obtained by fitting the experimental results of merged datasets with a linear regression by least-square fit, minimizing the square of the residuals. Taking the stress range  $\log \Delta\sigma$  as independent variable and the number of cycles  $\log N$  as dependent, the mean fatigue S-N curve is obtained by estimating both the slope  $m$  and the intercept  $\log C$ :

$$C = \Delta\sigma^m N \Rightarrow \log N = \log C - m \log \Delta\sigma \Rightarrow y = b - ax$$



$$a = \frac{SS_{xy}}{SS_{xx}} ; b = \bar{y} - a\bar{x} ; SS_{xy} = \sum_{i=1}^n x_i y_i - \frac{(\sum_{i=1}^n x_i)(\sum_{i=1}^n y_i)}{n} ; SS_{xx} = \sum_{i=1}^n x_i^2 - \frac{(\sum_{i=1}^n x_i)^2}{n}$$

A second regression analysis is then performed with fixed slope  $m$ . For welded joints the slope is fixed to  $m=3$  for uniaxial normal stress and to  $m=5$  under shear, leaving only one parameter estimated by the regression in this case.

By defining the S-N model by linear regression, the residuals are assumed normally distributed, independent and homoscedastic (variance independent from  $\log \Delta\sigma$ ). To check the accuracy of the linear model, the residuals are checked for normality with a quantile plot and for homoscedasticity by plotting them against the independent variable of the regression  $\log \Delta\sigma$ .

### Characteristic fatigue strength curves

Based on the mean S-N curve, the characteristic value for the fatigue strength (FAT) is defined according to (EN 1993 1-9, 2005) with a survival probability of 95% imposing a 75% confidence level on the estimation of the  $x_{0,05}$  fractile at  $2.10^6$  cycles. The experimental lives  $\log N$  are approximated by a Gaussian distribution and the one-sided confidence interval is defined for the 5% percentile of the distribution (ECCS, 1985).

The assumption about the normality of the experimental lives ( $\log C$ ) is checked with a probability plot of the least squares fit of the transformed data. The linearity of the cumulative frequency distribution of  $\log C$  function of  $\Phi^{-1}(F)$  is tested:

1. The  $t = \log C$  data is ordered and the Empirical Distribution (EDF) is computed with the mean rank estimator  $\hat{F}(t_i) = \frac{i}{n+1}$
2. Assuming a normal distribution  $F(t) = \Phi\left(\frac{t-\mu}{\sigma}\right)$  for  $t = \log C$ , the values  $x_i$  and  $y_i$  are computed as  $x_i = t_i$  and  $y_i = \Phi^{-1}(\hat{F})$
3. Probability plot with  $x_i$  versus  $y_i$  and linear regression to estimate  $y = ax + b \Rightarrow \Phi^{-1}(\hat{F}) = \frac{1}{\sigma}t - \frac{1}{\sigma}\mu$
4. The parameters of the normal distribution  $F(t) = \Phi\left(\frac{t-\mu}{\sigma}\right)$  given by  $\mu = -\frac{b}{a}$  and  $\sigma = \frac{1}{a}$ . A CDF plot is analysed
5. Confidence test for the goodness of fit with the Filliben's test using a correlation factor : If  $Cr \geq 0$  the data can be assumed to follow a normal distribution

A one-sided confidence interval  $[\theta_{low}, \infty]$  with a  $\gamma$  confidence level is defined as:

## Appendix A. Uniaxial fatigue database

---

$$P(\theta_{low} \leq \theta) = \gamma$$

If the fractile  $x_p$  is the parameter  $\theta$  being estimated, the lower confidence limit may be formulated as:

$$P(P(X \leq x_p) = p) = \gamma \rightarrow P(P(X \leq m_x - k_p \cdot s_x) = p) = \gamma$$

where  $m_x = \frac{\sum x_i}{n}$  is the mean and  $s_x = \sqrt{\frac{\sum (x_i - m_x)^2}{n-1}}$  the standard deviation for the normal distribution of  $x$ ,  $\gamma$  is the probability that  $p\%$  of the population is below  $m_x - k_p \cdot s_x$ .

While the  $x_p$  percentile is estimated in a normal distribution of  $\log N$  the  $\gamma$  confidence probability is described by a t-student distribution. To find the deviate  $k_p$ , the previous equation is rewritten as (Wampler, 1976):

$$P(T_f \leq k_p \cdot \sqrt{n} \mid \delta = x_p \cdot \sqrt{n}) = \gamma$$

where  $T_f$  is given by the inverse cumulative function of the noncentral t-distribution with  $f$  degrees of freedom and non-central parameter  $\delta$ . If the slope  $m$  of the mean  $m_x$  is estimated by regression analysis  $f = n - 2$ , otherwise with the slope fixed based on previous knowledge, only the intercept is estimated and the number of degrees of freedom for the noncentral t-distribution is  $f = n - 1$ , (Schneider and Maddox, 2003).

The characteristic value for the fatigue resistance is then defined by:

$$\text{Log}(N) = \text{Log}(C) - k_{0,05} \cdot \text{stdv} - m \cdot \text{Log}(\Delta\sigma) \quad \text{Log}(FAT) = \frac{\text{Log}(2.10^6) - \text{Log}(C) + k_{0,05} \cdot \text{stdv}}{-m}$$

where  $k_{0,05}$  is the one-sided confidence limit factor defined for  $p=0,05$  failure probability and  $\gamma=0,75$  confidence.

The definition of characteristic resistance values with a survival probability of  $p=0,95$  and a  $\gamma=0,75$  confidence lower limit has traditionally been used in statistical methods for material properties (ISO 2394, 2008), (ISO 12491, 1997). For a normal distribution the  $x_{0,05}$  fractile is given by  $k_{0,05}=1,64$  but when the number of tests in the sample is small, such as in the case of high-cycle fatigue experiments, the parameters from the sample distribution,  $m_x$  and  $s_x$ , may not be good estimators of the population parameters  $\mu_x$  and  $\sigma_x$ . In this case the estimation parameters are themselves assumed to follow a statistical distribution so that the probability of the population being included in the sample estimate is defined by the confidence level.

This approach defined in (EN 1993 1-9, 2005) is based on the coverage method to define the deviate  $k_p$ . The latest definition in Eurocode 0 - Annex D, is slightly different in that the deviate  $t_p$  is used to estimate a prediction limit for the mean  $m_x$  so that an additional random single observation from the population  $x_{n+1}$  would occur below  $x_p$  with a probability  $p$ .

## A.2. Flange tip attachments

The coverage method is adopted in our approach because confidence limits are sample statistics that estimate population parameters, rather than the prediction limits for future samples.

In any case it is noted that the coverage method gives more conservative values comparing with the prediction method. Table A.1 shows a comparison of both parameters for  $p = 0,05$  and  $\gamma = 0,75$ .

n	4	5	6	8	10	20	30	$\infty$
$k_p$	2.68	2.46	2.34	2.19	2.10	1.93	1.87	1.64
$t_p$	2.63	2.33	2.18	2.00	1.92	1.76	1.73	1.64

Table A.1 – Comparison of  $k_p$  (coverage method) with  $t_p$  (prediction method)

It is worth noting that other fatigue standards such as (DNV, 2014) or (BS7608, 2014), define the characteristic design curve at  $2 \cdot 10^6$  cycles, based on a shift of two standard deviations of  $\log N$  below the mean as originally introduced by Gurney and Maddox (1973). Although a good estimation for small sample sets, for  $n > \approx 15$  it leads to over-conservative characteristic FAT values, representing a 97,7% survival probability.

## A.2 Flange tip attachments

Rectangular flange tip attachment are classified in Eurocode 3 as a FAT40 category while IIW Recommendations classifies according to the attachment length, table A.2 . For attachments  $L_{attach} \leq 150mm$  this represents a difference up to 25% in allowable stress at  $2 \cdot 10^6$  cycles, which means roughly a factor of 3 in life for the high-cycle regime.

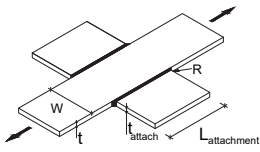
Standart	FAT	Geometrical conditions	Detail
<b>Eurocode 3 (2005)</b>	40		
<b>IIW (2013) (*)</b>	50	$L_{attach} < 150 \text{ mm}$	
	45	$150 \text{ mm} \leq L_{attach} < 300 \text{ mm}$	
	40	$L_{attach} \geq 300 \text{ mm}$	
(*) 1,12 FAT if $t_{attach} \leq 0,7t$			

Table A.2 – FAT categories for rectangular flange tip attachments

Table A.3 summarises the database of experimental results considered in our analysis.

## Appendix A. Uniaxial fatigue database

Reference	$f_y$	Rect.	Inters. flange	Tapered	Transition radius		Wing
	[MPa]	L [mm]	L [mm]	L [mm]	R [mm]	plates R/W	L [mm]
Puchner 1959	245	250		440	50	0,41	
Gurney 1959	290	250					
Gurney 1962	292						200/100
Gunnert 1963	230	200					
Harrison 1966	181						200
Neumann 1966	230	100			30	0,33	
Kramer 1967	230	60					
Hirt 1975	360	100/200			70	0,41	
Roberts 1977	250	305					
Haibach 1979	420/510	200/400	200/400	400	20/100	0,1/0,5	
Bergers 1979	394	200					
Daniels 1980	250	406			150	0,75	
Tilly 1980							150
Bergers 1982	394	200			60	0,3	
Yamada 1982	373	200			10	0,059	
Yamada 1984	400/430	50/100/200					200
Yamada 1986	373	200					200
Yamada 1989	373	200					
Yamada 1998	394	200	200				
Kondo 2002	400/430	100					
Shimokava 1985	833				15/40/60	0,083 / 0,2	
Wagner 1998	431	300					
Maddox 1999	448	100					
Woo 2000	308	100					
Lee 2003	315	300					
Bae 2004	310/570/700	80/150/300			30	0,33	
Choi 2006	700	150					
Tominaga 2007	286	200					
Kim 2008	299	50/100/200/250					
Nagata 2009	398	200					
Zhang 2009	385	510					150
Kinoshita 2013					20/40	0,2/0,14/0,28/0,5	

Table A.3 – Database of experimental results for flange tip lateral attachments

It is a common assumption that fatigue results may be combined regardless of the symmetry of the detail (Gurney and Maddox, 1973), (Brozzetti et al., 1989). Non-symmetrical specimens give higher fatigue lives due to the “beneficial” effect from the compressive bending stress due to the additional eccentricity, by which the pure tension stress on the weld toe is reduced. Fatigue test are usually performed in symmetrical specimens, see table A.4, because the probability of weld imperfections and thus fully propagating lives is higher since four weld toes are tested, instead of only two in the non-symmetrical configuration. This leads to a lower bound of the possible fatigue lives (Gurney, 1979), (Maddox, 1994). The only experimental study with both types specimens within the same batch is (Gurney and Trepka, 1959). Despite having only 3 symmetrical results these can be seen to be clearly unfavorable (FAT50) even having a smaller attachment length (200 mm) while the non-symmetrical tests were performed on specimens with a 250 mm attachment (FAT71).

Another common assumption confirmed by the comparison of several setups in the database is that tests on plain specimens give the same fatigue life than attachments tested on beams (Gurney, 1979). All cracks, were observed to propagate from the sealing weld toe through the width of the main plate, transversally to the normal stress.

The results for wing plates, although not being the same detail, are usually included in the rectangular flange tip attachment re-analysis (Gurney and Maddox, 1973), (Olivier

## A.2. Flange tip attachments

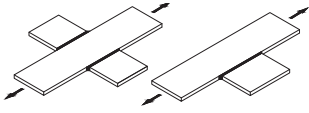
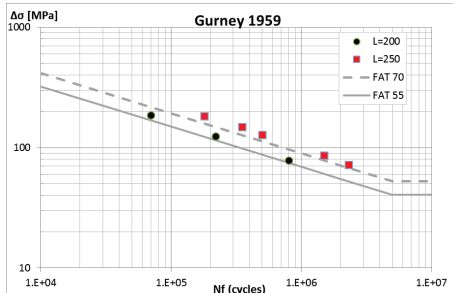
Reference	Symmetric	Non-symmetric	Comparison
Gurney 1959	x	x	
Puchner 1959		x	
Neumann 1966		x	
Hirt 1975		x	
Kim 2008		x	
Kloppel 1960	x		
Gunnert 1963	x		
Harrison 1966	x		
Kramer 1967	x		
Muller 1968	x		
Haibach 1979	x		
Berger 1982	x		
Wagner 1998	x		
Maddox 1999	x		
Woo 2000	x		
Lee 2003	x		
Bae 2004	x		
Choi 2006	x		
Yamada 1982	x		
Yamada 1984	x		
Yamada 1986	x		
Yamada 1989	x		
Yamada 1998	x		
Kondo 2002	x		

Table A.4 – Experimental setups with symmetrical and non-symmetrical specimens

and Ritter, 1982) and (Aygül et al., 2013). However, crack propagation rate is higher on out-of-plane attachments because while the cracks propagate in the main plate, instead of getting out of the stress concentration zone as in the case of in-plane attachments, the fillet weld in the interior part of the attachment increases the stress intensity factor. It can be seen by varying  $W_{attachment}$  to  $\approx 20mm$  in the Stress Intensity Factor derived by (Hobbacher, 1992) that wing plates give higher propagation rates.

(Yamada, 1984) tested out of plane vertical attachments 200mm long and 10mm thick in a 10mm tick main plate 200mm wide. A reduction of 20% in fatigue life was identified when comparing wing plates with in-plane attachments. Stress concentration factors were measured with chainette strain gage and compared to rectangular attachments. Wing plates showed higher stress concentration factors comparing to in-plane attachments with the same length. The collected data for wing plates is plotted against the in-plane FAT 40 curve in figure A.1. The results were obtained in specimens with attachment lengths of 100 and 200m and they are clearly lower than lateral tip attachments.

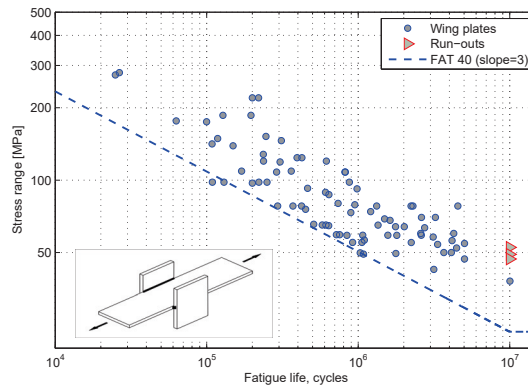


Figure A.1 – S-N curve for “wing plates”

### Discussion of parameters

Fatigue strength of flange tip attachments depends both on the attachment length and the main plate width (Maddox, 2003). The size effect is usually important when the dimension in the crack propagation direction increases which in this case is the width of the main plate. This question was addressed by (Gurney, 1989) where tests on plates with wing plates were compared for four different plate widths, 40, 80, 125 and 200 mm, all other dimensions remaining constant, stress relieved and tested in tension with  $R_\sigma = 0$ . A clear decrease in fatigue strength with the wider main plates was observed, a size effect equivalent to plate thickness in cruciform joints, but in this case depending on the plate width. Gurney suggested  $S = S_B \left(\frac{W_B}{W}\right)^{0,25}$  where  $W_B = 100\text{mm}$  is the basic plate width and  $W' = \min(W, L, 100 \text{ mm})$  where  $L$  is the attachment length.

Hobbacher (1992) showed that the welded length, i.e. the attachment length, has an even greater effect than the width, and the SCF increases with the attachment length  $L$  up to  $(L/W)$  about 2 (Maddox, 2003). The same was later proven by (Xiao and Yamada, 2004) where the fatigue strength were literally seen independent from the main plate width, as soon as  $W > 100\text{mm}$ , which is the usual case in bridges.

The influence of the main plate thickness was studied in (Maddox, 1991) where he concluded that no thickness effect exists. More recently also (Xiao and Yamada, 2004) showed that stress distribution at weld toe is not dependent on the thickness of the main plate and tests in 40, 75 and 100 mm thick plates performed by (Lee et al., 2003) and (Bae, 2004) proved the same.

On the other hand, the thickness of the attachment influences fatigue life. In IIW (2008), if the thickness ( $t_2$ ) of the attachment is smaller than the main plate ( $t_1$ ), the increase in FAT category is estimated in 12%, for any attachment length if  $t_2 < 0,7t_1$ . AASHTO (2002) allows an increase of 37,5%, from Class E' to E, 40 to 55 MPa, depending if the attachment thickness is less than 25mm. Experiments reported by (Lee et al., 2003) have shown that for tests on 40, 75 and 100 mm thick plates with the attachment thickness varying between 16, 24 and 32 mm, fatigue life was seen to decrease with thicker attachments plates, confirming the relative ratio rule from IIW instead of the absolute thickness value of 25 mm from AASHTO (2002). Same conclusions were reported by (Bae, 2004) and (Leander et al., 2013) where stress correction factor  $M_k$  for Stress Intensity Factors were proposed with due account for the relation  $(t_1/t_2)$ .

The attachment length is thus the main geometric factor influencing the fatigue resistance of the detail. Longer attachments allow higher load transfers to the attachment, increasing the stress concentration at the weld toe. For the classification in nominal stress, the size effect may be accounted for by classifying the fatigue resistance based on the attachment length. Results in database can be organized according to the attachment length ( $L_{attachment}$ ), with the FAT categories defined by IIW (2008), figure A.2.

## A.2. Flange tip attachments

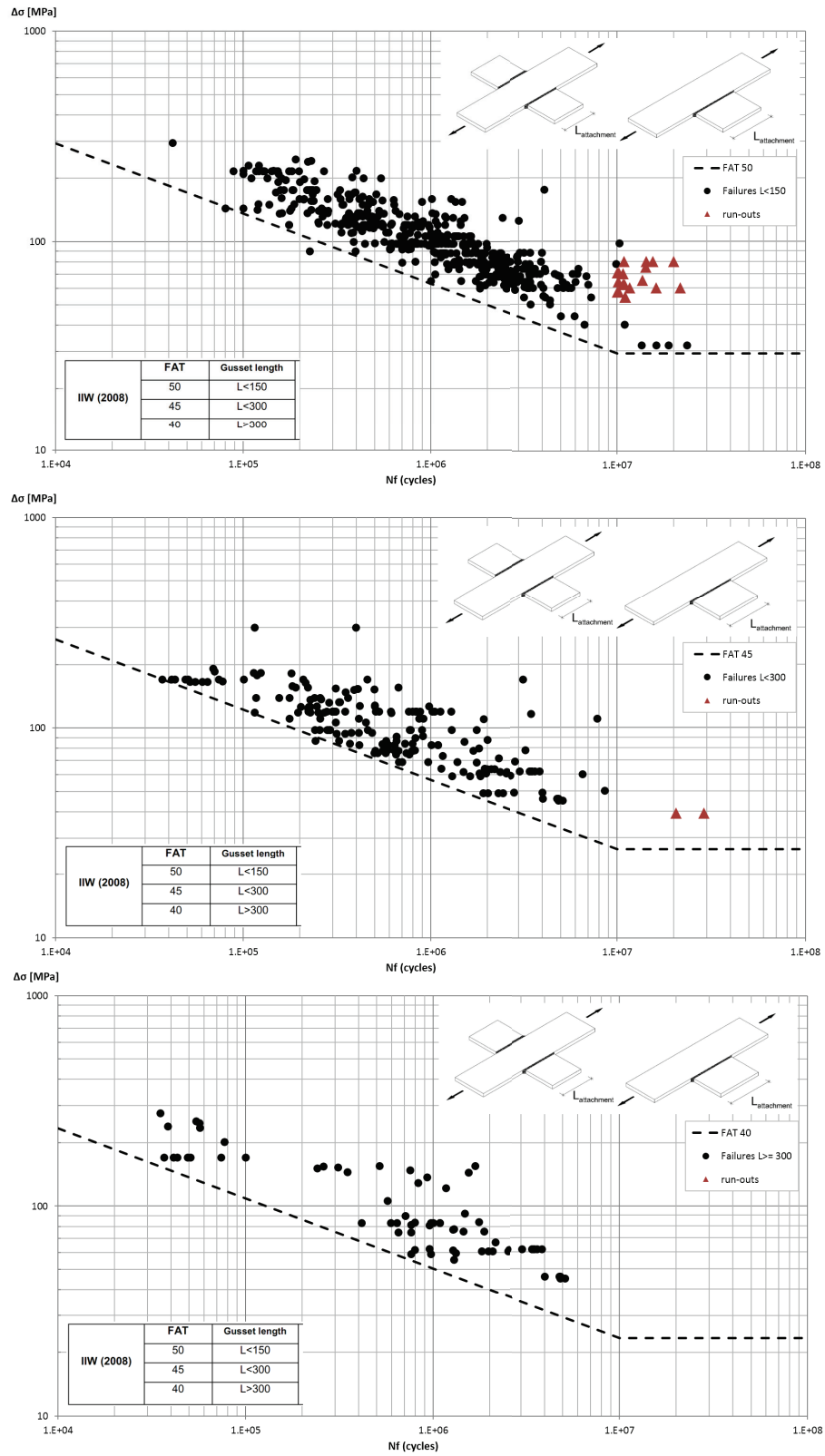


Figure A.2 – S-N curve for flange tip attachments according to IIW

## Appendix A. Uniaxial fatigue database

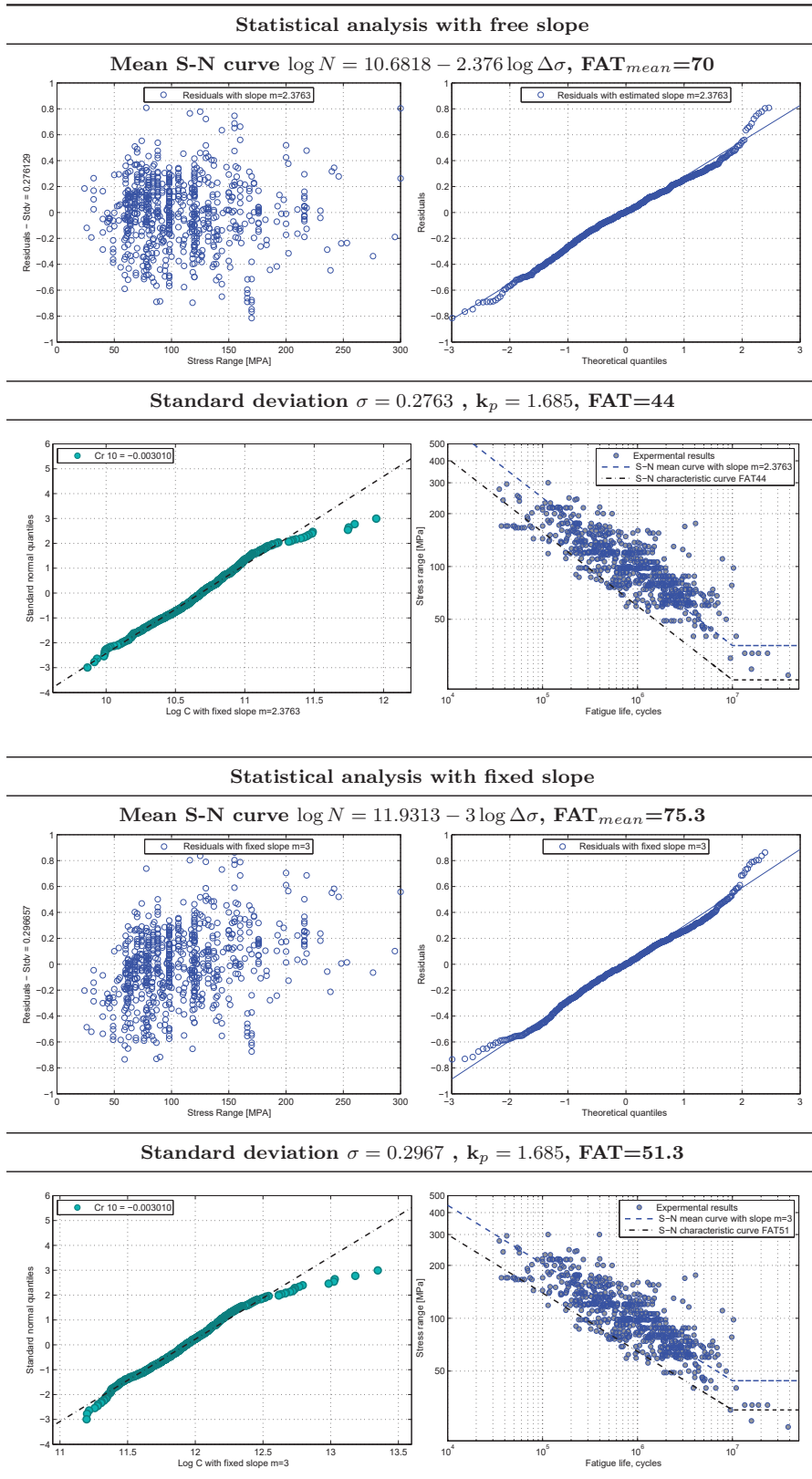


Figure A.3 – Statistical analysis of rectangular flange tip attachments



#### Recommendations

The statistical analysis for the flange tip attachments allows to define them as FAT50. Eurocode 3 classification FAT40 is not justified by tests and was probably set by inspection or using  $k_p = 2$  standard deviations while our database with a sample size  $n = 721$  allows for  $k_p = 1,685$ . Note that in this case the CAFL is defined at  $10 \cdot 10^6$  cycles.

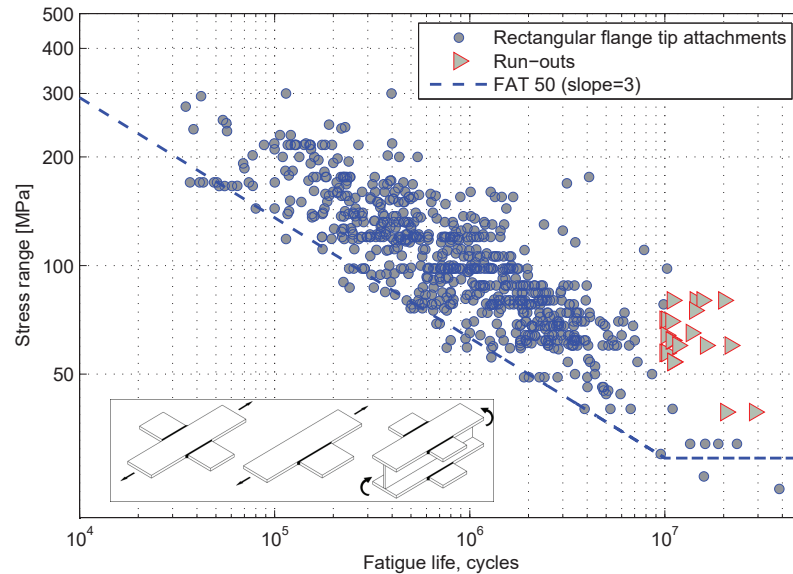


Figure A.4 – FAT classification for rectangular flange tip attachments

### A.3 Flange tip attachments with transition radius

The classification based on the R/W ratio dependence was proposed with the drafting of the European Fatigue Recommendations (ECCS, 1985). The beneficial effect of a smooth transition radius between the lateral attachment and the tip of the main plate is recognised in the fatigue classification of the Fatigue Design Codes, table A.5.

The fatigue results collected from literature are plotted with the Eurocode 3 classification in figure A.5. The plot for FAT 90 with  $R/W > 1/3$  includes plates with transition radius of 40, 70, 100 and 150 mm.

The analysis of the database shows that no real improvement can be achieved by small shaping of the attachment or by grinding the sealing fillet weld of a rectangular attachment. The minimum radius to allow an increase on the FAT category should be fixed at 50 mm.

Fatigue tests reported by (Shimokawa et al., 1985) on thick plates, 30 and 45 mm, with large attachments, 280 and 380mm, having transition radius of 15, 40 and 60 mm showed that no life improvement was achievable with transition radius smaller than 60 mm. Also

## Appendix A. Uniaxial fatigue database

Standard	FAT	Geometrical conditions	Detail
Eurocode 3 (2005)	90	$R/W \geq 1/3$ or $R \geq 150\text{mm}$	
	71	$1/6 \leq R/W < 1/3$	
	50	$R/W < 1/6$ (*)	
IIW (2013)	90	$R/W > 1/3$	
	71	$1/6 \leq R/W < 1/3$	
	50	$R/W < 1/6$	

(\*)  $R \geq 50$  mm should be specified

Table A.5 – FAT classification for “Flange Tip Attachments with Transition Radius”

Yamada and Hirt (1982) conducted tests on I beams with rounded attachments and results with transition radius of 10 and 50mm showed no significant improvement.

The lack of good shape and removal of weld toe imperfections is also the main reason why no improvement can be achieved with tapered attachments because the weld toe and its imperfections are not eliminated. The experimental programs that have tried to investigate the beneficial effect of a tapered transition between the lateral attachment and the main plate showed that no significant difference was achieved when comparing tests on rectangular and tapered attachments (Puchner, 1959), (Haibach, 1979), (Comeau and Kulak, 1979).

The effect of shaping the attachment weld toe is very small unless the weld toe is also completely grounded removing the weld toe concentration and most important his imperfections. This was shown by (Gurney, 1993) with experiments in specimens with three different shapes of the sealing fillet weld: (1) as-welded; (2) grounded to a 15 mm radius with the weld ending almost tangential to the stressed plate but without completely removing the weld toe; and (3) grounded to a 15 mm radius with the grinding continuing to a depth of around 0,5 mm into the edge of the main plate completely removing the weld toe and his inherent weld imperfections. Only the specimens where the grinding completely removed the weld toe and smoothed on the main plate edge, showed some improved fatigue life, figure A.6.

The same was shown by (Fisher et al., 1980) where rectangular attachment classified in AASHTO (2002) Category E could be improved to Category D by simply grinding the ends of groove welded flange attachment.

A series of tests in as-welded specimens with the weld toe grounded to a radius of 3 mm were performed by (Yamada, 1987), enough to remove weld toe imperfections, but no improvement on fatigue life could be seen. Another batch with the sealing fillet weld ground had been tested before and the same conclusion could be drawn (Yamada, 1984).

### A.3. Flange tip attachments with transition radius

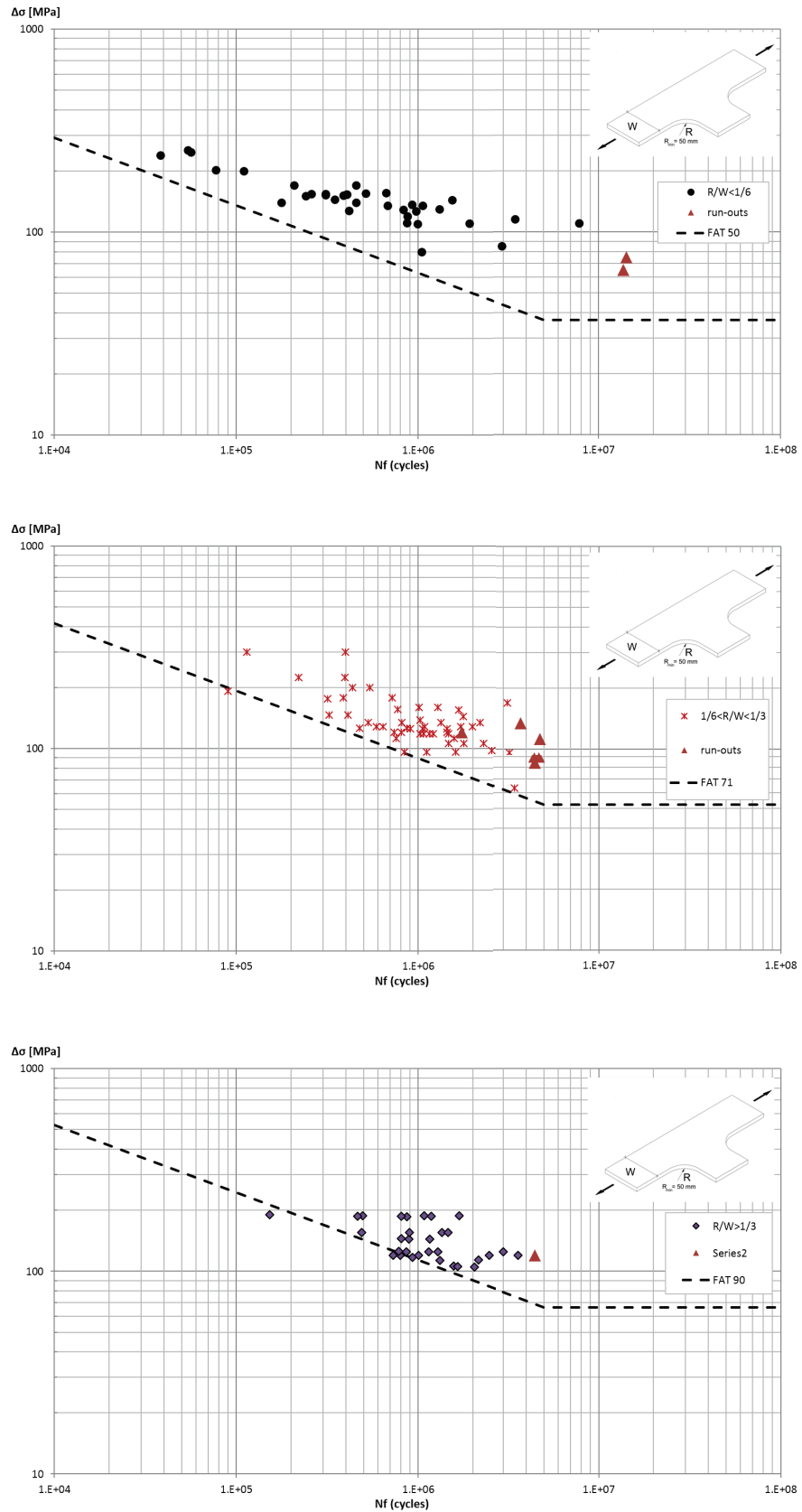


Figure A.5 – S-N curve for flange tip attachments with transition radius 209

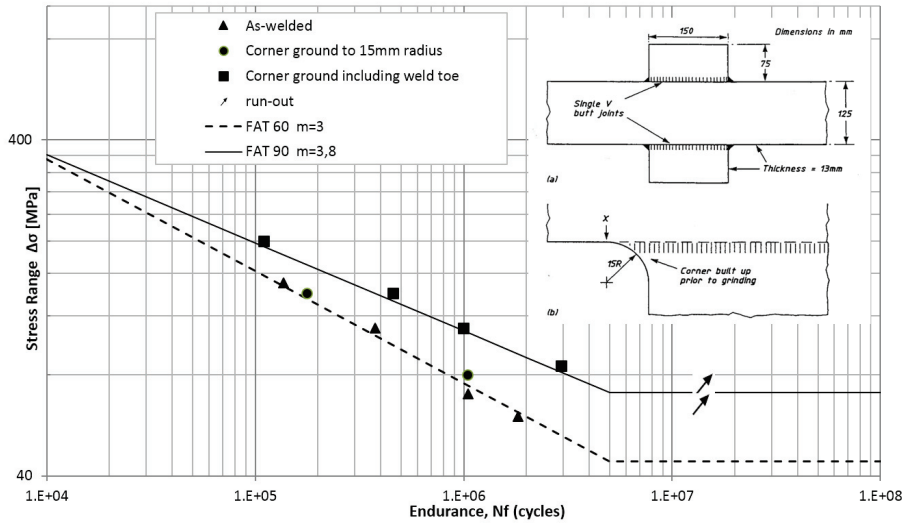


Figure A.6 – Tests with grounded 15mm transition radius (Gurney, 1993)

The effects of grinding can even be unfavorable, as reported in cases where sub-surface defects appear on the surface after grinding (Miki, 2010), (Keating and Fisher, 1986). In the test battery performed by (Daniels et al., 1980) in groove welded attachments with a 150 mm transitions radius, three of eight failed specimens were found to have large imperfections near the point of tangency, internal discontinuities from the weld that were brought to surface with the grinding.

### Statistical analysis

The stress concentration factor (SCF) for lateral attachments with transition radius was derived in (Zettlemyer and Fisher, 1978) with geometric definitions of table A.5:

$$SCF = -1,115 \log \frac{R}{W} + 0,5370 \log \frac{L}{W} + 0,1384 \log \frac{W_a}{W} + 0,2848 \frac{t_a}{t_f} + 0,6881 \quad (A.1)$$

$$M_k = \frac{1,16}{1,16 + \alpha^{0,6}} \times SCF \quad \text{and} \quad \alpha = \frac{a_i}{W}$$

Fracture mechanics calculations are carried out with some geometrical ratios from equation A.1 fixed. The influence of the thickness ratio is maximum for  $\frac{t_a}{t_f} = 1$ , values of  $t_a > t_f$  being un-realistic. The attachment to flange width ratio is considered as  $\frac{W_a}{W_f} = 1$  and the attachment length to flange width ratio  $\frac{L}{W} = 3$ . Figure A.7 shows that fatigue strength at  $2 \cdot 10^6$  cycles cannot be translated into an absolute radius value R, because strong differences in strength are obtained by varying the plate width. The values were obtained adopting lower bound values  $C = 1,85 \cdot 10^{-13}$  and  $m=3$  in Paris Law. Fatigue results are plotted according to the R/W ratio, and a good agreement is obtained with the characteristic lower bound values of C in the Paris Law and  $a_i = 0,1$ . A simplified FAT category may be defined, by fitting the characteristic value of each test

batch performed at a defined R/W ratio. Note that Eurocode 3 classifies rectangular attachments up to  $R \leq 50\text{mm}$  as FAT40, which is incoherent for small radius because there is a jump from FAT40 to FAT50.

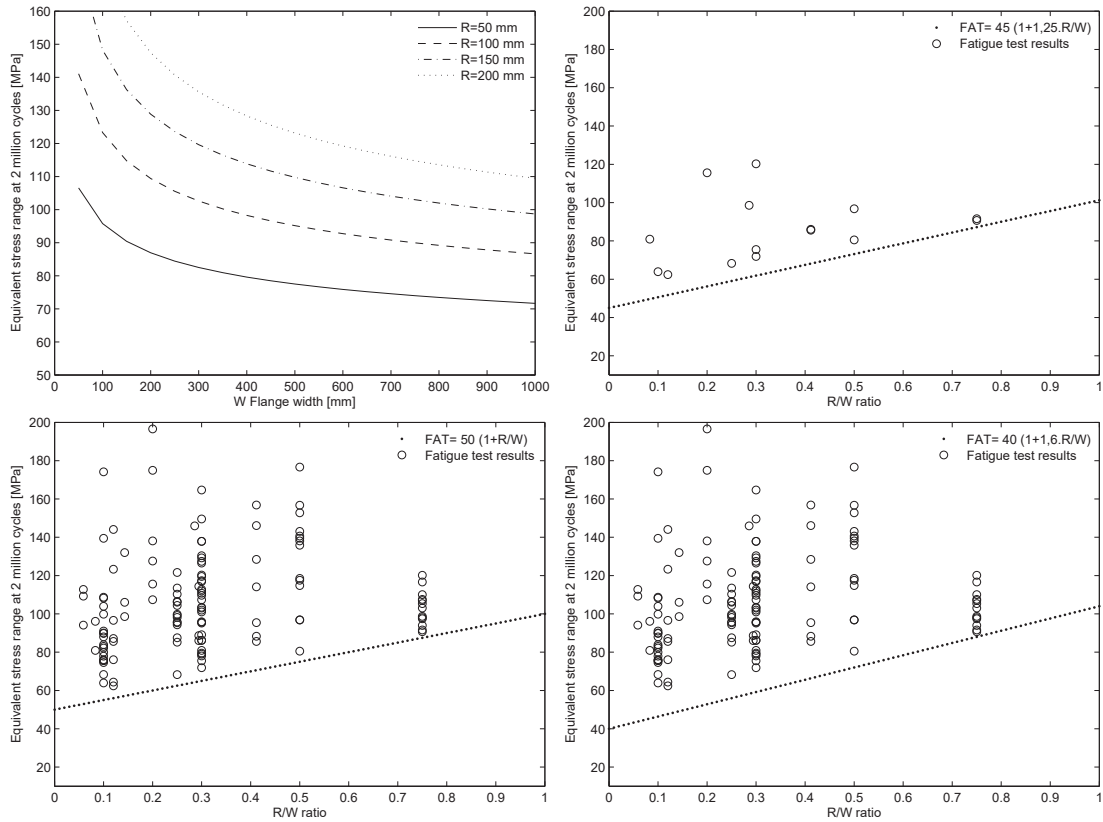


Figure A.7 – FAT category, influence of geometry on SCF and comparison with tests

## A.4 Transversal attachments

Non-load carrying fillet welds, a typical case of transversal attachments, figure A.8, is a detail with wide-spread use and considerable experimental data exists in literature.

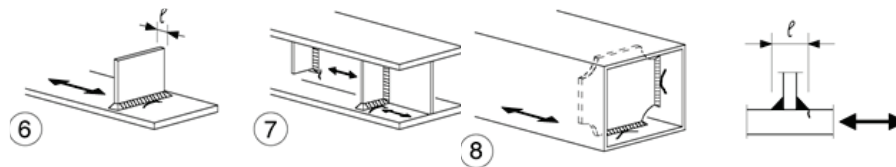


Figure A.8 – Typical details with transversal attachments (EN 1993 1-9, 2005)

Several databases and reviews for experimental results in transversal attachments can be found, (Gurney and Maddox, 1973) and (Olivier and Ritter, 1980). Some of the datasets used are described below. Our database is summarised in table A.6.

## Appendix A. Uniaxial fatigue database

Reference	Main plate thickness [mm]	EC3 Size factor [mm]	Stress ratio $R_\sigma$	N° of tests
Klöppel 1957	14	33,6	-1 , -0,5	15
Weck 1958	19	45,6	0	12
Gurney 1960	12,7	25,4	0.0-0.07	18
Navrotskii 1963	12	28,8	0.2-0.3	25
Ostermann 1965	12	28,8	(-)1-0	86
Harrison 1965 b	12,7	28,58	0	13
Wintergerst 1966	14	34-100	(-)1-0.5	104
Haibach 1966	10	24	(-)1-0.33	149
Gönnel 1967	14	33,6	0,1	28
Caracostea 1967			(-)1-0	73
Friis 1968	20	48	0,1	8
Haibach 1968	10	24	(-)1-0	166
Caracostea 1970			(-)1-0.2	90
Frank 1971	15,88	41,28	0.18-0.40	21
Odegard 1970	20	48	0,1	24
Mummery 1971	12	28,8	0	38
Disselmeyer 1973	10	24	0	117
N. N. 1975	12	28,8	(-)1-0.83	482
Lieurade 1975	12	28,8	0	55
EUR 5357 e 1975	11.0-13.0	25-27	(-)1-0.52	266
Ikedo 1976	15	36	(-)1-0.6	27
Bargel 1976	14	33,6	0.06-0.30	162
Knight 1977	12,5	30	0	93
Minner 1977, 1978, 1979	12	28,6	(-)3-0.8	726
Maddox 1987	13-100	26-82	0	40
Haibach 1980	10	24	-1	29
Gurney 1991	13-100	13-250	0	144
Gurney 1992	13-25	23-58	0	22
Ohta 1994	20-40	67.3-134.7	0-0.83	20
Kihl Sarkani 1997	6.0-25.0	10.7-43.5	-1	94
Kihl Sarkani 1999	11,1	16,32	0 - 0.82	65
Yamada 2004 (multiAxial)	9	22,1		27
Yamada 2004				52

Table A.6 – Database of literature tests on transversal attachments

Gurney presented an interesting study on transversal attachments, (Gurney, 1960), with tests both on plates and beams, having similar welded attachments. He concluded that tests on plates with welded attachments lead to the same results than tests on beams with similar welding details. An extensive analysis was presented in (Gurney, 1991) to investigate the size effect of the detail on plates with thickness varying from 13 to 100 mm, yield stress values ranging between 290-405 MPa and stress ratio maintained at zero. The loading conditions were axial and 4 point bending both in as-welded and stress relieved specimens. Fatigue strength of transverse non-load carrying fillet welds was shown dependent both on the thickness of the main plate and on the toe-to-toe width of the attachment. Under axial loading, the fatigue strength of a plate with a given thickness ( $t$ ) decreases with increasing toe-to-toe length ( $l$ ) up to  $l=2t$ , figure A.8. Further increases in the toe-to-toe length ( $l$ ) produced no further reduction.

Maddox (1987) carried out tests to investigate the effect of plate thickness varying ( $t$ ) between 13, 50 and 100 mm, yield strength from 360 to 630 MPa, in both as-welded and

stress relieved state. For the 13 mm thick reference tests, as-welded and stress relieved gave similar fatigue strength, higher than the 50 and 100mm thick specimens. As-welded joints in 50 and 100mm plates gave lower fatigue strength than stress-relieved ones.

The thickness effect is specified in the Offshore industry based on correlations as figure A.9, that shows fatigue data at  $2 \cdot 10^6$  cycles for equal plate and attachment thickness.

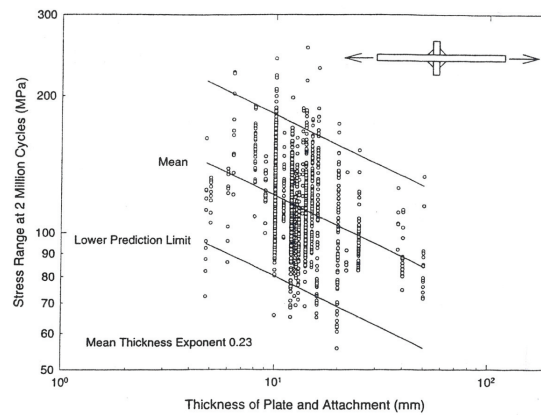


Figure A.9 – Thickness effect on offshore design after Gordon et al. (1997)

The effect is not considered in EN 1993 1-9 (2005) due to the weak correlation between the thickness and the fatigue life. Haibach presented several experimental studies on this detail, reviewed and presented in (Olivier and Ritter, 1980). One of the experimental sets presents 123 tests at the same stress level  $\Delta\sigma = 354\text{MPa}$ . Kihl and Sarkani (1997) carried out tests to determine the thickness effect in high strength steel (HSLA-80) at different thickness between 6 and 25 mm. They concluded that results were relatively insensitive to thickness effects with 94 tests at 4 different stress levels. By mixing these 2 datasets, a subset of 217 results at 5 different stress levels is obtained, figure A.10.

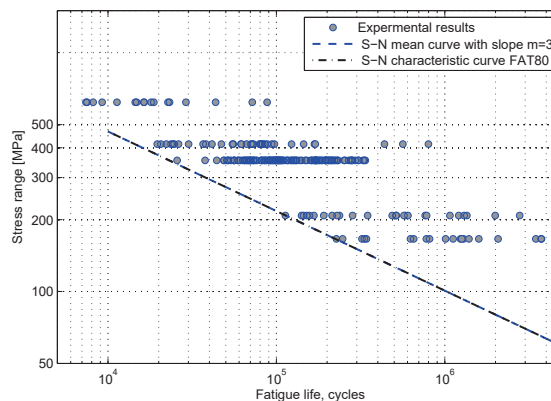


Figure A.10 – Datasets with results at the five different stress range level

This sub-set of data can be used to check the assumption of normality of the  $\log N$  data. As can be seen four out of five levels can be assumed to follow a normal distribution,

# Appendix A. Uniaxial fatigue database

with a confidence of 10% on the goodness of fit for  $Cr \geq 0$ , figure A.11.

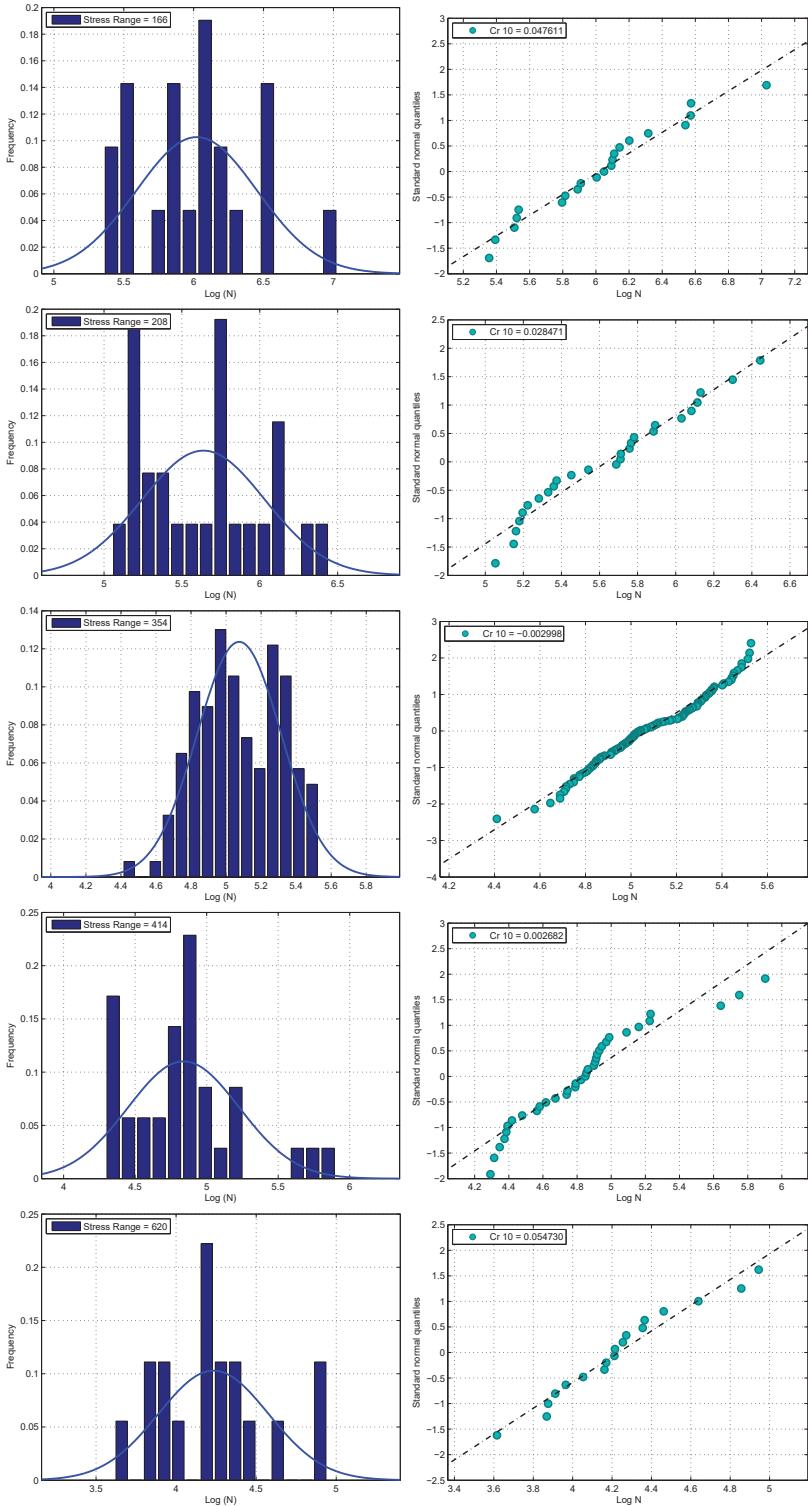


Figure A.11 – Normality of fatigue tests on transversal attachments



Out of 3100 failure points in the database, 985 were performed at  $R_\sigma < 0$ , figure A.12. The linear regression with fixed slope ( $m=3$ ) for the failures at  $R_\sigma \geq 0$  gives FAT76.

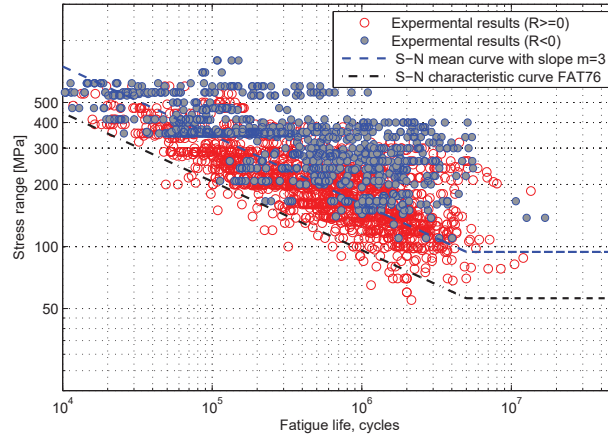


Figure A.12 – Experimental results for transversal attachments by  $R_\sigma$  ratio

Kihl and Sarkani (1999) investigated the mean stress effect with constant amplitude tests at zero and non zero mean stress. Tests indicated the modified Goodman equation to be generally conservative at low tensile stress and the Gerber correction to be suited at high tensile stress levels. Under compression mean stress, none of the relationships proved accurate and the stress range approach without mean stress consideration was conservative. Ohta et al. (1994) carried out test on plates 20 and 40 mm thick, yield stress  $f_y$  between 364 and 397 MPa and  $R_\sigma=0$  with  $\sigma_{max} = f_y$ . Fatigue strength stress range  $\Delta\sigma + \sigma_{res} < f_y$  was higher than  $\Delta\sigma + \sigma_{res} > f_y$

For the definition of the characteristic FAT, only failures at  $R_\sigma \geq 0$  are considered. The classification in EN 1993 1-9 (2005) is FAT80 for  $l < 50$  and FAT71 for  $50 \leq l \leq 80$ . There is no experimental data to justify this classification, so the size factor distinction is made here for  $l=80$ mm. The statistical analysis done for the two cases of size factor for  $l \leq 80$  figure A.14 and  $l > 80$  figure A.15, classified FAT80 and FAT56 respectively, figure A.13.

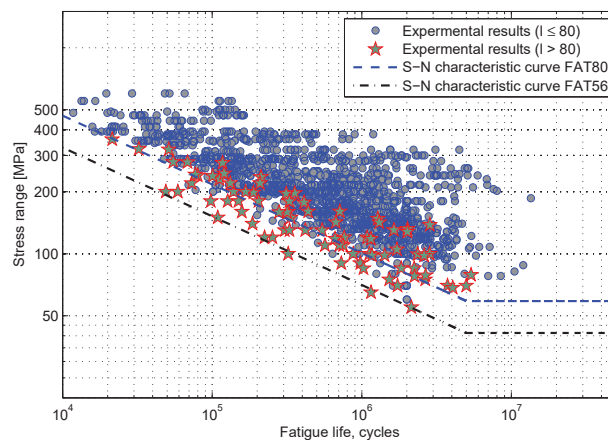
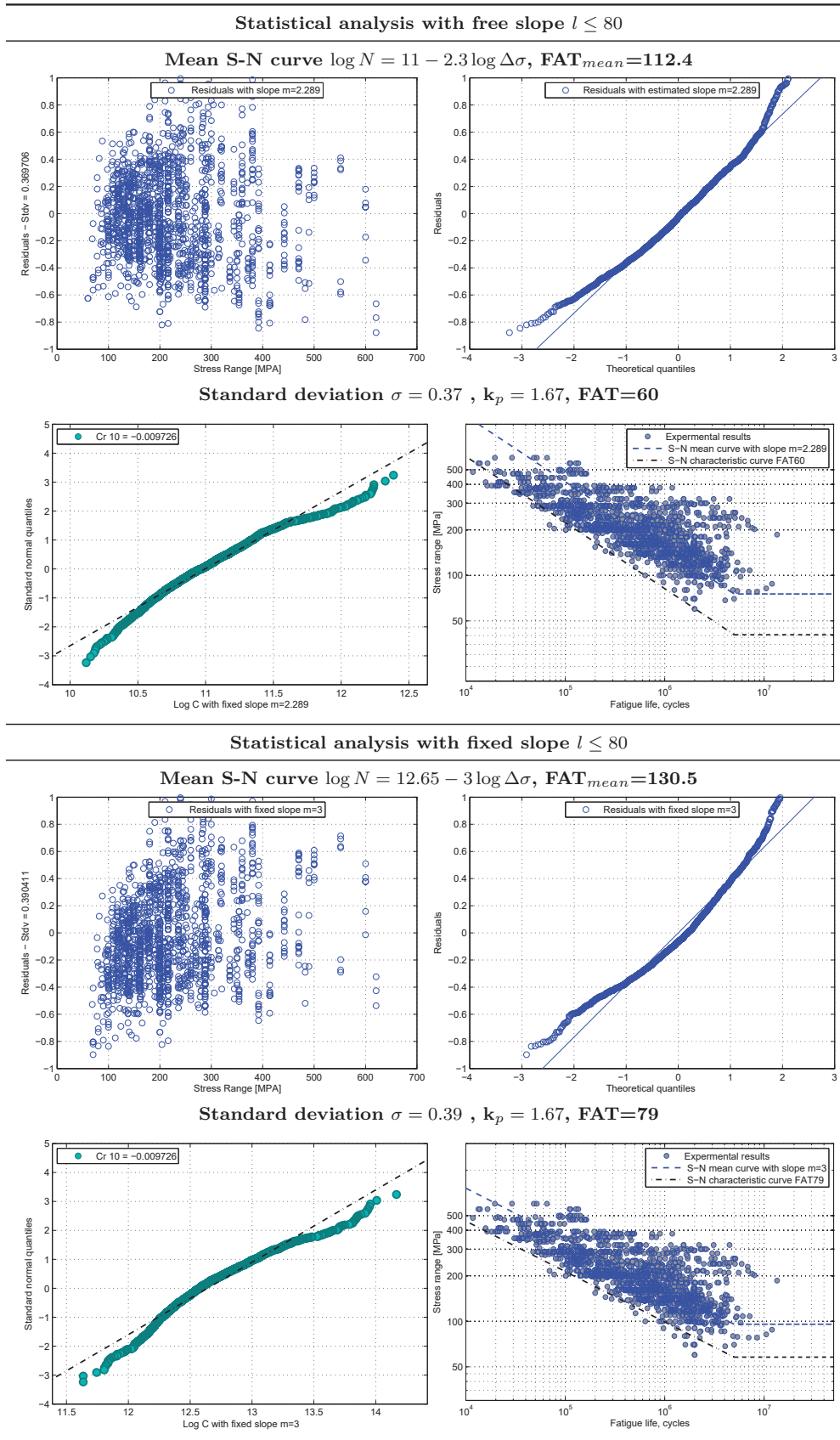


Figure A.13 – FAT classification for transversal attachments

## Appendix A. Uniaxial fatigue database



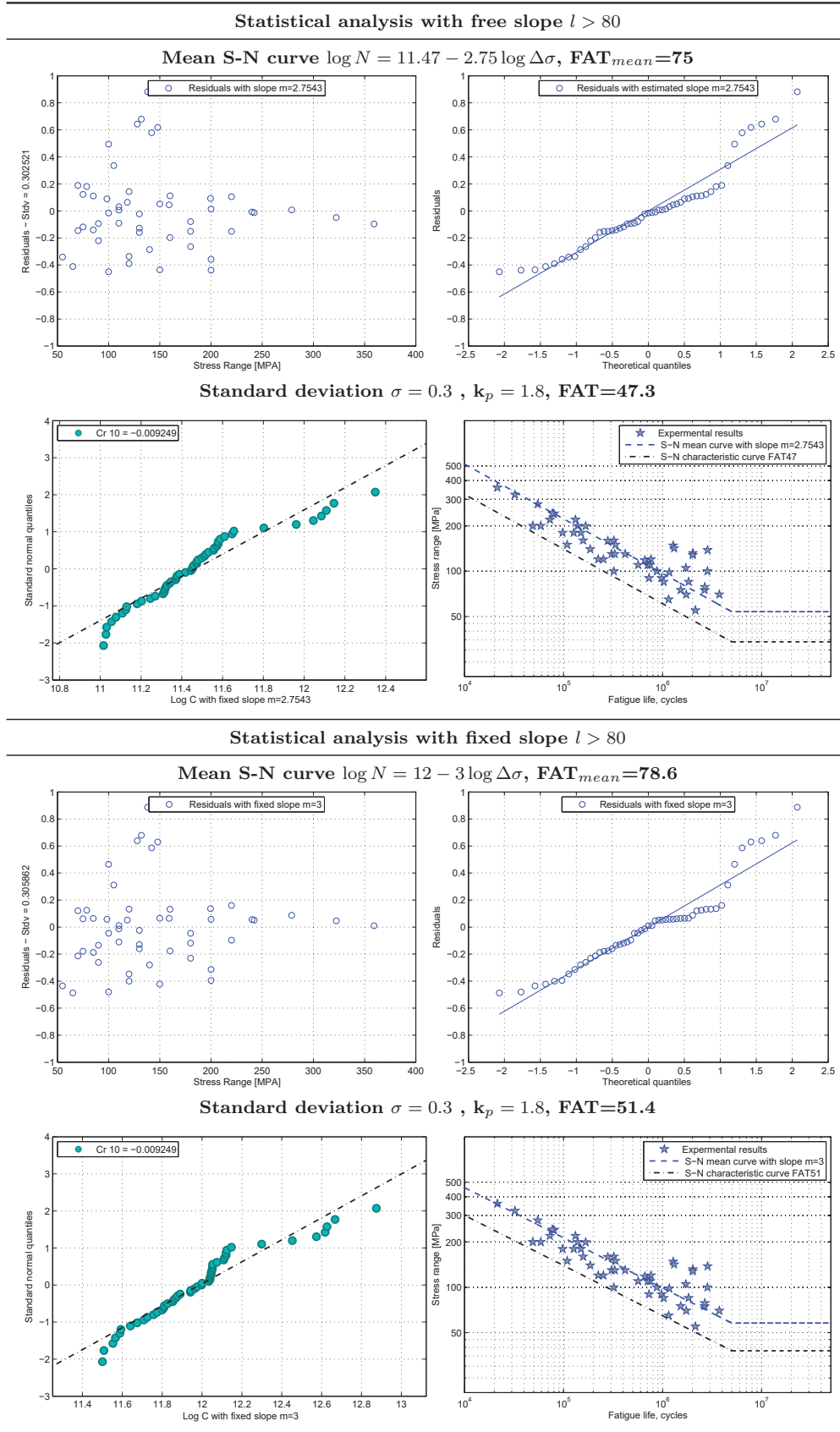


Figure A.15 – Statistical analysis of transversal attachments ( $l > 80$ )

### A.5 Longitudinal attachments

The database for longitudinal attachments includes 798 experimental results with 35 runouts that are not considered valid not taken into account: The experimental results considered in our database are summarised in table A.7.

Reference	Main plate thickness [mm]	EC3 Size factor [mm]	Stress ratio $R_\sigma$	N <sup>o</sup> of tests
Weck 1958	19	100	0	18
Gurney 1960	12,7	157,5	0	18
Gurney 1962	12,7-25	152,5	0	63
Gurney 1966	12,7	152,5	0	58
Maddox 1974	12,7	152	0	18
Booth 1978	25-38	150	(-)1-0	43
BWJ 1968	12,7	152,4	(-)1-0	80
Gurney 1970	12,7	152,4	(-)1-0,33	54
Gurney 1970a	12,7	152,4	0	15
Hirt 1975	12	50-100-200	0	16
Tilly 1980	12,7	150	0	14
Yamada 1980	10	100	0	32
Sperle 1980	15	150	0	39
Berge 1981	12	150	(-)1-0	60
Mang 1982		200	0,1	20
Mang 1982 a	8	50	0,1-0,5	19
Berger 1982		150	(-)1-0,5	25
Castiglioni 1988	20	100-200	0,1	8
Hirt 1992	20	100-200	0,1	6
Bogren 1993	12	140	0	19
Dimitrakis 2001	13	140	0,1	14
Choi 2005	10	150	0,1	18
Chen 2012	8	100	0,1	5
Kim 2008	10	150	0.04-0.13	19
Maddox 2008	30	230	0,7	3
Ting 2009	8	50	(-)1-0.45	54
Mori 2012	12	110	0-0.5	17
Hansel 2012	12	150	-1	36
Baumgartner 2013	12	150	(-)1-0	31

Table A.7 – Database for fatigue experiments in longitudinal attachments

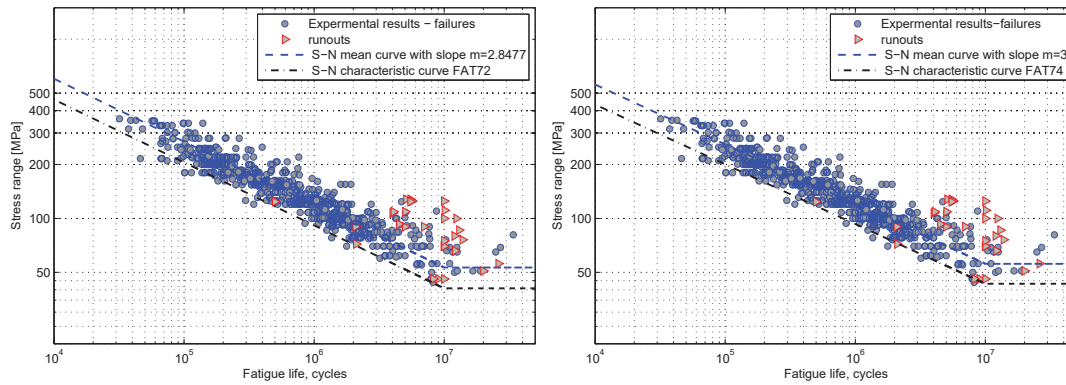


Figure A.16 – General plot for the database of longitudinal attachments

Discussion of parameters

An overview of the results is shown in figure A.16. One can immediately see by inspection that: 1) the slope of the S-N line is very close to 3; 2) several failures are reported after  $5 \cdot 10^6$  cycles; 3) the knee-point of the S-N curve is consistent at  $10 \cdot 10^6$  cycles; 4) long attachments could be classified as FAT74 regardless of the attachment length.

Stress ratio has little influence on the endurance expressed by stress range. The values for positive or negative stress ratios obtained by several individual studies are generally inside the same scatter band (Booth, 1978). This can be seen in our database. Considering the slope fixed to 3, a regression analysis gives FAT75 accounting only for  $R_\sigma \geq 0$ , figure A.17, the same as obtained when considering also negative stress ratios, figure A.16

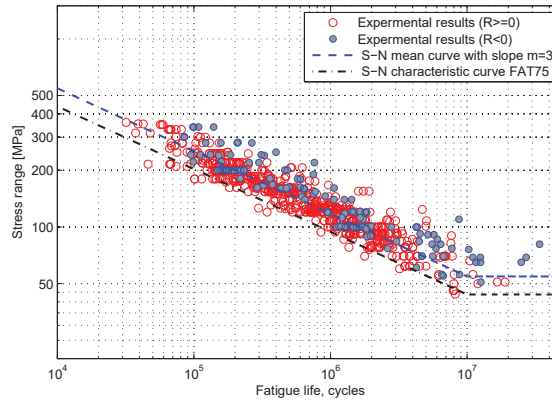


Figure A.17 – Longitudinal attachments distinguished by R ratio

As for the classification of tapered attachments, the few experimental results in literature generally found no increase in endurance compared to the rectangular ones (Hirt, M. A., Crisinel, 1975), (Booth, 1978). The endurance of trapezoidal stiffeners is similar to rectangular ones with the same length, figure A.18.

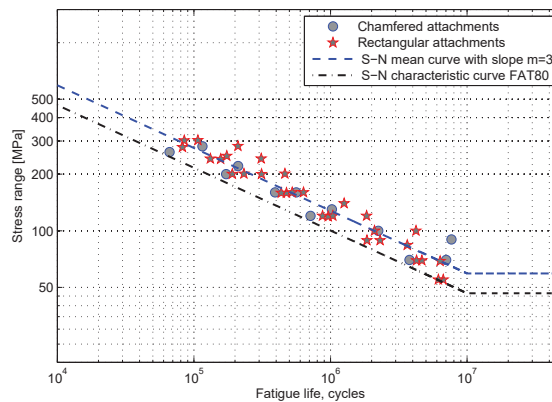


Figure A.18 – Longitudinal attachments with tapered transition

## Appendix A. Uniaxial fatigue database

The chamfer results in a very small redistribution of stress corresponding to the removal of the corners of a rectangular attachment. The stress concentration at the fillet weld end controls fatigue behaviour and tends to be independent from the stiffener chamfer because weld toes remain as-welded in both solutions.

Distinction is made in Eurocode for attachment with a round transition and weld toe flush grounded with the attachment tip. Results for this type of detail were produced at ICOM (Imhof et al., 2001) and are shown in figure A.19. Few failures were obtained and in this case linear regression is done considering also runouts. A characteristic FAT100 is obtained and shown also is the FAT80 recommended by Eurocode which should be maintained due to the lack of results to allow a consistent re-classification.

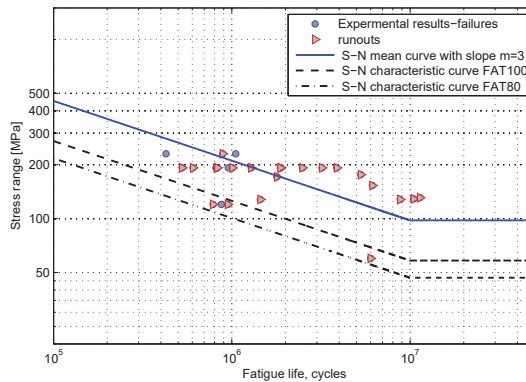


Figure A.19 – Longitudinal attachments with rounded transition

The attachment length has been shown to be the main parameter. However, the division adopted in Eurocode 3 seems rather exaggerated and not supported in a sound experimental basis. We divide thus the FAT categories according to attachments lengths bigger or smaller than 100mm, figure A.20, and present the statistical analysis on this basis. Figures A.21 and A.22 show the statistical analysis for failures at any  $R_\sigma$  and size factor  $L_{attachment} \leq 100$  (FAT80),  $L_{attachment} > 100$  (FAT71).

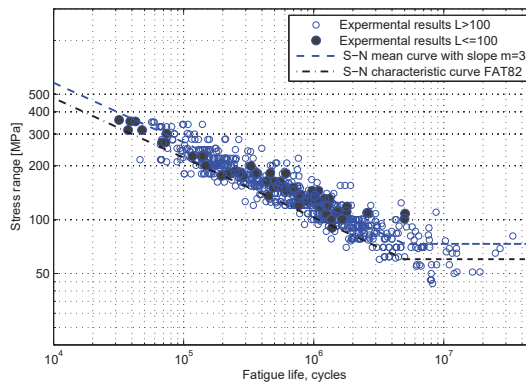


Figure A.20 – Longitudinal attachments distinguished by attachment length

## A.5. Longitudinal attachments

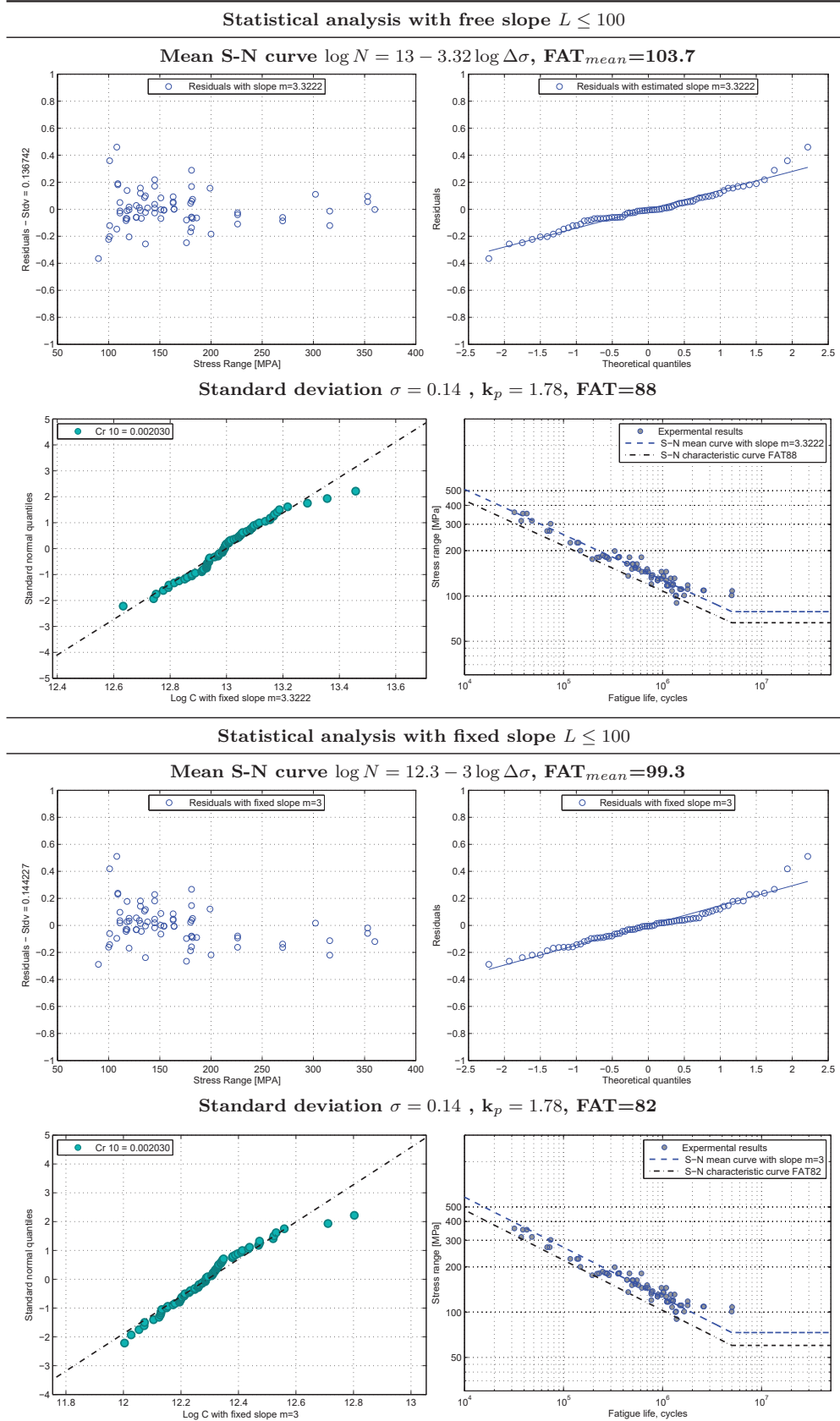
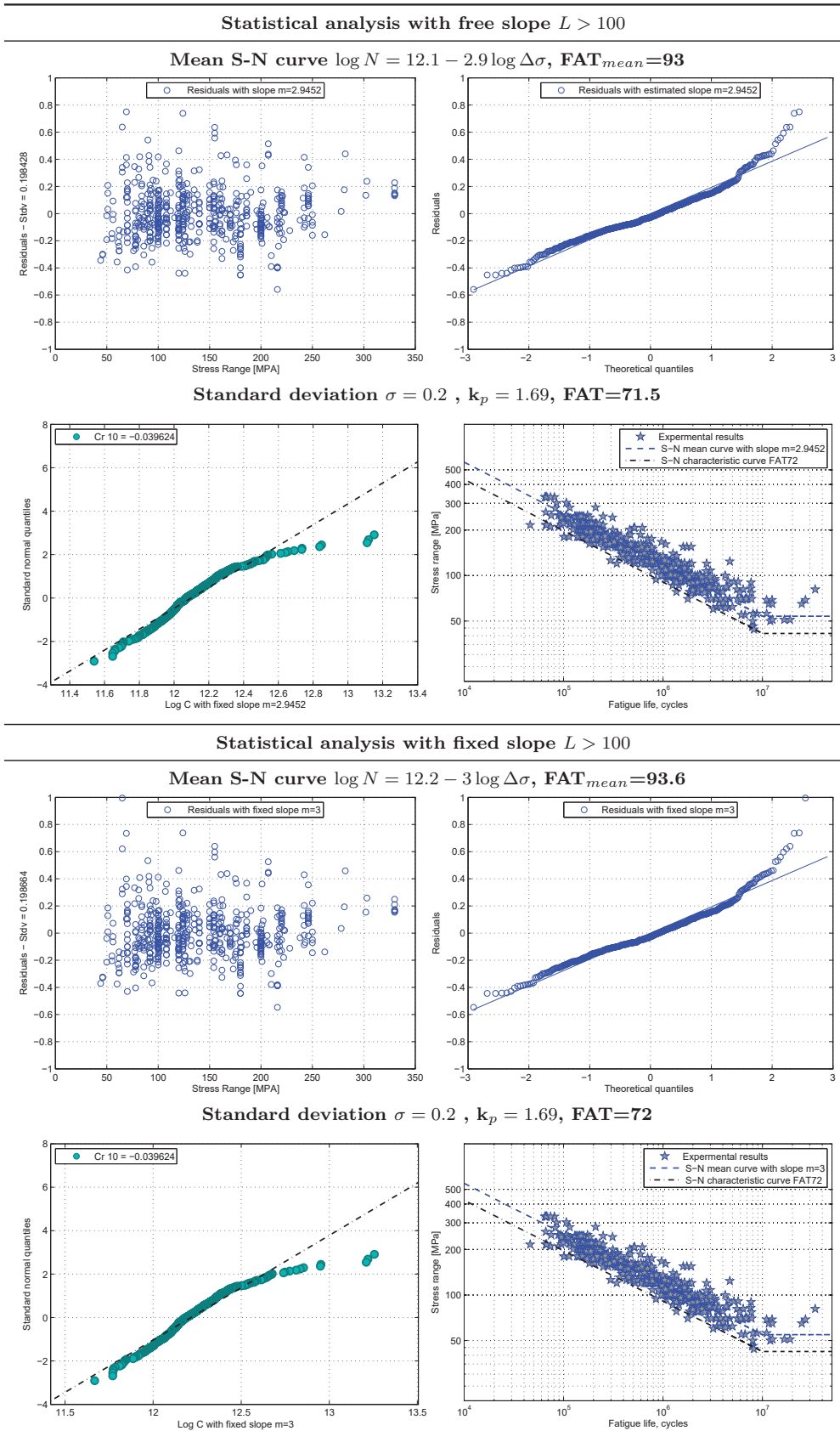


Figure A.21 – Statistical analysis of longitudinal attachments ( $L_{attach} \leq 100$ ) 221



# Appendix A. Uniaxial fatigue database



222 Figure A.22 – Statistical analysis of longitudinal attachments ( $L_{attach} > 100$ )



## A.6 Shear

Fatigue endurance of welds under shear has typically been tested on circular tubes, welded to an end flange and loaded in torsion. The most complete and coherent dataset, carried out explicitly to define the nominal shear endurance was presented by (Bohme et al., 1981), (Seeger and Olivier, 1987) and (Olivier and Seeger, 1992). Their experimental setup used circular tubes, welded on both extremities to an end plate, with fillet or half-V butt welds, and a torque applied to the end plate, figure A.23.

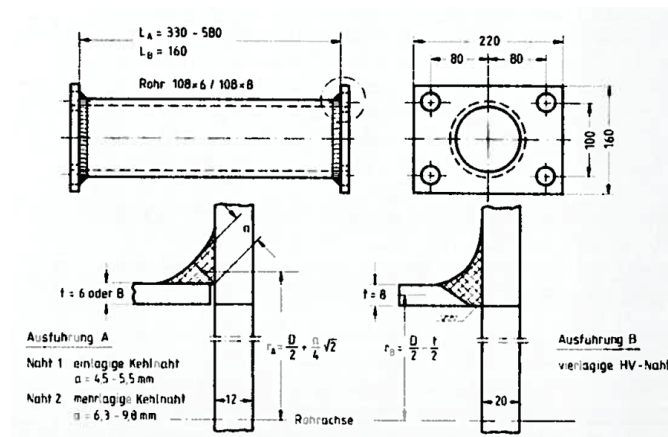


Figure A.23 – Experimental setup for tubes under pure shear (Seeger and Olivier, 1987)

Many experiments reported in literature used the same setup as figure A.23 in experimental campaigns under multiaxial fatigue. Their reference pure shear tests are included. These results are analysed in Appendix B. The authors included in the shear database are: (Yung and Lawrence, 1986), (Siljander et al., 1992), Razmjoo (1996), (Sonsino et al., 1999), (Amstutz et al., 2001), (Yousefi et al., 2001) and (Lotsberg, 2009). Recent tests on circular cold drawn seamless tubes welded to end plates in torsion were reported by Barsoum (2008) and are also included. The residual stresses were measured experimentally by saw cutting and X-ray diffraction and tensile residual stresses were found at the weld toe and compressive at the weld root.

Very few experimental results were found for shear in welded plates. Again, some data can be found on multiaxial fatigue setups reported in literature, see details in Appendix B. Dahle et al. (1997) presented tests on box beams under torsion. These produced longitudinal cracks (L) in the fillet weld between the flange and the web, starting at the root, figure B.4. Multiaxial tests on welded box beams with two longitudinal attachments were reported by Archer (1987). The shear tests are shown in figure B.2. These tests on plate specimens are not include because they are not directly comparable.

The statistical analysis is shown in figure A.24. Although EN 1993 1-9 (2005) classifies shear on welds at FAT80 for welded plates, the re-analysis supports an update to FAT100. The non-existence of a CAFL up to  $100 \cdot 10^6$  cycles is confirmed by experimental results.

# Appendix A. Uniaxial fatigue database

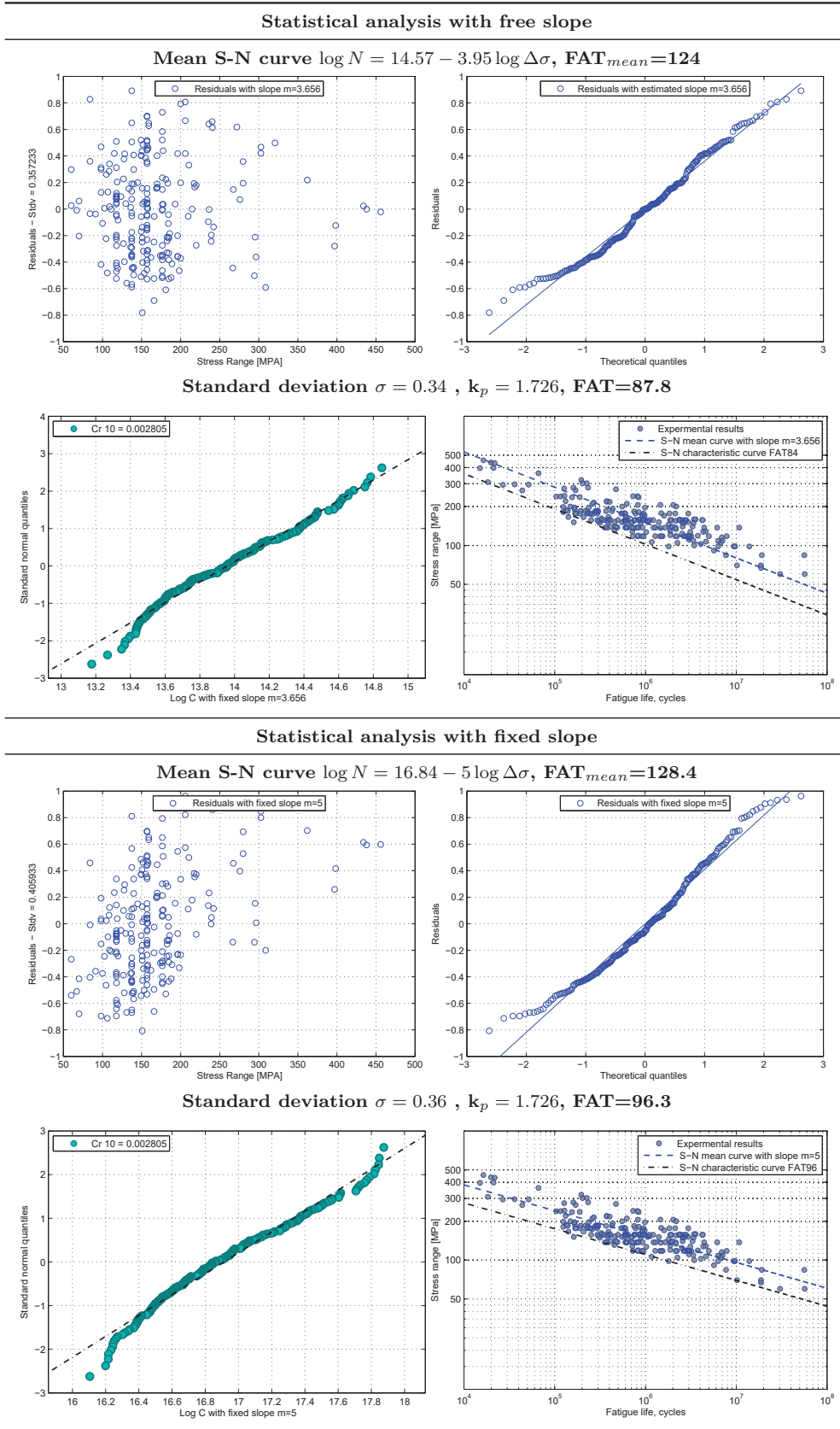


Figure A.24 – Statistical analysis of shear in tubes

## A.7 Plates with holes

Plates with holes are classified in Eurocode 3 as FAT 90 for the net cross-section nominal stress,  $\Delta\sigma_{net} = \Delta\sigma_{gross}(w/(w-d))$  where  $w$  is the plate width and  $d$  is the hole diameter. This classification is based on 3 sets of results (Mang et al., 1991), (JSSC, 1995), (Valtinat and Huhn, 2003), see (Sedlacek et al., 2003), without any requirements for the quality of the hole edges. Our re-analysis shows this FAT category to be non-conservative and that fatigue strength is highly dependent on the execution quality of the hole. They can be classified into two detail categories, FAT 71 and FAT 90.

The analysis was extended to the characterisation of the notch resistance to use in finite element models with local approaches such as the “notch stress method”. Two values of characteristic notch stress were proposed, FAT170 and FAT225, dependent on the hole edge quality. Details of this re-analysis are reported in (Baptista and Nussbaumer, 2014).

The fatigue tests collected from literature were carefully selected, limiting the scope to experiments on typical bridge steels. Only tests in plates under axial loading with the fabrication method and crack path clearly specified were considered. The database with a total of 491 fatigue results is considered suited for an analysis in the scope of Eurocode 3, because it represents a variety of steel types and working methods. An overview of the test data considered is given in table A.8 where out of a total of 491 fatigue results, 67 are “run-outs” not considered in the regression analysis.

Table A.8 – Database for fatigue experiments in plates with holes

Reference	Steel	Thickness [mm]	Diameter of hole [mm]	Hole method	N° of tests
Kloppel and Weihermuller (1960)	St52	14	17.0	Drilled	38
Gurney (1965)	BS15, BS968 QT	13	3.2	Reamed	31
Haibach (1975)	Fe355, Fe460	12	12.1	Reamed	134
Mang et al. (1991)	St37, St52, StE690	12, 20, 30	20-25	Flame, Plasma	79
JSSC (1995)				Drilled	37
Valtinat and Huhn (2003)	S235 JR G2	10	15.0	Drilled, Punched	57
Sánchez et al. (2004)	S355N, S460Q, S690Q	15	15.0	Drilled, Punched	34
Bergers et al. (2006)	S460MC, S960/1100QL	10	100.0	Plasma cut	9
Bennett et al. (2007)	HPS-485W (70 W)	15 - 25	24 -32	Drilled, Punched	30
Brown et al. (2007)	A36, A572, A588	12.7-25.4	17.46-23.8	Ream, Drill, Punch	43

### Discussion of parameters

The re-analysis of the data set shows the fabrication method of the hole to be the most important parameter influencing the fatigue life. Two different groups of holes were identified based on the rugosity profile Rz5. This parameter is obtained from the roughness profile height distribution ( $z$ ) recorded over a length ( $L$ ) and represents the ten-point roughness, average height from the five highest peaks and five lowest valleys over a given length (EN 9013):

$$R_z = \frac{1}{5} \left( \sum_{r=1}^5 (Z_r)_{max} + \sum_{r=1}^5 (Z_r)_{min} \right)$$

## Appendix A. Uniaxial fatigue database

---

All fabrication methods contained in the database are allowed by EN 1090-2, namely drilling, punching, laser, plasma or flame cut, with the requirement that local hardness and quality of the cut surface is checked. However, local hardness values measured by Mang et al. (1991) and Valtinat Valtinat and Huhn (2003) for punched, flame and plasma cut holes were inside the allowable range (380HV10 for steel up to S460 and 450HV10 for steel up to S690). Also residual stresses were measured with values close to the hole edge being low. The most important parameter distinguishing the 2 groups is the surface roughness in the hole, which may eliminate the initiation life, and introduce severe notches. The limits of roughness are defined according to EN 1090-2 for the Execution Class 4 (EXC4) as Range 2, which means a maximum value of  $Rz5=40+(0.8*t[\text{mm}])$  [ $\mu\text{m}$ ]. For the maximum plate thickness  $t = 30\text{mm}$  in the database, leads to  $64 \mu\text{m}$ .

The dependence of fatigue strength on the execution class is confirmed with linear elastic fracture mechanics, with due account for the initiation life in the Quality Group 1. The initiation life is estimated with a method proposed by (Haibach, 2006) with endurance limit  $\Delta\sigma_d = 0,45f_u$  where  $f_u$  is the tensile strength. The stress concentration factor is given for the net section as:

$$K_{tn} = 2 + 0,284 \left(1 - \frac{d}{w}\right) - 0,6 \left(1 - \frac{d}{w}\right)^2 + 1,32 \left(1 - \frac{d}{w}\right)^3$$

where  $d$  is the hole diameter and  $w$  the plate width. The threshold of the endurance curve is  $N_{th} = 10^{N_0}$  and  $N_0 = 6,4 - \frac{2,5}{m}$ .

The initiation period is completed when the microcrack growth is no longer dependent on the microstructure or surface conditions, and thus, the crack growth resistance of the material starts to control the crack growth. The size of the microcrack at the transition stage is thus material dependent. We adopt the Range 2 limit  $Rz5=40+(0,8*t[\text{mm}])$  [ $\mu\text{m}$ ],  $64 \mu\text{m}$ .

For the propagation stage, two types of cracks are considered to propagate the initial crack to a through thickness crack. Observations have shown that cracks propagate as corner or semi-elliptical cracks Mang et al. (1991). Tests on punched holes revealed that the cracks started at the edge where the punch goes in, propagating as a corner crack until the crack reached the edge on the opposite surface. The specimens with drilled holes showed cracks mainly initiated in the mid-thickness of the plate, propagating as a semi-elliptical crack. In the final propagation stage, a through-thickness edge crack is considered. For modeling the total life, two cases are distinguished: a) Quality Group 1: Initiation, then propagation first as semi-elliptical and final propagation as through-thickness crack; b) Quality Group 2: No initiation, propagation first as corner crack and final propagation as through-thickness crack.

Bowie's solution is adopted for the stress intensity factor (Broek, 1986):  $K = \sigma\sqrt{\pi a}f\left(\frac{a}{r}\right)$ . The function  $f\left(\frac{a}{r}\right)$ , where  $a$  is the crack length and  $r$  the hole radius is taken from (Paris

and Sih, 1965) and approximated by  $f\left(\frac{a}{r}\right) = \frac{0,65}{(0,08+0,5\frac{a}{r})^{0,58}} + 0,61$ . Since characteristic values have been adopted for the Paris law parameters, namely:  $C = 2.10^{-13}[mm^{3/2}/cycle]$  and  $m = 3$ , the estimated lives with fracture mechanics are close to the lower bounds of each of the quality group, curve 90 for quality group 1 and curve 71 for quality group 2. The results are shown in figure A.25.

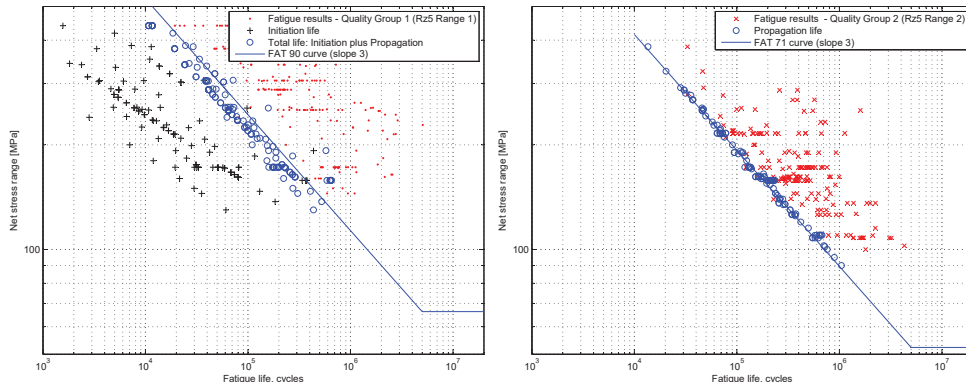


Figure A.25 – Characteristic fatigue curves obtained with fracture mechanics

### Statistical analysis

The data pooling check is in this case done for data in Quality Group 1 (Drilled and Reamed holes) against data in Quality Group 2 (Punched, Flame and Plasma cut holes). The hypothesis of equivalence is rejected because  $C_r = 0,43 > 0$  which means that these groups are considered different populations, figure A.26. For datasets of Quality Group 1, the datapooling check indicates that very few sets can be combined:

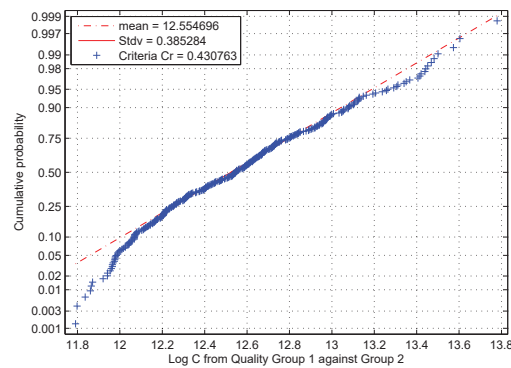


Figure A.26 – Data pooling check for plates with holes (Quality Group 1 and 2)

	Gurney 1965	Haibach 1975	Valtinat 2003	Sanchez 2004	Brown 2007
Kloppel 1960	0,11	0,28	0,60	0,09	0,38
Gurney 1965		<b>-0,01</b>	0,33	<b>-0,19</b>	0,11
Haibach 1975			0,28	<b>-0,12</b>	0,06
Valtinat 2003				0,21	0,15
Sanchez 2004					<b>0,00</b>

# Appendix A. Uniaxial fatigue database

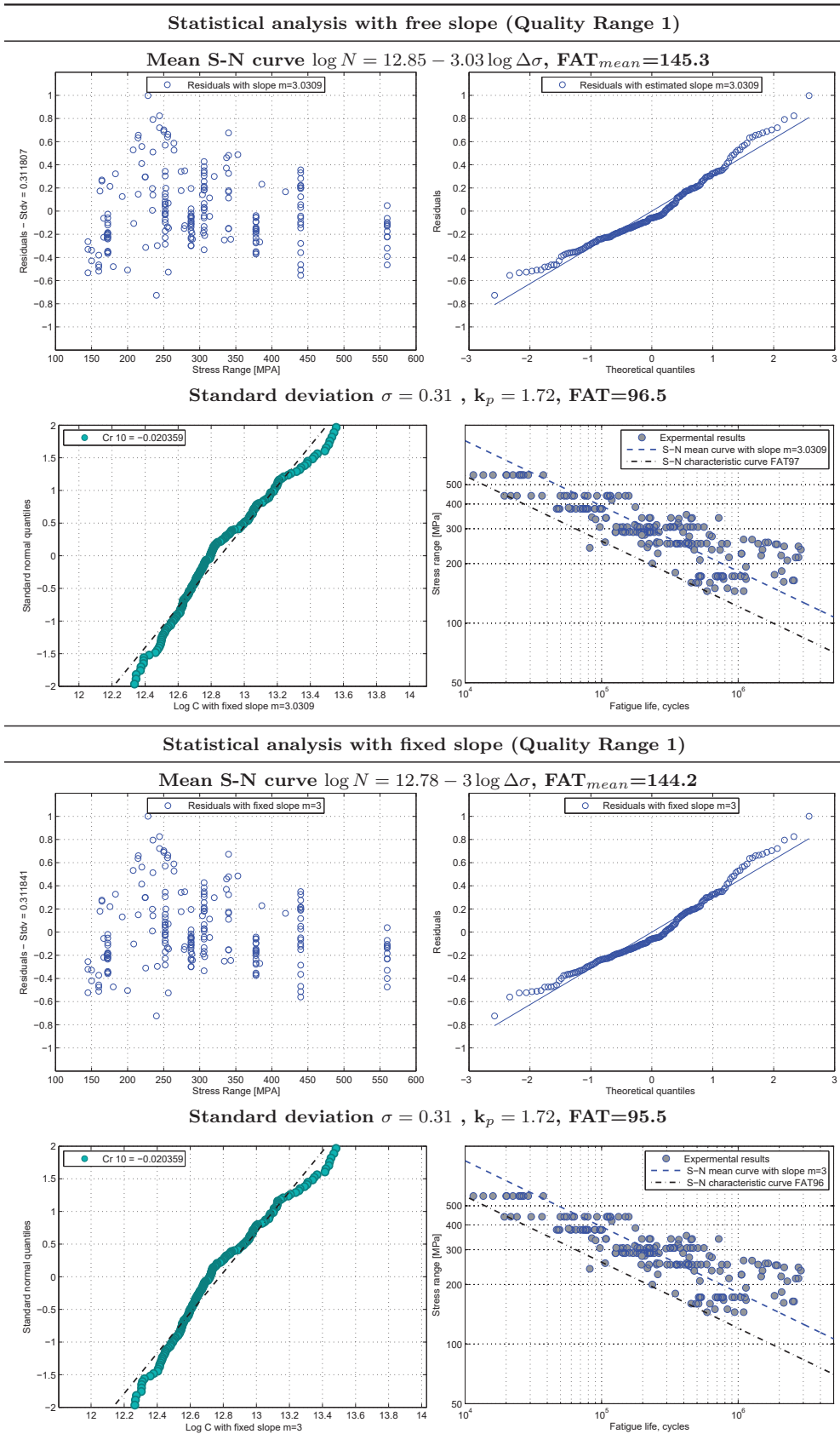


Figure A.27 – Statistical analysis of plates with holes (Quality group 1)

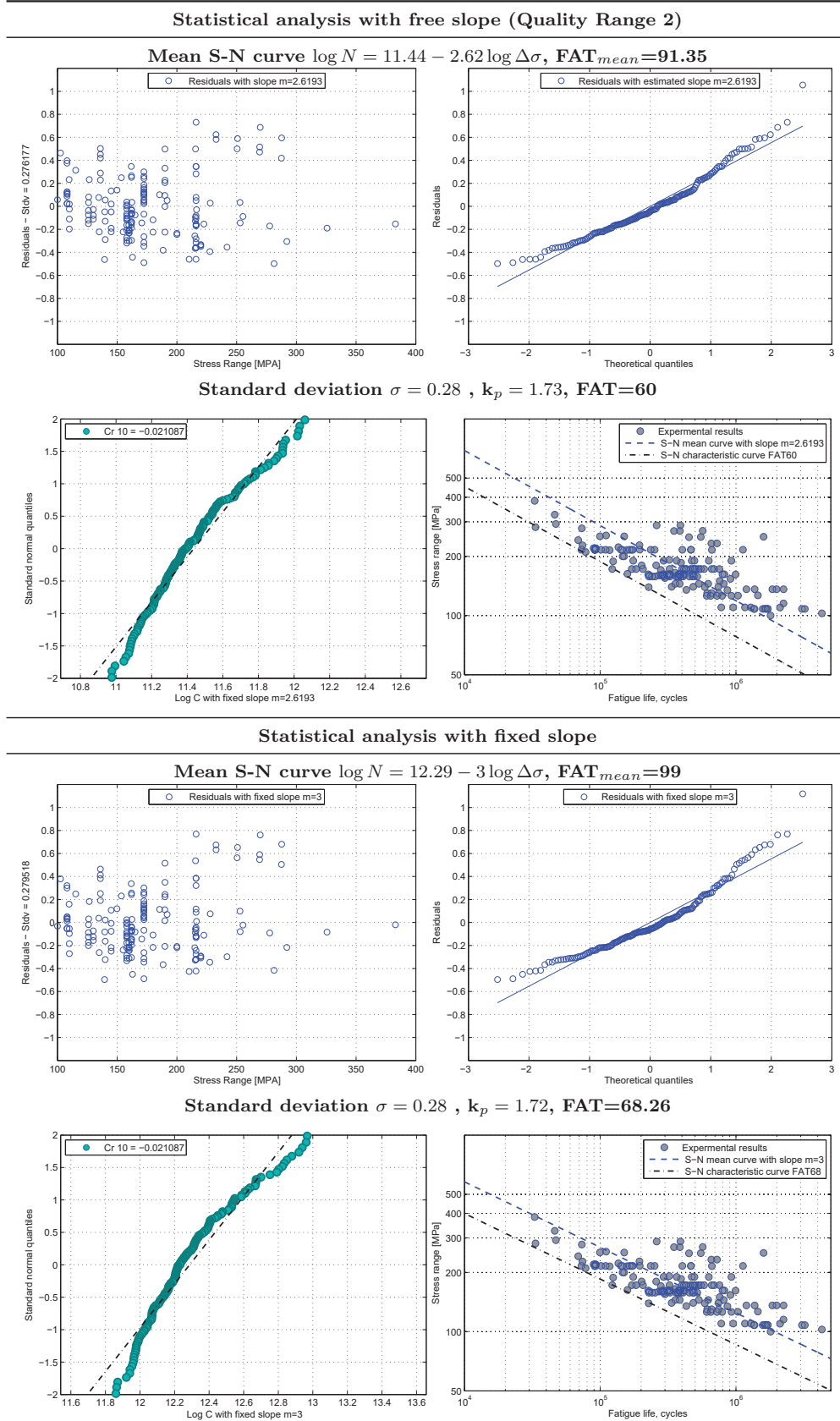


Figure A.28 – Statistical analysis of plates with holes (Quality group 2)



## Recommendations

The fatigue resistance of plates with holes in nominal net cross-section stress should be considered according to the rugosity profile of the hole edges, correlated with the fabrication method:

- **FAT90** - Quality Group 1 (Rz5 Range 1):  
Drilled and Reamed holes
- **FAT71** - Quality Group 2 (Rz5 Range 2):  
Punched, Flame and Plasma cut holes

For EXC4 structures subjected to fatigue loads, Range 1 should be adopted:  $Rz5=10+(0,6*t[\text{mm}])$  [ $\mu\text{m}$ ]. The characteristic fatigue curves are shown in figure A.29.

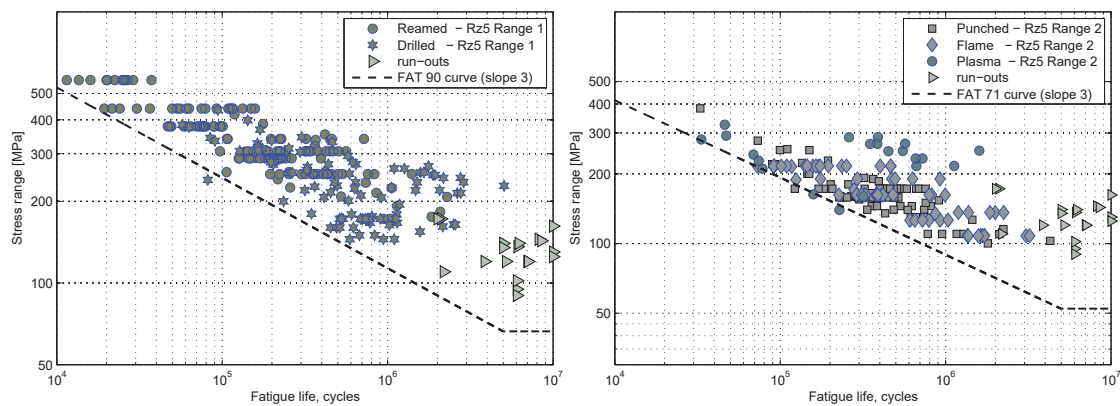


Figure A.29 – Nominal net-stress FAT classification for plates with holes

## A.8 Tubular connections

Tubular end connections are generally made with the end plates welded in a slit on the tube. The weld on the tube around the tip of the plate is the critical fatigue spot and many parameters influence its fatigue behavior. Eurocode 3 (EN 1993 1-9, 2005) defines fatigue categories only for circular tubes with wall thickness  $t_{tube} \leq 12,5\text{mm}$  without limitation on the tube diameter. The chamfer angle on the tube is given as the relevant parameter and the presence of open holes is specified, table A.30. Although the crack is shown in the plate, the relevant stress range is computed in the tube, because the hole edges are in this case the critical spot. However, the fatigue strength of the connection with open holes cannot be taken as granted, as indeed no tests in high cycle fatigue were found in literature. Our re-analysis of existing data in literature showed Eurocode curves (FAT71 for  $\alpha \leq 45^\circ$  and FAT63 for  $\alpha > 45^\circ$ ) to be clearly unrepresentative and nonconservative. Furthermore, an experimental campaign with twenty-four new tests



was done, showing the weld type to be the most important parameter and that tubes with open holes at the end of the slit, although a good detailing solution, do not attain the FAT category specified in Eurocode.


Standard	FAT	Geometrical conditions	Detail
Eurocode 3 (2005)	71	$\alpha \leq 45^\circ, t_{tube} \leq 12.5mm$	
	63	$\alpha > 45^\circ, t_{tube} \leq 12.5mm$	

Figure A.30 – FAT classification for tube to plate connections

The data set

The few experimental results that could be found in literature are tests performed mainly in circular hollow sections. Results reported by JSSC (1974), Uchino and Matsui (1974), Zirn (1975) and Harada and Kurobane (1982) were analysed in a report issued by Karlsruhe University (Mang et al., 1987) showing that a FAT45 category with  $m=3$  should be used for slitted tubes without chamfer, for both fillet or full penetration welds. The largest, most coherent and complete dataset is the one reported by Zirn (1975) with tests in CHS tubes,  $\phi = 88,9 mm, t_{plates} \leq 20 mm$ , with sealing plates at the end of the tubes. Several configurations of tube and gusset plate chamfers were tested, as well as fillet and full-penetration welds. All tests were done at stress ratio  $R = \frac{\sigma_{min}}{\sigma_{max}} = 0, 1$ . Most of the cracks started from the weld toe at the end of the gusset plate welded to the tube. Different steel grades were tested but no significant difference was identified.

Our experimental program involved twenty-four exploratory fatigue tests in four types of connections, six tests per connection and three of each at different stress levels, stress ratio  $R_\sigma = 0, 1$  and frequencies between 7 and 10 Hz. Specimens were fabricated with CHS 114,3x5 and CHS 114,3x5,6 tubes, figure A.31, (Baptista 2016).

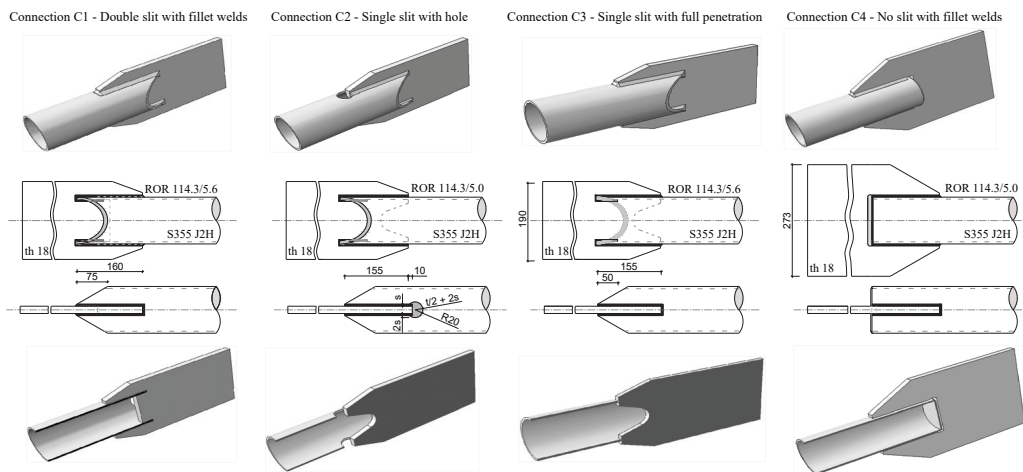


Figure A.31 – Specimen configuration for tubular experiments

Discussion of parameters

The re-analysis of the results obtained by (Zirn, 1975) taking the chamfer angle of the tube as the main parameter, gives characteristic values at  $2.10^6$  cycles  $s(\mu - 2\sigma)$  FAT 80 (with  $m = 4,26$ ) for  $\alpha < 45^\circ$  and FAT 60 (with  $m = 3,91$ ) without chamfer. The difference between tube chamfer as a parameter vanishes however when using a slope 3 as shown in figure A.32. The re-analysis shows the weld type to be the most important parameter for correlating stress range with fatigue life. Linear regression taking the weld type as the main parameter, gives again slopes close to  $m=4$  with characteristic values at  $2.10^6$  cycles  $(\mu - 2\sigma)$  FAT 73 (with  $m = 3,83$ ) for full-penetration welds and FAT 55 (with  $m = 3,84$ ) for fillet welds. Fixing the slope to 3 gives FAT 56 for full penetration welds and FAT 45 for fillet welds. These curves are shown in figure A.32 with the experimental results separated into two groups depending on the weld type.

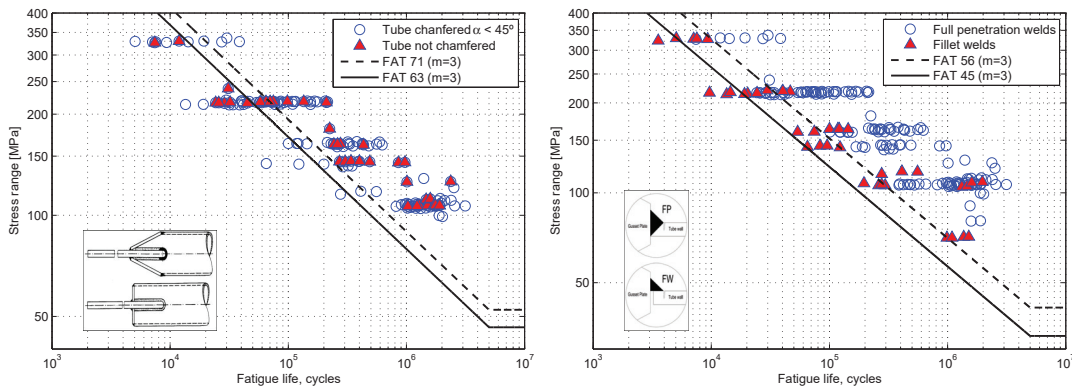


Figure A.32 – Re-analysis of tests reported by Zirn (1975)

Our experimental campaign in connections C1 to C4 showed that a single group of details, equivalent to full-penetration details, could be defined including: Double slit with fillet welds (C1), Single slit with a hole (C2) and Single slit with full-penetration welds (C3).

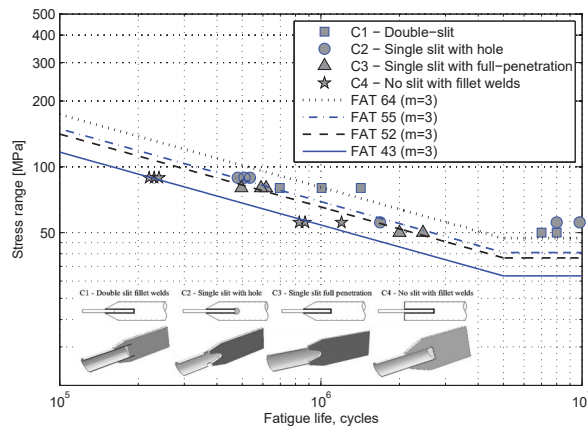
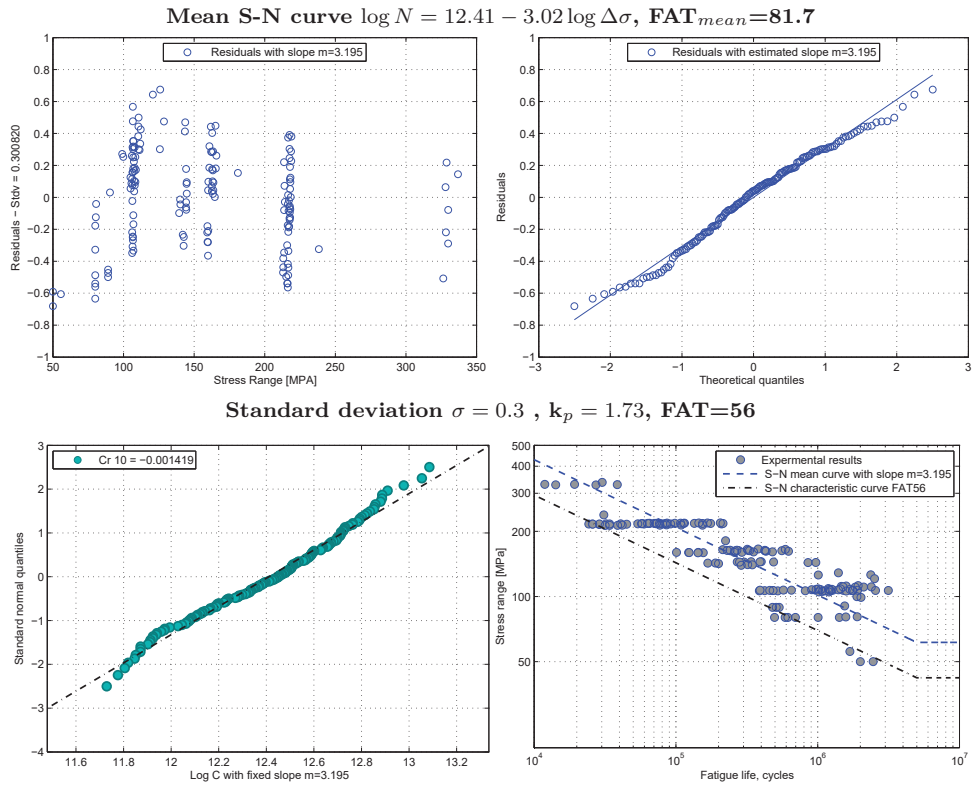


Figure A.33 – Fatigue tests in tubular connections

Statistical analysis with free slope (full penetration welds, holes and double slit)



Statistical analysis with fixed slope (full penetration welds, holes and double slit)

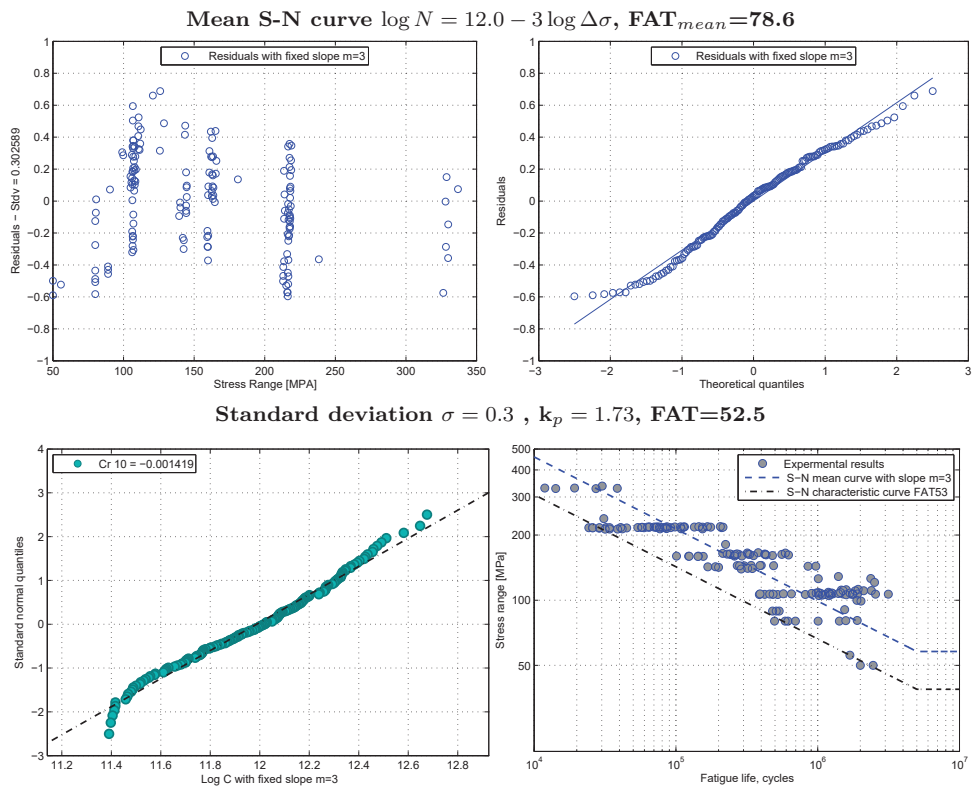
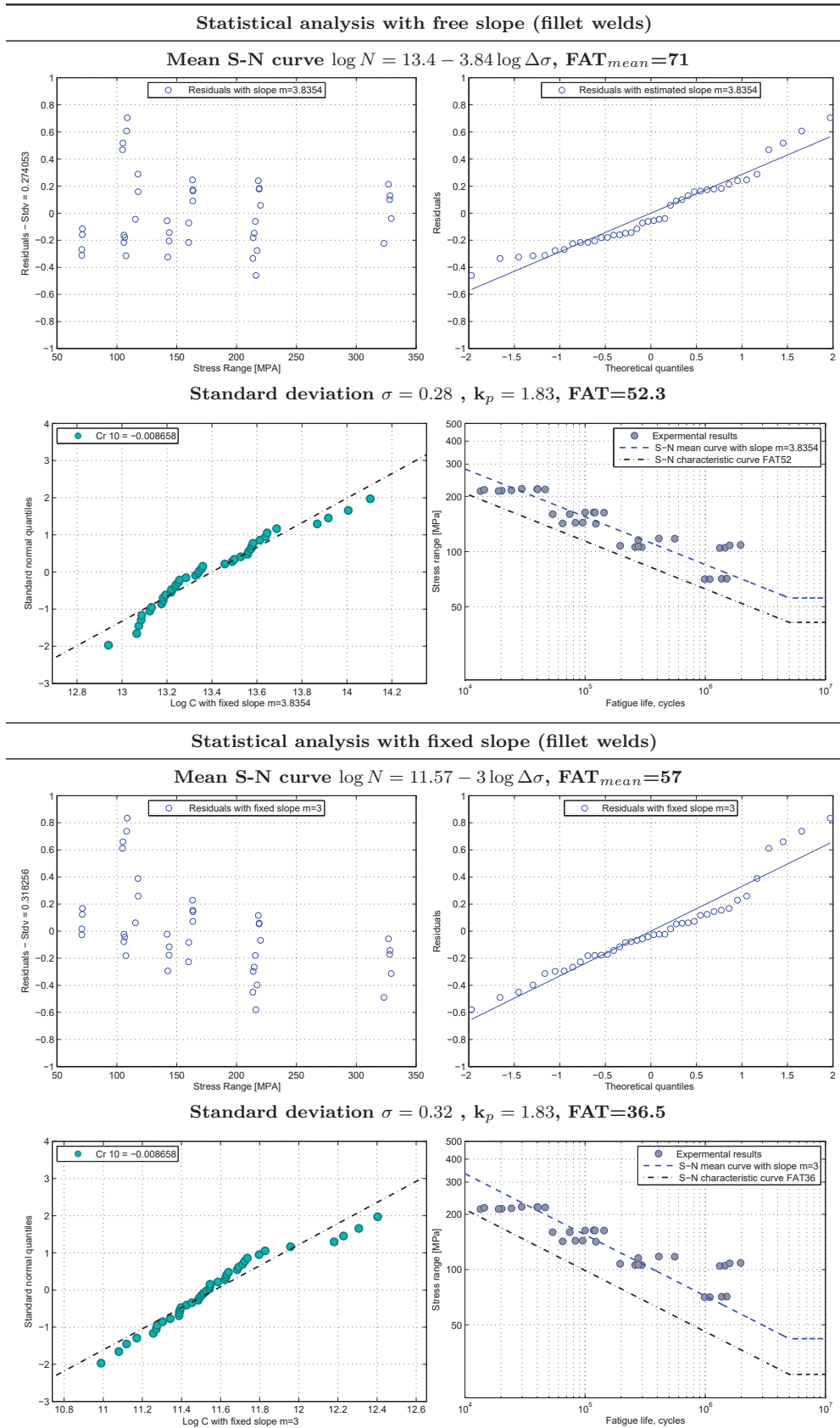


Figure A.34 – Statistical analysis of tubular connections

## Appendix A. Uniaxial fatigue database



Statistical analysis

The statistical is performed for 2 groups of tubes: one including full-penetration welds, single slit with a hole and double slit with fillet welds and a second group including tubes with single slits and fillet welds performed by (Zirn, 1975) that cannot be included in the previous group.

Based on the conclusions of the tests performed in connections C1 to C4 and the analysis of previous fatigue experiments performed by Zirn (1975), a single group of details may be defined as including full-penetration welds, single slit with a hole and double slit with fillet welds. This corresponds to a FAT56, below Eurocode 3 best category, FAT71 that experimental results do not confirm. A second group including tubes with single slits and fillet welds has to be defined with FAT45, figure A.37. Solutions with open hole cannot be recommended for exposed connections because of the waterproofing requirements but they may be used for details inside hermetic box girders. Connections protected from exposed environments where waterproofing is not required, slitted tubes with elongated holes with a length double its width are recommended. The hole edges should be reamed to quality group 1, the tube should be chamfered and sealing plates at the edge adopted. The gusset is to be shaped in a semi-circular form on the extremity inside the tube. For exposed connections, the double slit solution has the best performance. Sealing plates will be mandatory to isolate the tube interior and these have a beneficial effect on fatigue resistance. If these solution proves to be too expensive then a single slit, chamfered and full penetration welds should be used with sealing plates.

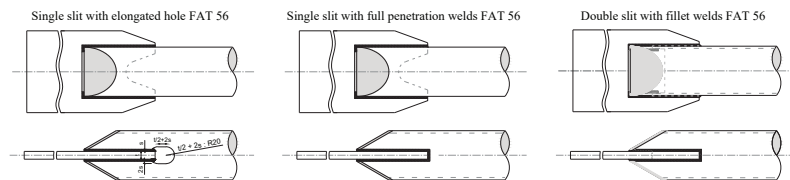


Figure A.36 – Recommended connections for different exposed environments

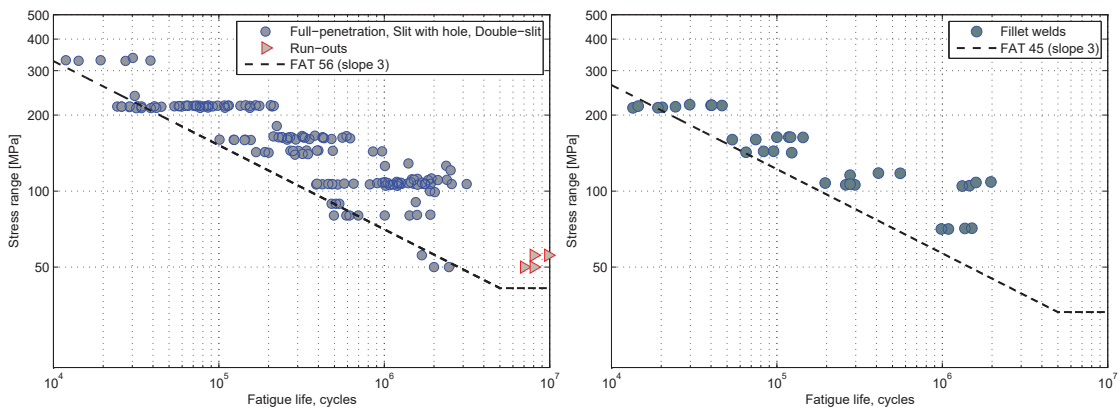


Figure A.37 – FAT classification for tubular connections

### A.9 Cope holes

Cope holes are adopted in welded joints mainly for two reasons. They prevent brittle failure by avoiding the intersection of welds on different directions and they provide access to welding and inspection operations of the joint. However, while the brittle failure is prevented, a potential fatigue problem is introduced, the detail being as low as FAT71, it is often the critical detail in fatigue assessment of steel bridges. Cope holes are classified in Eurocode 3 as a FAT 71 detail for the nominal stress in the flange. However, fatigue tests have shown a strong dependence of life on the ratio of shear stress to normal stress ( $\tau_a/\sigma_m$ ) (Miki and Tateishi, 1997), so that an equivalent stress ( $\sigma, \tau$ ) should be used. IIW chosed instead to put this influence on the resistance side so that the classification depends on the level of shear. If shear is negligible the FAT 71 detail applies, otherwise it is corrected by the formula:

$$FAT = 71 \cdot \left(1 - \frac{\Delta\tau}{\Delta\sigma}\right) \text{ with a minimum FAT36}$$

The classification of the cope hole according to the shear ratio was in the first version of Eurocode (ENV 1993) but was not adopted in final version, (Sedlacek et al., 2000).

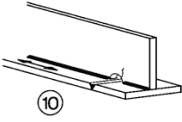
Detail category	Constructional details		Description	Requirements
71	$\Delta\tau/\Delta\sigma =$	0		10) Longitudinal butt weld, fillet weld or intermittent weld with cope holes, cope holes not higher than 40 % of web.
63		0,0 – 0,2		
56		0,2 – 0,3		
50		0,3 – 0,4		
45		0,4 – 0,5		
40		0,5 – 0,6		
36		> 0,6		

Figure A.38 – Cope hole classification in ENV 1993 (Sedlacek et al., 2000)

Cracks found in cope holes may be typified in the three cases, see figure A.39. In this review, only cracks type A are considered.

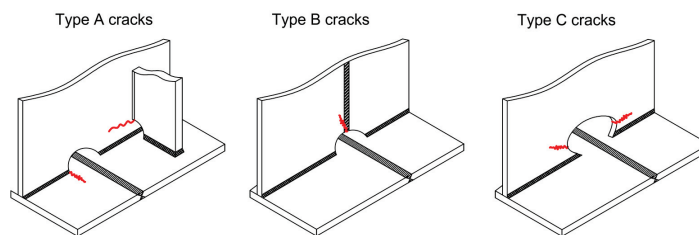


Figure A.39 – Cope holes cracks

The analysis of the fatigue tests in cope holes show that FAT71 is the appropriate notch category. In order to account for high shear stresses, a classification as IIW may be specified as  $FAT = 71 - 50 \frac{\Delta\tau}{\Delta\sigma}$ , see also (Heshmati, 2012). Satatistical analysis is shown in figure A.40.

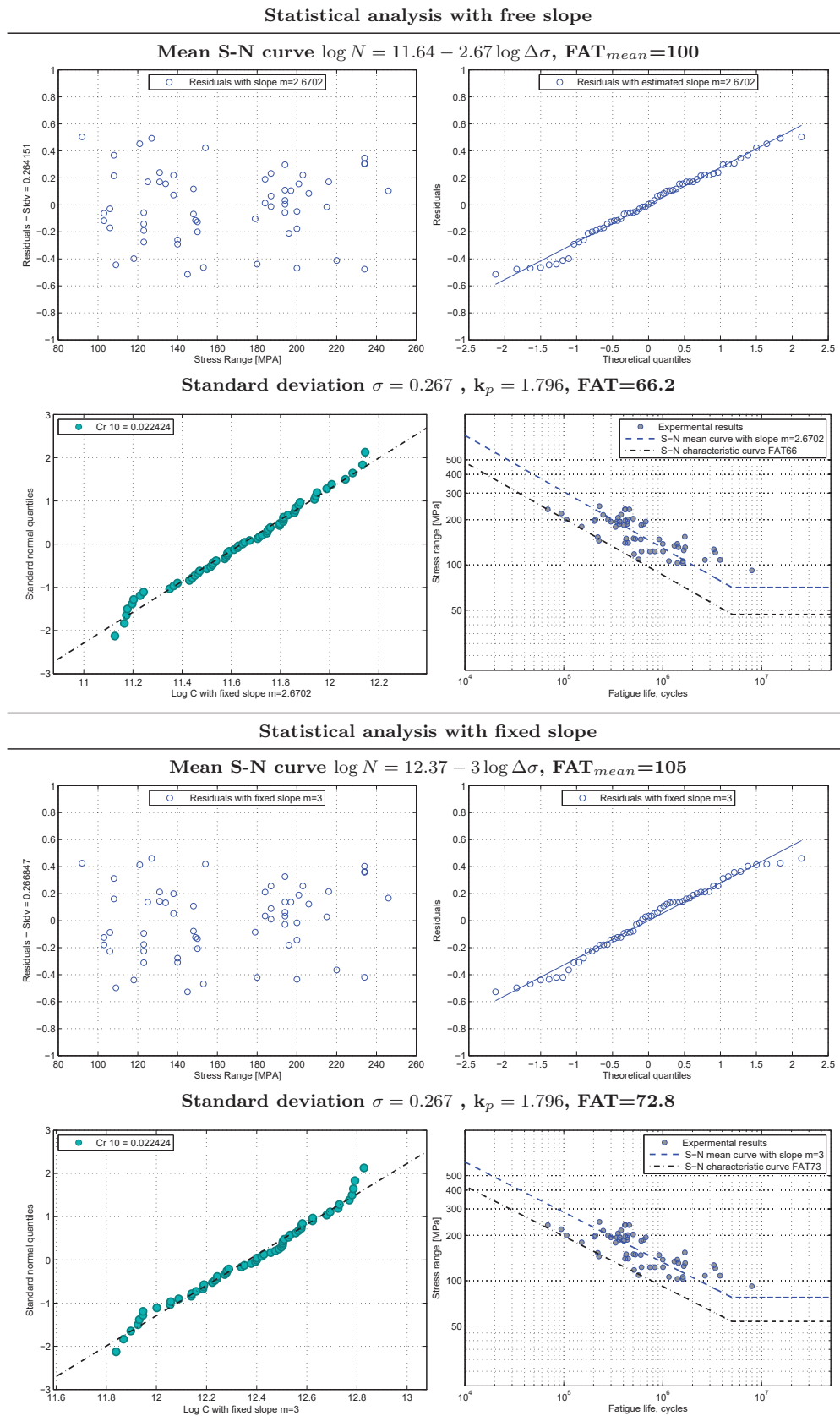


Figure A.40 – Statistical analysis of cope holes





# B Multiaxial fatigue database

This Appendix presents the database of multiaxial experiments collected from literature, as well as the statistical re-analysis of each detail. This review is restricted to weld toe failures and shear studs.

## B.1 Plate specimens

### B.1.1 Longitudinal attachments

Multiaxial tests on welded box beams with two longitudinal attachments were reported by Archer (1987). The attachments were welded laterally with fillet welds on webs with reduced thickness, figure B.1. A total of 31 tests in as-welded conditions were presented. The shear to normal stress ratio,  $\rho = \frac{\Delta\tau}{\Delta\sigma}$ , ranged from 0,9 to 1,0. Stress ratios were constant:  $R_\sigma = 0$ ;  $R_\tau = -1$ .

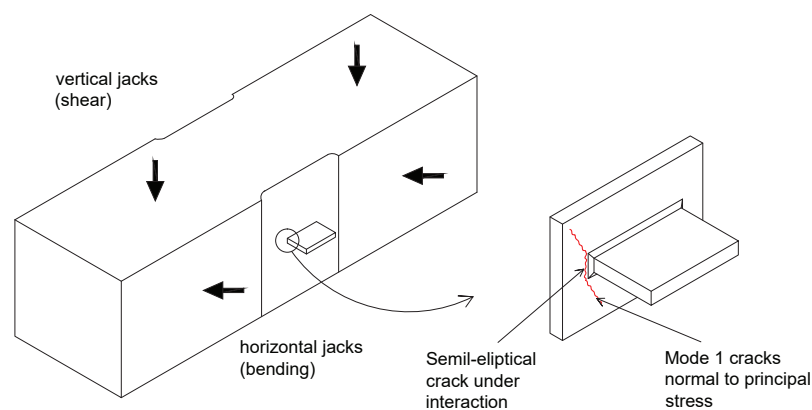


Figure B.1 – Box beam with longitudinal attachments tested by Archer (1987)

Twelve test were performed under pure shear (vertical jacks only). Excluding two run-outs, they lead to  $\Delta\tau_{mean,2.10^6}=115$  MPa. One single uniaxial bending test was performed

## Appendix B. Multiaxial fatigue database

(horizontal jacks only) resulting in  $\Delta\sigma_{mean,2.10^6}=112$  MPa, figure B.2. Both proportional and non-proportional tests, clearly resulted in lower fatigue lives than the uniaxial ones, showing the detrimental influence of shear stress, without distinction however between proportional or non proportional loads.

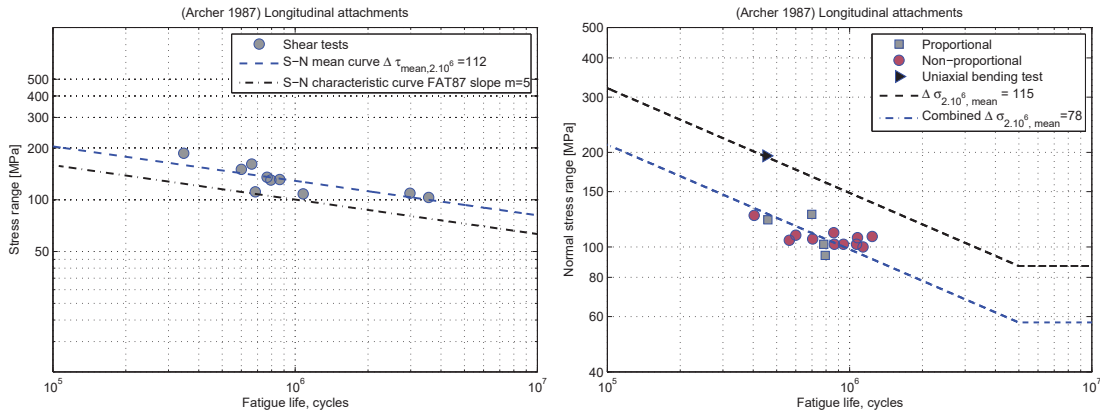


Figure B.2 – S-N curves for tests by Archer (1987)

Specimens failed at the weld toe of the longitudinal attachment tip and deviated according to the principal stress field with cracks in Mode I, figure B.1. Since the majority of life is spent in propagating a semi-elliptical crack at the attachment tip, these are considered in shear-normal interaction.

### B.1.2 Welded box beams

A total of 53 tests in welded box beams were reported by Dahle et al. (1997). Tests were done on two types of beams: with and without full transverse butt-weld splices. The longitudinal welds between web and flanges are partial penetration fillet welds, without chamfer in the web neither backing strip, figure B.3. This type of flange to web weld detail is very economical and often used in bridge girders but in box-girders they are prone to shear cracking from the root imperfections, driven by global torsion. Ratio  $\rho = \frac{\Delta\tau}{\Delta\sigma}$  ranged from 0,58 to 2 and stress ratios were constant  $R_\sigma = R_\tau = -1$ . One single test at  $R=0$  is not considered here and only steel type equivalent to S355 is included.

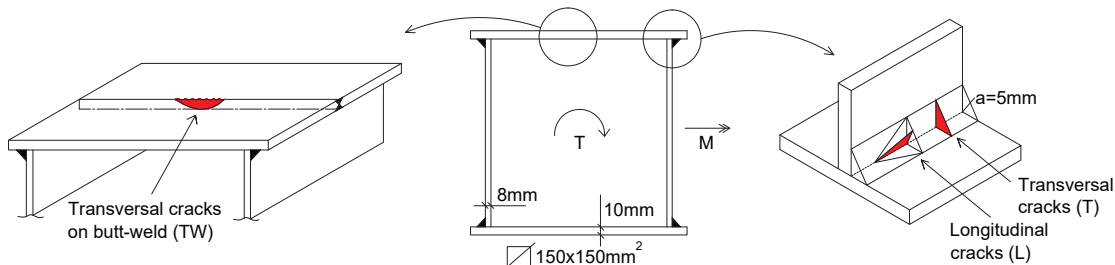


Figure B.3 – Welded box beams tested by Dahle et al. (1997)

To analyse the results, they are separated according to the 3 types of cracks observed with tests: (T) transversal cracks on fillet weld; (L) longitudinal cracks on fillet weld; (TW) transversal cracks on splice butt-weld, see figure B.3.

**(L) longitudinal cracks on the fillet weld**

15 tests under pure torsion produced longitudinal cracks (L) along the fillet weld, driven by shear and starting at the root. Linear regression with free slope gives  $\Delta\tau_{mean,2.10^6}=102$  MPa with  $m=5,76$  and  $\Delta\tau_{mean,2.10^6}=97$  MPa with fixed slope  $m=5$ , figure B.4.

Under combined bending and torsion, the majority of cracks were also longitudinal. This indicates that no major interaction from bending is expected for this type of cracks, because they are parallel to the bending stress. Indeed, figure B.4 shows that the majority of the combined results could be predicted only by considering the shear from torsion. A few show some degree of interaction. However this is probably due to an increase in shear due to longitudinal shear flow from bending, for which no interaction based on nominal FAT categories can be considered. These are root cracks not considered in our interaction analysis.

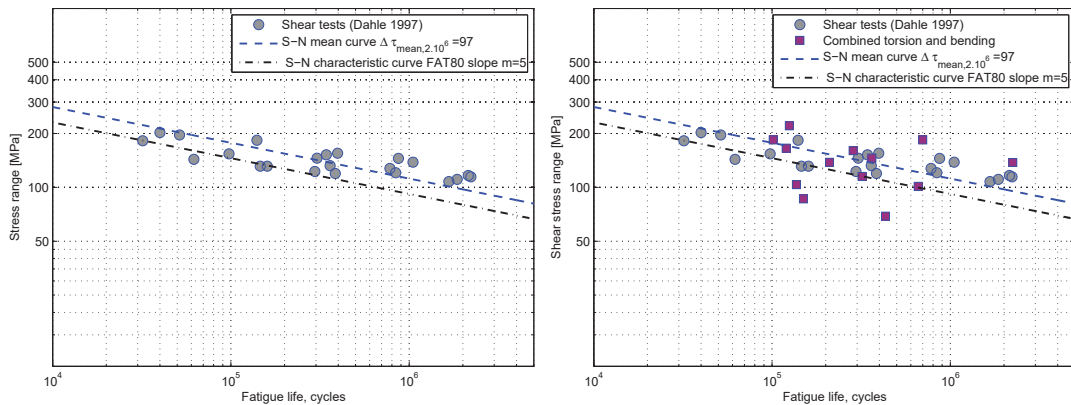


Figure B.4 – Results for longitudinal shear cracks on fillet welds (L)

**(T) transversal cracks on fillet weld**

Three uniaxial bending tests were presented for beams without butt-welds. These produced transversal (T) cracks on the fillet weld, perpendicular to the weld throat, figure B.3. These cracks are usually initiated at start/stop weld positions, weld inclusions or defects. The mean value obtained by linear regression with  $m=3$  is  $\Delta\sigma_{mean,2.10^6}=177$  MPa, figure B.5, well above Eurocode’s FAT100 classification. This is a case where good quality welds play a role. Under combined loads, fatigue life was considerably lower. Excluding one non-proportional point with an extremely low life, the results for combined loads traduced by normal stress, have a mean curve  $\Delta\sigma_{mean,2.10^6}=88$  MPa.

(TW) transversal cracks on the splice butt-weld

Three bending tests on beams with transversal butt-weld splices produced transversal cracks (TW), perpendicular to longitudinal stress, at the butt-weld, see figure B.3. Linear regression with slope  $m=3$  defines  $\Delta\sigma_{mean,2.10^6}=102$  MPa. Five tests under proportional bending/torsion produced the same type of cracks. If traduced only by normal stress, a clear decrease in fatigue life is observed,  $\Delta\sigma_{mean,2.10^6}=66$  MPa, so these data is considered with an interaction criteria, figure B.5.

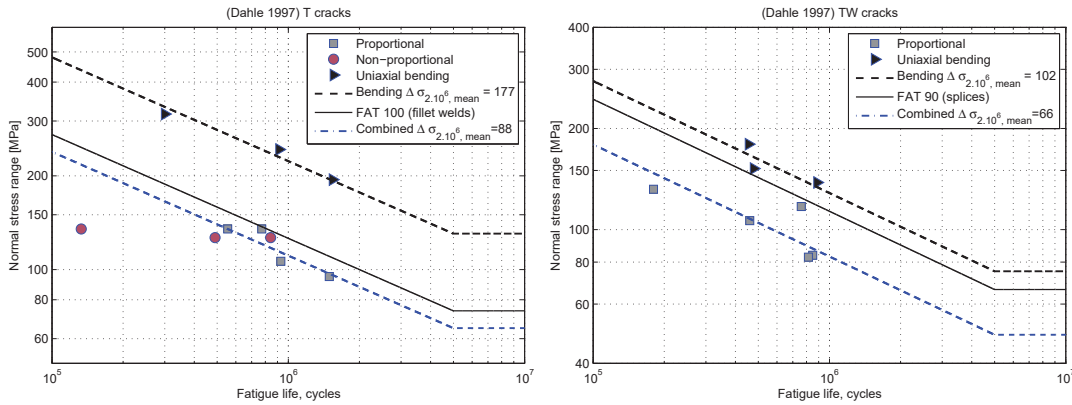


Figure B.5 – Results for transversal cracks (T) and (TW)

B.1.3 Transversal attachments

Multiaxial proportional tests on plates with welded attachments are reported in (Kim and Yamada, 2005). A total of 48 tests were carried out on specimens made in steel equivalent to European S355 and S420. The main plate is continuous, 10mm thick, and transversal attachments are welded inclined from  $\alpha = 0^\circ$  (corresponding to a transversal attachment) to  $\alpha = 15^\circ, \alpha = 30^\circ, \alpha = 45^\circ, \alpha = 60^\circ$  and  $\alpha = 90^\circ$  (corresponding to a longitudinal attachment), figure B.6. This angle variation of the attachment produced a proportional multi-axial stress state at the weld toe, induced by a uniaxial tension load.

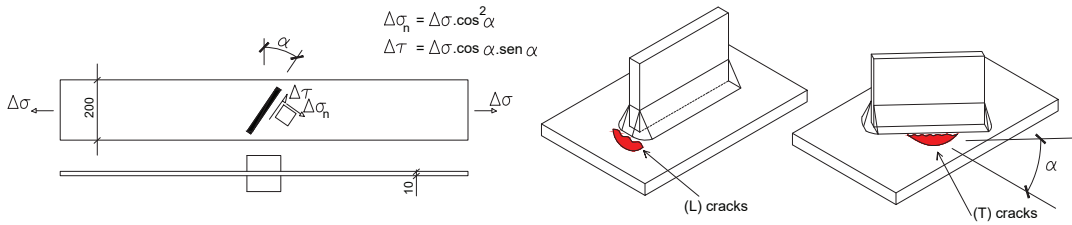


Figure B.6 – Transversal attachments tested by Kim and Yamada (2005)

Two types of cracks were observed. Type (L) cracks, initiated at the tip of the longitudinal attachment, typical failure path with  $\alpha = 90^\circ$ . Tests at  $\alpha = 90^\circ$  give the uniaxial

resistance for longitudinal attachments (L).  $\Delta\sigma_{mean,2.10^6}=73$  MPa is obtained with 4 results, a rather low value when compared to FAT72 obtained for longitudinal attachments, refer to figure A.22 ( $L_{attach}=200$ mm). Some (L) cracks were also obtained with  $\alpha = 30^\circ$ ,  $\alpha = 45^\circ$  and  $\alpha = 60^\circ$ . These are shown in figure B.7 along with the results for  $\alpha = 90^\circ$ . (L) type cracks are not further considered to interaction, because they can essentially be estimated with the main stress range on the plate  $\Delta\sigma$ .

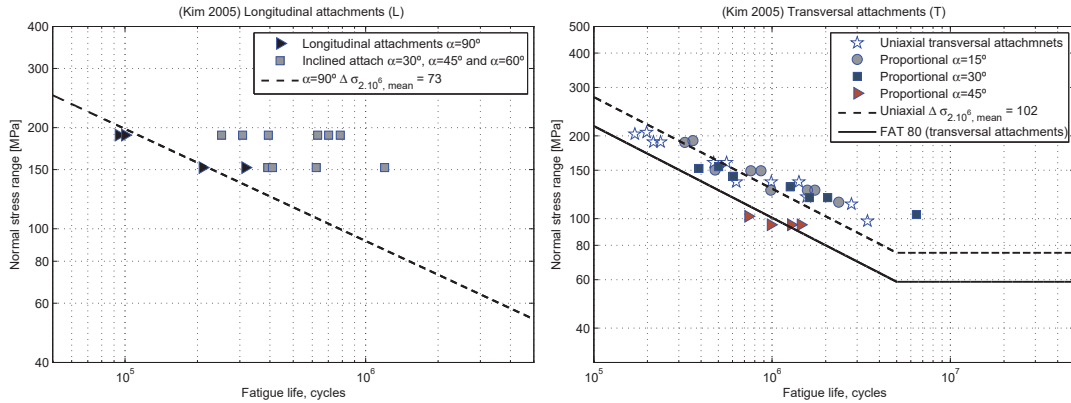


Figure B.7 – Results for longitudinal (L) and transversal (T) attachments

Type (T) cracks are obtained at the weld toe of the transversal attachments, comparable to our experimental results in Chapter 3. Uniaxial tests at  $\alpha = 0^\circ$  allow the definition of the transversal attachments (T) normal stress resistance.  $\Delta\sigma_{mean,2.10^6}=102$  MPa is obtained for a FAT80 detail, well in line with the re-analysis of transversal attachments, see figure A.14, as well as with our experimental results reported in figure 3.7. Increasing the attachment angle, decreases fatigue life, specially for the proportional case at  $\alpha = 45^\circ$ , figure B.7. The setup does not allow a pure shear resistance to be calculated, so that  $\Delta\tau_{mean,2.10^6}=128$  MPa with  $m=5$  and FAT80 is assumed, according to figure A.24. Cracks (T) type are considered for nominal stress criteria interaction.

## B.2 Tubular Specimens

### B.2.1 Circular tubes with flanges

Tests under proportional bending/torsion in circular tubes with welded flanges were reported by Yung and Lawrence (1986), figure B.8. The majority of specimens were tested in the as-welded condition. Four tests on stress-relieved specimens showed a considerable life decrease. This was attributed to the relieve of favorable compressive residual stresses measured in the longitudinal direction of the tube, at the weld toe. Tests were done at  $R_\sigma = R_\tau = -1$  and  $\rho = \frac{\Delta\tau}{\Delta\sigma}$  ranging from 0,34 to 0,58. Run-outs and tests below 100.000 cycles were ignored. Linear regression for pure bending with  $m=3$  gives  $\Delta\sigma_{mean,2.10^6}=100$ MPa and for uniaxial shear  $\Delta\tau_{mean,2.10^6}=102$  MPa with  $m=5$ . Results

## Appendix B. Multiaxial fatigue database

under proportional bending/torsion are shown in figure B.9 represented by their normal stress range  $\Delta\sigma$  and separated by stress-relieved and as-welded specimens.

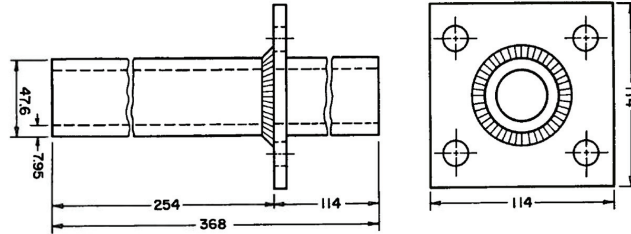


Figure B.8 – Tubes with welded flanges Yung and Lawrence (1986)

Biaxial tests in circular tubes welded to a flange plate were reported by (Siljander et al., 1992), with similar specimens and setup as Yung and Lawrence (1986), figure B.8. A total of 40 tests, in stress-relieved conditions in bending, torsion and combined loading, both in proportional and non-proportional regime were presented. The ratio  $\rho = \frac{\Delta\tau}{\Delta\sigma}$  ranged between 0,13 to 1 and stress ratio constant  $R_\sigma = R_\tau = 0$ , except for 3 bending tests at  $R_\sigma = -1$ .

A total of 9 uniaxial bending tests were performed but run-outs and tests below 100.000 cycles were excluded. Linear regression for pure bending with  $m=3$  gives  $\Delta\sigma_{mean,2.10^6} = 163$  MPa and FAT100. The results under proportional and non-proportional bending/torsion are shown in figure B.9, represented by their normal stress range  $\Delta\sigma$ . The non-proportional load case is seen to be more severe. A total of 6 torsion test, for uniaxial shear, resulted in  $\Delta\tau_{mean,2.10^6} = 148$  MPa with  $m=5$ .

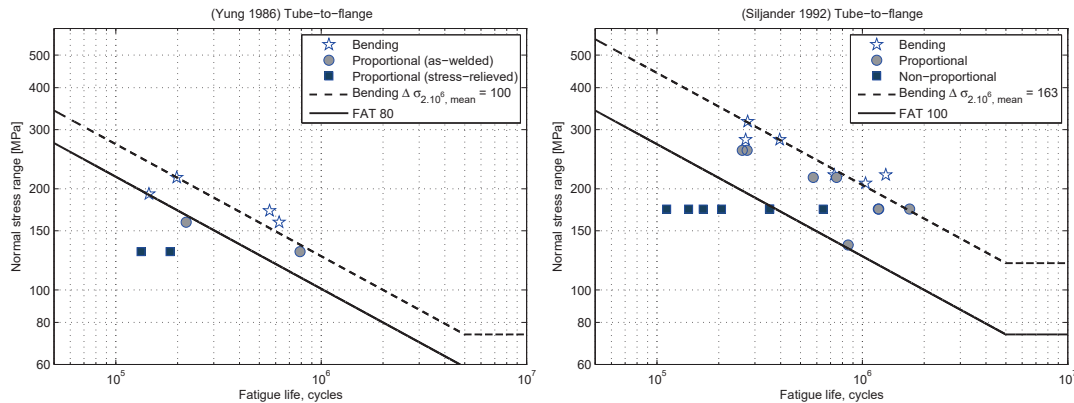


Figure B.9 – Tube-to-flange data (Yung and Lawrence, 1986), (Siljander et al., 1992)

Experiments under tension/torsion on circular tubes with fillet weld flanges were reported by Razmjoo (1996). Although the tube thickness is only 3,2mm, these results are included because they represent the only experimental setup with tubular specimens where normal tensile stress was obtained by pure tension loads. Tests were conducted on as-welded specimens at constant stress ratio  $R_\sigma = R_\tau = 0$ . Under combined loads, failures were

## B.2. Tubular Specimens

at weld toe while under shear, failure occurred on the weld throat. Linear regression for pure bending with  $m=3$  gives  $\Delta\sigma_{mean,2.10^6}=81$  MPa. The results under proportional and non-proportional tension/torsion are shown in figure B.10 represented by the normal stress range  $\Delta\sigma$ . The non-proportional load case is seen to be more severe. Under uniaxial shear,  $\Delta\tau_{mean,2.10^6}=120$  MPa with  $m=5$  is obtained. The lowest data in figure B.10 corresponds to a  $\rho = \frac{\Delta\tau}{\Delta\sigma}=3$ , while other data ranged from  $\rho=0,5$  to  $1,4$ .

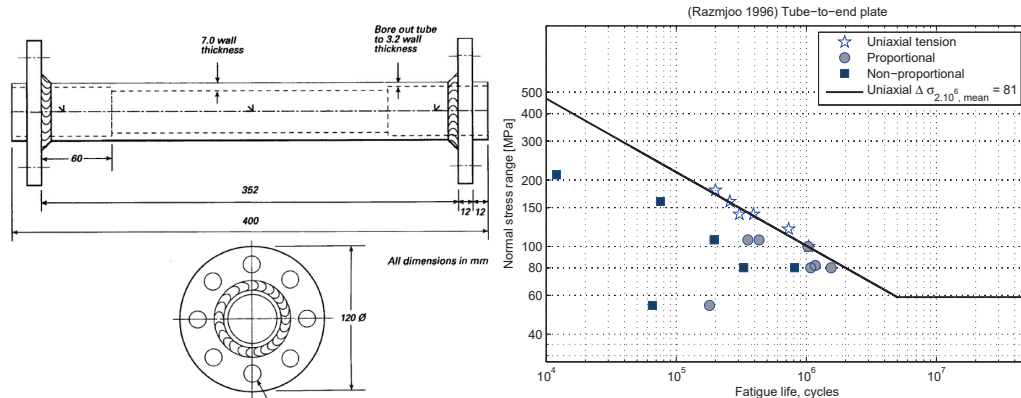


Figure B.10 – Results for tube to end-plate Razmjoo (1996)

### B.2.2 Circular tubes with end plate

Fatigue tests on tubes welded to an end plate were reported in (Sonsino, 1997) and (Sonsino et al., 1999) under both constant and variable amplitude, in as-welded and machined weld toes, with stress-relieved specimens, specimen configuration as figure B.11. Only constant amplitude on as-welded toes are considered here. Tests were done at  $R_\sigma = R_\tau = -1$  with  $\rho=0,58$ . For pure bending  $\Delta\sigma_{mean,2.10^6}=140$  MPa with  $m=3$  is obtained, considering only 60% of the compression range for tests at  $R_\sigma = -1$ . Under pure shear  $\Delta\tau_{mean,2.10^6}=178$  MPa with  $m=5$ . Figure B.11 shows the proportional and non-proportional bending/torsion results. The non-proportional case gave the lowest lives.

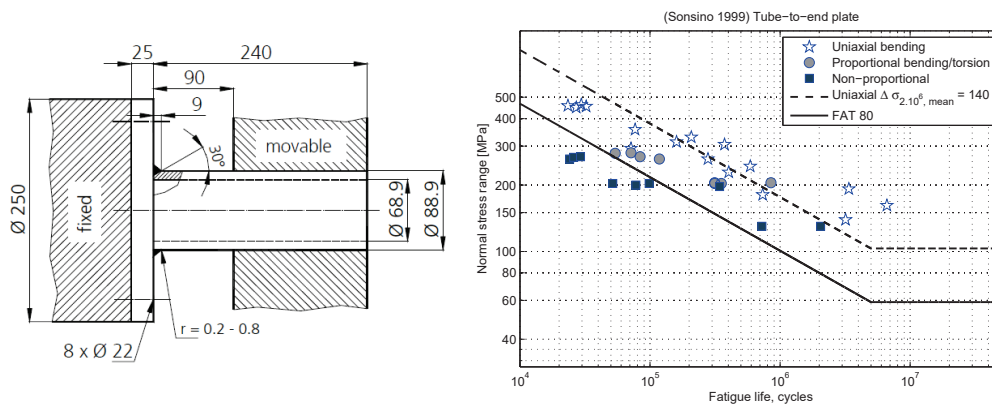


Figure B.11 – Results for tube to end-plate Sonsino et al. (1999)

## Appendix B. Multiaxial fatigue database

A similar setup and specimens as presented by Sonsino (1997) was used for tests reported in (Amstutz et al., 2001) and Yousefi et al. (2001). Circular tubes welded to an end plate were tested under bending, torsion and combined bending/torsion. Specimens were stress relieved and stress ratios  $R_\sigma = R_\tau = 0$  and  $-1$  were tested. For the bending stress at  $R_\sigma = -1$  only 60% of the compression range is considered to account for the stress relief. Tests reported by Amstutz et al. (2001), for pure bending, give  $\Delta\sigma_{mean,2.10^6} = 124$  MPa with  $m=3$  and  $\Delta\tau_{mean,2.10^6} = 131$  MPa with  $m=5$  for pure shear. The results are shown in figure B.12 without significant difference between proportional and non-proportional loads. Tests by Yousefi et al. (2001) give  $\Delta\sigma_{mean,2.10^6} = 144$  MPa with  $m=3$  for pure bending and  $\Delta\tau_{mean,2.10^6} = 184$  MPa with  $m=5$  for pure shear, figure B.12.

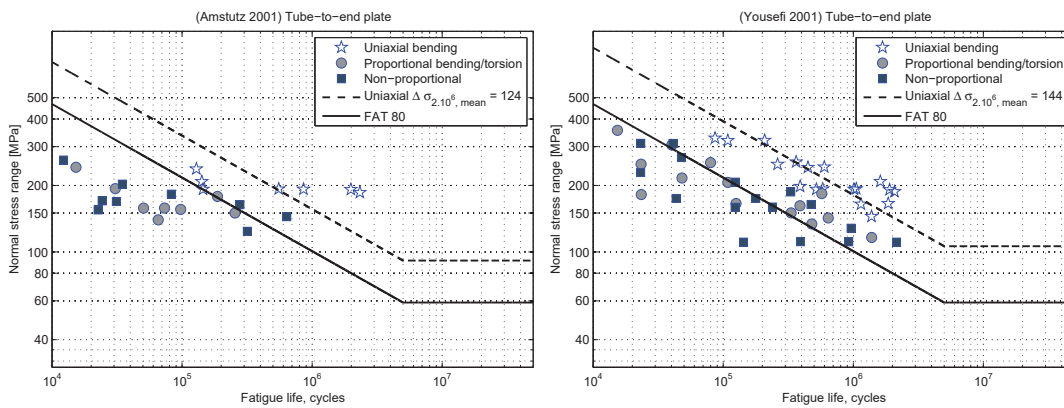


Figure B.12 – Tubes to end-plate by Amstutz et al. (2001) and Yousefi et al. (2001)

If the results of these three authors, with similar setups and specimens, are regrouped together, the result in terms of nominal normal stress are seen in figure B.13. For shear stress a linear regression of all three setups gives  $\Delta\tau_{mean,2.10^6} = 166$  MPa with  $m=5$ . Under pure bending, the slope of the free linear regression is  $m=4$ . By fixing it to  $m=3$ ,  $\Delta\sigma_{mean,2.10^6} = 139$  MPa but the tendency of a shallower slope is clear in figure B.13. The distinction between proportional and non-proportional loadings becomes less clear.

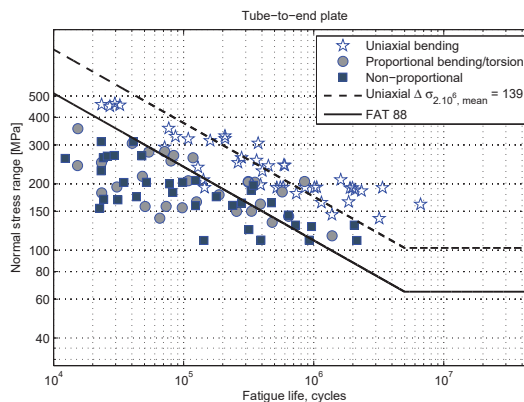


Figure B.13 – S-N curve for tubes to end-plate



B.2.3 Square tubes with end plate

Fatigue tests on square tubes SHS 100x100x5 mm<sup>3</sup> (S355) welded to an end plate were reported by Bäckström (2003), figure B.14. Test were done under bending, shear and combined proportional and non-proportional. A total of 22 tests, in as-welded conditions with ratio  $\rho = \frac{\Delta\tau}{\Delta\sigma}$  ranging from 0,34 to 1,1. For pure bending  $\Delta\sigma_{mean,2.10^6} = 87$  MPa with  $m=3$  is obtained, and under pure shear  $\Delta\tau_{mean,2.10^6} = 159$  MPa with  $m=5$ . No clear distinction between proportional or non-proportional case could be found.

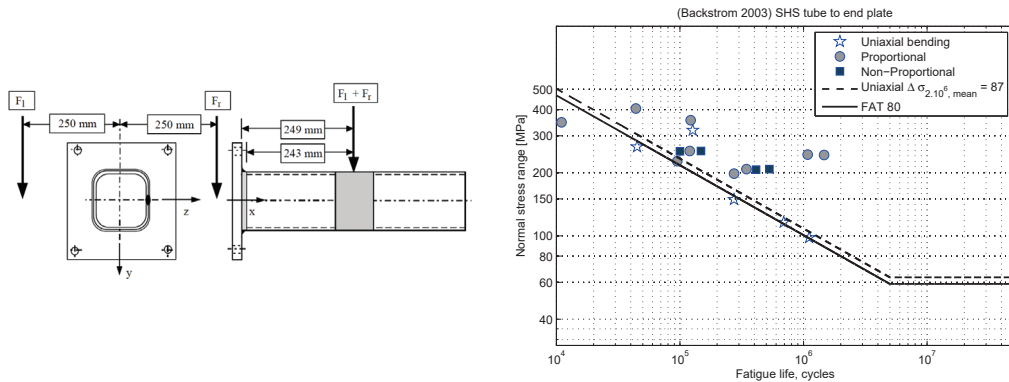


Figure B.14 – Square tubes to end-plate Bäckström (2003)

B.3 Stud connectors

A special case of multiaxial fatigue are shear studs under interaction between shear on the stud and normal stress on the base plate. The failure mechanisms shown in figure B.15, may be divided by:

- *Normal stress in the base plate:* cracks initiate and propagate in the base plate, perpendicular to the normal stress in the base plate
- *Shear:* cracks initiate from the weld notch and propagate perpendicular to the stud cross section, either through weld metal, through the stud cross section or at the interface of the Heat Affected Zone with the base plate
- *Combined shear and normal stress:* cracks initiate in the weld notch, either between the weld and the stud, either between the weld and the base plate, and propagate in the base plate, approximately perpendicular to the local principal stress direction

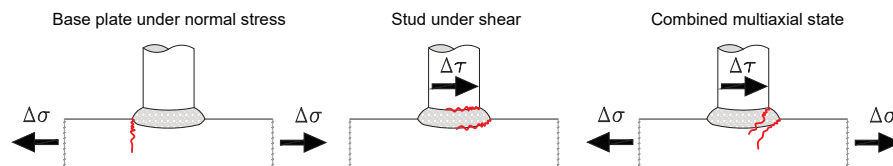


Figure B.15 – Failure modes for shear studs, (Roik and Holtkamp, 1986), (Radaj, 1990)

## Appendix B. Multiaxial fatigue database

The multiaxial interaction based on uniaxial FAT categories, requires each of the uniaxial case to be characterised. The notch case of a plate with welded studs is similar to the typical case of transversal non-load carrying fillet weld like longitudinal or transversal attachments. It is classified as FAT 80 with slope 3 which is confirmed by the re-analysis. For studs under shear, Eurocode defines FAT 90 which over-estimates the characteristic value, and a slope 8 that is unrepresentative of the data set which in turn is more in line with a typical shear behaviour with slope 5.

### B.3.1 Normal stress on base plate

In the re-analysis of several fatigue details made in 1973 by Gurney and Maddox (1973) plates under normal stress were classified as FAT 85 based on the results of (Selby et al., 1963), (Harrison, 1965b) and (Roshardt, 1966). Eurocode Background (Sedlacek et al., 2003), (Stötzel et al., 2007) classified the detail based on the results from (JSSC, 1995) as FAT80. These results are included in our database as well as some others from literature (Welz and Dietrich, 1971), (Welz and Dietrich, 1981), (Herion and Müller, 2000) and (Fricke and Tchuindjang, 2013).

The database is summarised in table B.1. An important dataset is found in the German database (Olivier and Ritter, 1985) with results under stress ratio  $R_\sigma = -1$ . These are included just for discussion of  $R_\sigma$  parameter. In general, none of the run-outs was considered to be valid and only results between 10.000 and 10.000.000 cycles are considered.

Residual stresses, manufacturing quality or higher tensile steel grades have little influence on the fatigue resistance of plates with welded studs under normal stress (Radaj, 1990). The lower influence of residual stress is confirmed by analysing tests at  $R_\sigma = -1$ . Figure B.16 shows the results from the database separated in two groups:  $R_\sigma = -1$  and  $R_\sigma \geq 0$ . If compression cycles are ignored, the plot shows no influence of the residual stress.

Reference	Thickness [mm]	Diameter of stud [mm]	Stress ratio Load $R_\sigma$	N° type	of tests
Selby et al. (1963)	13	20	0,5	Axial	14
Harrison (1965a)	12	25	0	Axial	14
Roshardt (1966)	15-25	20	0	Axial	16
Welz and Dietrich (1971)	12	22	-1	Bending	11
			0	Bending	16
Welz and Dietrich (1981)	20	22	0.09-0.39	Axial	28
			0.09-0.40	Bending	25
Olivier and Ritter (1985)	12	22	-1	Bending	73
			JSSC (1995)	Axial	57
Herion and Müller (2000)	8	12/14.6			19
Fricke and Tchuindjang (2013)		8.0-12.0	0-0.35	Axial	123

Table B.1 – Database for fatigue experiments in plates with studs

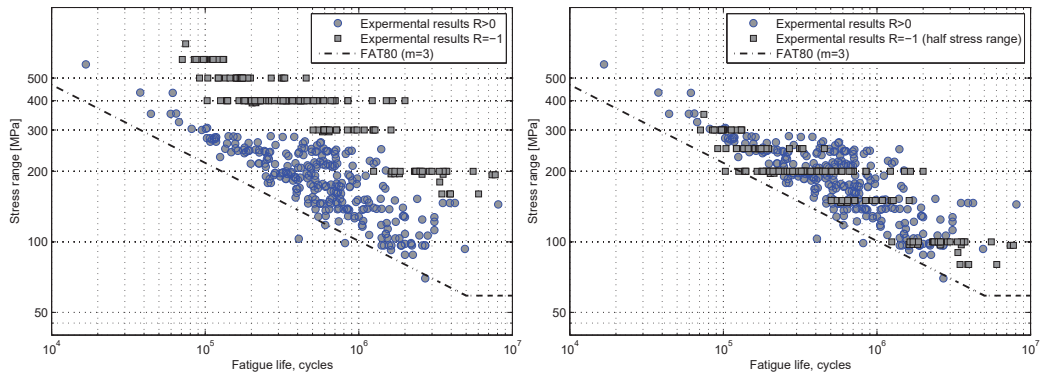


Figure B.16 – Influence of stress ratio  $R_\sigma$  on plates with studs

Statistical analysis and FAT classification is done only with results at  $R_\sigma \geq 0$ , figure B.17. FAT80 category with slope 3 is confirmed by the re-analysis. However no tests are available to confirm the CAFL endurance.

### B.3.2 Shear stress on stud

Detailed literature reviews about the tests considered in our database can be found in (Roik and Hanswille, 1990) and (Xie and Valente, 2011). A careful selection of the existing experimental results was done in order to achieve a reasonable classification for studs under shear, and a realistic estimate of the slope. The experimental results considered in the statistical analysis were obtained in symmetric push-out tests. Asymmetrical setups were excluded due to the additional tensile stress induced by the load eccentricity. None of the run-outs was considered to be valid and only tests above 10.000 cycles are considered. Only tests that comply with  $P_{max} \leq 0,6P_u$  are included and with  $R_\tau \leq 0,5$ . Table B.2 resumes the validated setups and number of tests considered.

Reference	Stud $\Phi$ [mm]	Height [mm]	N° tests
Mainstone and Menzies (1967)	19	100	10
Roderick and Ansorian (1976)	19	100	4
Hallam (1976)	19	76	13
Lo (1978)	16	-	32
Roik and Hanswille (1987)	22	100	6
ECSC (1999)	25	100	16
Faust et al. (2000)	22	125	11
Lee et al. (2001)	19	150	9
Badie et al. (2002)	32	140	19
ECSC (2002)	25	100	14
Seracino et al. (2003)	12.7	75	15
Lee et al. (2005)	25/27/30	155	9
Ahn et al. (2007)	16	125	9
Hanswille et al. (2007)	22	125	11
Kwon et al. (2010)	22	127	9

Table B.2 – Database for fatigue experiments in plates with studs

## Appendix B. Multiaxial fatigue database

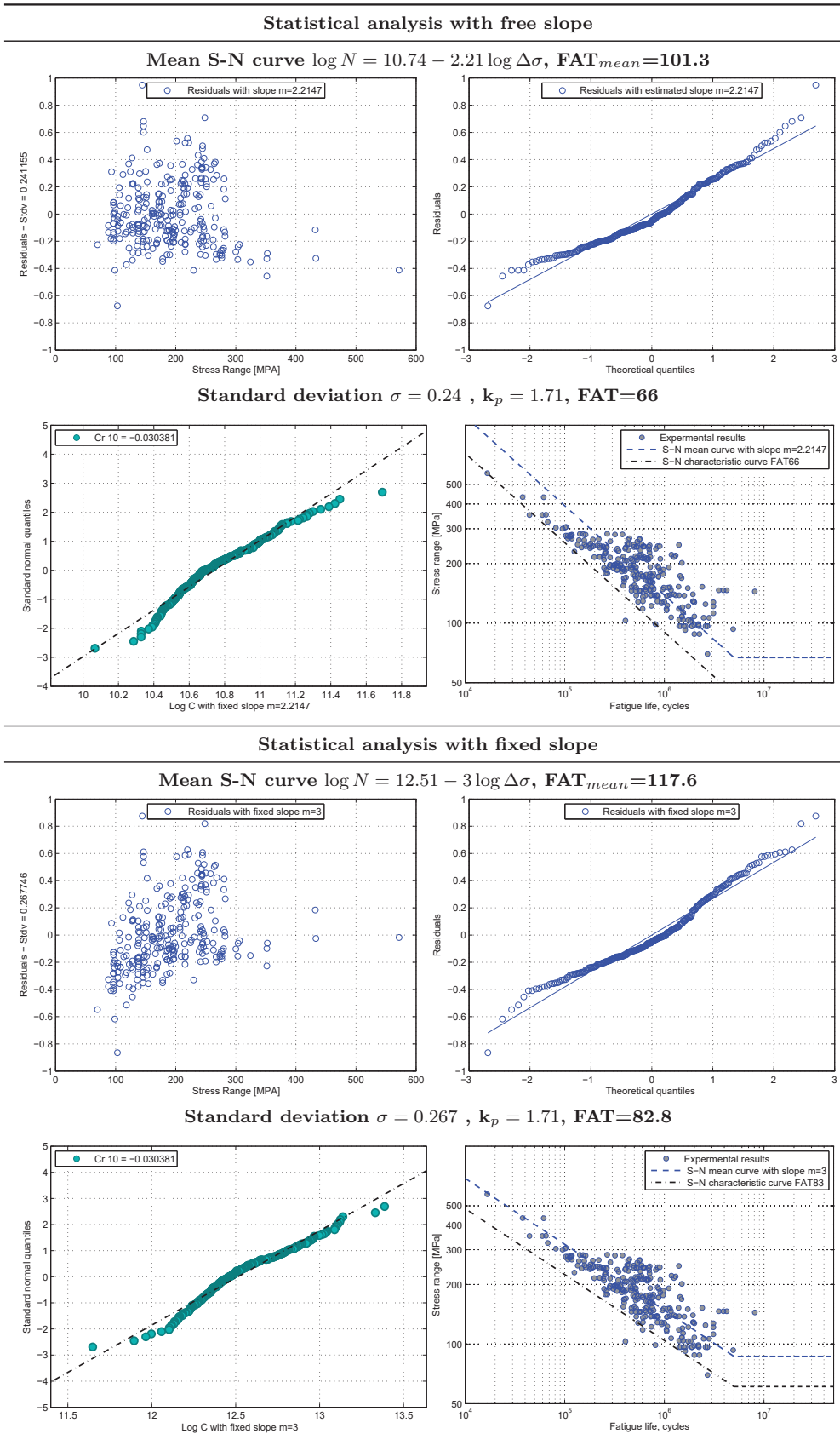
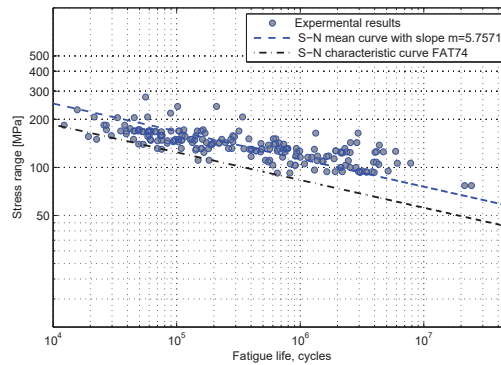


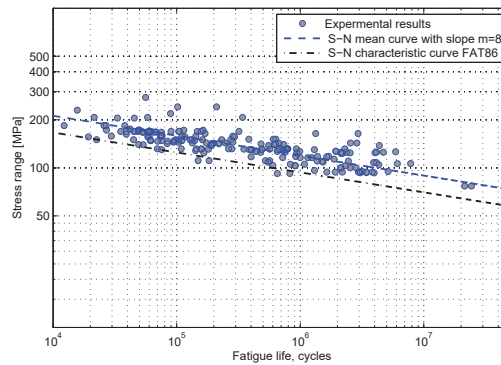
Figure B.17 – Statistical analysis of plates with studs

Shear studs are classified in Eurocode Background (Sedlacek et al., 2003) as FAT90 with slope 8 based on two datasets (ECSC, 1999) and (ECSC, 2002). This classification is not in line with our re-analysis, mainly because the slope of the regression line is close to 5 (actually  $m=5,76$ ) as expected for a welded element under shear, figure B.18.

Mean S-N curve  $\log N = 17.82 - 5.76 \log \Delta\sigma$ ,  $FAT_{mean}=100$ ,  $\sigma = 0.44$ ,  $k_p = 1.72$ ,  $FAT=74$



Mean S-N curve  $\log N = 22.6 - 8 \log \Delta\sigma$ ,  $FAT_{mean}=110$ ,  $\sigma = 0.49$ ,  $k_p = 1.72$ ,  $FAT=86$



Mean S-N curve  $\log N = 16.2 - 5 \log \Delta\sigma$ ,  $FAT_{mean}=96$ ,  $\sigma = 0.45$ ,  $k_p = 1.72$ ,  $FAT=67$

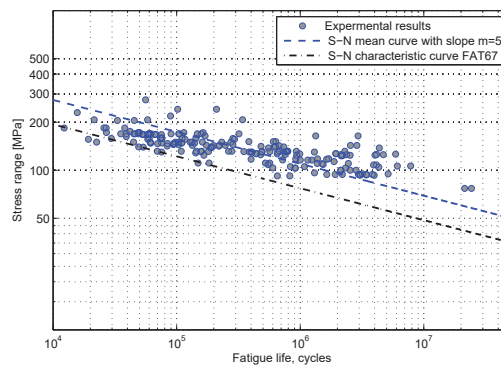


Figure B.18 – Statistical analysis of studs in shear

The slope  $m=8$  originates on the work of Roik and Holtkamp (1989) by doing the linear regression of  $\Delta\tau$  on the independent variable  $\log N$ . Figure B.18 shows that the difference between assuming  $\Delta\tau$  or  $\log N$  as the independent variable, roughly defining S-N slopes

## Appendix B. Multiaxial fatigue database

between  $m=5$  and  $8$ , respectively. Furthermore, it was seen that under pure shear, no CAFL could yet be established by experiments, with observed failures up to  $60 \cdot 10^6$  cycles, extending the S-N curve “ad-infinitum”, figure A.24. The same holds for shear studs, where no experimental evidence of the CAFL is reported. Although linear in log-log scale, the S-N curve is still a power law, and the difference between exponent  $m=5$  and  $m=8$  may severely under-estimate fatigue life for the high-cycle regime, characteristic for bridges. Further discussion about the slope  $m=8$  can be found in (Johnson, 2000).

### B.3.3 Shear-normal stress interaction

A review of the existing experimental data for shear studs under interaction was done in (Maddah and Nussbaumer, 2014). The data is scarce, and by limiting the database to tests above 10.000 cycles,  $P_{max} \leq 0,6P_{u,stud}$  and  $R_\tau \leq 0,5$  the only coherent datasets considered here are the ones reported by (Roik and Holtkamp, 1989) and (Mensinger, 2000). The experimental data by Roik and Holtkamp (1989) was originally analysed with  $\Delta\sigma_{mean,2 \cdot 10^6} = 105$  MPa with  $m=2,75$  and  $\Delta\tau_{mean,2 \cdot 10^6} = 93,8$  MPa with  $m=9,2$ , and the IIW elliptical criteria was proposed, equation 6.6. The criteria defined in Eurocode is however linear, defined as:

$$\left( \frac{\Delta\sigma_{Ed,2}}{FAT_\sigma} \right) + \left( \frac{\Delta\tau_{Ed,2}}{FAT_\tau} \right) \leq 1,3 \quad (\text{B.1})$$

where for each individual stress quantity, maximum damage 1,0 has to be respected. The experimental results are shown along with the interaction criteria B.1 in figure B.19. The correlation between the experimental results and the interaction formula is weak.

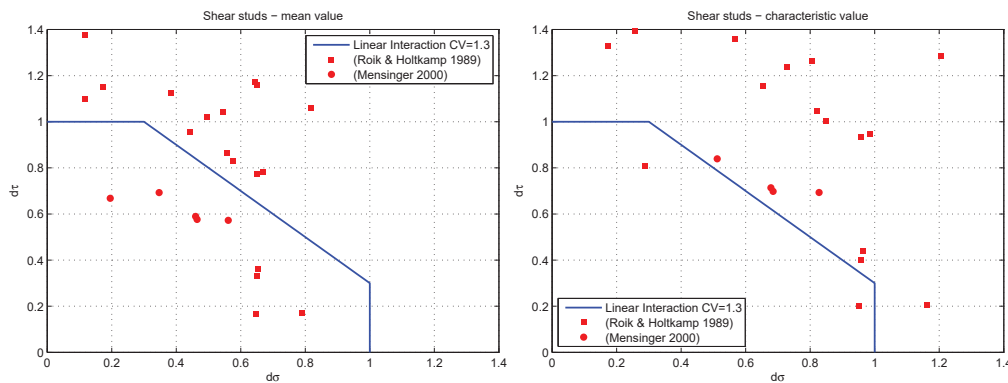


Figure B.19 – Multiaxial fatigue interaction for shear studs

The data on this referential is very scattered and life estimation with equation B.1 is equally scattered. Good experimental results under interaction are difficult to obtain, and the parameters related to concrete behaviour and rebar influence, add complexity to the problem. In order not to increase uncertainty in the analysis of general multiaxial interaction formulas, shear studs are not included in Chapter 6.

## C Experimental results

## Appendix C. Experimental results

### C.1 Experiments under constant amplitude

#### LA-CA-1

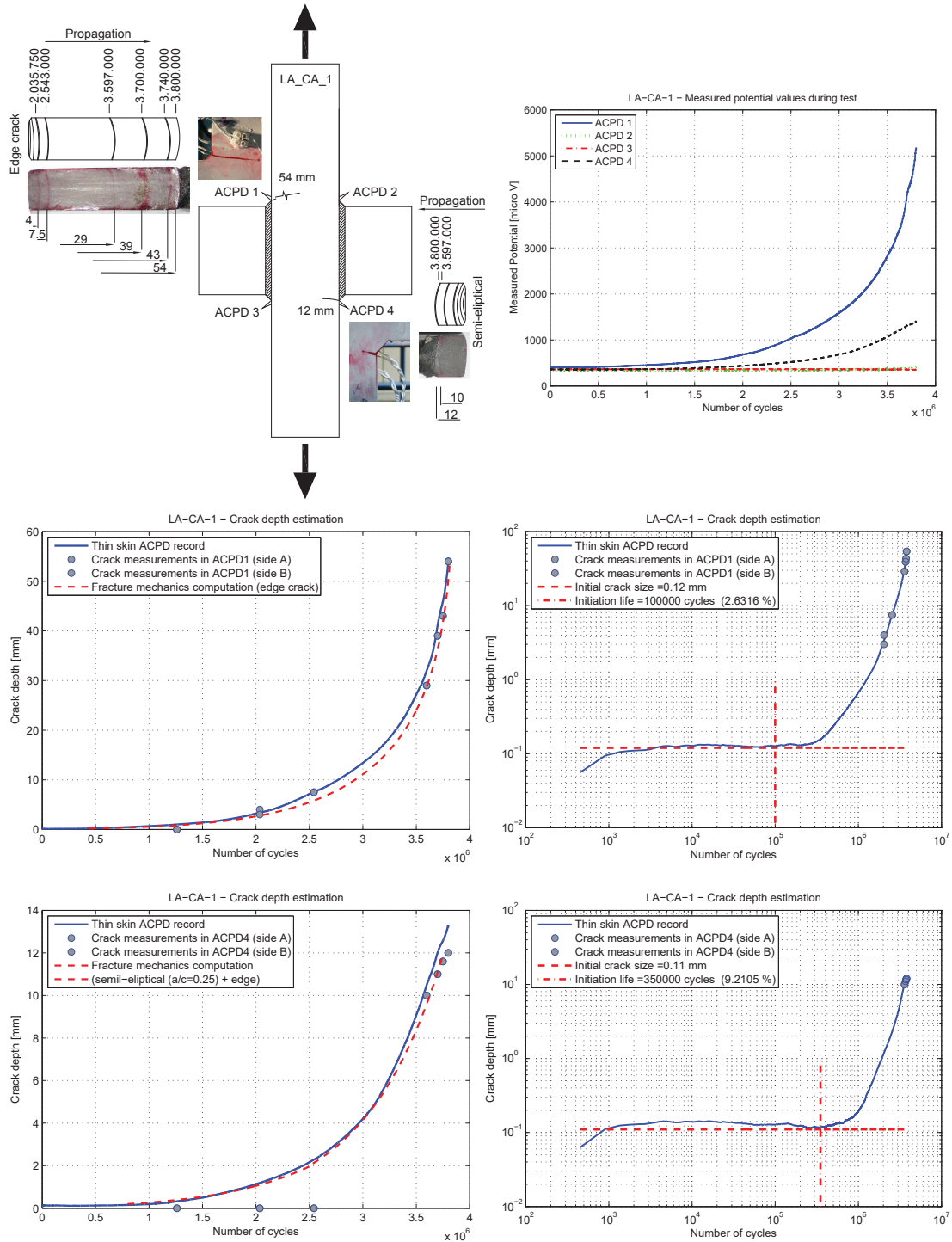


Figure C.1 – LA-CA-1: ACPD potential, estimated and measured crack depths



## C.1. Experiments under constant amplitude

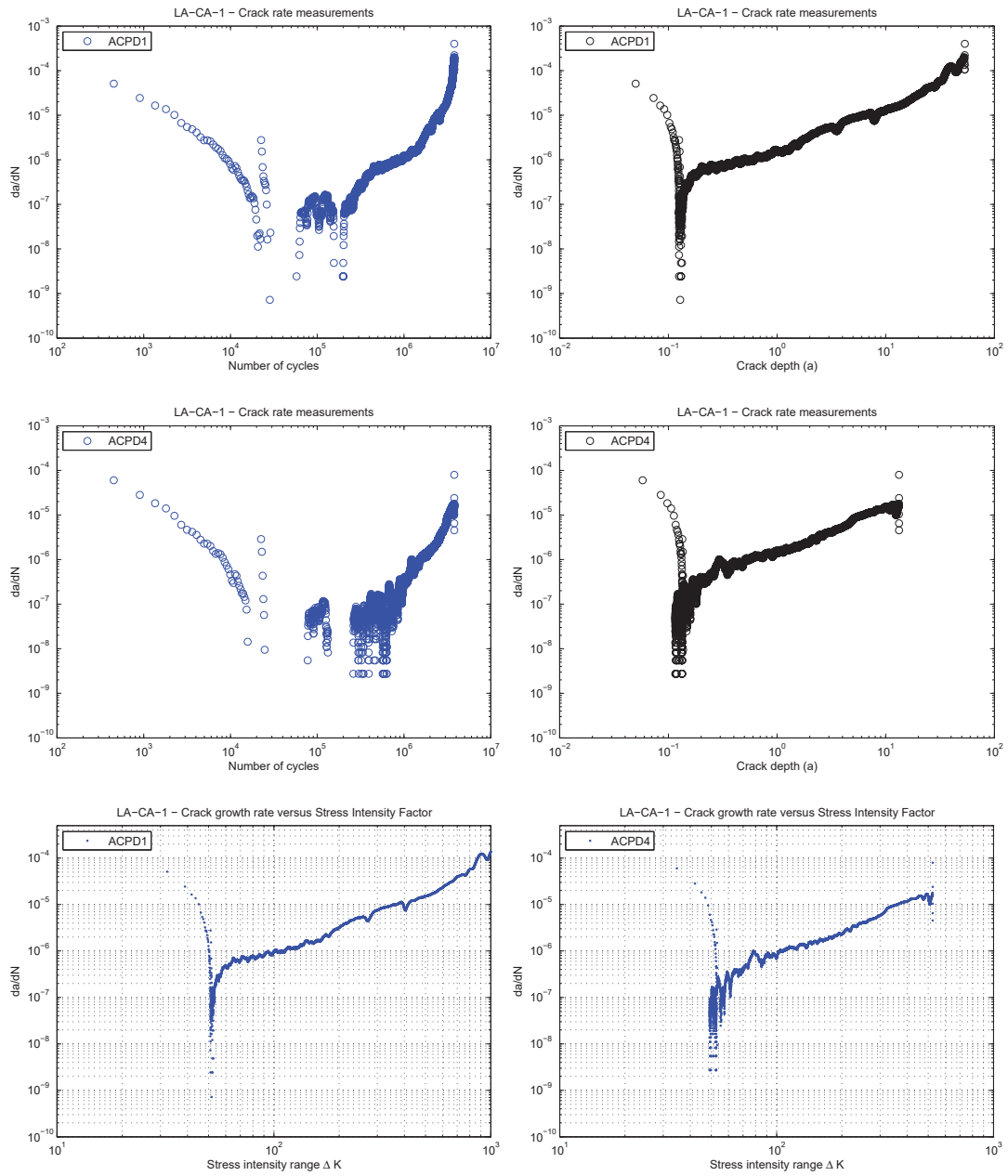


Figure C.2 – LA-CA-1: Crack growth rate

# Appendix C. Experimental results

## LA-CA-3

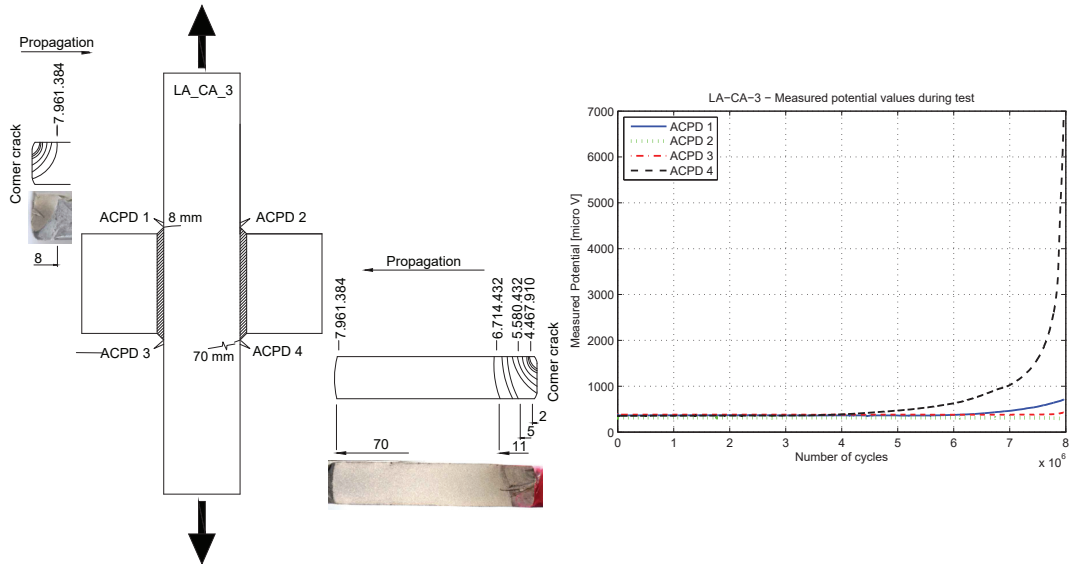


Figure C.3 – LA-CA-3: ACPD probes and measured potential values

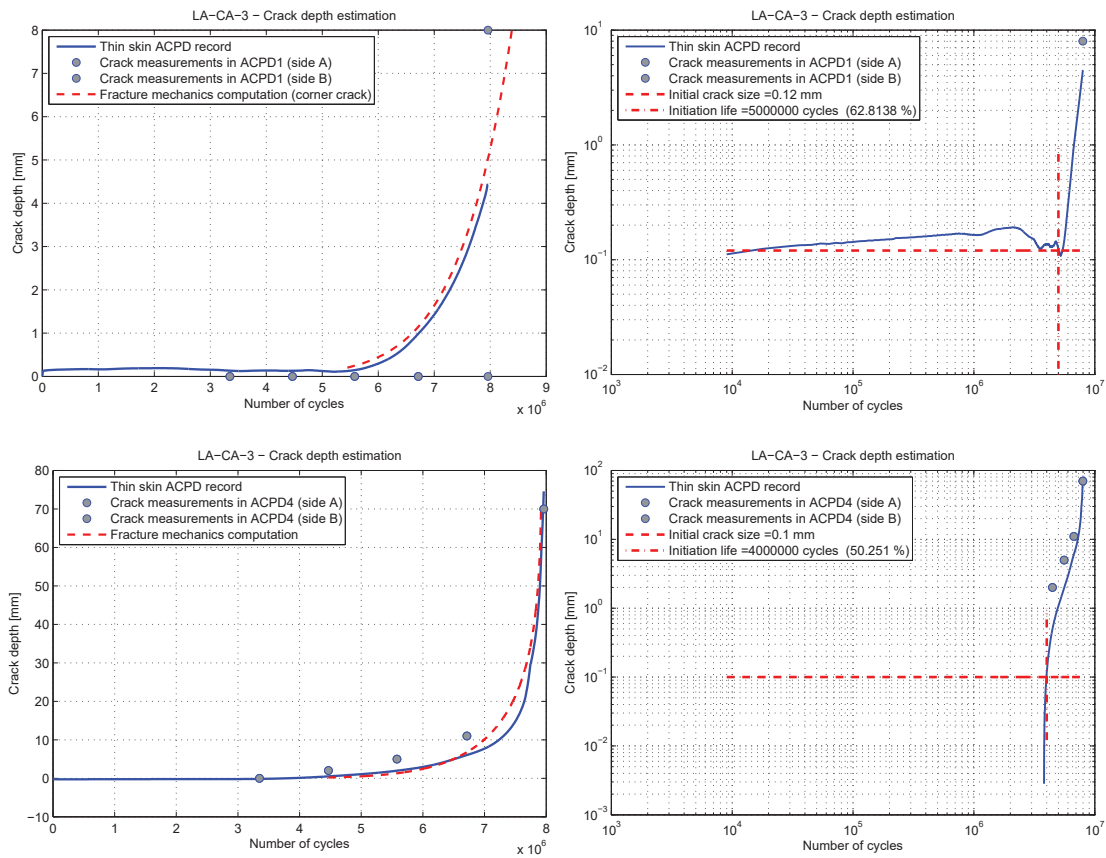
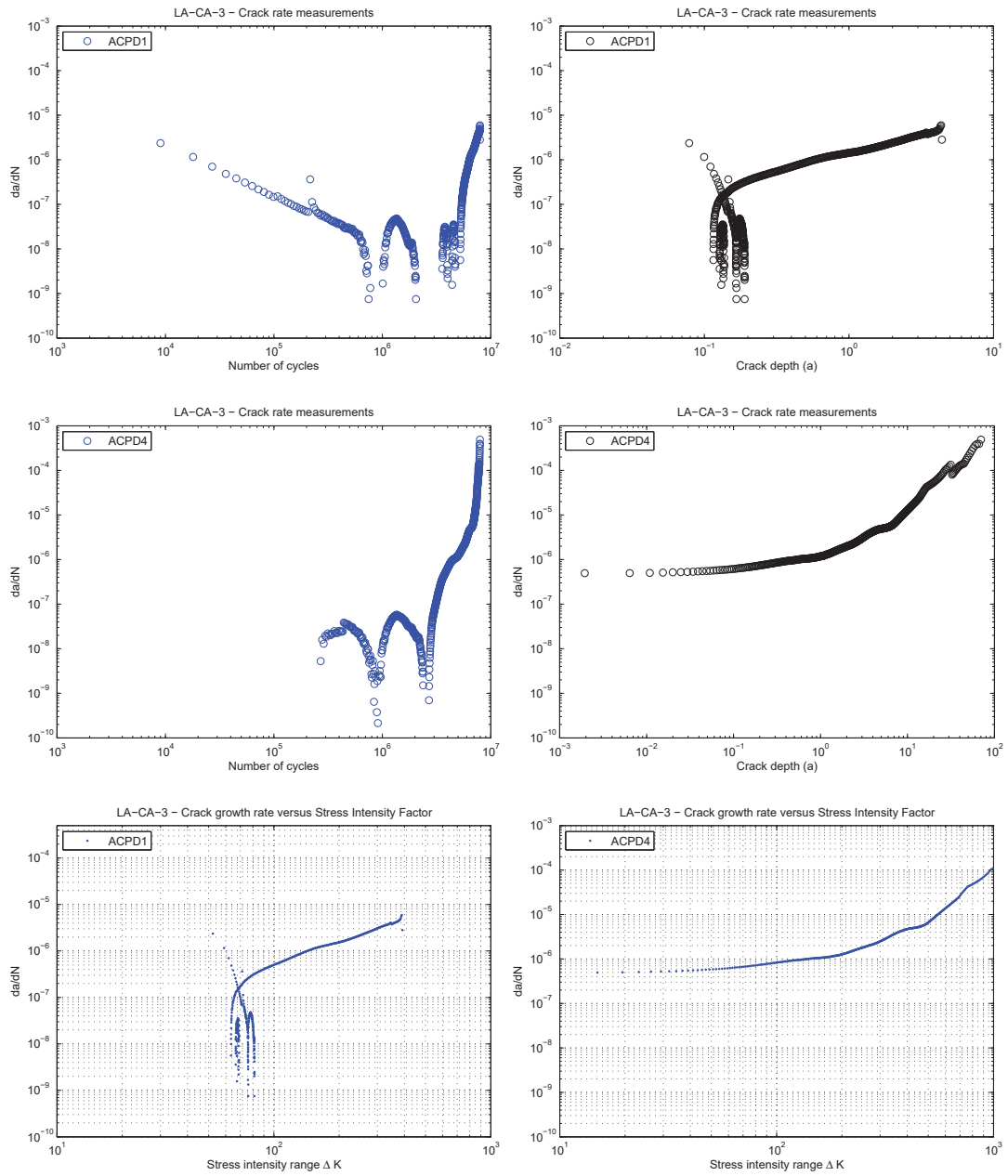


Figure C.4 – LA-CA-3: ACPD potential, estimated and measured crack depths

## C.1. Experiments under constant amplitude



Appendix C. Experimental results

LA-CA-4

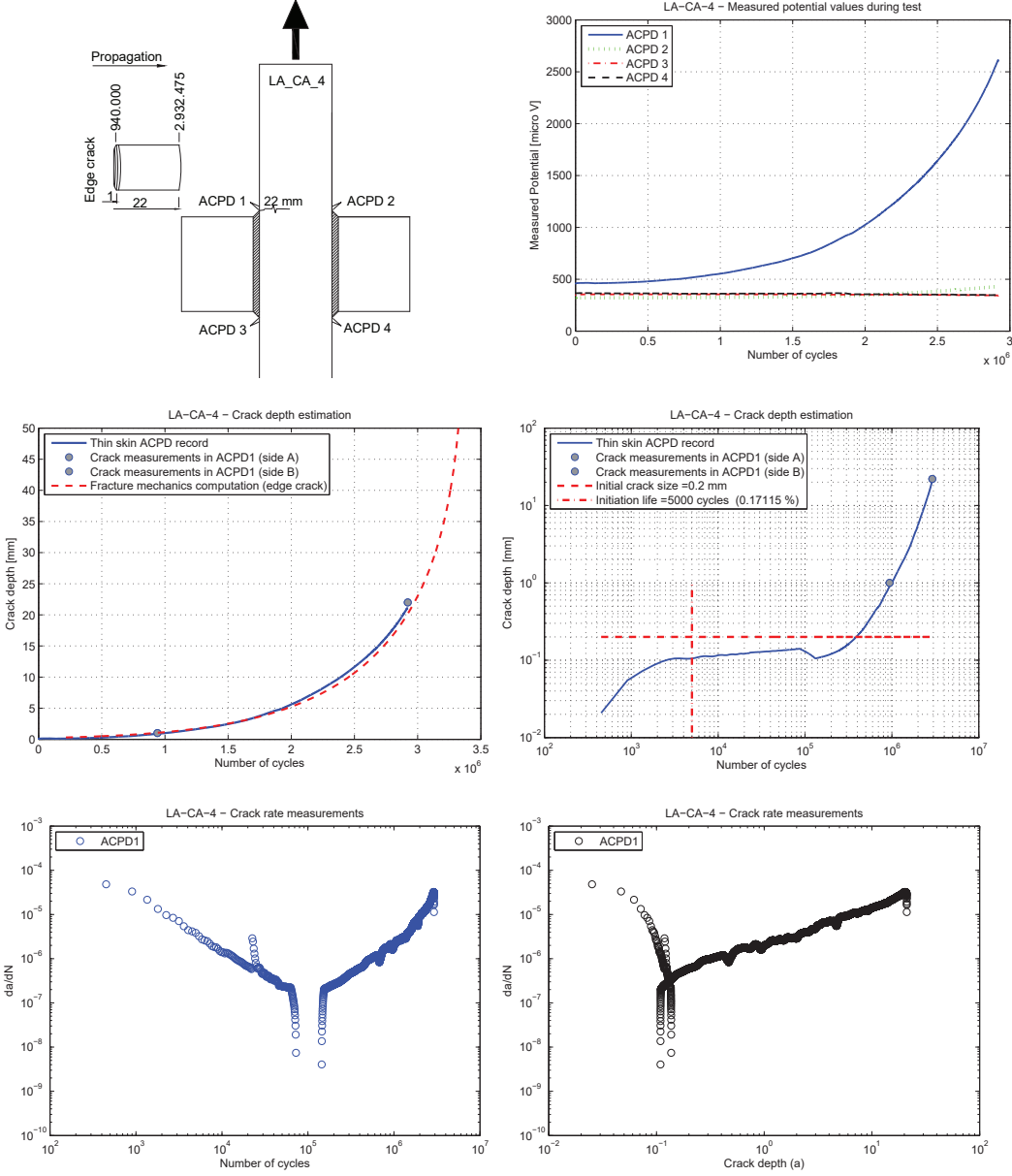


Figure C.5 – LA-CA-4: Estimated and measured crack depths

## C.1. Experiments under constant amplitude

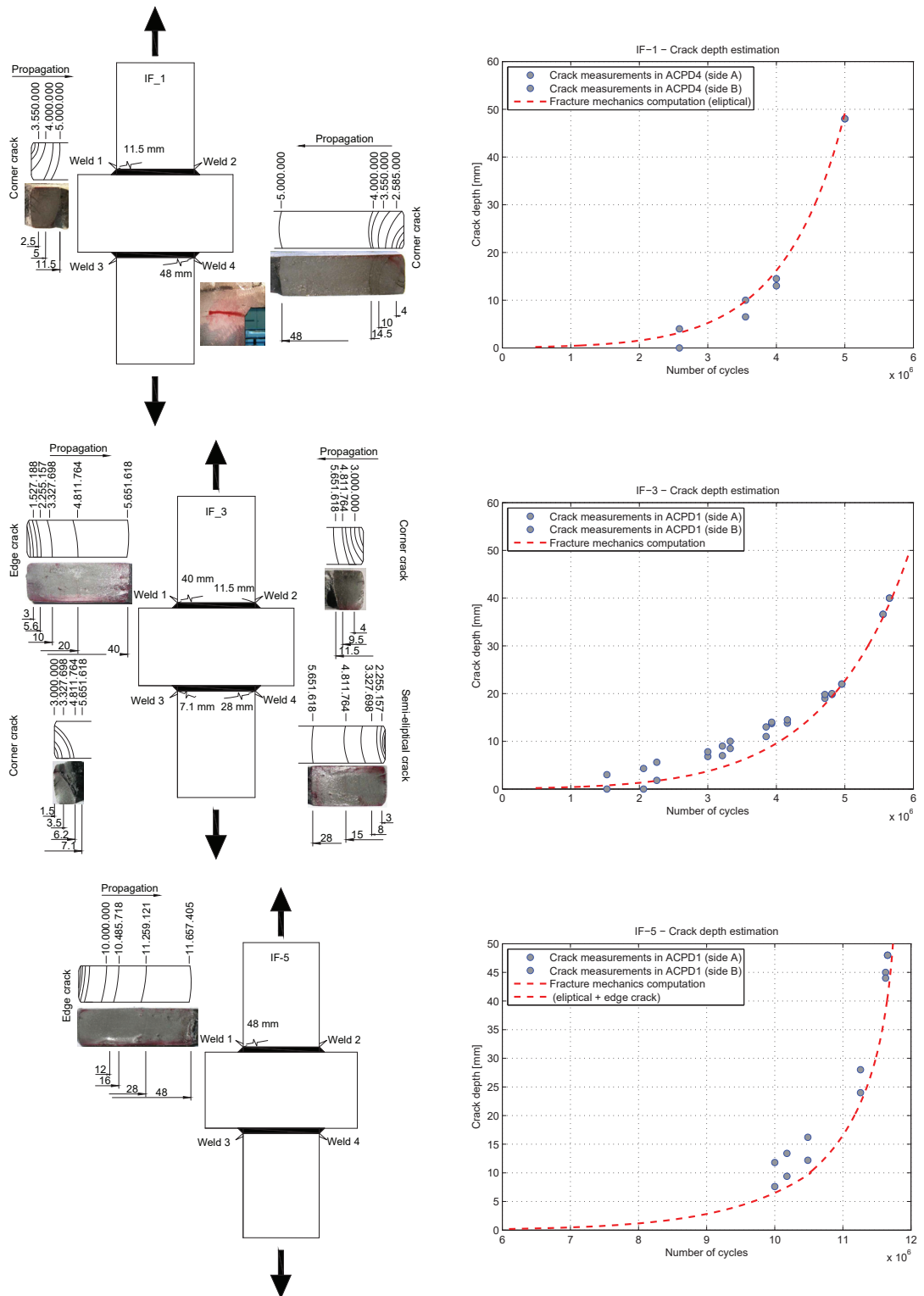


Figure C.6 – IF-1, IF-3 and IF-5: Crack measurements and fracture mechanics

# Appendix C. Experimental results

## IF-6

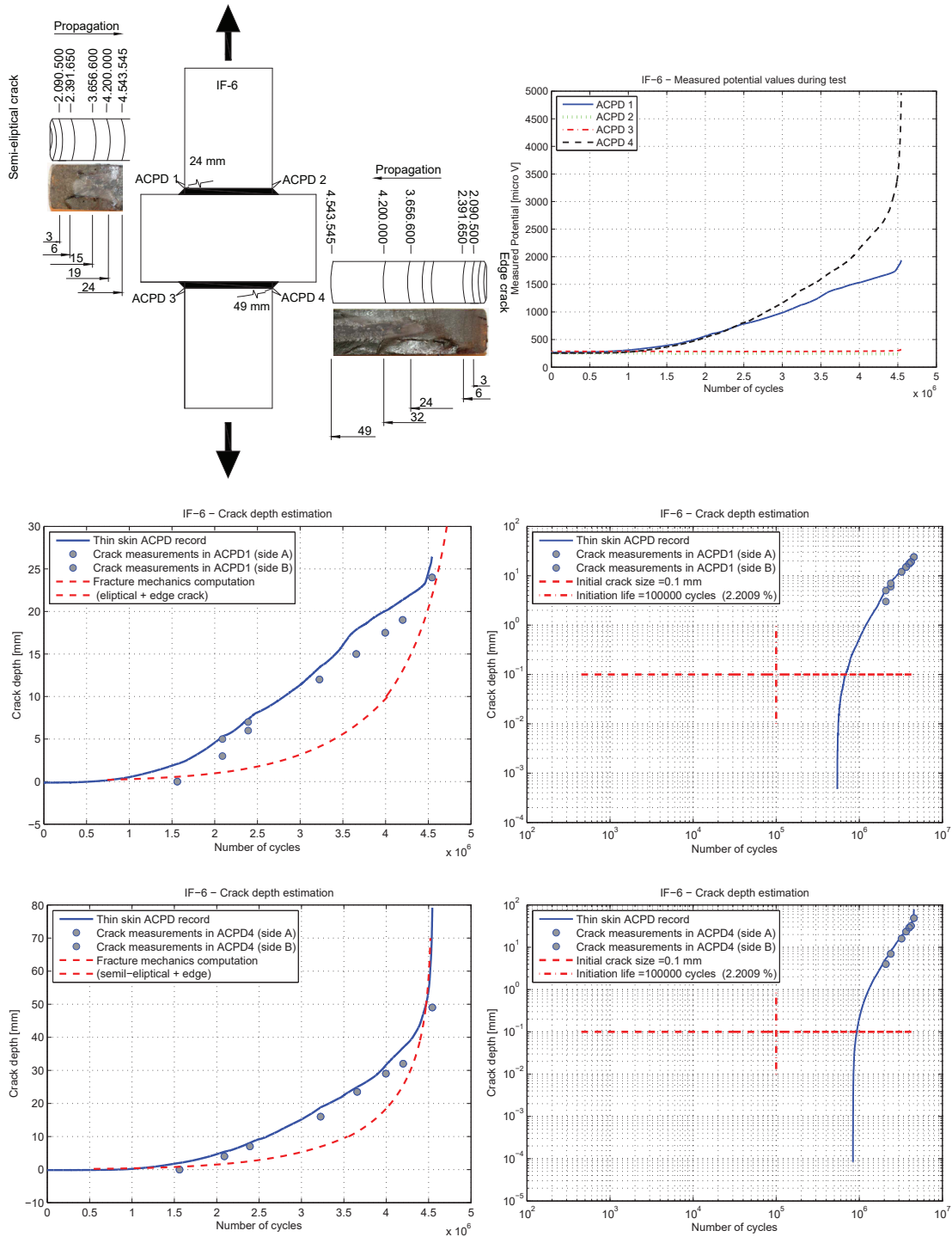


Figure C.7 – IF-6: ACPD potential, estimated and measured crack depths

## C.1. Experiments under constant amplitude

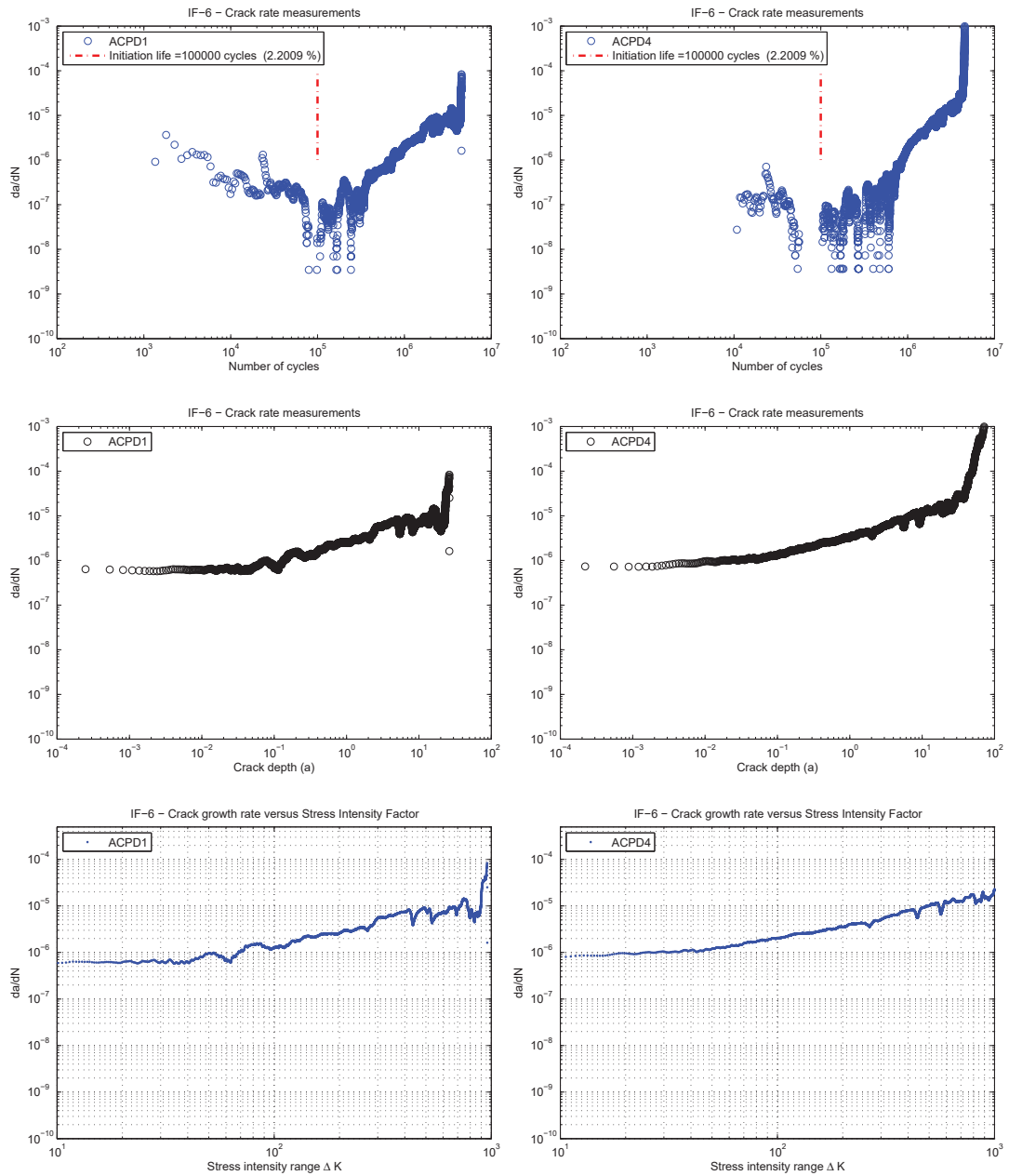


Figure C.8 – IF-6: Crack growth rate

# Appendix C. Experimental results

## IF-7

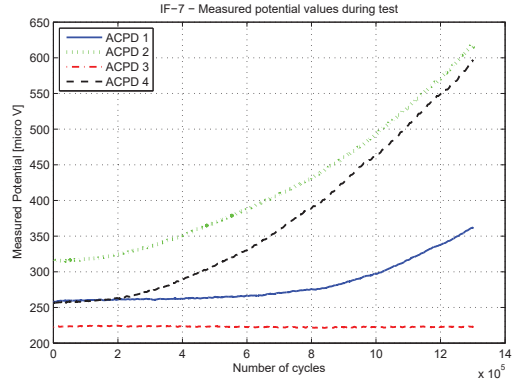
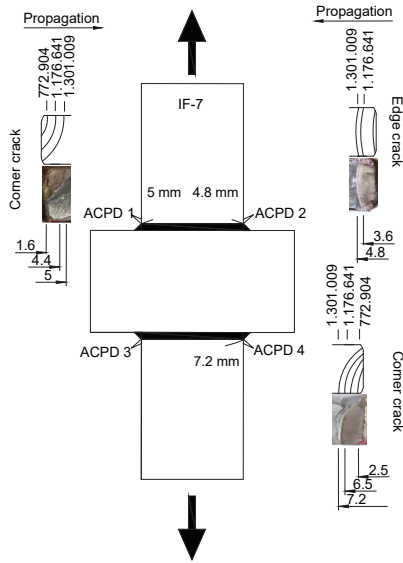


Figure C.9 – IF7: ACPD probes and measured potential values

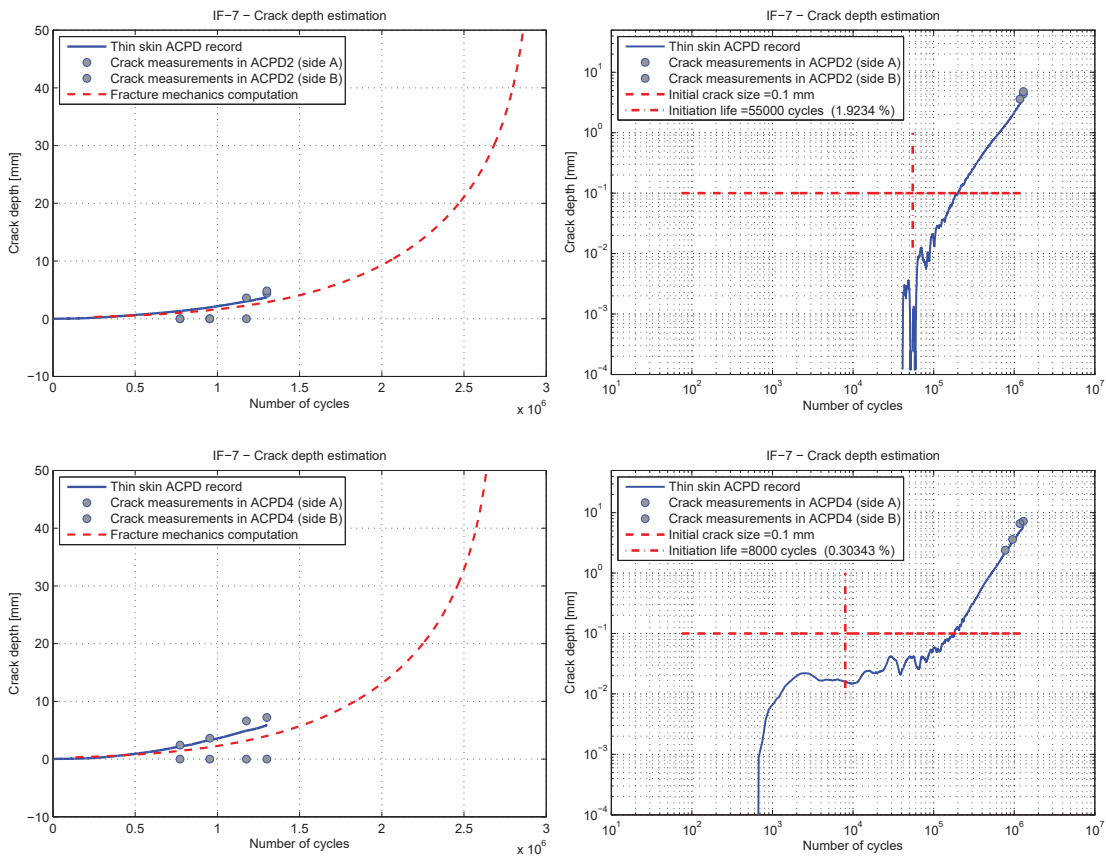


Figure C.10 – IF-7: ACPD potential, estimated and measured crack depths



## C.1. Experiments under constant amplitude

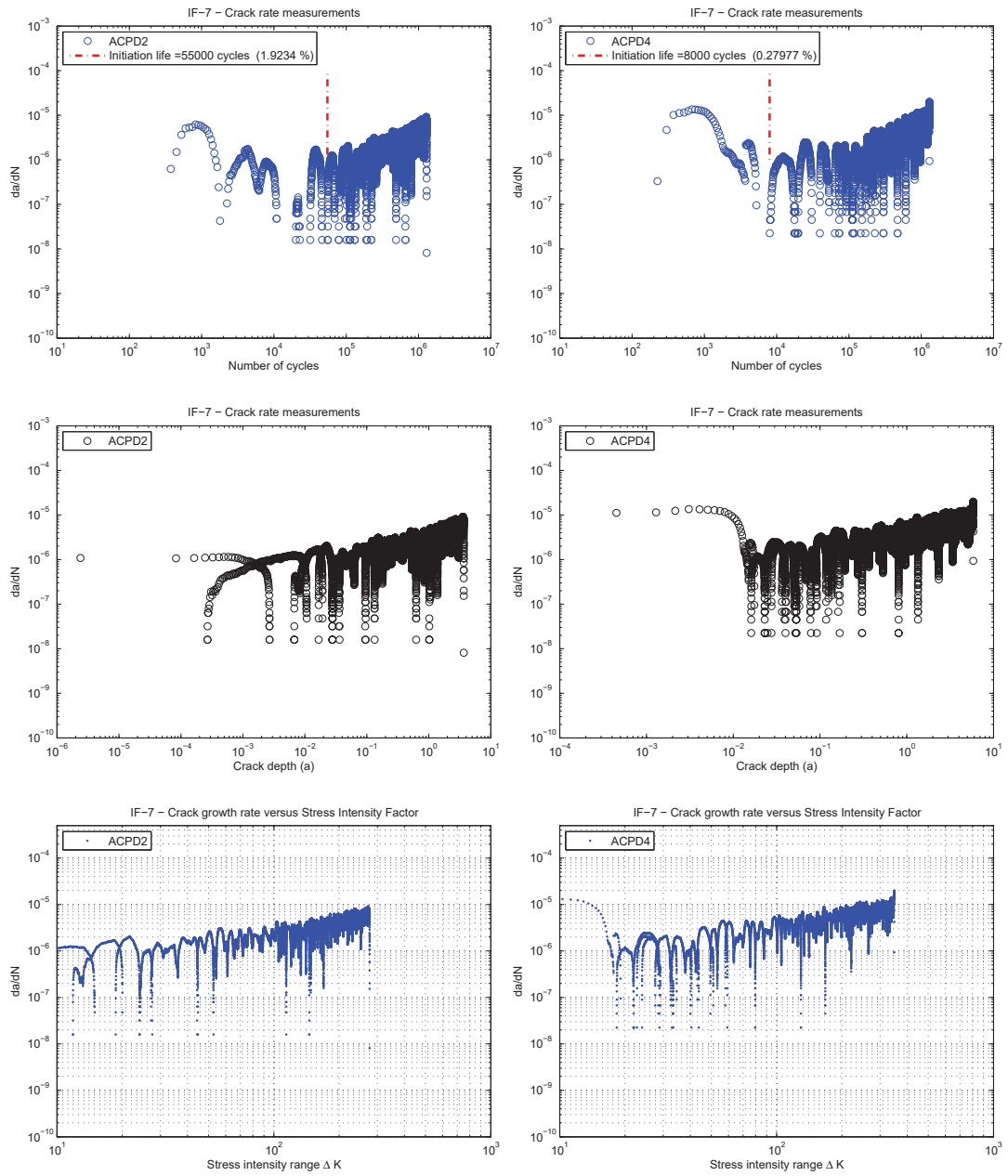


Figure C.11 – IF-7: Crack growth rate

# Appendix C. Experimental results

## IF-8

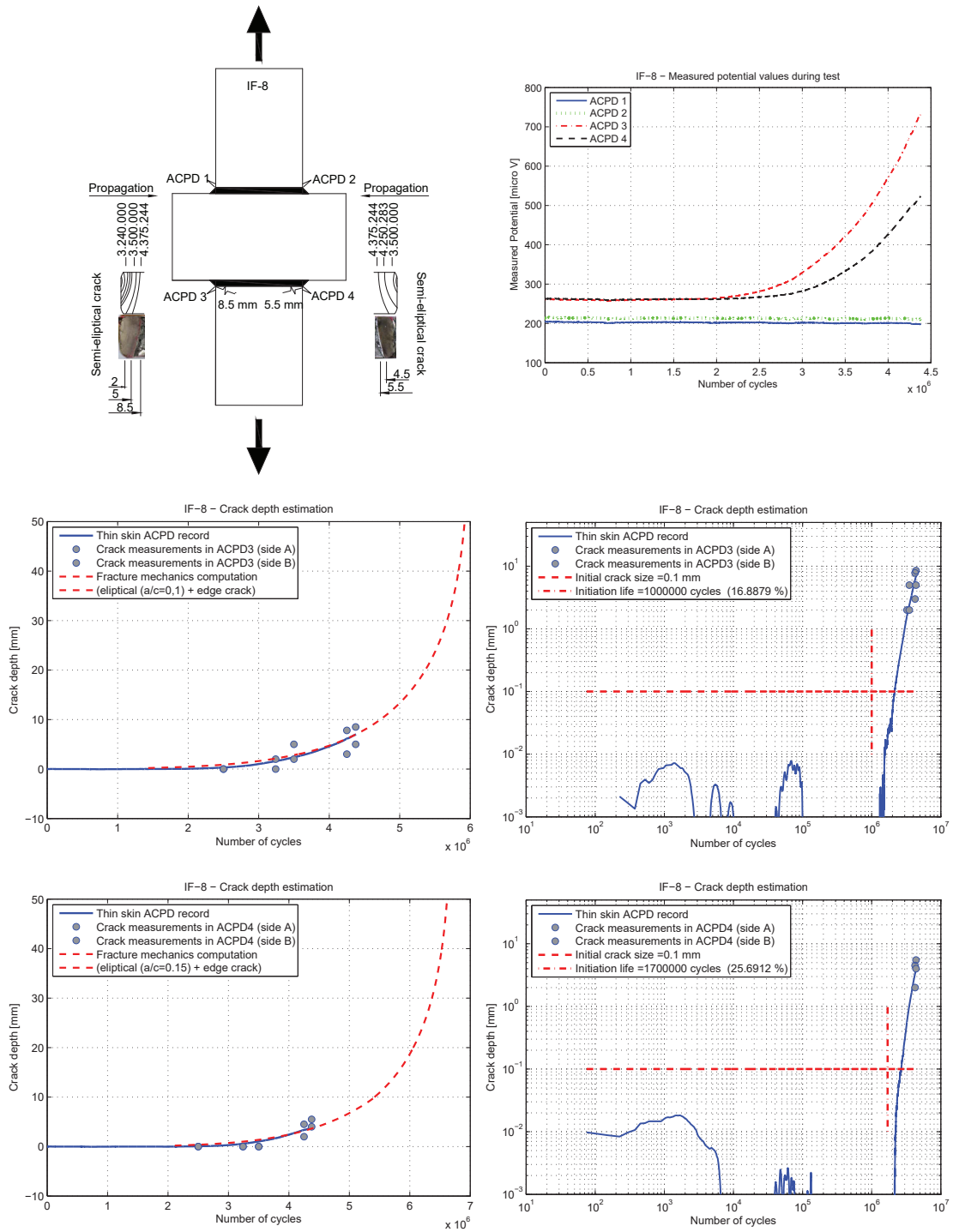


Figure C.12 – IF-8: ACPD potential, estimated and measured crack depths

## C.1. Experiments under constant amplitude

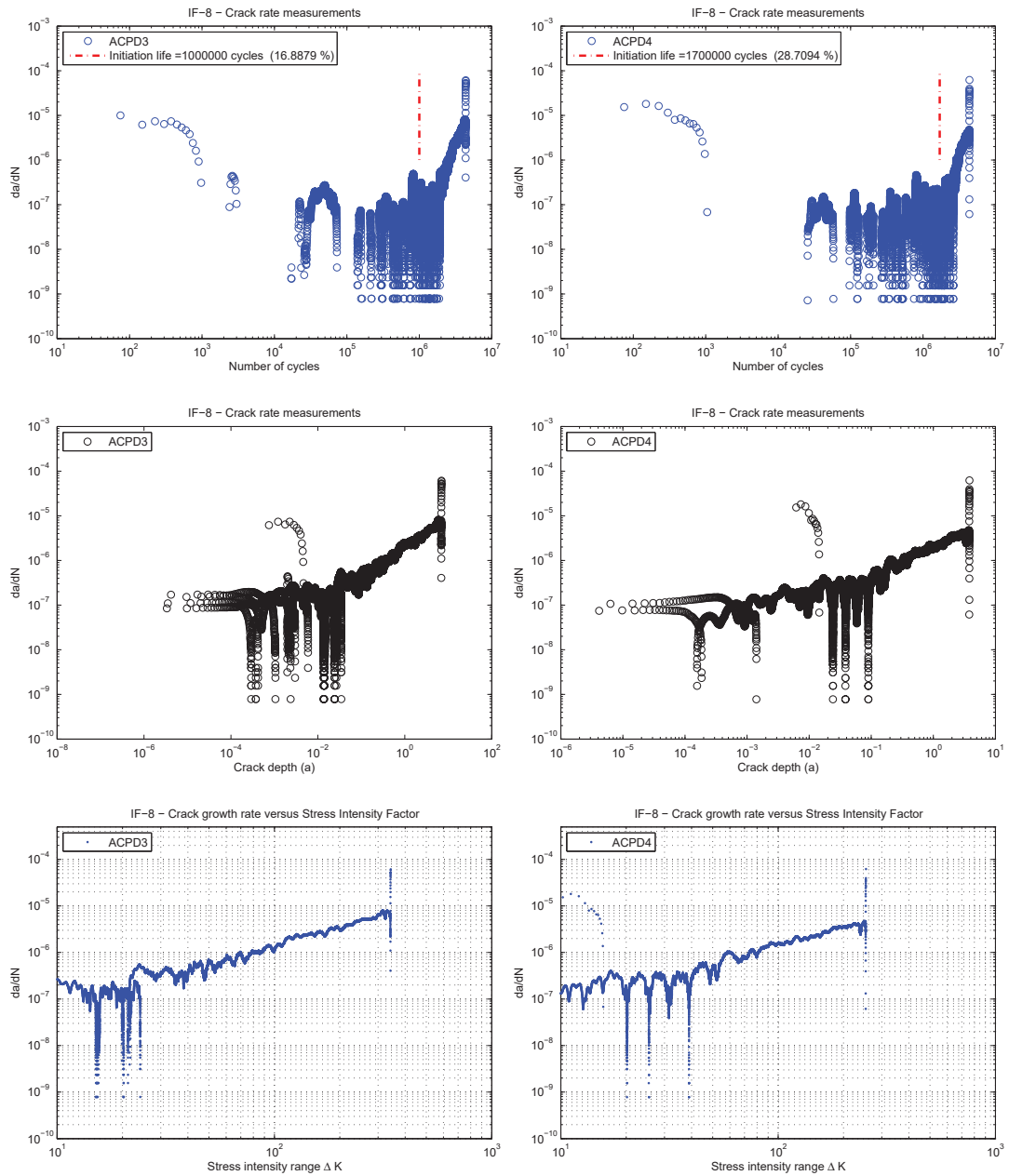
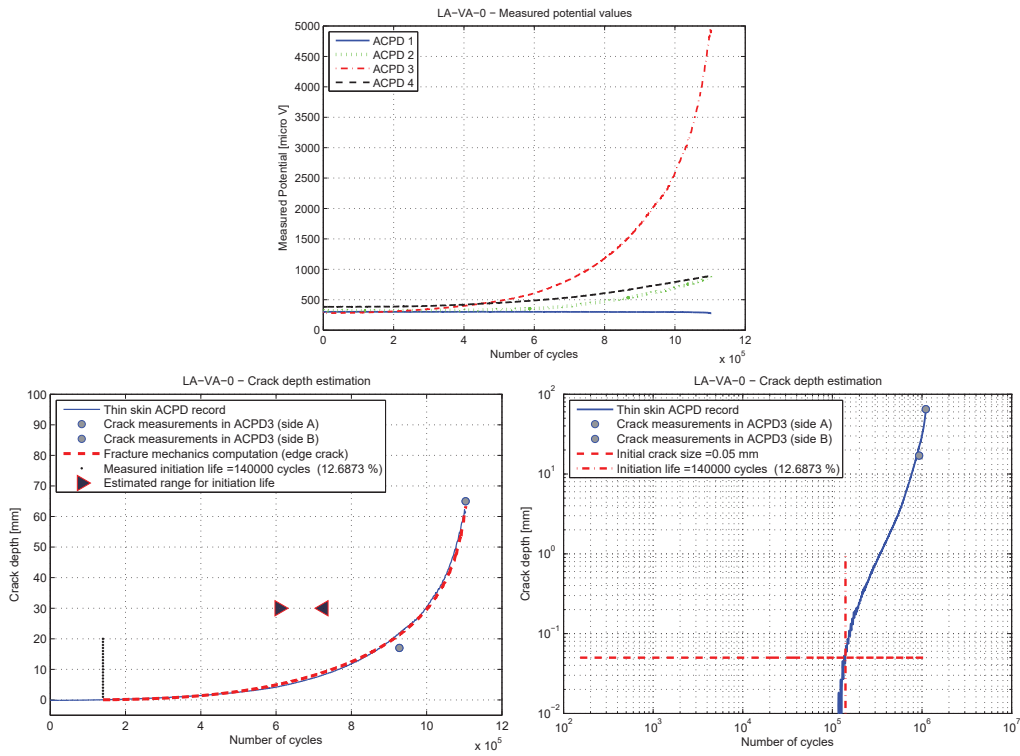


Figure C.13 – IF-8: Crack growth rate

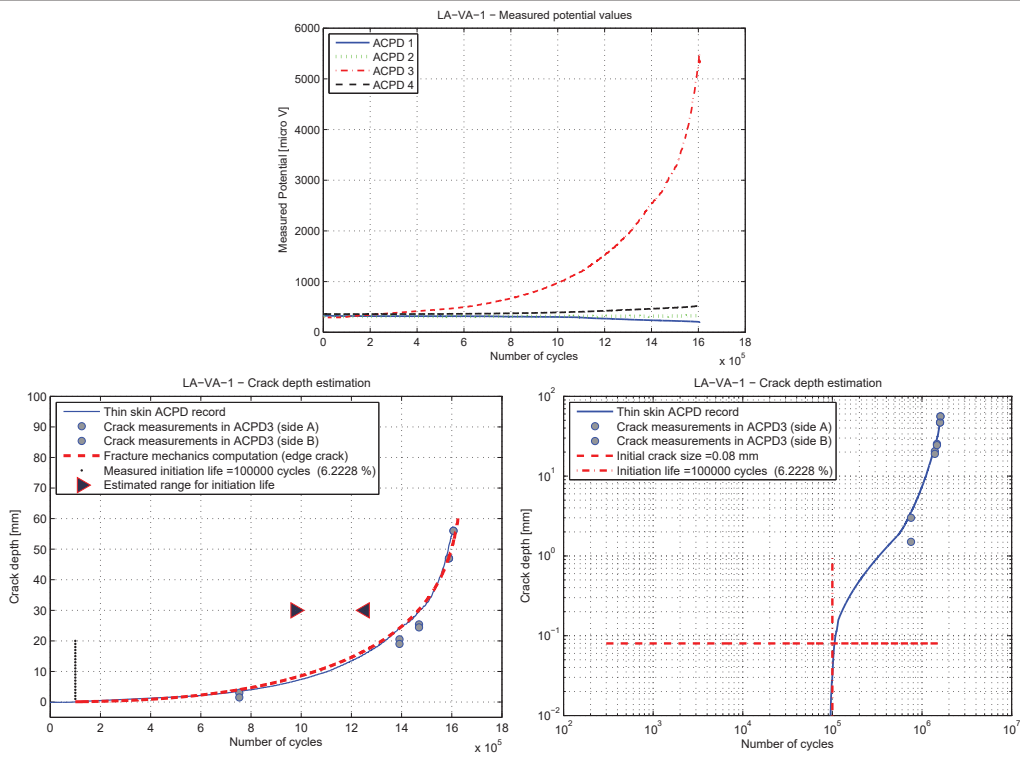
Appendix C. Experimental results

C.2 Experiments under variable amplitude

LA-VA-0

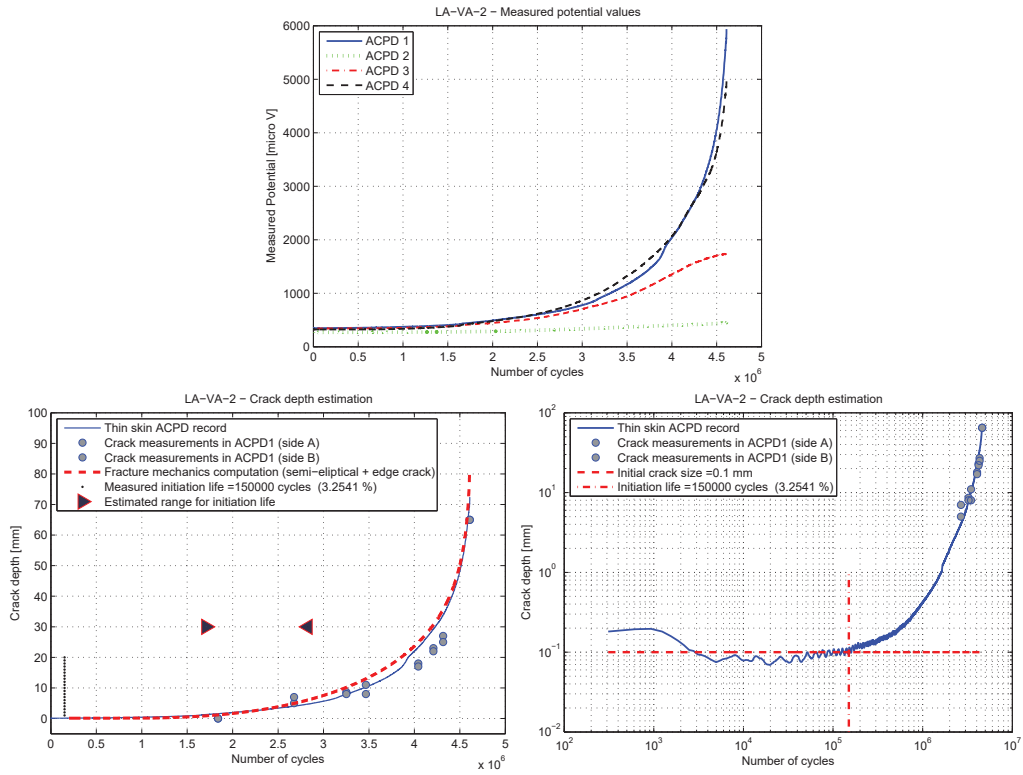


LA-VA-1

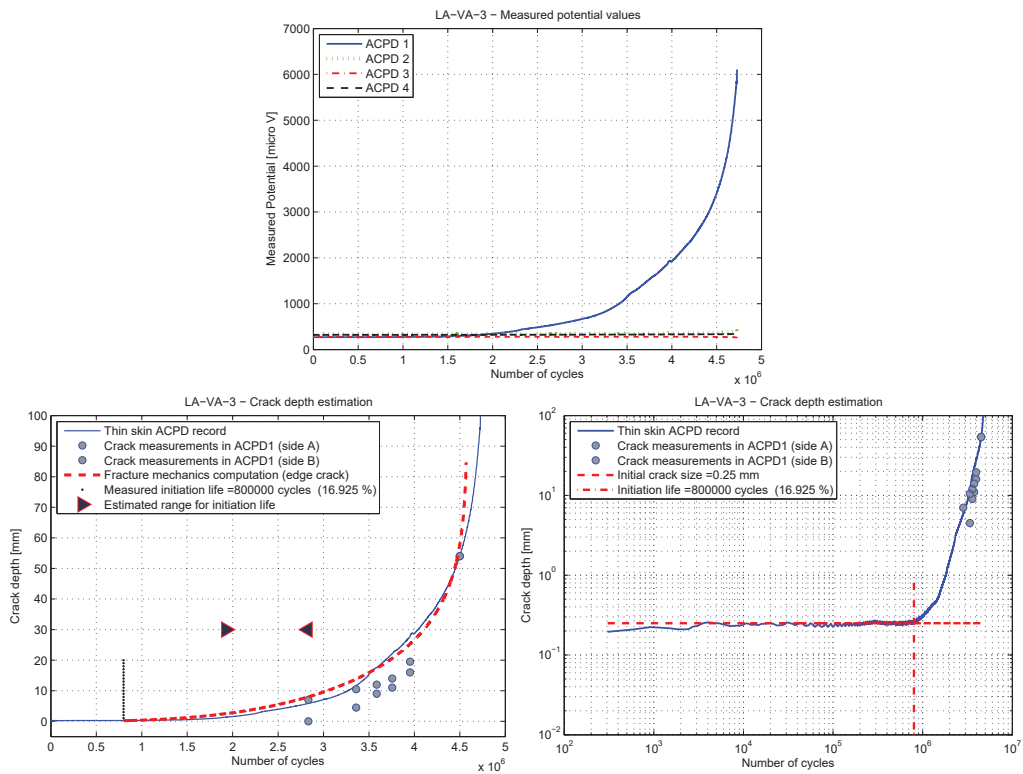


## C.2. Experiments under variable amplitude

### LA-VA-2

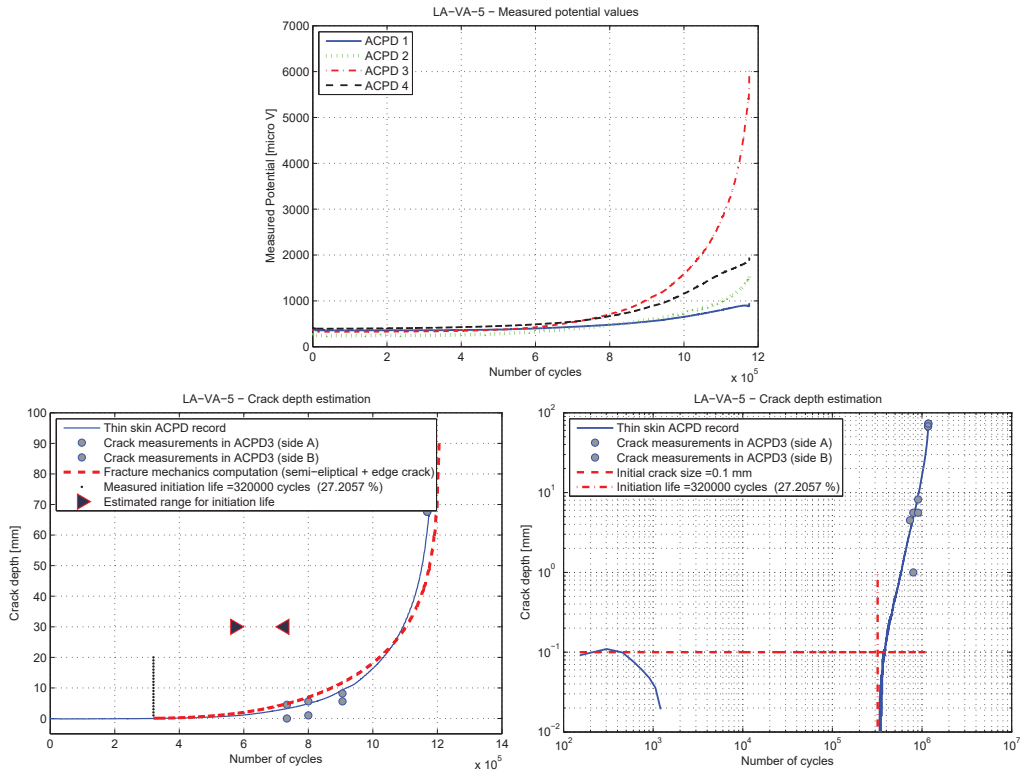


### LA-VA-3

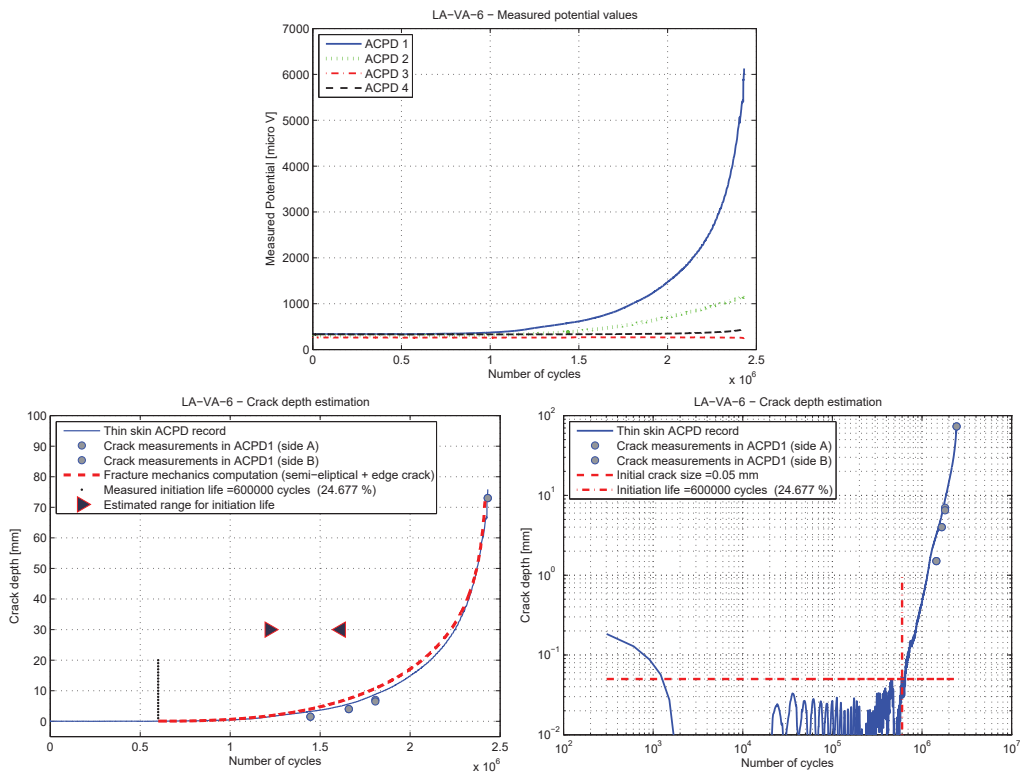


# Appendix C. Experimental results

## LA-VA-5

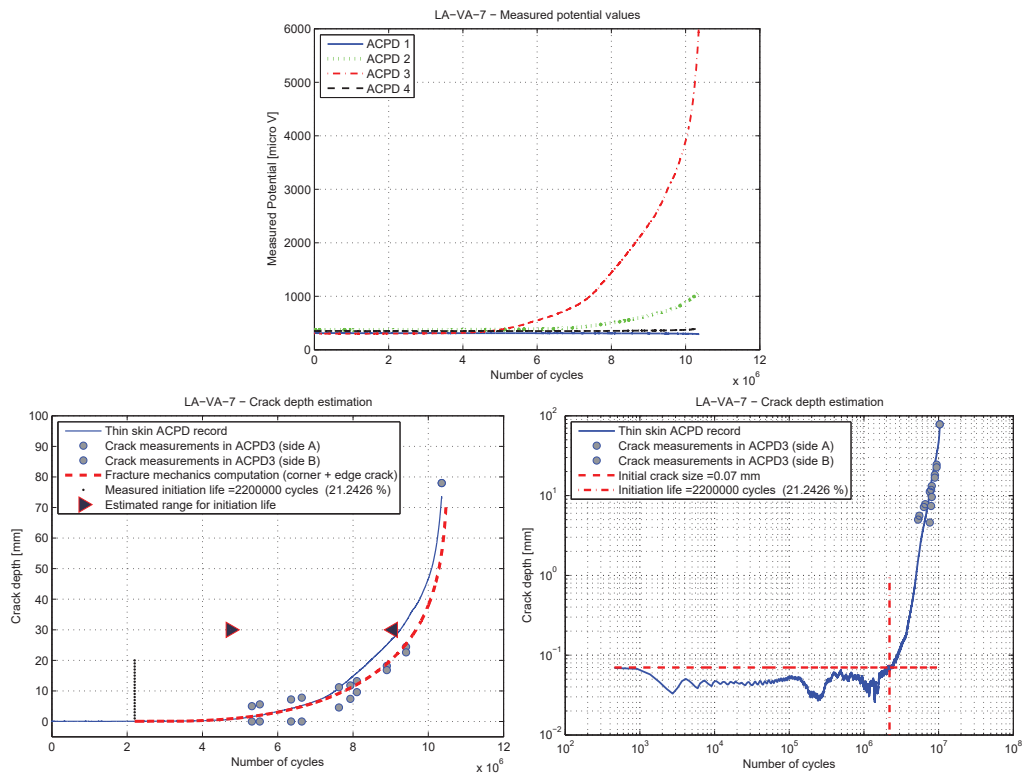


## LA-VA-6

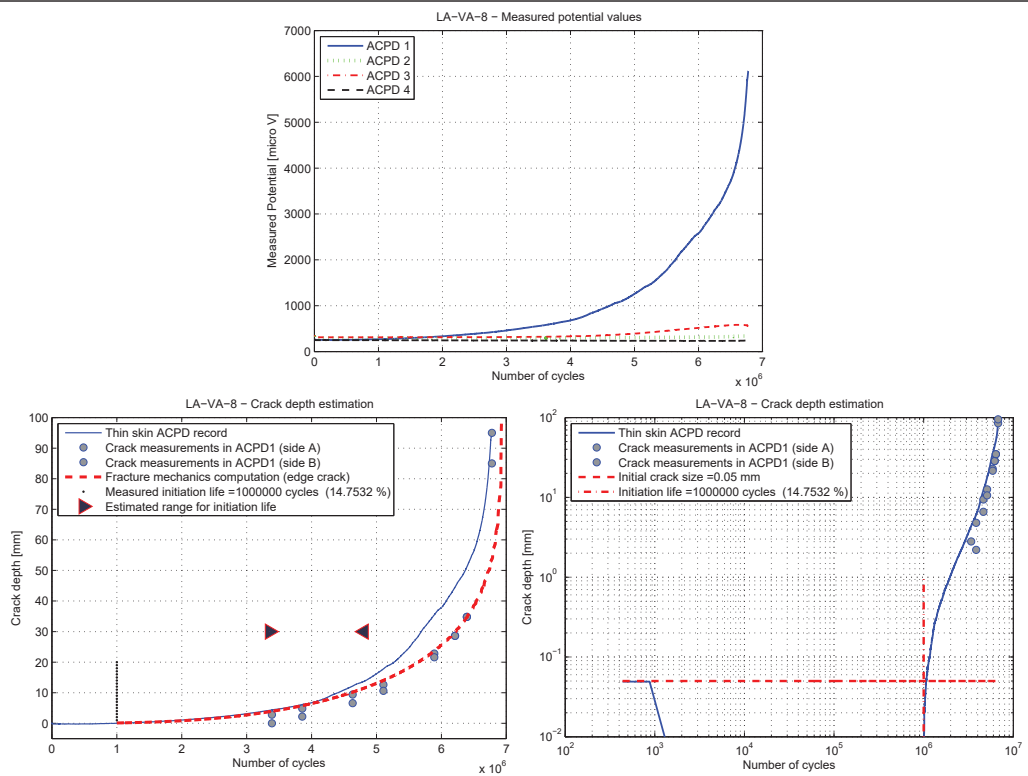


## C.2. Experiments under variable amplitude

### LA-VA-7

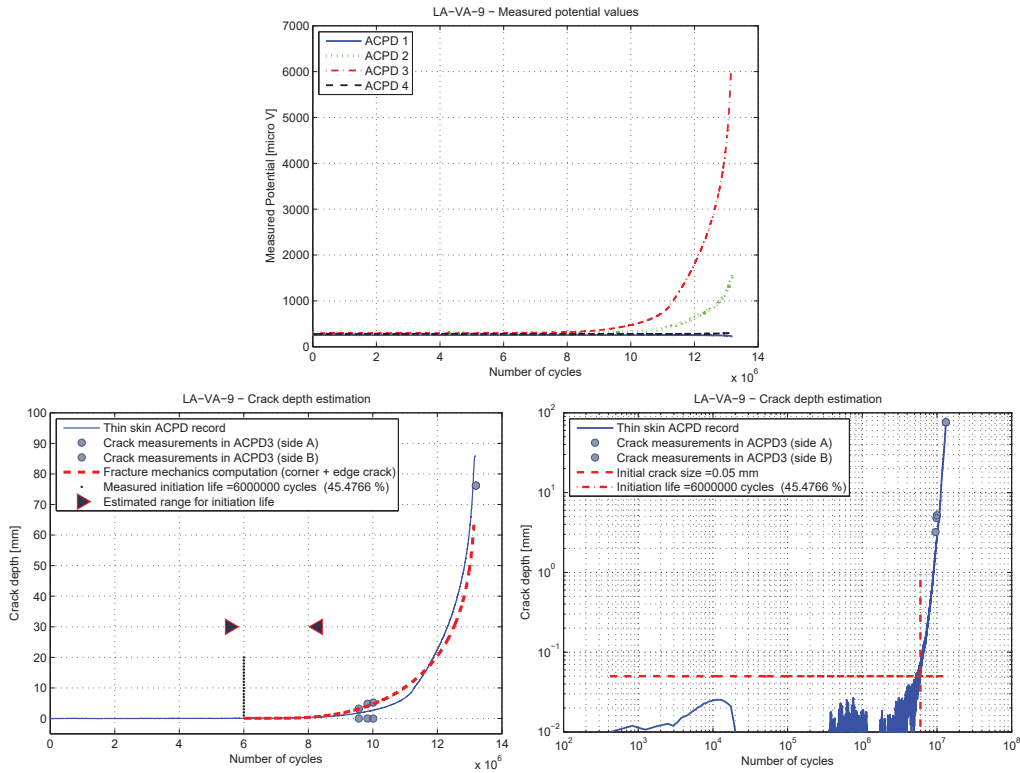


### LA-VA-8

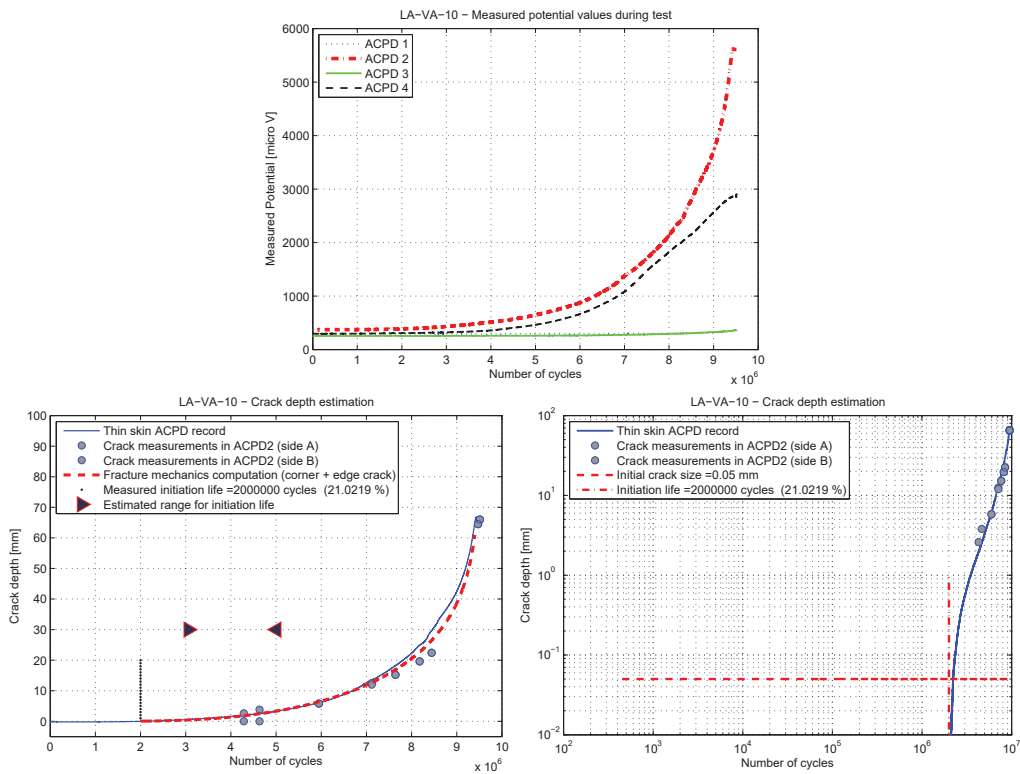


# Appendix C. Experimental results

## LA-VA-9



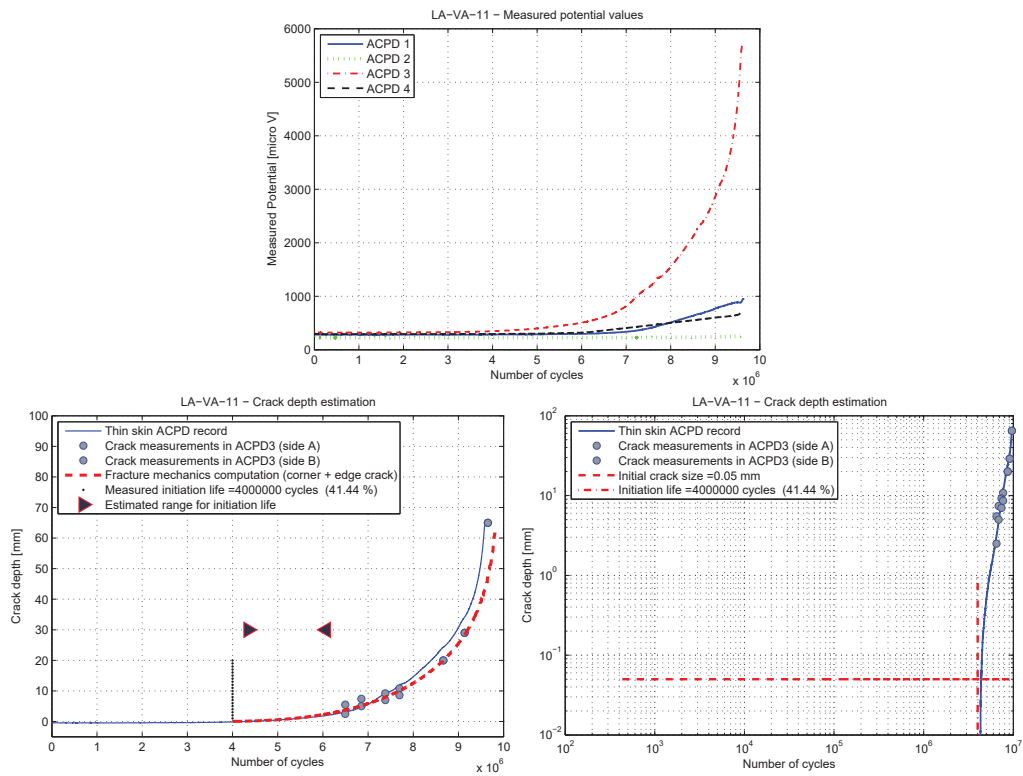
## LA-VA-10



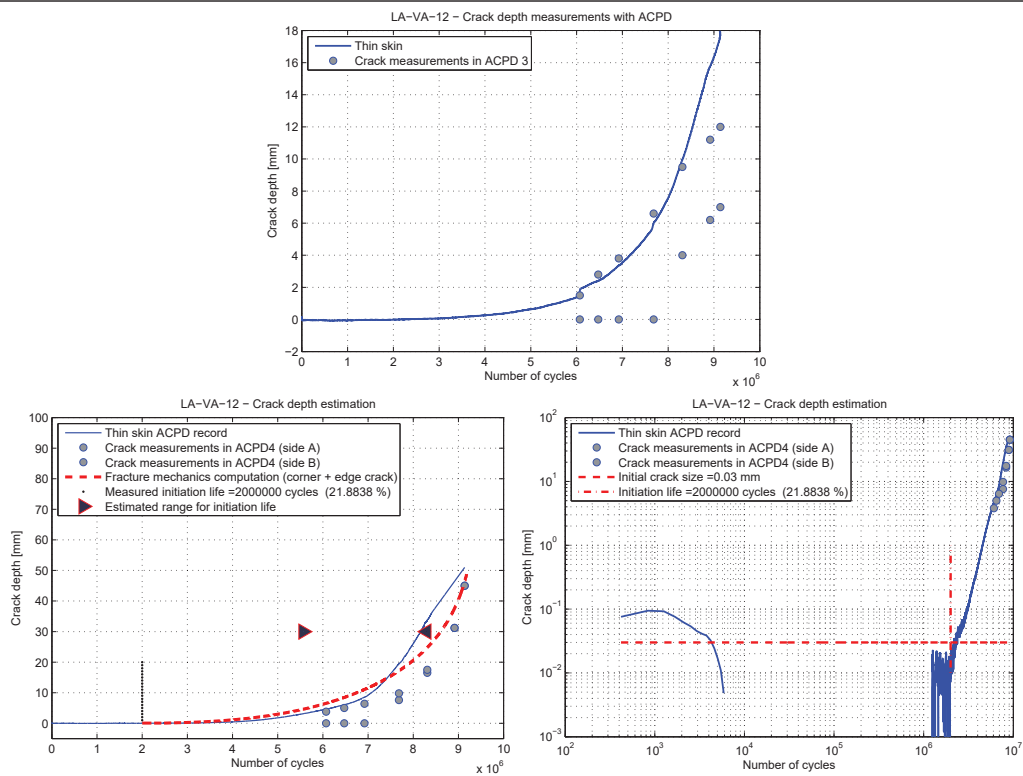


## C.2. Experiments under variable amplitude

### LA-VA-11

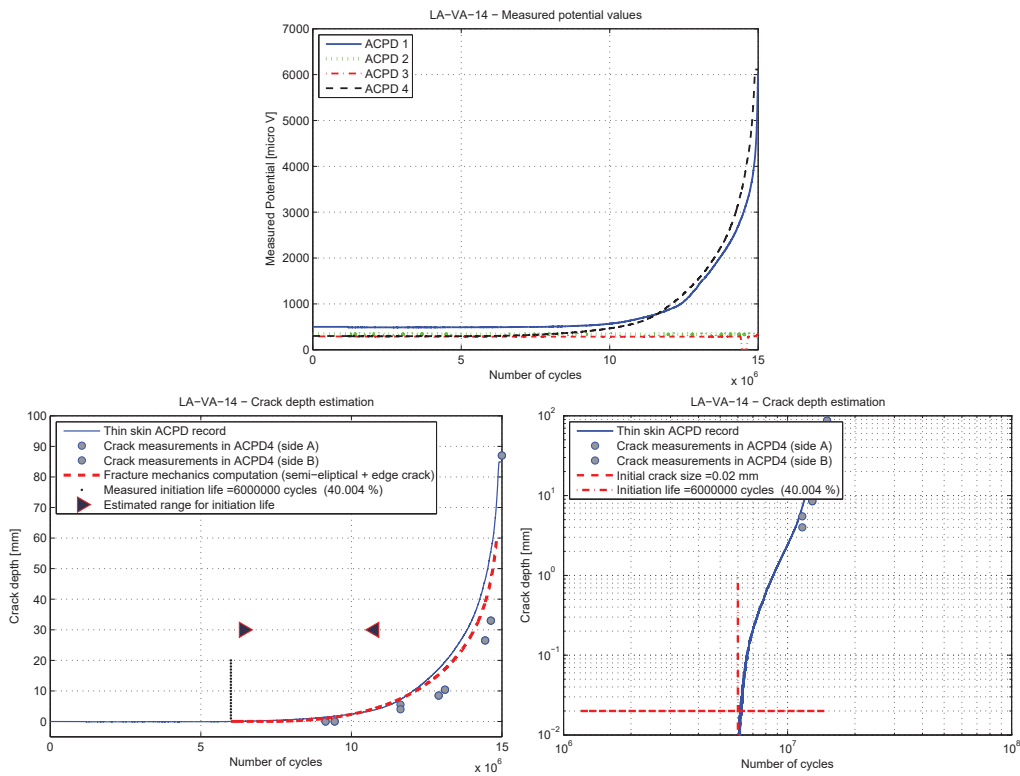


### LA-VA-12

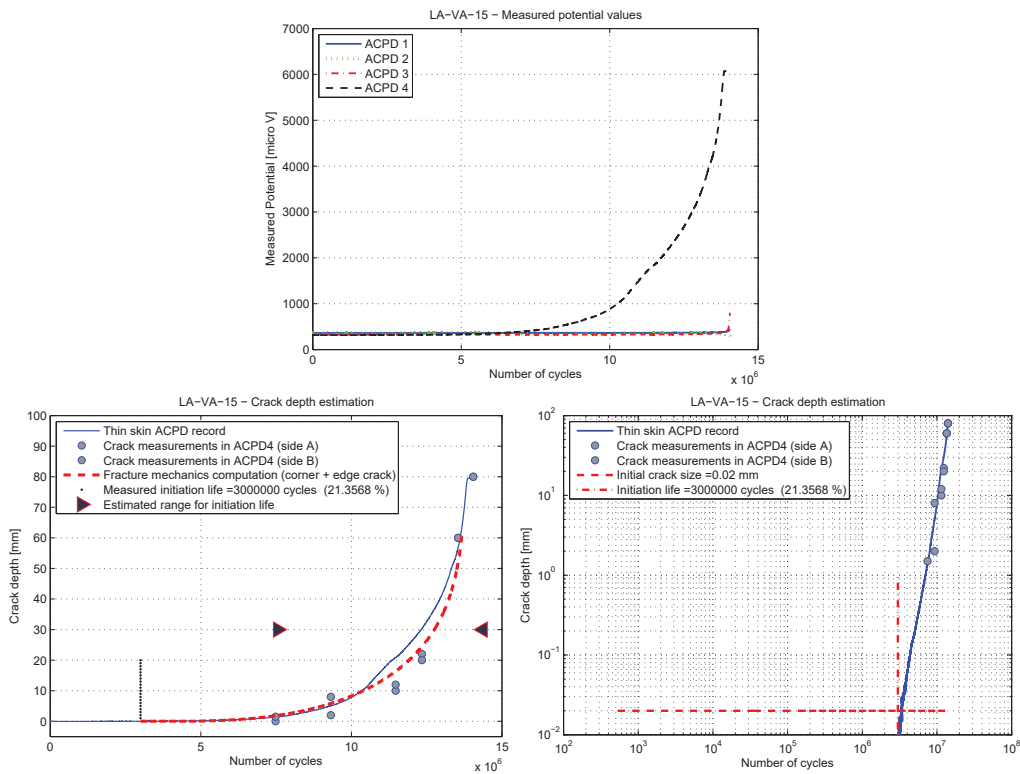


## Appendix C. Experimental results

### LA-VA-14

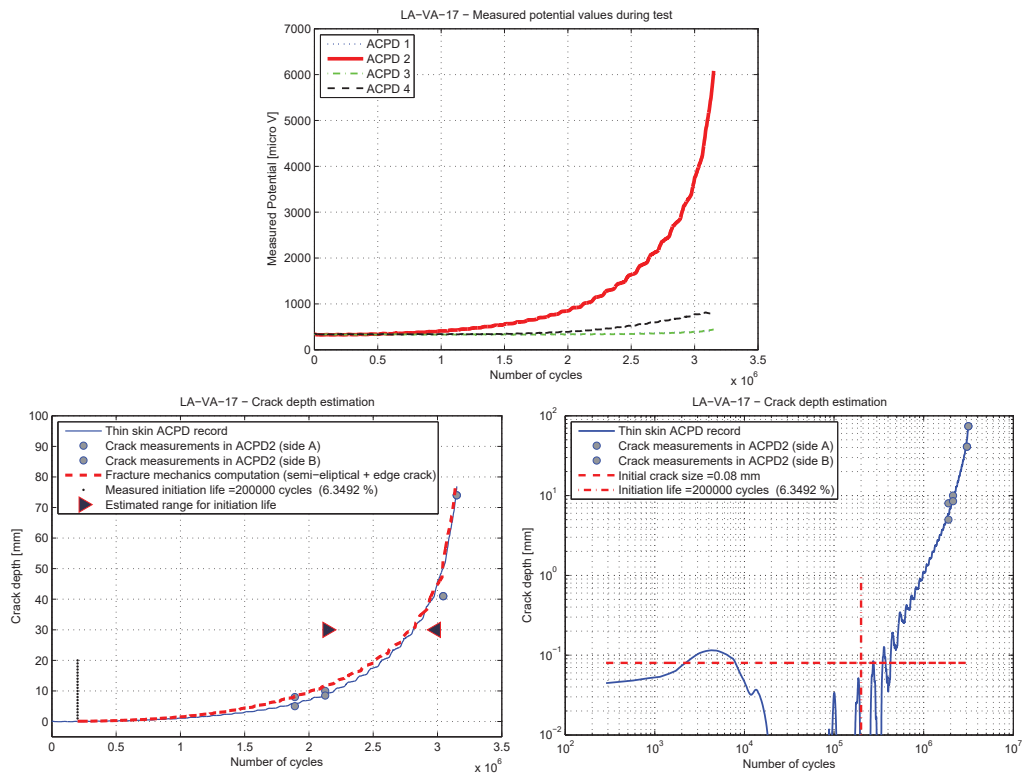


### LA-VA-15

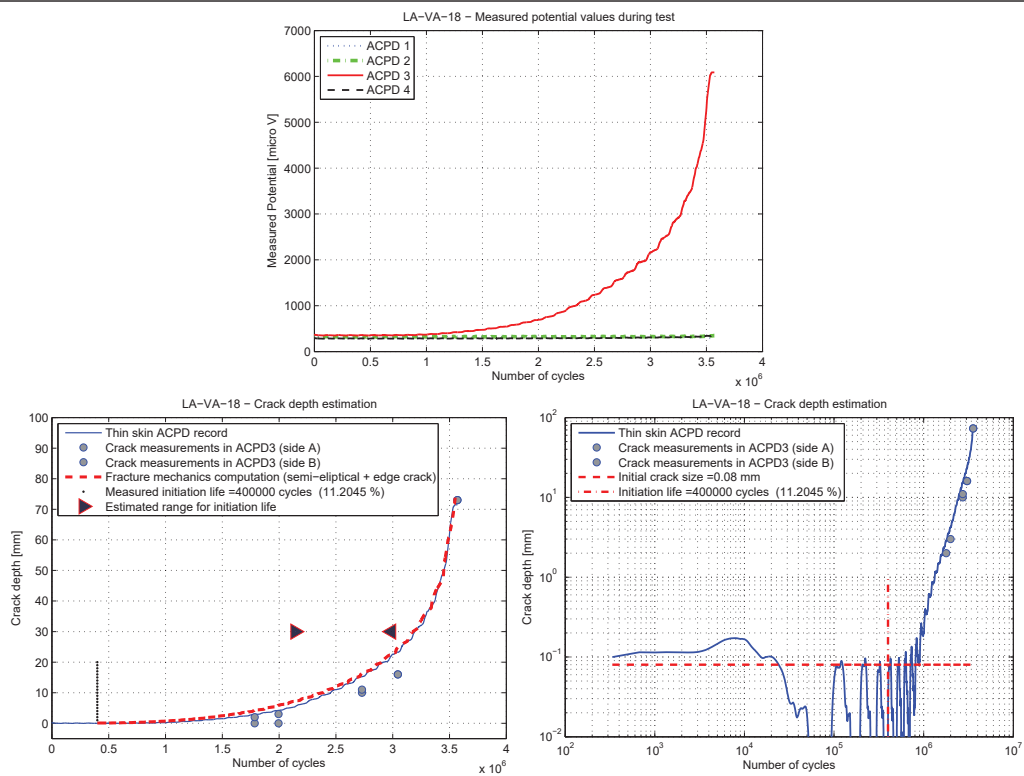


## C.2. Experiments under variable amplitude

### LA-VA-17

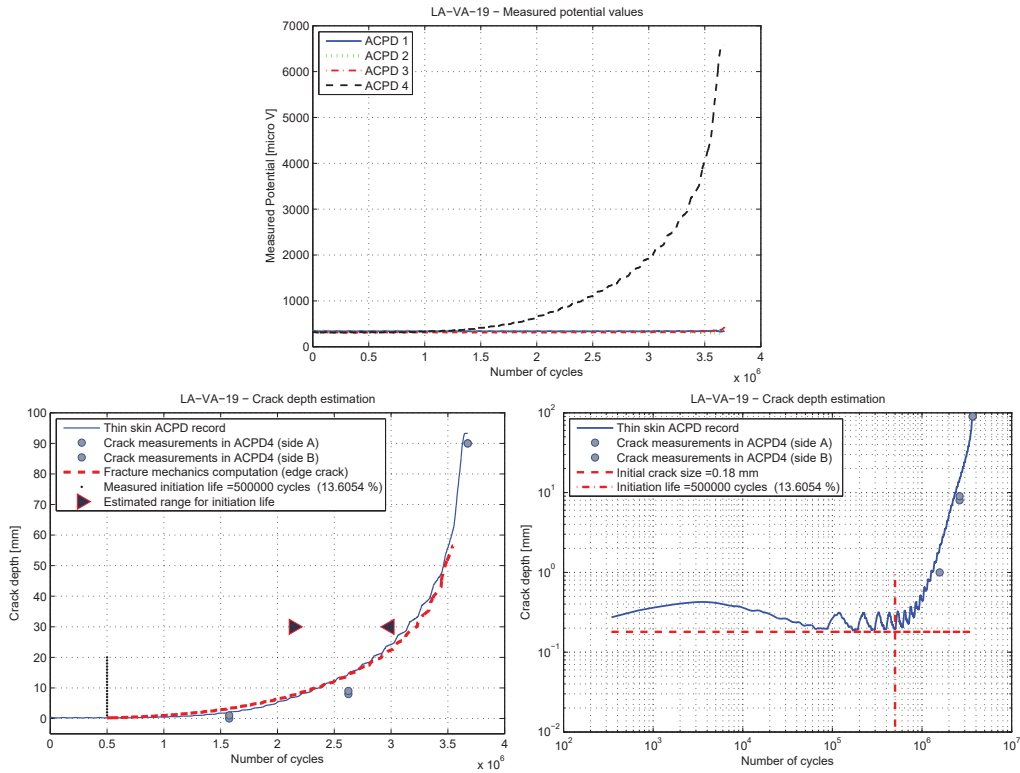


### LA-VA-18

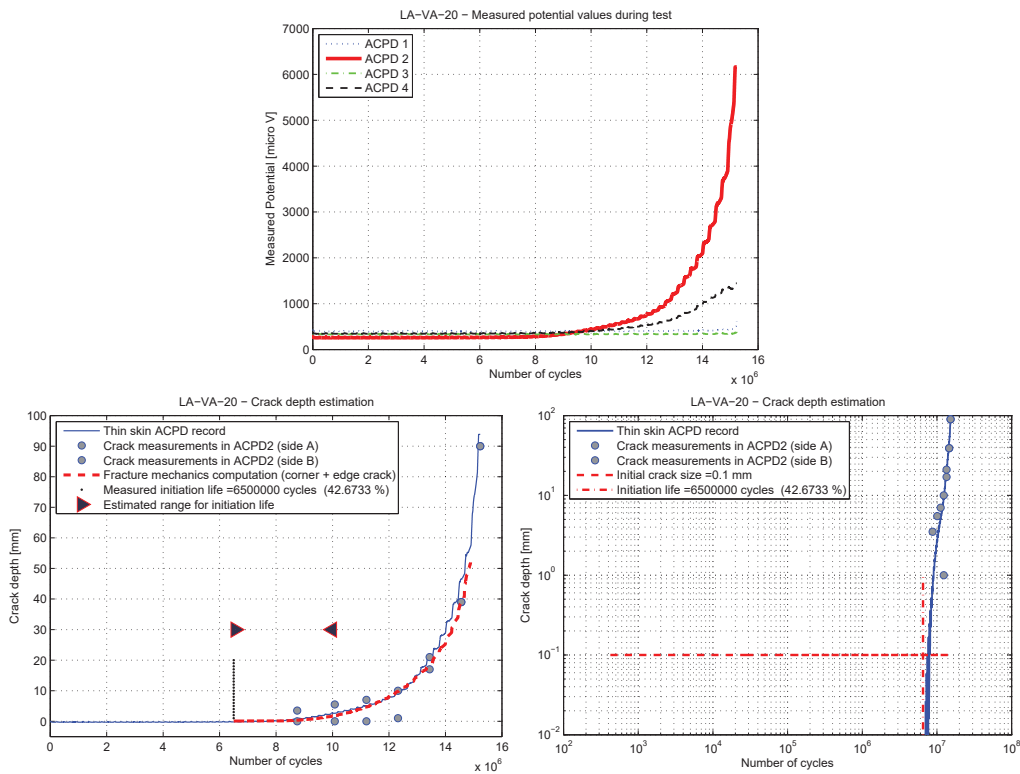


## Appendix C. Experimental results

### LA-VA-19



### LA-VA-20



## C.2. Experiments under variable amplitude

Specimen	N <sub>failure</sub> cycles	crack size [mm]	crack location ACPD	Figure
LA-VA-0	1.103.466	65	3	
LA-VA-1	1.607.006	56	3	
LA-VA-2	4.609.552	74	4	
LA-VA-3	4.726.744	120	1	
LA-VA-5	1.176.222	50	3	
LA-VA-6	2.431.418	50	3	
LA-VA-7	10.356.540	50	3	

Table C.1 – Crack surfaces - 1

## Appendix C. Experimental results

Specimen	$N_{\text{failure}}$ cycles	crack size [mm]	crack location ACPD	Figure
LA-VA-8	6.778.200	70	1	
LA-VA-9	13.193.600	70	1	
LA-VA-10	9.513.900	65	2	
LA-VA-11	9.652.500	65	3	
LA-VA-12	9.139.200	46	4	
LA-VA-14	14.998.500	87	4	
LA-VA-15	14.047.080	87	4	

Table C.2 – Crack surfaces - 2

## C.2. Experiments under variable amplitude

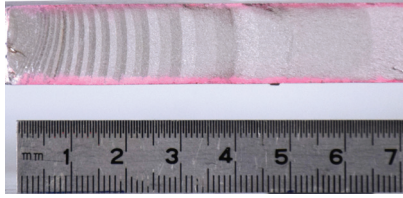
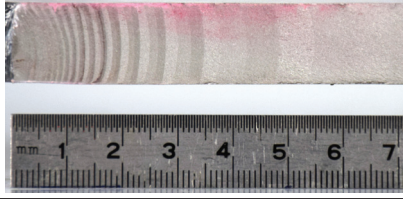
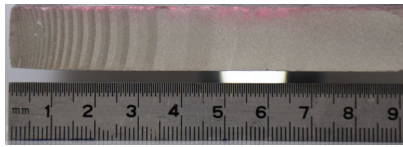
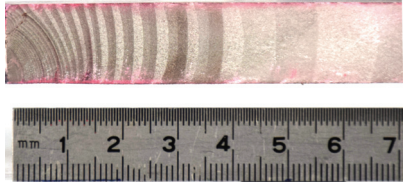
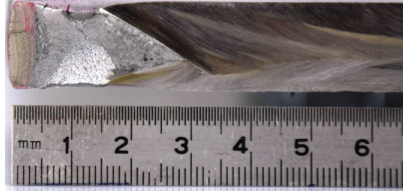
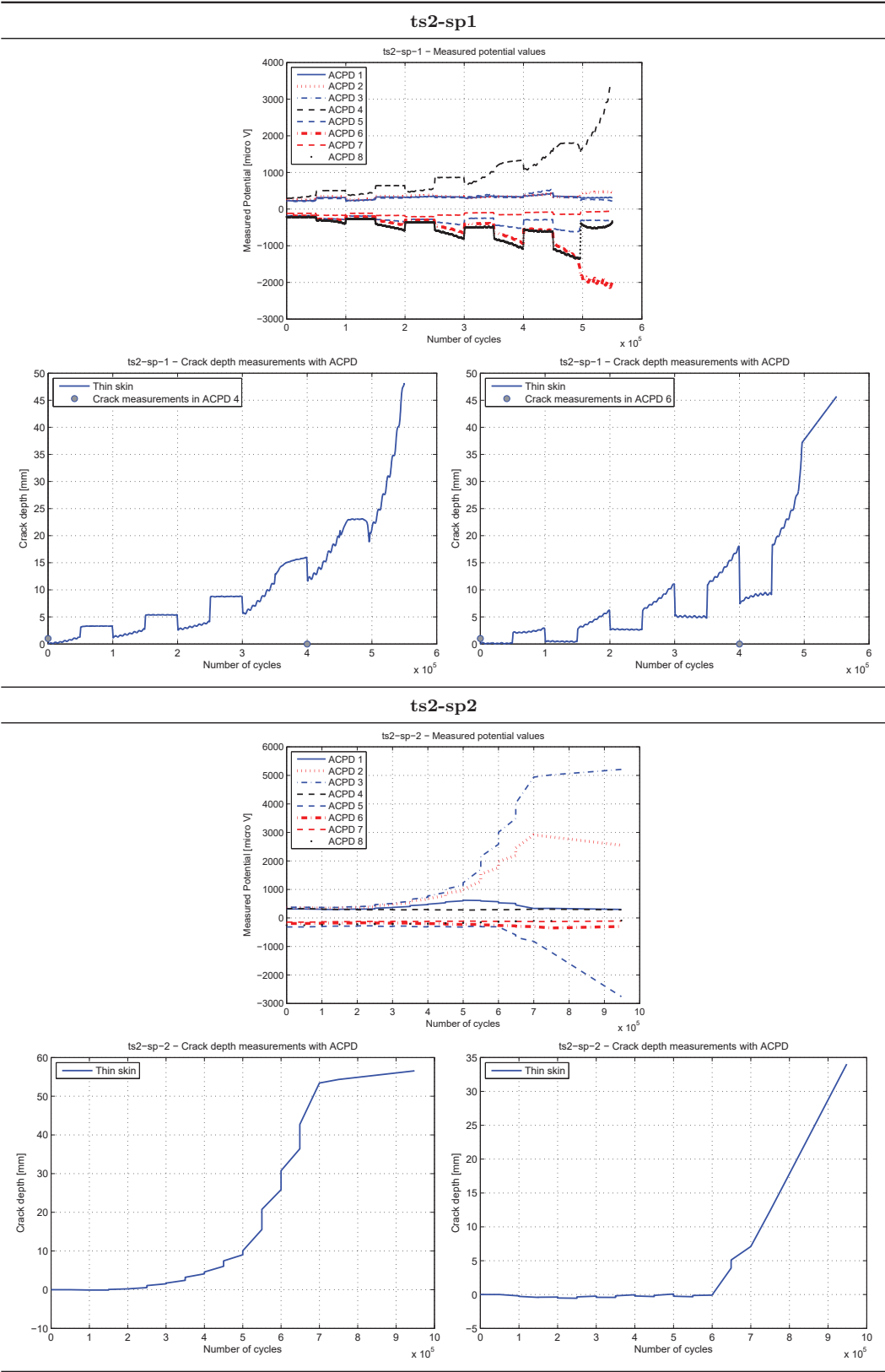
Specimen	$N_{\text{failure}}$ cycles	crack size [mm]	crack location ACPD	Figure
LA-VA-17	3.150.000	87	4	
LA-VA-18	3.570.000	87	3	
LA-VA-19	3.570.000	87	3	
LA-VA-20	3.570.000	87	3	
LA-VA-21	3.570.000	87	3	

Table C.3 – Crack surfaces - 3



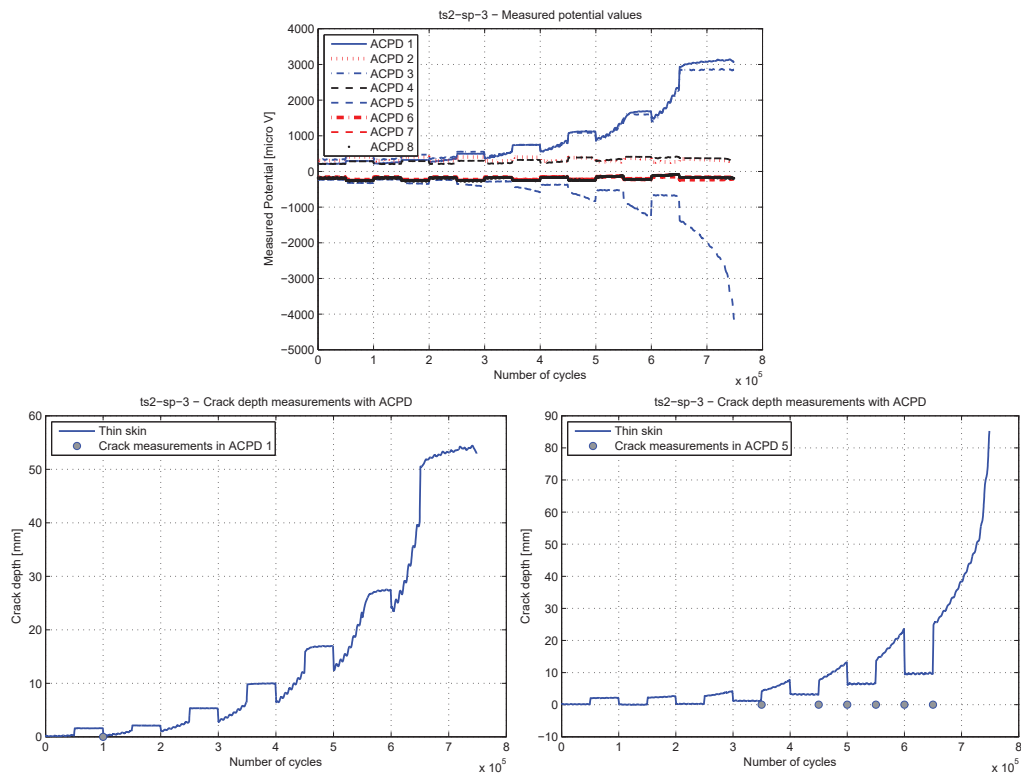
### C.3 Experiments under non-proportional load



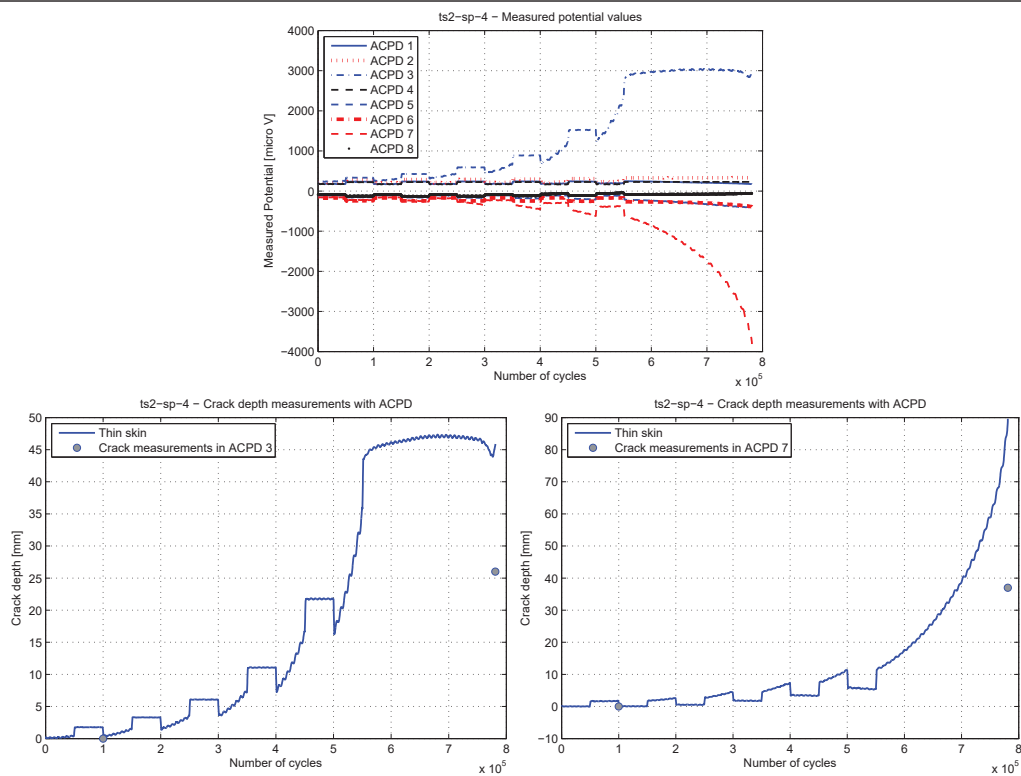


### C.3. Experiments under non-proportional load

#### ts2-sp3

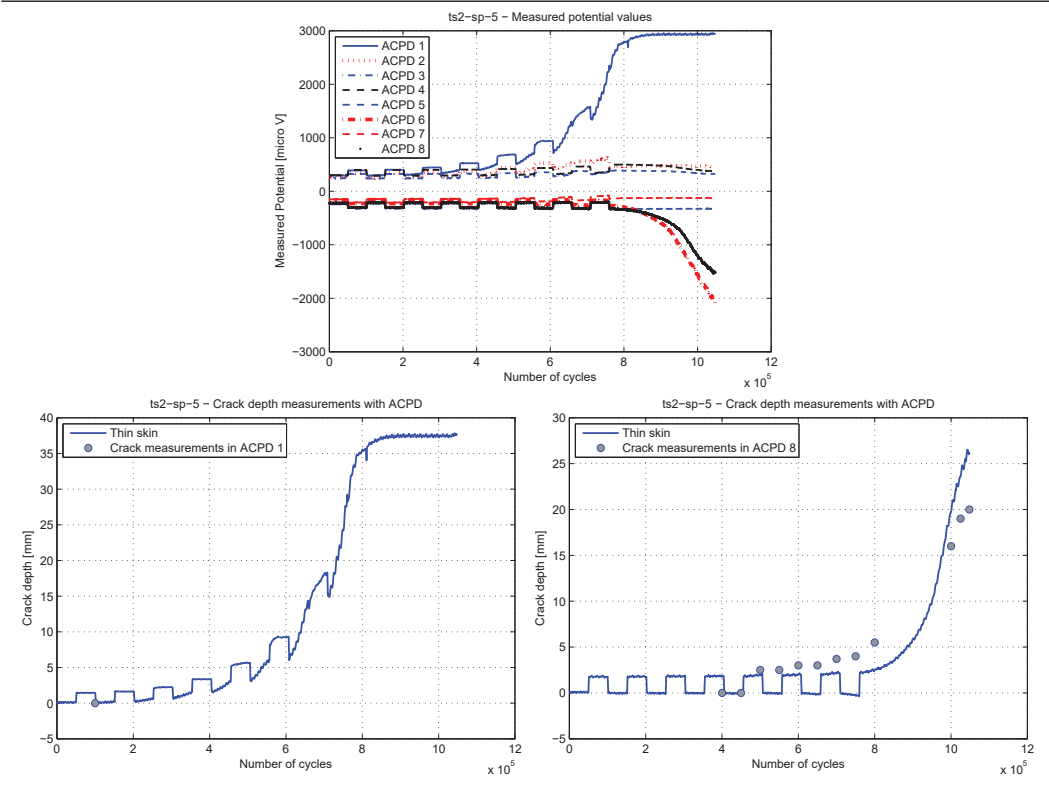


#### ts2-sp4



Appendix C. Experimental results

ts2-sp5



# Bibliography

- AASHTO (2002). *Standard Specifications for Highway Bridges*. AASHTO.
- Ahn, J., Kim, S., and Jeong, Y. (2007). Fatigue experiment of stud welded on steel plate for a new bridge deck system. *Steel and composite structures*, 7(5):391–404.
- Albrecht, P. and Lenwari, A. (2009). Variable-Amplitude Fatigue Strength of Structural Steel Bridge Details: Review and Simplified Model. *Journal of Bridge Engineering*, 14(4):226–237.
- Albrecht, P. and Yamada, K. (1977). Rapid calculation of stress intensity factors. In *Journal of the Structural Division. ASCE 103 (ST2)*, pages 377–389.
- Amstutz, H. and Olivier, R. (2011). Fatigue strength of shear loaded welded joints according to the notch stress concept. *Materialwissenschaft und Werkstofftechnik*, 42(4):254–262.
- Amstutz, H., Störzel, K., and Seeger, T. (2001). Fatigue crack growth of a welded tube–flange connection under bending and torsional loading. *Fatigue and Fracture of Engineering Materials and Structures*, 24(5):357–368.
- Archer, R. (1987). Fatigue of welded steel attachments under combined direct stress and shear stress. In *International Conference on Fatigue of Welded Constructions*, page Paper no. 50, Brighton. The British Welding Institute.
- Aygül, M., Bokesjö, M., Heshmati, M., and Al-Emrani, M. (2013). A comparative study of different fatigue failure assessments of welded bridge details. *International Journal of Fatigue*, 49:62–72.
- Bäckström, M. (2003). Multiaxial fatigue life assessment of welds based on nominal and hot spot stresses. *VTT Publications 502*.
- Bäckström, M. and Marquis, G. (2001). A review of multiaxial fatigue of weldments: experimental results, design code and critical plane approaches. *Fatigue and Fracture of Engineering Materials and Structures*, 24(5):279–291.

## Bibliography

---

- Backstrom, M. and Marquis, G. (2004). Interaction equations for multiaxial fatigue assessment of welded structures. *Fatigue and Fracture of Engineering Materials and Structures*, 27(11):991–1003.
- Badie, P., Tadros, K., Kakish, H., Splittgerber, and Baishya, P. (2002). Large Shear Studs for Composite Action in Steel Bridge Girders. *Journal of Bridge Engineering*, (June):195–203.
- Bae, D. (2004). Experimental study on fatigue strength of in-plane welded gusset joints. *KSCE Journal of Civil Engineering*, 8(1):89–93.
- Bailey, S. and Bez, R. (1999). Site specific probability distribution of extreme traffic action effects. *Probabilistic engineering mechanics*, 14:19–26.
- Bannantine, J. (1990). Fundamentals of metal fatigue analysis. *Prentice Hall*.
- Banz, A. and Nussbaumer, A. (2001). Fiabilité des ponts métalliques vis à vis de l'état limite combiné fatigue et rupture. *ICOM - Report 446/ICOM*.
- Baptista, C. and de Castro e Sousa, A. (2013). An approach to multiaxial fatigue analysis on steel components. *EPFL - Design of Experiments Doctoral course*.
- Baptista, C. and Nussbaumer, A. (2014). *A re-analysis of the fatigue strength of steel plates with holes, for application of the notch stress approach*. ICOM - Report EPFL 201786.
- Baptista, C. and Nussbaumer, A. (2015). *Traffic load generation for the fatigue assessment of the 3rd Bosphorus bridge*. ICOM - Report EPFL 209910.
- Barsoum, Z. (2008). Residual stress analysis and fatigue of multi-pass welded tubular structures. *Engineering Failure Analysis*, 15(7):863–874.
- Barsoum, Z. and Jonsson, B. (2008). Fatigue assessment and LEFM analysis of cruciform joints fabricated with different welding processes. *Welding in the World*, 52(7-8):1–23.
- Barsoum, Z. and Samuelsson, J. (2006). Fatigue assessment of cruciform joints welded with different methods. *Steel Research International*, 77(12):882–888.
- Bathias, C. (2010). Influence of the metallurgical instability on the gigacycle fatigue regime. *International Journal of Fatigue*, 32(3):535–540.
- Bathias, C. and Paris, P. (2005). *Gigacycle fatigue in mechanical practice*. CRC Press.
- Baumel, A. and Seeger, T. (1990). *Materials data for cyclic loading. Supplement 1*. Elsevier Science Publishers, Amsterdam.
- Bennett, C. R., Swanson, J. A., and Linzell, D. G. (2007). Fatigue Resistance of HPS-485W Continuous Plate with Punched Holes. *Journal of Bridge Engineering*, 12(1):98–104.

- Berger, C., Eulitz, K., and Heuler, P. (2002). Betriebsfestigkeit in Germany—an overview. *International Journal of Fatigue*, 24:603–625.
- Bergers, J., Herion, S., Höhler, S., Müller, C., and Stötzel, J. (2006). Beurteilung des Ermüdungsverhaltens von Krankonstruktionen bei Einsatz hoch- und ultrahochfester Stähle. *Stahlbau*, 75(11):897–915.
- Blitz, J. (1997). *Electrical and Magnetic Methods of Non-destructive Testing*, volume 3. Springer Science & Business Media.
- Blom, A. (1995). Spectrum fatigue behaviour of welded joints. *International Journal of Fatigue*, 17(7):485–491.
- Boer, D. (2010). Adapted Eurocode related traffic load models for new bridges for National Annex to EN 1991-2.
- Bohme, V., Olivier R, and Seeger T (1981). Einfluss von Fertigungsbeschichtungen auf die Schwingfestigkeit schubbeanspruchter Kehlahte. *Der Stahlbau*, 11:335–338.
- Bokesjö, M., Al-Emrani, M., and Svensson, T. (2012). Fatigue strength of fillet welds subjected to multi-axial stresses. *International Journal of Fatigue*, 44:21–31.
- Boller, C. and Seeger, T. (1987). *Materials Data for Cyclic Loading: Part B Low-alloy Steels*. Elsevier Science Publishers, Amsterdam.
- Booth, G. (1978). Constant amplitude fatigue tests on welded steel joints performed in air. In *European Offshore Steels Research Seminar*.
- Bouley, J. (1993). Un pont Warren a poutres laterales pour le franchissement du canal de la Deule a Henin-Beaumont. *Bulletin de Ponts Metalliques*, (16).
- Braithwaite, A. and Gurney, T. (1967). Fatigue tests on cross girder connections. *British welding journal*, 14(2):71–80.
- Bremen, U. (1989). *Amélioration du comportement à la fatigue d'assemblages soudés: étude et modélisation de l'effet de contraintes résiduelles*. Phd thesis, EPFL.
- Broek, D. (1986). *Elementary engineering fracture mechanics*. Martinus Nijhoff Publisher, The Hague.
- Brose, W., Dowling, N. E., and Morrow, J. (1974). Effect of Periodic Large Strain Cycles on the Fatigue Behavior of Steels. In *Automotive Engineering Congress*. SAE Technical Paper No. 740221.
- Brown, J., Lubitz, D., Cekov, Y., Frank, K., and Keating, P. (2007). *Evaluation of Influence of Hole Making Upon the Performance of Structural Steel Plates and Connections*. Center for Transportation Research - Report No. FHWA/TX-07/0-4624-1, University of Texas at Austin.

## Bibliography

---

- Brozzetti, J. and Chabrolin, B. (1986). Méthodes de comptage des charges de fatigue. *Revue Construction Métallique* (1).
- Brozzetti, J., Hirt, M., Ryan, I., Sedlacek, G., and Smith, I. (1989). Background Documentation to Eurocode 3, Chapter 9. Document 9.01: Background information on fatigue design rules. Statistical evaluation (Final draft v.1). Technical report, Eurocode 3 Editorial board.
- Bruls, A. (1996). *Resistance des ponts soumis au trafic routier: modelisation des charges, reevaluation des ouvrages*. PhD thesis, Universite de Liege, Faculte des sciences appliquees.
- BS 5400: Part 10 (1980). *Steel, concrete and composite bridges. Part 10. Code of practice for fatigue*. British Standards Institution.
- BS 7910 (2005). *Guide to methods for assessing the acceptability of flaws in metallic structures*. British Standards Institution.
- BS7608 (2014). *Guide to fatigue design and assessment of steel products*. British Standard Institution.
- Calgaro, J., Tschumi, M., and Gulvanessian, H. (2010). *Designers' Guide to Eurocode 1: Actions on Bridges*. Thomas Telford, London.
- Caramelli, S. and Croce, P. (2010). *Influence of heavy traffic trend on EC1-2 load models for road bridges*. ENEA, Rome.
- Chabrolin, B. (1988). Détermination des coefficients partiels de sécurité à prendre en compte pour la vérification à la fatigue d'un élément de structure. *Construction Métallique*, 4:12.
- Comeau, M. and Kulak, G. (1979). Fatigue Strength of Welded Steel Elements. *Alberta University Reports*, (79).
- D Angelo, L. (2015). *Probabilistic approach for fatigue evaluation of welded connections with application to road steel bridges*. Phd thesis, EPFL.
- Dahle, T. (1993). Spectrum fatigue life of welded specimens in relation to the linear damage rule. In *Fatigue under Spectrum Loading and in Corrosion Environments*, pages 133–147, Copenhagen. EMAS.
- Dahle, T. (1994). Long-life spectrum fatigue of welded joints. *Fatigue*, 16(August):392–396.
- Dahle, T. and Larsson, B. (1992). Full scale spectrum testing and fatigue life predictions of welded bogie beams. In *International symposium of fatigue design*, pages 99–109, Helsinki.

- Dahle, T., Olsson, K., and Jonsson, B. (1997). High strength welded box beams subjected to torsion and bending - test results and proposed design criteria for torsion/bending interaction. In Blom, A. F., editor, *Welded High-Strength Steel Structures*, pages 143–161, London. EMAS.
- Daniels, J. H., Fisher, J. W., and Yen, B. T. (1980). *Fatigue of curved steel bridge elements. Design recommendations for fatigue of curved plate girder and box girder bridges*. FHWA-RD-79-138 Final Rpt.
- Dawes, M. (1965). Analysis of residual stresses in welded I beam connections. *British Welding Journal*, October:507–516.
- DNV (2014). *Fatigue design of offshore steel structures, RP-C203*. Det Norske Veritas.
- Dowling, N. E. (1993). *Mechanical behavior of materials: engineering methods for deformation, fracture, and fatigue*. Prentice hall.
- ECCS (1985). Recommendations for the Fatigue Design of Steel Structures - ECCS 43.
- ECCS (2000). *Good design practice: A guideline for fatigue design - ECCS 105*. European convention for Constructional Steelwork, Brussels.
- ECSC (1999). *Use of High Strength Steel S460 - Final Report*. ECSC Steel RTD Programme.
- ECSC (2002). *Composite Bridge Design for Small and Medium Spans - Final Report*. ECSC Steel RTD Programme.
- Elber, W. (1971). The significance of fatigue crack closure. In *Damage tolerance in aircraft structures - ASTM STP 486*.
- Elber, W. (1976). Equivalent constant-amplitude concept for crack growth under spectrum loading. *Fatigue crack growth under spectrum loads - ASTM STP 595*.
- EN 1991-2 (2003). Eurocode 1: Actions on structures - Part 2: Traffic loads on bridges. Technical report, European Committee for Standardization (CEN), Brussels.
- EN 1993 1-9 (2005). *Eurocode 3 : Design of steel structures - Part 1-9 : Fatigue*. European Committee for Standardization (CEN), Brussels.
- Engesvik, K. and Moan, T. (1983). Probabilistic analysis of the uncertainty in the fatigue capacity of welded joints. *Engineering Fracture Mechanics*, 18(4):743–762.
- Enright, B. and O'Brien, E. J. (2011). *Cleaning Weigh-in-Motion Data: Techniques and Recommendations, International Society for Weigh-In-Motion*.
- Faber, M. and Sorensen, J. (2002). Reliability based code calibration. *The Joint Committee on Structural Safety, Zurich*.

## Bibliography

---

- Faust, T., Leffer, A., and Mesinger, M. (2000). Fatigue of headed studs embedded in LWAC. In *Second international symposium on structural lightweight aggregate concrete*, pages 212–220.
- Fisher, J. (1979). Detection and repair of fatigue damage in welded highway bridges. *NCHRP Report 206*.
- Fisher, J., Albrecht, P., and Yen, B. (1974). Fatigue strength of steel beams with welded stiffeners and attachments. *NCHRP Report 147*.
- Fisher, J., Barthelemy, B., Mertz, D., and Edinger, J. (1980). Fatigue behavior of full-scale welded bridge attachments. *NCHRP Report 227*.
- Fisher, J., Frank, K., Hirt, M., and McNamee, B. (1970). Effect of weldments on the fatigue strength of steel beams. *NCHRP Report 102*.
- Fisher, J., Mertz, D., and Zhong, A. (1983). Steel bridge members under variable amplitude long life fatigue loading. *NCHRP Report 267*.
- Fisher, J., Nussbaumer, A., Keating, P., and Yen, B. (1993). Resistance of welded details under variable amplitude long-life fatigue loading. *NCHRP Report 354*.
- Fricke, W. (2008). *Guideline for the fatigue assessment by notch stress analysis for welded structures*. International Institute of Welding.
- Fricke, W. (2013). IIW guideline for the assessment of weld root fatigue. *Weld World*, 57(6):753–791.
- Fricke, W., Cui, W., Kierkegaard, H., Kihl, D., Koval, M., Mikkola, T., Parmentier, G., Toyosada, M., and Yoon, J.-H. (2002). Comparative fatigue strength assessment of a structural detail in a containership using various approaches of classification societies. *Marine Structures*, 15(1):1–13.
- Fricke, W. and Kahl, A. (2007). Local stress analysis and fatigue assessment of bracket toes based on measured weld profile. *International Institute of Welding*.
- Fricke, W. and Paetzoldt, H. (1995). Fatigue strength assessment of scallops—an example for the application of nominal and local stress approaches. *Marine structures*, 8:423–447.
- Fricke, W. and Tchuindjang, D. D. (2013). Fatigue strength behaviour of stud-arc welded joints in load-carrying ship structures. *Welding in the World*, 57(4):495–506.
- Fryba, L. (1996). *Dynamics of railway bridges*. Thomas Telford.
- Glinka, G. and Chattopadhyay, A. (2009). Stress analysis and fatigue life assessment of welded structures. *IIW document*.



- Gordon, J., Mohr, W., Dimitrakis, S., and Lawrence, F. (1997). Fatigue Design of Offshore Structures. In *International Conference on Performance of Dynamically Loaded Welded Structures*, pages 74–97. Welding Research Council.
- Gough, H. and Pollard, H. (1935). The strength of metals under combined alternating stresses. *Proc. Inst. Mech Engrs*, 131:3–103.
- Guerrera, U. (1982). *Draft proposal for the fatigue strength of the main details of a welded structure (technical background report for ECCS 43)*.
- Gurney, T. (1960). Fatigue Strength of Fillet Welded Joints in Steel. *Welding in the world*, 7(3):178–187.
- Gurney, T. (1962). Further Fatigue Tests on Mild Steel Specimens with Artificially Induced residual stresses. *British Welding Journal*, 8(November):609–613.
- Gurney, T. (1965). Some Exploratory Fatigue Tests on Notched Mild and High Tensile Steels. *British Welding Journal*, 12(9):457/61.
- Gurney, T. (1978). *An analysis of some fatigue crack propagation data for steels subjected to pulsating tension loading*. Welding Institute.
- Gurney, T. (1979). *Fatigue of welded structures*. Cambridge University Press.
- Gurney, T. (1989). The influence of thickness on fatigue of welded joints-10 years on (a review of British work). *Proc 8th Int Conf on Offshore Mech and Arctic Eng*, III:1–8.
- Gurney, T. (1991). *The fatigue strength of transverse fillet welded joints: A study of the influence of joint geometry*. Elsevier.
- Gurney, T. (2001). Exploratory Investigation of the significance of the low stresses in fatigue loading spectrum. *IIW document No XIII-1899-01*.
- Gurney, T. (2006). *Cumulative damage of welded joints*. Woodhead Publishing Limited.
- Gurney, T. and Maddox, S. (1973). A re-analysis of fatigue data for welded joints in steel. *Welding Research International*, 3(4):1–54.
- Gurney, T. and Maddox, S. (1982). An alternative to Miners rule for cumulative damage calculations. In *Fatigue of Structures and Materials*, pages 189–198, Lausanne. IABSE.
- Gurney, T. and Trepka, L. (1959). Influence of local heating on fatigue behaviour of welded specimens. *British Welding Journal*, J 6:491–497.
- Gurney, T. R. (1993). Fatigue tests in two types of joint to establish joint classification. *IIW Document XII 1519-93*.
- Haibach, E. (1968). *Die Schwingfestigkeit von Schweißverbindungen aus der Sicht einer örtlichen Beanspruchungsmessung*. Fraunhofer-Institut für Betriebsfestigkeit, Darmstadt.

## Bibliography

---

- Haibach, E. (1970). *Modifizierte lineare Schadensakkumulations-hypothese zur Berücksichtigung des Dauerfestigkeitsabfalls mit fortschreitender Schädigung*. Laboratorium für Betriebsfestigkeit.
- Haibach, E. (1971). The allowable stresses under variable amplitude loading of welded joints. In *Proceedings Conference Fatigue of Welded Structures*, volume Vol 2, pages 328–339.
- Haibach, E. (1975). *Fatigue investigation of higher strength structural steels in notched and in welded condition. Synthesis of results and tentative conclusions*. ECCS Report, eur5357 edition.
- Haibach, E. (1976). Cumulative damage in marine welded structures. In *Boss '76, First International Conference on Behavior of off-shore structures*, Trondheim University, Norway.
- Haibach, E. (1979). Fatigue investigation of typical welded joints in steel Fe E460 as compared to steel Fe E355. Final report of a common investigation by seven European laboratories. FB-147. Technical report, LBF-Bericht.
- Haibach, E. (2006). *Betriebsfestigkeit - Verfahren und Daten zur Bauteilberechnung*. VDI-Verlag, Düsseldorf.
- Hallam, M. (1976). *The behavior of stud shear connectors under repeated loading*. School of civil engineering, University of Sydney.
- Hanswille, G., Porsch, M., and Ustundag, C. (2007). Resistance of headed studs subjected to fatigue loading Part I: Experimental study. *Journal of Constructional Steel Research*, 63:101–116.
- Harada, K. and Kurobane, Y. (1982). *Fatigue of welded tube to gusset plate joints applicable for the use in transmission towers*. Trans. of AIJ.
- Harrison, J. (1965a). Further fatigue tests on fillet welded specimens subjected to prior overloading. Technical report, BWRA Report.
- Harrison, J. D. (1965b). Some tests on the effect of friction welded studs on fatigue. *British Welding Journal*, August:420–423.
- Herion, S. and Müller, C. (2000). Untersuchung kranzspezifischer Kerbdetails. *Stahlbau*, 69(4):251–267.
- Heshmati, M. (2012). *Fatigue Life Assessment of Bridge Details Using Finite Element Method*. Chalmers University.
- Heuler, P. and Klatschke, H. (2005). Generation and use of standardised load spectra and load–time histories. *International Journal of Fatigue*, 27(8):974–990.

- Hirt, M. A., Crisinel, M. (1975). La resistance a la fatigue des poutres en ame pleine composees-soudees. Effect des plaquettes et goussets soudes a l' aile - ICOM 017. Technical report, EPFL, Institut de la Construction Metallique.
- Hobbacher, A. (1992). Stress intensity factors of plates under tensile load with welded-on flat side gussets. *Engineering fracture mechanics*, 41(6).
- Hobbacher, A. (2010). New developments at the recent update of the IIW recommendations for fatigue of welded joints and components. *Steel Construction*, 3(4):231–242.
- Husset, Lieurade, Maltrud, T. (1985). Fatigue crack growth monitoring using a crack front marking technique. *Welding in the World*, 23(11/12):276–282.
- Huther, M., Galtier, A., Parmentier, G., and Marquis, G. (2011). Guidance for the Application of the Best Practice Guide on Statistical Analysis of Fatigue. *IIW Doc. XIII-WG1-149-11*, pages 1–27.
- IIW (2008). *Recommendations for fatigue design of welded joints and components*. Edited by Hobacher, A., International Institute of Welding.
- Imhof, D., Bailey, S., and Hirt, M. A. (2001). Modele de charge (trafic 40 t) pour l'evaluation des ponts-routes à deux voies avec trafic bidirectionnel. *ICOM 444-4*.
- ISO 12491 (1997). *Statistical methods for quality control of building materials and components*. International organization for standardization, Zuriqye.
- ISO 2394 (2008). *General principles on reliability for structures*. International organization for standardization, Zuriqye.
- Johnson, R. P. (2000). Resistance of stud shear connectors to fatigue. *Journal of Constructional Steel Research*, 56(2):101–116.
- JRC (2008). Background document to EN 1991-Part 2-Traffic loads for road bridges-and consequences for the design. *JRC Scientific and Technical Reports*.
- JSSC (1974). *Recommendations for Fatigue Design*, volume 10.
- JSSC (1995). *Fatigue design recommendations for steel structures*.
- Keating, P. and Fisher, J. (1986). Review of Fatigue Tests and Design Criteria on Welded Details. *NCHRP Report 286*, 1(86).
- Keating, P. B. and Fisher, J. W. (1989). High-cycle, long-life fatigue behavior of welded steel details. *Journal of Constructional Steel Research*, 12(3-4):253–259.
- Kihl, D. and Sarkani, S. (1997). Thickness effects on the fatigue strength of welded steel cruciforms. *International journal of fatigue*, 19(1).

## Bibliography

---

- Kihl, D. P. and Sarkani, S. (1999). Mean stress effects in fatigue of welded steel joints. *Probabilistic Engineering Mechanics*, 14(1-2):97–104.
- Kim, I. and Yamada, K. (2005). Fatigue life evaluation of welded joints under combined normal and shear stress cycles. *International journal of fatigue*, 27:695–701.
- Kim, M.-H. and Kang, S.-W. (2008). Testing and analysis of fatigue behaviour in edge details: a comparative study using hot spot and structural stresses. *Proceedings of the Institution of Mechanical Engineers, Part C: Journal of Mechanical Engineering Science*, 222(12):2351–2363.
- Kloppel, K. and Weihermuller, H. (1960). Dauerfestigkeitsversuche mit Schweissverbindungen aus St 52. *Der Stahlbau*, 29(8):129–137.
- Kondo, A. and Yamada, K. (2002). Variable amplitude fatigue tests on in-plane gussets in long life region. *Journal of Structural Engineering, JSCE, (in Japanese)*, 48(A):1039–1046.
- Krebs, J. and Kassner, M. (2007). Influence of Welding Residual Stresses on Fatigue Design of Welded Joints and Components. *Welding in the World*, 51(7-8):54–68.
- Kuehn, B. and Lukić, M. (2008). Assessment of existing steel structures: recommendations for estimation of remaining fatigue life. *JRC Scientific and Technical Reports*.
- Kulak, G. and Smith, I. (1993). *Analysis and design of fabricated steel structures for fatigue: A primer for civil engineers*. Department of Civil Engineering, University of Alberta.
- Kunz, P. (1992). *Probabilistisches verfahren zur beurteilung der ermuedungssicherheit bestehender bruecken aus stahl*. Phd thesis, EPFL.
- Kwon, G., Engelhardt, M. D., and Klingner, R. E. (2010). Behavior of post-installed shear connectors under static and fatigue loading. *Journal of Constructional Steel Research*, 66(4):532–541.
- Lawrence, F., Mattos, R., Higashida, Y., and Burk, J. (1978). Estimating the fatigue crack initiation life of welds. *ASTM STP*.
- Leander, J., Aygül, M., and Norlin, B. (2013). Refined fatigue assessment of joints with welded in-plane attachments by LEFM. *International Journal of Fatigue*, 56:25–32.
- Lee, J.-k., Yoon, T.-y., and Chang, S.-p. (2003). The Fatigue Performance of Plate Girder in Korea High-Speed Railway Bridge. *IABSE Symposium Report*, 87(1):129–135.
- Lee, P., Shim, C., and Chang, S. (2001). Design of shear connection in composite steel and concrete bridge with precast decks. *Journal of Constructional Steel Research*, 57(203-219).

- Lee, P.-G., Shim, C.-S., and Chang, S.-P. (2005). Static and fatigue behavior of large stud shear connectors for steel–concrete composite bridges. *Journal of Constructional Steel Research*, 61(9):1270–1285.
- Lesniak, Z. (1960). Fatigue tests of flanges with welded gusset plates. *Welding production*.
- Lo, K. (1978). Fatigue testing of stud shear connectors. *M.Eng. Thesis, University of Melbourne*.
- Lotsberg, I. (2009). Fatigue Capacity of Load Carrying Fillet-Welded Connections Subjected to Axial and Shear Loading. *Journal of Offshore Mechanics and Arctic Engineering*, 131(4):041302.
- Maddah, N. (2013). *Fatigue life assessment of roadway bridges based on actual traffic loads*. Phd thesis, EPFL.
- Maddah, N. and Nussbaumer, A. (2014). *Fatigue limit state of shear studs in steel-concrete composite road bridges*. Number 661. OFROU - Office fédéral des routes.
- Maddah, N., Nussbaumer, A., and Meystre, T. (2012). *Traffic simulation parameters based on Switzerland measurements*. Report EPFL ICOM-169876.
- Maddox, S. (1970). Fatigue crack propagation in weld metal and HAZ. *Metal Construction and British Welding Journal*, 2(7):285–289.
- Maddox, S. (1973). Some Further Fatigue Crack Propagation Results Relevant to Welded Joints in Steel. *Welding Research International*, 3(1):72–99.
- Maddox, S. (1974). Assessing the significance of flaws in welds subject to fatigue. *Welding Journal*, 53(9).
- Maddox, S. (1975). An analysis of fatigue cracks in fillet welded joints. *International Journal of Fracture*, 11(2):221–243.
- Maddox, S. (1987). *The effect of plate thickness on the fatigue strength of fillet welded joints*. The Welding Institute.
- Maddox, S. (1991). *Fatigue strength of welded structures*. Abington Publishing, 2nd edition.
- Maddox, S. (1992). Fatigue design of welded structures. *Pergamon Press (UK)*.
- Maddox, S. (2001a). Hot-spot fatigue data for welded steel and aluminium as a basis for design. *International Institute of Welding (IIW), Paris, France*.
- Maddox, S. (2001b). Recommended hot-spot stress design SN curves for fatigue assessment of FPSOs. In *Proceedings of The Eleventh International Offshore and Polar Engineering Conference*. International Society of Offshore and Polar Engineers.

## Bibliography

---

- Maddox, S. (2003). Key developments in the fatigue design of welded constructions. *Welding in the World*, 47:7–40.
- Maddox, S. and Razmjoo, G. (2001). Interim fatigue design recommendations for fillet welded joints under complex loading. *Fatigue and Fracture of Engineering Materials and Structures*, (January):329–337.
- Maddox, S. J. (1994). Statistical analysis of fatigue data obtained from many welds. *International Institute of Welding*.
- Mainstone, R. and Menzies, J. (1967). Shear connectors in steel-concrete composite beams for bridges. Part 1 Static and fatigue tests on push-out specimens. *Concrete*, 1(9):291–302.
- Maljaars, J. and Steenbergen, R. (2012). Safety assessment of existing highway bridges and viaducts. *Structural Engineering International*, pages 112–120.
- Mang, Bucak, and Klingler (1987). *Wöhlerlinien katalog für Hohlprofilverbindungen*. Universität Karlsruhe, Karlsruhe.
- Mang, F., Bucak, O., and Obert, K. (1991). Investigation into the fatigue life of specimens with flame-cut holes and plasma cutting of steel. In *New Advances in Welding and Allied Processes: Proceedings of the International IIW Conference*, Beijing, China. IIW.
- Marquis, G. (1995). *High cycle spectrum fatigue of welded components*. Phd thesis, VTT.
- Martinez, L. L. and Korsgren, P. (1993). Characterization of initial defect distribution and weld geometry in welded fatigue test specimens. In *Fatigue under Spectrum Loading and Corrosive Environment*, pages 3–21.
- Mayer, H. (2007). Fatigue damage of low amplitude cycles under variable amplitude loading condition. In *Proc VHCF 4*, pages 333–340.
- Meggiolaro, M. (2004). Statistical evaluation of strain-life fatigue crack initiation predictions. *International Journal of Fatigue*, 26(5):463–476.
- Melchers, R. (1999). *Structural Reliability. Analysis and Prediction*. Ellis Horwood Limited, Chichester, UK.
- Mensingher, M. (2000). *Zum Ermüdungsverhalten von Kopfbolzendubeln im Verbundbau*. Phd thesis d 386, Universität Kaiserslautern.
- Merzenich, G. and Sedlacek, G. (1995). Hintergrundbericht zum Eurocode 1 - teil 3.2: "Verkehrslasten auf Strassenbruecken". *Forschung Strassenbau und Strassenverkehrstechnik*, (711).

- Michael, D. H. and Collins, R. (1982). The ac field around a plane crack in a metal surface when the skin depth is large. *Journal of Nondestructive Evaluation*, 3(1):19–24.
- Miki, C. (2010). Retrofitting Engineering for Fatigue Damaged Steel Structures. *IIW document No XIII-2284r1-09*.
- Miki, C., Murakoshi, J., Toyoda, Y., and Sakano, M. (1989). Long life fatigue behavior of fillet welded joints under computer simulated highway and railroad loading. *Proc. of JSCE*, 6(1):41–48.
- Miki, C. and Tateishi, K. (1997). Fatigue strength of cope hole details in steel bridges. *International Journal of Fatigue*, 19(6):445–455.
- Miki, C., Toyoda, Y., Mori, T., and Enokido, N. (1990). Fatigue of large scale welded girders under simulated highway loadings. *Structural Engineering/Earthquake Engineering*, 7(2):283–291.
- Mikkola, E., Remes, H., and Marquis, G. (2015). Influence of residual stresses on elasto-plastic response in HFMI-treated welded joint under different load ratios different load ratios. *International Institute of Welding IIW-XII-2591-15*.
- Miner, M. A. (1945). Cumulative damage in fatigue. *J. Appl. Mech*, 12 (3):159–164.
- Mladen, L., Al-Emrani, M., and Al., E. (2010). *Bridge Fatigue Guidance (BriFaG), Mid-term Report*. Research program RFCS.
- Nagata, Y., Gotoh, K., and Toyosada, M. (2009). Numerical simulations of fatigue crack initiation and propagation based on re-tensile plastic zone generating load criterion for in-plane gusset welded joints. *Journal of Marine Science and Technology*, 14(1):104–114.
- Neuber, H. (1961). Theory of stress concentration for shear-strained prismatical bodies with arbitrary nonlinear stress-strain law. *Journal of Applied Mechanics*, 28(4):544–550.
- Neuber, H. (1968). A physically nonlinear notch and crack model. *Journal of the Mechanics and Physics of Solids*, 16(4):289–294.
- Niemi, E. (1997). Random loading behaviour of welded components. In *Proc. of the IIW International Conference on Performance of Dynamically Loaded Welded Structures*, pages 14–15.
- Niemi, E. (2000). Hot spot stress determination for welded edge gussets. *Welding in the world*, 44(5):31–37.
- Niemi, E. (2002). Structural stress approach to fatigue analysis of welded components. *IIW document*, XIII-1819-.



## Bibliography

---

- Niemi, E., Fricke, W., and Maddox, S. I. (2006). *Fatigue analysis of welded components - Designer's guide to the structural hot-spot stress approach*. Woodhead Publishing Limited.
- Nussbaumer, A. and Schumacher, A. (2002). Fatigue of hollow section structures in bridges. *Stahlbau*, 71(8):564–570.
- Nussbaumer, A; Borges, L; Davaine, C. (2011). *Fatigue Strength Fatigue design of steel and composite structures*. ECCS.
- Ohta, A., Matsuoka, K., Suzuki, N., and Maeda, Y. (1994). Fatigue strength of non-load-carrying cruciform welded joints by a test maintaining maximum stress at yield strength. *Engineering fracture mechanics*, 49(4):639–645.
- Olivier, R., Köttgen, V. B., and Seeger, T. (1989). *Schwingfestigkeitsnachweis für Schweissverbindungen auf der Grundlage örtlicher Beanspruchungen - Schweißverbindungen I - FKM 143*. Frankfurt.
- Olivier, R., Köttgen, V. B., and Seeger, T. (1994). *Untersuchung zur Einbindung eines neuerartigen Zeit- und Dauerfestigkeitsnachweises von Schweißverbindungen in Regelwerken-Schweissverbindungen II - FKM 180*. Frankfurt.
- Olivier, R. and Ritter, W. (1980). *Wöhlerlinienkatalog für Schweissverbindungen aus Baustählen. Teil 2: Quersteife*. Deutscher Verlag für Schweißtechnik (DVS) GmbH, Düsseldorf.
- Olivier, R. and Ritter, W. (1982). *Wöhlerlinienkatalog für Schweissverbindungen aus Baustählen. Teil 4: Längssteife*. Deutscher Verlag für Schweißtechnik (DVS) GmbH, Düsseldorf.
- Olivier, R. and Ritter, W. (1985). *Wöhlerlinienkatalog für Schweissverbindungen aus Baustählen. Teil 5: Längskehlnaht, aufgeschweißter bolzen, Brennschnittkante*. Deutscher Verlag für Schweißtechnik (DVS) GmbH, Düsseldorf.
- Olivier, R. and Seeger, T. (1992). Neigung und Abknickpunkt der Wöhlerlinie von schubbeanspruchten Kehlnähten. *Stahlbau*, 61(5):137–142.
- Paris, P. and Erdogan, F. (1963). A Critical Analysis of Crack Propagation Laws. *Journal of Basic Engineering*, 85(4):528.
- Paris, P. C. and Sih, G. (1965). Stress Analysis of Cracks. In *Fracture Toughness Testing and its Applications, STP 381*, pages 30–83.
- Pedersen, M., Mouritsen, O., Hansen, M., Andersen, J., and Wenderby, J. (2010). Re-analysis of fatigue data for welded joints using the notch stress approach. *International Journal of Fatigue*, 32(10):1620–1626.



- Puchner, O. (1959). Augmentation de la résistance à la fatigue par chauffage localisé de plats et de poutres comportant des goussets soudés. *IIW-Doc IIS 27-59*.
- Pyttel, B., Schwerdt, D., and Berger, C. (2011). Very high cycle fatigue – Is there a fatigue limit? *International Journal of Fatigue*, 33(1):49–58.
- Radaj, D. (1990). *Design and analysis of fatigue resistant welded structures*. Elsevier.
- Radaj, D. (1996). Review of fatigue strength assessment of nonwelded and welded structures based on local parameters. *International Journal of Fatigue*, 18(3):153–170.
- Radaj, D., Sonsino, C., and Fricke, W. (2006). *Fatigue assessment of welded joints by local approaches*. Woodhead publishing, CRC.
- Ramberg, W. and Osgood, W. R. (1943). Description of stress-strain curves by three parameters.
- Raoul, J. and Günther, H. (2005). *Use and application of high-performance steels for steel structures*. IABSE Vol 8.
- Razmjoo, G. (1996). *Fatigue of load-carrying fillet welded joints under multiaxial loading*. Woodhead.
- Reis, A. (2001). Bridge decks: composite systems for improved aesthetics and environmental impact. In *Proc.3rd Int. Meeting on Composite Bridges*, pages pp 645–59, Madrid.
- Reis, A. (2008). Steel concrete composite bridges: options and design issues. In *Proc. 7th International conference on steel bridges*, Guimarães.
- Reis, A. and Oliveira Pedro, J. (2011). Composite Truss Bridges: new trends, design and research. *Steel Construction*, 4(3):176–182.
- Roderick, J. and Ansorian, P. (1976). Repeated loading of composite beams. *Institution of Engineers (Australia) Civ Eng Trans 2*, Paper No.
- Roik, E. and Hanswille, G. (1990). *Background Report on Eurocode 4: Limit state of fatigue headed studs*. Bochum.
- Roik, K. and Hanswille, G. (1987). Zur Frage der Rissbreitenbeschränkung bei Verbundträgern. *Bauingenieur*, 62:273–285.
- Roik, K. and Holtkamp, H. (1986). *Untersuchungen zur Dauer- und Betriebsfestigkeit der Verdübelung von Verbundträgern mit Hilfe von Kopfbolzendübeln*. Ruhr-Universität Bochum.
- Roik, K. and Holtkamp, H. (1989). Untersuchungen zur Dauer- und Betriebsfestigkeit der Verdübelung von Verbundträgern mit Hilfe von Kopfbolzendübeln. *Stahlbau*, 58(2):53–58.

## Bibliography

---

- Roshardt, W. (1966). Einfluss des Aufschweissens von Bolzen auf das Grundmaterial. *Schweizerische Bauzeitung*, 84(51):906–908.
- Rother, K. and Rudolph, J. (2011). Fatigue assessment of welded structures: practical aspects for stress analysis and fatigue assessment. *Fatigue and Fracture of Engineering Materials and Structures*, 34(3):177–204.
- Saguy, H. and Rittel, D. (2005). Bridging thin and thick skin solutions for alternating currents in cracked conductors. *Applied Physics Letters*, 87(8).
- Saguy, H. and Rittel, D. (2007). Flaw detection in metals by the ACPD technique: Theory and experiments. *NDT and E International*, 40(7):505–509.
- Samuelsson, J., Jonsson, B., and Barsoum, Z. (2008). Service fatigue design of complex welded construction equipment. *Materialwissenschaft und Werkstofftechnik*, 39(10):734–739.
- Sánchez, L., Gutiérrez-Solana, F., and Pesquera, D. (2004). Fatigue behaviour of punched structural plates. *Engineering Failure Analysis*, 11(5):751–764.
- Sanpaolesi, L. and Croce, P. (2005). *Handbook 4: Design of bridges-Guide to basis of bridge design related to Eurocodes supplemented by practical examples*. Leonardo Da Vinci Pilot Project CZ/02/B/F/PP-134007.
- Schaumann, P. and Steppeler, S. (2013). Fatigue Tests of Axially Loaded Butt Welds up to Very High Cycles. *Procedia Engineering*, 66:88–97.
- Schijve, J. (1988). Fatigue crack closure: observations and technical significance. *Mechanics of fatigue crack closure*, STP 982.
- Schilling, C. and Klippstein, K. (1978). Fatigue of Welded Steel Bridge Members Under Variable-Amplitude Loadings. *NCHRP Report 188*.
- Schijve, J. (2003). Fatigue of Structures and Materials in the 20th Century and the State of the Art. *International Journal of Fatigue*, 25(September):679–702.
- Schneider, C. and Maddox, S. (2003). Best practice guide on statistical analysis of fatigue data. *International Institute of Welding*.
- Schönborn, S. and Nitschke-Pagel, T. (2015). Einflussgrößen auf die Lage des Abknickpunktes der Wöhlerlinie für den Schwingfestigkeitsnachweis von Schweißverbindungen. *Fraunhofer-Institut für Betriebsfestigkeit und Systemzuverlässigkeit LBF, Darmstadt TU Braunschweig Institut für Füge- und Schweißtechnik, Braunschweig*.
- Schönhof, M. and Helbing, D. (2007). Empirical features of congested traffic states and their implications for traffic modeling. *Transportation Science*, 41(2):135–166.

- Sedlacek, G. (2010). *Traffic loads on road bridges*. RWTH University of Technology Aachen.
- Sedlacek, G., Feldmann, M., and Kühn, B. (2008). *COMMENTARY AND WORKED EXAMPLES to EN 1993-1-10 "Material toughness and through thickness properties and other toughness oriented rules*. JRC Scientific and Technical Reports.
- Sedlacek, G., Hobbacher, A., Schleich, J. B., Nussbaumer, A., Maddox, S. J., Brozzetti, J., Chabrolin, B., Helmerich, R., Piraprez, E., and Kleineidam, P. (2003). 1st Draft of the Background Document prEN1993-1-9. Technical report, RWTH Institute of steel construction.
- Sedlacek, G. and Jaquemoud, J. (1984). Herleitung eines Lastmodells für den Betriebsfestigkeitsnachweis von Strassenbrücken. *Forschung Strassenbau und Strassenverkehrstechnik*, (Heft 430).
- Sedlacek, G., Sedlacek, G., Müller, C., and Müller, C. (2000). Die Neuordnung des Eurocode 3 für die EN-Fassung und der neue Teil 1.9 - Ermüdung. *Stahlbau*, 69:228–235.
- Seeger, T. and Olivier, R. (1987). Ertragbare und Zulässige Schubspannungen Schwingbeanspruchter Schweiss-Verbindungen. *Stahlbau*, 8(56):231–238.
- Selby, K., Stallmeyer, J., and Munse, W. (1963). *Fatigue Tests of Plates and Beams with Stud Shear Connectors*. Number July. University of Illinois.
- Seracino, R., Oehlers, D., and Yeo, M. (2003). Behaviour of stud shear connectors subjected to bi-directional cyclic loading. *Advances in structural engineering*, 6(1):65–75.
- SETRA (1996). *Ponts métalliques et mixtes. Résistance à la fatigue*. SETRA, Paris.
- Shimokawa, H., Takena, K., Itoh, F., and Miki, C. (1985). Fatigue strengths of large-size gusset joints of 800MPa class steels. *Proceedings of JSCE, Structural Eng./Earthquake Eng*, 2(1):279–287.
- Signes, E., Baker, R., Harrison, J., and Burdekin, F. (1967). Factors Affecting Fatigue Strength of Welded High Strength Steels. *British Welding Journal*, (March).
- Siljander, A., Kurath, P., and Lawrence, F. (1992). Nonproportional fatigue of welded structures. In Mitchell, M. R. and Landgraf, R., editors, *Advances in Fatigue Lifetime Predictive Techniques, ASTM STP 1122*, pages 319–338, Philadelphia. ASTM, Philadelphia.
- Slockblower, R. and Fisher, J. (1978). *Fatigue Resistance of Full Scale Cover-Plated Beams*. Lehigh University.
- Smith, I. and Smith, R. (1982). Measuring fatigue cracks in fillet welded joints. *International Journal of Fatigue*, (January):41–45.

## Bibliography

---

- Smith, I. and Smith, R. (1983). Fatigue crack growth in a fillet welded joint. *Engineering Fracture Mechanics*, 18(4):861–869.
- Socie, D. F. and Marquis, G. B. (2000). *Multiaxial Fatigue*. Warrendale, PA: Society of Automotive Engineers, Warrendale, PA.
- Sonsino, C. (1997). Fatigue strength of welded components under complex elasto-plastic, multiaxial deformations. *Report EUR 16024*.
- Sonsino, C. (2007a). Course of SN-curves especially in the high-cycle fatigue regime with regard to component design and safety. *International Journal of Fatigue*, 29(12):2246–2258.
- Sonsino, C. (2007b). Fatigue testing under variable amplitude loading. *International Journal of Fatigue*, 29(6):1080–1089.
- Sonsino, C. (2009). Multiaxial fatigue assessment of welded joints – Recommendations for design codes. *International Journal of Fatigue*, 31(1):173–187.
- Sonsino, C., Küppers, M., and Gäth, N. (1999). *Fatigue behaviour of welded high strength components under combined multiaxial variable amplitude loading - Report FB 218*.
- Sonsino, C., Maddox, S., and Haagenzen, P. (2005). A Short Study on the Form of the SN-curves for Welded Details in the High-Cycle-Fatigue Regime. *IIW-Doc. No. XIII-2045-05*.
- Spindel, J. E. and Haibach, E. (1981). Some considerations in the statistical determination of the shape of S-N curves. In *ASTM STP 744*, pages 89–113. American Society for Testing and Materials.
- Stötzel, J., Sedlacek, G., Hobbacher, A., Tschickardt, D., and Nussbaumer, A. (2007). *Background document to EN 1993-1-9, Draft version (unpublished)*. RWTH Aachen, Germany.
- Susmel, L., Sonsino, C., and Tovo, R. (2011). Accuracy of the Modified Wöhler Curve Method applied along with the  $r_{ref}=1\text{mm}$  concept in estimating lifetime of welded joints subjected to multiaxial fatigue loading. *International Journal of Fatigue*, 33(8):1075–1091.
- Tilly, G. and Nunn, D. (1980). Variable amplitude fatigue in relation to highway bridges. *Proceedings of the Institution of Mechanical Engineers*, 194(1):259–267.
- Topper, T. and Haddad, M. (1981). Fatigue strength prediction of notches based on fracture mechanics. In *Int. Symposium on Fatigue Thresholds*, page 7.
- Topper, T., Wetzel, R., and Morrow, J. (1967). *Neuber's rule applied to fatigue of notched specimens*. ILLINOIS UNIV AT URBANA DEPT OF THEORETICAL AND APPLIED MECHANICS.

- TRB (2000). *Highway Capacity Manual*. Transportation Research Board, National Research Council, Washington.
- Treiber, M., Hennecke, A., and Helbing, D. (2000). Congested traffic states in empirical observations and microscopic simulations. *Physical Review E*, 62(2):1805.
- Uchino, K. and Matsui, A. (1974). Experimental study on the fatigue strength of welded tube to gusset joints. *IIW Doc.XII-726-74*.
- UIC (1979). *Statistical distribution of axle loads and stresses in railway bridges*. UIC International union of railways.
- UIC 775 R (1984). *Emploi des techniques des soudages dans la construction des ponts-rails*. UIC International union of railways.
- UIC/ORE (1971). Bending tests of structures consisting of two beams welded at right angles - Question D86/Report 3/E. Technical report.
- Valtinat, G. and Huhn, H. (2003). Festigkeitssteigerung von Schraubenverbindungen bei ermüdungsbeanspruchten, feuerverzinkten Stahlkonstruktionen. *Stahlbau*, 72(10):715–724.
- Vasudevan, A., Sadananda, K., and Iyyer, N. (2016). Fatigue damage analysis: Issues and challenges. *International Journal of Fatigue*, 82:120–133.
- Virkler, D. A., Hillberry, B. M., and Goel, P. K. (1979). The Statistical Nature of Fatigue Crack Propagation. *Journal of Engineering Materials and Technology*, 101(2):148.
- Vormwald, M. (2015). Classification of Load Sequence Effects in Metallic Structures. *Procedia Engineering*, 101:534–542.
- Vrouwenvelder, A. C. W. M. and Waarts, P. H. (1993). Traffic Loads on Bridges. *Structural Engineering International*, 3(3):169–177.
- Wagner, M. (1998). Fatigue strength of structural members with in-plane notches. *IIW document No XIII-1730-98*.
- Walbridge, S. (2005). *A probabilistic study of fatigue in post-weld treated tubular bridge structures (EPFL Phd Thesis No. 3330)*. Phd thesis, EPFL.
- Wampler, R. H. (1976). One-sided tolerance limits for the normal distribution. *Journal of research of the National Bureau of Standards - Mathematical Sciences*, 80(2):343–346.
- Watkinson, F., Bodger, P. H., and Harrison, J. D. (1971). The fatigue strength of welded joints in high strength steels and methods for its improvement. In Proc. Conf. Fatigue of Welded Structures. In *Proceeding of Conference on Fatigue of welded structures*, Welding Institute, UK, pages 97–113.

## Bibliography

---

- Welz, W. and Dietrich, G. (1971). Festigkeitsuntersuchungen an Bolzenschweißverbindungen. *Schweißen und Schneiden*, 23(8):308–311.
- Welz, W. and Dietrich, G. (1981). Dauerfestigkeit von Konstruktionen mit aufgeschweißten Bolzen. *Schweißen und Schneiden*, 33(2):63–66.
- Wirsching, P. H. (1984). Fatigue Reliability for Offshore Structures. *Journal of Structural Engineering*, 110(10):2340–2356.
- Xiao, Z. and Yamada, K. (2004). A method of determining geometric stress for fatigue strength evaluation of steel welded joints. *International Journal of Fatigue*, 26:1277–1293.
- Xie, E. and Valente, I. (2011). *Fatigue strength of shear connectors*. Universidade do Minho.
- Yakubovski, V. and Valteris, I. (1989). Geometrical parameters of butt and fillet welds and their influence on the welded joint fatigue life. *IIW Doc. No. XIII*, pages 1326–1369.
- Yamada, K. (1984). Fatigue of tensile plate with gussets and stop holes as crack arrest. *JSCE, Journal of Structural Mechanics and Earthquake Engineering*, 341:129–136 (in Japanese).
- Yamada, K. (1987). Fatigue of Tension Members With Welded Gussets and Repair of Cracks. In *IIW International Conference on Fatigue of Welded Structures*.
- Yamada, K. and Hirt, M. (1982). Fatigue life estimation using fracture mechanics. In *IABSE Symposium. Fatigue of steel and concrete structures*, Lausanne.
- Yamada, K., Kainuma, S., Suzuki, M., and Kondo, A. (1998a). Fatigue tests of Gusset-Welded Specimens with side static load. In *The sixth East Asia-Pacific Conference on Structural Engineering and Construction*.
- Yamada, K., Nagatsu, S., and Mitsugi, Y. (1989a). Evaluation of scatter in fatigue life of welded details using fracture mechanics. *Structural Engineering/Earthquake Engineering*, 6(1):13–21.
- Yamada, K., Nagatsu, S., and Mitsugi, Y. (1989b). Evaluation of scatter in fatigue life of welded details using fracture mechanics. *Structural Engineering/Earthquake Engineering*, 6(1):13–21.
- Yamada, K. and Sakai, Y. (1986). Weld Repair of Cracked Beams and Residual Fatigue Life. *Proceedings of JSCE, Structural Eng./Earthquake Eng.*, 3(2):373–382.
- Yamada, K. and Shigetomi, H. (1989). Fatigue tests of welded details in long life region and fracture mechanics analysis. *Proceedings of JSCE, Structural Eng./Earthquake Eng.*, 6(1):23–30.

- Yamada, K., Tanaka, H., Okado, N., and Kondo, A. (1998b). Fatigue strength of tensile plates with side gussets subjected to transverse static load. In *The sixth East Asia-Pacific Conference on Structural Engineering and Construction*.
- Yang, J. and Manning, S. (1980). Distribution of Equivalent initial flaw size. In *Proceedings of the annual reliability and maintainability symposium*, pages 112–120.
- Yousefi, F., Witt, M., and Zenner, H. (2001). Fatigue strength of welded joints under multiaxial loading: experiments and calculations. *Fatigue & Fracture of Engineering Materials & Structures*, 24(5):339–355.
- Yung, J. and Lawrence, F. (1986). *Predicting the fatigue life of welds under combined bending and torsion*. University of Illinois at Urbana-Champaign.
- Zettlemoyer, N. and Fisher, J. (1978). Stress gradient correction factor for stress intensity at welded gusset plates. *Welding Research Supplement*, pages 57–62.
- Zhang, Y. and Maddox, S. (2009). Investigation of fatigue damage to welded joints under variable amplitude loading spectra. *International Journal of Fatigue*, 31(1):138–152.
- Zhao, Z., Haldar, A., and Breen, F. L. (1994). Fatigue Reliability Evaluation of Steel Bridges. *Journal of Structural Engineering*, 120(5):1608–1623.
- Zirn, R. (1975). *Schwingfestigkeitsverhalten geschweißter Rohrknotenpunkte und Rohrlaschenverbindungen*. PhD thesis, Universität Stuttgart.







# Curriculum Vitae

**Claudio Alexandre Pereira Baptista**

Born: 25 September 1975, Hamburg, Germany

Nationality: Portuguese

**Address:**

Av. Almirante Reis N°74 F, 2º Andar  
1150-020, Lisboa

**ACADEMIC DEGREES**

**Phd candidate in Structural Engineering**

by “École polytechnique fédérale de Lausanne” EPFL and Technical University of Lisbon (IST/UTL), 2012-2016

**DFA Advanced Degree in Structural Engineering**

by Technical University of Lisbon (IST/UTL), 2010

**Civil Engineer (5 years)**

by Technical University of Lisbon (IST/UTL), Structural Engineering , Lisbon, 2006

Final thesis: Geometric non-linear analysis of suspension bridges

**PROFESSIONAL EXPERIENCE**

<i>Structural Engineer</i>	2006 – 2016
Grid International, Consulting Engineers <a href="http://www.grid.pt/">http://www.grid.pt/</a>	(Lisbon)
<i>Metalworker</i>	1997 – 2002
SesAlcoa, aluminum and steel	(Alcobaça)

- "BlueWaters" pedestrian bridge Dubai, UAE, (2015)  
Stay cable steel box-girder pedestrian bridge, Bid design
- Third Bosphoro Bridge, Turkey (2014-2015)  
Detail design for exterior prestress anchorages  
Traffic generation and fatigue analysis for diaphragm connections
- Suspension Bridge over Save river, Mozambique (2013-2014)  
Suspension Bridge with 810m, prestressed concrete deck with 5 suspended spans  
Inspection and Strengthening/Rehabilitation Design
- Cable stayed bridge in Xai-Xai, Mozambique (2013-2014)  
Prestressed concrete and steel deck  
Inspection and Strengthening/Rehabilitation Design

- "Stadium Allianz Riviera", Nice, France (2011-2012)  
Design Manager on site for the Detail Design of concrete structures
- Suspension Bridge over Zambezi river at Tete, Mozambique (2008-2011)  
Suspension Bridge with 720m (90m + 3 x 180m + 90m)  
Strengthening and Rehabilitation Design, Supervision of construction works
- Rehabilitation of 4 Bridges in Ziguinchor, Senegal (2010-2011)  
4 concrete bridges with precasted prestressed concrete girders  
Inspection and Rehabilitation Design
- Rosso Bridge, between Senegal and Mauritania (2010-2012)  
Balanced cantilever bridge with 700m and approach viaducts of 1000m  
Preliminary Design, Technical Assistance for bridge location and Bid documents
- High Speed Railway Line Lisbon-Madrid (2010-2012)  
Steel truss bridges, Base case design
- Bridge over S.Vicente river, Madeira Island (2009-2011)  
Two steel bow-string arch bridges with 33m span and prestressed concrete decks  
Inspection works, Rehabilitation Design, Survey and Technical Assistance
- "Estádio do Barreiros", Funchal, Portugal (2009-2010)  
Detail design for steel structures
- Bridge over Zambezi River at Caia, Mozambique (2006-2009)  
Balanced cantilever main bridge 720m and box girder approach bridge 1500m  
Detail Design Review, analysis of erection stages, technical assistance to site team
- Adaptation to the Oriente Station, High-Speed Train, Lisbon (2009)  
Review of detailed design
- 3 Bridges in Bioko, Equatorial Guiné (2007-2009)  
Balanced Cantilever Bridges in prestressed concrete  
Detail Design, Camber and Construction stages, Technical assistance to site team
- Bridge over Ribeiro Seco, Madeira Island (2008)  
Hydraulic reinforced concrete box culvert with 800 meters  
Detail Design and Technical Assistance
- Suspension footbridge over Ibar River, Serbia (2007)  
Prestressed concrete bridge, Bid Design
- Roadway link in Expressway Fajã da Ovelha - Ponta do Pargo, Madeira (2006)  
Preliminary Design, 2 balanced cantilever bridges and 8 viaducts

## PUBLICATIONS

### Journal papers

- Baptista, C., S. Kannuna, J. Oliveira Pedro, and A. Nussbaumer. 2016. “Fatigue Behaviour of Tubular Bracings in Steel Bridges.” *International Journal of Fatigue* *In press*
- Reis, António, and Claudio Baptista. 2013. “Rehabilitation of the Suspension Bridge over Zambezi River in Mozambique.” *Structural Engineering International* 23 (1): 89–93.

### Conference papers

- Baptista, C., L. Borges, S. Yadav, and A. Nussbaumer. 2015. “Fatigue Behaviour and Detailing of Slotted Tubular Connection.” In *International Symposium of Tubular Structures - ISTS 2015*. Rio de Janeiro.
- Baptista, C., J. Oliveira Pedro, and A. Nussbaumer. 2015. “Fadiga em Ligações Tubulares de Tabuleiros Metálicos e Mistos.” In *X Congresso de Construção Metálica*, edited by L. Simoes da Silva et al, 171–80. Coimbra
- Reis, A., and C. Baptista. 2012. “A Ponte Suspensa sobre o Rio Zambeze em Tete, Moçambique: Reforço e Reabilitação.” In *Encontro Nacional Betão estrutural - BE2012*, FEUP, 24-26 October 2012. Porto.
- Reis, A., and C. Baptista 2012 “Rehabilitation of the Suspension Bridge over Zambezi River in Mozambique.” In *Sixth International IABMAS Conference*, Stresa, Lake Maggiore, Italy, 8-12 July 2012, edited by D. Frangopol and F. Biondini. CRC Press.

### Technical reports

- Baptista, C., and A. Nussbaumer. 2015. *Traffic Load Generation for the Fatigue Assessment of the 3<sup>rd</sup> Bosphorus Bridge*. ICOM - Report EPFL 209910
- Baptista, C., and A. Nussbaumer. 2014. *A Re-Analysis of the Fatigue Strength of Steel Plates with Holes, for Application of the Notch Stress Approach*. ICOM - Report EPFL 201786

## AWARDS

IABSE Outstanding Paper 2014 for the Paper::

«Rehabilitation of the Suspension Bridge over Zambezi river in Mozambique»

